CARL
VON
OSSIETZKY
universität OLDENBURG

Real-time investigations of energy dissipation processes at interfaces between semiconductors and thin metallic films

Von der

Fakultät für Mathematik und Naturwissenschaften der
Carl von Ossietzky Universität Oldenburg

zur Erlangung des Grades und Titels eines

Doktors der Naturwissenschaften (Dr. rer. nat.)

angenommene

Dissertation

von Herrn

Dirk Hoogestraat

geboren am 29. April 1979 in Emden

Gutachterin:	Prof. Dr. Katharina Al-Shamery
Zweitgutachter:	Prof. Dr. Thorsten Klüner

Tag der Disputation: 28. April 2014

Abstract

In the present work the second order nonlinear optical properties of bare n-doped native oxide terminated GaAs(100) semiconductors and GaAs-Pt hetero-interface samples were investigated by static and time-resolved measurements and related to their chemical and structural characteristics. The second harmonic generation (SHG) process describes the nonlinear response of a material upon irradiation with intense laser pulses in which light at twice the excitation frequency is emitted. Although this process is bulk allowed in GaAs, its higher attenuation length and the phase matching makes it a very surface and interface sensitive analysis tool. Different experimental set-up were built to study the SHG response as a function of beam polarization, wavelengths and crystallographic alignment with respect to the plane of incidence. For the time-resolved measurements a pump-probe technique was used to create a transient non-thermal distribution of hot carriers within the absorption length inside the semiconductor and detect its temporal effect on the SHG efficiency. In native oxide covered n-doped GaAs samples charged defect states at the interface induce a band bending and thus a depletion zone at the surface. Similar to findings from Germer [1] the SHG signal obtained from rotation scans could be separated into a bulk term and one related to the electric field inside the depletion zone. A linear relationship was found between the strength of the depletion field term and the power of the laser pulse, which indicates a self photomodulation by screening of the space charge field by the probing laser pulse itself. Using the established bulk second order susceptibility term, it was possible to determine the strength of the depletion field terms and their dispersive behaviour. Both substrates showed a different behaviour regarding the contribution of the depletion field and its dispersive behaviour, although doped with Si i.e Te to a similar level. Accompanying chemical and structural analysis by x-ray photoelectron spectroscopy and different scanning probe microscopy techniques revealed an oxide mainly consisting of Ga_2O_3, As_2O_3 and Ga_2O and a varying oxide layer thickness between $2.3 - 3.6$ nm. Time-resolved measurements showed a fast response of the bulk term within the time span of the pump pulse ($27 - 35$ fs), which was attributed to transient band filling effects and a two step effect in the depletion zone: a fast process with a similar lifetime as the bulk process and a slower response which was attributed to the drift dynamics of hot electrons and holes in the depletion field ($233 - 256$ fs). The modulation of this signal is caused by the coherent phonon motion. An analysis of this revealed that the lattice oscillation is dominated by the longitudinal optical (LO) bulk mode at 8.7 THz inside the carrier free space charge region. Beside this, two coupled modes with small amplitudes could be found: A LO-hole plasma coupled mode direct at the interface (8.3 – 8.5 THz) and one linked to the electron plasma at the back of the depletion zone (7.7 – 7.9 THz).

For the metal-interfaced samples different amounts (3 – 5 Å) of Pt were evaporated at varying process temperatures (100 – 570 K). Room temperature preparations yielded the highest surface quality with respect to roughness, they exhibited a terraced structure with monoatomic steps. Additionally a protrusion of gallium through the layer forming a nodule and crater structure was found on all samples. XPS measurements supported this findings and indicated the formation of $PtAs_2$ as well as $PtGa_2$. The static SHG measurements showed that already at this ultra thin metal coatings Schottky barrier interfaces are established. The measurements were found to be very sensitive to the interface quality, which manifests itself in the ratio between depletion zone and bulk effects and the total intensity of non-linear reflectivity. The strongest depletion field term was found in the room temperature preparations. A simple modelling indicated that $PtAs_2$ is responsible for the barrier formation in these samples. The time-resolved measurements showed a general deceleration of the dynamic response (fast process: $\approx 100 - 130$ fs, slow process: $\approx 760 - 1360$ fs) indicating longer lifetimes of the excitation and a similar dependency of the signal to the interface quality. Also the structure of the transient signal itself was changed. The metallization had also a strong effect on the phonon spectra, but a clear trend between the phonon signal and the preparation parameters is not evident. In general the Schottky barrier type samples exhibited an increased strength of phonon signals in the range of 6.0 – 8.5 THz. An distinct additional signal at 9.0 – 9.7 THz was found in many of these spectra, which till now can not be assigned to any known phonon mode but may be related to the metal-semiconductor interface.

Kurzzusammenfassung

Im Rahmen dieser Arbeit wurden die nichtlinearen optischen Eigenschaften zweiter Ordnung von n-dotierten und mit einer nativen Oxidschicht bedeckten GaAs Halbleitern sowie von GaAs-Pt Metall-Halbleiter-Grenzflächen mittels statischer und zeitaufgelöster Messungen untersucht und mit ihren chemischen und strukturellen Eigenschaften verglichen. Der “second harmonic generation” (SHG) Prozess, also die Erzeugung des zweiten harmonischen Obertons, beschreibt die nichtlineare optische Antwort eines Materials auf die Anregung mittels eines intensiven Laserstrahls, in dem Licht mit der doppelten Frequenz des eingestrahlten Strahlung emittiert wird. Auch wenn dieser Prozess aus

Symmetriegründen innerhalb von Galliumarsenid erlaubt ist, ist das SHG Signal bedingt durch die stärkere Absorption und die Phasenanpassung ein nützliches Analysewerkzeug mit einer hohen Oberflächen und Grenzflächenempfindlichkeit. Zur Untersuchung der SHG Effekte wurden eine Reihe verschiedener Experimente durchgeführt, die eine Analyse in Abhängigkeit von der Strahlpolarisation, der Wellenlänge und der kristallographischen Ausrichtung innerhalb der (100) Ebene in Bezug auf die Einfallsebene des Lichtes erlaubte. Für die zeitaufgelösten Untersuchungen wurde eine so genannte Pump-Probe Technik verwendet um eine große Anzahl heißer Ladungsträger mit einer nichtthermischen Verteilung im Material innerhalb der Absorptionstiefe zu erzeugen und den Einfluss dieser auf die SHG-Effizienz zu untersuchen. In GaAs Halbleitern mit einer nativen Oxidschicht stellt sich eine Bandverbiegung und damit eine Raumladungszone ein, die durch geladene Defektzustände an der Oxidgrenzfläche hervorgerufen wird. Ähnlich wie in den Arbeiten von Germer [1] konnte das SHG Signal aus Rotationsmessungen in einen Volumen Anteil und einen Beitrag, der vom elektrischen Feld in der Raumladungszone abhängt, aufgespalten werden. Für den letzteren Anteil wurde ein linearer Zusammenhang mit der eingestrahlten Leistung beobachtet. Dies deutet auf eine Selbstmodulation hin, bei der der Abfragepuls durch Injektion von Ladungsträgern zu einer partiellen Depolarisation des elektrischen Feldes in der Verarmungszone führt. Unter Berücksichtigung der literaturbekannten nichtlinearen Suszeptibilität im Volumen-Material konnte die Stärke und das Dispersionsverhalten der Suszeptibilität in der Raumladungszone bestimmt werden. Hierbei zeigten die vermessenen Substrattypen ein unterschiedliches Verhalten im Hinblick auf den Einfluss des Verarmungszonenanteils und der Dispersion, trotz einer vergleichbaren Dotierungsstärke (Te bzw. Si Dotierung). Eine begleitende chemische und strukturelle Charakterisierung mittels Röntgenphotoelektronen-Spektroskopie und verschiedener Rastersondenmikroskopie-Verfahren ergab ein Oxidschicht, die zum größten Teil aus Ga_2O_3, As_2O_3 und Ga_2O besteht und deren Schichtdicke zwischen $2.3 - 2.6$ nm variiert. Zeitaufgelöste Messungen zeigten einen schnellen Prozess des Volumen-Anteils mit einer Lebenszeit in der Grössenordnung des Anregungspulses ($27 - 35$ fs). Dieser wurde mit einer kurzlebigen Abnahme der Absorption, bedingt durch ein sogenanntes “band filling”, in Verbindung gebracht wurde. Für den Raumladungszonenbeitrag ergab sich dagegen ein zweistufiges Verhalten bestehend aus einem ähnlich schnellen Schritt wie der des Volumen-Anteils und einem langsameren, der auf Ladungsträgerdrift im Raumladungsfeld zurückgeführt wurde ($233 - 256$ fs). Die gemessenen zeitaufgelösten Signal wiesen eine Modulation auf, die durch die Schwingung kohärenter Phononen verursacht wird. Eine Analyse dieser Modulation ergab ein

Phononenspektrum, welches von der longitudinal optischen (LO) Schwingungsmode bei 8.7 THz innerhalb der ladungsträgerfreien Verarmungszone dominiert wird. Daneben fanden sich zwei weitere, schwächere Signale. Sie gehören zum Einen zu einer gekoppelten Schwingung des LO-Phonons mit dem Lochplasma direkt an der Grenzfläche (8.3 – 8.5 THz) und zum Anderen zu der entsprechenden Kopplungsschwingung mit dem Elektronenplasma an der Grenze zwischen Verarmungszone und dem Volumen (7.7 – 7.9 THz).
Bei der Herstellung der Metallproben wurden verschieden dicke Platinschichten (3 – 5 Å) bei variierenden Prozesstemperaturen (100 – 570 K) abgeschieden. In Bezug auf Rauheit, zeigten hierbei die Proben die bei Raumtemperatur präpariert wurden, die höchste Qualität. Ihre Oberfläche besteht aus terassenförmigen, ebenen Schichten, die durch monoatomare Stufen getrennt sind. Zusätzlich wurden bei allen Temperaturen ein Gallium-Durchbruch durch die Schicht beobachtet. Dies wurde durch XPS Messungen bestätigt die Hinweise auf $PtAs_2$ und $PtGa_2$ Verbindungen geben. Die statischen SHG Messungen konnten zeigen, dass bereits bei ultra dünnen Metallbedeckungen Schottky Kontakte entstehen. Des weiteren zeigte sich, dass Rotationsmessungen sehr empfindlich bezüglich der der Oberflächen-, bzw. Grenzflächen-Qualität sind. Dies spiegelte sich im Verhältnis zwischen Raumladungs- und Volumen-Anteil sowie in der Gesamtintensität des reflektierten SH Signals wieder. Der stärkste Einfluss der Verarmungszone wurde in den Raumtemperaturproben gemessen. Eine einfache Modellierung lässt vermuten, dass bei diesen Proben $PtAs_2$ für Höhe der Energiebarriere verantwortlich ist. Zeitaufgelösten Messungen ergaben eine generelle Entschleunigung der dynamischen Prozesse (Schneller Prozess: ≈ 100 – 130 fs, Langsamer Prozess: ≈ 760 – 1360 fs) und eine ähnliche Abhängigkeit von der Prozesstemperatur wie die statischen Messungen. Darüberhinaus wurde auch die Struktur des zeitaufgelösten Signals verändert. Auch auf die Phononenspektren hat das Aufbringung der Metallgrenzfläche einen starken Einfluss, allerdings ließ sich kein entsprechender Trend wie in den Messungen zuvor ermitteln. Im Allgemeinen zeigten sich verstärkt Schwingungsmoden im Bereich zwischen 6.0 – 8.5 THz. Ein weiteres Signal im Bereich zwischen 9.0 – 9.7 THz konnte in vielen Messungen gefunden werden. Auch wenn eine exakte Zuordnung bislang noch nicht vorgenommen werden konnte, ist es möglich dass es sich hierbei um einen Effekt in Verbindung mit der Metallgrenzfläche handelt.

One shouldn't work on semiconductors,
that is a filthy mess;
who knows whether they really exist.
Wolfgang Pauli, 1931

You can't rush science, Gibbs!
You can yell at it and scream at it,
but you can't rush it.
Abby Sciuto,
character in the TV series Navy CIS

Contents

List of Abbreviations

2PPE	Two photon photoemission
2TM	Two temperature model
AC	Alternating current
ADP	Acoustic deformation potential
AES	Auger electron spectroscopy
AFM	Atomic force microscopy
ARXPS	Angle-resolved XPS
BAP	bare atom picture
BBO	Beta barium borate
BE	Binding energy
BTE	Boltzmann transport equation
CAD	Computer aided design
CCD	Charge coupled device
CW	Continuous wave
DAP	Dressed atom picture
DC	Direct current
DDE	Drift diffusion equation
DECP	Direct excitation of coherent phonons
DFT	Density functional theory
EDX	Energy dispersive x-ray spectroscopy
EFISHG	Electric field induced SHG
EMA	Exponential moving averager
EPD	Etch pit density
FCC	Face centred cubic
FROG	Frequency resolved optical gating
FWHM	Full width at half maximum
GIXR	Gracing incidence x-ray spectroscopy

GVD	Group velocity dispersion
HAS	Helium atom scattering
HOPG	Highly ordered pyrolytic graphite
HP-X	High intensity peak number x
HWHM	Half width at half maximum
IGS	Induced gap states
IMFP	Inelastic mean free path
IR	Infrared
IRRAS	Infrared reflection absorption spectroscopy
ISRS	Impulsive stimulated Raman scattering
KLM	Kerr lens mode-locking
LA	Longitudinal acoustic (phonon)
(L)DOS	(Local) Density of states
LEED	Low energy electron diffraction
LID	Laser induced desorption
LO	Longitudinal optical (phonon)
LOPC	Longitudinal optical-plasma coupled (phonon)
LP-X	Low intensity peak number x
LPSVD	Linear prediction singular value decomposition
MBE	Molecular beam epitaxy
MIGS	Metal induced gap state
ML	Monolayer
MOCVD	Metal-organic chemical vapour deposition
MOS	Metal oxide semiconductor
MQW	Multi quantum well
NEO	Nonlinear optical sampling
NMR	Nuclear magnetic resonance
ODP	Optical deformation potential
OFHC	Oxygen free high conductive copper
PES	Potential energy surface / Photoelectron spectroscopy
PID	Proportional integral derivative (controller)
PL	Photoluminescence
PMT	Photomultiplier tube
POP	Polar optical phonon

P-polarisation	Parallel polarisation (with respect to the plane of incidence)
PPP	p-polarised input, p-polarised output, p-polarised pump
PPS	p-polarised input, p-polarised output, s-polarised pump
PVD	Physical vapour deposition
PZ	Piezo-electric
QED	Quantum electrodynamics
REOS	Reflectivity electro-optical sampling
RHEED	Reflective high energy electron diffraction
SIBA	Simultaneous ion bombardment and annealing
SIMS	Secondary ion mass spectroscopy
SEM	Secondary electron multiplier / Scanning electron microscopy
SEMI	Semiconductor Equipment and Materials International
SNOM	Scanning nearfield microscopy
SNR	Signal to noise ratio
SNIR	Signal to noise improvement ratio
SPIDER	Spectral phase interferometry for direct electric-field reconstruction
S-polarisation	Senkrechte (perpendicular) polarisation (with respect to the plane of incidence)
SPP	s-polarised input, p-polarised output, p-polarised pump
SPM	Self phase modulation / Scanning probe microscopy
SPS	s-polarised input, p-polarised output, s-polarised pump
STM	Scanning tunnelling microscopy
TA	Transversal acoustic (phonon)
TDFS	Transient depletion field screening
TE	Transversal electric
TEM	Transversal electromagnetic / Transmission electron microscopy
TFC	Transmission function correction
THG	Third harmonic generation
TIR	Total internal reflection
TO	Transversal optical (phonon)
TPD	Thermal programmed desorption spectroscopy
(TR)-SF(G)	(Time-resolved) sum frequency (generation)

(TR)-SH(G)	(Time-resolved) second harmonic (generation)
UHV	Ultra-high vacuum
UPS	Ultraviolet photoelectron spectroscopy
UV	Ultraviolet
VIGS	Virtual induced gap state
XPS	X-ray photoelectron spectroscopy

List of Symbols

A_I^{ex}, A_j^{dec}, A_0	Exponential fitting amplitudes of excitation and decay process and constant offset
A_n	Complex amplitude of $\cos(n\phi)$ in rotation SHG fitting
a_x	Bohr radius of an exciton
α	Absorption coefficient
$\vec{B}$	Magnetic field
B_{12}, B_{21}	Einstein coefficients of absorption
B_n	Complex amplitude of $\sin(n\phi)$ in rotation SHG fitting
c, c_0	Speed of light, speed of light in vacuum
χ	Susceptibility
$\vec{D}$, D	Electric Displacement, its magnitude
D_C	Deformation potential
$\vec{E}$, E	Electric field, its magnitude / Energy
e	Elementary charge
E_g	Band gap energy
$\widetilde{\epsilon_r}$	Complex relative permittivity
ϵ_0	Permittivity of free space
ϵ', ϵ''	Real and imaginary part of $\widetilde{\epsilon_r}$
F	Force
f	Laser frequency
g	Joint density of states factor
γ	Damping
$\vec{H}$	Magnetic field strength
h, $\hbar$	Planck constant, reduced Planck constant
H	Hamiltonian
I, I_0	Intensity, Initial intensity
i	$\sqrt{-1}$

j	Current density
k	Wave vector
k_B	Boltzmann constant
κ	Extinction coefficient
K_s	Spring constant
l	Length
L	Fresnel transmission coefficient
L_D	Depletion zone thickness
λ	Wavelength / Free path
m	Mass
M	Matrix element
m^*	Effective carrier mass
$1/\mu$	Reduced mass
μ	Chemical potential
n	Refractive index
$\widetilde{n}$	Complex refractive index
N	Atomic density
N_A	Numerical aperture
N_s	Scattering centre density
ν	Frequency
ω	Angular frequency, waist of Gaussian beam
Ω	Phonon frequency/ $\Omega = 2\omega$
p	Dipole moment / impulse
$\vec{P}$, P	Macroscopic Polarisation, its magnitude / Laser power
ϕ	Azimuthal angle
Φ	Potential
ψ	Wave function
$\vec{q}$	Phonon wave vector
R	(Nonlinear) reflectivity coefficient
$\vec{r}$	Vectorial Position
R_i	Rise time of excitation process number i
R_x	Rydberg constant
ρ	Density matrix operator
σ_S	Scattering cross-section

T	Temperature or Transmission coefficient
T_i	Decay time of process number i
t	Time
τ	Lifetime
θ	Angle of incidence
v	Velocity
V	Volume
$W_{1\rightarrow 2}$	Transition probability between states 1 and 2
x, y, z	Space coordinates

1. Introduction

Since sometime in the early 2000s humanity lives in the so called digital or information age. It happened in this period of time that the estimated amount of digital storage capacity exceeded the amount of analogue storage media. While in the year 2000 still 71 % of the 55 exabyte (5.5×10^{19} byte) capacity was related to printed matter, photographies and analogue video and audio media, in 2007 94 % of the then already 295 exabyte (2.95×10^{20} byte) capacity were provided by digital devices, mostly by computer hard drives [2]. Similar drastic changes can be found when looking at the development of telecommunication and computation power. The digital age is a result of the ongoing digital revolution which is seen with similar importance as the agricultural revolution or the industrial revolution 200 years ago [3]. It began with the invention of semiconductor based transistors in 1947 by Schockley, Bardeen and Brattain [4] replacing vacuum tubes as switching devices in early computers. While in the 1950s and 1960s computers were merely used by big organizations and governments, the 1970s brought the advent of home computers. In the next century microelectronic devices and digitalization held their way into other equipment of the daily life, most prominent is the launch of digital audio compact discs in 1982 by Philips [5]. The milestone of the 1990s is most likely the upcoming of the world wide web [6]. While already available in the early 1990s mobile communication is the booming trend in the first years of the new millennium, which in recent years led to a huge increase in wireless data transmissions related to web-enabled smart phones and tablet computers [7].

While the industrial revolution relied on the availability of resources like energy, water and manpower, the driving force in the digital revolution is the increase of computational power in combination with miniaturization and simultaneous reduction of average unit prices. Frequently cited and much stressed in introductory treatises on semiconductor research is Moore's law [8], which is basically an observation that the computational power of integrated devices doubles every 18 month. Sometimes it is interpreted as doubling the density of transistors on the wafer (die). Although postulated back in 1965 it proves to be accurate up to now, even if it has nowadays the tendency to be a self fulfilling prophecy: Many companies and research teams set their milestones for future development goals according to Moore's law. Much research and development is being carried out to advance the level of integration as for example establishing new ways to write small conducting structures on semiconductors [9] or to replace the gate oxide layers in metal on silicon field effect transistors (MOSFET) with new so called 'high-κ' materials [10]. In transistors with effective lengths of only 20 nm the thickness of the SiO_2 oxide layer used as insulating material at the gate contact in current silicon based devices would only be 1 nm thick, a regime where due to leak currents this technology reaches its limits [10]. Still the validity of Moore's observation will cease in the next years as the current development will come to a fundamental technological limit. Current central processing units (CPU) based on Intels®Haswell™microarchitecture are fabricated in so called 22 nm technology. Its name states the half distance between neighboured identical objects on the chip. The successor of this technology will be the 14 nm processing. At this transistor density heat dissipation becomes an important issue. The small dimensions of the conducting paths will favour cross talk effects by electric fields, increased leak currents through thin insulators by electron tunneling and other quantum mechanical effects like quantum confinement will become relevant. The transit times of such small transistors are in the range of a picosecond only and in some devices they can be as short as some hundred femtoseconds [11]. It is crucial to exactly understand the spatial and temporal behaviour of electrons inside those integrated circuits, the influence of defects, band bending, confinement and the heat dissipation by phonon coupling processes. In order to preserve the ongoing advancement of technology in this field, further careful research has to be made. This work tries to contribute to this goal by investigating the dynamics inside of semiconductors and hetero-structures.

While integrated circuits are commonly based on silicon semiconductors, GaAs wafers play an important role in applications which require higher performance. Compared to silicon GaAs has a higher electron drift velocity allowing transistor switching frequencies of up to 250 GHz [12, 13]. Thus gallium arsenide devices produce less electrical noise and therefore they are used in particular for high frequency components in cellular phones, radar systems and in satellite communications [14], although silicon based devices with lower costs and higher level of integration started to drive GaAs out of some mainstream markets [15]. GaAs is also commonly used in Schottky barrier diodes in combination with metal coatings [16–18] and in Gunn diodes, or more precisely transferred electron devices, used to generate microwave radiation [19]. Its direct band gap makes it suitable for optical devices such as light emitting diodes, as solid state lasers (e.g. in [20, 21]) or in solar cells in which GaAs based devices currently achieve the highest efficiency [22, 23].

Nevertheless, the electricity production costs resulting from the usage of photovoltaic devices are much higher than those obtained with conventional fossil fuels [24]. This is partly caused by the high purity requirements for the semiconductors needed to achieve the efficient absorption of photons and subsequent field induced separation of electron-hole pairs without quenching the excitation in combination with the conduction of the carriers to the respective current collectors all within the same material. Much research is going on to construct solar cells from low cost organic materials for example by preparing core-shell nano tubes with large interface regions between semiconducting polymers at which charge separation will take place [25]. The separation of the light absorption and the charge-carrier transport processes is also part of a solar cell demonstrated by McFarland et al. [26, 27]. In this device a dye layer applied to the metal surface of a Schottky barrier diode made from TiO_2 and Au is responsible for the initial absorption of photons. From there electrons from excited states will be injected into the metal layer. In a ballistic transport step these electrons can overcome the barrier and will be emitted into the conduction band of the semiconductor (internal emission). The dye will be reduced by electron replenishment from the gold layer, which together with a back contact at the semiconductor acts as an electrode of the photovoltaic device. Quenching of the initial excitation is thought to be related, among other processes, by electron phonon coupling. Experiments by Tisdale et al. demonstrated that hot electron transfer from nanocrystalline PbSe semiconductors into a TiO_2 electron acceptor induce the launch of coherent surface phonons at the interface [28]. The detailed understanding of excited carrier dynamics at metal-semiconductor interfaces and its relation to Schottky barrier height, as well as its coupling to phonons is important to further optimize this type of solar cells.

Finally there is also a strong chemical interest in the investigations on hot interface carriers and phonon dynamics. While photocatalytic reactions of larger organic molecules are mostly direct excitation processes, the reaction or photo desorption of small molecules like CO and NO is often induced by a metallic substrate mediated process [29–31]. Fast processes typically are related to an energy transfer from hot electrons in the metal layer into the adsorbed molecule ($\approx 0.1 - 1$ ps), while slower processes in the picosecond range are caused by transfer of vibrational energy from hot phonons into the metal-adsorbate bonding (friction model) [32]. Usually metallic films or nanoparticles are applied to oxidic supports (eg. [33]), which itself show no catalytic behaviour, but a change of activity and selectivity has been found for some reactions when the active material was used in combination with different oxide supports. It was suggested that the formation of a Schottky barrier and ballistic transport of hot electrons is responsible for this behaviour [34]. An experimental device similar to the McFarland type solar cell discussed before with the difference that platinum particles were deposited on top of a Au/TiO_2 diode surface instead of a dye layer, produced a chemicurrent upon light induced CO oxidation related to hot carrier injection into the semiconductor [35]. While GaAs itself is not well known for catalytic activity, a Pt-GaAs interface sample which forms Schottky barrier type contacts too, could be an interesting system to study the effect of electron dynamics onto desorption processes, for example of CO.

The optical properties of GaAs makes this semiconductor a convenient sample to investigate its electronic response by means of time-resolved ultrashort pulse pump-probe techniques. In this method a strong laser pulse creates a transient non-thermal carrier distribution within the absorption length inside the material and a second delayed and weaker pulse probes the temporal change of optical properties related to the electronic and lattice effects. Of special use is the detection of nonlinearly generated light at the second harmonic frequency of the probe photons (SHG process). Due to the stronger attenuation compared to the fundamental light and its inherent interface sensitivity it is an useful method to investigate near surface and interface properties. A commonly employed complementary technique is the two photon photoemission (2PPE) method, where electrons are extracted from the investigated sample after progressive absorption of two photons exciting the electron above the vacuum energy level. Analysis of the emitted electrons, allows the mapping of the initial and intermediate electronic states of the sample [36]. The advantage of the all optical SHG measurements over 2PPE is its previously mentioned surface sensitivity and its robustness towards high pump energy levels and space charge fields [37].

In this thesis time-resolved SHG experiments are performed to study the excitation dynamics in different n-doped GaAs substrates. Due to defect states at the interface between the bulk material and the native oxide layer, these samples exhibit a depletion zone caused by band bending. The static nonlinear response is analysed to separate bulk effects from those related to the depletion field. The pump-probe measurements will be separated into investigation of electronic effects, which will be discussed in the scope of depletion dynamics and into signals from coherent phonons. In the second step different amounts of platinum at different process temperatures are deposited onto both substrate types. Their behaviour is compared to that from the oxide covered samples and related to their chemical and morphological properties. In the first three chapters an introduction into linear and nonlinear light matter interaction is given, the generation and characterization of ultrashort laser pulses is described and the nature of phonons and in particular that of coherent phonons is explained. The next sections summarizes the structural, electronic and optical properties of gallium arsenide, platinum and metal-interfaced GaAs known from literature. The analysis methods used for the structural and chemical analysis of the various samples and the ultra-high vacuum based preparation methods for the GaAs-Pt samples are discussed in the following chapter. This chapter describes also the different set-ups build to investigate the optical properties. The results of these experiments are divided into three chapters: The chemical and structural characterization is given first. The next chapter shows the results of static optical experiments like rotational SHG and photoluminescence measurements, while the third part covers the time-resolved experiments. The work is concluded with a summarizing discussion and an outlook.

2. Linear and Nonlinear Optics on Surfaces and Interfaces

This chapter covers the fundamentals of linear and nonlinear optics with focus on light matter interaction necessary for the understanding of the dynamical processes on the Pt−GaAs hetero systems investigated in this work. The classical treatments in the following sections are based on findings and relations extracted from Maxwell equations of electrodynamics, summarized in appendix A.1.

2.1. Optical Constants

When light impinges on solid optical media, the interaction can be described by many different processes. In the simplest classification they can be grouped into propagation through the medium, reflection from its front R_1 and rear surface R_2 and transmission T. The propagation in the linear regime itself is governed by refraction, (in)elastic scattering and absorption processes. In the case of a transparent non absorbing medium the reflection and transmission coefficients have to sum up to one to fulfill energy conservation:

$$R_1 + R_2 + T = 1 \tag{2.1}$$

Both absorption and scattering cause an attenuation of the light. Considering a propagation in z direction and an initial intensity I_0 the absorption can be described by an exponential decay determined by a strongly frequency dependent absorption coefficient α. In the same way scattering can be described introducing a scattering centre density N_S and a cross-section σ_S.

$$\begin{aligned} I(z) &= I_0 \cdot exp(-\alpha z) \\ I(z) &= I_0 \cdot exp(-N_S \sigma_S z) \end{aligned} \tag{2.2}$$

The upper equation is known as Beer's law. For a medium of thickness z_l equations 2.1 and 2.2 can be combined to:

$$T = (1 - R_1) \cdot exp((\alpha + N_S \sigma_S) \cdot - z_l)(1 - R_2) \tag{2.3}$$

The refraction does not fit into the above formalism. It describes the velocity of light in the medium. Its measure is the refractive index n, which is defined as the ratio of the speed of light in vacuum c to that in the medium ν. The frequency dependence of this quantity leads to diffraction.

$$n = \frac{c}{\nu} \tag{2.4}$$

Introducing a complex refractive index allows both refraction and absorption to be expressed by a single parameter $\widetilde{n}$. The real part contains the standard refractive index n, while the imaginary part is given by the extinction coefficient κ. This can be shown by looking at a planar electromagnetic wave

$$E(z,t) = E_0 \cdot exp(i(kz - \omega t)) \tag{2.5}$$

where n affects the wave vector k by reducing its wavelength (via equation 2.4 and $\lambda \nu = c$) :

$$k = \frac{2\pi}{\lambda / n} = \frac{n\omega}{c} \tag{2.6}$$

Replacing n with $\widetilde{n} = n + i\kappa$ and inserting eq. 2.6 in eq. 2.5 results in:

$$E(z,t) = E_0 \cdot exp(-\kappa \omega z / c) \cdot exp(i(n \omega z / c - \omega t)) \tag{2.7}$$

The first exponential describes the decaying of the wave due to κ while n still acts on the phase velocity. The relation between κ and the absorption coefficient α can be obtained by squaring equation 2.7 to get the wave's intensity and comparing with Beer's law:

$$\alpha = \frac{4\pi\kappa}{\lambda} \tag{2.8}$$

Solving the Maxwell equations and including boundary conditions at the interface of different media allows also to relate the reflectivity coefficient to the complex refractive index. For normal incidence at an interface to air this is:

$$R = \left| \frac{\widetilde{n} - 1}{\widetilde{n} + 1} \right|^2 \tag{2.9}$$

For arbitrary angles also the polarization of the incoming light plays a role. This case is described by Fresnel's equations (cf. appendix A.2 and [38]). For thin films between two media, whose thickness is larger than atomic distances, the system can be treated as three-phase system and corresponding Fresnel equations can be derived. For very thin films a model of thin polarization layers acting as a source of electromagnetic waves can be applied to correctly determine the reflection and transmission behaviour [39].
The knowledge of the complex refractive index allows the calculation of many optical properties of a medium. Theoretical models describing light matter interaction like the Lorentz oscillator model discussed later, mostly yield the complex relative permittivity $\widetilde{\epsilon_r}$. The connection between this and the refractive index can also be deduced from the Maxwell equations. Using $\widetilde{\epsilon_r} = \epsilon' + i\epsilon''$ gives:

$$\begin{aligned} n &= \frac{1}{\sqrt{2}}(\epsilon' + \sqrt{\epsilon'^2 + \epsilon''^2})^{\frac{1}{2}} \\ \kappa &= \frac{1}{\sqrt{2}}(-\epsilon' + \sqrt{\epsilon'^2 + \epsilon''^2})^{\frac{1}{2}} \end{aligned} \tag{2.10}$$

2.2. Linear Light Matter Interaction

The light matter interaction is governed by the interplay of the electromagnetic field of the light and the permanent or induced dipole moment (polarization) in the medium. For a full microscopic understanding of the polarization, quantum electrodynamic approaches (QED) have to be used. Here only a classical concept is presented to give a general overview. In this model the interaction of light with free or bound electrons and lattice vibrations is described by simple dipole oscillations, defined by spring constant K_S, which is related to the reduced mass $\frac{1}{\mu}$ and resonance frequency ω_0:

$$\omega_0 = \sqrt{\frac{K_S}{\mu}} \tag{2.11}$$

For the case of bound electrons, an electromagnetic wave at frequency ω exerts a force on the dipole, which results in a varying displacement of the electrons, while the motion of the heavy nucleus can be neglected. The hereby induced dipole moment p is given by the oscillating displacement x(t) and the elementary charge:

$$p(t) = e \cdot x(t) \tag{2.12}$$

This oscillating dipole generates electromagnetic radiation which affects in turn the external field. When ω is close to ω_0 the the amplitude of the materials response increases and energy from the wave is effectively transferred into the medium (absorption). In the off-resonance case the system oscillates at the driving frequency with a small amplitude and a phase offset which is induced by damping. In the course of the propagation through the medium the phase term sums up to a retardation of the wave front, an effect which is characterized by the real refractive index.

In the Lorentz model the (electron) displacement in x direction is described by an equation of motion which consists of an acceleration term, a damping term with constant γ and a restoring force due to the binding. The motor of this motion is the electric field.

$$\frac{d^2x}{dt^2} + \gamma\frac{dx}{dt} + \omega_0^2 x = -\frac{e}{m}E \tag{2.13}$$

Here m refers to the mass of the oscillatory electron. The exact determination of γ is not possible without the use of QED. The above expression is an approximation known as Lorentz-Abraham equation which describes the damping purely phenomenologically. The stationary solution is:

$$x(t) = X_0 \cdot exp(-i(\omega t)) \tag{2.14}$$

where the complex amplitude X_0 is given by

$$X_0 = -\frac{e}{m} \cdot \frac{1}{\omega_0^2 - \omega^2 - i\gamma\omega} E_0 \tag{2.15}$$

with ω as the frequency of the electromagnetic radiation and E_0 its complex amplitude. The macroscopic polarization P for a system with a single resonance can be obtained by combining eq. 2.14, 2.15 and 2.12 and multiplying with the atomic density N:

$$P = N \cdot e \cdot X_0 \cdot exp(-i(\omega t)) \tag{2.16}$$

Introducing the electric displacement $\vec{D}$ or flux density,a ϵ_0 as the permittivity of free space:

$$\vec{D} = \epsilon_0 \vec{E} + \vec{P} \tag{2.17}$$

which in an isotropic medium is proportional to the electric field:

$$\vec{D} = \epsilon_0 \widetilde{\epsilon_r} \vec{E} \tag{2.18}$$

allows to calculate the complex relative permittivity by combination of eq. 2.17 and 2.18 and inserting the solution for $\vec{P}$. With this result it is possible to calculate the refractive index and the extinction coefficient as discussed in the section before.

$$\widetilde{\epsilon_r}(\omega) = 1 + \frac{Ne^2}{\epsilon_0 m} \cdot \frac{1}{\omega_0^2 - \omega^2 - i\gamma\omega} \tag{2.19}$$

The real and imaginary parts of $\widetilde{\epsilon_r}$ for the single resonance model are shown in figure 2.1. The real part ϵ' exhibit mainly the properties of the refraction, while the imaginary part ϵ'' shows features of the absorption. The slopy behaviour of ϵ' around the resonance is responsible for diffraction. At the low frequency side ϵ' approaches the static value $\widetilde{\epsilon}_{st} = \widetilde{\epsilon_r}(0)$. At high frequencies it converges to $\widetilde{\epsilon}_{inf} = \widetilde{\epsilon_r}(\infty)$ which is one for a single resonance system.

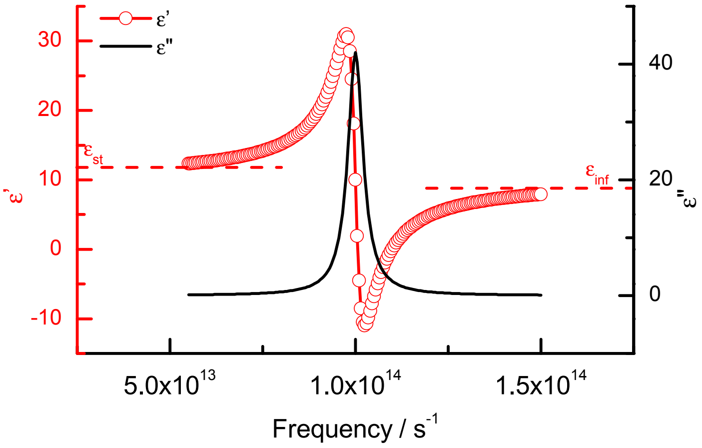

Figure 2.1.: Real and imaginary part of the complex relative dielectric function for a model system.

The influence of other resonances on the polarization can simply be included by an additional $\epsilon_0 \chi \vec{E}$ term in eq. 2.17. As a consequence equation 2.19 will become:

$$\widetilde{\epsilon_r}(\omega) = 1 + \chi + \frac{Ne^2}{\epsilon_0 m} \cdot \frac{1}{\omega_0^2 - \omega^2 - i\gamma\omega} \tag{2.20}$$

and thus $\widetilde{\epsilon}_{inf} = 1 + \chi$. Here χ, the electric susceptibility, contains the cumulated response of the higher frequency surrounding. Starting from the high frequencies, every single resonance changes the dielectric function by an amount related to:

$$\widetilde{\epsilon}_{st} - \widetilde{\epsilon}_{inf} = \frac{Ne^2}{\epsilon_0 m \omega_0^2} \tag{2.21}$$

Alternatively the response of all resonances can be implemented in $\vec{P}$ by summing up all resonance terms NeX_0 (eq. 2.16) (cf. [38]).

In a dense dielectric medium the interaction between the external electric field and the individual dipoles is influenced by the surrounding dipoles. For a correct treatment this can be included in the above equations by an additional modelled local electric field E_{local} [40].

When adapting with the reduced mass, this description can also be applied to vibrations in molecules or solids. Of course this is only valid in systems, where an oscillation in the dipole moment can be induced by the electric field. Transversal optical phonons, delocalized excitations in well ordered ionic or at least polar crystals belong to this class of interaction (section 2.4). Naturally the resonances of these interactions fall into the infrared region, while the bound electrons respond in the ultraviolet (UV) or visible region.

For free electrons the spring constant is zero and an equation analogue to 2.19 without the single electron resonance ω_0 can be found for the dielectric function. Instead a plasma frequency:

$$\omega_p = \sqrt{\frac{Ne^2}{\epsilon_0 m}} \tag{2.22}$$

can be defined which corresponds to a resonance of the complete electron gas. The dielectric function becomes:

$$\widetilde{\epsilon_r}(\omega) = 1 - \frac{\omega_p^2}{\omega^2 + i\gamma\omega} \tag{2.23}$$

For a damping free system ($\gamma = 0$) ϵ_r is real and its obvious that for an optical frequency smaller than the plasma frequency it becomes negative and thus the refractive index will be purely imaginary and the reflectivity unity. At $\omega = \omega_p$ the dielectric function is zero and so is the electric displacement in eq. 2.17. The effects of the transversal electric (TE) field of the light and the polarization cancel each other out. This implies a longitudinal oscillation of the plasma. The quasiparticles of this motion are called plasmons (cf. plasmons in XPS spectra in section 5.1.2.1). At higher frequencies the electron gas becomes transparent as the light drives only transversal oscillations. In figure 2.2 the behaviour of a system obeying the full eq. 2.23 is plotted.

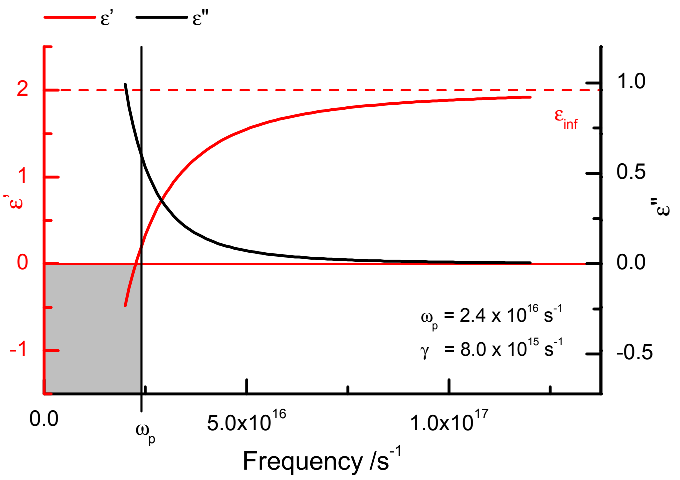

Figure 2.2.: Real and imaginary part of the relative dielectric function of a model plasma. The zero-crossing in the real part is slightly offset from ω_p caused by the strong damping.

The damping γ can be understood as loss of momentum of the electrons through scattering processes. This can be made clear by inserting the momentum $p = mv = m\frac{dx}{dt}$ into equation 2.13. The damping reduces the overall reflectivity and smears out its instantaneous change at ω_p. This approach also allows to express ϵ_r as a function of the electrical alternating current (AC) and direct current (DC) conductivity, by relating the modified eq. 2.13 with the current density (Drude-Lorentz model) (cf. [41]).
The interplay of phonon resonances, oscillations of bound and free electrons, and significantly the intra-, interband transitions, which will be discussed with focus on GaAs in section 4.1.3, determine the overall optical properties of solids in the linear regime.

2.2.1. Interband Transitions and Photoluminescence

In semiconductors the main resonances in linear and nonlinear optically response are interband transitions between valence and conduction band. By quantum mechanics the absorption coefficient can be obtained by calculating transition rates to which it is directly related. According to Fermi's golden rule the transition probability $W_{1\rightarrow 2}$ can be expressed by a matrix element M and a weighted joint density of states factor $g(\hbar\omega)$ of the initial and final bands:

$$W_{1\rightarrow 2} = \frac{2\pi}{\hbar}|M_{12}|^2 g(\hbar\omega) \qquad (2.24)$$

The matrix element describes the effect of the light's electric field on an electron in the irradiated atom by means of time-dependent perturbation theory. Applying electric dipole approximation M results in:

$$\begin{aligned} M_{12} &=< 2|H'|1 >= \int \psi_2^*(\vec{r})H'(\vec{r})\psi_1(\vec{r})d^3\vec{r} \\ H' &= \vec{p_e} \cdot \vec{E} \end{aligned} \tag{2.25}$$

where ψ_1 and ψ_2 are the wave functions of the involved states and $\vec{r}$ is the electron position. The perturbation Hamiltonian H' with the electron's dipole moment $\vec{p_e}$ and the electric field $\vec{E}$ is the same as for a simple dipole in an external electric field. Using Bloch functions for the wave functions of the initial and final states:

$$\Psi(\vec{r}) = \frac{1}{\sqrt{V}} u_i(\vec{r})\ exp(i\vec{k} \cdot \vec{r}), \tag{2.26}$$

with V as the normalization volume and u_i as the periodic envelope function of the lattice and describing the light by a planar wave, gives:

$$M_{12} = \frac{e}{V} \int u_2^*(\vec{r})\ exp(-i\vec{k_2} \cdot \vec{r}) \left(\vec{E_0} \cdot \vec{r}\ exp(\pm i\vec{k} \cdot \vec{r}) \right) u_1(\vec{r})\ exp(i\vec{k_1} \cdot \vec{r}). \tag{2.27}$$

This can be further simplified by conservation of momentum considerations. The joint density of states factor incorporates the fact that both initial and final level are continuous energy bands. It can be obtained by evaluating the individual density of state terms of the involved bands. For a simplified parabolic band with effective carrier mass m^* these terms are:

$$g(E) = \frac{1}{2\pi^2} \left(\frac{2m^*}{\hbar^2} \right)^{\frac{3}{2}} \sqrt{E}. \tag{2.28}$$

In summary the transition probability can be calculated when the parameters of the band structure and the lattice envelope functions are known. For group IV or III-V compound semiconductors using a simple model with four parabolic bands the absorption coefficient is approximately:

$$\begin{aligned} &\alpha(\hbar\omega < E_g) = 0 \\ &\alpha(\hbar\omega \geq E_g) \propto \sqrt{\hbar\omega - E_g}, \end{aligned} \tag{2.29}$$

where excitonic effects and the influence of impurities or defects are neglected.

Photoluminescence

Interband transitions induced by absorption of photons with an energy well above the band gap result in a non-equilibrium distribution of electrons in the excited states from where they quickly relax to the bottom of the conduction band by emitting phonons. Due to the fast electron-phonon coupling compared to the luminescence lifetime, which is in the range of a few nanoseconds for GaAs, the carriers accumulate (cf. section 4.1.4). They form a quasi-equilibrium thermal distribution, before they either re-emit photons in a radiative electron-hole recombination step or lose their energy in non-radiative pathways. The intensity of emission at a given frequency is depending on the transition probability given by equation 2.24 and on the population of upper state.

In the low carrier density limit the thermalization of the excited carriers can be described by Boltzmann statistics. Assuming a frequency independent matrix element the shape of emission spectrum is determined by:

$$I(\hbar\omega) \propto \sqrt{(\hbar\omega - E_g)} \cdot exp(-\frac{\hbar\omega - E_g}{k_B T}) \tag{2.30}$$

where the square root term is the frequency dependent part of $g(\hbar\omega)$ causing a sharp rise in intensity towards the band gap energy on the low energy side of the signal. The exponential term is the occupancy given by Boltzmann statistics. It creates a decaying intensity tail on the high energy side with a time constant of $k_B T$. In the high carrier intensity regime Fermi-Dirac statistic has to be applied and photons are emitted not only near E_g, but over the complete range of band gap and Fermi energies of valence and conduction band $(E_g + E_F^C + E_F^V)$. The corresponding spectra exhibit a plateau in this energy range.

2.3. Nonlinear Optics

Nonlinear optics deal with light matter interaction effects which occur at high optical powers, where the optical constants become a function of the electric field amplitude. When in the linear regime the polarization can be expressed by the linear electric susceptibility $\chi^{(1)}$, the nonlinear effects can be included by adding higher order nonlinear susceptibility terms. The polarization and the relative dielectric functions become:

$$\begin{aligned} \vec{P} &= \epsilon_0 \chi^{(1)} \vec{E} + \epsilon_0 \chi^{(2)} \vec{E}^2 + \epsilon_0 \chi^{(3)} \vec{E}^3 + \cdots \\ \widetilde{\epsilon_r} &= 1 + \chi^{(1)} + \chi^{(2)} E + \chi^{(3)} E^2 + \cdots \end{aligned} \tag{2.31}$$

The nonlinear susceptibilities depend on the microscopic structure of its medium and again quantum mechanical calculations are necessary for a correct treatment. Experimentally nonlinear optical effects were first demonstrated in form of second harmonic generation from a pulsed ruby laser by Franken et al., shortly after the advent of optical masers [42, 43].

Non resonant processes

When considering only non-resonant responses of the system, so called virtual processes, where the energies of the involved photons don't match to any transition inside the medium, the high order polarization can be deduced i.a. from a modified Lorentz oscillator approach as discussed above for the linear regime [41, 44] or by the free electron gas model [44].
The harmonic restoring force term $\omega_0^2 x$ in the equation of motion 2.13 can be converted into an anharmonic potential by a power expansion in the form of:

$$F(x) = \omega_0^2 x + a_2 x^2 + a_3 x^3 + \cdots \tag{2.32}$$

The anharmonic coefficients are small compared to the linear resonance frequency which dominates the response at low intensity. At higher optical powers and thus larger displacements the anharmonic coefficients become relevant. The restoring force will be asymmetric due to the power dependence on the displacement, the resulting polarization contains harmonic frequencies. The following consideration covers only second order effects and neglects the spatial dependence of the oscillations. It can be seen from equation 2.31 that the polarization contains terms oscillating at 2ω, caused by the $\vec{E}^2$ term. The formulation for the displacement is therefore chosen to be:

$$x(t) = X_1 \cdot exp(i\omega t) + X_2 \cdot exp(2i\omega t) + c.c. \tag{2.33}$$

The driving EM field is expressed by:

$$E(t) = \frac{1}{2} E_0 \cdot (exp(i\omega t) + exp(-i\omega t)) \tag{2.34}$$

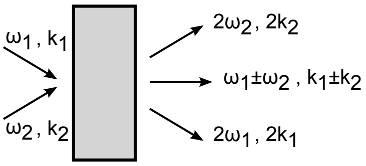

Figure 2.3.: Spatial dependency of the incoming and outgoing beams in a second order nonlinear process.

To find a solution for the nonlinear polarization equations 2.33 and 2.34 are inserted into the anharmonically expanded equation of motion. Treating the anharmonic components as a perturbation, the coefficients X_i of eq. 2.33 can be calculated in an iterative procedure. First, by neglecting terms at 2ω, the linear solution X_1 is found to be equal to eq. 2.15. Next X_2 is obtained by including higher frequency components and approximating the anharmonic force by $a_2 X_1^2 \cdot exp(2i\omega t)$. From the calculated displacements the polarization and further an expression for the nonlinear susceptibility can be established:

$$\chi^{(2)} = \frac{m_0 a_2 \chi^{(1)}(\omega)^2 \chi^{(1)}(2\omega)\epsilon_0^2}{N^2 e^3} \tag{2.35}$$

A more sophisticated version of a second order solution including two driving electromagnetic waves at different frequencies (ω_1, ω_2)and thus containing second harmonic terms ($2\omega_i$), sum frequency / difference frequency parts ($\omega_1 \pm \omega_2$) and DC components can be found in [44]. The spatial dependency effects are worked out in [45], where the various terms generated by squaring two different EM waves with individual frequencies and wave vectors, are discussed. Figure 2.3 illustrates the second-order beams generated in a nonlinear medium for a common geometry as used for example in auto- or crosscorrelation measurements (cf. section 3.2.1).

For a quantum mechanical treatment the density matrix formalism is a suitable method to describe the microscopic properties of nonlinear susceptibilities [44, 46]. Combining the expectation value of the polarization of an ensemble

$$\overline{\langle P \rangle} = \overline{\langle \psi | P | \psi \rangle} \tag{2.36}$$

with the density matrix operator

$$\rho = \sum_k P_k \cdot |\psi_k\rangle\langle\psi_k| \tag{2.37}$$

where P_k is the probability of the system to be in the kth pure state $|\psi\rangle$, gives

$$\overline{\langle P \rangle} = Tr(\rho P) \tag{2.38}$$

The density matrix operator can be determined using the Liouville - Von Neumann equation:

$$\frac{d}{dt}\rho = -\frac{i}{\hbar}[H_0 + H_{int} + H_{rand}, \rho] = -\frac{i}{\hbar}[H_0 + H_{int}, \rho] + \left(\frac{d\rho}{dt}\right)_{relax} \tag{2.39}$$

where the Hamiltonian H is composed of a system part H_0, a Hamiltonian describing the interaction with the electromagnetic field $H_{int} = E_0 \cdot \mu$ with the transition dipole operator μ and a component governing the relaxation processes with the thermal bath H_{rand}.

In the eigenstate basis $|n\rangle$ the diagonal matrix elements $\langle n|\rho|n\rangle$ of the density matrix operator contain information about the population of the nth state. In thermal equilibrium they can be described by particle statistics and the relaxation term of these elements in eq. 2.39 can be expressed by transition rates between the different states. The off diagonal elements $\langle n|\rho|n'\rangle$ represent the coherent superposition of states $|n\rangle$ and $|n'\rangle$. Due to their random phase relation in the ensemble they centre to zero. In simple cases their relaxation can then be expressed by an exponential decay.

So for straightforward systems, higher order polarizations can be found using perturbative expansion, where the density matrix operator is expanded into a power series treating H_{int} as a first order perturbation:

$$\begin{aligned} \rho^{(n)} &= \rho^{(0)} + \rho^{(2)} + \rho^{(3)} + \cdots \\ P^{(n)} &= \langle \rho^{(n)} P \rangle \end{aligned} \tag{2.40}$$

Detailed derivations and further information on the calculation of the nonlinear susceptibilities can i.e. be found in [44, 47].

Resonant processes

From the Lorentz oscillator approach (eq. 2.35) it can be seen that if the fundamental or second harmonic wave comes close to a resonance, the nonlinear susceptibility will strongly increase due to the influence of the $\chi^{(1)}$ terms. When considering a weakly damped system at resonance (compare equation 2.20), this influence causes the equation to break down, so a different concept has to be established for resonant nonlinearities.

Commonly observed resonant effects are shifting and broadening of absorption lines. The shifts are related to the optical Stark effect, which is the electric field analogue to the Zeemann effect. The light (AC) field shifts the atomic levels and lifts their degeneracy. It could be demonstrated for a large number of systems as for instance in dye solutions, semiconductors and quantum well structures [48–50]. The peak broadening of the absorption is caused by a power dependent saturation of absorption. While at low intensities the absorption can be calculated by Fermi's golden rule (cf. section 2.2.1), at high powers the initial state becomes considerably depleted and the stimulated emission has to be included into the calculation. For a two-level system the absorption coefficient can be found using the Einstein coefficients for absorption B_{12} and stimulated emission B_{21}. Assuming that $B_{12} = B_{21}$ it results in:

$$\alpha = B_{12}(N_1 - N_2)\frac{h\nu n}{c} \tag{2.41}$$

where $N_{1,2}$ are the populations of both states and n is the refractive index [41]. At low intensities with N_2 close to zero and a constant N_1 the absorption is in the normal linear regime. At high intensities N_2 increases significantly and thus the absorption decreases. This intensity dependence can be expressed by:

$$\alpha(I) = \alpha_0 - (\alpha_0/I_S)I \tag{2.42}$$

where a saturation intensity I_S and the linear absorption α_0 where introduced. Remembering that the intensity is proportional to E^2 and α is related to the relative permittivity (eqs. 2.8 and 2.10), reveals that this is a third order nonlinear process. In direct band gap semiconductors this effect can be observed at interband transitions, where the absorption saturation is caused by reducing the occupancy of the involved valence band states. Furthermore excitonic effects add to the nonlinear saturation behaviour [51, 52].

Due to the strong interaction of light and matter the perturbation approach is no longer applicable in the quantum mechanical picture. For simple systems which can be treated as an effective two or three level system, the bare or dressed atom pictures (BAP, ie. DAP) are usually applied, in which the interaction is described either in the bare, non-interacting atom eigenstate basis or in the dressed, combined atom-field eigenstates framework. An introductory treatment and comparison between BAP and DAP is given in [38, 53].

Phase-matching

The nonlinear susceptibilities are very small, so for an efficient frequency conversion (e.g. in a SHG process), it is necessary to exploit a large number of nonlinear polarization sources by using long optical media. Here the difference in the refractive indices of the fundamental and the generated second harmonic light produces a phase mismatch. Due to the different propagation speed of the fundamental beam, the SH light created at different positions in the conversion medium will experience a phase lag which in turn results in destructive interference. More precisely, for an incoming beam with $k_1 = \omega_1 n(\omega_1)/c$, the mismatch $\Delta\phi$ is given by discrepancy between the wavevector of the SH light $k_{2\omega_1}$ and that of the induced polarization $k_p = 2k_1$:

$$\Delta\phi = 2k_1 - k_{2\omega_1} \tag{2.43}$$

A coherence length l can be defined after which the phase lag equals 2π:

$$l = \frac{2\pi}{2k_1 - k_{2\omega_1}} = \frac{\lambda}{2(n_{2\omega_1} - n_{\omega_1})} \tag{2.44}$$

The conversion efficiency oscillates inside the medium with $1/l$. Therefore for an efficient process it is important to obtain a phase matching ($n_{2\omega_1} = n_{\omega_1}$). This can be achieved by exploiting the birefringent properties of common solid nonlinear conversion media, where the ordinary and extraordinary beams exhibit different refractive indices. Depending on the arrangement of the beams the phase adaption is known as type 1 or type 2 (for details see [38]). A basic treatment of phase matching is given by Ruddock [54].

Nonlinear susceptibility tensor and crystal symmetry

The second order nonlinear susceptibility derived in equation 2.35 is a tensor of third rank with 27 elements. Due to intrinsic permutation symmetry, the frequency elements can be exchanged along with their coordinate indices without changing the susceptibility. Consequently a reduced notation is commonly used where the polarization is expressed by the nonlinear coefficient tensor which operates on a column matrix of electric fields:

$$\begin{pmatrix} P_x^{(2)} \\ P_y^{(2)} \\ P_z^{(2)} \end{pmatrix} = \begin{pmatrix} d_{11} & d_{12} & \cdots & d_{16} \\ d_{21} & d_{22} & \cdots & d_{26} \\ d_{31} & d_{32} & \cdots & d_{36} \end{pmatrix} \begin{pmatrix} E_xE_x \\ E_yE_y \\ E_zE_z \\ 2E_yE_z \\ 2E_zE_x \\ 2E_xE_y \end{pmatrix} \tag{2.45}$$

Further for the non-resonant case in absence of absorption the susceptibility is real and invariant to a permutation of Cartesian indices (*Kleinman's* conjecture [55]) which moreover reduces the number of distinct elements. The general validity of this simplification is lately questioned by Dailey et al. who pointed out the mutually exclusive results of Kramers-Kronig relations [56]. The third simplification of the susceptibility tensor is related to the *Neumann* principle which says that the physical properties of a crystal must contain the symmetry elements of the crystals point group [57]. So the susceptibility has to be invariant to a symmetry operation of the crystal. For a centrosymmetric crystal with inversion symmetry this directly implies that all tensor elements are zero and thus second-order processes can not be observed. More precisely this is valid for electric-dipole approximation only. A small nonlinear polarization in centrosymmetric calcite was first observed by Terhune in 1968 [58]. It was attributed to second-order magnetic dipole and electric-quadropole contributions [59, 60].

2.3.1. Second Harmonic Generation in Reflection

The fundamental processes of nonlinear light matter interaction in reflection geometry were first discussed in 1962 by Bloembergen et al. [61]. Subsequently experiments in a large number of centrosymmetric media and in media without inversion symmetry followed and phenomenological models were discussed [62, 63]. In theses models, the emerging SH light ($\Omega = 2\omega$) is generated by a combination of a weak nonlinear bulk polarization term and a thin but strong sheet of polarization at the surface. The bulk part can be expressed by a multipole expansion:

$$\vec{P}_{bulk}^{(>1)}(\Omega) = \chi^{(2)}(\Omega)\vec{E}^2(\omega) + \chi_{quad}^{(2)}(\Omega)\vec{E}(\omega)\nabla\vec{E}(\omega) + \cdots \tag{2.46}$$

It converges quickly as the successive components vary like $ka \ll 1$ where a is the atomic dimension and k the wave vector, so only the leading non-vanishing term plays a role [64, 65]. For a centrosymmetric material this is the non-local electric-quadrupole and the magnetic dipole term. In other materials like GaAs the bulk part is much more pronounced or even dominating the SH response due to its electric-dipole contribution. The surface source first was assigned to quadrupole terms caused by the discontinuity of electric field across the surface border [63]. It was characterized in terms of pure bulk properties without a specific interface related aspect. Even though already discovered in 1969 by Brown et al. [66] the potential of second harmonic studies with respect to surfaces sensitivity didn't become widely recognized until the 1980s, where, for example, studies on surface roughness and molecular adlayers were performed [67, 68]. In fact the surface layer is always non-centrosymmetric due to the break of symmetry in the normal direction and thus it inherently adds a dipole term to the polarization source. Caused by reconstruction or relaxation processes the surface layer symmetry can be substantially different from the bulk. Further, when exposed to air, surface oxidation will change the composition of the surface region or create passivation layers and thus additional interfaces with distinct properties.

The geometry used in the following derivations is displayed in figure 2.4. It shows the interface layer with distinct optical properties given by $\epsilon_{int} = \widetilde{\epsilon}_{r,int}\epsilon_0$ between the two media 1 and 2 with permittivities ϵ_1 and ϵ_2. The incoming fundamental beam with wave vector $k_{1x,1z}$ propagates in the xz plane and hits the surface at $z = 0$. When dispersion in medium 1 can be neglected (air, vacuum), the reflected SH light radiates in the same direction as the reflected fundamental. Inside medium 2 dispersion changes the speed and direction of both beams according to Snell's law. The model holds for interfaces with a thickness smaller then the wavelength of the radiation.

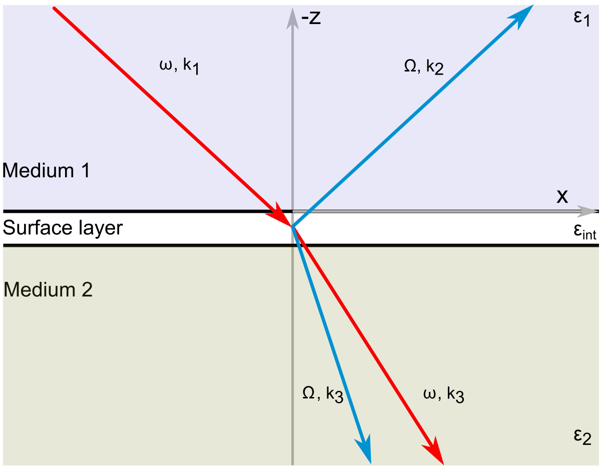

Figure 2.4.: Second harmonic generation in reflection at surfaces and interfaces. The surface layer was exaggerated for clarity. It is actually treated as a two dimensional plane.

Following the derivation given by Shen [64, 69] or Heinz et al. [65] the second order surface layer polarization term can be expressed by a sheet polarization source in the xy-plane and a delta function perpendicular to the surface :

$$\vec{P}^{(2)}_{surf.}(x,y,z,t) = \vec{P}^{(2)}_{surf.}(x,y,t)\delta(z) \tag{2.47}$$

Initially the sheet polarization term is implemented by an infinite planar, spatially varying wave with wave vector $\vec{k}$, frequency $\Omega = 2\omega$ and amplitude $P_s = |\vec{P}_s|$:

$$\vec{P}^{(2)}_{surf.} = \vec{P}_s \cdot exp(i\vec{k}\cdot\vec{r} - i\Omega t) + c.c \tag{2.48}$$

The electric and magnetic fields of the radiation generated on both sides of the surface sheet can be determined using Maxwell's equations (see appendix A.1) with the above polarization as the driving force:

$$\begin{aligned}
\nabla \cdot \vec{D} &= -4\pi\nabla_x \cdot \vec{P}^{(2)}_{surf.} \\
\nabla \cdot \vec{B} &= 0 \\
c\nabla \times \vec{E} + \frac{\partial \vec{B}}{\partial t} &= 0 \\
c\nabla \times \vec{H} - \frac{\partial \vec{D}}{\partial t} &= 4\pi \frac{\partial \vec{P}^{(2)}_{surf.}}{\partial t}.
\end{aligned} \tag{2.49}$$

The appropriate boundary conditions which ensure the continuity of $(D_\perp + 4\pi P^{(2)}_\perp)$, $E_\parallel$, $B_\perp$ and $H_\parallel$ (with $\perp = z$-direction and $\parallel$ as x, y-directions) across the surface layer are [65, 70, 71]:

$$\begin{aligned}
\Delta D_\perp &= -4\pi\nabla_\parallel \cdot P^{(2)}_{surf.,\parallel} \\
\Delta B_\perp &= 0 \\
\Delta E_\parallel &= -\frac{4\pi}{\epsilon_{int}}\nabla_\parallel \cdot P^{(2)}_{surf.,\perp} \\
\Delta H_\parallel &= \frac{4\pi}{c}\frac{\partial P^{(2)}_{surf.,\parallel}}{\partial t} \times \hat{z}.
\end{aligned} \tag{2.50}$$

Disregarding magnetic properties ($\mu = 1$) the expressions for the p- and s-polarized radiated fields in media 1 become:

$$\begin{aligned} E_p(\Omega) &= \frac{i4\pi|\vec{k}_1|}{\epsilon_2 k_{1z} + \epsilon_1 k_{2z}} \left[k_{2z} P_{surf.,x} + (\epsilon_2/\epsilon_{int}) k_x P_{surf.,z}\right] exp(i\vec{k}_1 \cdot \vec{r} - i\Omega t) \\ E_s(\Omega) &= \frac{i4\pi|\vec{k}_1|}{k_{1z} + k_{2z}} \left[\frac{\vec{k}_1 P_{surf.,y}}{\epsilon_1}\right] exp(i\vec{k}_1 \cdot \vec{r} - i\Omega t) \end{aligned} \tag{2.51}$$

where k_i are the corresponding wave vectors of the radiation. By swapping the indices and changing the direction of the z-direction depending elements, the expressions for the radiated field in media 2 can be found. Now the linear dielectric response is determined by repeating the calculation for the case $\epsilon_1 = \epsilon_2 = \epsilon_{int}$ and taking the ratios of the single field amplitudes. This yields the Fresnel transmission coefficients:

$$\begin{aligned} \left(\frac{E_p}{E_{p0}}\right)_x &= L_{xx} \equiv \frac{2\epsilon_1 k_{2z}}{\epsilon_2 k_{1z} + \epsilon_1 k_{2z}} \\ \left(\frac{E_p}{E_{p0}}\right)_z &= L_{zz} \equiv \frac{2\epsilon_1 k_{1z}}{\epsilon_2 k_{1z} + \epsilon_1 k_{2z}} \\ \left(\frac{E_s}{E_{p0}}\right)_y &= L_{yy} \equiv \frac{2k_{1z}}{k_{1z} + k_{2z}} \end{aligned} \tag{2.52}$$

which combine to the local field correction tensor L. The radiated electric fields in media 1 are related to those inside the sheet by:

$$\vec{E}_L(\Omega) = L \cdot \vec{E}_0(\Omega) \tag{2.53}$$

In the next step the simplified version of a polarization source in eq. 2.48 is replaced by an usual implementation with two planar and collinear pump waves and a susceptibility tensor:

$$\vec{P}^{(2)}_{surf.}(\Omega) = \chi^{(2)}_{surf.} : \vec{E}_L(\omega)\vec{E}_L(\omega). \tag{2.54}$$

This gives:

$$\begin{aligned}
E_p(\Omega) =& \frac{i4\pi\omega}{c}\left[L_{xx}(\Omega)\chi^{(2)}_{surf.,xjk}L_{jj}(\omega)L_{kk}(\omega) + \frac{k_x(\Omega)}{k_{1z}(\Omega)}L_{zz}(\Omega)\chi^{(2)}_{surf.,zjk}L_{jj}(\omega)L_{kk}(\omega)\right] \\
&\times E_{0,j}(\omega)E_{0,k}(\omega) \\
E_s(\Omega) =& \frac{i2\pi|\vec{k}_1|^2(\Omega)}{k_{1,z}(\Omega)\epsilon_1(\Omega)}\left[L_{yy}(\Omega)\chi^{(2)}_{surf.,yjk}L_{jj}(\omega)L_{kk}(\omega)\right]E_{0,j}(\omega)E_{0,k}(\omega).
\end{aligned} \tag{2.55}$$

The indices j and k imply a summation of all susceptibility term components (cf figure 2.4). The amplitudes of the incoming fields are given by their components in the coordinate frame of figure 2.4, while the radiated field amplitudes are given directly as p and s-polarizations. Both have to be corrected by the appropriate Fresnel coefficients when propagating across the interface layer. The terms are grouped by output components. The intensity depends on the square of the electric field:

$$I(\Omega) = \frac{1}{2}cn\epsilon_1(\Omega)|\vec{E}_0(\Omega)|^2. \tag{2.56}$$

By introducing Fresnel corrected polarization vectors $\vec{e}'(\Omega) \equiv L(\Omega)\cdot\hat{e}(\Omega)$ (the hat denotes an unit vector) and the SH transmission angle θ_Ω referenced to the surface normal, the intensity is:

$$I(\Omega) = \frac{8\pi^3\Omega^2\sec^2\theta_\Omega}{c^3\epsilon_1(\omega)\sqrt{\epsilon_1(\Omega)}}|\vec{e}'(\Omega)\cdot\chi^{(2)}_{surf.}:\vec{e}'(\omega)\vec{e}'(\omega)|^2 I^2(\omega) \tag{2.57}$$

Special care has to be taken with the directions of the wave vectors on both sides of the interface and to those of the electric field polarization vectors. This is worked out extensively in [61].

With this formalism for the surface nonlinear response it is convenient to incorporate the bulk response in a similar way. This is done by replacing the surface polarization in the above equations with an effective polarization term or an effective second-order susceptibility term respectively:

$$\begin{aligned}
P^{(2)}_{eff.,x,y} &= P^{(2)}_{surf.,x,y} + i\frac{P^{(2)}_{bulk,x,y}}{k_z(\Omega)+2k_z(\omega)} \\
P^{(2)}_{eff.,z} &= P^{(2)}_{surf.,z} + i\frac{\epsilon_2(\Omega)}{\epsilon_{int}(\Omega)}\frac{P^{(2)}_{bulk,z}}{k_z(\Omega)+2k_z(\omega)}
\end{aligned} \tag{2.58}$$

Here the bulk response is treated as another polarization sheet, with an effective thickness $l_{eff} = (k_z(\Omega) + 2k_z(\omega))^{-1}$ (phase matching length). In optical measurements only this effective term is accessible. In order to obtain surface sensitivity $\chi^{(2)}_{surf.}$ has to be larger then $\chi^{(2)}_{bulk}/2\vec{k}$ [64, 72]. As discussed before this ratio is strongly depending on the symmetry properties of the bulk structure and on those of the surface. In centrosymmetric crystals the ratio is in the order of d/a, with d as the surface layer thickness and a as the atomic size in the bulk [44]. In non-centrosymmetric materials this ratio is only about $2\pi d/\lambda$. In this case the surface elements can eventually be determined using special polarization geometries.

2.3.2. SHG as Surface Probe

Surface second harmonic generation is used in a variety of experiments both in static mode and with temporal resolution, where the time dependent experiments have to be distinguished between large timescale studies up to several hours and ultrafast pump-probe experiments [73, 74] which are introduced in section 5.3.2. One possible application in the large timescale field is the measurement of SHG intensity at an interface while adsorbing or desorbing molecular species [75]. Zhu et al. studied the adsorption of CO on a Ni (111) surface and its desorption [76] and correlated it with temperature programmed desorption [77–80]. In this case the effective susceptibility tensor can be described by a summation over the surface and bulk contributions of the substrate, the natural nonlinearity of the adsorbate and an additional term incorporating the interaction at the interface (equation 2.59) [74].

$$\chi^{(2)}_{eff} = \chi^{(2)}_{surf.} + \chi^{(2)}_{bulk} + \chi^{(2)}_{ads.} + \Delta\chi^{(2)}_{int.} \tag{2.59}$$

When the influence of the adsorbate on the overall SH intensity is small only, the change can be expressed by a constant C describing the maximum effect at $\theta = 1$, multiplied by the adsorbate coverage θ [81]:

$$\chi^{(2)\prime}_{eff} = \chi^{(2)} \cdot (1 + C\theta) \tag{2.60}$$

Similar experiments were performed at semiconductor surfaces, electrochemical silver electrodes and even on nano ceramic-metallic materials (cermets) composed from gold and titanium oxide [44, 64, 82]. SHG can also be used to probe diffusion dynamics at liquid interfaces. Bavli et al. showed by monitoring the SH response of metal liquidlike films (MELFS) consisting of spherical nano particles embedded between two unmixable liquids, reordering processes evoked by diffusion of the nano particles inside the film [83]. Another important aspect is the measurement of surface reactions, especially surface oxidation and reduction as demonstrated in [84] for a semiconductor or in [85] for metal interfaces.

The ultrafast timescale field covers a large number of experiments on various samples like metals [86, 87], semiconductors [88] and nanostructures [89, 90] probing the excitation and relaxation dynamics of carriers, collective excitations and magnetic properties [91] or surface reactions [92].

Static SHG methods can be used to perform spectroscopic analysis and orientation studies of molecular monolayers adsorbed on surfaces [67] or to probe the symmetry of anisotropic interface layers of single crystals [93, 94]. This technique, also used in this thesis to characterize the platinum - GaAs interfaces, is based on a combined variation of input and output polarizations while rotating the sample around its surface normal- It was first demonstrated on Si (111) surfaces by Driscoll [95, 96] and Heinz et al. in 1983/84 [97, 98] (see also section 5.3.3). Depending on the crystal class and the face of the surface, different relations for the radiated harmonic light can be established, as discussed in a number of publications [64, 65, 74, 84]. For example for the (100) and (111) faces of centrosymmetric materials with m3m symmetry the p- and s-polarized contributions are [65]:

$$\begin{aligned} E_p(\Omega) &= a + b_m \cos(m\phi) \\ E_s(\Omega) &= c_m \sin(m\phi), \end{aligned} \tag{2.61}$$

where ϕ is the azimuth angle, m is related to the symmetry ($m = 3$ for the (111) face and $m = 4$ for the (100) face). a, b_m and c_m are linear combinations of susceptibility tensor elements. These formulas are commonly given in beam coordinates, so a transformation of the $\chi^{(2)}_{surf.}$ elements normally given in crystallographic coordinates has to be performed. Further a careful symmetry analysis and decomposition of the susceptibility tensor in a set of spherical tensors has to be done [99].

In figure 2.5 the measurements done by Tom et. al [98, 100] on native oxide covered Si (100) surfaces are shown. They used a 532 nm Nd:YAG light source impinging onto the sample in an angle of incidence of 45°. The circles of both curves show the measured SH intensities while varying the azimuthal angle for s- and p-polarized output respectively.

The angle is referred to the {010} direction. Both results are fitted (dashed lines) by squaring the appropriate electric field expressions of equation 2.61. In this case the surface layer has a $4mm$ symmetry which is isotropic. The changes in the signal intensity due to rotation of the crystal can thus be attributed to bulk properties.

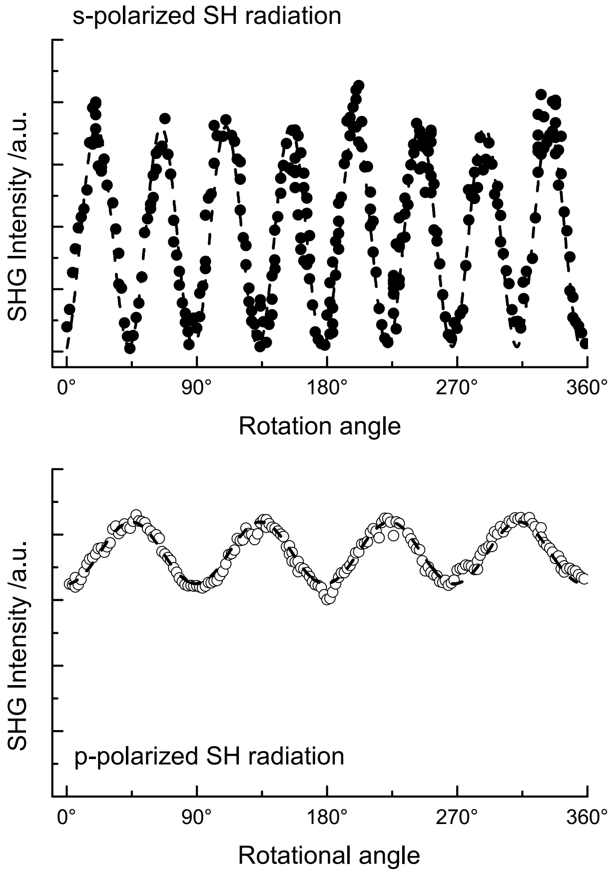

Figure 2.5.: SH rotational scans on native oxide covered Si(100) surface. For this measurements laser radiation at 532 nm was used at an angle of incidence of 45°. The upper graph shows the s-polarized part, the lower one the p-polarized output (circles). The fit is described in the text. The data was extracted from [98, 100].

2.4. Interaction with Phonons

Excitation of delocalized lattice vibrations is an important channel for energy dissipation in metals and semiconductors. The dynamics of phonons in these systems can be measured directly with the time-resolved methods presented in this thesis. Therefore this sections begins with an introduction to the fundamental vibrational modes, their classical treatment and interaction with light while the second part deals with the coherent excitation of phonons and their relaxation processes.

A crystalline solid can be excited to vibrate at its natural frequencies. Equivalent to vibrational modes in molecules, the collective oscillation has discrete energy levels. These are the so called phonons, the energy quanta of lattice vibrations. In the harmonic approach the energy is given by:

$$E = (n + \frac{1}{2})\hbar\Omega, \tag{2.62}$$

where Ω is the frequency of the vibrational mode and n is the quantum number representing the number of phonons occupying a given vibronic state. Phonons are defined by their frequency and a wave vector $\vec{q}$. Even though phonons don't have an impulse in a physical meaning, they interact with other (quasi) particles as if. Therefore the quantity $\hbar\vec{q}$ is called crystal impulse.

There are four principle phonon mode types, on one hand they either vibrate in transverse or longitudinal relation to their direction of propagation and on the other hand they can be classified into acoustic or optical modes, where the latter is only possible in crystals with at least two different constituents in the unit cell. In the acoustic modes, as shown in the upper half of figure 2.6a, all adjacent atoms oscillate in the same direction. Acoustic phonons are sound waves propagating through the solid. In optical modes however, the vicinal atoms vibrate in opposed direction around the centre of mass. When the atoms are ionic or the bond is at least polarized these phonons can couple to photons and the usual Raman and IR selection rules apply. In general for a crystal with a p atomic basis there are 3 acoustic and 3p-3 optical modes. In classical treatment phonons can be described by Hooke's law and the equation of motion:

$$M\frac{d^2u_s}{dt^2} = F_s = \sum_n f_n(u_{s+n} - u_s), \tag{2.63}$$

where F_s is the force acting on atom s with mass M, f_n is the force constant and $u_{s+n} - u_s$ is the displacement difference between the atom investigated and that n atomic planes away. For a correct treatment, the influence of all n atoms has to be considered. With an appropriate approach and limiting the wave vector to the first Brillouin zone, the solution gives the dispersion relation. For a solid consisting of atoms separated by the

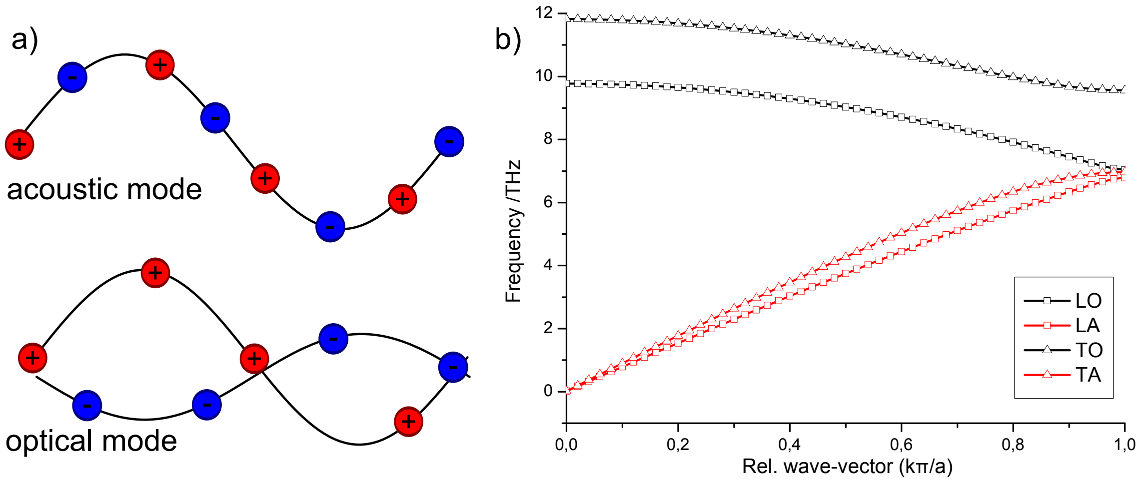

Figure 2.6.: a) Acoustic and optical transverse phonon modes. b) Example of a typical phonon dispersion relation.

atomic plane translation vector $\vec{a}$, the dispersion of the acoustic mode is:

$$\Omega = \sqrt{\frac{4f_1}{M}} \left| \sin \frac{\vec{q}\vec{a}}{2} \right| , \tag{2.64}$$

where for reasons of simplicity, only the effect of direct neighbours is regarded. For a system with two atoms per unit cell two motion equations have to be set up separately and the combined solution directly gives an acoustic and an optical branch as shown in figure 2.6b for the longitudinal and transverse modes. A more detailed classical and also quantum mechanical treatment can be found in many solid-state physics textbooks, for example in [40, 101, 102].

The interaction of photons and phonons requires the conservation of energy and momentum, which is fulfilled when the dispersion curves of both quanta cross in the dispersion relation. The slope of the photon dispersion is c/n, which is much larger than the sound velocity. So a coupling to acoustic phonons would be impossible neglecting the DC point at $k = 0$. The crossing with the optical branch occurs at small $\vec{q}$, where those phonons are nearly dispersionless ($\vec{q} \approx 0$). Due to its transversal nature photons only couple to transverse optical vibrations directly.

Analogue to the general discussion about light matter interaction in section 2.2 the coupling to phonons can be described by extending equation 2.63 with the electric field as the driving force, a damping term γ and the reduced mass μ. Finally the follwing expression for the relative dielectric constant is obtained (cf. equations 2.13 - 2.20):

$$\widetilde{\epsilon_r}(\omega) = \widetilde{\epsilon_\infty} + (\widetilde{\epsilon_{st}} - \widetilde{\epsilon_\infty})\frac{\Omega_{TO}^2}{\Omega_{TO}^2 - \omega^2 - i\gamma\omega} \tag{2.65}$$

The longitudinal optical mode can be found for the condition $\widetilde{\epsilon_r} = 0$ (cf. figure 2.2). Neglecting the damping term in eq. 2.65 this gives the frequency

$$\omega' = \sqrt{\frac{\epsilon_{st}}{\epsilon_\infty}}\,\Omega_{TO} = \Omega_{LO} \tag{2.66}$$

and further the Lyddane-Sachs-Teller relationship [41]:

$$\frac{\epsilon_{st}}{\epsilon_\infty} = \frac{\Omega_{LO}^2}{\Omega_{TO}^2}. \tag{2.67}$$

Figure 2.7 shows this situation for a sample system. In a damping free material the reflectivity is unity between the TO and LO frequency, which is therefore known as Reststrahlen band. In section 4.1.4 on carrier dynamics in GaAs the energy dissipation after the excitation with an ultrafast laser pulse involves coupling processes with phonons. For unpolar crystals the most important process of electron-phonon scattering is related to the deformation potential, which describes the change of valence and conduction band levels as a function of strain applied to the material. For the conduction band

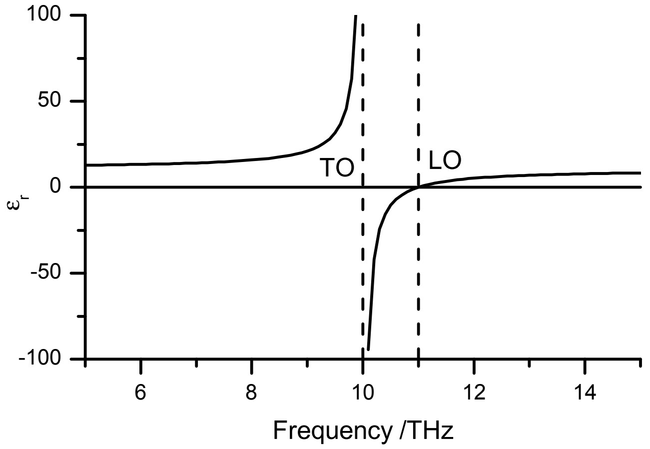

Figure 2.7.: Relative dielectric function of a sample system in the phonon frequency range. At resonance with the transverse optical mode it shows asymptotic behaviour. The longitudinal mode is determined by the zero-crossing of the real relative dielectric function.

level the relation is:

$$\delta E_C = D_C \frac{\delta a}{a}, \tag{2.68}$$

where D_C is the deformation potential and a is the lattice spacing. A longitudinal acoustic phonon with adjacent atoms moving in phase, locally changes the conduction band level by this deformation potential and thus creates a scattering potential for a moving electron. Caused by the longitudinal movement the change in lattice spacing is proportional to the gradient of displacement (acoustic deformation potential (ADP) scattering). In TA phonons the transverse displacement changes the lattice spacing only in second order and thus can be neglected. Finally at LO phonon modes, the out of phase oscillation of adjacent atoms directly affects the lattice spacing making this effect much stronger than its acoustic analogon (optical deformation potential (ODP) scattering). In polar materials the deformation potential scattering processes play a minor role compared to polar optical phonon (POP) scattering. In GaAs energy transfer to or from acoustic phonons can be neglected for temperatures > 40 K as these scattering events become nearly elastic [103, 104]. The electron-phonon interaction by POP scattering can be described by introducing the concept of polarons. These quasi-particles are formed by Coulomb interaction between an electron and the oscillating dipole induced by longitudinal vibrations of polarized lattice elements (Fröhlich interaction) [105, 106]. For systems with a strong coupling the deformation of the lattice caused by the moving electron can be interpreted as a permanent absorption and emission of local or virtual LO phonons. Finally acoustic modes in polar materials also create an oscillating dipole, however due to the in phase motion of vicinal lattice constituents, the effect is weak. It is referred to as piezo-electric (PZ) scattering [107, 108].

The second process, the coupling between phonons, mediates the fast decay of transverse optical phonons initially excited into acoustic vibration with larger wave vectors. It results from the anharmonicity in real systems resembling nonlinear optical effects and manifests itself by higher order terms to the restoring force in which the interaction of three or more phonons is made possible. The conservation of momentum is ensured by emitting phonons with opposite wave-vectors (figure 2.8). These large wave vector phonons can also interact with hot carriers by scattering them into side bands (intervalley scattering) as discussed also in section 4.1.4. A widespread method for the analysis of phonons, is inelastic scattering of photons. Depending on whether optical or acoustic vibrational modes are measured, the techniques are Raman or Brillouin scattering. In both cases the frequency shift between the incident and the emitted photons are measured. A drawback of this methods is the small range of wave vectors that can be probed and the weak signal intensity due to the high order process. Larger wave vector probes are helium atom or neutron scattering.

(Surface) polaritons

Before it was said, that light-phonon coupling depends on a frequency and wave vector matching. Figure 2.9 displays the dispersion relation of an uncoupled electromagnetic wave (red curve) and a transverse optical phonon (lower dashed black curve) in the close vicinity of the supposed intersection. In this case of a strong coupling the system shows a different behaviour (black solid curves) than expected, with a characteristic anti-crossing and the creation of a forbidden band between the frequencies of the longitudinal and transverse optical phonons. The gap is a direct implication from the phonons impact on the dielectric function as discussed before. These coupled modes close to the Reststrahlen band are called polaritons. Similar effects can be discussed for an interaction with plasma oscillations, where due to the nature of the dielectric response only the upper branch starting at $\omega(k=0)=\omega_p$ exists. A condition for the propagation of coupled excitations in the bulk of a medium is, that the dielectric function has values larger zero, otherwise the light wave will consist only of an exponential damped term (compare equations 2.7 and 2.10). On surfaces and interfaces however this leads to a different type of coupled excitations between light propagating along the surface and surface phonons or surface plasma oscillations. Their surface confinement is given by the penetration depths into the media on both sides of the interface which can be derived from the dispersion relation of surface polaritons (SP) [109]. The dispersion curves of those polaritons lay to the right hand side of the corresponding light waves, thus their wave vectors are to large to get excited directly. This can only be achieved by special excitation techniques, which adjust

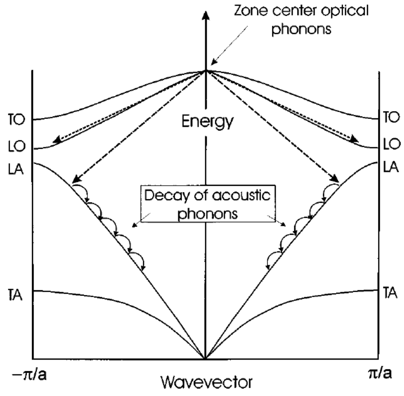

Figure 2.8.: Decay of optical phonons into acoustic modes in germanium. Reprinted from [11], with permission from AIP Publishing.

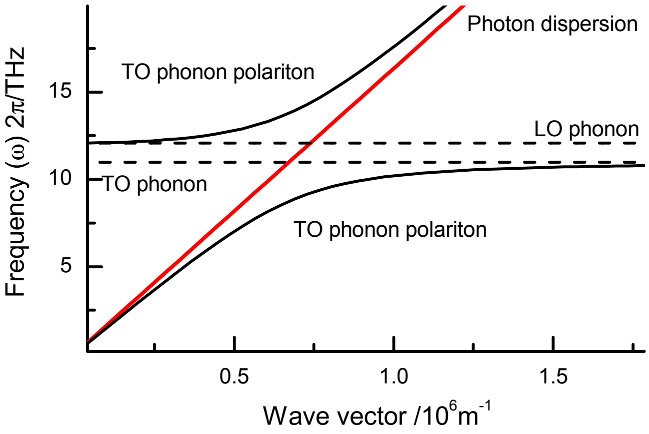

Figure 2.9.: Dispersion relation of phonon polaritons in a sample medium.

the wave vector of light either by passing it through a prism (Otto [110] or Kretschmann [111] configuration), or incorporate grating structures or grating like defects [112]. Particular interest lies in the excitation of surface plasmon polaritons in small structures to confine light into sub wavelength dimensions (e.g. [113, 114]).

2.4.1. Coherent Phonons

The thermal occupancy of phonons can be calculated by Bose-Einstein statistics and the density of states (DOS) of the individual phonon branches. For systems with monoatomic basis the Debye approximation can be used to approximate the DOS term, which finally result in the T^3 model for its heat capacity. At room temperature the occupancy is low and mostly acoustic modes with random phase relation are excited. By interaction with CW or long pulsed light additional optical, zone centre phonon states get occupied. They too have unlinked phases. Coherent phonons in contrast, are characterized by their defined phase relation. Ultrashort laser pulses as an approximation for delta functions with considerably smaller durations then the dephasing time of the coherence can be used to create those phonon states by a number of different mechanisms as discussed below. In principle mostly zone centre optical phonon levels get occupied by these processes.

In the quantum mechanical picture the evolution of the coherent vibration is generally treated by the density matrix formalism already introduced in section 2.3 on nonlinear optics [47, 115, 116]. When the phonon wave packet is constructed by a superposition of eigenstates, the density matrix operator (eq. 2.37) evolves in time as described by the Liouville - Von Neumann version (eq. 2.39) of the time dependent Schrödinger equation.

The relaxation term of eq. 2.39 can be expressed by phenomenological terms describing the dissipation effects [117]. One obtains for the evolution of the diagonal population elements ρ_{nn} and the off-diagonal coherence elements $\rho_{nn'}$ $(n \neq n')$:

$$\begin{aligned}
\frac{\partial \rho_{nn'}}{\partial t} &= \frac{i}{\hbar}\left[H_0 + H_{int}, \rho_{nn'}\right] - \gamma_{nn'}\rho_{nn'} \\
\frac{\partial \rho_{nn}}{\partial t} &= \frac{i}{\hbar}\left[H_0 + H_{int}, \rho_{nn}\right] + \sum_{E_{n'}>E_n} \Gamma_{nn'}\rho_{n'n'} - \sum_{E_{n'}<E_n} \Gamma_{n'n}\rho_{nn}
\end{aligned} \tag{2.69}$$

The population elements ρ_{nn} are affected by transitions from higher and decay to lower energy states determined by the sum over the decay terms of the individual transitions (summarized as $\Gamma_n = \sum_{E_{n'}<E_n} \Gamma_{n'n}$ and accordingly $\Gamma_{n'}$). The off diagonal elements decay in this simple picture with a dephasing term $\gamma_{nn'}$ driven by $\rho_{nn'} - \rho_{nn'}^{eq.}$, where $\rho_{nn'}^{eq.} = 0$ (loss of coherence). The coherence dephasing between two states is depending on the population of those, so $\gamma_{nn'}$ is defined by the population decay terms and a pure phase distortion rate (elastic scattering) $\gamma_{nn'}^{*}$:

$$\gamma_{nn'} = \frac{1}{2}\left(\Gamma_n + \Gamma_{n'}\right) + \gamma_{nn'}^{*}. \tag{2.70}$$

For a real or an assumed two-level system the decay rate from the lower state is zero. The lifetime of the diagonal elements is characterized by the population decay rate $1/T_1$ (longitudinal decay), while the off-diagonal elements describing the coherent superposition state decay with $1/T_2$ (transversal decay). This loss of coherence lifetime consists of a population decay contribution and pure dephasing part T_2^* [115]:

$$\frac{1}{T_2} = \frac{1}{2T_1} + \frac{1}{T_2^*}. \tag{2.71}$$

The latter describes phase fluctuations for example caused by elastic collisions. Classically a coherent phonon can be treated like an incoherent vibration by a Lorentz oscillator, as discussed above determining the influence of phonons on the dielectric function (eq. 2.65) and in section 2.2. Recapitulating equation 2.13 with the appropriate quantities:

$$\frac{d^2U}{dt^2} + \frac{2}{T_2}\frac{dU}{dt} + \Omega^2 U = \frac{F(t)}{\mu}, \tag{2.72}$$

where μ is the reduced mass of the oscillator and U is in contrast to eq. 2.63 not the displacement of an individual atom but of the whole coherent vibration. When the force $F(t)$ in form of an ultrashort light pulse impulsively creates the coherent wave packet, it shows a free induction decay:

$$u(t) \propto \sin(\widetilde{\omega} t - \phi) \cdot exp(-t/T_2), \tag{2.73}$$

here the frequency $\widetilde{\omega}$ of the under-damped oscillation differs from the pure harmonic resonance by

$$\widetilde{\omega} = \sqrt{\Omega_0^2 - 1/{T_2}^2}. \tag{2.74}$$

The term under-damping belongs to a classification which relates the damping to the natural frequency of the oscillation. At the critical level, where $\frac{1}{T_2} = \Omega$, the system returns the quickest way to the equilibrium position without any oscillation. Under-damping defines the behaviour with damping between zero (undamped) and the critical damping [118].

Coherent phonon pump-probe studies using femtosecond laser based excitation and probing different optical properties were performed on a number of different systems like molecular crystals [119], (semi)metals [120–122], semiconductors [120, 123], quantum wells [124–127] nano particles [128–132] and in prismatic nano structures [133–136]. For the well known coherent phonons in Bi recent calculations suggests, that ultrashort excitation not only creates coherent phonons but also induces coupling between different phonon modes [137]. In some systems coherent phonons are also found to re-emit electromagnetic radiation at their resonance frequency in the terahertz regime [138–140], which can be exploited for example in terahertz spectroscopy [141, 142].

2.4.2. Excitation Mechanisms

Direct resonant excitation

The direct excitation of the coherent wave packet by an ultrashort laser pulse, whose frequency spectrum contains a component in resonance with the phonon transition, is the most obvious excitation mechanism. The pulse has to be shorter than T_2 to create the coherence. The detection of the decay can be accomplished by time-resolved sum frequency generation (TRSFG), for example [143]. Quantum mechanically this enters the interaction Hamiltonian of equation 2.69 in form of a dipole moment operator μ by $H_{int} = -\mu \vec{E}(t, r)$. Alternatively the coherent state can be created by absorbing appropriate monochromatic coherent laser light. By analysis of the line shape in an absorption experiment, information on the decay process can be obtained.

Non-resonant impulsive Raman excitation

The impulsive stimulated Raman scattering (ISRS) is a second order process acting on the density matrix operator. Here different spectral components of a spectrally broad femtosecond laser pulse provide the energy for a transition to a virtual state and for the consequent stimulus for decay [123]. When the difference frequency between both matches a vibrational transition a coherent excitation is created (transparent excitation). As the vibration is created in the electronic ground state the oscillation shows a sinusoidal behaviour after the impulsive trigger [144]. The interaction Hamiltonian has the form of the common Raman tensor: $-1/2U \sum_{k,l} \left(\partial\alpha/\partial U\right)_{k,l} \vec{E}_k \vec{E}_l$, where α is the polarizability and $\vec{E}_{k,l}$ the involved light fields [145].

Resonant impulsive Raman excitation

In the resonant case, when the intermediate level is real, the excitation is enhanced and the oscillation starts either in the ground or in the electronically excited state, depending on the electronic dephasing time (opaque excitation). In the resonant case the imaginary part of the (resonant) Raman tensor dominates the vibration [146]. The ground state coherence emerges from interference between the wave packet dropping back from the transitional state after stimulation and that in the ground state. As the excited wave packet had moved on the excited potential energy surface (PES), the perpendicular transition back to ground state, launches a displacive coherent phonon. Similar the creation of a displacive coherent vibration in the excited electronic state is induced by the interference between the excited wave packet and the ground state wave packet transferred also to the excited PES by the stimulus [144]. This description is comparable to Menzel-Gomer-Redhead type process for the laser induced energy transfer into a molecule - surface vibration at metal surfaces [147, 148].

Displacive excitation of coherent phonons (DECP)

The DECP mechanism is completely phenomenological and does not explicitly include coherent elements in the density matrix [115]. It was introduced by Zeiger and Dresselhaus [120]. Here a reasonable strong excitation pulse creates a transition to an excited PES and the lattice starts to oscillate around the new equilibrium position. It is comparable to the Franck-Condon like transitions in molecules. Thus the initial phase also shows a cosine behaviour. In contrast to resonant Raman scattering, beside its intrinsic coherence, here only highly symmetric A_1 vibrations (breathing modes) can be excited.

Nevertheless it is used in the discussion of many different systems, mostly semiconductors or semimetals [120, 149]. The model includes an expression directly relating the vibrational displacement with the laser induced carrier density, which allows an estimation on the applicability of the model, when comparing to experimental results [150].

Transient depletion field screening (TDFS)

Related to the DECP mechanism is the transient screening of the depletion zone in a semiconductor surface [151, 152]. Due to absorption and consequent electron-hole pair generation the charge in the depletion zone (cf. section 4.1.2), is screened. The atoms relax to a new equilibrium position and start to oscillate. When this screening is short enough, the vibration becomes coherent. Due to the new equilibrium position the motion is of cosine character. As the light only is responsible for the injection of carriers, this mechanism should be independent of sample and light polarization orientation.

3. Generation and Measurement of Ultrashort Laser Pulses

The following sections give a brief introduction to femtosecond light sources and their differences to classic monochromatic lasers. Further the principles of characterization of ultrashort pulses are given. Both generation and measurement depend on nonlinear effects introduced in the chapter before.

3.1. Generation of Femtosecond Laser Pulses

Classical lasers are based on singular well defined light emitting electronic transitions, thus emitting light with a small bandwidth. They can be operated in continuous or pulsed mode, determined by the type of pumping. Using optical switches and cavity dumping, pulses of nanosecond to picosecond period can be generated [153]. In contrast to this, femtosecond lasers utilize the constructive interference of many longitudinal resonator modes to form a pulse shaped superposition travelling through the laser cavity. Necessary for the formation of a pulse is a constant phase relation between the individual modes, which otherwise would cancel out (destructive interference). The second requirement is a broad emission band of the employed laser material, allowing a large number of modes to be incorporated. Neglecting the spatial dependence, the complex electric field of the pulse can be obtained by summing up all $q = (2n + 1)$ spectral components:

$$E(t) = \frac{1}{2\pi} \sum_{q=-n}^{n} E_q \cdot exp(i\left[(\omega_0 + q \cdot \Delta\omega)t + \phi_q\right]) \tag{3.1}$$

The modes are distributed around the central frequency ω_0 equally separated by $\Delta\omega$. E_q is the amplitude and ϕ_q the spectral phase of the qth mode. For real femtosecond lasers a continuous emission with differential $d\omega$ and a Gaussian spectral intensity function can be approximated [38, 45]. Further it is a common procedure to separate the variables in a carrier wave term oscillating at ω_0 and the slow varying complex amplitude term

$A(t)$, also referred to as envelope (SVEA):

$$\begin{aligned} E(t) &= A(t) \cdot exp(i\omega_o t) \\ A(t) &= \frac{1}{2\pi}\int_{-\infty}^{\infty} E(\omega)\cdot exp(i(d\omega t + \phi(\omega)))d\omega \end{aligned} \tag{3.2}$$

The FWHM of the intensities in time and spectral domain are related by $\Delta\tau\Delta\nu \geq \kappa$ where κ is a factor describing the pulse shape (for a Gaussian beam κ is 0.441). For a flat phase, bandwidth limited pulse as shown in figure 3.1, the temporal width is directly connected to the spectral width by $\Delta\tau = \frac{\kappa}{\Delta\nu}$.

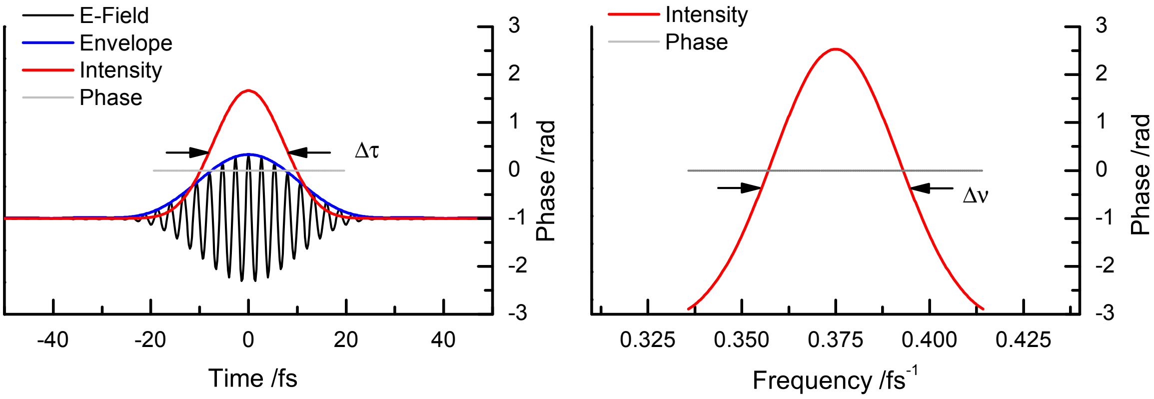

Figure 3.1.: Bandwidth limited laser pulse in time and spectral domain.

Most commonly a Ti-doped sapphire crystal is used as active material in femtosecond lasers. It has a broad emission spectrum in the range of 660 nm to 1050 nm and can be effectively pumped at around 530 nm. In addition it provides a passive phase locking by third-order nonlinear optical Kerr effects. The refractive index of a material has a nonlinear intensity dependent component n_2, which, due to its small coefficient, becomes only relevant at high intensities, for example when a laser pulse propagating through the cavity passes by. Assuming a Gaussian beam with a Gaussian TEM00 profile (see [153]), the intensity distribution across the beam front of such a pulse will create a lens like refractive index inside the laser crystal and thus leads to a focusing of the pulse. The better overlap with the pump laser favors an amplification of pulsed radiation. Additionally a pinhole can be used to block the unfocused radiation. The second Kerr effect important for the creation of a short pulse is self-phase modulation (SPM), a high order temporal phase modulation, which is induced by the longitudinal Gaussian profile of the pulse. The temporal intensity profile causes a red shift by retarding of the rising edge and blue shifts the falling side of the pulse. All in all this gives a spectral broadening of the pulse. This kind of mode-locking is called passive Kerr lens mode-locking (KLM).

The third essential element of a femtosecond source, next to the broad emitter and the phase lock, is the group velocity dispersion (GVD) compensation. As the refractive index is frequency dependent, the spectral components of the pulse propagate with different speeds, inducing a temporal divergence (cf. figure 3.2). Under normal dispersion conditions the effect of this 2nd order spectral phase component is called positive chirp. To counteract this behaviour, dispersive element assemblies build from prisms or gratings as shown in figure 3.3 are used to add a compensatory amount path difference between the different spectral components (of negative chirp). Dispersion and positive chirp effects of optical components are also an important factor outside the cavity, when the light is guided to the experiment.

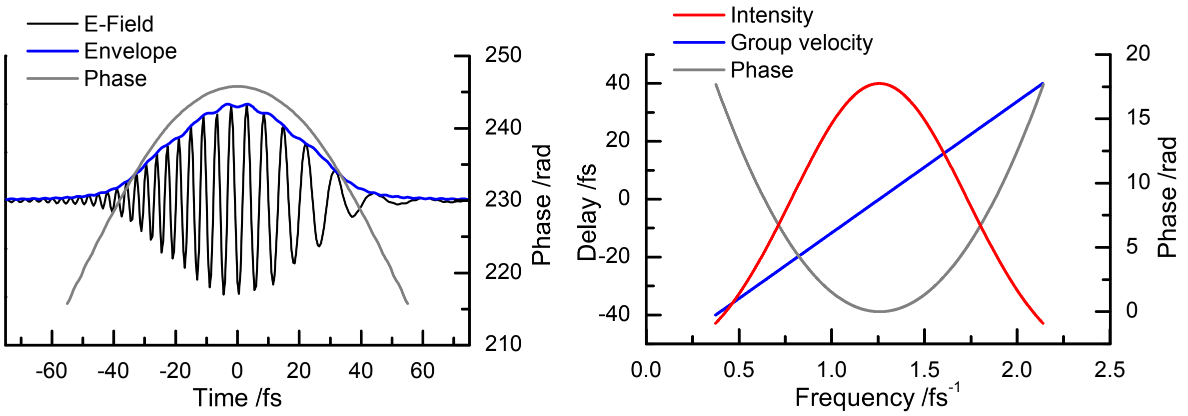

Figure 3.2.: Laser pulse with positive chirp in time and spectral domain.

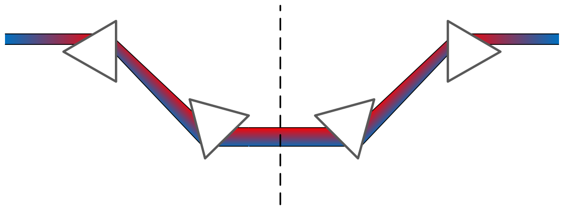

Figure 3.3.: Prism assembly for chirp compensation.

3.2. Pulse Measurement Techniques

For a full characterization of femtosecond laser pulses its intensity and phase in time or frequency domain have to be determined. Using spectrometers it is easy to obtain the intensity distribution of a pulse in the frequency domain. Common devices are based on a Czerny-Turner set-up, using a grating in combination with collimation and focussing mirrors. The detection is done with line CCD cameras recording the spatially dispersed spectral components at once, or by using a simple photo detector in combination with additional slits and rotating the grating. As it belongs to the class of one-dimensional phase-retrieval problems, the spectral phase can not be extracted, even when additional information is available. Obtaining information in the time domain is more complicated, as events in the femtosecond regime are too fast to be detected directly and shorter events as the femtosecond laser pulse are necessary for strobing. This led to the development of autocorrelation techniques and to more sophisticated methods such as frequency resolved optical gating (FROG) or spectral phase interferometry for direct electric-field reconstruction (SPIDER) discussed in the next sections.

3.2.1. Autocorrelation

As the name of this technique implies here the pulse is probed with itself. Therefore it is split and one part is delayed by a time τ using a delay stage to vary its optical path length. In the simplest approach both pulses are focused and overlapped non-collinearly in a nonlinear material like beta barium borate (BBO) (cf. figure 3.4). As discussed in section 2.3 second harmonic radiation is emitted in the direction of the two beams. Additionally SH light is emitted at an angle given by the sum of both wave vectors, with an electric field determined by both input E-fields. As this pulse is also to short to be resolved, detectors integrate over the complete signal. By scanning the delay the intensity autocorrelation function $A^2(\tau)$ can be obtained:

$$A^2(\tau) = \int_{-\infty}^{\infty} I(t)I(t-\tau)dt \tag{3.3}$$

A^2 has always its maximum at zero delay when both pulses overlap perfectly and is also strictly symmetric. The attempt to extract the temporal intensity of the pulse, fails again on a one-dimensional phase-retrieval problem, as there are infinite pulses producing the same autocorrelation trace. Even though, autocorrelation is a commonly used procedure to measure pulse lengths. When a specific, simple pulse shape is assumed, or determined by advanced methods, the full width at half maximum (FWHM) can be calculated from the autocorrelations FWHM (FWHM$_{AC}$). Normally a sech^2 or Gaussian shape is estimated, whereas the first is a more optimistic choice, resulting in a 1.54 shorter pulse referred to FWHM$_{AC}$. In this work autocorrelation measurements more conservatively are based on a Gaussian pulse shape assumption with a factor of $\sqrt{2} \approx 1.41$. Although only limited information can be extracted from intensity autocorrelation measurements, it is a quick and useful method for tuning the laser source or pulse compression assemblies, when the pulse shape is known. An advanced method is the interferometric SH autocorrelation in which both beams propagate collinearly through the nonlinear medium and interference of the fundamental and second harmonic signals add to the autocorrelation part [154]. Theses traces unveil distortions in the pulse more reliably. In 1989 Naguma et al. presented an algorithm based on interferometric AC and spectral information to calculate both intensity and phase of a laser pulse [155, 156], but it seems not to converge to a solution very well [45]. Lately Yang et al. improved this idea employing a combination of genetic algorithms and graduated optimization [157]. Finally when pulses from an amplifier system with a higher pulse to pulse noise should by characterized the above described multi-shot strategy averaging over many pulses will exhibit a large error. For this situation single-shot autocorrelators like the *SSA* from *Coherent* used in this work for quick analysis, circumvent this problem. Again the pulse is split, but this time both partial pulses undergo the same optical distance before they overlap with a large angle in a thick nonlinear crystal. Along the axis parallel to the plane of incidence and to the crystal surface the pulses arrive with different temporal relation, mapping the delay to the spatial domain. Using a line CCD camera and calibrating the time axis, the trace can be recorded with one frame.

Beside the above introduced second order nonlinear autocorrelation, also third order effect like third harmonic generation (THG), polarization gating (PG), transient grating (TG) etc. can be exploited, when the autocorrelation function (equation 3.3) is adapted accordingly.

3.2.2. FROG

Frequency resolved optical gating is from the experimental point of view only a small change to a normal intensity autocorrelation setp-up, replacing the photodetector with a frequency sensitive spectrometer and capturing the complete spectrum at every delay step (figure 3.4). Again the pulse is measured by stepwise gate out parts and spectrally resolve them. Instead of retrieving a temporal intensity distribution signal, FROG scans result in a spectrogram, a three dimensional plot showing intensity versus delay τ and frequency ω.

$$I_{FROG}(\omega,\tau) = |\int_{-\infty}^{\infty} E(t)E(t-\tau)\cdot exp(-i\omega t)\, dt|^2 \tag{3.4}$$

In equation 3.4 the case for a SHG based experiment is shown. To extract also phase information one has to solve a two-dimensional phase-retrieval problem which compared to the one-dimensional case, can be solved when some boundary conditions are given. A strong constraint in this scope is that the term describing the interaction between the pulses electrical field and the gate field is known (for SHG: $E(t)E(t-\tau)$). It is called nonlinear optical constraint. Beside some trivial ambiguities like absolute phase or time shift and temporal inversion (which can also be ruled out) this problem has a virtually unique solution. To get quantitative information about the pulse iterative methods mostly based on 2D phase-retrieval algorithms are used. For more details on the procedure compare [45].

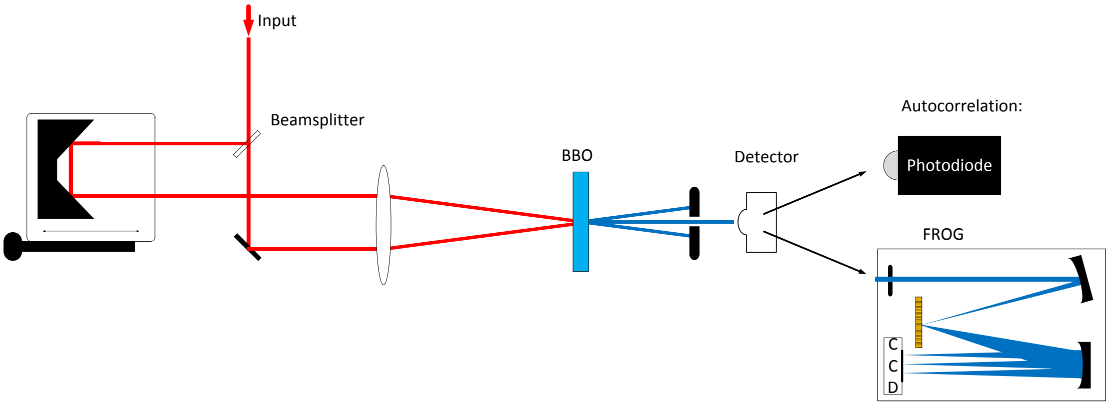

Figure 3.4.: General set-up for intensity autocorrelation using a photodiode or PMT and spectrally resolving FROG employing a spectrometer as detector.

The SHG type FROG used in this thesis is more sensitive compared to the third order options and offers the highest SNR. Of course, like in SHG autocorrelation and opposite to other types, the spectrogram is always symmetrical on the time axis and thus less intuitive. In figure 3.5 an intensity autocorrelation and a corresponding SHG FROG trace is shown for a chirped pulse represented by its temporal intensity profile. Pulses with positive or negative chirp give the same traces. To solve this, the direction of time axis can be determined by introducing a trailing satellite pulse. This can be generated by placing a piece of glass in the beam and exploiting double reflection on its surfaces [158].

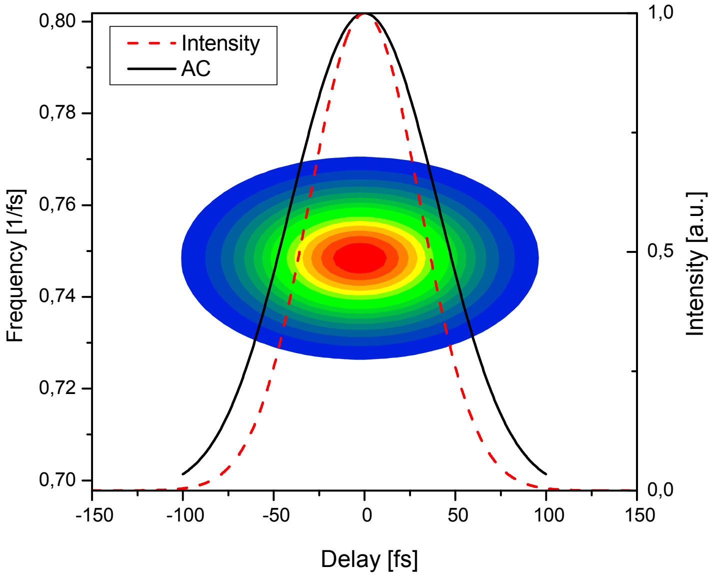

Figure 3.5.: SHG intensity autocorrelation and SHG FROG trace for a chirped pulse represented by its intensity.

4. Structural, Electronic and Optical Properties of GaAs and Pt

The metal-semiconductor hetero-structures investigated in this thesis consist of n-doped GaAs coated with thin platinum layers. Gallium arsenide itself as a binary compound with a strong oxidation affinity shows a complex behaviour of surface reconstructions, temperature depending diffusion and segregation as well as element specific oxidation. Upon deposition of metals further temperature depending processes set in, such as alloying and diffusion between the phases. Not only the morphology of the samples are affected but also their optical and especially their electronic properties. These properties are summarized in the following sections.

4.1. Gallium Arsenide

4.1.1. Structural Properties

Gallium arsenide crystallizes in the cubic zinkblende structure which belongs to the $\overline{4}3m$ space group. The unit cell contains 4 molecules of GaAs whereby every As atom is located at the tetrahedral position formed by 4 Gallium atoms and vice versa. This is shown in figure 4.1. The lattice constant at 300 K is $a = 5.65$ Å [159].

On the (100) face investigated here, the symmetry is reduced to $mm2$. The polar surface appears in many different reconstructions from Ga-rich to As-rich systems, were the detailed configuration depends sensitively on the surface preparation conditions and the crystal growth. After sputtering of epitaxial GaAs(100) layers at 770 K Van Bommel et al. found initially a (1×6) pattern with disorder lines [161]. From here two distinct configuration sets could be established by heat treatment at different temperatures. The first starts with the As-rich $c(2 \times 8)$ pattern and ends via a transition pattern in the

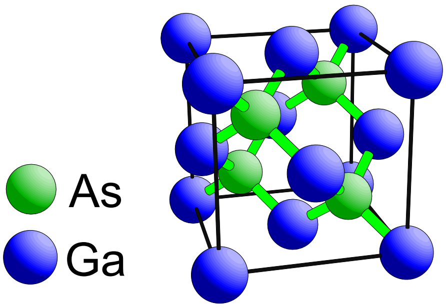

Figure 4.1.: Unit cell of GaAs.

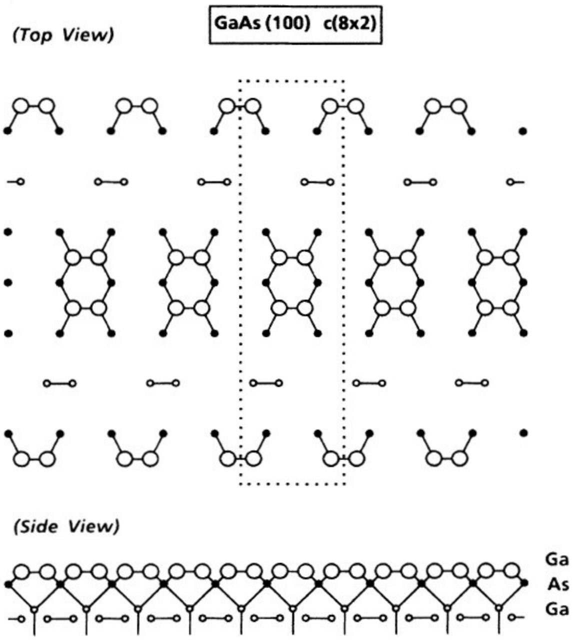

Figure 4.2.: The proposed model of the $c(8 \times 2)$Ga surface reconstruction based on STM measurements. Reprinted from [160] with permission from APS.

Ga-rich $c(8 \times 2)$ structure:

$$\mathrm{c}(2 \times 8) \underset{620\ \mathrm{K}}{\overset{720\ \mathrm{K}}{\rightleftharpoons}} \mathrm{c}(6 \times 4) \underset{720\ \mathrm{K}}{\overset{770-870\ \mathrm{K}}{\rightleftharpoons}} \mathrm{c}(8 \times 2).$$

After two to three complete heat treatment cycles (here a cycle refers to starting from a c(2×8) face, increase the temperature in steps to 870 K to obtain a c(8×2) reconstruction and afterwards decrease the temperature by the steps given above to finally return the starting configuration), the second set appears, where the two low temperature reconstructions are replaced by $c(1 \times 6)$ patterns with different disorder lines. Finally, after some further iterations, the only stable phase up to 870 K they could establish was $c(8 \times 2)$. This indicates that the initial diffusion of arsenic atoms ceases after a number of heat treatments. Also Drathen and co workers analysed molecular beam epitaxy (MBE) grown GaAs (100) samples with LEED and Auger electron spectroscopy (AES) [162]. In addition to the patterns reported by van Bommel and other groups, they found more intermediate and mixed structures. Using peak height analysis from AES referenced to a standard with known composition they estimated the As coverage in the top layer. This is summarized in table 4.1. Mendez et al. studied which of the patterns produced by MBE can be obtained also with simultaneous ion bombardment and annealing (SIBA) of single crystal samples [163]. It showed that the arsenic rich compositions are not accessible with this technique. The temperatures applied in the SIBA process are shown in the third column of table 4.1 at the corresponding patterns. The AES measurements of Mendez et al. are not in good agreement with those of Drathen as both use different reference surfaces in the Auger peak height analysis [163].

As coverage	**Structure**	**SIBA temperature /K**
0.22	$c(8 \times 2)$Ga	>800
0.27	(4×6)Ga	770-800
0.37	$c(6 \times 4)$	-
0.52	(1×6)	750
0.61	$c(2 \times 8)$As	-
0.75	(2×4) As*	-
0.86	$c(4 \times 4)$As	-

Table 4.1.: Surface coverage of As and the corresponding reconstructions of GaAs (100) as found by Drathen et al. [162] or, marked with a $\star$, by Armstrong et al. [164]. The SIBA temperatures were determined by Mendez et al. [163].

Later STM measurements by Biegelsen et al. unveiled some of the prominent stable structures [160, 165]. It was found that the (1×6) reconstruction consists actually of

(2×4) units containing two As-As dimers. The model surface for the high temperature $c(8 \times 2)$Ga phase, generated from the STM results, is shown in figure 4.2. It most likely consists of unit cells with two dimerized gallium atoms, but also other structures with one, three Ga dimers and even with an arsenic termination are discussed [166]. Both the LEED studies and the STM measurements yield that the (4×6)Ga pattern is actually an overlap of (4×1) and (1×6) regions.

A self limited surface oxidation process occurs on GaAs samples exposed to air and a so called native oxide layer is formed. Due to its technical importance the growth mechanisms of oxide layers have been investigated with many different methods like Raman scattering, AES, ellipsometry and TPD. Most experiments employ in-situ oxidation in a defined environment while monitoring changes on the substrate. Oxygen can adsorb on GaAs in molecular or dissociated form (sticking coefficient $\approx 10^{-5}$ [150]), whereby the dissociation is defect induced and can be exited thermally or by the kinetic energy of the incoming oxygen molecules [167]. In thermal desorption experiments on samples with low defect density the molecular O_2 desorption peak at 394 K dominates, while on defect rich specimen mostly Ga_2O is found. On undoped samples the initial oxidation step is a diffusion of oxygen into the substrate in compliance with Fick's law, which is followed by a second diffusion process in the course of the oxidation [168]. The process is limited by the formation of an arsenic layer at the oxide-GaAs interface, which exhibits a crystalline structure detectable by a phonon mode in Raman scattering experiments (7.8 THz). Negative doping on one hand hampers the crystallization of the As layer, while on the other hand reduces the speed of the first diffusion step.

The oxide layer thickness on different, in ambient air oxidized samples, was found to be in the range of 23 to 29 Å, determined by ellipsometry and gracing incidence X-ray diffraction (GIXR) [169]. Other authors specify the oxide layer thickness with 50 – 80 Å [150, 170]. With the x-ray method also surface roughness parameters were determined to be in the range of 4 to 6 Å, for both surface and interface. Corresponding measurements by AFM yielded a roughness of only 2 to 3 Å. X-ray photoelectron spectroscopy suggest a multi layered architecture with As, As_2O_3 and Ga_2O_3 species close to the bulk - oxide interface and mixed oxides comprising of $GaAsO_3$ and $GaAsO_4$ close to the surface of the oxide layer [171]. In deoxidation routines by controlled heating in a vacuum, the low temperature desorption of Ga_2O was confirmed. Additional As_2O_3 was found to desorb in this range. At high temperatures (850 to 1000 K) Ga_2O_3 is removed from the surface [169]. Allwood and coworkers also recorded AFM pictures for the different de-oxidation temperatures (see figure 4.3). At low temperatures the surface is amorphous, while

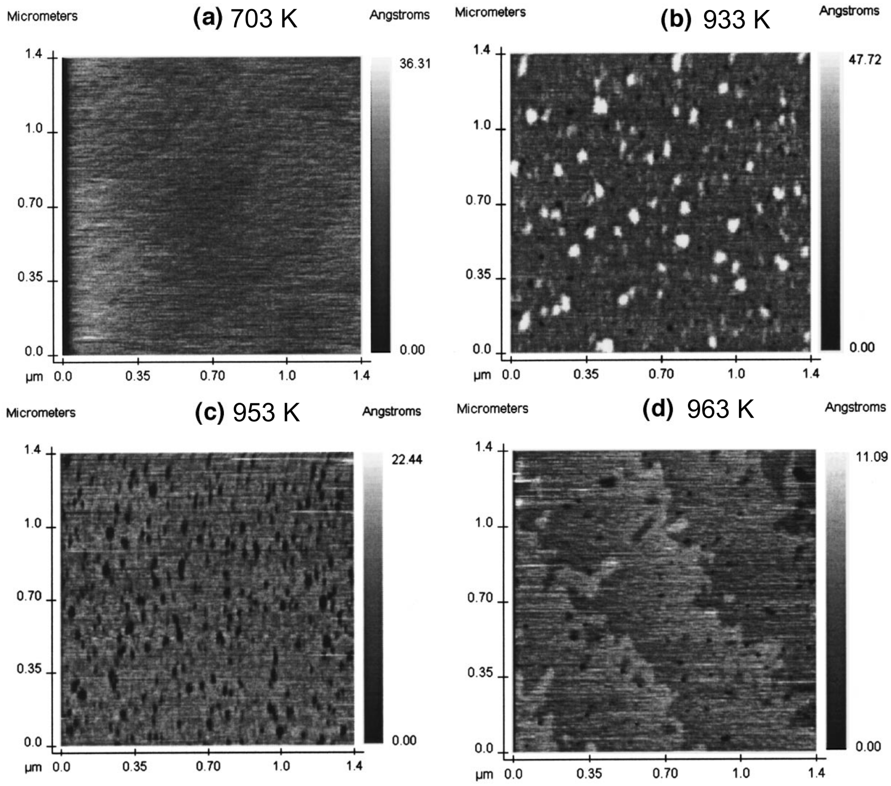

Figure 4.3.: AFM pictures of partly de-oxidized GaAs samples. Reprinted from [169], with permission from Elsevier.

with increasing temperature islands in a height range comparable to the measured oxide thickness appear. On samples deoxidized at 963 K atomic steps become visible. Based on STM measurements on native oxide covered n-doped GaAs (100) samples Torkhov proposed the formation of a grained structure of nanoclusters made of gallium and arsenic oxides [172]. They too witnessed the formation of an As layer at the oxide/bulk interface, in contrast to the findings on n-doped samples of Rim and Beserman [168] discussed before. The discrepancy may be explained by the lack of crystallinity.

4.1.2. Electronic Properties

The band structure of bulk GaAs as a typical III-V compound semiconductor is displayed in figure 4.4. The $\Gamma \rightarrow X$ direction corresponds to $\langle 100 \rangle$, while $\Gamma \rightarrow L$ points at the $\langle 111 \rangle$ direction. The valence band maximum is located at the Γ point in the zone centre (Γ_8). Here the levels of the light and heavy holes are degenerated and together with the split-off band, which is shifted to lower energies due to spin-orbit coupling, have p like character. The direct band gap transition to the s-like conduction band minimum (Γ_6) is allowed by selection rules.

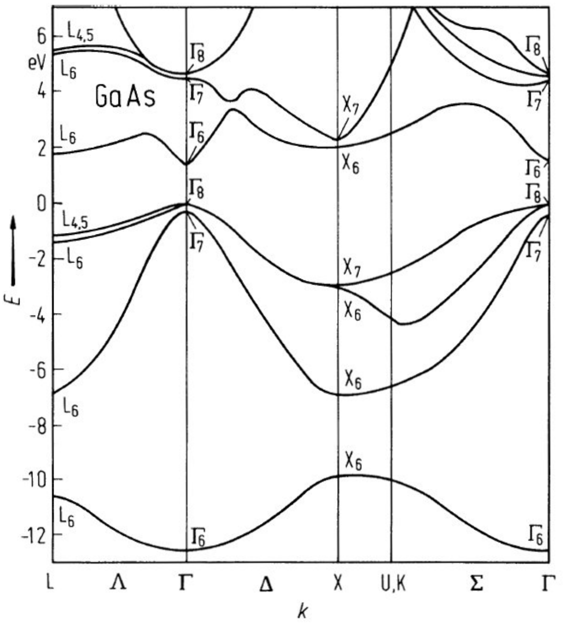

Figure 4.4.: The band structure of GaAs obtained by non-local pseudopotential calculations. Reprinted from [173], with permission from Springer.

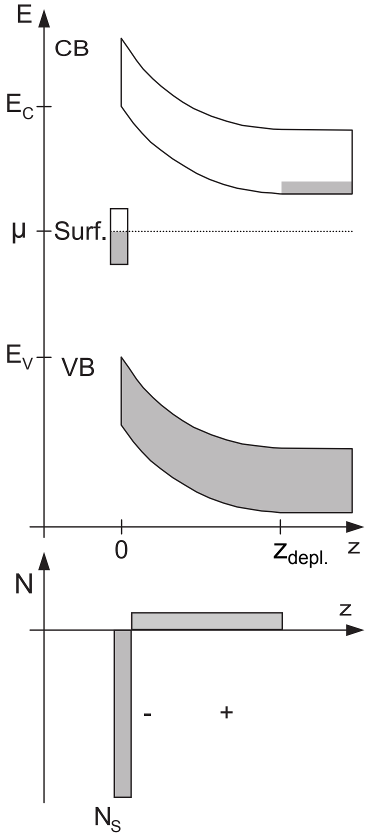

Figure 4.5.: Band bending in the depletion zone of a n-doped semiconductor. Adapted from [174].

E_g /eV (0 K)	E_g /eV (300 K)	Δ /eV	m_e^*	m_{hh}^*	m_{lh}^*	m_{so}^*
1.519	1.424	0.34	0.067	0.5	0.08	0.15

Table 4.2.: Band structure parameters of GaAs [41]. Δ is the spin-orbit splitting energy, the subscripts in the effective mass terms stand for electrons, heavy holes, light holes and split-off holes.

The energy dispersion of valence (E_V) and conduction bands (E_C) close to the Γ point can be described by the nearly free electron model:

$$\begin{aligned} E_C(k) &= E_g + \frac{\hbar^2 k^2}{2m_e^*} \\ E_V(k) &= -\frac{\hbar^2 k^2}{2m_h^*} \end{aligned} \tag{4.1}$$

where E_g is the direct band gap energy and m_e^* and m_h^* are the effective masses of holes and electrons. The deviation of the latter quantities from the free electron mass m_0 reflect the influence of the periodic lattice potential [41]. Vice versa, usually the effective mass is calculated from the curvature of the bands:

$$m^* = \hbar^2 \frac{dk^2}{d^2E} \tag{4.2}$$

The parameters of GaAs are enlisted in table 4.2, where the masses are given in multiples of m_0. In general, surface reconstruction of the (100) face induced by dangling bonds leads to the formation of localized states whose energy levels are situated within in the band gap (figure 4.5). These states are formed by valence and conduction band states, so their occupation is defined by the number of electrons taken from the valence band. The total neutrality is not affected. Depending on the position of the surface states with respect to the Fermi level, they can be donor or acceptor states. In n-doped samples at temperatures $T \gg 0$ K, the dopant excess electrons are located mostly in the conduction band, from where they can make a transition into the acceptor states driven by a reduction of the overall energy. This trapping of impurity electrons in a small layer within the surface results in a surface charge denoted by a charge density N_S. As a consequence free electrons within a defined volume below the surface states (depletion region) are repelled by this potential leaving behind naked holes, compensating the surface charge. On one hand the local change of the equilibrium concentration between

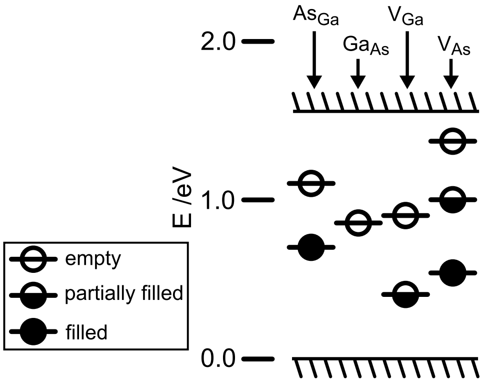

Figure 4.6.: Defect states and their energy level in GaAs. $\mathrm{Ga_{As}}$ and $\mathrm{As_{Ga}}$ are anti sites, $\mathrm{V_{As,Ga}}$ label vacancies. Adapted graph from [176, 177].

holes and electrons changes the position of the Fermi level relative to the valence and conduction band, while on the other hand at the surface it is pinned to the surface states. To retain a constant Fermi level throughout the crystal the bands have to bend upwards [101]. The length of the depletion zone is a function of the material parameters as dopant type and concentration and can be calculated using Poissons equation [175] (cf chapter 7). For a GaAs crystal n-doped with Si ($\approx 3 \times 10^{18} cm^{-3}$) Chang calculated the surface field to be −720 kV/cm and a depletion width of 136 Å [150]. For GaAs(100) the Fermi pinning is usually not attributed to the formation of dangling bonds but to a native point defect with acceptor properties. This mid band gap state is commonly labelled EL2. Figure 4.6 shows typical defects for GaAs [176, 177].

4.1.3. Optical Properties

In figure 4.7 the real and imaginary parts of the complex refractive index of GaAs are shown [178]. The calculated reflectivity, transmission and absorption coefficients for a 500 µm thick sample at normal incidence are displayed in figure 4.8. In the near infrared region the band gap at 1.424 eV (871 nm) is the most dominant feature in the transmission and absorption data. The dopant type and its concentration influences the absorption properties in the close vicinity of this transition [179]. In the lower end of the visible spectrum, close to the range of the Ti:Sa laser second harmonic frequencies and below (cf. section 3), the optical properties are determined by electronic transitions (e.g. the two photon resonance of the band gap at 436 nm). More detailed measurements of the reflectivity in a lager energy range can be found in [180]. In the infrared region between 1 to 5 µm (not shown), the measured absorption is an overlap of transitions between the zone center conduction band minimum and the indirect minimum X_6 and

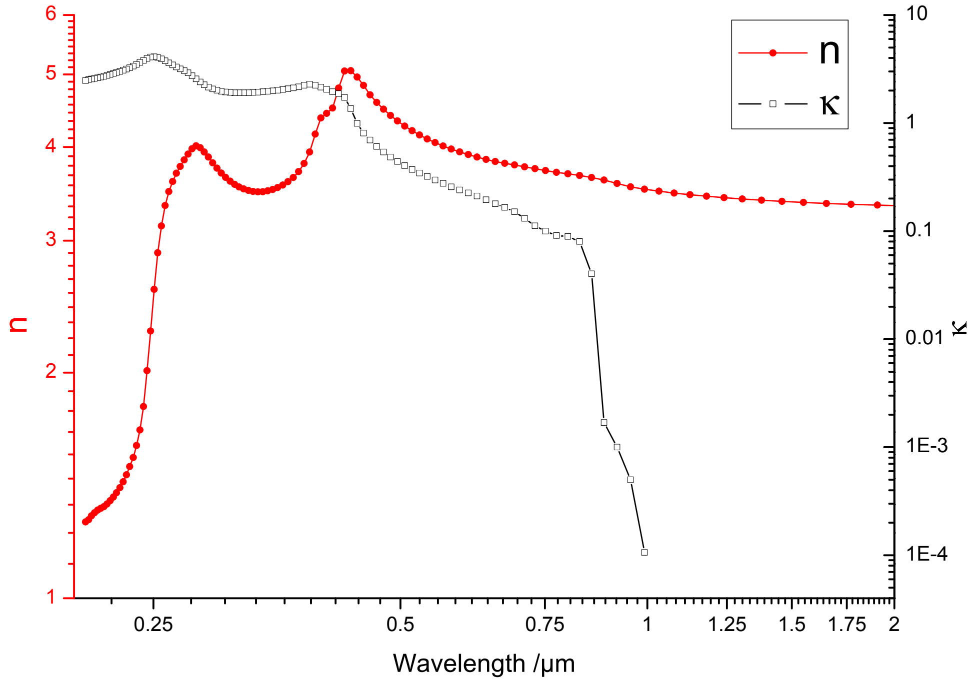

Figure 4.7.: The real and imaginary part of the refractive index of GaAs from [178].

free carrier absorption [181]. At higher wavelengths the free carrier absorption is dominating [179]. The dielectric constant ϵ_∞ for GaAs is 12.9, for the native oxide covered samples a value of 12.7 is found [150].

In n-doped GaAs the negatively charged surface states induce a band bending by driving the free electrons away from the surface layer. The resulting DC electric field lowers the symmetry from $\bar{4}3m$ to $mm2$ inside the depletion region and thus changes its optical properties.

For electric dipole approximation the non-vanishing elements of the second order nonlinear susceptibility tensor $\chi^{(2)}$ are summarized in figure 4.9 in the nonlinear coefficient tensor notation (compare section 2.3) for the relevant crystal classes. For the bulk region of GaAs the non-vanishing elements are: $\chi^{(2)}_{xyz} = \chi^{(2)}_{yzx} = \chi^{(2)}_{zxy}$. For the surface layer they are: $\chi^{(2)}_{xzx} = \chi^{(2)}_{zxx}$, $\chi^{(2)}_{yyz} = \chi^{(2)}_{zyy}$ and $\chi^{(2)}_{zzz}$ (when Kleinman symmetry applies). The directions of the indices are given in table 4.3.

Qi et al. treated the effect of the depletion layer to the nonlinear response as a perturbation of bulk susceptibility elements [182]. As effects on tensor elements which are zero in the bulk were to small to be detected, only a change in the bulk $\chi^{(2)}_{xyz}$ element has to be considered. Here the depletion area adds destructively, with a term proportional to the square of the static depletion field, leading to a lowering of the measured SHG intensity

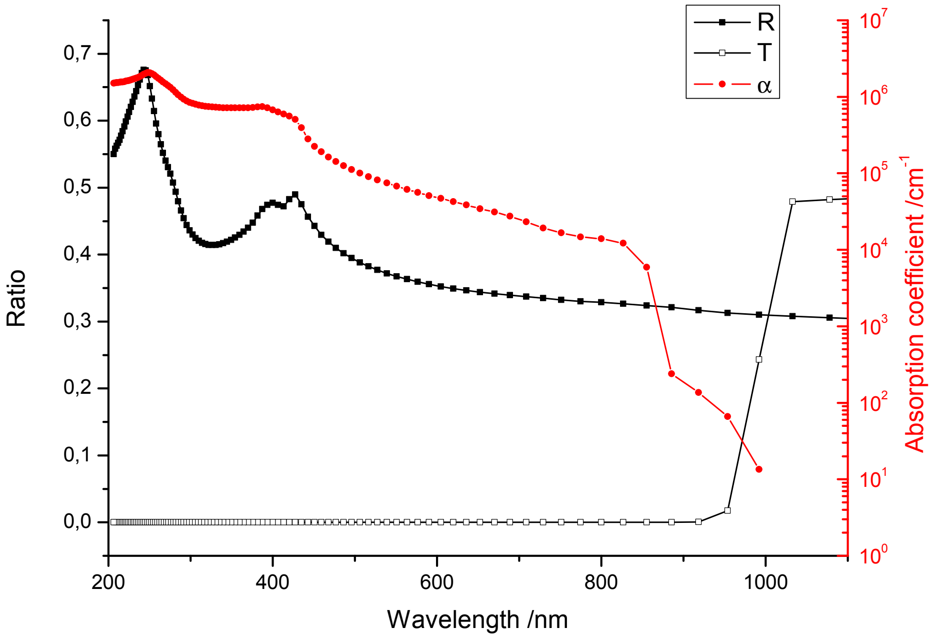

Figure 4.8.: Reflectivity, transmission and the absorption coefficient calculated from the complex refractive index shown in figure 4.7.

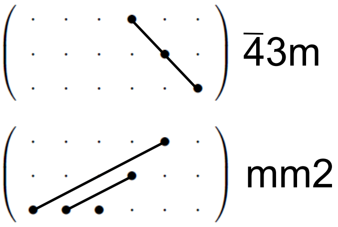

Figure 4.9.: Non-vanishing second-order nonlinear coefficient tensor elements for GaAs bulk and GaAs 100 surfaces. The bold dots represent non zero elements. The lines connect elements of same value, when Kleinman symmetry is applicable.

Index	$\bar{4}3m$	$mm2$
x	{010}	{011}
y	{001}	{0$\bar{1}$1}
z	{100}	{100}

Table 4.3.: Symmetry axes used for the point groups.

with increasing depletion field. These effects belong to the class of electric-field induced second harmonic generation (EFISHG) first discovered by Lee et al. [183]. The static fields lead to a higher order tensor contribution to the radiated second order light. As the depletion field is perpendicular to the surface, only elements related to the z component of the static field have to be considered. Thus the overall depletion polarization term is [150, 184]:

$$\begin{aligned}\vec{P}^{(2)}_{depl.}(\Omega) = \epsilon_0 \sum_{j,k=1}^{3} \chi^{(2)}_{ijk}\vec{E}_j(\omega)\vec{E}_k(\omega) + \epsilon_0 \sum_{j,k=1}^{3} \chi^{(3)}_{ijkz}\vec{E}_j(\omega)\vec{E}_k(\omega)\vec{E}_z(0)\\ + \epsilon_0 \sum_{j,k=1}^{4} \chi^{(4)}_{ijkzz}\vec{E}_j(\omega)\vec{E}_k(\omega)\vec{E}_z(0)\vec{E}_z(0),\end{aligned} \tag{4.3}$$

where the tensor elements are given in bulk coordinates (refer to table 4.3). The surface and the bulk terms are equal to the formulation in eq. 2.58, where non-local contributions of the bulk can be neglected. The effective total second-order polarization term in GaAs finally assembles to:

$$\begin{aligned}P^{(2)}_{eff.,x,y}(\Omega) &= P^{(2)}_{surf.,x,y}(\Omega) + i\frac{P^{(2)}_{bulk,x,y}(\Omega) + P^{(2)}_{depl.,x,y}(\Omega)}{k_z(\Omega) + 2k_z(\omega)}\\ P^{(2)}_{eff.,z}(\Omega) &= P^{(2)}_{surf.,z}(\Omega) + i\frac{\epsilon_2(\Omega)}{\epsilon'(\Omega)}\frac{P^{(2)}_{bulk,z}(\Omega) + P^{(2)}_{depl.,z}(\Omega)}{k_z(\Omega) + 2k_z(\omega)}\end{aligned} \tag{4.4}$$

It is possible to separate the different surface, bulk and depletion zone tensor elements by choosing appropriate combinations of input and output polarization and rotational alignment. Stehlin et al. calculated effective Fresnel factors and analysed the bulk and surface contributions upon rotation and in this way could determine the parameters with surface sensitivity [185], although they didn't consider a depletion zone effect. They verified their findings by monitoring the change of SH response of a GaAs (100) surface while evaporating Sn. Surface sensitivity can be achieved on a (100) face for example with p polarization for both pump and detected light, while aligning the {001} axis of the crystal with the plane of incidence (see also table 4.4).

Rotational SHG measurements on GaAs plates were first published by Krasnov et al. [187]. They used either the fundamental 1.064 µm or the second harmonic output at 532 nm of a Nd:YAG laser to probe (111) and (100) GaAs surfaces. For the (111) faces

Input polarization	**Output polarization**	**Sample rot. angle (deg)**[a]	**Tensor element of $\chi^{(2)}$**
p	p	0	zzz[b]
p	s	45	yyz = xxz
s	p	0	zyy = zxx
s	s	-	none

---

[a] Azimuthal angle relative to the {001} direction.

[b] The zzz component is measured among other elements, but is dominant.

Table 4.4.: Surface specific polarization and sample orientation combinations and the appropriate tensor elements. The data is taken from Stehlin [185], the table layout from Armstrong [186].

Krasnov found a substantial contribution from SH light generated upon reflection from the backside of the sample to the signal generated at the top side. When probing samples with a rough backside, the overall signal was found to be smaller by nearly a factor of ten. The backside reflection could be suppressed by using above band gap light which reduces the effective attenuation length below the sample thickness, but also the overall SH intensity. On the (100) faces they could not detect any SH signal, when the back reflection was eliminated.

Armstrong et al. [186] took a closer look at the interface of native oxide covered GaAs (100) samples, probing with different polarization configurations to work out the individual susceptibility tensor elements as calculated by Stehlin. Their results are summarized in figure 4.10 [186, 188, 189]. The upper curve shows the p-in s-out configuration which is surface sensitive at a rotational angle of 45°, and subsequently at 135°, 225° and 315°, because of the fourfold symmetry. In the initial publication [190] where the plot was erroneously shifted 45°, the peaks were detected at these angles and Armstrong claimed that the intensity of all of those is equal [sic], and that this is an indication for the isotropic surface structure. According to the authors this is consistent with a model in which the dominant SHG source is located at the buried GaAs oxide interface and where the contribution of the amorphous oxide layer is weak only. Unfortunately they did not update their argumentation, after correcting the graph. The lower curve shows the p-in p-out configuration and a strong anisotropy between the [011] and $[01\bar{1}]$ directions. It was assumed that this arises from a varying oxide layer thickness like on Si samples. Yamada argued that these differences arise from an interference between the isotropic surface response and a fourfold bulk contribution [188, 191] which lowers the symmetry to C_{2v}. Steps in the surface layer or different oxide layer diameters should

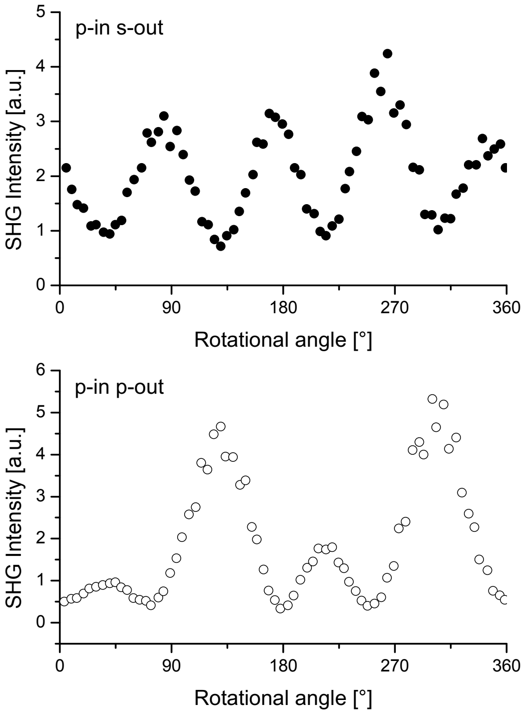

Figure 4.10.: Rotational SHG measurement in two different configurations (cf. table 4.4) on native oxide covered GaAs(100). After Armstrong (corrected version) [186, 188, 189].

further lower the surface symmetry to C_1 (m) and thus manifest themselves in different intensities of all peaks. Bearing in mind the measurement uncertainty, this could be seen in the p-in p-out results of Armstrong (figure 4.10).

This idea was picked up by Takebayahi et al. [192] and they demonstrated the use of rotational SHG measurements to determine the tilt angle of a GaAs (100) wafer surface in comparison to x-ray methods. In their analysis they fitted the tensor elements, tilt angle and direction iteratively between all four polarization combinations probed. As a result of fitting to purely bulk elements of the tilted substrate they found configurations with s-polarized incident light to be very sensitive to changes in the tilt angle, making it the dominant indicator for wafer miscut. Further Takebayahi et al. pointed out that the low symmetry of the p-in p-out results can be used to distinguish between the [011] and $[01\bar{1}]$ directions also on untilted samples, which is raised by a 180° phase shift in the electronic wave functions along the two directions. This in turn is caused by opposite distribution of Ga and As atoms along the chains.

Yamada and Kimura developed a model to include the effects of interference and surface steps by deriving the model originally published by Sipe for centrosymmetric materials [99, 193].

As discussed in section 2.3.2 for a specific symmetry, the rotational SHG response can be fitted by the following general model:

$$I_{\alpha,\beta}^{(\Omega)} \propto \left| \sum_{n=0}^{m} A_n^{\alpha,\beta} \cos(n\phi) + \sum_{n=1}^{m} B_n^{\alpha,\beta} \sin(n\phi) \right|^2 . \tag{4.5}$$

Here α and β are the polarizations of the pump and emitted light, m specifies the symmetry (eg. $m = 2$ for a twofold response), the fitting coefficients A_n and B_n are linear combinations of nonlinear susceptibility tensor elements from bulk, surface and depletion region and ϕ is the azimuthal angle.

In his thesis Chang shows rotational SHG scans on n-doped GaAs (100) samples were he takes into account depletion field effects. Figure 4.11 shows the individual tensor contributions in the different layers to the rotational fitting coefficients. In contrast to the work of Qi also third order terms add to the signal. From this figure it can be seen that in no configuration the isotropic coefficient is determined by surface contributions only, but is always mixed with depletion zone effects. But this influence can be removed or at least reduced by an intense preceding pump pulse to screen the depletion field ($\vec{E}_{depl.} = 0$) (see section 4.1.4). At the same time Germer at al. [1] investigated the influence of doping density and excitation wavelength on the fitting parameters in rotational SHG measurements. They too developed an EFISHG model and concluded that the depletion field contribution to SHG surpasses any surface effects. In this model the depletion zone SHG affects the isotropic response to first order only and the anisotropic component at second order. Here it interferes with the unperturbed bulk response.

Looking at the discussion above it shows that the many different contributions to the SHG signal in GaAs in combination with the large parameter space, which includes polarizations, incidence angles, rotational angles, wavelength dependence, coherence length as much as material parameters like tilt angles, surface and backside roughness etc. make the discussion complex. This can be illustrated with a publication from Kravetsky et al. [190] in which once more GaAs (100) samples with different tilt angles were probed with the NIR radiation from a Nd:YAG laser. For all samples a signal in s-in / s-out configuration was detected, which according to Takebayahi et al. [192] should vanish for 0° tilt. They explained it by a possible leakage of p-polarized light through the analysing polariser.

Configuration		Bulk	Depletion zone			Surface
p-in / p-out $\lvert A_0 + B_2 sin(2\phi)\rvert^2$	B2	$\chi^{(2)}_{bulk}$	$\chi^{(2)}_{bulk}$	$\chi^{(3)}_{bulk}E_{depl.}$	$\chi^{(4)}_{bulk}E_{depl.}E_{depl.}$	$\chi^{(2)}_{surf}$
	A0			$\chi^{(3)}_{bulk}E_{depl.}$		$\chi^{(2)}_{surf}$
p-in / s-out $\lvert A_2 cos(2\phi)\rvert^2$	A2	$\chi^{(2)}_{bulk}$	$\chi^{(2)}_{bulk}$		$\chi^{(4)}_{bulk}E_{depl.}E_{depl.}$	$\chi^{(2)}_{surf}$
s-in / p-out $\lvert A_0 + B_2 sin(2\phi)\rvert^2$	B2	$\chi^{(2)}_{bulk}$	$\chi^{(2)}_{bulk}$			
	A0			$\chi^{(3)}_{bulk}E_{depl.}$		$\chi^{(2)}_{surf}$

Figure 4.11.: Susceptibility tensor contribution to the rotational fitting coefficients. From Chang [150]

4.1.4. Dynamic Electronic Properties and Their Optical Response

Interband transitions in GaAs triggered by ultrashort laser pulses with photon energies above the band gap can be treated as delta functions initially creating a large density of excited carriers with a narrow energy distribution and defined momentum. The fastest process with a timescale of 10^{-14} s is the randomization of momentum by (in)elastic scattering events [11, 194]. In a time span of up to 10^{-13} s electrons and holes establish individual temperatures as they thermalize into Fermi-Dirac distribution by carrier-carrier scattering. Under standard conditions, the carrier temperatures are fundamentally higher than that of the lattice ($T_e \neq T_h > T_L$). Ippen et al. found that the initial relaxation times are depending on the carrier density and on the band gap, which they modified by adding Al to the gallium arsenide lattice. In their experiments they found relaxation times between $13 - 30$ fs [195]. The dominating process in thermalizing lattice and carrier temperatures in gallium arsenide is the emission of optical phonons with small wave vector (intra valley carrier-phonon scattering). Furthermore electrons can be scattered into the side valleys of the conduction bands (L and X) by interacting with large wave vector optical phonons (cf. section 2.4). The energy dissipation into phonons takes some 10^{-12} s in which the electrons move towards the conduction band

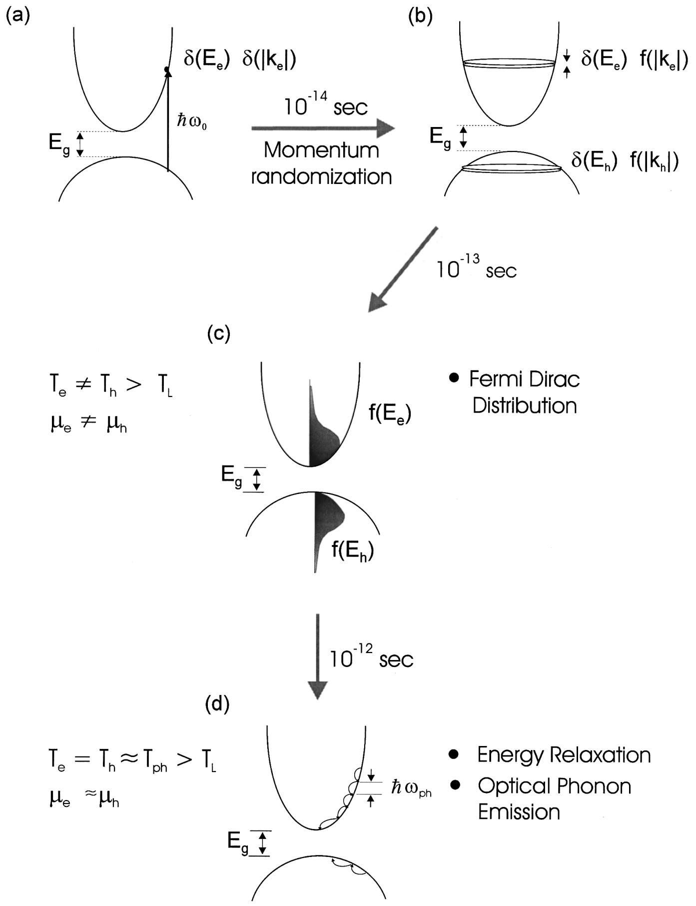

Figure 4.12.: Schematic flow of carrier relaxation into band minima after excitation by an ultrashort laser pulse above the band gap [11]. Reprinted with permission from AIP Publishing.

minimum and the holes to the valence band maximum, respectively. These steps are shown in figure 4.12 [11].

The carriers reside at the band edge until they either recombine emitting a photon (see section 2.2.1) or lose their energy in a non-radiative way like Auger recombination. Depending on their density they form a thermal quasi-equilibrium according to Boltzmann statistics in the low excitation regime or have to be treated by Fermi-Dirac statistics at high laser intensities. The latter case also causes carrier degeneracy broadening the emission spectrum [41]. The optical phonons itself decay by phonon-phonon scattering ($\approx 10^{-11}$ s) into low energy modes. The temporal difference of optical phonon generating processes to the annihilation events can lead to an accumulation of high energetic optical phonons (hot phonons) which hinder carrier relaxation by re-absorption [196, 197]. These processes are summarized in the flow chart depicted in figure 4.13 [11, 194].

In time-resolved transient absorption measurements Shah et al. investigated the change

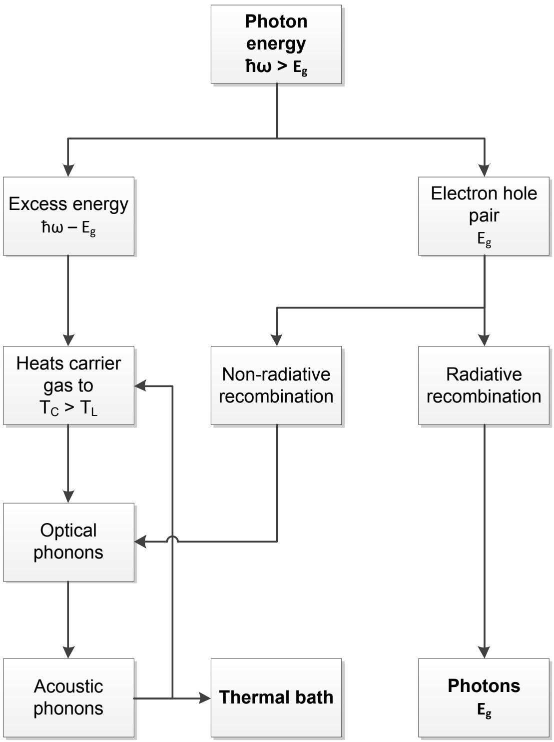

Figure 4.13.: Flow chart of carrier relaxation processes in GaAs. After [11, 194].

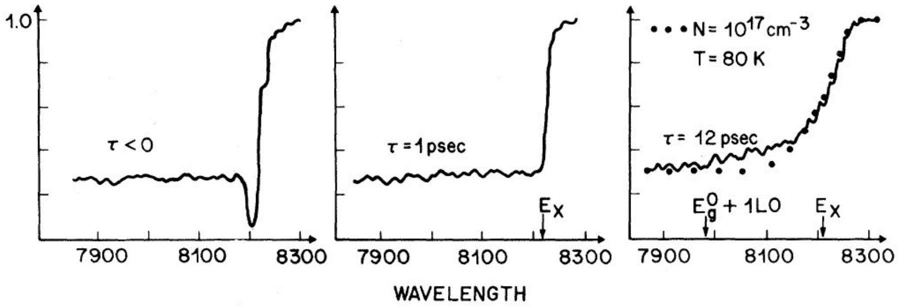

Figure 4.14.: Time-resolved transmission spectra of GaAs after excitation with an ultrashort laser pulse [198]. Reprinted with permission from APS.

in near band gap transmission of thin GaAs samples cooled to 80 K after strong excitation by an ultrashort laser pulse. They used a < 0.5 ps pump pulse at 750 nm for excitation, the transmission was probed by a delayed broadband sub picosecond continuum pulse. Their results for different temporal intervals between excitation and probing are shown in figure 4.14. Without excitation the transmission spectra displays features of free exciton absorption at 820 nm and the absorption for above band gap photons (left panel). One picosecond after the excitation the exciton absorption is screened and the band edge is shifted to higher frequency due to band gap renormalization caused by the large density of free carriers. At higher delays the relaxation of carriers into states near the band edge lead to a reduction of absorption which is shown in the right frame of figure 4.14 (band-filling).

Additionally spatial effects have to be considered as the excitation is localized into a volume defined by the light spot diameter and the absorption depth of GaAs. A combined diffusion of holes and electrons (ambipolar diffusion) sets in, which lasts for a timescale of nanoseconds. The diffusion coefficient in the excitation region is substantially influenced by the elevated carrier temperatures.

Some experimental and theoretical results indicate that the excitation of a large number of hot carriers induces a destabilization of the covalent bonds and that optical pump-probe measurements scan the subsequent change in the electronic band structure rather than the previously discussed (cf. section 2.2) effects of free carriers [199, 200].

Also second harmonic generation effects can be used in combination with pump-probe experiments to study the different relaxation processes of hot electron and phonons in GaAs samples [201–203]. In figure 4.15 the results of a time-resolved SHG measurement on a clean GaAs (110) sample in p-in / p-out configuration using a femtosecond laser source delivering 35 fs pulses at 850 nm are shown.

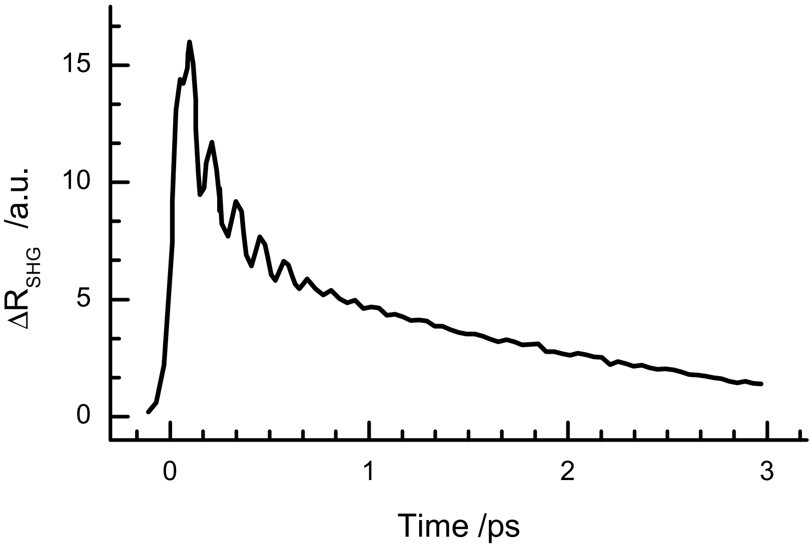

Figure 4.15.: Time-resolved SHG measurements on a GaAs (110) faced sample. The surface was prepared and held under UHV conditions. The laser is incident on the {001} plane and is p-polarized. The detected signal was also analysed in p-polarization. Data from [203].

The SHG signal consists of a sharp rise at the zero delay point between pump and probe pulse and a consequent decay process. This curve is modulated by a distinct underdamped oscillation waveform. Because of the larger surface sensitivity of the SHG signal compared to linear reflectivity used in previous works, the signal is naturally more influenced by surface carriers and especially from depletion zone dynamics. The rising edge is explained by the injection of hot carriers $\partial\chi^{(2)}/\partial n_{e,h}$ and the resulting screening of the depletion field which reduces the constant electric field terms in equation 4.4. The decaying part reflects the different recombination, scattering and diffusion processes as described in section 8.2.1 [202, 203].

The oscillation is related to the coherent lattice vibrations which are discussed in section 2.4.1. This contributes to the nonlinear susceptibility tensor in form of hyper-Raman tensor elements [115, 202, 203]:

$$\chi^{(2)} = \chi_0^{(2)} + \sum_n \frac{\partial\chi^{(2)}}{\partial\hat{u}_n}|_0 U_n, \tag{4.6}$$

where U is the amplitude of phonon n and $\hat{u}_n$ is its normalized polarization vector. The non phonon related contributions are summarized in the $\chi_0^{(2)}$ term. In the case of a thermalized system the random distribution of phonon modes extinguish the phonon contribution to the signal. As the SHG intensity measured in an experiment is proportional to the susceptibility terms, the phonon oscillation contributes in two ways:

$$I(2\omega) \propto |\chi_0^{(2)}|^2 + |\chi_{phon.}^{(2)}|^2 + 2Re(\chi_0^{(2)} \cdot \chi_{phon.}^{(2)}), \tag{4.7}$$

where $\chi_{phon.}^{(2)}$ represents the phonon term which will be small and negligible. A larger effect is contributed from the third term, thus the detection relays on a heterodyne method and the oscillation may only be detectable in systems with an additional strong non-phonon susceptibility, like it is the case for gallium arsenide [115].

4.1.5. Phonon Properties

Figure 4.16 shows the calculated (solid lines) and measured (open circles and triangles) values for the phonon dispersion in gallium arsenide [204]. The optically active LO and TO modes at the zone centre have frequencies of 8.76 and 8.07 THz respectively.

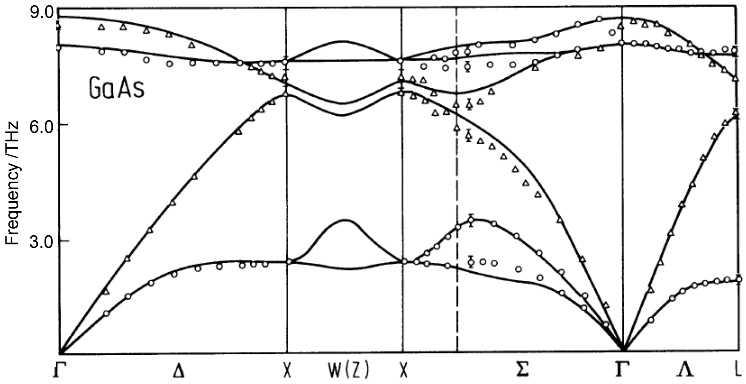

Figure 4.16.: Calculated phonon dispersion in GaAs (solid lines). The open circles and triangles are results from neutron scattering. Reprinted from [204], with permission from Springer.

The first studies on coherent phonon excitation in GaAs were performed by Kurz, Kütt et al. [151, 205]. They found a strong excitation of the $\vec{k} = 0$ LO phonon mode at 8.8 THz with a dephasing time of 2 ps for an injected carrier density of 1×10^{-17} cm^{-3}, decreasing to 0.7 ps at 1×10^{-18} cm^{-3} carrier density in reflectivity electro-optical sampling (REOS) [206] measurements on intrinsic GaAs(100). The amplitude of this vibration is controlled by the strength of the initial space-charge field [123]. Changing the depletion field by biasing revealed a linear relation. They eliminated ISRS as driving mechanism by symmetry considerations and addressed acceleration of carriers in the depletion field as the source of ultrashort polarization responsible for launching coherent phonons

(TDFS mechanism). Simulations based on drift-diffusion equation (DDE) supported this assumption quantitatively [207]. Additionally they found the rise of the TO phonon mode at 8 THz in the high carrier density regime (5×10^{18} cm^{-3}), which finally dominates the response at very high excitations. This can be explained by considering the coupling of phonons to plasma oscillations [208]. Kuznetov and Stanton performed numerical calculations on the coupling between coherent plasmons [209] and LO phonons in GaAs by solving the coupled equations of motion for both excitations, each driven by the external light field and linked by polarization and the lattice displacement [210]. Figure 4.17a shows the carrier concentration dependency of the LOPC frequency. The anti-crossing behaviour already discussed for polaritons, causes the occurrence of two coupled branches ω_- and ω_+. In the low density regime the plasma oscillation is overdamped and the phonon oscillates at the LO frequency, at high concentrations the lattice can't follow the fast plasma motion. This screening shifts the phonon frequency to the TO limit. The absence of LOPC related frequencies in the REOS measurements and the concurrent presence of both TO and LO peaks, which according to figure 4.17a should be impossible, is an effect of the inhomogeneous excitation in real experiments. The Gaussian intensity distribution of common femtosecond laser pulses induces different carrier concentrations in its waist and centre region. In the probing process this leads to interference between the plasmon modes and thus to a complete smearing of plasmon contributions.

In later experiments Kurz et al. used nonlinear optical sampling (NEO) with near band gap pulses [211] on n-doped gallium arsenide. In contrast to the linear variation, the isotropic NEO exploiting the Franz-Keldysh effect, shows an increased sensitivity close to optical transitions. To minimize the spatial inhomogeneity the probe diameter was reduced to a fifth of the excitation pulse. For fixed laser energy and differently doped samples they found resonances (figure 4.17b) which are in accordance to the calculation shown in figure 4.17a or to light scattering data [208] only, when adding up all free carriers. This indicates that both, induced carriers and majority carriers from the doping, participate in the coupled mode. The dephasing time varies between the longer LO phonon lifetime of $2-4$ ps and the shorter plasmon dephasing period < 1 ps in the same way as the LOPC is more phonon or plasmon like character for different carrier densities.

Tom, Chang et al. investigated surface phonons by TR-SHG in a number of gallium arsenide faces and their reconstructions. For the UHV prepared, (1×1) relaxed, (110) surface they found a number of modes between $4.5-9$ THz by iterative fitting of 4

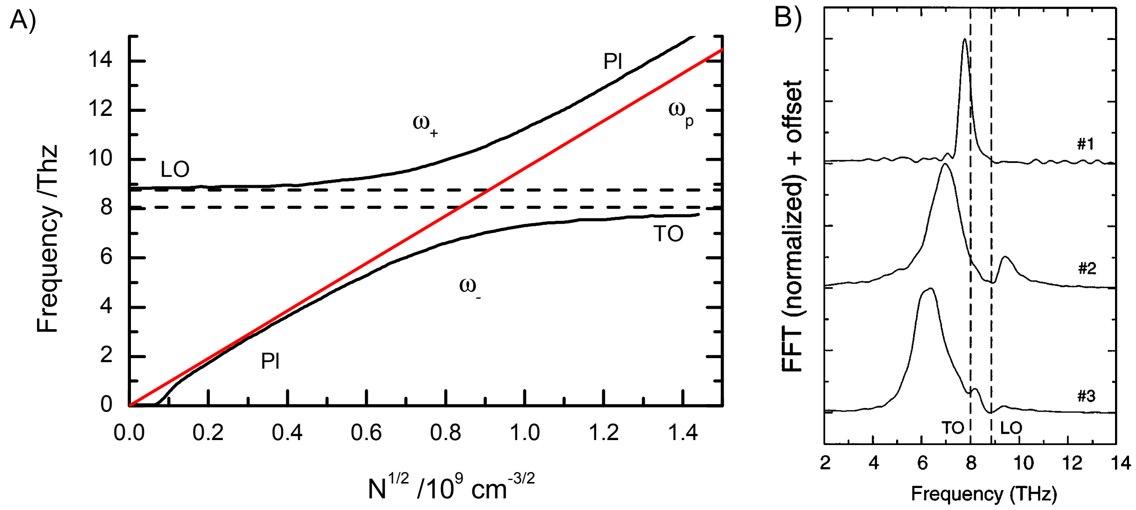

Figure 4.17.: A) Coupling between LO phonon and plasma oscillation ω_p in GaAs as function of carrier density. The LOPC branches ω_- and ω_+ are extracted from calculation in [210]. B) Time-resolved reflectivity measurements by Kurz et al. [212]. The injected carrier density was kept constant at $4 \times 10^{17}\ \mathrm{cm}^{-3}$, while the majority carrier density was increased from $7.7 \times 10^{16}\ \mathrm{cm}^{-3}$ at #3 to $3 \times 10^{17}\ \mathrm{cm}^{-3}$ at #2 and $2 \times 10^{18}\ \mathrm{cm}^{-3}$ at #1. Reprinted with permission from APS.

traces with different probe polarization and crystal orientation simultaneously in time and spectral domain [203] (figure 4.18a and b). As the carrier concentration is kept low, the dominating signal originates from the LO bulk phonon mode (non-centrosymmetric crystal) without LOPC character at 8.76 THz, driven by transient depletion field screening. From calculations and information depth considerations the displacement of this mode is estimated to be 1 pm located 3 nm below the surface. The other modes are confined directly to the topmost surface layers and are easily affected by surface modifications (like oxidation, sputtering etc.). At 8.35 THz the surface TO optical mode is identified and some more modes related to motions in the top three layers were detected between 7 to 8 THz. The Fuchs-Kliewer mode [213], typically visible in scattering experiments, can be ruled out by its large wave vector. Those findings were supported by *ab-initio* calculations. The excitation mechanism for the surface phonons is probably (resonant) ISRS, as the polarization dependency showed.

Highly n-doped GaAs (100) covered with a native oxide layer also boasts the LO phonon mode at 8.78 THz [201, 214]. With increasing carrier density the LOPC mode develops and shifts from 7.52 to 7.67 THz (figure 4.18c). By controlled oxidation experiments under UHV conditions of initially cleaned (4×6) reconstructed GaAs (100) surfaces a peak at 8.48 THz was confined to a surface localized mode, probably comparable to those found on the (110) face in the same spectral region, biased by oxidation strain.

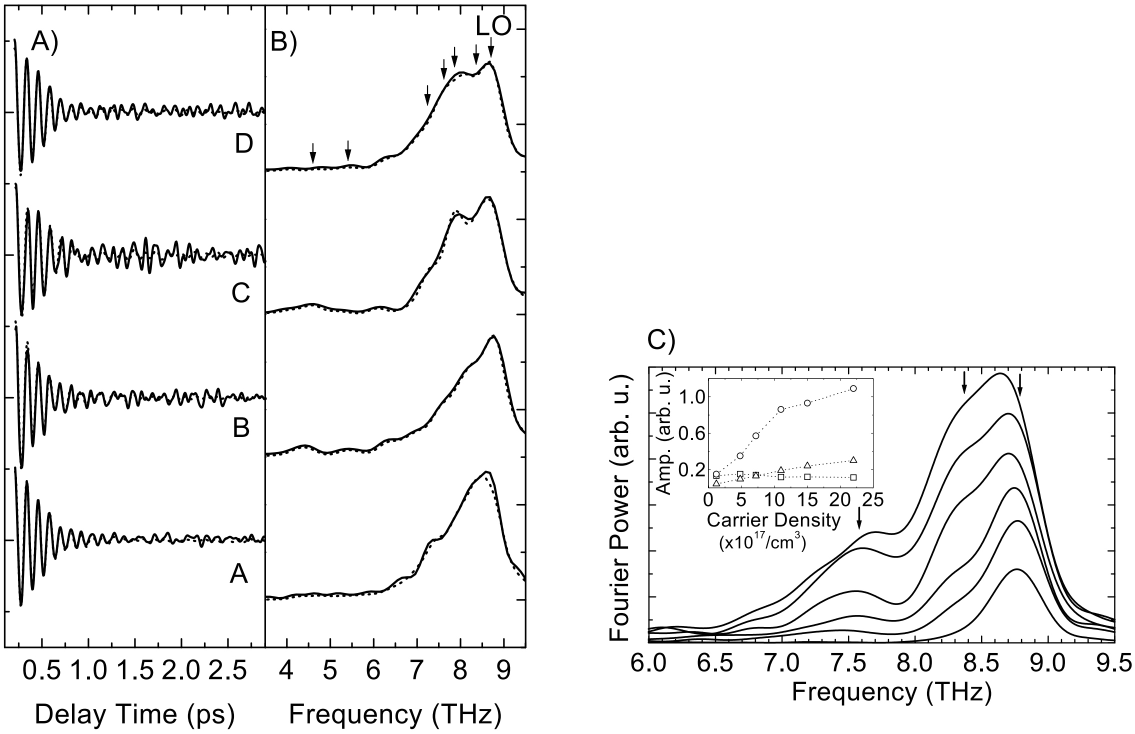

Figure 4.18.: A)-B) TR-SHG traces and corresponding spectra of measurement on GaAs (110). from bottom to top: A: [001], s-pol. pump. B: [001], p-pol. pump. C: $[1\bar{1}0]$, s-pol. pump. D:$[1\bar{1}0]$, p-pol. pump. C) TR-SHG spectra from native oxide covered GaAs (100) with increasing carrier density. The shift in the 8.78 and 8.4 THz modes is an artefact of their coherent superposition [203]. Figures from [201, 214], with permission from APS and Springer.

Also for the (1×6) and (4×1) reconstructions, phonon spectra were recorded, showing different but not in general new modes [202]. The strength of plasmon coupling of phonons can be controlled in two-pump experiments by varying the pump-pump delay[215, 216]. By this method Chang also found evidence for LO-hole plasma coupled modes, which before were thought to be undetectable due to the hole plasmas strong overdamping [215, 217]. Their dephasing increases with the plasma density.

Measurements on $c(8 \times 2)$ reconstruction, the high temperature surface modification of gallium arsenide (100) faces, were performed by Matsumoto et al. under UHV conditions on highly n-doped wafers in the usual p-polarized probe and p-polarized detection scheme [218]. In their experiments the crystal was aligned with the $[1\bar{1}0]$ direction parallel to the plane of incidence. Beside the LO phonon mode, they found a peak at 8.4 THz and a sharp dip at 8.7 THz. By simulation using two underdamped oscillators, they found that a phase difference of 69° is responsible for the dip. The low frequency component was identified as a surface mode, showing a pronounced response on surface treatment. With increasing pump power from 70 to 210 mW both modes undergo a red shift and while the bulk mode dephasing time arbitrarily varies between $2.0 - 3.0$ ps, the surface mode halves its lifetime from 0.4 to 0.24 ps. The initial phase shift between both resonances increases from 69° to 103°.

4.2. Platinum and GaAs-Pt Interfaces

4.2.1. Structural Properties

Platinum crystallizes in the face centred cubic (fcc) type which exhibits $m3m$ symmetry. The lattice constant is 3.92 Å. Most prominent in surface scientific experiments are the (111), (100) and (110) faces. The first forms layers of spherical packing, with two types of steps. One with a (100) orientation and a thermodynamically preferred (111) step [219]. The growth of (111) layers is determined by the energetic difference of diffusion processes along the terraces compared to the jump energy across steps. When the first requires less energy, two-dimensional films dominate, while in the other case the growth of $3D$ islands is amplified. Reconstructions only occur at high temperatures ($T > 1330$ K) or in the presence of a high concentration of adsorbates. The reduced coordination of the surface atoms is compensated by the formation of a double striped reconstruction with separated hcp and fcc areas [220]. With increasing temperature above the threshold a continuous transformation into an incommensurate fluid phase begins [221].

Pt(100) surface are known to reconstruct severely by changing from fcc to a quasi-hexagonal surface [222], simply by thermal activation. This goes along with an increase of surface atom density of about 25%. The stable form of (110) surfaces is the (1×2) reconstruction. Here every second atomic row is missing along the [001] direction [223]. The unreconstructed face can be obtained by adsorbing CO at 425 K under UHV conditions [224].

Theoretical calculations on the mechanisms of adsorbate induced reconstructions of platinum surfaces can be found in [225].

4.2.1.1. Growth of Thin Films

The initial factor determining the grows of evaporated materials is the sticking coefficient, which specifies the ratio of stuck atoms to the number impinged atoms. Platinum is known to have a weak adhesion and to grow as soft films. The second step is the nucleation, which is related to properties like substrate roughness, diffusion energies and defect concentration. The actual growth of thin films can be classified by three funda-

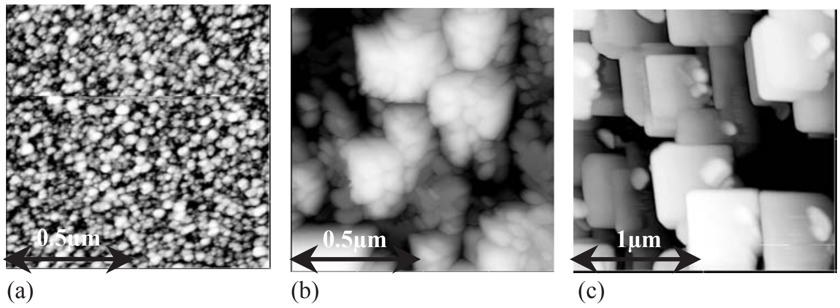

Figure 4.19.: AFM pictures of 60 nm Pt films on $SrTiO_3$. a) Room temperature. b) 770 K. c) 970 K. Reprinted from [234], with permission from Elsevier.

mental modes: When the energy of substrate surface is equal to that of the first adsorbate monolayer a two-dimensional layer by layer growth is expected, known as Frank-van-der-Merwe growth [226]. When the energy of the adsorbate is lower, the growth of three-dimensional islands is preferred [227]. In systems where the energy of the first adsorbate layer is higher then on the substrate surface, a complete monolayer forms before the growth of islands sets in (wetting layer) [228]. The quality of the interface is determined by the lattice mismatch of the involved materials. For conductor-semiconductor junctions the interface quality is in general low and diffuse over many interatomic distances with a pronounced change in electronic properties across the boundary [229, 230]. A more detailed review of the nucleation and growth of platinum with focus on Al_2O_3/NiAl is given in [29].

Pt films on GaAs are used as Schottky devices, where typically platinum layers in the range of $100 - 500$ nm are deposited [16, 231, 232]. Further thin films of Pt are used as diffusion barriers in gold gallium arsenide devices, as Au alloys with Ga already at room temperature [233]. STM measurements on $2.5 - 7.5$ nm thick platinum layers on GaAs revealed a rough structure, with increasing grain size ($Ra = 0.66 - 1.25$ nm) [18].

On oxidic supports Pt usually grows as islands. Zhao et al. found epitaxial growth of platinum films on functional oxides with small lattice mismatch like $SrTiO_3$, deposited by a sputtering technique. AFM pictures of 60 nm thick platinum films show small island growth for room temperature deposition (figure 4.19 a). With increasing temperature (770 K) bigger grains arise which are partly aligned with the substrate (figure 4.19 b). At high deposition temperatures around (970 K) large square and flat islands with (100) configuration can be observed as shown in panel c of figure 4.19 [234]. On MgO substrates similar experiments by McIntyre et al. at 970 K revealed even a mixture of (100) and (111) facets [235].

For films in the range of 1 nm and below as they are deposited in this work little information is available. Al-Shemmary and Buchwald performed experiments on photochemistry of small molecules adsorbed at Pt particles deposited on thin Al_2O_3/NiAl substrates [29, 31, 235, 236]. For this purpose small platinum amounts between $0.5 - 3$ nm were evaporated on an in-situ prepared epitaxial alumina film employing the same equipment used for the experiments presented in this thesis. Ex-situ AFM measurements for different platinum amounts and for deposition temperatures of 100 and 300 K indicate growth of well separated islands at room temperature, while at the low temperature preparations the islands are smaller and densely packed. The measured cluster heights were up to two times larger than those reported by Klimenkov et al. and Bäumer before for Pt/Al_2O_3/NiAl[30, 237, 238], which was attributed to accuracy limitations of the used microbalance. Klimenkov found a monotonic increase of cluster size with increasing amount of deposited platinum, while the particle density passes through a maximum at 0.5 ML [237].

Alloying and diffusion

In silicon platinum is highly soluble and diffuses by substitution of interstitials [239]. Two different equilibria compete: The balanced reaction of filling vacancies by interstitial Pt leading to silicon lattice sites occupied by impurity platinum and the two-directional process of replacing impurity atoms by self introduced interstitials (Si in interstitial positions) [240]. In GaAs the same mechanism is assumed with an activation energy of 0.95 eV. The diffusion coefficient of Pt in n-GaAs (1.32×10^{-8} cm^2/s) and GaAs based light emitting diode structures was found to be smaller than that in silicon. The difference is explained by the higher density of gallium arsenide. In the investigated temperature range of $773 - 1173$ K the surface roughness measured by AFM rises from $Ra = 2.91$ nm to 34.96 nm [241]. The diffusion also affects the photoluminescence recorded at 20 K where emission at 894 nm dominates the optical response, indicating the installation of platinum acceptor levels in the 1173 K samples at $E_V + 0.125$ eV [239]. In the lower temperature samples this signal is missing.

A chemical reactivity between Pt and GaAs was found by Murarka, Chang et al. resulting in formation of $PtAs_2$ at the interface and a Ga-Pt phase away from the boundary for annealing temperatures larger than 470 K [17, 242]. Begley et al. found similar results by depth profiling secondary ion mass spectroscopy (SIMS) and additionally revealed a fast diffusion of Ga atoms even through thick (200 nm) platinum films [243]. The semiconductor-metal reaction at 620 K is fast enough to completely consume Pt films up to 200 nm, before self limitation, probably due to the formation of a continuous layer of $PtAs_2$, stops the process [230]. The activation energy for this reaction as extracted from Arrhenius plots is about 2.3 eV. From those also the kinetic hindrance at low temperatures is confirmed. The phase diagram for the ternary system Pt/Ga/As can be found in [244] along with cross-sectional microscopic images of micrometer scaled composite samples.

Generally many different thermodynamically stable phase like eutectics or intermetallics can be formed at elevated temperatures, but at thin metal film samples they are usually not established and only metastable configurations can be found [230]. All in all the fast diffusion of gallium atoms at the interface reduces the ratio between Ga and As (< 1). The doping in the top layers of gallium arsenide may be considerably different from that in the bulk semiconductor due to the indiffusion of metal atoms.

4.2.2. Electronic Properties

4.2.2.1. Ohmic and Schottky Contacts

Electric contacts between metals and semiconductors can be classified in to Ohmic contacts, which boast a linear relation between the applied voltage and the resulting flow of current obeying Ohm's law and nonlinear Schottky contacts with rectifying properties. In figure 4.20 the steps of electronic realignment are shown, when contacting a metal with a n-doped semiconductor [174]. The metals Fermi level (or chemical potential μ_M) lies within the band gap of the semiconductor which is characterized by its valence and conduction band energies (E_V and E_C) and its Fermi level (μ_{SC}) close to the conduction band, typical for a n-type material. The metal contact creates states inside the band gap region located close to the surface of the semiconductor (figure 4.20A). These induced gap states (IGS) are partly filled and create a surface Fermi level (μ_S), comparable to the surface states described in section 4.1.1.

Frame B of figure 4.20 shows the equalizing of the Fermi levels μ_M and μ_S which is driven by the flow of electrons from the metal into lower energy surface states. The holes left behind in the metal induce a band bending by an amount defined by the difference of workfunctions of μ_M and μ_S: $\Delta\mu = \Phi_M - \Phi_S$. This would be the final state for an intrinsic semiconductor. For a n-doped device the different Fermi levels in the bulk and on the the surface have of course to be levelled too. This is done by a transfer of donor level electrons into the surface in the same way as described in the section before, creating a second bending in the opposite direction. All in all this process forms a barrier as shown in figure 4.20C. Its height is given by $V_S = \Phi_M - \chi_e + \Delta\mu$ and is

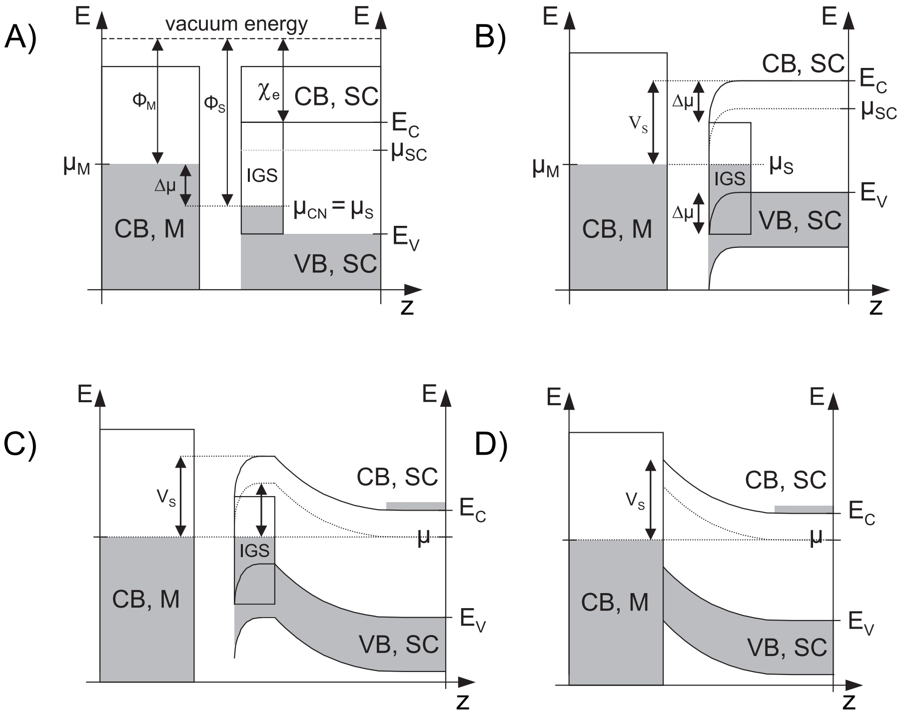

Figure 4.20.: Band diagrams as a function of depth z into a metal / n-doped semiconductor hetero-structure showing the formation of a Schottky type electric contact. For detailed information see text. From [174].

related as such to the chemical potential of the surface states which is complicated to obtain. The width is dominated by the doping concentration in the semiconductor. In the more simple Schottky model the surface states are neglected and the barrier height is only determined by the workfunction of the metal and the electron affinity of the conduction band (figure 4.20D).

For a flow of current across the contact electrons have to overcome the barrier, either by tunnelling or by increasing its energy. The nonlinear behaviour of a Schottky contact results from an exponential dependence of the tunnel current from the barrier height and width. By applying a voltage across the boundary, the work function of the metal can be adjusted and thus the barrier properties. A biasing enhances the current, while a reverse bias suppresses it. A more Ohmic behaviour of a metal semiconductor contact can be obtained by a high doping level, which narrows the barrier width and thus increases the tunnelling. Also alloying or the formation of silicides in silicon based contacts can help to create Ohmic contacts [174]. The fabrication of good Ohmic contacts is difficult. Rideout argues that: ‘Ohmic contact technology has developed thus far more as a technical art than as a science.’ [245]. A common system for Ohmic contacts to GaAs consists of Au

and Ge where germanium act as an impurity to reduce the barrier width [231].
The experimentally obtained barrier height for Pt/n-GaAs is 0.94 eV [242]. Ohmic contacts to n-GaAs can be established using platinum in multimetalic alloys [239, 241]. In p-type gallium arsenide Ohmic contacts to platinum can be created by sintering [246]. The accumulation of $PtAs_2$ at the interface stabilizes the formation of Schottky barriers, which manifests itself in a small increase of barrier height by 0.05 eV [230].
Beside the direct application in electronics, Pt-GaAs contacts can be used as sensors. Lechuga and coworkers presented a Schottky based device for detection of hydrogen [16]. H_2 dissociates on the catalytically active Pt and diffuses to the metal semiconductor interface, leading to a change of the barrier height. The amount of hydrogen can be related to the drop of capacitance in the diode.

4.2.3. Optical Properties

Linear Properties

In figure 4.21 the real and imaginary parts of the complex refractive index of Pt as specified in [247] are displayed. The inset shows the calculated (cf. equation 2.9) reflectivity in the spectral region of interest. Measurements of the reflectivity over a larger energy scale can be found in [248]. The plasma frequency of platinum is located at 241 nm [249]. In the visible range of the spectrum it shows the expected featureless response. Similar optical properties are found at small Pt particles in the size regime between $2 - 10$ nm [250].

Nonlinear properties

Platinum with its face centred cubic bulk structure has $m3m$ inversion symmetry, so there is no dipole contribution to SHG from the bulk. For the common surface faces of Pt the non-vanishing surface susceptibility elements are summarized in table 4.5. At the surface the atoms tend to relax or reconstruct differently depending on the face and temperature (i.e. [251] and references therein).
The nonlinear response of metals is mostly governed by the polarization of the conduction and valence band electrons at the boundary [252]. Changes in the SHG upon adsorption of foreign atoms or molecules can be traced to modifications of the surface electronic states. But only in some cases a direct relation to surface electron density and the work function could be established as in the work of Grubb et al. in which the kinetic of CO and H_2 absorption on Pt(111) is studied by SHG [253].

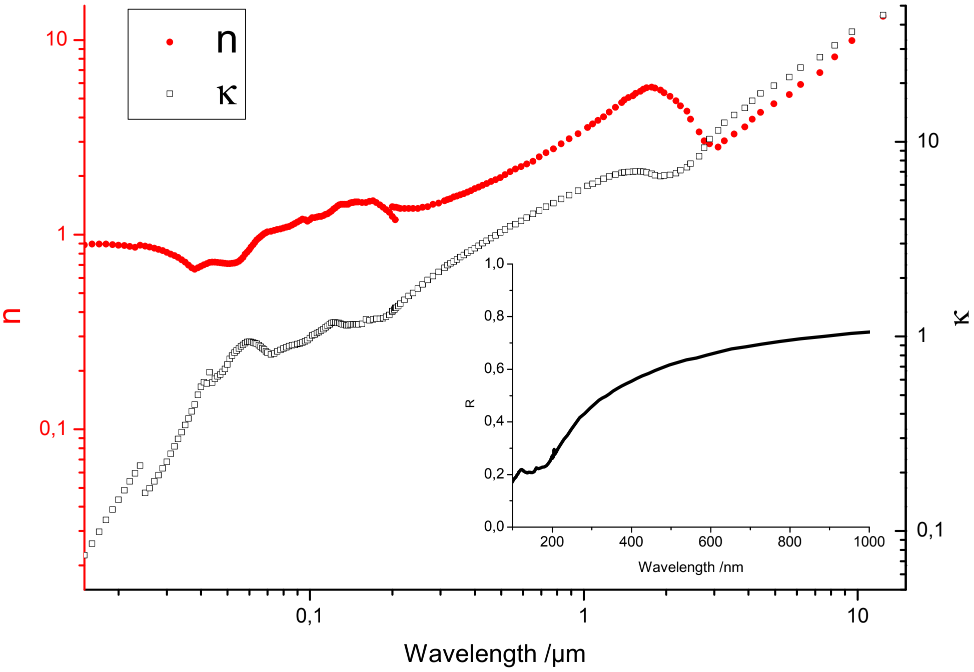

Figure 4.21.: The real and imaginary part of the refractive index of platinum from [247]. The inset shows the calculated reflection coefficient in the spectral region of interest.

The first experiment in which an anisotropic SH signal from a metallic surface was discovered, were published by Tom and Aumiller in 1986 [254]. They investigated (111) surfaces of Cu which exhibits the same symmetry as platinum, with the typical fundamental light of a Nd:YAG laser. With probing different polarizations one surface tensor element ($\chi^{(2)}_{xxx}$) and part of the quadrupole bulk response was found to be responsible for anisotropy, manifesting in the expected threefold waveform. While at semiconductors the oriented SH signal can be explained by an effect of the electrons in the directional atomic bonds, the free electrons in a metal should not cause any anisotropic signal. Tom

Face	**Symmetry**	**Non-vanishing** $\chi^{(2)}_{surf.}$
(100)	C_{4v} $(4mm)$	zzz, zxx, xxz
(111)	C_{3v} $(3m)$[a]	zzz, zxx, xzx, xxx
(110)	C_{2v} $(mm2)$	zzz, zxx, xzx, zyy, yzy

---

[a] Due to the influence of the second layer, the $6m$ symmetry of the top layer is reduced.

Table 4.5.: Non-vanishing surface susceptibility tensor elements of second-order for common faces of face centred cubic crystals in the general form without Kleinman symmetry. From [65].

and Aumiller discussed a large contribution to the polarization from interband transitions involving d-band electrons. SHG measurements on platinum surfaces can mostly be found in the context of electrochemical systems using Pt electrodes. Here the pure optical method is nearly unchallenged to measure surface transitions or surface reactions at the metal surface-liquid interfaces.

Lynch et al. studied the multistage preparation of a well ordered platinum surface in an electrochemical environment by measuring the SHG anisotropy with 605 nm photons generated from a dye laser in p-in / s-out and s-in / p-out polarization configuration [255–257]. Before its transfer into the electrochemical cell, the electrode was flame annealed and cooled in iodine vapour steam. The black circles in figure 4.22 show the corresponding rotational scan. In the second step the iodine is replaced by CO forming a well ordered overlayer (blue squares). Finally the ordered Pt surface is obtained by electrochemical oxidizing carbon monoxide (green open circles). For the polarization combinations used, the rotational signal of the (111) surface can be fitted by:

$$\begin{aligned} I_{sp}^{(\Omega)} &= |A + C\cos 3\phi|^2 \\ I_{ps}^{(\Omega)} &= |B\sin 3\phi|^2\,, \end{aligned} \tag{4.8}$$

where A, B and C are the complex fitting coefficients as defined before.

For the iodine wetted surface, the symmetry of the p-in / s-out is changed compared to the expected C_{3v} form. A possible reason for this may be an additional anisotropic influence of the adsorbate itself or an induced lowering of the surface symmetry (C_3) (equal distribution of two different overlayer domains). Upon replacement with CO the rotational SHG response changes significantly, which is interpreted as a sign for a change in the electronic structure consistent with the findings in [253]. Finally the pure platinum surface shows the straight C_{3v} symmetry, described by the fitting functions in equation 4.8 although with a low intensity.

The nonlinear effects of gold-silicon interface samples as an example of coinage metal semiconductor boundaries are in detail analysed by McGilp et al. in many publications (e.g. [258, 259]). They performed normal incidence rotational measurements on a 7×7 reconstructed Si (111) surface in UHV, while different amounts of gold in the range of 2 to 12 monolayers were evaporated. It could be shown, that neither bulk or the formed gold silicide contributes to the SHG signal and that its origin must be the interface in between both materials. For small amounts of gold a reduction in the symmetry of the rotational signal is found and addressed to a formation of localized interface states

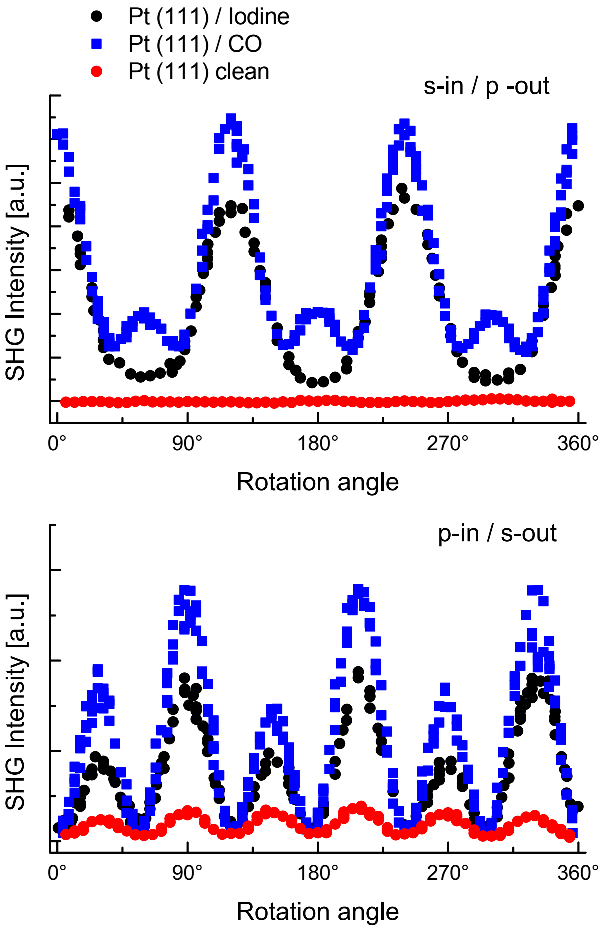

Figure 4.22.: Rotational SHG from Pt(111) with different adsorbates. Data from [256].

along steps on the surface due to the absorption of gold. With increasing thickness a $3m$ symmetric compressed gold layer builds up and coexists with the steps. At the same time an increase in SHG intensity was found. This was discussed with a possible resonance in the interface states whose possible more s, p_x or p_y orbital like character compared to the dangling bonds on pure silicon allows a better interaction with the normal incidence pump light. This electronic resonance was further verified with $\chi^{(2)}_{surf.}$ tensor element resolved SHG intensity measurements depending on the Au coverage.

The change of SHG intensity at metal-metal interfaces is analysed by Song et al. on Ag (110) covered with different layers of Rb [260]. For one monolayer coverages a huge increase of SH efficiency is observed (depending on the pump wavelength the change is up to a factor of 1600). With further deposition the signal gradually decreases and shows a damped oscillatory behaviour. While the initially effect is addressed to a resonance of the adsorbed atoms, the latter is discussed as a result of electron density fluctuations at the surface, caused by the impinging electro magnetic wave. These fluctuation give rise to a longitudinal oscillating electric field within the Thomas Fermi screening length at the surface.

4.2.4. Dynamic Electronic Properties and Their Optical Response

Carrier dynamics in metals can be explained by the same concepts introduced in the description of carrier dynamics in gallium arsenide. An intense ultrashort excitation first creates a non-thermal hot carrier distribution, which thermalizes into a Fermi-Dirac distribution by scattering between hot carriers. In a second step the hot electrons thermalize with the lattice by phonon emission ($T_{el} = T_{la}$). Electrons in the initial state are thought to couple with unoccupied molecular adsorbate states and trigger surface reactions (see figure 4.23a). These relaxation processes can be described by the two temperature model (2TM) [261]. While in early experiments on thin metal films transport effects could be neglected [262, 263], in bulk metals again spatial effects have to be considered and incorporated into the 2TM [264] (figure 4.23b). On very thin gold films (5 nm) Meech et al. found that the two-temperature model has to be further modified to regard the strong impact of film morphology on phonon mediated cooling of thermalized carriers observed, which only weakly influences the thermalization process itself [265].

In hetero systems consisting of GaAsP and 10 nm Au films Chang found that ballistic transport of hot electrons from the metal into the semiconductor and the consequent screening of the depletion zone induce the emission of coherent phonons (cf. section 2.4 and section 4.2.5) [266]. An opposite effect was found by Hasselbrink et al. for thin silver films coated on Si wafers. They studied the photochemistry of adsorbed NO_2 using Nd:YAG laser photons at different energies [267, 268] and discussed an effect of hot electrons inside the semiconductor responsible for the increase in reaction cross section with decreasing film thickness observed. Those non-thermalized carriers cross the metal film in a ballistic transport process and couple to the adsorbate. The relevant energy levels lie within a gap in the band structure of the silver films, explaining the low cross sections at higher film thicknesses. The electron transport through this thin layers may be explained by quantization effects. The principle theoretical prediction of those kind

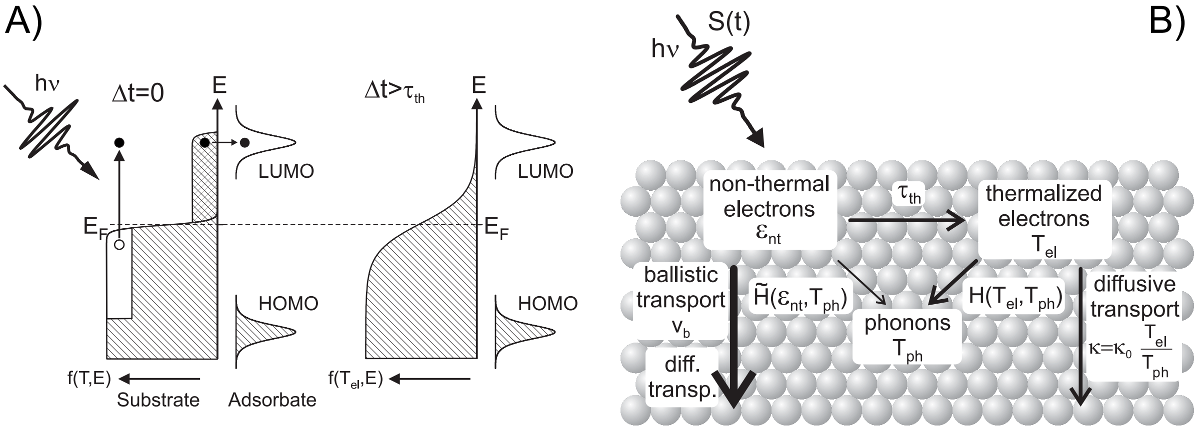

Figure 4.23.: a.) Energy distribution in metals after excitation with an ultrashort laser pulse. Directly after the stimulus electrons in their non-thermal distribution can couple to molecular adsorbate states firing surface reactions. b) Energy dissipation pathways in a bulk metal. Reprinted from [264], with permission from Springer.

of effects was previously published by Zhdanov and Kasemo [269].

Finally when metals are incorporated into the bulk of a semiconductor they mostly act as traps for excited electrons and thus control the lifetime of excited states [270]. For the case of low temperature grown GaAs it is known that the excess of arsenide, typical for this type of samples, can act as a metallic impurity itself [271].

Only a few experiments are known using pump-probe techniques and employing the nonlinear response of a metal to characterize the thermalization of carriers. More widespread in this field, is two photon photo emission (2PPE) in which the photoelectric effect of metals is exploited by using two consecutive ultrashort laser pulses, to emit an electron in a two step process. By varying both, the delay and the frequency of one of the pulses allows a time-resolved mapping of electron density [264, 272, 273]. Matsumoto et al. investigated coherent vibrations of Cs and K adatoms on Pt (111) surface using a SHG pump-probe technique with 150 fs laser pulses from a Ti:Sa laser source at 800 nm and a p-in / p-out polarization configuration. For the pure platinum surface they found only a weak response, shown in figure 4.24, which is around seventy times smaller than the signal from the alkali metal covered samples [274, 275].

The decaying curve was fitted by two exponentials with time constants $\tau_1 = 410$ fs and $\tau_2 = 2.76$ ps. Along with the ΔSH curve, calculated plots of the electron and lattice temperature dynamics are shown. A good agreement between these calculations and the experimental data is found. The adsorbate induced changes to these signal is discussed in section 4.2.5.

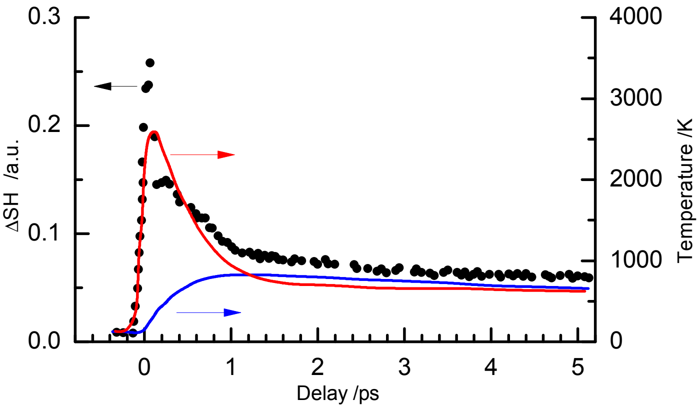

Figure 4.24.: Time-resolved SH signal of a Pt (111) surface and the modelled electron and lattice temperature curves. Data from [275].

4.2.5. Phonon Properties

Figure 4.25 shows the phonon dispersion on Pt (111) surfaces, measured by helium atom scattering. Between the two directions $\Gamma \rightarrow K$ and $\Gamma \rightarrow M$ a pronounced asymmetry of the surface phonons can be observed [276, 277]. Their frequencies at the M-point are 2.7 and 3 THz, while a the K-point the corresponding are 2.6 and 3.1 THz. As expected no optically active phonon modes are present at the Γ-point.

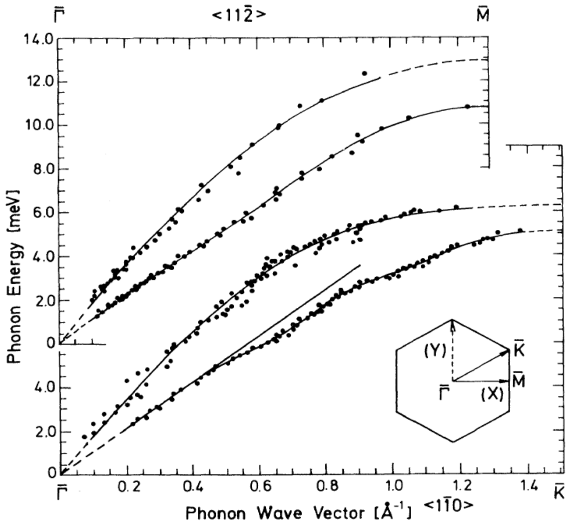

Figure 4.25.: Phonon dispersion on Pt(111) measured by helium atom scattering. Reprinted from [276], with permission from APS.

Consequently time-resolved SHG measurements, as shown in figure 4.24 in section 4.2.3, show only contributions from hot carriers and their relaxation processes. However on the

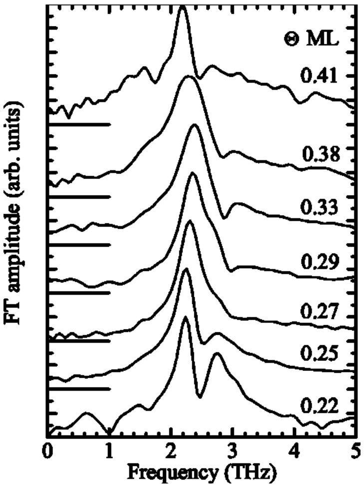

Figure 4.26.: Pump-probe phonon spectra for different coverages of Cs on Pt (111) showing two features from Cs–Pt stretching and Pt Rayleigh mode. Reprinted from [275], with permission from APS.

deposition of alkali metals (Cs, K) follows a huge increase in second harmonic photon yield and a signature of optically active coherent oscillations [274, 278, 279]. The increase depends on the coverage of alkali metal and it is related either to local field enhancement at the vacuum interface or to transitions between interband states induced by the two-dimensional quantum well like metal layer [279]. The main contribution to the oscillation signal comes from the Cs–Pt, respectively K–Pt, stretch mode. They are driven by ISRS in the ground state and show a strong relaxation component of pure dephasing at elevated excitation fluences, caused by (in)elastic scattering of hot electrons from the substrate [278]. When the Cs coverage is systematically varied, not only the Cs–Pt oscillation (≈ 2.3 THz) slightly shifts due to adsorbate dipole-dipole coupling but also a second resonance appears at $\approx 2.7 - 2.9$ THz (figure 4.26) [275]. A strong dip between both modes again implies a strong phase shift. The oscillation parameters, obtained by LPSVD (see section 8.1), reveal frequencies matching the surface acoustic mode (Rayleigh mode) of Pt measured by He atoms scattering (HAS) [276]. It is discussed that the superstructure formed by the adsorbate at specific concentrations, fold the Rayleigh phonon mode from the Brillouin boundary at the M-point to the Γ-point at the zone centre, making it optically available [275]. Similar observation were found on the system K/Pt were the modes are easier to resolve as the K–Pt stretch mode is located at $4.5 - 5.2$ THz [280]. Coherent control experiments using adjustable femtosecond pulse trains allow the direct excitation of the platinum surface phonon [281].

As an example for a GaAs-metal hetero-interface Chang investigated a commercial

(*Hamamatsu*) Schottky diode by TR-SHG [266]. The diode consisted of a 10 nm Au coating on top of a 10 μm n-doped $GaAs_{0.6}P_{0.4}$ layer on a GaAs (100) substrate. He observed two phonon modes, one LO-GaAs like at 8.5 THz and a LO-GaP like resonance at 11.5 THz. The carrier relaxation occurs on a timescale smaller than 1 ps. The polarization invariance and the linear behaviour of the phonon amplitude on the pump power lead to the proposal of a ballistically transport of hot carriers created in the metal layer into the semiconductors depletion zone as the phonon driving mechanism. The band gap of GaAsP is larger than the photon energy, a direct screening would than be a two photon process, leading to a quadratic pump intensity dependence.

5. Experimental

This chapter is dived into three main sections. The first part describes the analysis methods employed in the characterization of the investigated samples, the second part covers the sample preparation, in particular the fabrication of the platinum GaAs interfaces under ultra-high vacuum conditions. In the third section the optical set-ups and experiments are described.

5.1. Analysis Methods

The structural and chemical configuration of the investigated samples was determined with spectroscopic, diffractive and microscopic methods, mainly by x-ray photoelectron spectroscopy (XPS), low energy electron diffraction (LEED) and scanning probe microscopy (SPM). These techniques and their theoretical foundations are presented briefly in the following sections. For further discussion reference is made to text books and special literature as stated within the section.

5.1.1. LEED

The low energy electron diffraction technique is based on findings of Davisson and Germer which discovered the wave nature of electrons in 1927 as they performed electron scattering experiments on a nickel single-crystal [282]. They found a pronounced angular dependency of the detected intensities which is comparable to that expected from x-ray diffraction and can be described by Laue equations. In a typical LEED experiment electrons from a hot filament are impinged onto the sample with a kinetic energy in the range of 50 to 500 eV. After elastic and inelastic collision processes the backscattered electrons are filtered and re-accelerated onto a phosphor screen and thus made visible. The filtering of inelastic electrons and the speed-up is done by a number of grids, which are positioned hemispherical around the specimen (figure 5.1a). On the screen a diffraction pattern is depicted, representing a direct image of the reciprocal (surface) lattice of the sample (figure 5.1b).

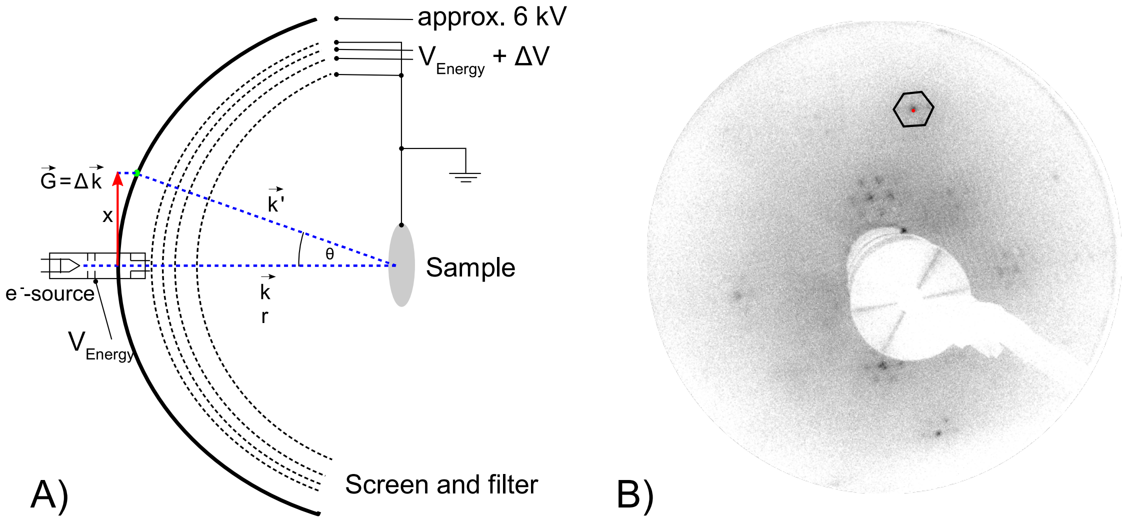

Figure 5.1.: A) Schematic drawing of a LEED device. B) Diffraction pattern of a 7x7 reconstruction on Si(111). To enhance the visibility the hexagonal surface reconstruction pattern (black curve) surrounding the bulk (111) spot (red dot) is highlighted for an arbitrary point in the diffraction patttern.

To obtain the surface mesh parameters, first the reciprocal lattice has to be constructed by transformation of screen coordinates into reciprocal lattice dimensions. The constructive interference conditions are defined by the Laue equations $\vec{G} = \Delta\vec{k}$ saying that every scattering vector $\Delta\vec{k}$ is equal to a reciprocal lattice translation. The scattering vector is the difference of the incoming and diffracted electron beam wave vectors (blued dashed lines in figure 5.1a). The wave vector of the incoming electron beam is defined by distance between screen and sample r and it's kinetic energy. This gives:

$$|\vec{G}| = |\Delta\vec{k}| = |\vec{k}| \cdot sin(\theta) = |\vec{k}| \cdot \frac{x}{r} = \frac{\sqrt{2m_e E_{kin}}}{\hbar} \cdot \frac{x}{r}, \tag{5.1}$$

where x is the screen distance of the points connected by $\vec{G}$. Stepwise determination of simple translation vectors $\vec{G} = \vec{b}_i$, where $\vec{b}_i$ is a basis vector of reciprocal space, allows the construction of the reciprocal mesh, which than can be transformed back to real space.

The derivation is based on single scattering events and is called kinematic theory and a more detailed treatment including the transformation between real and reciprocal space can be found in appendix A.3. It is sufficient for the rather qualitative application the technique is used in the scope of this work. More detailed investigations can be made by recording the spot intensity as a function of the electron energy (I-V curves) and compare the results with calculations based on a dynamical, multiple scattering theory.

More details about scattering descriptions and the reciprocal lattice can be found in [101]. An interesting review of development in LEED instrumentations and technical details are presented by Lagally and Martin in [283].

5.1.2. X-ray Photoelectron Spectroscopy

The photoelectron spectroscopy (PES) is based on the photoelectric effect, which describes the emission of electrons from metals after irradiation with electromagnetic waves (for molecules the equivalent is photo ionization). It originates from the experimental work of people like Hertz, Hallwachs, Innes and Rutherford [284–287] on one hand and on the other from theoretical considerations of Einstein [288]. When using a well defined, preferably monochromatic light source, the measured energy reveals information about the binding energy of the electrons. Depending on the photon energy the PES is classified into large wavelength ultraviolet photoelectron spectroscopy (UPS) for the detection of valence band electrons and in short wavelength X-ray photoelectron spectroscopy (XPS) for the investigation of core level electrons.

The kinetic energy of the photoelectrons E_{Kin} is equal to the difference between the x-ray photon energy and the ionization energy, which for solids, is the sum of the binding energy E_B (referenced to the Fermi level E_F) and the work function Φ (figure 5.2). By electrical connecting sample and analyser to a common earth, the Fermi energies of both systems level. After calibration of the spectrometer (determination of $\Phi_{\text{Spectrometer}}$), the electron binding energy can simply be obtained from its kinetic energy E'_{Kin} measured in the analyser:

$$E_B = h\nu - E'_{Kin} - \Phi_{\text{Spectrometer}} \tag{5.2}$$

The kinetic energy of the emitted photoelectron lays in the range between $0 - 1486.6$ eV ($0 - 1253.6$ eV) based on the typically used Al (Mg) K$_\alpha$ x-ray source. As shown in figure A.2 in appendix A.3 the inelastic mean free path of these electrons λ_I makes XPS a surface sensitive method. The attenuation length λ_A is a quantity of the Lambert-Beer formalism, describing the transparency of the material. It is defined as the length over which the number of electrons drops to $1/e$. The information depth d_i is in the range of $d_i = 3\lambda_A \approx 10$ nm. For simplification λ_I and λ_A are used synonymously [9, 289].

λ_I and λ_A are experimentally accessible, for example by TEM measurements on thin samples, or can be obtained by empirical equations as the one proposed by Seah and Dench [290]:

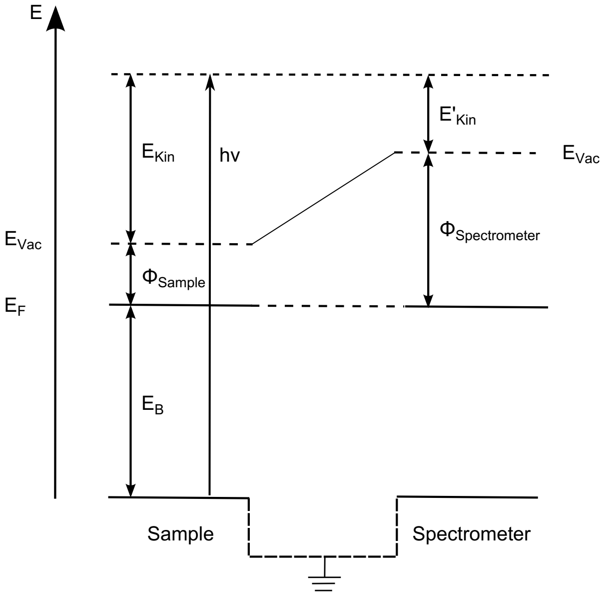

Figure 5.2.: Energy diagram of sample and analyser. The electron is leaving the sample with E_{Kin} and enters the analyser with the kinetic Energy E'_{Kin}. Due to the common grounding between both parts, the binding energy E_B is no longer dependent on the samples work function Φ_{Sample} but on the empirically determinable work function of the spectrometer $\Phi_{Spectrometer}$ [289].

$$\lambda_I(E) = 538\frac{a}{E^2} + 0.41 \cdot a^{\frac{3}{2}} \cdot E^{\frac{1}{2}} \tag{5.3}$$

where λ_I is specified as a function of the electrons kinetic energy and a term $a = \sqrt[3]{\frac{M}{1000 \cdot \rho \cdot N_A}}$ which is depending on the molecular weight M of the material and its density ρ. A method to convert λ_A and λ_I is published by Seah, too [291]. More recent calculations with a modified model can be found i.a. in [292].

5.1.2.1. Structural Elements of XPS Spectra

Figure 5.3 shows a typical survey spectrum of a metallic sample. The primary structure of this spectrum includes the valence band electrons (d) close to the primary excitation energy and the Fermi level (smallest binding energies), the core level signals which spread over the complete energy range (b) and signals from the emission of Auger electrons (c). The core level signals are commonly accompanied by satellite peaks due to plasmon excitation or two-electron processed (shake-up/down processes). The huge and growing background is caused by the Bremsstrahlung radiation tail emitted from the photon source, which excites electrons with an undefined energy. The stepwise background increment towards low kinetic energy is a result from an effect called inelastic loss tail.

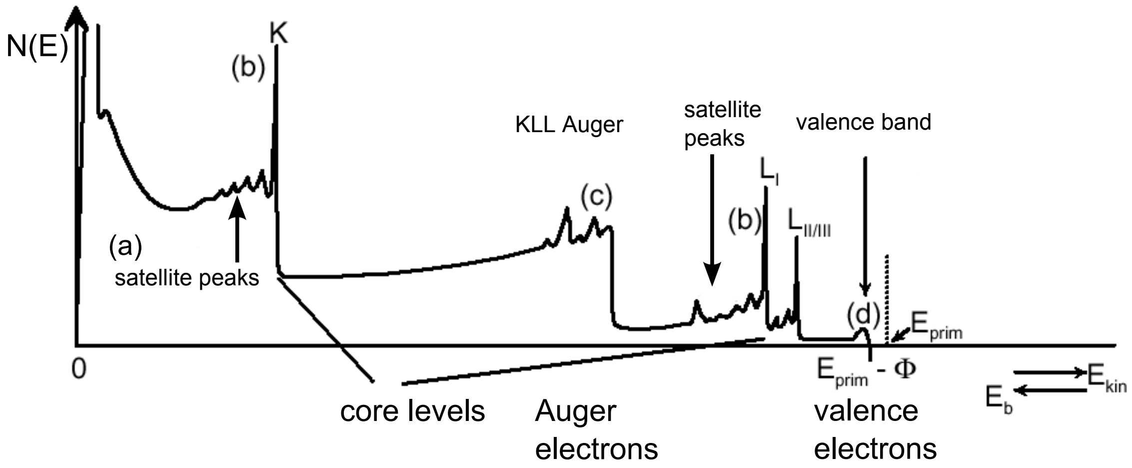

Figure 5.3.: Schematic illustration of a typical survey scan of a solid, showing the different structural features emerging in a XPS scans. The processes are explained in the text. Based on [293].

A part of the emitted photoelectrons lose continuously energy by inelastic scattering events, which shifts their kinetic energy to the lower energy side of the corresponding main peak.

Further signals in a spectrum originate from the photon source. In non-monochromatic instruments, photons emitted by less intense side emission lines give rise to x-ray satellites. Impurities on the target material (oxidation, contamination) or a cross talk between both targets will add further peaks, called x-ray ghosts.

Core level signals

The core level signals found in a XPS spectrum are characteristic and reveal the electron structure of the elements in the sample. Their nomenclature is assembled from the element symbol and the quantum number of the ionized energy level in spectroscopic notation. In contrast to the simple picture in figure 5.2 the signal is not a discrete peak, instead its line width and energetic position is determined by a number of effects. The peak broadening is induced by the bandwidth of the x-ray source ΔE_{Source} (expressed as full width at half maximum (FWHM) with the assumption of a Gaussian shape), the resolution of the analyser $\Delta E_{Analyser}$ and the inherent or natural line width of the excited level $\Delta E_{inherent}$, which by Heisenbergs uncertainty principle, is coupled to the excited states lifetime:

$$\Delta E = \sqrt{\Delta E_{Source}^2 + \Delta E_{Analyser}^2 + \Delta E_{inherent}^2} \tag{5.4}$$

The peak position and fine structure are affected by a number of final- and initial-state effects. Final-state effects describe the processes that take place in the changed core level state after the emission and change the energy of the emitted electron, while initial-state effects, describe influences of the core levels electronic surrounding onto the photo electron before the emission. The measured binding energy is the sum over the effects [294]:

$$E_{B,\text{detected}} = E_{B,\text{atom}} + \Delta E_{chem} + \Delta E_{Mad} + \Delta E_{\text{relax}} + C \tag{5.5}$$

The most dominant is the chemical shift ΔE_{chem}. This initial-state effect expresses the local charge distribution at the atom. It can be used to distinguish between oxidized and clean species. A similar initial-state effect is the change in the core level energy in ionic crystals by the periodic electrostatic potential of the lattice, this contribution (if applicable) is given by $\Delta E_{Madelung}$. The relaxation term E_{relax} is a final-state effect and depends on the excitation speed. In a fast Franck-Condon like process, the vibrational relaxation inside of the excited electronic state is slow and will not influence the kinetic energy of the photo electron, in contrast in a slow excitation, the relaxation energy can be (partly) transferred to the ejected electron.

On non conducting samples a positive charge C builds up the more electrons are extracted. Normally its amount is limited to some electronvolt due to compensation by secondary electrons emitted from the Al window of the x-ray source (see section 5.1.2.2) and can be estimated to a constant factor.

Another important final-state effect is the spin-orbital coupling induced level split-up. The electron removed by the x-ray photon from a fully occupied core level, leaves behind an unpaired one and an overall spin of $s = \pm\frac{1}{2}$. The total angular momentum can now take two different values, which induces a split of the level into a doublet from which photoelectrons can be emitted in a well defined ratio.

Auger signals

The Auger process is an important radiationless relaxation process, where the core level hole, created by the the photo emission, recombines with an electron from a higher energy level. Subsequent the excess energy is transfered to a third electron, which is ejected and detected in the spectrometer, or dissipated by emission of a photon (x-ray fluorescence). The Auger signals are not depending on the primary excitation energy, and can be identified by varying the excitation source. In figure 5.3 a KLL series is shown. The notation is derived from the core levels involved. For the KL$_I$L$_{II}$ process the hole in the K shell recombines with an electron from the L$_I$ level and the detected electron is emitted from L$_{II}$. For different elements of the periodic table, different Auger series can be observed, giving a characteristic 'fingerprint'.

5.1.2.2. XPS Instrumentation

Figure 5.4 shows the schematic principle of the XPS set-up used for the measurement shown in this thesis. The source is of the common double anode type. Electrons from a hot filament are accelerated to a target material (here aluminium or magnesium) which is deposited on the tapered end of the anode. This impact ionization process extracts electrons from the coating, in the subsequent relaxation characteristic x-ray photons are emitted according to the core levels involved. For Al this is the $K_\alpha = 1486.6$ eV line [289]. The heat dissipation and charge balancing is accomplished by the well-spaced water cooling on the inside of the anode tip. The Al window at the exit of the source filters the Bremsstrahlung tail emitted simultaneously.

The sample should be placed in the focus of both the analyser and the source. For the realisation of angle-resolved measurements the sample should be rotatable around an axis defined by the intersection point of source and analyser beam and the direction perpendicular to the plane spanned by those.

The analyser consists of three components, an electrostatic lens system, a monochromator and the actually detector. The first is used to focus the electrons, confine their acceptance angle and to adjust their kinetic energy (see below). The standard design of an electron monochromator is that of a concentric hemispherical analyser (CHA). Here the electrons are deflected by an adjustable potential (see figure 5.4) and only those with a specific kinetic energy will reach the opening at the exit slit. The detection is usually done by a secondary electron multiplier (SEM) or a channeltron. The principle of a SEM is shown in figure 5.5. The incoming electron is accelerated to a dynode, where after the impact several secondary electrons n are ejected. Those in turn are accelerated to the next dynode and so on. The total amplification for a m staged device is n^m, typically values of 10^4 to 10^6 are reached. Channeltrons are based on the same principle, but with a continuous voltage drop over a funnel or horn-shaped electrode made of glass covered with a semi-conducting layer.

As indicated above the kinetic energy of the electrons inside the analyser (the transmis-

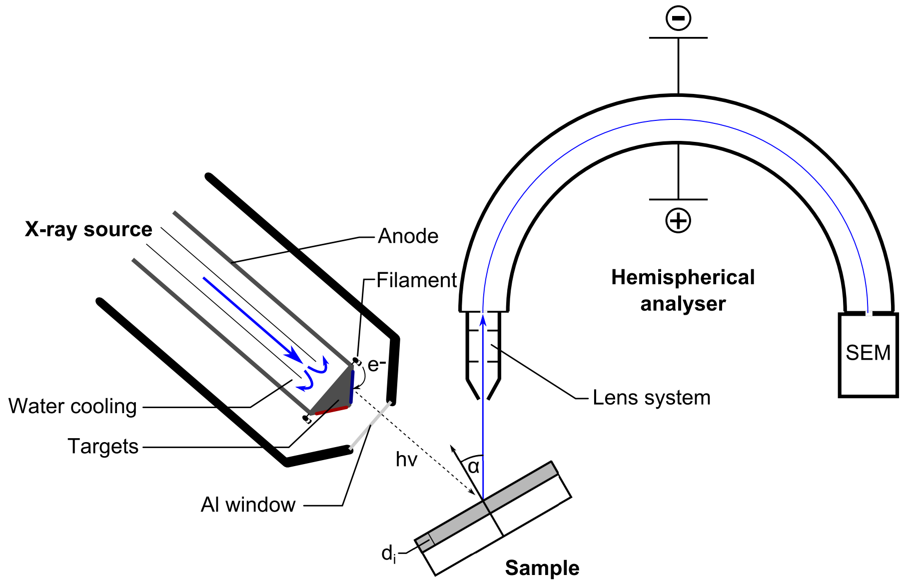

Figure 5.4.: Schematic, unscaled drawing of a photo emission set-up, consisting of a double anode x-ray source, a rotatable sample and a hemispherical analyser with an attached secondary electron multiplier. Based on work from [9, 289].

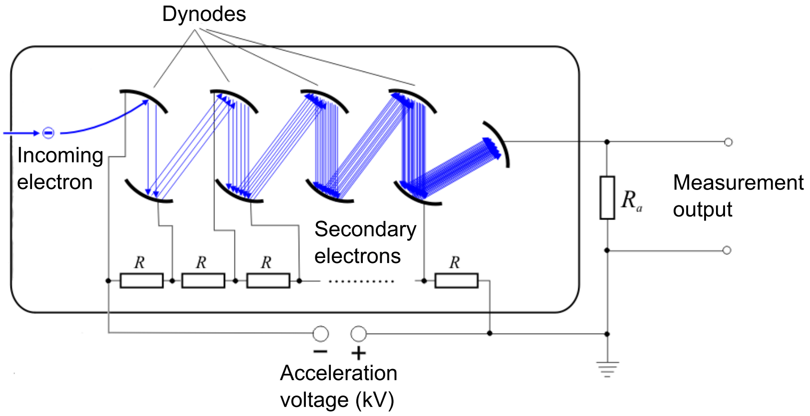

Figure 5.5.: Principle of a secondary electron multiplier. Based on work from Jan Krieger under public domain [295].

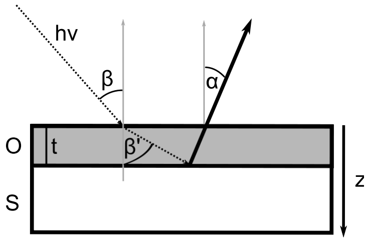

Figure 5.6.: Parameters used for the calculation of the overlayer and substrate signal intensities as function of rotation angle.

sion energy E$_T$) determines the resolution and the sensitivity; a low E$_T$ gives a higher resolution but a smaller signal. The detector can be operated in two modes:

In the constant retarding ratio the retarding field is varied with the kinetic energy, so that $\frac{\Delta E}{E} = constant$. The relative resolution is invariable and the sensitivity increases with higher E$_{kin}$, while the absolute resolution dwindles. In the fixed analyser transmission (FAT) mode, the retarding field is hold constant, resulting in a decrease of signal strength but with a steady absolute resolution ($\Delta E = constant$). This mode is used throughout the complete measurements shown within this thesis.

5.1.2.3. Angle-Resolved XPS (ARXPS)

While the IMFP stays constant, d_i (compare figure 5.4) changes upon variation of take-off angles α between the sample surface normal and the analyser beam:

$$d_i = 3\lambda_A \cdot cos(\alpha) \tag{5.6}$$

By rotating the sample away from the analyser, the surface contribution to the signal increases. When the signal intensity of a film constituent or of the underlying substrate is recorded for different angles, this can be used for depth profiling to determine the thickness of surface layers. [289, 296]

For the following mathematical description a couple of assumptions are made concerning, among other, the ideal and homogeneous flux of the x-ray source and the propagation of photons and electrons and their interaction with material. The most important prerequisite is that the sample has to be flat on an atomic scale; otherwise a detailed a priori knowledge about the surface roughness is to be included into the model.

The electron intensity I_O of an overlayer of thickness t can be established in a Lambert-Beer approach:

$$\begin{aligned} I_O(\alpha) &= I_O^\infty \left[1 - exp\left(\frac{-t}{\lambda_O(O)cos(\alpha)}\right)\right] \\ I_O^\infty &= C\lambda_O(O), \end{aligned} \tag{5.7}$$

where $\lambda_O(O)$ is the attenuation length of electrons emitted from inside the overlayer and C a constant involving the x-ray flux density, geometrical parameters and analyser parameters. It can be seen that I_O^∞, the intensity of a very thick overlayer, does not depend on the rotation angle. The intensity from the substrate is similar to that of the infinite thick overlayer with an additional damping of the substrate photoelectrons in the overlayer, described by $\lambda_O(S)$:

$$\begin{aligned} I_S(\alpha) &= I_S^\infty \; exp\left(\frac{-t}{\lambda_O(S)cos(\alpha)}\right) \\ I_S^\infty &= C\lambda_S(S). \end{aligned} \tag{5.8}$$

The ratio of both intensities at a given angle α is:

$$\frac{I_O}{I_S} = R^\infty \frac{1 - exp\left(\frac{-t}{\lambda_O(O)cos(\alpha)}\right)}{exp\left(\frac{-t}{\lambda_O(S)cos(\alpha)}\right)}, \tag{5.9}$$

with $R^\infty = I_O^\infty / I_S^\infty$. For the simple case of $\lambda_O(O) \approx \lambda_O(S)$ (which, for example is valid for most oxide layers) this ratio can be simplified and rearranged to:

$$\ln\left(\frac{I_O}{I_S R^\infty} + 1\right) = \frac{t}{\lambda \cos\alpha}. \tag{5.10}$$

Plotting this linear expression for different take-off angles allows the determination of the overlayer thickness t. This is valid for small angles at which elastic scattering is insignificant ($\alpha \approx\leq 60°$). As more detailed derivation can be found in appendix A.4.

5.1.3. Scanning Probe Microscopy (SPM)

Nearly all SPM techniques are based on the same fundamental design. This includes a sharp tip probe made from metal or other stiff material that is scanned in xy-direction across a sample surface and whose z position (the probe-sample distance) is sensed by analysing a specific tip-sample interaction. This information is fed into a feedback unit, mostly a proportional-integral-derivative controller (PID), to control the z-position. The principle is shown in figure 5.7A by means of a scanning tunnelling microscope (STM). The three dimensional movement is implemented using the piezoelectric effect of certain crystals, who create an inhomogeneous charge distribution when put under mechanical strain and vice versa react with mechanical deformation when a voltage is applied. This allows a slow but precise movement in the nanometre regime. Also common for many types of SPM are two operation modes. The first is the constant height mode (CH) in which the feedback is turned off and, as the name implies, the tip is moved across the sample at a fixed position. This speeds up the measurement, but can only be used on very flat samples because of the danger of a tip crash. In the resulting picture the change of interaction quantity is plotted as function of xy-position. Obviously the second mode is the constant interaction mode. Here the tip is continuously repositioned along the z-direction to keep the interaction quantity constant. The image is created by plotting the z-voltage applied to the corresponding piezo, needed to keep constancy in the interaction.

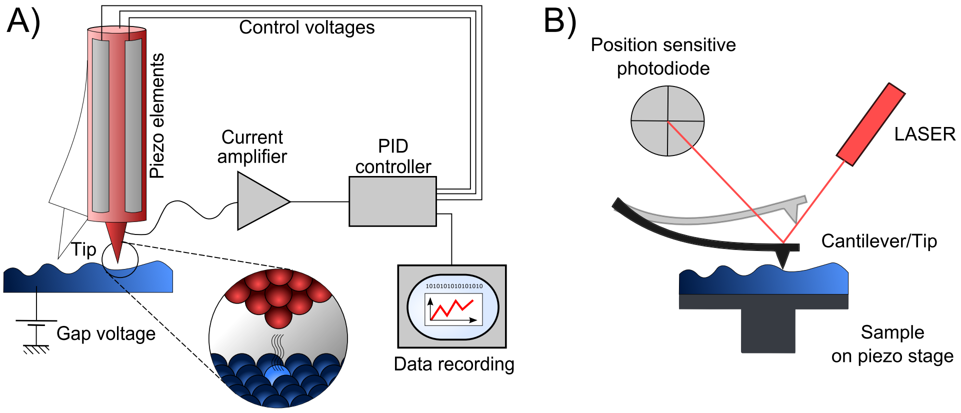

Figure 5.7.: A) Schematic drawing of a STM. Based on work from Michael Schmid, TU Wien [297], published under cc-by-sa [298]. B) Cantilever AFM in tapping mode. The deflection is measured by a laser beam reflecting from the back of the cantilever into a position sensitive photodiode. (published under public domain).

A number of different interactions were utilized to create SPM types, like spin, magnetism or electrochemical potential. The most popular are the atomic force microscope (AFM) and the STM, which was the first SPM technique, invented in 1981 by Binning and Rohrer at IBM Labs in Zürich [299]. This method utilizes the tunnel current of electrons between the sample and the tip after applying a bias voltage. Consequently both parts have to be (semi) conductive. In a simplified form, a more detailed and adequate description can be found in [300], the quantum mechanical principle for this effect and the distance current relation can be deduced, from solving the Schrödinger equation for an one dimensional particle in a box with finite potential walls. With appropriate boundary conditions non zero solutions can be found for electrons within the box and outside. The current distance d dependence for a given tunnelling barrier Φ can be related to the outside wave equation directly:

$$\begin{aligned} I_{tunnel} \propto \Psi^2 &= D^2 e^{-2\gamma d} \\ \gamma &= \frac{1}{\hbar}\sqrt{2m_e\Phi} \end{aligned} \tag{5.11}$$

Here D is a the pre-exponential factor of the general solution. The current is decreasing exponentially with distance, so a tip-sample separation of only a few nanometres has to be established. In the direct proximity to the surface the change is so pronounced, that a vertical resolution of several picometres can be realised. The in plane resolution is determined by the tip-sample interaction volume and so from the apex size, a sub nanometre precision is also possible and thus atomic resolution. As the tunnelling intensity is a function of the local density of states (LDOS) the resulting image is not implicitly a topographic image but an electron density distribution. The method also allows the spectroscopy of local surface states, by recording IV-curves [301]

Atomic force microscopy is based on measuring the attractive or repulsive force between the apex of a tip attached to a cantilever and the atoms of the sample surface below (figure 5.7B). The force distance relation can be described by a Lennard-Jones Potential from which two operation modes can be derived - the contact mode at small tip-sample distances sensing the Pauli repulsive forces and the non-contact mode in the long distance attractive area (Van der Waals, electrostatic and magnetic forces). In the contact regime the constant height and constant force modes both exert a mechanical stress to the sample, which could lead to damage. To reduce the interaction a third method, the tapping mode, was developed. Here the cantilever, driven at its resonance frequency, touches the sample surface only at the lower return point of the oscillation. This operation mode gives additional phase information. In the non-contact regime a similar oscillating mode is used either with amplitude or frequency modulation. A mathematical treatment of the separation depend interaction energy can be found in [301, 302].

The third method, mainly used for film thickness determination, is scanning near-field optical microscopy (SNOM). It combines features of AFM with optical microscopy beyond the diffraction limit. In classical optics the minimal resolvable distance d between two objects is (Abbe 1873):

$$\begin{aligned} d &= 0.61 \cdot \frac{\lambda_0}{N_A} \\ N_A &= n \cdot sin(\theta) \end{aligned} \tag{5.12}$$

where λ_0 is the vacuum wavelength of the light used for imaging and N_A is the numerical aperture of the employed lens element (with the refractive index n and the convergence angle θ). Good lenses offer a N_A of about 1.3, so the Abbe limit is around $\lambda/2$. To overcome this limit the investigated sample has to be brought into the near-field of the light source. The intensity I of the evanescence near-field decays rapidly with increasing distance d form the source ($I \propto d^{-4}$), so a separation around 10 nm or less has to be maintained [301]. This idea was first proposed by Synge in 1928 and due to technical limitations not realized until the mid 1980 (Pohl) [303, 304]. In its current form it was presented by Betzig, where a tapered optical fibre is used as near-field probe [305] (left side of figure 5.8). The distance control is established by dithering the tip laterally to the surface at its resonance frequency. When approaching to the sample surface the resonance is shifted due to shear-force damping, thus the amplitude and phase are changed [306]. This can be measured optically, with a position sensitive detector and a lock-in tuned to the resonance, or by measuring the current flow through the dithering element like a piezo or a tuning fork [302, 307].

On the right side of figure 5.8 the fibre holder of SNOM (DualScope DS 95-50/200, *DME*) is shown. Here the oscillation is provoked by an excitation piezo and the response measured by a second detection piezo.

In figure 5.9 the fundamental different optical modes of operation are summarized. A and D describe the most common modes where the probe is either used as a near-field photon source (A) or as a near-field detector (D). In (B) the light reflected from (opaque) samples is detected. (E) shows a photon scanning tunnelling microscopy (PSTM) set-up where the sample is attached to a dielectric medium which is illuminated from one side in a total internal reflection (TIR) arrangement. An evanescent near field is created at the surface of the dielectric and propagates through the sample before it is collected by the tip. In this way the modulation of the near-field, induced by the sample, is measured. Finally mode (C) describes the back reflection of the signal into the fibre. Due to passing the tip apex twice, the resolution in this mode is higher but at the same time the intensity of the response is low, and superimposed with back reflections inside

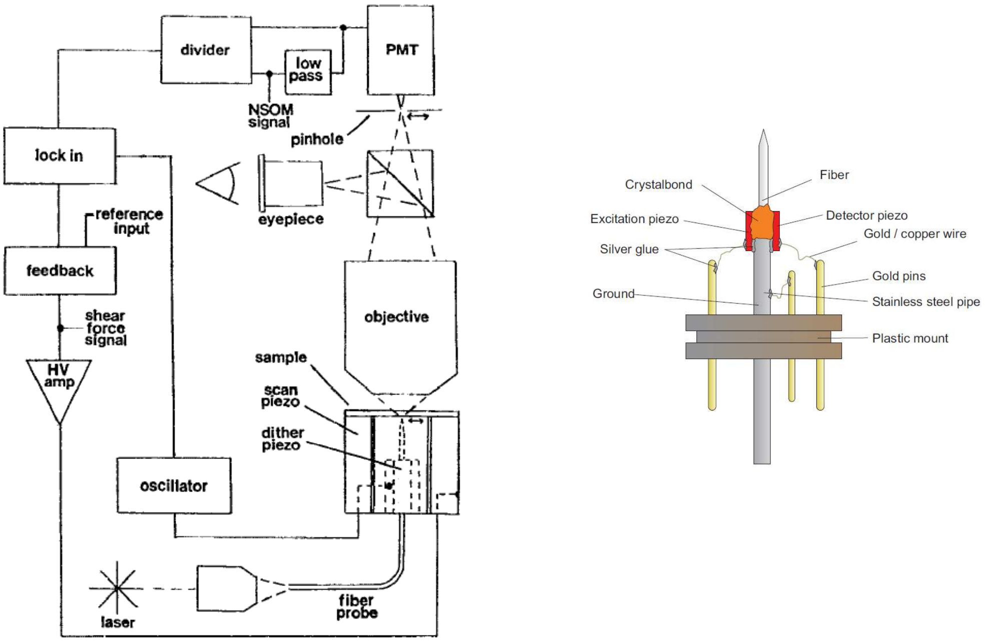

Figure 5.8.: Left: SNOM implementation with optical force detection by Betzig. Reprinted from [306], with permission from AIP Publishing. Right: Drawing of a tip holder of a commercial SNOM (*DME*) [308].

the fibre and from the optical components used in the fibre coupler.

Today there are two well-established methods to prepare probe tips, the use of a common capillary puller, which creates very reproducible sharp tips, or by self controlled etching in hydrofluoric acid [309]. The methods differ in the taper properties of the tip. Further both probes can be metallized to increase the optical resolution. The various advantages and disadvantages between the different tips, concerning factors like light throughput, heating, and topographic vs. optical resolution, are discussed in detail in various publications, i.e [302, 307, 309–311].

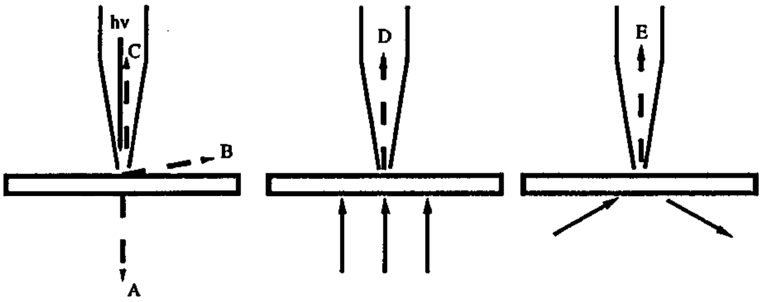

Figure 5.9.: Different optical modes of operations of a SNOM, which are explained in the text. [311, 312] Reprinted with permission from John Wiley and Sons.

	GaAs:Si	**GaAs:Te**
Orientation	(100)	
Miscut	$< 1°$	
Shape	10×0.4 mm discoid	$8 \times 10 \times 0.5$ mm rectangular
Doping /cm^{-3}	1.5×10^{18} Si (n-type)	$1.1 - 2.2 \times 10^{18}$ Te (n-type)
EPD /cm^{-2}	$< 8 \times 10^{4}$	

Table 5.1.: Specifications of the used GaAs samples. Etch pit density (EPD) is a measure of surface quality. As the name implies it describes the density of pits caused by etching. As the pit formation is a result of increased etching speed at surface defects, the EPD is related to the number of defects.

5.2. Sample Preparation

Two types of GaAs (100) substrates (*Crystec*) were used in the experiments. Their specifications are summarized in table 5.1. Both wafers are negatively doped to a comparable level, but with different dopants. For the circular, Si doped sample the angular orientation of the (100) layer is unknown. The tellurium doped wafer is marked by a flat according to SEMI specification and cut in a way that the long side of the rectangular pieces is parallel to the $\left[01\bar{1}\right]$ direction (figure 5.10).

To remove the protective coating and residues from processing the samples were cleaned by ultrasonication in acetone and isopropyl alcohol. For the experiments on pure, native oxide capped samples, the wafers were directly mounted to the optical set-up after this procedure. For the fabrication of platinum covered GaAs the samples were introduced into an ultra-high vacuum (*UHV*) chamber.

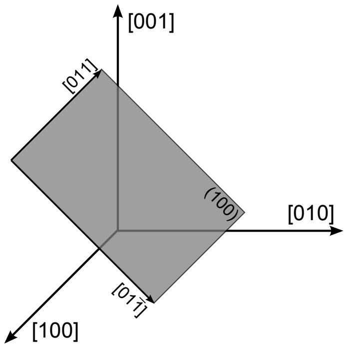

Figure 5.10.: Crystallographic orientation of the rectangular shaped Te doped GaAs(100) substrates

To create a defined interface between gallium arsenide and platinum processing under UHV conditions is inevitable. At a base pressure of 10^{-10} mbar the surface of a sample remains clean for around 10^4 s before it is covered with a monolayer of contamination, considering a simple Langmuir isotherm absorption and a sticking coefficient of 1. As GaAs is quite reactive and tends to form complex oxide layers easily, a residual gas free and in particular an oxygen free environment is required while preparing the interface, not just to prevent the cleaned surface from contamination, but also from reoxidation. Not only the chemical composition of the final sample is strongly influenced by the atmospheric environment, also the formation of highly ordered reconstruction or relaxation layers is only possible under UHV conditions. Beside the direct effect on the sample itself, nearly all of the employed UHV preparation and analysis techniques require a low density of gaseous molecules, as they employ electron or ion beams and therefore need a specific mean free path. The UHV machine used in this work is explained in the next section.

5.2.1. The UHV Chamber

The apparatus was originally developed and installed by Ulrich Leist in 1999 [313]. It consists of a spherical chamber with a movable cooling finger at its centre. This manipulator, to which the sample is attached (cf. section 5.2.2), allows rotational and xyz-directional movement as well as cooling of the sample. Depending on the specific sample holder system employed, temperatures of around 80 K can be achieved by filling the cooling finger with liquid N_2. Beside the infrared spectrometer, all the preparation and analysis devices available are arranged circularly around the central sample position. For surface cleaning purposes the chamber is equipped with a sputter gun (*Tectra*); the resulting crystallographically well defined interfaces can be analyzed by a three grid low energy electron diffraction optics (*Specs*). Further it is possible to evaporate platinum on to the sample by using an electron beam evaporator (*OmniVac*), which is loaded with a 1.0 mm diameter Pt (99.997%) wire (*Alfa Aesar*). Finally a quadropole mass spectrometer (*Pfeiffer*) is attached to the machine to analyse the composition of residual gas and to perform temperature programmed desorption experiments (TPD).
The vacuum is generated mainly by a turbomolecular pump (*Pfeiffer*) in cooperation with an oil free scroll prevacuum pump (*Varian*). In addition, the chamber is equipped with a combined $N_{2(l)}$ cryo- and Ti getter-pump. In this way a base pressure around 1×10^{-10} mbar is obtained. Details about the design and construction of the chamber, as well as details about the methods the chamber is equipped with can be found in

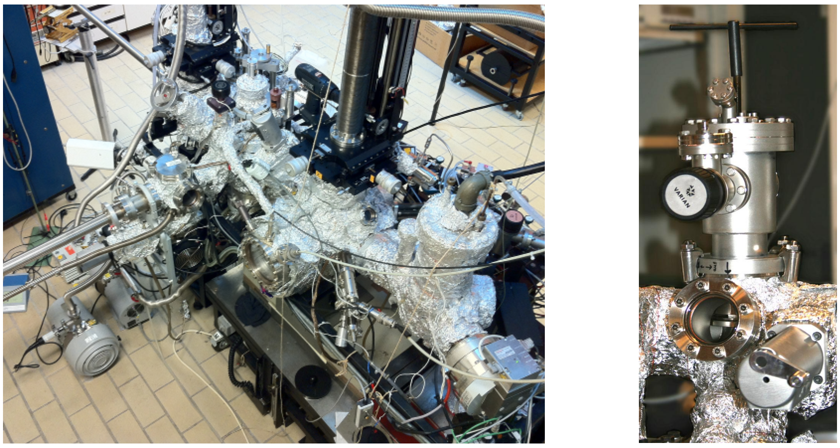

Figure 5.11.: Left: The extended UHV chamber as it was used in this work. Right: Sample transport container attached to the XPS UHV chamber. The image was taken from [9]

[313–315].

This original set-up was extended by Robert Buchwald [31] with a number of new elements such as a new, interchangeable sample mounting, which was developed by Leist and Winkler [316] and is discussed in section 5.2.2. Also a parking station, which allows the storage of up to three sample holders in a separate compartment of the chamber at a base pressure of about 5×10^{-10} mbar, and a sample interlock was added to the device. Beside these modifications, a complete secondary chamber was installed, mainly for scanning tunneling microscopy and specific laser desorption experiments, which is not important in the scope of this work. Figure 5.11 shows an image of the complete new set-up.

5.2.2. The Sample Holder

The first sample mount layout consisted of four tantalum rods which were attached to a sapphire block. This block was in turn connected by a copper adapter to the cooling finger. The sample was wired to two of the rods. The other two were used as holder and electric connection for a tungsten or tantalum filament. This layout was designed for the use of metallic single crystals with a typical thickness of some millimeters. It is shown on the left side of figure 5.12.

In order to allow a sample exchange without opening the UHV chamber a new holder system was developed in this work-group by Ullrich Leist and Alexander Winkler together with Jens Büsow from the mechanical workshop of the university [314, 316, 318, 319]. On the right side of figure 5.12 an early implementation of the new design is shown.

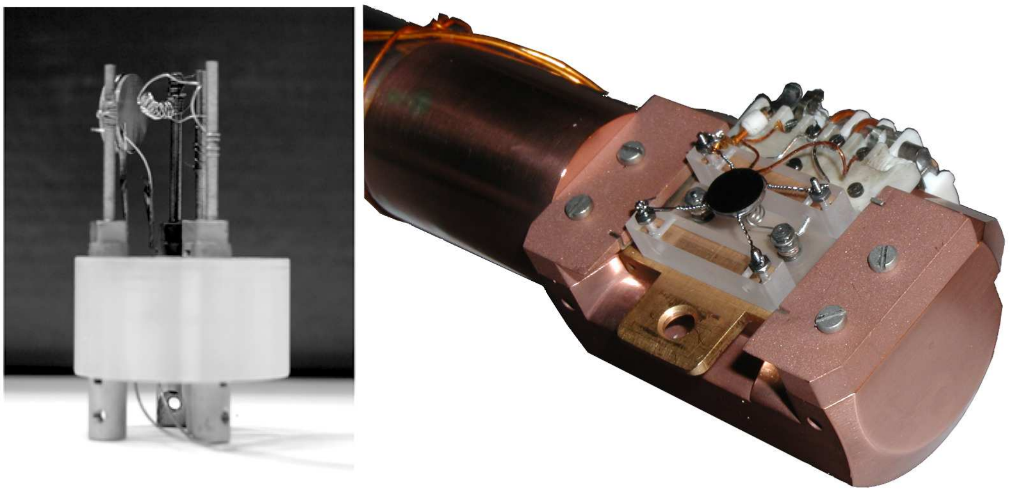

Figure 5.12.: Left: Old fixed, sample mount (picture from [317]). Right: New interchangeable holder inserted into the cooling finger.

In this figure one can see the copper docking station attached to the cooling finger and a docked sample holder. Electrical connections are established by a contact stripe on the docking station side and by a number of plugs, in form of sheet metal brackets, on the sample holder. To achieve a high cooling efficiency the sample holders ground plate is gold coated and the sample is mounted to two sapphire blocks, which exhibit a high thermal conductivity at low temperatures. Heating is done by a Ta or W filament, which is placed below the sample. By applying a high voltage up to 1000 V to the filament an additional heating by electron bombardment can be realized. The sample itself is mounted to the holder by wires, as shown in figure 5.12, or by clamping it directly onto the sapphire blocks (for details refer to [31]), using two sheet metals. The sample temperature is measured by a thermocouple which is spot welded to one side of the sample.

Here a problem becomes evident, when using small and thin semiconductor samples. On one hand it is neither possible to clamp them directly, due to its small size and high brittleness, nor can they be fixed by wires and on the other hand it is impossible to spot weld a thermocouple. As the wafer pieces are used only for a single experiment, the fixing should support a quick sample exchange in combination with a reliable and reproducible temperature measurement. To meet these objectives a new wafer fixing was developed and mounted onto the sapphire blocks. The clearance of this fixing was designed to fit the standard sample geometry exactly; the two curved metal sheets clamp the wafer to this position. Beside a reliable fastening, the lowering of the sample, compared to

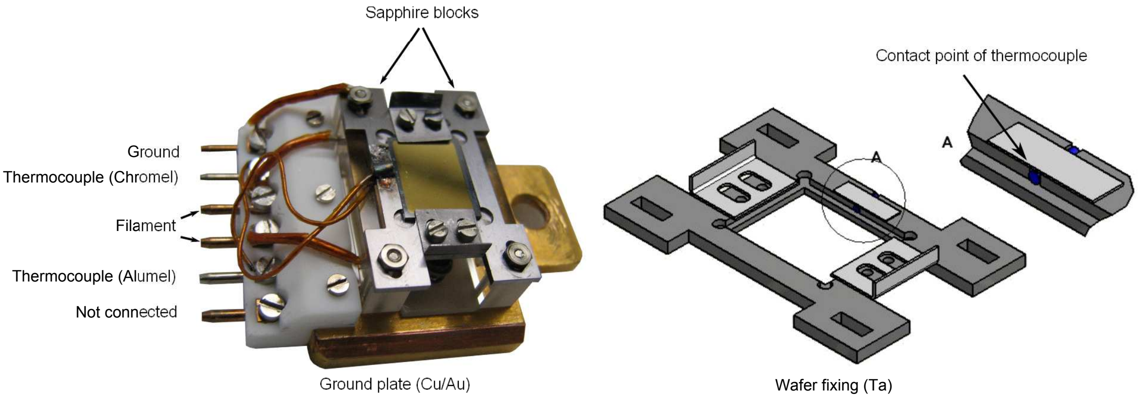

Figure 5.13.: Left: Sample holder with wafer fixing and new electrical connectors. For testing purposes it is equipped with a gold covered silicon sample. Right: CAD model of the wafer fixing. The thermocouple contacts the sample from the side.

the Ta plate's surface, reduces the sample filament distance and hence increases the heating performance. The thermocouple is embedded in a notch and should contact the sample from the side, directly at the welding between the alumel and chromel part. This advanced holder is depicted in figure 5.13. On the left side the complete assembly is shown. That version already comes with a revised electrical connection, developed by Ralf Nustedt and Stephanie Neuendorf, with conic male plugs on the holder and spring loaded jacks at the docking station. This modifications lead to a more reliable and durable electrical connection. Details about this can be found in [31, 320, 321]. The right side in figure 5.13 displays a CAD model of the wafer fixing, in particular the contact point of the thermocouple and the sample.

While for the preparation of different GaAs surface reconstructions temperatures up to 850 – 870 K are necessary, for the growth of the platinum films temperatures down to 100 K should be accessible. This temperature range is in general easily obtainable. With the standard sample holder, e.g. the holder shown on the right side of figure 5.12 the sample can be cooled down to 80 K, when filling the cooling finger with L-N_2 and heated up to temperatures larger then 1100 K, by operating the filament at around 40 W and additional electron bombardment. Nevertheless using the wafer-fixing sample holder, it was not possible to measure temperatures larger then 240 K, even when heating at 50 W filament power. As for the time of the development and testing of this holder modification no additional UHV temperature measuring method was available in the group, it was not finally solved whether this problem was one of insufficient heating power or incorrect temperature measurement.

The rather bulky tantalum element not only adds a large quantity of heat capacity to the system, the large contact area between the metal and the sapphire blocks could also increase the heat transport away from the sample into the cooling-finger. A similar tendency was also found in earlier experiments where a massive Ta sheet was used as sample support (cf. [315]).

In a thermocouple based temperature measurement the temperature dependent contact potential between two dissimilar metals or alloys is measured. In the ideal case this contact point is small and well defined, in practice is is created by welding, and it's dimension is thus related to the size of the electrodes used. Also the insulating Kapton ® (*DuPont*) cleading will be rapidly pyrolyzed, leading to additional mechanical tunnelling contact points between the two elements of the thermocouple and thus to an additional influence on the signal. Overall these limitations in combination with the geometry in which the thermocouple is surrounded by the tantalum frame from three sides and only loosely contacted to the wafer, will induce a large error to the measured temperature.

Further development of this device was stopped, when a third holder type became available, that was before successfully used in deposition and decomposition experiments of metallic and rare-earth inorganic precursors on silicon wafers [9, 322]. It is another more complex implementation of the interchangeable holder, where a second, smaller sample holder, called sample plate, is attached to the sapphire blocks by two clamping elements. This plate has a bored hole in the middle, over which the sample is placed and two female connectors for the thermocouple (fig. 5.14b).

This set-up has it's origin in another chamber equipped with a scanning tunnelling microscope (*Omicron*). There the smaller sample plate is necessary to introduce the sample into the STM. Although this system, just like the wafer fixing setup described before, contains an additional Ta layer it is possible to reach temperatures between 100 K and 1200 K, even though the cooling rate at lower temperatures is very small. Maybe this is due to the divided structure of the sample plate and clamping and its merely mechanical contact.

The temperature is measured by a thermocouple clipped on to the sample surface by a piece of s-shaped tantalum sheet (fig 5.14a). In the previous experiments this holder was used, the tip of the temperature sensor was capped with a drop of a ceramic adhesive (see figure 5.14c) [9, 322]. This was necessary because of the large reactivity of silicon with the Ni contained in the thermocouple [323]. Since a similar behaviour, especially in combination with Ge, is known for GaAs too, this arrangement was adopted [324–326]. As a protective coating an inorganic compound based on zirconium oxide was

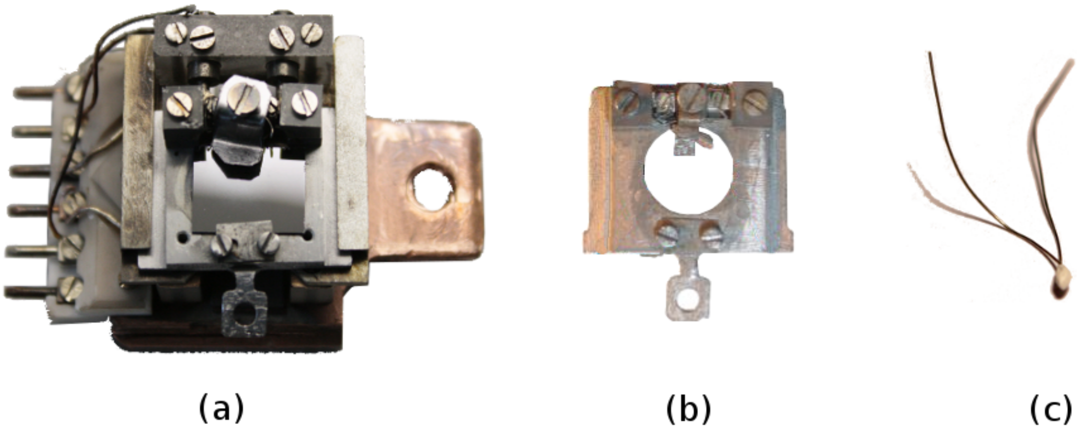

Figure 5.14.: The third implementation of the interchangeable holder model. (a) The complete assembly. (b) The sample plate with attached thermocouple. (c) Sealed thermocouple.

used (ULTRA-TEMP 516, *T-E-Klebetechnik*). In its final state it is non degassing and characterized by a high thermal stability up to 2030 K and high thermal conductivity of 111 W/m K (compared to 44 W/m K of GaAs [327]), it is thus very suitable for the UHV processes. To check the accuracy of the temperature measurement a calibration was performed which is described in appendix B.1.

5.2.3. Preparation of Platinum Covered Samples

In the following section the individual steps for the preparation of the platinum covered samples and the use of the non-optical analysis methods introduced above are described briefly. After the initial cleaning with organic solvents the wafer piece was mounted to the sample holder and introduced to the load lock of the UHV chamber (cf. section 5.2.2). As soon as a pressure of less than 10^{-8} mbar was reached, the sample was transferred into the main chamber.

Surface Cleaning

To create a clean and well defined crystalline GaAs surface different methods can be applied. On one hand there are growth processes like molecular beam epitaxy (MBE) or metal-organic chemical vapour deposition (MOCVD) [328] and on the other hand there are the ablative techniques, as cleaving, etching or sputtering. In the experiments presented in this work the latter method was used in which Ar^+ Ions, generated by electron impact from a hot filament, are accelerated on to the sample at angle of incidence

Duration	Process	Temperature	Parameter
20 min	Sputtering	$620 - 670$ K	1000 eV, $p_{Ar} = 5 \cdot 10^{-5}$ mbar 3 µA emission current
15 min	Annealing	$790 - 850$ K	

Table 5.2.: Default parameters of the sputtering and annealing cycles for gallium arsenide wafers

of 45°. The fast nonreactive noble gas ions mechanical remove the surface layers of the target by impulse transfer. By controlling the partial pressure of Ar and the acceleration voltage the amount and energy of the impinging ions can be adjusted. Typically a voltage between $600 - 1000$ V, a pressure $\mathrm{p_{Ar}}$ of 5×10^{-5} mbar and elevated sample temperatures where used for cleaning of GaAs surfaces in this chamber. On GaAs surfaces exposed to air the main contamination beside carbon containing residuals from the initial cleaning, is the native oxide layer. For basic cleaning, repeated cycles of sputtering and subsequent annealing at higher sample temperatures had to be conducted. This is sometimes abbreviated with (S)IBA - *(simultaneous) ion bombardment and annealing* (see also section 4.1.1). While the sputtering roughens the target surface, the heating in the latter phase increases the mobility of the atoms in the surface layers, leading to a curing by relaxation or reconstruction processes. The standard parameters for SIBA cleaning are summarized in table 5.2. It should be pointed out that due to the binary composition of gallium arsenide crystals a great number of different surface configurations can be established which exhibit different microscopic geometries and surface compositions. The specific formation is strongly depending on the cleaning or preparation method and the temperature of the annealing phase [162]. Details about the different surface configurations can be found in section 4.1.1.

LEED

To monitor the cleaning progress and the morphology change during the cleaning and annealing processes, LEED measurements were made between the cycles with a three grid LEED device (ErLEED, *Specs*). Due to the chamber design it was not possible to do this while sputtering. The pictures were recorded using a standard digital camera attached to a stand and placed in front of the view port. For the analysis the spot centres were marked and the average distance between all neighbouring spots was used. In this way the bulk lattice parameters of GaAs were calculated using equation 5.1. Technically this was done using GIMP (gnu image manipulation program), taking the known screen diameter as a reference length. The sample-screen distance r was extracted from the construction plans of the chamber.

Platinum deposition

After the desired surface reconstruction was created, a specific amount of Pt was deposited onto the sample surface by physical vapour deposition (PVD) from an electron beam evaporator source. In the evaporator a 1 mm diameter Pt Rod of 99.997% purity is heated by electron bombardment from a surrounding filament (2 A heating current, 1000 V acceleration voltage). The outlet port of the evaporator is equipped with a shutter to control the evaporation time and an ion trap to remove ionized platinum particles and thus reduce possible sputtering effects. At the same time this acts as a flux monitor, measuring the ion induced current. This current is proportional to the evaporation rate and for a given high voltage and sample position also to the platinum flux onto the sample. In all preparations the flux was kept constant and in tune with the settings used in other experiments (for instance [236]). The actual atom flux rate was calibrated using a quartz microbalance (*Tectra*) which was put in place of the sample. Due to the position requirements of the balance the thickness could not be measured concomitantly, the required evaporation time for a specific platinum amount had to be determined in a separate processing step. In the microbalance an oscillation circuit excites a standing acoustic wave, utilizing the piezoelectric effect, inside a quartz crystal which is used as evaporation target. A change of the mass of this crystal by depositing platinum leads to a shift in the resonance frequency which is measured. With a given density and the correct tooling factor accounting the geometric alignment between the quartz surface and the evaporation source, the coating thickness can be established with an accuracy up to 0.1 nm. The thickness resolution of the used controller (IL150, *Intellemetrics*) is 0.1 nm, the evaporation rate can be resolved with 0.1 nm/s. For the experiments in this thesis, a Pt amount between 0.3 to 0.5 nm was deposited, which is at the hard limit of the measuring accuracy of this method. In this regime distortions due to electric fields inside or around the chamber will influence the measurement. Another important factor is the pyroelectric effect which occurs when the shutter of the evaporator is opened and the radiation from the filament heats the quartz crystal. Unless a new thermal equilibrium is established by the water cooling the resonance is increased, resulting in a negative evaporation rate reading. In figure 5.15 calibration curves of some preparations are shown. The evaporation rate is extremely small in the range of 8 pm/min. Even though there is a small offset between the individual preparations, the deposition speed

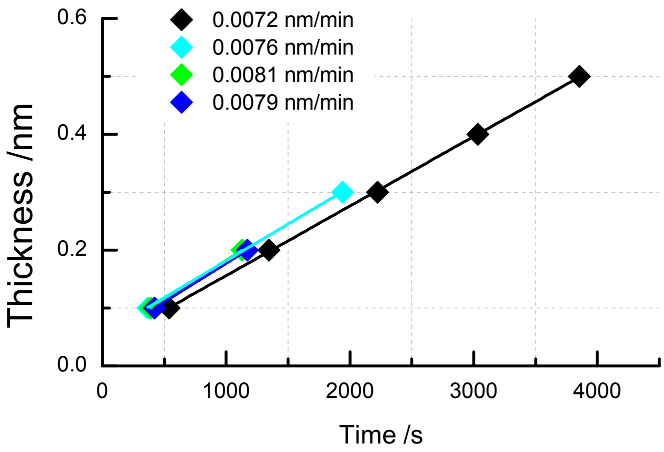

Figure 5.15.: Evaporation calibration curves from different preparations. The evaporation rate is extremely small, but constant.

is constant and comparable. To validate the coating thickness, additional measurements were performed, as described in the following sections.

Beside the above mentioned different amounts of platinum, the substrate temperature was varied to create differently structured surfaces. From experiments on oxidic supports it is known that the latter parameter affects the mobility of the Pt adatoms and thus controls the growth mode and the formation of islands or film like coatings [29, 236, 237]. Also the strongly temperature dependent platinum diffusion into the GaAs substrate and vice versa plays an important role [239]. This is discussed in detail in section 4.2.1.1. After the preparation the sample was stored as long as possible under UHV conditions in the park station to prevent the system from reoxdiation.

X-ray photoelectron spectroscopy

To examine the quality of the prepared samples, which is defined by a complete removal of surface contaminations and the native oxide layer as well as a distinct amount of non-oxidized platinum, the sample could be transferred in an evacuatable sample transportation container to a second chamber which is equipped with a x-ray photoelectron spectroscopy (XPS) device.

The right side of figure 5.11 shows the container attached to the load lock of the XPS chamber. The sealing of the transport container is provided by a Viton ® (*DuPont*) o-ring permitting the device to maintain a vacuum of about 10^{-5} mbar for a short while, when dismounted from the chamber. Even when the sample is handled quickly between the chambers, a recontamination with small amounts of oxygen could not be completely prevented.

The XPS equipment consists of a non monochromatic Mg / Al double anode x-ray source (XR 50, *Specs*) and hemispherical electron energy analyser (EA-10P, *Leybold-Heraeus*) in combination with a secondary electron multiplier. The sample was mounted to a cooling finger in the same way as in the preparation chamber, which allows a rotation of the sample and thus different angular alignments between the specimens surface and the inlet of the analyser. The double water cooling facility in the x-ray source, one direct behind the anode, which is also used for grounding the anode, and a second at the anode casing, together with the possibility to cool the sample with $N_{2(l)}$ prevents the sample to heat up during long analysis. To counteract a charging while measuring, the sample was grounded. For a semiconductor the effect of this procedure is of course limited. An additional electron source which would compensate the charge-up was not available. The technical data of the source and the analyser are summed up in table 5.3 and 5.4 (according to [9, 289, 329] and references therein).

X-ray source:	
Acceleration voltage	12 kV
Emission current	25 mA
Orientation to sample	45°

Analyser:	
Analyser work function	4.9 eV
Mode	ΔE = const.
Pass energy	50 eV
Resolution	~ 0.5 eV

Table 5.3.: Technical specification and operation parameters of the x-ray source and the electron energy analyser [9, 289, 329]

Anode material	Energy	Linewidth
Mg $K_{\alpha 1,2}$	1253.6 eV	0.7 eV
Al $K_{\alpha 1,2}$	1486.6 eV	0.85 eV

Table 5.4.: X-ray energy and linewidth of the two provided sources [9, 289].

The spot size of the analyser is not adjustable and covers an area of $5 - 10$ mm [9]. Thus the excitation spot illuminates the complete sample. The response is thus always an averaged signal over a larger volume. Because the sample surface is not in line with the rotation axis of the cooling finger, a number of precalibrated sample positions were used for the angle-resolved measurements [320], compensating the movement of the sample.

The analyser is controlled and read out by 'SPECTRA Windows Version 8.0-A-1' (*Scientific Instrument Consultants*).

For the spectral processing the data was exported into a spectral processing software ('SDP 4.5' by Vince Christ (*XPS International*)). The database of this software was also used to remove the non-monochromatic x-ray satellites from Al or Mg sources, prior to the actual analysis. For a first classification of the peaks found in a spectrum, the signatures from various compounds, comprising of the characteristic photo electron signals from different core levels, were assigned based on tabulated data from different databases as for example [330, 331]. The detailed analysis of the individual peaks was done by peak synthesis. Both the necessity and the quality of fitting depends on the signal to noise ratio (SNR) of the peaks and their full width at half maximum (FWHM) which is determined by the analysers resolution and the energetic width of the x-ray emission line, as summarized in equation 5.4 in section 5.1.2.1. Only the first factor of influence can be adjusted by repeated scans. The increase of SNR is proportional to $\sqrt{n_{Scans}}$.

In principle the broad convoluted peak is fitted by a sum of curve profiles and a baseline function. To prevent overfitting it is important to constrain the fit by *a priori* information about the peak and sample, for example by specification of intensity ratios and energy differences for peaks with spin-orbit coupling. The peak shape used in the fit is of pseudo Voigt type, a linear combination of a Lorentzian and a Gaussian. The first is the natural shape of the x-ray emission line and of the photo emission, the later describes the statistical variance. For the baseline correction the Shirley fit is widely used, as it successfully reproduces the stepped inelastic loss tail [332].

Surface probe microscopy

Scanning probe microscopy, mainly in form of atomic force microscopy, was used to characterize the surface structure of the native oxide covered samples and to investigate the growth and diffusion properties of the platinum deposition. In addition to the XPS and LEED measurements and knowledge gained from previous experiments on alumina, information obtained by SPM allows to complete the picture of the samples chemical and structural properties [29, 236].

The AFM measurements (Dimension 3100, *Digital Instruments / Veeco*) were performed in tapping mode using RTESP cantilevers from *Veeco* and *Olympus*.

To a small degree a scanning tunnelling microscope (EasyScan, *Nanosurf*) was used on the metal covered samples. In the compact and simple device a fissured tip made from platinum iridium wire is used as probe. The scan area of this device has a maximum size 500 × 500 nm. A shift of the lateral scan coordinates beyond this limits is not possible, so only a small part of the sample can be scanned. The quality of the self made tips and the accuracy of the lateral displacement of the piezos was checked by calibration (see appendix B.2). The samples were glued to the holder by conducting carbon pads, normally used for scanning electron microscopy. Additionally the sample surface was contacted by conducting silver glue (Acheson Silver DAG 1415, *Agar Scientific*). With this preparation it was possible to investigate the metal covered samples, while the oxide covered GaAs specimen did not exhibit stable tunnelling current. The problem of scanning GaAs surfaces at air is commonly faced by cleaning or cleaving the crystal under UHV conditions and passivating the surface by evaporation of a thin Au layer [333, 334], sometimes in combination with a high dopant concentration [335]. Both counterproductive approaches for the scope of the experiments discussed here. The scanning parameters found to produce stable and reproducible images are summarized in table 5.5.

Scan mode	Constant current
Bias voltage	-2.5 V
Current set point	-0.2 nA
Line speed	$0.07 - 0.3$ s^{-1}

Table 5.5.: STM scanning parameters. The negative sign for the voltage and current indicates a positively biased sample.

In the course of the experimental work a scanning near-field optical microscope (SNOM) was installed (DS95-200, *DME*). In the shear force mode the tip of the microscope oscillates parallel to the surface, resulting in a height resolution of about ten picometres. The lateral scan size covers an area of 200 × 200 μm, a coarse positioning can be done by a manual micrometer screw driven xy-table. The lateral resolution is limited by the size of the tip which is typically 50 to 100 nm thick. The optical part consists of a back reflection set-up with a 650 nm HeNe laser coupled into an uncoated, apertureless fibre and a photodiode as detector. The received image was merely used to get additional contrast between the uncovered and Pt areas. The calibration routines of the AFM and SNOM are also shown in appendix B.2.

In some cases further analyses with methods like optical microscopy, scanning electron microscopy (SEM) or energy dispersive x-ray spectroscopy (EDX) were performed.

5.3. Optical Experiments

Previously to this work and with the exception of some static SHG experiments on organic nanofibres [109], the laser equipment was mainly used for laser induced desorption (LID) experiments on model catalysts under UHV conditions with frequency-doubled amplified pulses. A major part of the work was to gain know-how in tuning the light sources, designing optical set-ups, assembling the electro-optical measurement techniques and implementing software for data acquisition and experiment control. In the following sections the results of this process and the different optical experiments used are presented.

5.3.1. Light Sources

The time-resolved experiment presented in this work were performed using either a femtosecond oscillator or a regenerative amplifier system. The oscillator, a MiniTS from Kapteyn-Murnane Labs (*KML*), is pumped by a frequency doubled Nd:YVO_4 cw laser (Millenia Vs, *Spectra-Physics*). It generates sub 35 fs laser pulses [336] with around 3.16 nJ per pulse at 95 MHz. It employs passive Kerr lens modelocking and a prism assembly for dispersion compensation. Additionally a movable slit (S) is placed in the Fourier plane in front of the second prism (P2) (see figure 5.16). By a combined movement of P2 and S it is possible to tune the lasers central wavelength in the range of 790 nm and 850 nm. Outside the cavity a small portion of the beam is split off and analysed with a compact fibre optics spectrometer and a fast photo diode for tuning and synchronisation purposes. When experiments were performed with the amplifier system, the KML oscillator is used as a seed.

The amplifier (Legend, *Positive-Light*) is designed as a chirped pulse amplifier with a regenerative multi pass core. To prevent the laser rod from self focusing induced damages, the peak power of the pulse to be amplified is reduced by prefixing a grating based pulse stretcher. The principle is equivalent to the dispersion compensation in the oscillator but with opposite effect, inducing a large positive chirp. After the amplification process, the pulse is recompressed by a similar compressor set-up. The actual amplifier consists of a complete Ti:sapphire laser cavity, which is pumped by a frequency doubled (527 nm) 8 mJ Nd:YLF laser at 1 kHz. With the help of synchronized high speed electronics con-

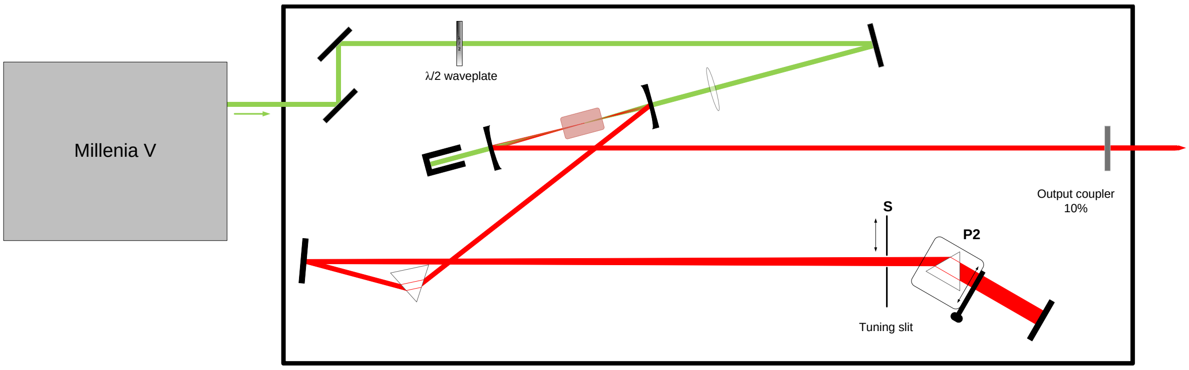

Figure 5.16.: Layout of the KML femtosecond laser.

trolling Pockels cells inside the cavity a single pulse from the seed source is trapped in the resonator precisely timed after the pump pulse created the population inversion inside the active material. In this way the trapped seed pulse induces the emission. After a number of round trips, when the energy stored in the crystal is consumed, the pulse is dumped by a second Pockels cell and a polariser (more details can be found i.a. in [153]). The resulting femtosecond pulses have an energy of up to 1 mJ (at 1 kHz) after compression and a temporal width of about 50 to 80 fs.

5.3.2. Pump-Probe Measurements

Pump-probe measurements are a common method to study processes on an ultrashort timescale, which may be defined as the low picosecond range down to the sub femtosecond range, not accessible by conventional detection schemes involving electronics or even fast streak cameras [11, 115, 281]. They are based on a two pulse sequence at least in which the first pump pulse triggers the event, for example creating a population of hot electrons in the conduction band of a semiconductor or transferring a molecule in an excited electronic/ vibronic state, and a second, in general weaker, delayed pulse which interrogates this pump induced change. Different optical properties can be exploited in the probing process. Most prominent in the linear regime are changes in the reflectivity or transmission respectively and Raman scattering. Regarding the special surface sensitivity, second harmonic generation is also highly suitable. By varying the central frequency of the pump pulse also spectroscopic aspects can be included, like it is done in time-resolved infrared spectroscopy related sum frequency generation experiments [143]. Related to these pure pump-probe techniques are time-resolved luminescence experiments. Here the pump pulse induces the emission of light (e.g. photoluminescence) which is collimated and focussed onto a nonlinear medium. The delay gated pulse couples with this emission by parametric up conversion. The generated sum frequency signal can then be detected as a function of gate pulse delay. The common method to produce a defined delay is to convert the temporal problem into the spatial domain, by splitting off a small amount from the excitation pulse and delaying it with the help of a precise translation stage in an interferometer set-up.

To gain insight into the carrier and lattice dynamics at the interface regions of the GaAs-Pt samples, time-resolved SHG measurements are performed, where the probe pulse interacts with the various nonlinear tensor elements described in section 2.3.1. For each delay step, the produced SH signal is filtered off the strong reflection signal of the fundamental and then its intensity is measured and averaged over a large number of pulses. Of course now the detector is integrating the intensity over the complete probe pulse, resulting in a convoluted response which limits the temporal resolution to the range of the FWHM of the probe.

5.3.2.1. TR-SHG with Amplified Femtosecond Pulses

The need to inject a high number of carriers into the semiconductor (see section 4.1.4), makes the amplifier system which generates high energy pulses with a 5 mm diameter wide spatial profile, a suitable light source for the planned experiments. Also, a high pulse energy eases the spatial and temporal alignment of both pulses onto the sample without the need of a strong focusing. The second harmonic generated at the GaAs sample is visible by eye, which makes the routing of the reflected beam inside the analyser less difficult. The complete layout of the set-up is shown schematically in figure 5.17. In the upper left corner, the pulse generation as described before is shown. Noteworthy is the fast photo diode placed after the oscillator. It's signal is amplified by a circuit designed at the university's workshop and then lead into a synchronisation device, which matches the timing of the 1 kHz of the regent amplifier with the fast repetition rate of the oscillator. The triggering of the detection circuit is obtained from this device too. The output of the amplifier is guided to the pump-probe set-up by a periscope, which routes the beam to the standardized optical height and rotates the polarization of light to vertical, as needed for the beamsplitter. This splits the beam at a 80/20 ratio into a strong pump beam and a weaker probe pulse. The pump is retro reflected from a mirror assembly attached to a computer controlled delay stage (*Physikalische Instrumente*) and guided through a chopper (*Thorlabs*) and a waveplate for polarisation control. The probe beam is folded due to space limitations on the optical table (Beside that the experiment can be easily extended by removing retro reflector 1 and routing one pulse through pulse shaping arrangements). It is also passed through a waveplate and a manual delay stage, before it is reflected from the edge of a steering mirror M1 in the sample direction. In autocorrelation measurements with a commercial single shot autocorrelator (SSA, *Positive Light*) of the individual beams, no influence on the temporal width due to the more complex path of the probe beam interacting with a larger number of optical elements could be found by this rather simple measurement. Both pump and probe beams are then focused by a convex lens placed on a moveable xy stage. The non parallel beam alignment before the lens leads to an overlapping of pump and probe on the sample out of focus, which otherwise would damage the sample. The sample is placed on a rotatable stage with a 45° orientation towards the centre of the incoming beams. After blocking the pump and cross correlation beams the reflected light is re collimated and feed into the analyser assembly which is covered by a reflectivity reduced black housing. To reduce the stray light contribution, another pinhole and a tube is placed at the entrance. Inside, the second harmonic radiation is purified by a colour glass filter, a polariser and a narrow-bandwidth interference filter, centred at 400 nm before it is finally focused on the entrance slit of a photomultiplier (PMT) (R943-02, *Hamamatsu*), which is based on a secondary electron multiplier as shown in figure 5.5 in section 5.1.2.2 with an additional photo cathode converting an incoming photon into an electron (external photoelectric effect) [337]. The PMT is optimized for photon counting and operated at 2000 V creating a gain of $5 \cdot 10^6$ and cooled by a thermoelectric cooler down to -30 °C to reduce the dark count to less than 2 /s.

The inset shows a detailed picture of the beams close to the sample. When a delay is set within the temporal pulse width, the slightly focused beams overlapping on the sample result in five outgoing rays: Two reflected fundamental beams and collinear to those, their SHG counterparts and a second harmonic beam representing the autocorrelation for the given delay pointing in a direction given by the sum of the wave vectors of involved pump and probe beams. As for the analysis only the modulated probe is of interest, the other components have to be carefully blocked as shown in the figure using a pinhole. For the experiments with the amplifier, the samples are mounted to a 2" disc made of anodized aluminium, which in turn is mounted to a standard mirror holder placed on a rotatable platform. For the coarse alignment the sample can be replaced by a thin beta barium borate (BBO) crystal also mounted to such a disc. By tuning the manual delay stage and steering mirror M1 the spatial and temporal overlap is optimized by creating a bright cross correlation spot with high spatial quality. Additionally intensity autocorrelation and FROG traces were recorded by placing a fibre optic spectrometer

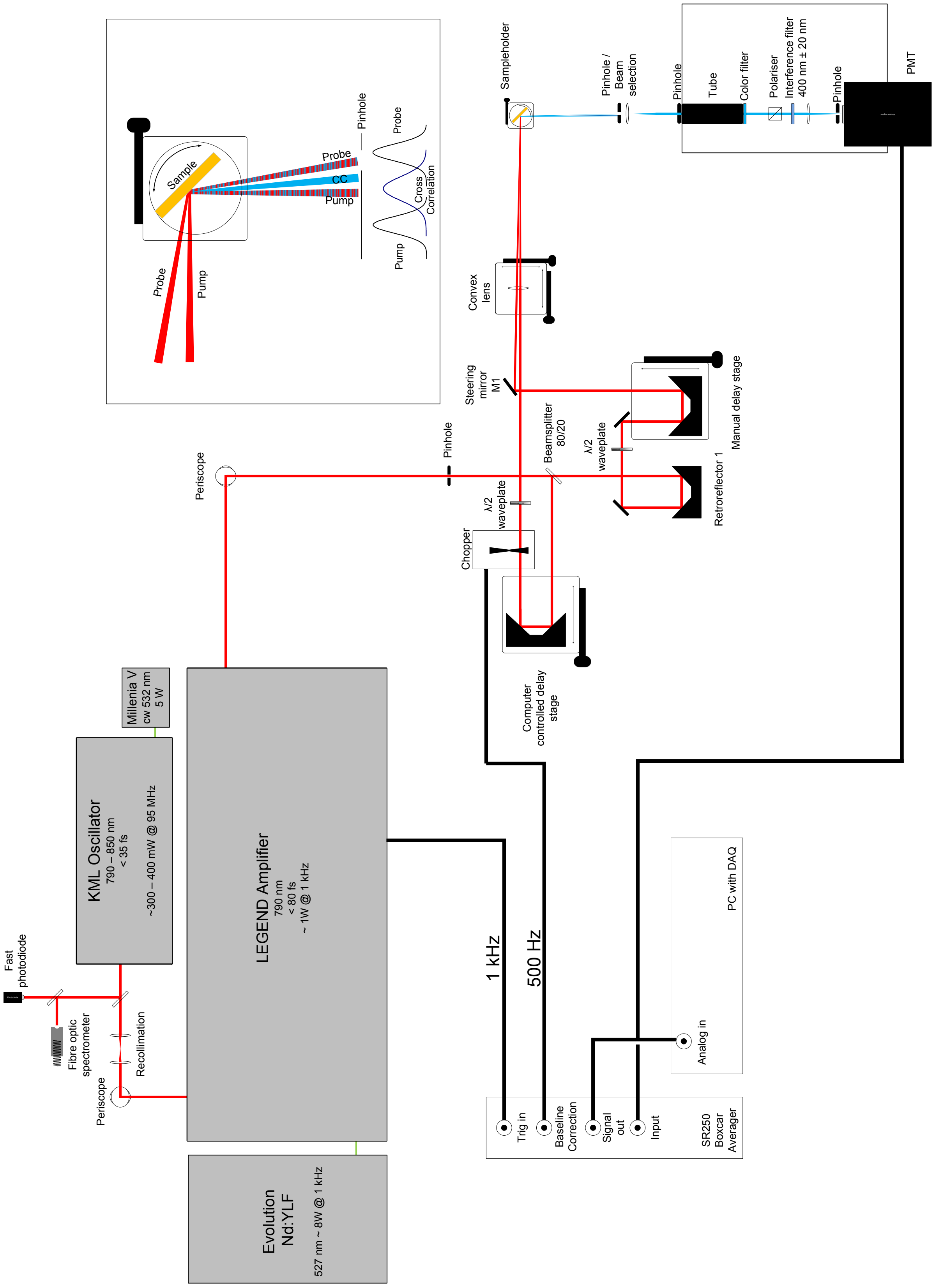

Figure 5.17.: Pump-probe set-up for amplified pulses.

behind the crystal and using a self written software (cf. section 3.2.2).
The third section found in figure 5.17 depicts the detection scheme. The SHG light entering the detector is still in the femtosecond regime and can be treated as a delta function in the scope of the PMT. The temporal character of the current pulse produced by the device is determined by the rise time, the electron transit time and its statistical spreading. Nevertheless the approximately 10 ns long pulses are very short compared to the 1 ms period of the laser repetition rate, thus the duty cycle is too low for using lock-in techniques. In combination with the high count rate the appropriate detection scheme is boxcar averaging, also known as gated integration (cf. figure 5.18).

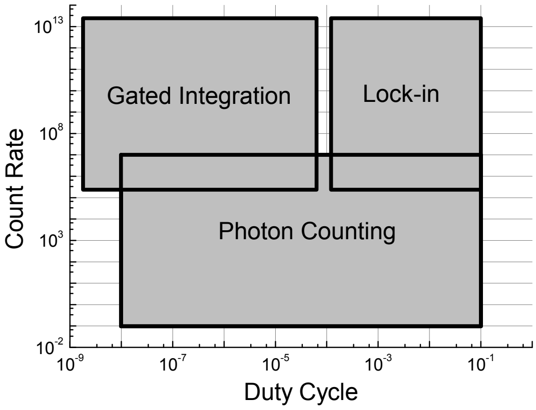

Figure 5.18.: Scheme showing count rate and duty cycle and the appropriate measurement techniques. According to [338].

The electron bunch ejected from the PMT is converted by a resistance into a small voltage impulse. To shorten the pulse and suppress ringing the cable termination is designed as a snubber network, a piece of 50 Ω coaxial cable with a specific length and a variable termination resistance ($< 50\ \Omega$). When feed into the gated integrator, the signal is temporally overlapped with a tunable boxcar to control the timing of the integration circuit. After integration and normalization to the boxcar width the signal averages over a defined number of pulses. In this way the absolute probe SHG intensity for different delay steps can be measured. The pump induced change in the probe signal is small compared to its absolute intensity. To improve the SNR of the experiment only the differential signal is recorded using the active baseline correction feature of the gated integrator. For this purpose the pulse repetition rate received from the synchronization electronics of the Legend amplifier is divided by a factor of two and send to a chopper placed in the path of the pump beam. The chopper consists of a stabilized motor rotating at a given frequency to which a slitted blade is attached. When aligned concerning the

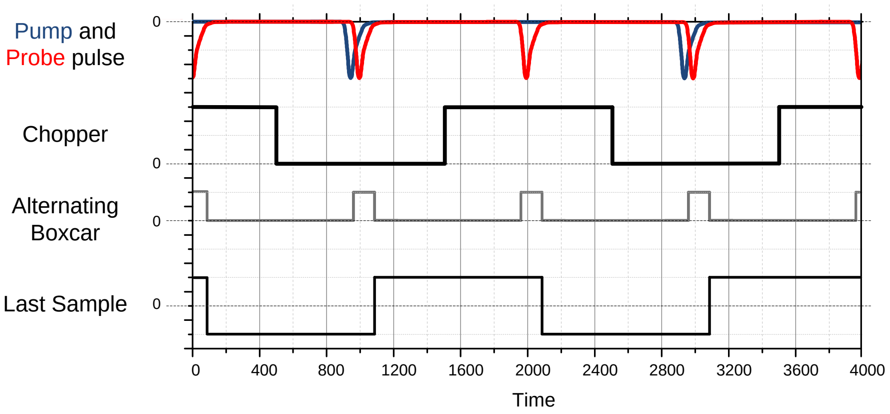

Figure 5.19.: Timing diagram of the boxcar averager setup.

phase shift induced by the delay in the cables, the chopper blocks every second pump pulse. At the same time the integrator inverts the sign of every second signal. As a result the averaging stage of the gated integrator subtracts the intensity of the unmodulated probe SH beam from the combined signal and giving the mean value of the differential part. The timing is summarized in figure 5.19. The 'Last Sample' is read out before the averaging section. The difference of the absolute values of the positive and negative level is the requested pump induced change.

According to measurements done by Chang, the pump induced change in the SH intensity is in the range of 1 to 10 % of the absolute SH intensity [150]. The response due to carrier dynamics is about 10 % of the SH signal and the phonon oscillations cause a modulation with an initial amplitude in the range of 1 %. To reveal both, the carrier and the phonon features a signal to noise ratio of 100 or higher has to be achieved. As only the differential signal is measured and recorded information on the absolute SH intensity is not available directly. The signal to noise ratio information given in this text are referenced either to the combined signal amplitude in the differential pump-probe scan A_{comb} or to the amplitude of the dominant phonon mode A_{phonon}. Further, because of the strongly decaying and oscillating nature of the signals, taking the mean value for the SNR calculations is unhandy. As one aim of this work is to investigate the dynamics of the non-thermal electron and phonon population it is reasonable to reference the SNR to the peak amplitude of the according signal dropped to $1/e$. So the signal to noise ratio is defined as:

$$SNR = \frac{A_{max} \cdot e^{-1}}{A_{noise}} \tag{5.13}$$

where A_{max} is the maximum of either A_{comb} or A_{phonon} and A_{noise} is the noise amplitude defined by it's standard deviation σ_{noise}. Taking the above mentioned amplitudes of the individual signal components as a design target in the layout of data processing, it is a justified claim to demand a SNR_{phonon} of at least 1, or a $\mathrm{SNR}_{comb} \geq 10$ respectively. The amplifiers pulse to pulse fluctuations is specified with 2 %, which, due to the quadratic intensity dependence of the second order nonlinear process, results in a 4 % SHG intensity fluctuation. Considering this as the dominant noise, the initially obtained SNR_{phonon} should be in the range of $1/(4e) = 0.092$.

In the presence of merely frequency independent white noise, like shot noise picked up by the photomultiplier, the signal improvement (signal to noise improvement ratio SNIR) in a linear averager is proportional to $\sqrt{n}$, where n is the number of samples. In the exponential moving averager (EMA) stage of the boxcar, which works like a low pass filter, the SNIR is a function of the window size, or likewise the time constant RC, speaking in the filter picture. It obeys the same $\sqrt{RC}$ relation. The SNR obtained by the boxcar averager in active baseline correction mode is smaller by a factor of $0.5\sqrt{2}$. This has two reasons. First due to the alternating subtraction of a background the amplitude of the signal is halved. Secondly for one differential signal, two probe pulses have to be measured, one with the pump turned on and one without. The total number of scans is thus twice the number of scans in a standard boxcar measurement, adding the factor $\sqrt{2}$. Respecting this in the SNIR calculation, a window size of 237 differential samples in the averaging stage of the boxcar analyser are necessary to create a SNR_{phonon} of 1.

Figure 5.20 shows a typical pump-probe trace obtained with this set-up. The differential SHG intensity change is normalized to the signal peak. The delay step width is 20 fs. To overcome the limitations in the window size of the boxcar averager and to reduce the influence of slow drifts in the signal, the number of averaged samples in a single scan was chosen to keep the measurement time moderate. The final traces were obtained by averaging over a number of scans. The black curve shows such a single scan with the boxcar averaging over 500 differential samples (1000 pulses), while the red curve represents an average of 25 single scans (12500 differential samples), calculated by the self written control and recording software PumpProbeController. Even though the combination of EMA and linear averaging increases the SNR by 111, no phonon signal could be detected. The noise in the single scan, extracted from the negative delay part, is 13 % of the peak signal amplitude ($\mathrm{SNR}_{comb} = 2.8$). In the averaged curve the noise contribution is about 1.5 % ($\mathrm{SNR}_{comb} = 26$), so the phonon oscillation should become

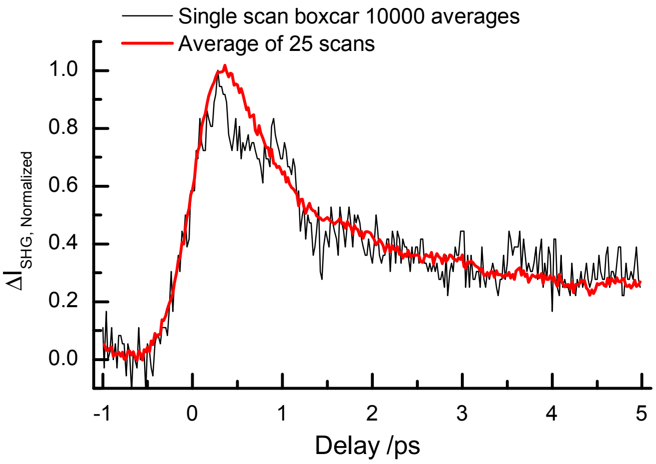

Figure 5.20.: Typical pump-probe measurement on a n-doped GaAs sample using the amplifier system. The black curve shows one scan using a 500 differential sample window. The red curve is an average of 25 such scans.

visible, if the above made assumptions about the phonon intensity are valid and coherent phonons were launched by the pump pulse. A single scan of this measurement with a readout after 3RC and taking account of the translation of the delay stage takes about 20 min, the complete experiment is finished within 8.33 h. This is at the hard limit of the time the amplifier behaves stable, without large power fluctuations or even drop outs. In particular the synchronisation between the seed laser and the regenerative amplifier, which is governed by the photo diode / preamplifier combination and the fast triggering electronics of the Legend, becomes unstable or suffers from a phase drift. This is very crucial for the timing of the chopper to reliably block the pump pulses in the background sampling. These limitations don't allow a further increasing of the window size in the boxcar (5000 averages max.) and additional averaging scans.

The rising edge of the electronic excitation can be fitted by a Gaussian with a 400 fs half width at half maximum (HWHM), which is quite large, compared to the later experiments performed with the oscillator system. This indicates temporal broad pulses which may be incapable of launching coherent phonons by the processes described in section 2.4.1. However on the left side of figure 5.21 the temporal intensity profile of the pulses from the Legend amplifier at the time of the experiment were shown and the autocorrelation pulse width is about 75 fs, corresponding to a 53 fs wide Gaussian pulse. Thus the pulse is considerably shorter then the period of the estimated dominant phonon mode with around 120 fs. Also clearly visible in this figure is the distorted pulse form compared to the nearly pure Gaussian shape of the seed laser. These high order

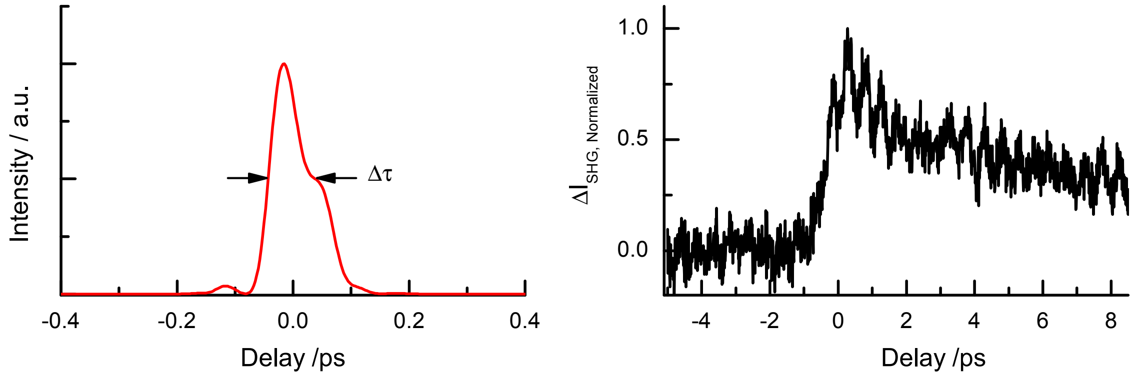

Figure 5.21.: Left: Legend amplifier laser pulse intensity profile, measured with FROG technique. The autocorrelation pulse width is 75 fs. Right: Single scan with 500 diff. samples dominated by a superimposed periodic noise.

phase terms are mostly induced in the re-compression stage in the regenerative amplifier and can not be completely compensated. Depending on the daily performance of the system, these effects are more or less distinct. This complex pulse shape may hinder the launching of the coherent phonon modes. Beside this effect on the pulse shape the amplifier regularly exhibits a strong periodic intensity modulation as shown on the right side of figure 5.21. Here a single scan with the same amount of samples as in figure 5.20 is displayed. The periodic oscillation has a period of around 50 s and is strongly varying in amplitude. Due to its large period compared to the maximum window size in the boxcar, it is difficult to average it out.

In conclusion it is obvious that the stability and pulse quality of the amplifier system in the current state make reliable measurements impossible. Even if the high power and the in principle precise timing and triggering facilities would have made it a suitable excitation and probing light source.

5.3.2.2. TR-SHG with Unamplified Tunable Femtosecond Pulses

As a consequence of the stability problems of the amplifier, the experiments were switched to use the weaker pulses from the oscillator directly. The advantage of this approach is that the pulses are shorter and have a simple Gaussian shape, which should enhance the creation of coherent phonons. Further the pulse energy is tunable over a limited range, allowing the sample to be exited below and above the band gap energy of pure GaAs. Due to their small temporal width, the oscillator pulses are subject to a larger chirp broadening when travelling through air. As the oscillator is mainly used as a seed of the amplifier, its output is turned away from the experiment and the pulses have to travel a rather long way to the sample. The much lower pulse energy requires a stronger focusing to create the needed carrier density, which also makes the overlapping of pump and probe beams on the sample surface more complicated. Finally the non-clocked 95 MHz output demands a different sample detection and processing scheme.

Chopper based measurements

In the first implementation the fundamental previous set-up was used and the above listed requirements were incorporated. This is shown in figure 5.22. For chirp compensation a pulse compressor was installed half way to the sample. Its layout is equal to that used inside the cavity, a four prism set-up to induce a frequency dependent path length difference. For space and cost reasons it is folded by mirror M2, reflecting the beam with a small vertical angle. The prisms are made of SF10. The compression can be tuned by changing the insertion of the second prism and performing FROG measurements at the sample position. Next to this are mirrors M3 and M4. Their purpose is to restore the standard beam height and to uncouple the sensitive alignment of the interferometer from beam displacement in the first part of the set-up, caused by oscillator tuning. The rest of the design remains unchanged, except that the waveplate of the pump path is positioned in front of the beam splitter to create a s-polarized beam needed for splitting the light in the specified ratio. Further the convex lens L1 is realigned to focus the beam onto the sample surface. To ensure that spot overlap and focussing are lined up correctly, the probe and pump beam are adjusted with L1 removed, to propagate parallel over at least 10 meters, using mirrors M5 and M6. With this coarse adjustment and L1 reinserted the temporal overlap can be established using a thin BBO crystal at the sample position. The important fine tuning is done in an iterative procedure, by alternately tuning the spot overlap on the sample surface using M6 and adjusting the focus by replacing the sample with the thin BBO and varying the distance of lens L1. The spot overlap is monitored using a CCD camera equipped with zooming optics.

The SHG intensity in the oscillator experiments is still well above the photon counting regime and with the high repetition rate of 95 MHz the current output of the photomultiplier can be treated as a direct current (DC) resulting in a duty cycle of 1. Comparing figure 5.18 lock-in detection is an appropriate measurement technique. In this set-up the chopper is used as reference clock which modulates the pump beam with a frequency of 2.85 kHz and routes this synchronization signal into a dual phase lock-in amplifier (LIA-

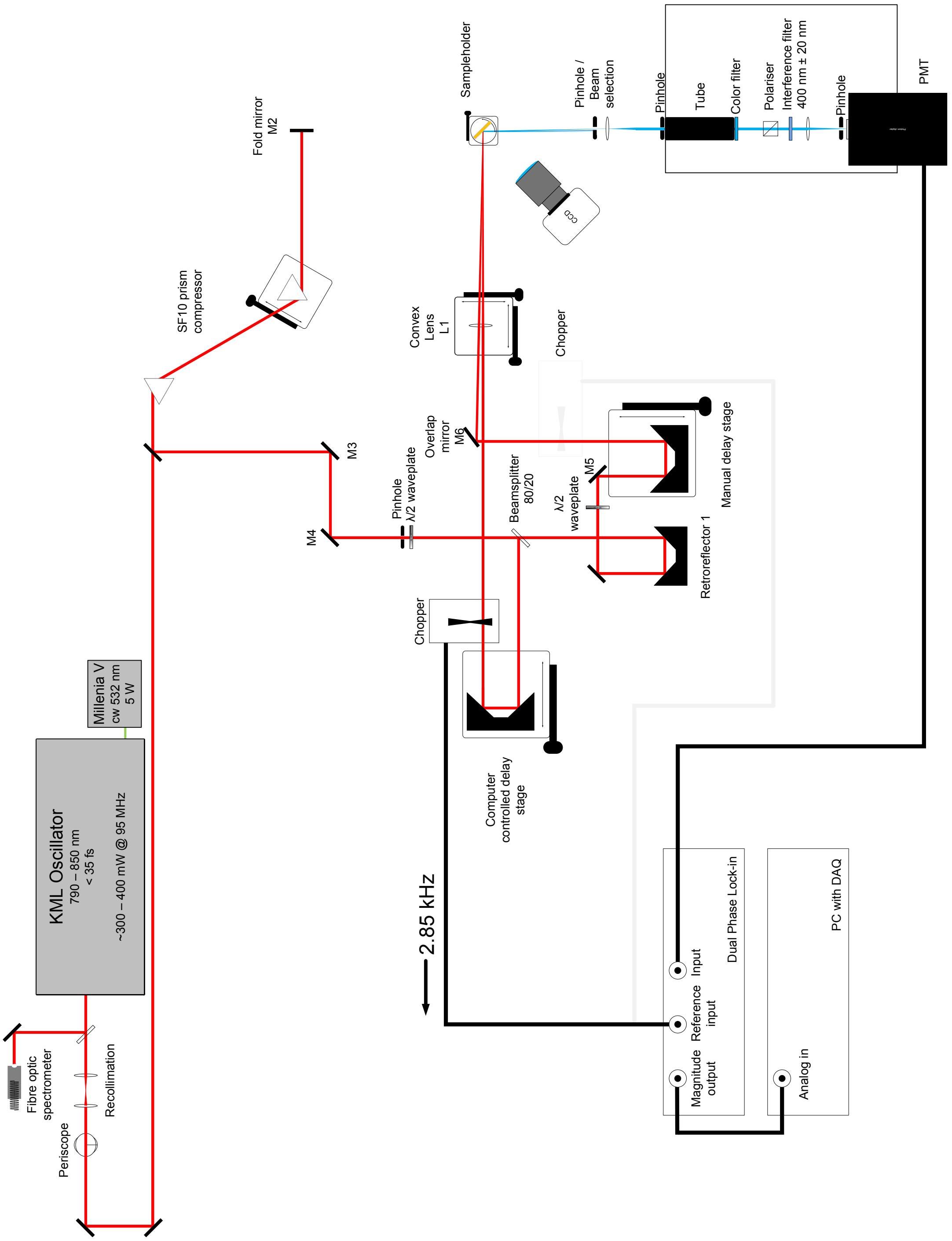

Figure 5.22.: Pump-probe set-up for experiments with the oscillator.

MVD-200, *Femto*). The current response from the PMT is feed directly into the lock-in, where a transimpedance amplifier converts it into a voltage signal, without putting a load on the PMT dynodes. After preamplification the voltage signal is split up and mixed with two 90° phase shifted reference signals in the phase sensitive detector. The output signals X and Y are both processed by low-pass filters to eliminate the non DC noise components. In the final step the vector magnitude R of X and Y is calculated (see figure 5.23). Using this output, the influence of a phase shift during long measurements is eliminated, but as a drawback, only the magnitude of the differential SH response can be obtained. The SNR improvement is, equal to that of the boxcar set-up introduced in the section before, proportional to $\sqrt{RC}$. The default time constant used is 1 s and the signal is read out after 3RC.

The high chopping frequency was chosen to reduce the total amount of noise. For the same reason meticulous care was taken for the electrical signal and power connections, especially for noise-loop free grounding (cf. [339]).

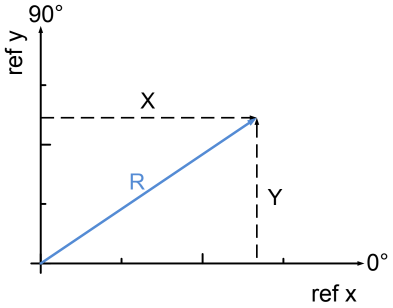

Figure 5.23.: Working principle of a dual phase lock-in amplifier. Mixing the input signal with two orthogonal reference signals allows the reconstruction of the signal magnitude without knowing its phase.

In figure 5.24 a typical result of a measurement performed with this set-up is shown. It displays a normalized linear average over 10 scans. The signal to noise ratio of the combined signal (SNR_{comb}) using the noise in the prepump part of the scan is 151. The maximum phonon amplitude is approximately 4 % of the electronic signal and thus less than half of what is claimed by Chang [150]. The obtained SNR_{phonon} is 6. The relative phonon amplitude and the achievable SNR is strongly dependent on the type of sample, beam polarization and the intensity ratio of pump and probe beam, which is discussed in section 8.3. Most commonly 30 to 50 scans were necessary to resolve the phonon oscillations, so the total scan times were in the same region as those of the amplifier experiments.

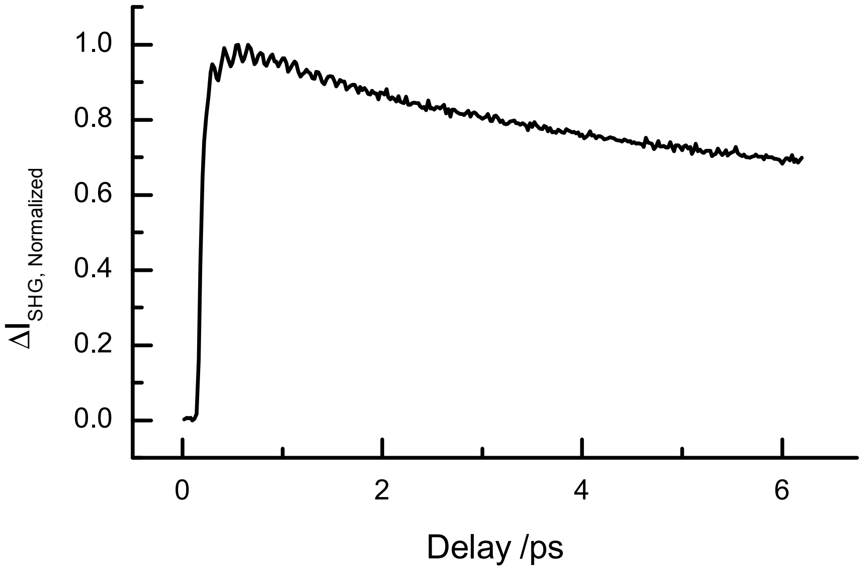

Figure 5.24.: Typical pump-probe measurement on a n-doped GaAs sample using the oscillator and chopper based set-up. The curve is an average of 10 scans, each recorded with a time constant of 1 s.

Shaker based measurements

In an attempt to reduce the measurement time and increase the temporal resolution, a third modification of the experimental set-up was introduced, were the differential measuring using a chopper was abandoned, favouring a fast, straight forward absolute measurement design. Here the pump delay is accomplished using a fast oscillating shaker and the data is accumulated by a digital storage oscilloscope. The commercial hardware (AixScan, *AMO*) is based on developments of Kurz and Tang [151, 340], who used this design for studying the dynamics of large molecules and semiconductors. The computer controlled delay stage in the pump beam was moved into the probe beam replacing retroreflector 1. In the pump path a shaker, originally made for vibration tests of small objects (*Brüel&Kjaer*), fixed to a horizontal mount was placed. The output of the PMT is converted into a voltage signal by a stand alone transimpedance amplifer (DLCPA-200, *Femto*) before it is fed into the recorder. The movement of the shaker and the delay stage as well as the fast recording of the data points is managed by a special program running on the PC based oscilloscope and control unit. The reference design and the works cited before involve a second signal path, were a part of the probe beam is separated and recorded in an additional detector, free of pump perturbation, In contrast to this it was not possible to install a second channel to perform differential measurements. The changes in the set-up are summarized in figure 5.25. The shaker can be driven with up to 100 Hz depending on the chosen amplitude. The scope can read data with a rate of up to 100 MS (megasample per second), allowing a much better temporal resolution than the delay stage. Due to the sinusoidal movement of the shaker mirrors, the time axis is not linear (the movement is slower at the reversal points and thus the temporal resolution is higher in this regions) and has to be calibrated for every combination of amplitude, frequency and sampling rate setting. This can be done in a semi automatic procedure using a BBO crystal in autocorrelation configuration and a fast amplified photo diode to provide an intense and well defined peak shape signal. A time axis can be defined by letting the pump delay oscillate and recording data over a number of periods. The peak separation of consecutive oscillations changes when the temporal balance point is shifted closer to the reversal points of the shaker by moving the probe with the calibrated motorised stage. The end points can be identified as that point were the peaks merge, between these extremes, the time axis can be determined using their temporal distance.

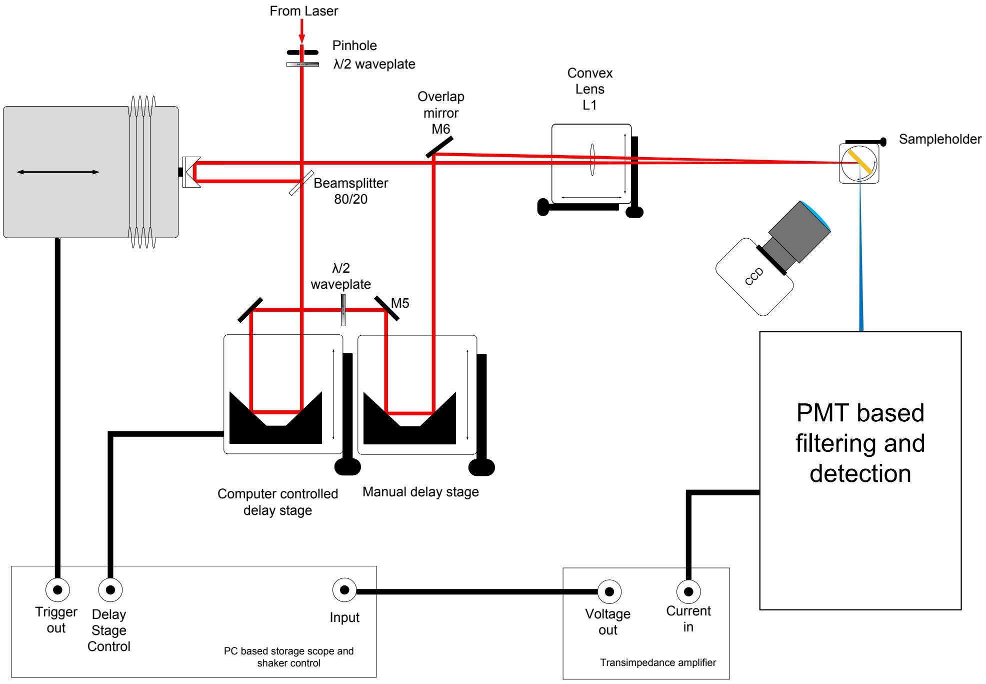

Figure 5.25.: Modifications in the oscillator set-up to implement the shaker delay.

With this set-up good results could be achieved, although a reduction of measurement time could not be attained and millions of data points have to be recorded for a reas-

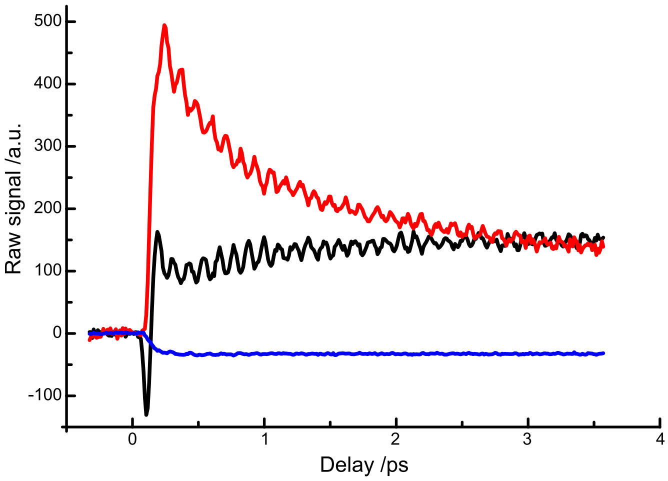

Figure 5.26.: Typical rsults obtained using the shaker setup. Shown here are measurements on GaAs at different rotational axis (see next section). The black curve is recorded by taking one million averages. The other curves are averages over five hundred thousand scans.

onable SNR. This most likely results from the lack of a reference channel. The benefit of this technique is the possibility to obtain absolute changes as shown in figure 5.26. It depicts measurements on GaAs at different rotational angles (see next section) with parallel polarized pump and probe beams. The black curve is a result of linear averaging over one million scans (SNIR = 1000), while the others are aggregates over five hundred thousand scans. For the red curve the SNR_{comb} is 33. The phonon's signal to noise ratio is about 10. The other curves apparently don't follow the simple biexponential decay process.

5.3.3. Rotational Second Harmonic Generation (SHG)

To probe the nonlinear susceptibility tensor elements of the samples, static rotational second harmonic generation experiments are performed. As discussed in the section about nonlinear, optical surface probes (section 2.3.2), information about the different tensor elements within the information depth of the reflected SH signal can be obtained by measuring the SH signal intensity as a function of the incoming and outgoing polarizations as well as the azimuthal angle between the plane of incidence and specific crystal directions. The principle set-up of such a measurement is displayed in figure 5.27. The polarization of the fundamental input beam is controlled by a polariser in combination with a waveplate, and the reflected second harmonic signal is analysed by a second polariser and a photodetector. Thereby the sample is rotated around its surface normal.

Instead of a dedicated experiment, the facility of performing those measurements was included into the pump-probe set-up. For this purpose the pump beam is blocked and the chopper moved into the probe beam (cf. figure 5.22). The same detection scheme as described in the section about chopper based pump-probe measurements is used, except that the software now controls a motorised rotation stage (*thorlabs*). In this type of experiments the strongly changing absolute SHG intensity is measured and a single scan with a RC of 3 s is sufficient to achieve a good SNR. As the samples are either glued to a metal disc by means of carbon tape or in the later experiments, clamped to this disc, they are not precisely aligned perpendicular to the rotation axis. This results in beam walk and slight focus variations while rotating. When time-resolved measurements at different angles should be performed, also the spot overlap is affected by this. Further, the sample should be hit at its centre, since otherwise a circular path on its surface gets scanned and inhomogeneities like dust or scratches, distort the signal. To face these effects the sample holder was modified enabling multi axis adjustability. The sample is mounted on a goniometer table, which rests on the motorized rotation stage. A xy table beneath, allows an in plane movement of the sample surface. The complete assembly is mounted to a rigid mirror holder which provides the steering of the reflected SH signal into the detector.

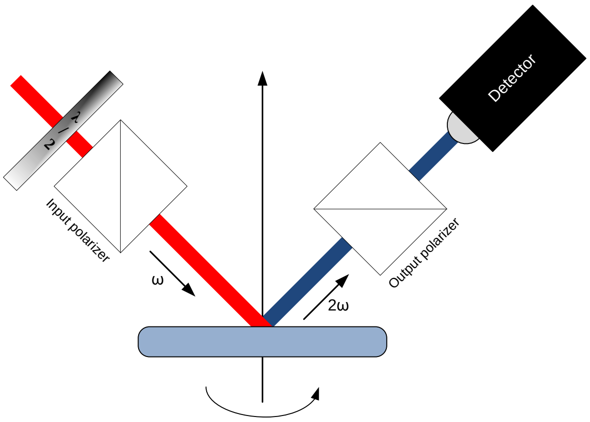

Figure 5.27.: Principle setup of a surface symmetry measurement using SHG. The input and output polarizations are controlled while the sample is rotated around its surface normal.

5.3.4. Time-Resolved Reflectivity

Linear reflectivity measurements can be performed with both, chopper and shaker based set-ups, only the filters have to be replaced. The total signal intensity in this experiments is much larger and neutral density filters are used to prevent detector saturation. The influence of scattered light of the pump beam propagating in the detector direction is much stronger, while at the same time phonon signals are less pronounced with an amplitude in the range of 10^{-6} of the absolute intensity (according to [150]). This method was not regularly used within this work as only weak or no phonon signal could be obtained.

5.3.5. Photoluminescence

In order to probe the samples electronic structure in the band gap region, photoluminescence measurements can be performed. As excitation source the Nd:YLF pump laser of the Legend amplifier is used. Its 527 nm output is slightly focused on the sample surface. A collection lens in front of the sample collects the emitted luminescence, a second lens in sequence focuses the light into the fibre of compact grating and CCD camera based spectrometer (*OceanOptics*). To block the scattered excitation light filters a placed in front of the spectrometer. As no cryostat is available only room temperature measurements can be performed, consequently the resulting spectra are broad due to the large k_BT term (see also section 2.2.1 and [41]).

6. Results: Chemical and Structural Characterization

The following chapter discusses the experiments conducted to reveal the chemical and structural composition of the bare substrates and the platinum covered samples. For the chemical characterization XPS is used, while the morphology is investigated by various scanning probe techniques and LEED.

6.1. Preliminary Remarks

6.1.1. SPM

The discussion of scanning probe measurements results reveals a non-uniform morphology across the sample surface, which can be classified into different regions (figure 6.1). Region 1 and 2 define the areas below the retaining brackets. Region 3 labels the sample centre, while region 4 covers the outer parts. This definition is related to the larger rectangular GaAs:Te samples only. On the round and small silicon doped substrates this classification turned up less useful. The AFM measurements recorded with the *Digital Instruments* microscope were in large part carried out by Peter Clawin and Heinrich Driemeyer, whose help is gratefully acknowledged. The given statistical values are always affected by the properties (shape, interaction volume) of the tip, especially when comparing results from cantilever AFM scans with less precise SNOM measurements in shear force AFM mode.

6.1.2. XPS

On the investigated semiconducting gallium arsenide samples the x-ray induced extraction of electrons creates a charging which consequently shifts the measured binding energies significantly (cf equation 5.5). To quantify and compensate this shift it is a

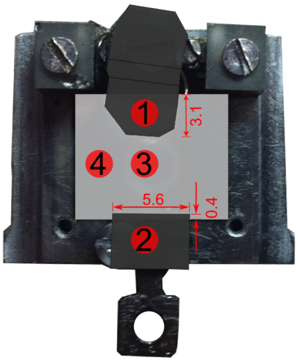

Figure 6.1.: Schematic mapping of different, significant regions on a typical UHV prepared GaAs:Te sample.

common procedure to reference the energy scale to the binding energy of the 1s electrons from adventitious carbon [9, 331, 341]. In publications between 1986 and 1993 the C 1s level was pinned to 284.6 eV, while later investigations showed the substrate dependency of the exact C 1s binding energy, shifting on native oxide covered metals between $284.4 - 287.0$ eV [331]. Further the chemical nature of the carbon species reflects on its 1s energetic position. Details can be found in [331, 342]. As an average value Crist uses 285.0 eV as reference energy in his spectral libraries [330, 331]. Sullivan et al. discussed the impracticality using the carbon line on GaAs samples, giving erroneous results [343] (and references therein). Alternatively they suggest to reference the energy scale to the well characterized As 3d peak at 41.4 eV.

For quantification purposes and peak deconvolution a careful device calibration with respect to the energy scale, sensitivity factors and peak widths is inevitable. The performance of the XPS spectrometer used was thoroughly analysed by Necke with reference samples relevant to his experiments [9]. The energy scale was checked by measuring oxygen free high conductive copper (OFHC) and comparing the core level signals to reference values published by Crist and others [330]. The relative sensitivity factors were corrected for analyser transmission and electron attenuation length effects on the basis of detailed Au (111) reference data measured by Stoever and Ahlf [344]. Peak areas of different core level signals over a widespread energy range were balanced using a correction function as suggested by Crist for copper samples [9, 345] in combination with a nonlinear minimization routine provided by Matlab®. The optimized parameter (transmission function correction (TFC) coefficient) of this correction function is found to vary between 0.89 and 1.17 for different data sets due to its high sensitivity to integration boundaries and background function of weak transition signals. For a TFC of 0.95 the peak area error is below 10 % for all gold data sets investigated and is therefore used together with Scofield cross sections to determine the atomic concentrations given in this chapter.

According to equation 5.4 the line width of a XPS signal depends on the inherent line width of the excited level and on source and analyser properties. In order to deconvolute broad peaks it is important to determine the broadening caused by the device. Peak FWHM values of principle atom levels are mostly given for monochromatic x-ray sources. Crist suggests to multiply those by 1.5 to estimate the corresponding signal widths for non-monochromatic set-ups. Table 6.1 shows binding energies (BE) and FWHM values for different calibration measurements and the corresponding literature values. These are used for the evaluation of peak fitting results. The non metallic signals are synthesized by a Voigt profiles, which are generated by convolution of a Gaussian and a Lorentzian, with different ratios for different samples classes [345].

Signal	Sample	BE (FWHM) /eV	Reference /eV [331]
Cu 2p 3/2	OFHC [9]	932.63 (1.57) [9]	932.67 (0.88)[a] 932.7 (1.22)[b]
Au 4f 7/2	Au(111)[c] [9]	83.95 (1.2) [9]	83.98 (0.68)[a] 84 (0.66)[b]
Si 2p 3/2	Si(111)[d] [9]	98.89 (1.06) [9]	99.35 (0.45)[a] 99.8 (0.58)[b]
Pt 4f 7/2	Pt(111)[c] [344]	72.09 (1.23)	71.15 (0.88)[a] 71.1 (0.96)[b]

[a] Ion etched
[b] Under native oxide
[c] Sputtered
[d] Flash evaporated

Table 6.1.: X-ray photoelectron spectrometer calibration measurements and reference values.

The analyser was set to 50 eV pass energy and a dwell of 0.1 s for all spectra shown, unless otherwise noted. The surveys were recorded with a resolution of 0.5 eV and averaged over five or ten scans, as required. For the detailed spectra the resolution was increased to 0.09 eV and the averaging set to twenty. By default a Shirley type background is subtracted.

6.2. Native Oxide Covered Samples

First the structure and the chemical properties of the two different types of native oxide covered samples, henceforth referred to as GaAs:Te and GaAs:Si were investigated. Their specifications are summarized in table 5.1.

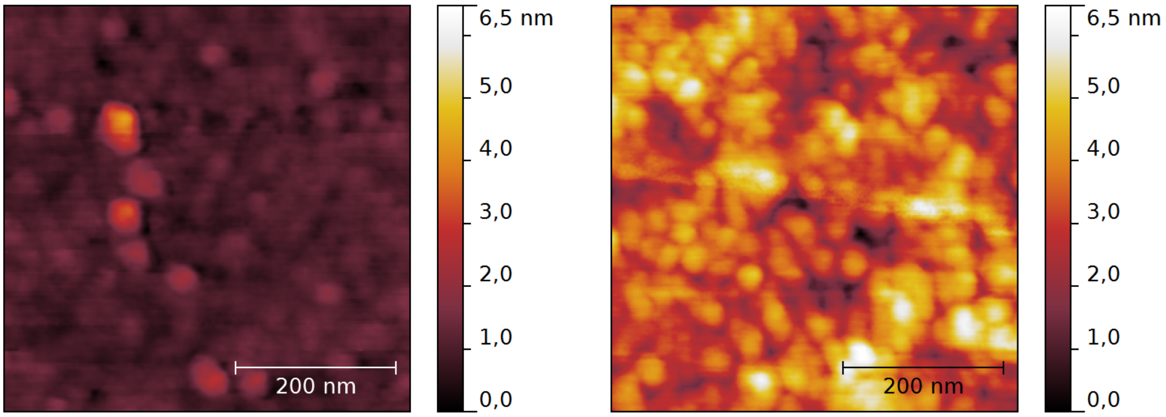

Figure 6.2.: AFM images of GaAs:Si covered with an amorphous native oxide layer. Left: As received. Right: After ultrasonication in acetone and isopropyl alcohol.

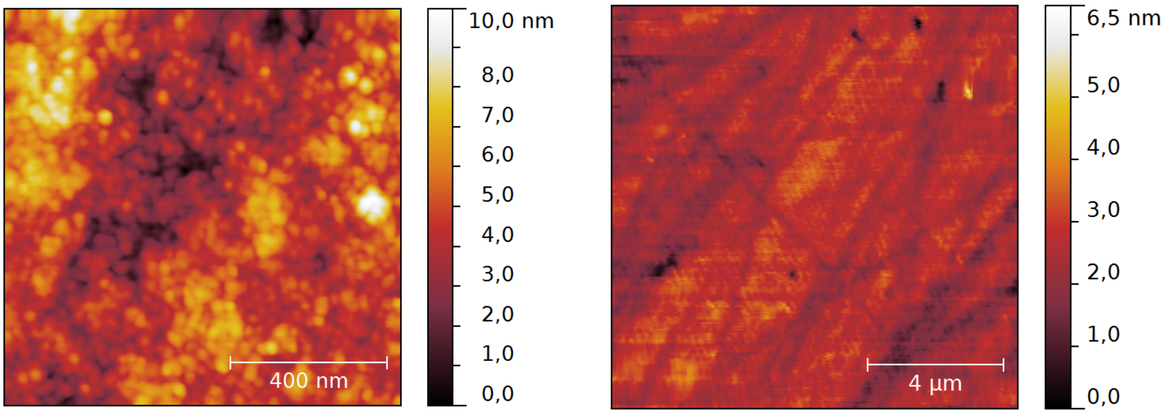

Figure 6.3.: Left: AFM images of GaAs:Si covered with an amorphous native oxide layer. After ultrasonication in acetone and isopropyl alcohol. Left: *Veeco* AFM scan. Right: SNOM shearforce AFM image.

SPM

On the sub micrometer scale all oxidized samples show the same uniform grainy surface (figure 6.2 and left side of figure 6.3). In their as-received state (left side of figure 6.2) the average surface areal roughness S_A has a value of 0.214 nm. After removing the protective coating by ultrasonication in solvents the roughness rises to 0.758 nm. This increase may simply reflect the uncovering of the surface features upon removal of the coating, but could also be an effect of solvent intrusion into the oxide. On a larger scale, images of shearforce AFM measurements reveal 0.3 nm deep and ≈ 300 nm wide ditches. These may be induced by sample handling or in the ultrasonication process. The determined roughness parameters from this type of measurements range in the region of ≈ 0.4 nm. The measured roughness values correspond to the published values obtained by GIXR [169]. No principle differences between the silicon and tellurium doped samples could be found. With STM measurements it was not possible to obtain reliable images, as a stable tunnelling contact to the insulating oxidic surface could not be established.

XPS

The focus of the XPS analyses on this samples is the characterization of oxidation state and the detection of further contaminations. After the ultrasonication step, the otherwise untreated samples were transferred directly into the XPS vacuum chamber and scanned at a residual gas pressure of 1×10^{-9} mbar. Figure 6.4 shows a survey spectrum for native oxide covered GaAs:Te, recorded with Mg K_α excitation at 1253.6 eV. Charge referencing is made according to section 6.1.2, the measured binding energy of the C 1s electrons is 286.9 eV. The peaks are assigned on the basis of reference values published by Crist and Moulder [341, 345]. Beside various signals from Ga and As levels, a pronounced oxygen 1s and Auger signal can be identified. Further a structured C 1s peak is found. There are no visible signals from further inorganic contaminations or the Te doping.

The principle peaks for gallium and arsenic are the 3d photoelectron lines. The information depth at this energy is in the range of $8 - 14$ nm [290, 346, 347]. Figure 6.5 displays the corresponding spectral details, also recorded using the Mg K_α source. The gallium 3d peak on the left side is fitted under the assumption of convoluted spin-orbit split signals. The $3d_{3/2}$:$3d_{5/2}$ area ratio is fixed to the theoretical value of 2/3 and the relative positions are constrained to 0.45 eV [348]. Also their peak width is coupled. The spectrum shows GaAs bonding states at 18.94 eV and 19.39 eV respectively, similar to those found by Kang et al. [348] and in the typical energy range for GaAs [330, 341, 349]. The additional weaker and broader peaks, shifted to 20.34 and 20.79 eV can be assigned to Ga in Ga_2O_3 in accordance with literature [349, 351]. Sullivan et al. however synthesized the Ga 3d line with three peaks (no spin-orbit splitting) at 19.1, 20.1 and 20.7 eV and assigned those to Ga$-$As, Ga_2O and Ga_2O_3 [343]. Reference data beyond the lib-

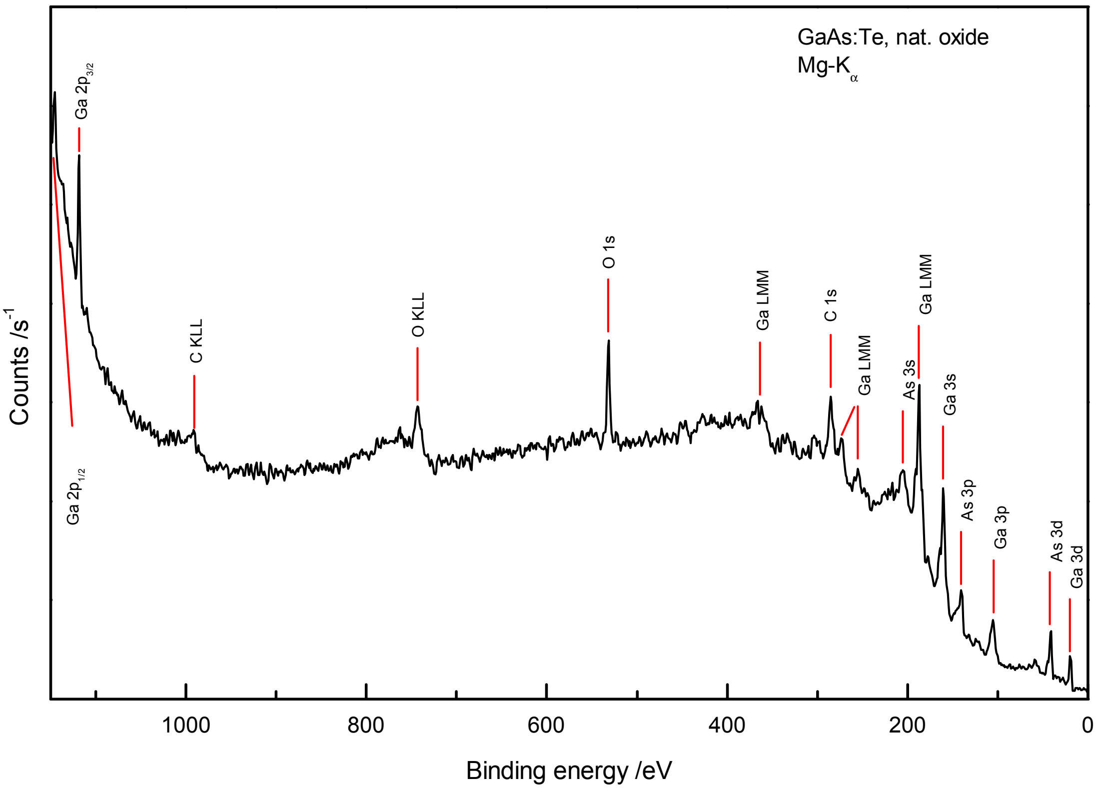

Figure 6.4.: XPS survey spectrum of a GaAs sample, doped with Te, using the Mg x-ray source.

raries from Crist and Moulder for various gallium and arsenic species are summarized in appendix C.1.1. The peak width of the Ga-As bonding states is 1.18 eV which agrees very well to the monochromatic FWHM published by Crist (0.66 – 0.72 eV) considering the same broadening factor as for Si (cf. table 6.1). The oxidic species has a FWHM of 1.30 eV and thus is less inflated compared to the bulk state as found in the Crist data (0.96 – 1.18 eV), making an unrevealed convolution with a second oxidic species less likely. Furthermore the Auger parameters for the dominant Ga LMM emission were extracted from the XPS spectra to support the chemical species assignment. Beside an unambiguous doublet LMM of covalently bound Ga in GaAs, the LMM signal with an Auger parameter of 1083.2 eV points to an Ga^{3+} species, but could also be related to Ga^{1+} in Ga_2O. The general existence of a Ga_2O species inside the oxide layer seems to be unlikely comparing the data presented here and other various XPS studies (e.g. [171]). Rather it is formed at the surface upon heating of Ga_2O_3 under reductive conditions [352] (cf. section 4.1.1).

The As 3d peak is fitted using similar boundary conditions with a spin-orbit splitting of

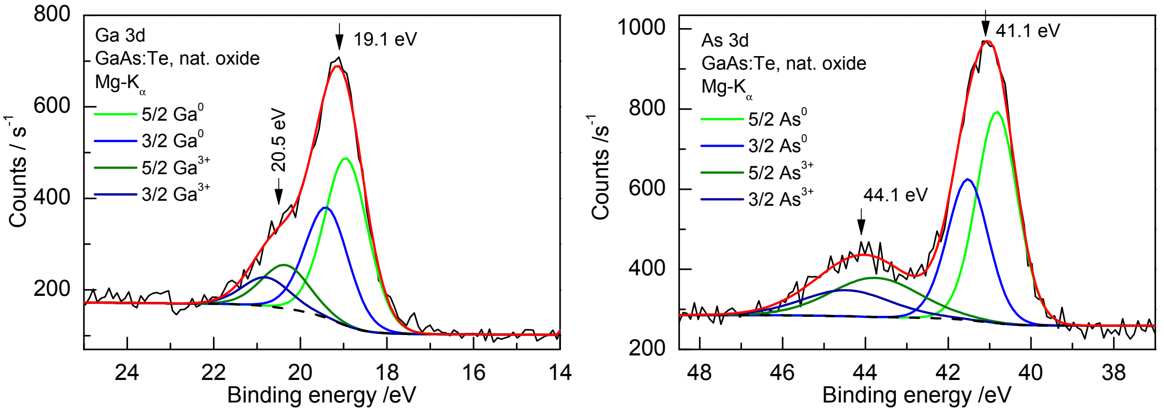

Signal	**Species**	**BE (FWHM) /eV**	**Lit. BE /eV**	**Area /a.u.**	**Conc. /%**
Ga $3d_{5/2}$	Ga-As	18.94 (1.18)	18.8 [348]	313	10.9
Ga $3d_{3/2}$	Ga-As	19.39 (1.18)	19.3 [348]	206	
Ga^{3+} $3d_{5/2}$	Ga_2O_3	20.34 (1.3)	20.4-20.6 [349, 350]	90	3.2
Ga^{3+} $3d_{3/2}$	Ga_2O_3	20.79 (1.3)		59	
As $3d_{5/2}$	As-Ga	40.83 (1.17)	40.8 [341]	275	9.7
As $3d_{3/2}$	As-Ga	41.53 (1.17)	41.5 [341]	183	
As^{3+} $3d_{5/2}$	As_2O_3	43.77 (2.48)	44.3 [343]	108	3.9
As^{3+} $3d_{3/2}$	As_2O_3	44.47 (2.48)		72	
O 1s		531.84	531.7 [345]	1437	29.0
C 1s		285.0	285.0 [345]	2048	43.3
Ga LMM	Ga_2O_3	A.P.: 1083.2	1082.8 [349]		
Ga LMM	Ga-As	A.P.: 1085.5	1085.4 [343]		
Ga LMM	(Ga-As)	A.P.: 1089.2	1091.3 [343]		

Figure 6.5.: XPS spectral details of Ga 3d (left frame) and As 3d (right frame) in GaAs:Te using the Mg x-ray source. The carbon and oxygen concentration is calculated from the raw peak integral, while the arsenic and gallium species are quantified using the fit. All semiconductor peaks are synthesized by a 70% Gaussian Voigt shape.

0.70 eV (see figure 6.5, right frame) [341, 348]. The mass centre of the As–Ga bonding states is at 41.1 eV, justifying the C 1s charge referencing on this sample. The FWHM of these peaks are equal to the corresponding gallium lines. The oxide is shifted to 44.05 eV with a FWHM of 2.48 eV. This matches the As_2O_3 region given in [343], while other sources show slightly higher values for this oxidation state (44.4 – 45.3 eV) [330, 349]. The As^{5+} photoelectron line of As_2O_5 is expected at 45.3 – 46.3 eV [342, 343, 349]. The peaks used for fitting the oxidic species are quite broad, compared to literature values and to those in the gallium peak, but adding a second oxidic species to the fit does not give reasonable results. For both gallium and arsenic the relative oxide concentration is between 22 to 40 %.

The O 1s signal (not shown) is well fitted by a single 70 % Gaussian at 531.8 eV. The

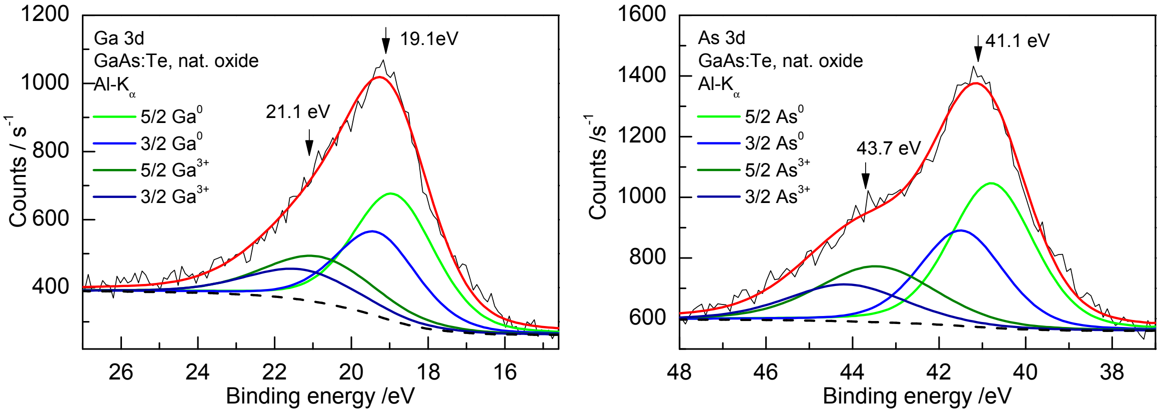

Signal	**Species**	**BE (FWHM) /eV**	**Lit. BE /eV**	**Area /a.u.**	**Conc. /%**
Ga 3d$_{5/2}$	Ga-As	18.96 (2.47)	18.8 [348]	831	17.08
Ga 3d$_{3/2}$	Ga-As	19.41 (2.47)	19.3 [348]	549	
Ga^{3+} 3d$_{5/2}$	Ga$_2$O$_3$	20.86 (3.43)	20.4-20.6 [349, 350]	454	9.33
Ga^{3+} 3d$_{3/2}$	Ga$_2$O$_3$	21.31 (3.43)		300	
As 3d$_{5/2}$	As-Ga	40.78 (2.31)	40.8 [341]	618	12.7
As 3d$_{3/2}$	As-Ga	41.48 (2.31)	41.5 [341]	408	
As^{3+} 3d$_{5/2}$	As$_2$O$_3$	43.44 (3.22)	44.3 [343]	333	6.84
As^{3+} 3d$_{3/2}$	As$_2$O$_3$	44.14 (3.22)		220	
O 1s		531.5	531.7 [345]	2969	36.77
C 1s		284.6	285.0 [345]	1394	17.26
Ga LMM	Ga$_2$O$_3$/Ga$_2$O	A.P.: 1082.4	1082.8 [349]		
Ga LMM	Ga-As	A.P.: 1085.4	1085.4 [343]		
Ga LMM	(Ga-As)	A.P.: 1089.3	1091.3 [343]		
As LMM	As$_2$O$_3$	A.P.: 1262.7	1263.2 [343]		
As LMM	As-Ga	A.P.: 1266.0	1266.1 [343]		

Figure 6.6.: XPS spectral details of Ga 3d (left frame) and As 3d (right frame) in aged GaAs:Te using the Al x-ray source. All semiconductor peaks are synthesized by a 70% Gaussian Voigt shape. Compared to the Mg source the aluminium radiation has a larger linewidth (see table 5.4) and a longer free path inside the sample resulting in a larger information depth.

carbon signal (also not shown) is more complex, consisting of the main peak referenced to 285.0 eV and a weak shoulder at 285.6 eV. The overall carbon concentration of 42.7 % is quite high and points to an adsorbed hydrocarbon overlayer, maybe a residue of the protection coating, which typically gives a carbon concentration of 20-40 % [9].

Later an aged but otherwise identical prepared sample from the same wafer was measured using the aluminium x-ray source, including the high binding energy 2p orbitals. The survey is similar to that in figure 6.4, with no contaminations, beside oxygen and carbon. The C 1s signal is weak and interferes with an As LMM Auger signal [330], so charge referencing was made to the As 3d peak (3.1 eV shift). Figure 6.6 depicts the 3d peaks of Ga and As.

At first glance it is noticeable that the peaks of the Ga-As bonding states are two times broader than those in the Mg K_α based measurements. In the gallium signal the oxidic contribution is best fitted by a wide peak doublet of 3.43 eV FWHM each, making an assignment unprecise. Compared to the previous measurement the signal is shifted to higher binding energies pointing to a Ga_2O_3 species, rather than to Ga_2O. The same situation of broad peaks can be seen in the arsenic signal. The oxidic component exhibits a signal at 43.7 eV, which is on the lower side of the published values for an As^{3+} photo electron from As_2O_3. The signal broadening may be understood that the sample, compared to the previous measurement, was exposed to air over a much longer period resulting in a thicker and more complex native oxide layer (the relative oxide concentration is increased to 53 %). At the high energy tail, the signal curve eventually indicates the rise of a third emission at ≈ 45.0 eV of an As^{5+} species, but the peak synthesis for this situation gives unsatisfying peak width distributions. As discussed in section 4.1.1 the self limitation of the oxidation process is related to the formation of a metallic arsenic layer. This species with a chemical shift of 1.4 eV relative to the GaAs species is frequently found in XPS studies and forms a flattop signal, especially at low take off angles [171]. The peak broadening of the As 3d core level could thus be a sign of a metallic arsenic contribution. The As Auger LMM parameter supports the assignment of the oxidic species, but a metallic arsenic is expected to have an AP of $1266.6 - 1267$ eV. Moreover both the Ga as well as the As 3d lines show the increased linewidth, which thus could also be a sign of increased charging effects.

In contrast to 3d photo emission and Auger signals the more surface sensitive (≈ 2 nm) $2p_{3/2}$ peak of As shows two species, a dominant As^{3+} oxide at 1326.4 eV and a signal at 1323.2 eV which is at the edge between the GaAs and metallic As region (right side of figure 6.7) [343]. The gallium $2p_{3/2}$ signal at 1118.0 eV shown on the left side of the same figure, can be perfectly fitted by a single component matching the observed energy region of Ga^{3+} in thermally evaporated Ga [343]. The complete 2p signal of gallium is shown in figure C.1 in appendix C.1. An accurate assignment is difficult due to the limited amount of reference data and overlapping energy regions. In the same publication a Ga^{1+} species in Ga_2O_3 powder is discussed at 1118 eV. The possible presence of gallium in a lower oxidation state at the surface of the oxide layer could also be a x-ray induced effect, similar to that found on cerium oxides [353].

Also in the XPS spectrum of GaAs:Si a higher internal consistency could be achieved by referencing the energy scale to the dominant As 3d signal at 41.1 eV. Only a small charge build up of 0.5 eV binding energy shift is observed. The survey spectrum once

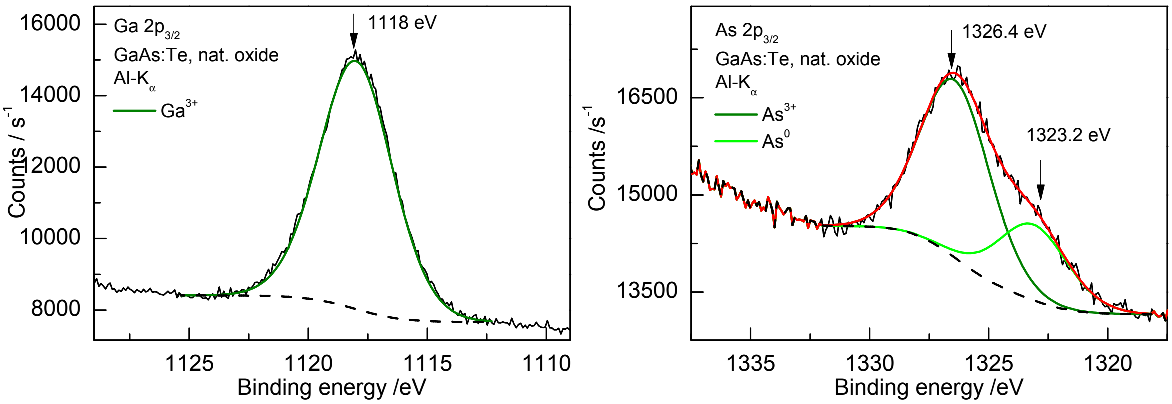

Signal	**Species**	**BE (FWHM) /eV**	**Lit. BE /eV**	**Area /a.u.**	**Conc. /%**
Ga $2p_{3/2}$	Ga_2O Ga_2O_3	1118.0 (3.66)	1118.0 [343] 1118.8 [343]	2648	17.30
As $2p_{3/2}$	metallic As Ga-As	1323.2 (3.44)	1323.2-1323.8 [343] 1322.7-1323.0 [343]	652	9.11
As $2p_{3/2}$	As_2O_3	1326.4 (3.44)	1325.8-1327.3 [343]	1515	21.17

Figure 6.7.: XPS spectral details of Ga and As $2p_{3/2}$ in GaAs:Te covered with native oxide layer using the Al x-ray source. All semiconductor peaks are synthesized by a 70% Gaussian Voigt shape. The increased surface sensitivity of the 2p region manifests in higher oxide concentration.

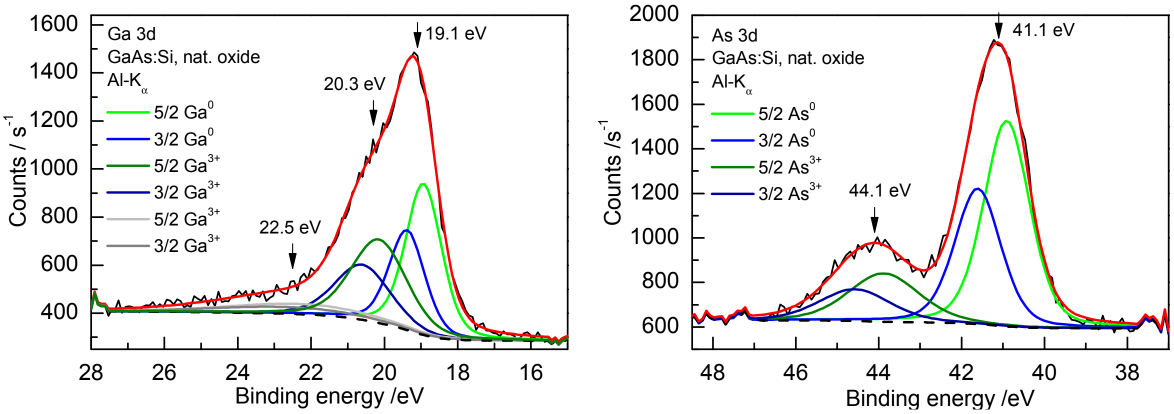

Signal	**Species**	**BE (FWHM) /eV**	**Lit. BE /eV**	**Area /a.u.**	**Conc. /%**
Ga $3d_{5/2}$	Ga-As	18.93 (1.16)	18.8 [348]	672	11.46
Ga $3d_{3/2}$	Ga-As	19.38 (1.16)	19.3 [348]	444	
$Ga^{1+}/^{3+}$ $3d_{5/2}$	Ga_2O, Ga_2O_3	20.15 (1.78)	20.1-20.6 [343, 349]	571	9.73
$Ga^{1+}/^{3+}$ $3d_{3/2}$	Ga_2O, Ga_2O_3	20.60 (1.78)		377	
Ga^{3+} $3d_{5/2}$	$(Ga(OH)_3)$	22.35 (4.61)	21.6 [343]	182	3.1
Ga^{3+} $3d_{3/2}$	$(Ga(OH)_3)$	22.80 (4.61)		120	
As $3d_{5/2}$	As-Ga	40.91 (1.31)	40.8 [341]	679	11.56
As $3d_{3/2}$	As-Ga	41.61 (1.31)	41.5 [341]	448	
As^{3+} $3d_{5/2}$	As_2O_3	43.88 (2.01)	44.3 [343]	245	4.17
As^{3+} $3d_{3/2}$	As_2O_3	44.58 (2.01)		162	
O 1s		530.96	531.7 [345]	2558	41.08
O 1s		532.24		1445	
C 1s		284.85	285.0 [345]	1842	18.9
Ga LMM	Ga_2O_3	A.P.: 1082.5	1082.6 [349]		
Ga LMM	Ga-As	A.P.: 1085.6	1085.4 [349]		
Ga LMM	(Ga-As)	A.P.: 1089.1	1091.3 [343]		
As LMM	As_2O_3/As_2O_5	A.P.: 1263.6	1263.2 [343]		
As LMM	As-Ga	A.P.: 1266.2	1266.1 [343]		

Figure 6.8.: XPS spectral details of Ga 3d (left frame) and As 3d (right frame) in GaAs:Si using the Al x-ray source. All semiconductor peaks are synthesized by a 70% Gaussian Voigt shape.

	GaAs:Te fresh, Mg-Source	**GaAs:Te** aged, Al-Source	**GaAs:Si** aged, Al-Source	**Comment**
Ga oxide ratio	0.29	0.54	1.19	
As oxide ratio	0.40	0.53	0.34	
Ga/As	1.06	1.35	1.46	
O rel. conc.	0.29	0.37	0.42	
C rel. conc.	0.43	0.17	0.18	
Oxide layer /nm (full TPP-2M)	2.28 (1.79)	3.36 (2.61)	3.61 (2.83)	Weighted average

Table 6.2.: Relative concentrations of the relevant elements and calculated native oxide layer thickness for the fresh and aged GaAs:Te and GaAs:Si samples. TPP-2M refers to a predictive formula to calculate inelastic mean free paths in materials introduced by Tanuma, Powell and Penn [292, 347]. The Ga, i.e. As oxide ratio describes the relation between the oxidic components and the corresponding elemental signal from bulk GaAs in the 3d region.

again exhibits no contaminations beside oxygen and carbon. The detailed spectra of the characteristic 3d peaks in figure 6.8 basically are similar to those in figure 6.5, with single oxidic species in the arsenic photo electron line, assigned to As_2O_3. Also the FWHM are comparable. The Ga 3d signal however exhibits a weak, but clearly recognisable tail at the high energy side. It can be fitted by a broad peak doublet at 22.5 eV. A similar species was also found on some samples investigated by Sullivan et al. There it was identified as $Ga(OH)_3$ by selective surface preparation [343]. This is backed up by the second feature in the O 1s region usually related to hydroxide groups [341]. Alternatively it can be a signature of $GaAsO_4$ which however would also appear in the arsenic signal in the same energy range as As_2O_5 [354]. A third possible explanation is an interference with the weak O 2s species expected at 23 eV [355]. On this sample exposed to air for a longer period of time, the relative oxide concentration of 77 % (averaged) is even higher than on the less aged tellurium doped sample. Specific for this sample is the high gallium oxide content and thereby the resulting high Ga/As ratio of 1.46. This Ga enrichment in naturally oxidized GaAs results from the thermodynamically favoured formation of Ga_2O_3 and is comparable to findings from Negrila et al. [356].

In the 2p region the arsenic response is similar to the previous sample. The Ga 2p signal is convoluted by three species, belonging to gallium in GaAs at 1117.6 eV, the dominant surface oxide Ga_2O_3 or Ga_2O and a third weak species which could be $Ga(OH_3)$ [343] found only on samples with thick oxide layer [357].

In summary both wafer types show no further contamination next to carbon within the sensitivity of the XPS instrumentation. The oxide composition confirms the expected

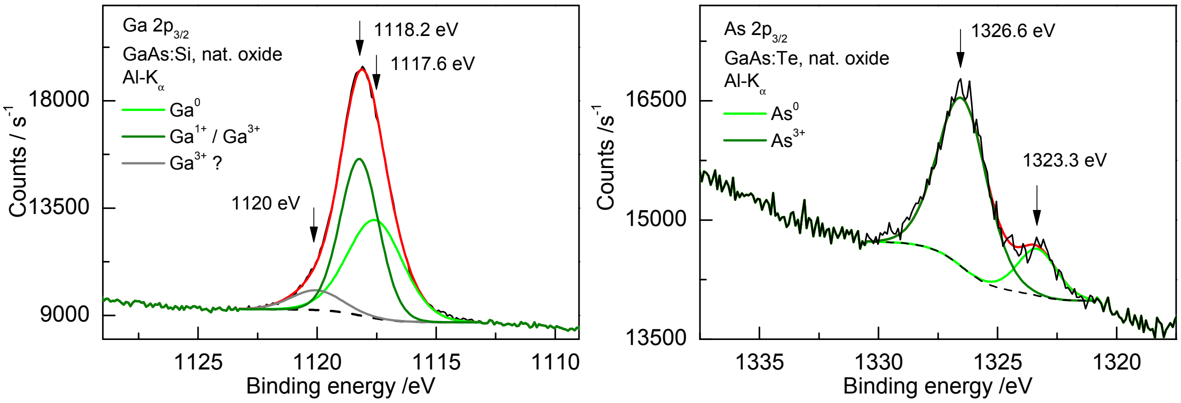

Signal	Species	BE (FWHM) /eV	Lit. BE /eV	Area /a.u.	Conc. /%
Ga $2p_{3/2}$	GaAs	1117.6 (2.74)	1117.0-1117.4 [343, 358]	1153	7.39
Ga $2p_{3/2}$	Ga_2O, Ga_2O_3	1118.2 (1.91)	1118.0 [343] 1118.8 [343]	1284	8.23
Ga $2p_{3/2}$	Ga_2O_3, $Ga(OH)_3$	1120.0 (2.47)	≈ 1118.8 [357]	211	1.35
As $2p_{3/2}$	metallic As, Ga-As	1323.3 (1.95)	1323.2-1323.8 [343] 1322.7-1323.0 [343]	187	2.56
As $2p_{3/2}$	As_2O_3	1326.5 (2.44)	1325.8-1327.3 [343]	860	11.77

Figure 6.9.: XPS spectral details of Ga and As $2p_{3/2}$ in GaAs:Si covered with native oxide layer using the Al x-ray source.

behaviour, with a Ga_2O_3 species and arsenic in the As^{3+} state and sometimes signs of an As^{5+}. The surface of the oxide layer sometimes eventually contains a small amount of gallium and arsenic in low oxidation states (Ga_2O and metallic As). With increasing exposure to air the relative amount of oxidized species, in particular the amount of gallium oxides, increases (cf table 6.2). The oxide thickness t is calculated by a simplified formula related to the derivations in section 5.1.2.3 on ARXPS [359, 360]:

$$t = \lambda_{ox} \cos\alpha \ln\left(1 + \frac{R}{R^{\infty}}\right), \tag{6.1}$$

where λ_{ox} is the inelastic mean free path of photoelectrons in the oxide overlayer, α the analyser take-off angle and R the sensitivity factor corrected intensity ratio of the oxide to substrates signals. Finally R^{∞} is the intensity ratio for infinite thick samples and can be calculated from inelastic mean free paths (IMFP), densities and molecular weights. For each sample the calculation is applied to the gallium and arsenic oxide and elemental core level 3d signals. The thickness is obtained by a weighted average depending on the respective Ga/As ratio. The mean free paths are calculated using TPP-2M, a predictive formula established by Tanuma, Powell and Penn (TPP) in the implementation of the NIST database [347, 361]. In general these predictions fit well to experimental data. Only for GaAs calculated values from optical data deviate considerably [347]. Thickness values are calculated for both, using optical data for GaAs and full TPP-2M based IMFP values (table 6.2 values in brackets). The accuracy is in the range of 10 to 20 %, primarily caused by the errors in the calculated mean free path (sic!) and in the transmission correction. The obtained oxide layer thickness values are smaller than those found by Chang [150], but are in good agreement with GIXR experiments by Allwood [169]. The calculation supports the growth of a thicker oxide layer on the aged samples, which too was found by Allwood on aged samples. Further it is of comparable size on both types of aged substrates, indicating the self limitation of the oxide growths. The Ga/As ratio is related to the overall elemental composition of covalent and oxidic species. Beside the suspicious $Ga(OH)_3$ or O 2s signal, no general difference in chemical states between both sample types was found. Rather the specific surface composition varies with each individual sample. It seems that this reflects the rather undefined process parameters of the wet chemical cleaning and the storage in ambient environment.

6.3. Platinum Covered Samples

Temperature programmed desorption

The annealing of a GaAs:Te sample after sputtering at the typical conditions given in table 5.2 was monitored by temperature programmed desorption (TPD) [77–80]. In this method the sample is heated with a constant temperature ramp, while the desorbing molecules are monitored with a mass spectrometer (QMS200, *Pfeiffer*). Figure 6.10 shows on the lower and left axis the raw ion currents recorded for the masses of C^+, O^+, Ga^+ and As^+ and the temperature ramp on the upper and right axis. Due to the limitations of the sample holder (cf. section 5.2.2) the temperature ramp is inhomogeneous and exhibits a strong kink at approximately 770 K, with slow heating to larger temperatures. The peaks and valleys in the ion currents between 755 and 782 K are possibly produced by the sudden slow down in heating. Nevertheless it can be seen that starting at 620 K, all signals start to increase, culminating in a peak or a shoulder at 703 K. The volatile As shows the strongest relative signal increase up to the maximum temperature at 850 K.

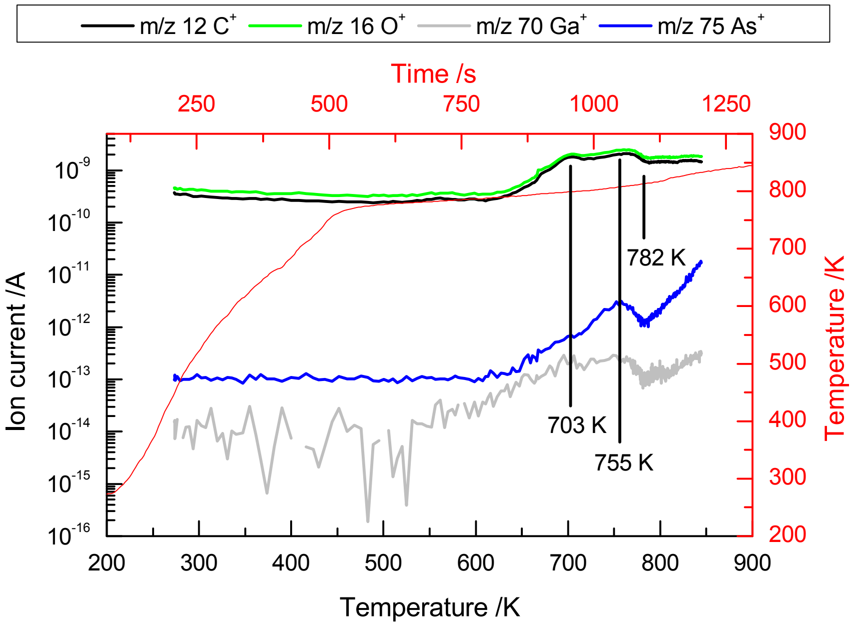

Figure 6.10.: Thermal desorption spectrum of the annealing process of a sputtered GaAs:Te sample.

Guillén-Cervantes et al. also observed first oxide species to desorb from GaAs (100) at 623 K studied by reflective high energy electron diffraction (RHEED), AFM and by monitoring the chamber pressure [362]. They claim that at low temperatures first unstable As oxides desorb. With increasing temperature the reduction reaction of otherwise stable As_2O_3 with GaAs produces Ga_2O_3 and volatile As_2 or As_4. They too found a saddle point in the chamber pressure at 752 K before a second desorption process sets in. SpringThorpe et al. determined the characteristic oxide desorption temperature of thermally oxidised GaAs samples at 855 K [363].

Low energy electron diffraction

As described in section 5.2.3 the cleaning and the surface conditioning of the GaAs wafers prior to the platinum deposition was controlled by LEED measurements. Directly after the initial wet chemical cleaning no surface structure can be observed by LEED due to the unordered oxide layer and the residual surface contaminations. During the cleaning process, after sputtering an annealing up to 620 K, electron diffraction images as given in figure 6.11a, showing the expected pattern of the GaAs (100) bulk, are obtained. The weakly defined spots and the intense background signal at the centre still indicate a distinct disorder at the sample surface. However even after a large number of SIBA cycles, a spot quality comparable to that from clean metallic single crystals could never be achieved.

By averaging over a large number of spots on different samples the bulk lattice parameters of GaAs were calculated using equation 5.1. The distance between two adjacent lattice points was found to be 3.97 ±0.23 Å. The published value of 3.99 Å [364] is within the error margin. One has to bear in mind that the lattice constant of GaAs is 5.65 Å, but the nearest distance between two spots in figure 6.11a is defined by the green surface mesh shown in the right part figure 6.11b [364]. The accuracy is reproduced in all measurements and is completely satisfying for the identification of the different surface reconstructions. According to Auger peak height interpretations by Mendez, the surface bilayer at this preparation conditions and with the observed (1×1) pattern consists of either 0.5 ML (mono layer) Ga on top and a pure arsenic layer below, or vice versa, of 0.5 ML As above a complete layer of gallium [163]. Here one mono layer corresponds to an atomic concentration of 6.26×10^{14} cm^{-2} [163].

After the SIBA cleaning process with parameters given in table 5.2 and annealing up to 850 K, a LEED pattern with sharp spots and a strongly reduced background, as depicted in figure 6.12a, can be observed. The pattern is a (4×1) reconstruction along the

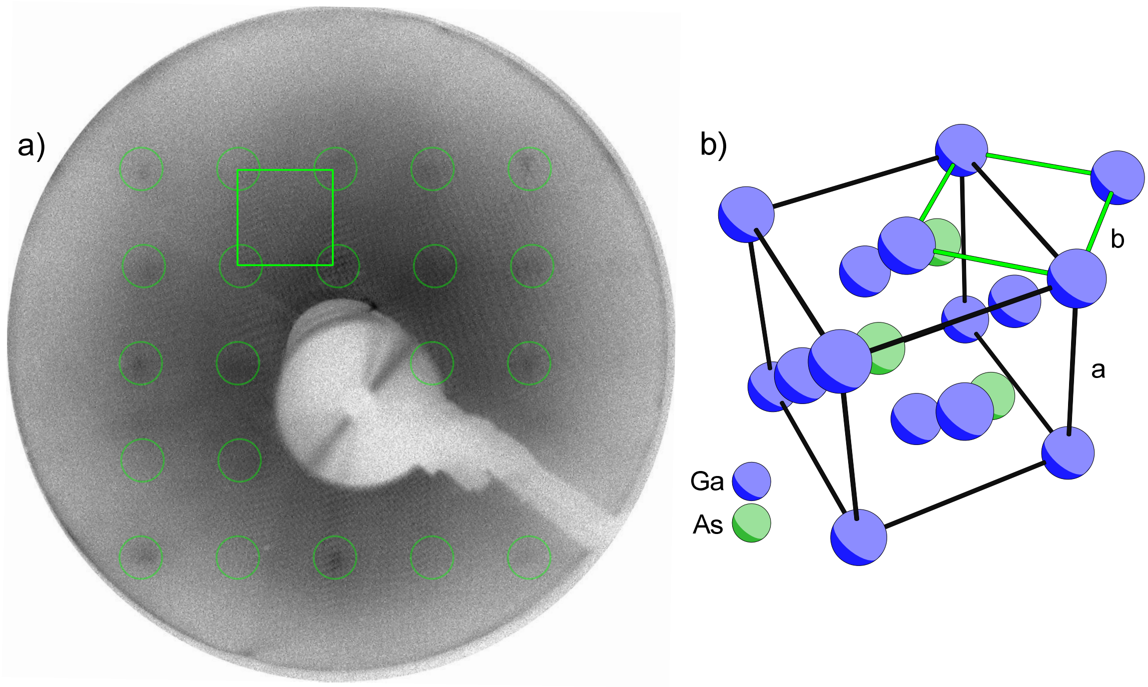

Figure 6.11.: a) LEED picture of GaAs bulk structure at 200 eV. b) Model of the Zinkblende structure of GaAs. The lattice constant *a* is 5.65 Å. The surface mesh imaged by LEED is defined by the green frame. The distance *b* is 3.99 Å. For simplicity the different radii of Ga and As are neglected.

(011) face, with a calculated interval of 16.00 Å. As discussed in section 4.1.1 Biegelsen found (4×1) regions on samples with a (4×6) LEED pattern and described those as a repeated stripes appearing to be regions of incompletely ordered $c\,(8 \times 2)$. According to Drathen the As surface coverage is about 0.27 [162]. Taking a closer look at figure 6.12a, other weak vertical lines can be recognized. In some preparations (figure 6.12b), the LEED pictures resolve individual spots. This pattern belongs to the full $c\,(8 \times 2)$ reconstruction. The corresponding model surface worked out by Biegelsen is shown in figure 4.2. AES measurements by Mendez indicate a 0.5 ML Ga over 0.75 ML As surface coverage which are in agreement with the STM obtained model [163]. Drathen claimed an arsenic surface concentration of 0.22

The surface cleaning process successfully removes contaminations and the oxide layer and creates a gallium rich surface with an at least partial $c\,(8 \times 2)$ ordering. The subsequent deposition of Pt at any temperature does not produce crystalline layers observable by electron diffraction.

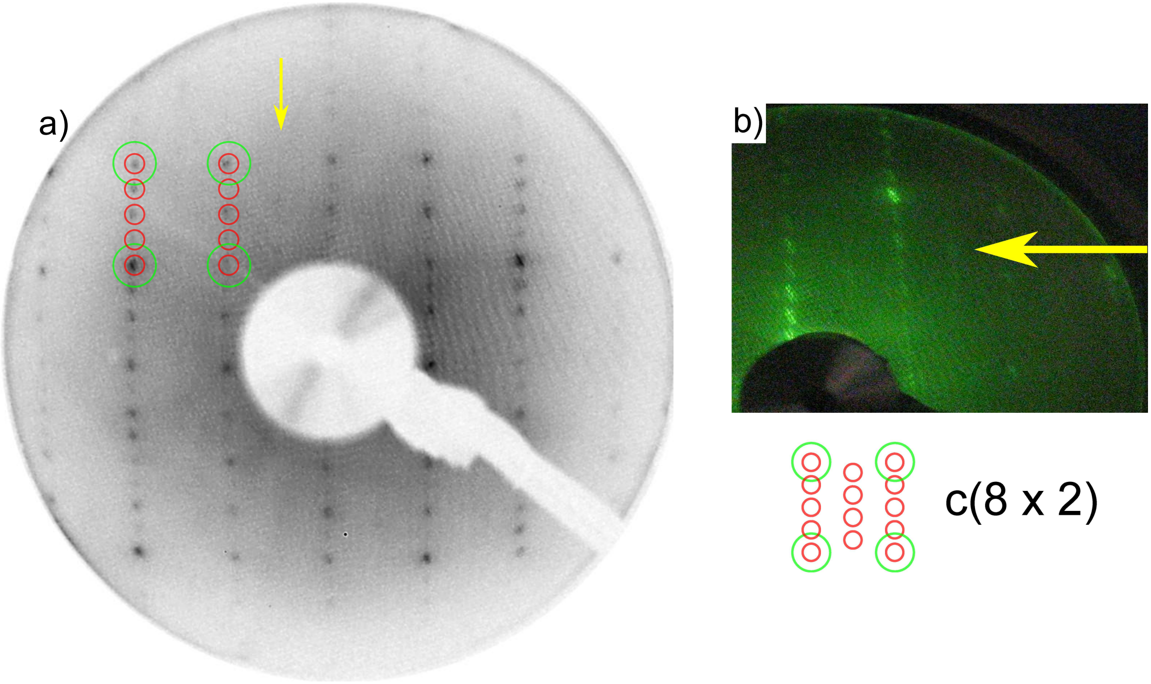

Figure 6.12.: Reconstructed LEED pattern of a cleaned GaAs:Te surface, after annealing to 850 K recorded at 210 eV. a) (4×1) reconstruction. b) Complete $c\,(8 \times 2)$ reconstruction.

SPM

Upon sample preparation under UHV the retaining brackets protect the surface in regions 1 and 2 from sputtering and platinum deposition (cf. section 6.1.1 and figure 6.1). After the cleaning process and metallization at 100 K the otherwise flat clamping region 2 is speckled with up to 72 nm deep holes and ≈ 1.5 nm high dislocation lines (figure 6.13). The surface roughness on the remaining area is increased to $S_A = 1.48$ nm. AFM measurements by Guillén-Cervantes et al. who investigated the thermal oxide desorption from GaAs revealed that already the vaporization of the unstable low temperature As oxides creates pits in the surface as deep as 12 nm [362]. In the outer zone away from the brackets (region 4) granular features as seen on the native oxide covered samples become apparent again. Here, however, with a larger particle size of up to 30 nm, resulting in a roughness parameter of 3.25 nm (left side of figure 6.14).

Moving closer to the centre of the sample into region 3, the particle/island density decreases and unveils the beginning of a layered structure beneath. This is shown in the right side of figure 6.14 where a nonlinear colour mapping is used to increase the visibility. The roughness including the particles decreases to $S_A = 2.68$ nm.

Taking the roughness as a measure, a weak trend in surface quality improvement can

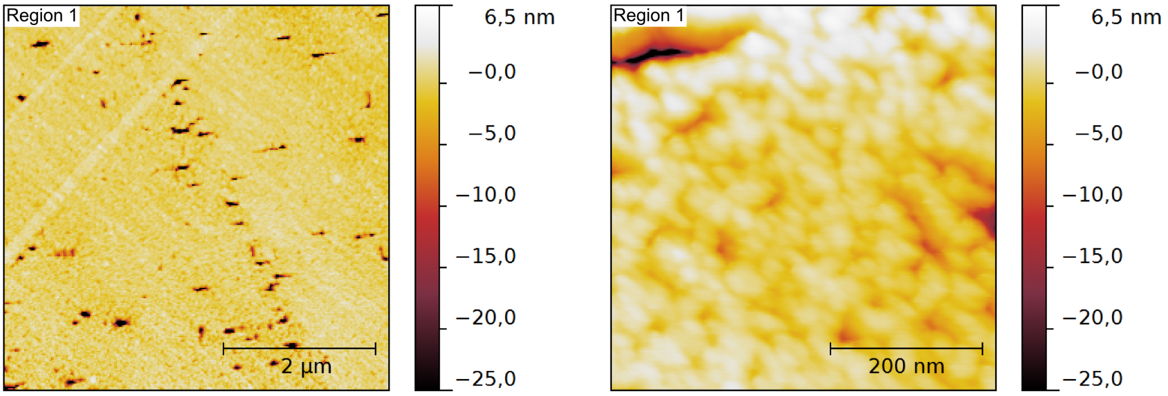

Figure 6.13.: AFM images of sputtered and annealed GaAs:Te covered with 5 Å Pt evaporated at 100 K in region 1 (cf. figure 6.1) below the retaining bracket.

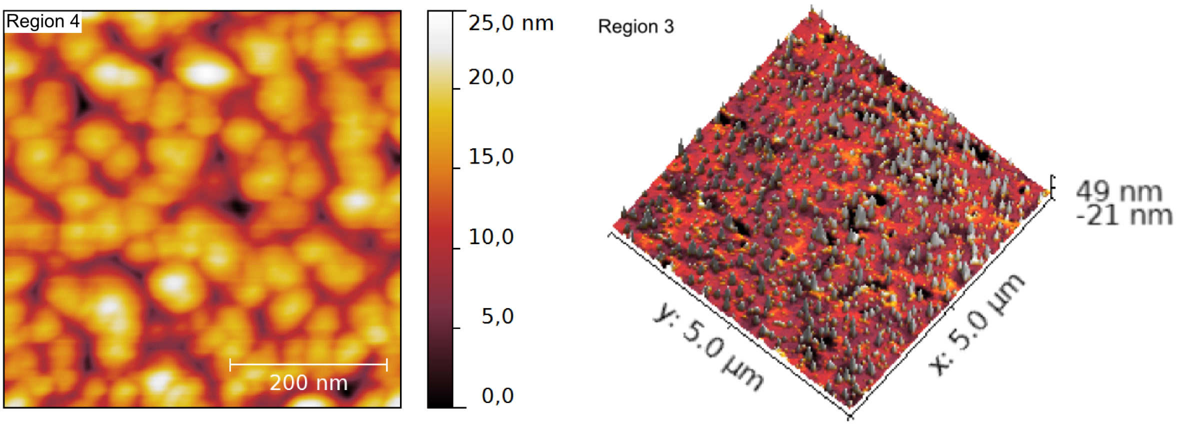

Figure 6.14.: AFM images of sputtered and annealed GaAs:Te covered with 5 Å Pt evaporated at 100 K. Left: Outer region of the sample (region 4, cf. figure 6.1). Right: Centre of the sample (region 3, cf. figure 6.1) with nonlinear colour mapping.

be observed when increasing the process temperature from cryogenic levels to ambient temperature. In particular this observation applies to the regions 3 and 4, important for the optical experiments (figure 6.15). Beside region 3, the roughness corresponds rather to those found on thicker platinum layer of 7.5 nm published by Masó [18]. When evaporating at higher substrate temperatures the roughness starts to rise again. At 300 K the uniformity of the layer structure in region 3 is responsible for the small areal roughness (figure 6.16), even though a new species of particles starts to grow on top, resembling of impact craters. From height distribution analysis (masking the particles) an average step height of 0.25 nm was extracted, which is in the dimension of mono atomic steps. The impact crater structures typically consist of an approximately 200 nm wide and 4 nm deep crater with a 30 − 40 nm thick and 4 nm high nodule at its centre.

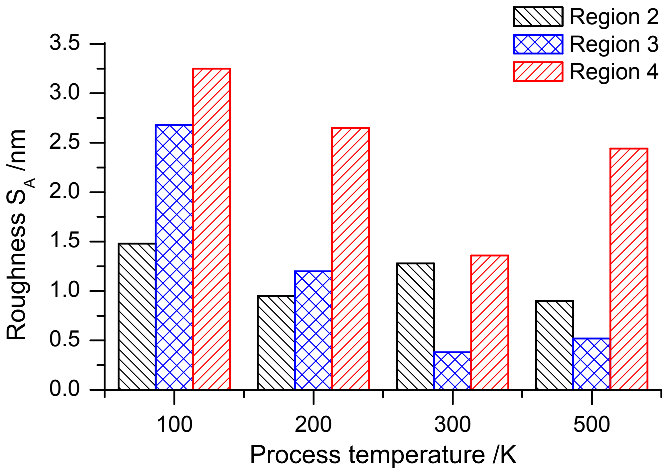

Figure 6.15.: Roughness parameter S_A as function of substrate temperature at the evaporation process given for different sample regions as defined in figure 6.1.

STM measurements on this sample reveal similar structures in regions 3 and 4, although the image quality and repeatability is poor compared to AFM experiments (figure 6.17). At 500 K the central nodule grows to a width of $35-50$ nm and reaches a height of $8-16$ nm, while the density of this particles is smaller than on the room temperature preparation. The previously smooth terraces begin to decompose into arrays of droplets (right side of figure 6.18).

The spatial inhomogeneity of the surface morphology is caused on one hand by the spatial inhomogeneous particle density in the process beams (evaporated Pt and Ar^+ ions of the sputter cleaning) and on the other hand and more important by a temperature gradient across the sample. The later effect is caused by the sample plate design, in particular by the circular notch at its centre (figure 5.14b in section 5.2.2) and the heating filament position. LEED measurements taken from different positions at the sample surface after the cleaning cycle already indicate this effect. The proposed lower sample temperature and smaller sputter intensity in the outer region prevents a complete removal of the native oxide layer and/or creates a rough, defect rich surface which either easily reoxidizes by residual oxygen or leads to a different nucleation behaviour in the metallization step. The central region is characterized by terraces of well defined $c\,(8\times 2)$ reconstructions as observed by LEED. The steps may be caused by a small miscut or by the directional sputtering. The AFM measurements by Allwood recorded at different steps (temperatures) of thermal deoxidation show a similar trend, with a particle like distribution at lower temperatures and a monoatomic layers after complete oxide removal

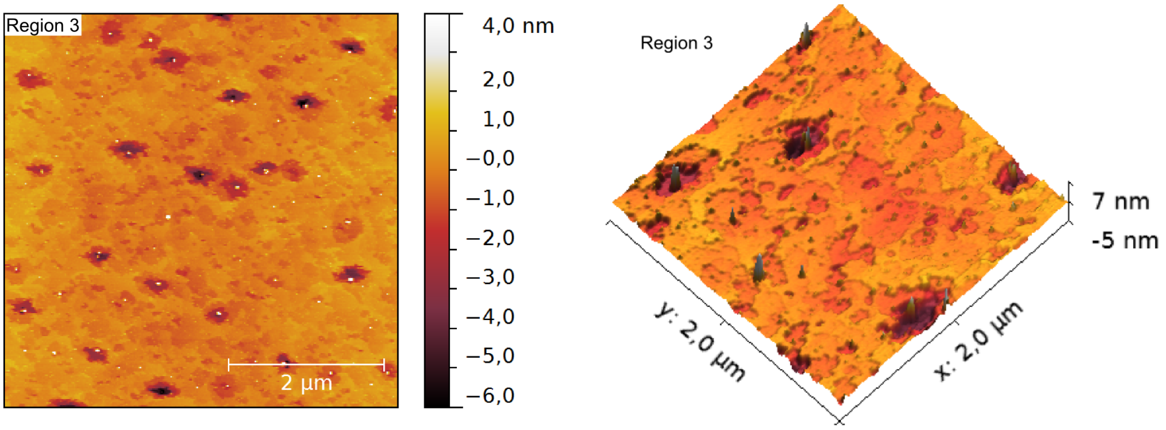

Figure 6.16.: AFM images of the central sample region (region 3, cf. figure 6.1) from sputtered and annealed GaAs:Te covered with 5 Å Pt evaporated at 300 K.

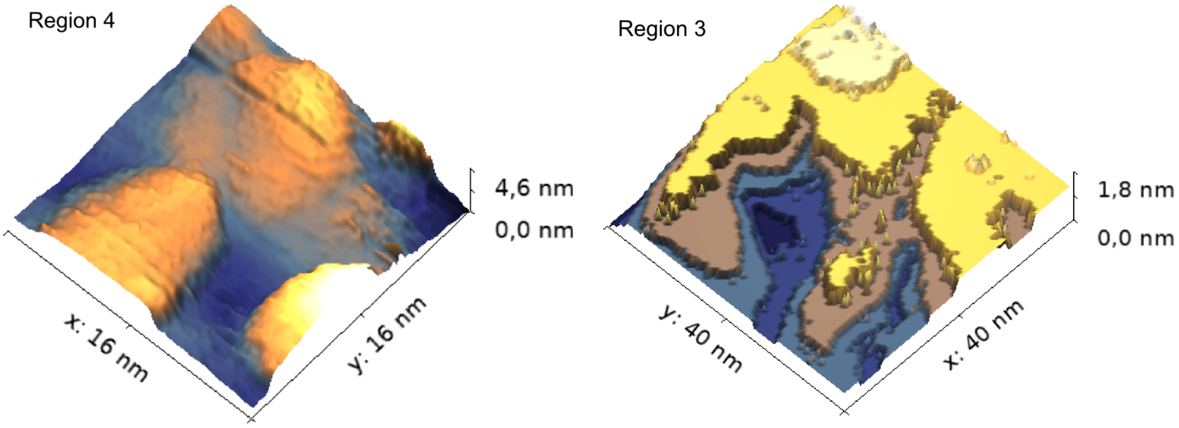

Figure 6.17.: STM images of sputtered and annealed GaAs:Te covered with 5 Å Pt evaporated at 300 K. Left: Out sample region (region 4). Right: Sample centre (region 3).

(see figure 4.3 in section 4.1.1) [169].

Since sometimes several days passed between the ambient air AFM measurement and the removal of the samples from the UHV chamber, a bare, exposed GaAs 100 surface would suffer reoxidation. Also there is no indication for a the growth of highly ordered gallium and arsenic oxides.

Platinum with its high surface free energy of $\approx 2.5\ \mathrm{J/m^2}$ does not readily wet most substrates. On oxidic model catalyst supports Pt forms well separated three-dimensional islands in a Vollmer-Weber like growth, while at low temperatures the structures is more like an amorphous layer of small particles. The difference is attributed to the temperature dependency of diffusion coefficients and different nucleation modes [29] (cf. section 4.2.1.1). In contrast to that system, the GaAs $\{100\}$ surface exhibits a

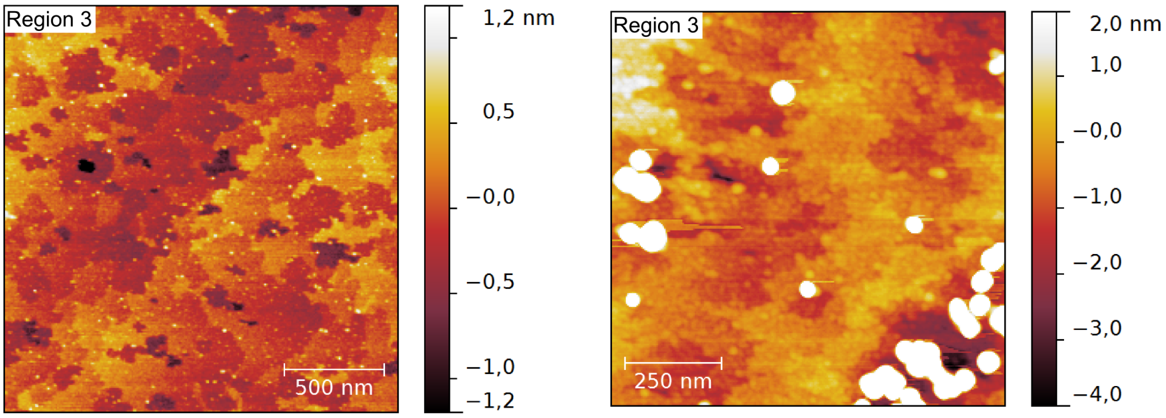

Figure 6.18.: AFM images at the sample central (region 3, cf. figure 6.1) from sputtered and annealed GaAs:Te covered with 5 Å Pt evaporated at 500 K.

surface Gibbs energy of 2.94 J/m^2 which should in principle allow the formation of a wetting layer [365]. Also the lattice mismatch between Pt (3.92 Å) and the surface mesh of the {100} surface layer (3.97 Å) is small enough (1.3 %) to allow a layer by layer growth. The observed structure is thus attributed to a thin layer of Pt on top of the reconstructed GaAs, preserving its morphology at the centre. This is also supported by indirect evidences obtained in STM and infrared spectroscopy experiments (see appendix C.3.1).

While the small evaporation rate of ≈ 8 pm/min allows a growth under thermodynamic control, the reduced surface mobility of the ad-atoms favours a meta stable kinetic controlled state at low temperatures. This may be the dominating cause for the particle like distribution at the low temperature samples, compared to the completely wetted surface at room and elevated process temperatures (comparing right side of figure 6.14 and figure 6.16). Increasing the substrate temperature to 500 K the diffusion and reactivity across the interface gains importance. The observed droplet formation on the terraces thus may be a stress relief process or an alloying. The later discussed static nonlinear optical response measured by rotational SHG indicates an optimum in interface quality (in the context of Schottky barriers) for the room temperature samples too.

Observations similar to the impact craters found in region 3, but on a larger scale (approximately 2 µm wide craters on 200 nm thick platinum depositions) investigated by scanning electron microscopy (SEM) were published by Begley [243]. Additional x-ray emission spectroscopy measurements revealed a high gallium content at the central nodule. They discussed the effect as a local gallium diffusion through the metal layer at hidden film imperfections and the formation of an alloy.

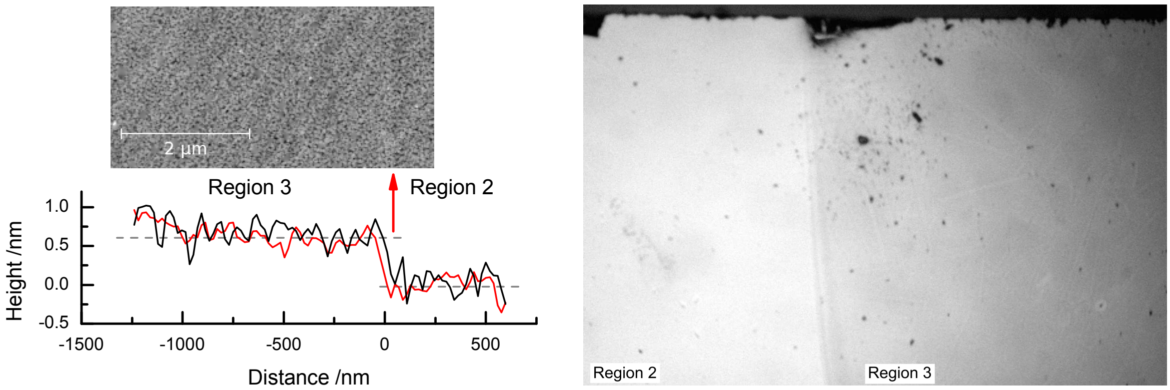

Figure 6.19.: AFM image and height profiles (left) and microscopy image (right) at the boundary between region 2 and 3 from sputtered and annealed GaAs:Te covered with 5 Å Pt evaporated at 200 K.

An attempt was made to determine the evaporated platinum thickness by taking AFM scans across the clamping boundary between region 2 and 3. While in incident light microscopy the two different regions on low temperature evaporated 5 Å GaAs:Te samples can be easily identified, the contrast in atomic force microscopy images is weak (figure 6.19). Cross sections perpendicular to the edge marked by the red arrow however, reveal a step of approximately 0.62 nm. It is tempting to interpret this as the platinum coverage, but the mechanical stress in the clamping region and the removal of the 2 – 3 nm thick native oxide layer has a larger impact on the measured step height, than the thin metal layer. On other samples, especially the high temperature species, also transitions with negative step height were found. Difficulties with this approach of thickness determination also emerged when investigating platinum films deposited on glass substrates (cf. appendix C.2.1).

XPS

The XPS characterization of the platinum covered samples focuses on the effects of reoxidation, platinum coverage and on signatures of potential alloying or reactions between Pt and the substrate elements. As described in the experimental section the sample has to be transferred from the preparation to the XPS chamber by an evacuatable transportation container. An oxygen contamination during the exchange and transport procedure could not be prevented. This becomes evident in the majority of investigated GaAs-Pt samples.

The first platinum sample discussed is prepared by only two sputter and annealing

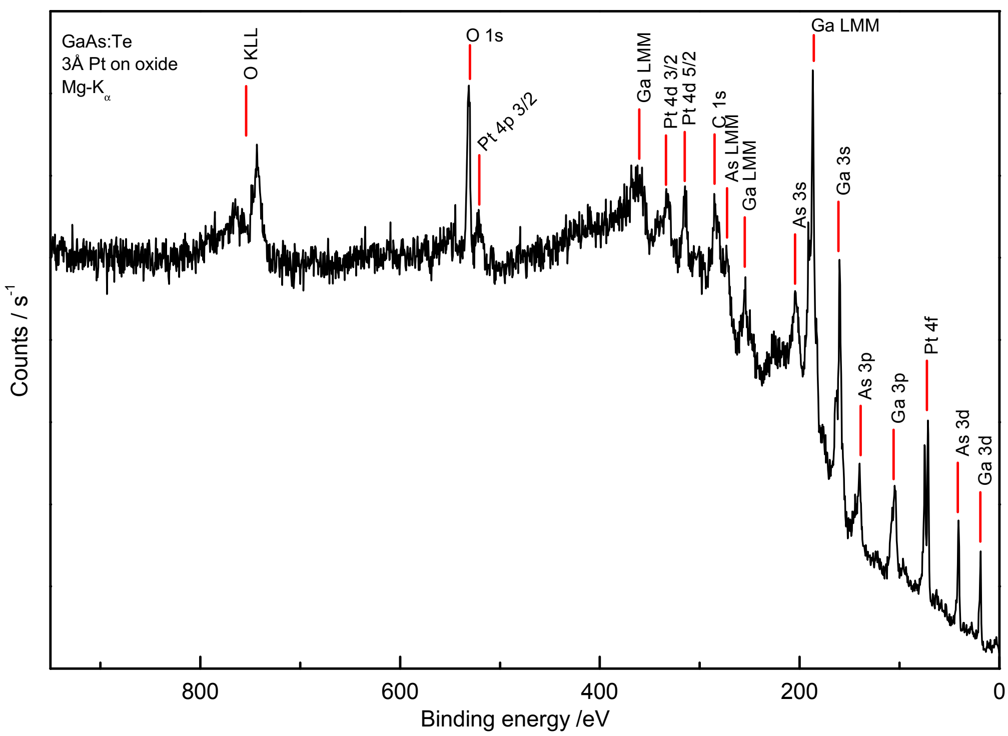

Figure 6.20.: XPS survey spectrum of a GaAs:Te sample covered with residual oxide layer and 3 Å Pt, using the Mg x-ray source.

cycles to remove the topmost contaminations and oxide. In this way a clean platinum on oxide interface is created. Figures 6.20 and 6.21 show the corresponding survey and the Ga/As 3d regions, investigated using the Mg x-ray source. With respect to the previous discussion this sample is the platinum covered version of the first GaAs:Te sample (figures 6.4 and 6.5). From the survey it can be seen that the preparation introduced no additional contaminations beside platinum and that the transport between the UHV chambers leads to a readsorption of carbon. The structure of the gallium 3d region is identical to the unmetallized sample; also the relative concentrations of oxygen and carbon are unchanged. The difference is found in the arsenic 3d region. The main As^{0+} peaks of Ga-As are best fitted with an asymmetric contribution in shape of a Voigt peak modified by an exponential blend function. The high energy tail covers either a buried low oxidation state species or more likely a small amount of metallic arsenic (or intermetallic $PtAs_2$) which is expected between 41.6 – 42 eV [343]. A metallic arsenic species is not surprising considering the annealing at 850 K and the subsequent diffusion of As and the reduction reaction of As_2O_3. Only with this fit the oxidic As^{3+} species at 43.8 eV could be synthesized with reasonable parameters. In contrast to the bare native oxide samples the signal of this species is shifted by approximately −0.2 eV which may indicate a lower, non stoichiometric oxide. While the Ga/As ratio and the relative amount of gallium oxides stays constant with respect to the unprocessed sample, it shows that the surface reactions and the partial sputtering preferentially removes the arsenic oxides (As oxide ratio of 0.1).

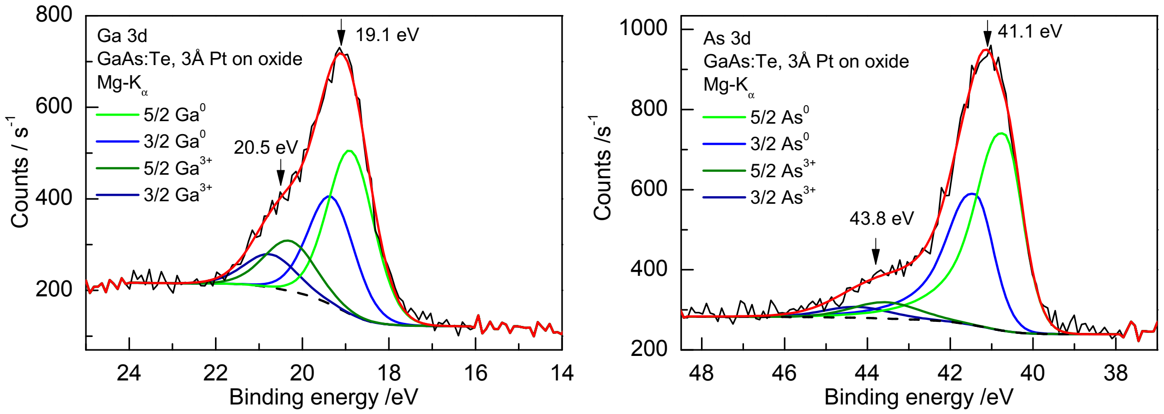

Signal	Species	BE (FWHM) /eV	Lit. BE /eV	Area /a.u.	Conc. /%
Ga 3d$_{5/2}$	Ga-As	18.90 (1.25)	18.8 [348]	324	9.98 (10.9)
Ga 3d$_{3/2}$	Ga-As	19.35 (1.25)	19.3 [348]	214	
Ga^{3+} 3d$_{5/2}$	Ga-O	20.29 (1.39)	20.4-20.6 [349, 350]	110	3.4 (3.2)
Ga^{3+} 3d$_{3/2}$	Ga-O	20.74 (1.39)		73	
As 3d$_{5/2}$	As-Ga	40.70 (1.07)	40.8 [341]	333	10.3 (9.7)
As 3d$_{3/2}$	As-Ga	41.40 (1.07)	41.5 [341]	222	
As^{3+} 3d$_{5/2}$	As-O	43.56 (1.89)	44.3 [343]	34	1.1 (3.9)
As^{3+} 3d$_{3/2}$	As-O	44.26 (1.89)		23	
O 1s		531.1	531.7 [345]	1571	29.1 (29.0)
C 1s		285.0	285.0 [345]	2245	41.6 (43.3)

Figure 6.21.: XPS spectral details of Ga 3d (left frame) and As 3d (right frame) in GaAs:Te with residual oxide layer and 3 Å Pt using the Mg x-ray source. The arsenic 3d peaks of GaAs are fitted with an additional exponential blend with an amplitude of 1.2. The concentrations of the individual components on the oxide covered unmetallized GaAs:Te sample discussed before are given in parentheses.

Applying the oxide thickness calculation to this sample gives a residual oxide layer of 1.48 (1.01) nm (full TPP-2M in parentheses) (cf. table 6.3), but for a correct treatment the effects of the platinum overlayer have to be included.

The strongest signal of the metallic overlayer is the Pt 4f doublet at 71.6 eV with a spin-orbit coupling separation of 3.31 eV (figure 6.22). It is synthesized with an asymmetric contribution to account for multiplet splitting too. In contrast to measurements on uncleaned and sputtered Pt(111) single crystal samples with the same equipment [344],

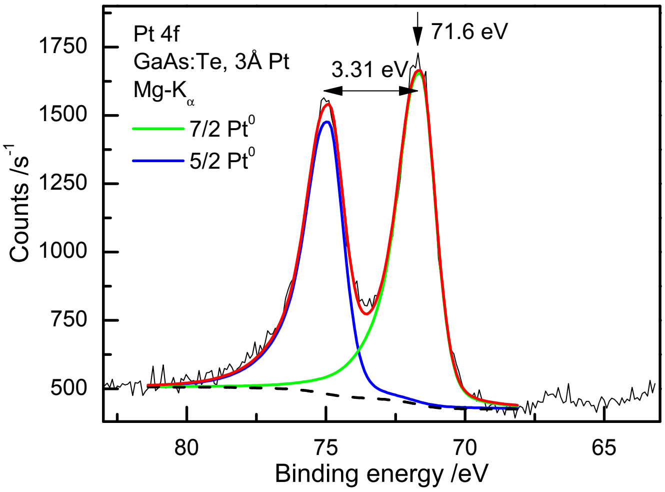

Signal	Species	BE (FWHM) /eV	Lit. BE /eV	Area /a.u.	Conc. /%
Pt $4f_{7/2}$	metallic Pt	71.60 (1.30)	71.1 [366, 367]	134	4.54
Pt $4f_{5/2}$	metallic Pt	74.91 (1.30)		111	

Figure 6.22.: XPS spectral details of Pt 4f in GaAs:Te with 3 Å Pt using the Mg x-ray source. The peaks are fitted with an additional exponential blend with an amplitude of 1.2.

the signal is shifted to higher binding energies by ≈ 0.5 eV and can be fitted by a single doublet (i.e. with less asymmetry). From reference data and the measurements on the single crystal the pure metallic species gives photoelectrons at 71.1 eV [366, 367]. While both Pauli and Allred-Rochow scale agree on the electro-negativity values of gallium (≈ 1.8) and arsenic (≈ 2.2) they significantly differ at the Pt value [368, 369]. The Pauli electro-negativity (EN) value of 2.2 and the redox-potentials suggest a shift to lower binding energies in any of the possible compound with Ga and As. In contrast the observed shift rather indicates an oxidized platinum and thus matches the EN value of Allred-Rochow (1.44). A positive BE shift of the same magnitude was also observed in alloying reactions between Pt and Re and other metals [370] (and references therein). Experiments by Kuroda, Kim and others suggest the formation of kinetically stable, at least under UHV conditions, $PtGa_x$ phase at the sample surface (not at the interface between Pt and the native oxide) [371–373]. This fits to the observation of gallium rich protrusions on the clean interface samples. The XPS measurements shown in figure 6.21 with their metallic arsenic signal and corresponding Auger signals indicate an interaction with arsenic, e.g. in form of $PtAs_2$ at the interface.

The platinum layer thickness is determined by the THICKOGRAM technique introduced by Cumpson. It is a graphically method which, in contrast to the simple Hill equation 6.1,

	GaAs:Te 3Å Pt @ 100K oxide, Mg-Source	**GaAs:Te** 5Å Pt @ 300K Al-Source	**GaAs:Si** 3Å Pt @ 300K Al-Source	**GaAs:Te** 5Å Pt @ 570K Al-Source
Ga_2O_3/Ga	0.34	0.32	0.12	0.00
As_2O_3/As	0.10	0.31	0.25	0.11
O	0.29	0.42	0.49	0.38
C	0.42	0.14	0.13	0.00
Ga/As	1.18	1.51	1.27	1.27
Oxide /nm (full TPP-2M)	1.48 (1.01)	2.36 (1.76)	1.70 (1.24)	0.67 (0.48)
Pt /nm	0.38	0.31	0.15	0.20

Table 6.3.: Relative concentrations of the relevant elements and calculated native oxide layer and Pt thickness for the GaAs:Te / GaAs:Si samples. The oxide layer parameters are calculated using the Hill formula (equation 6.1), the platinum thickness is determined by the THICKOGRAM technique [374].

allows the analysis of overlayer and substrate signals with large kinetic energy differences. It's application and derivation, based on the same Lambert-Beer foundation as the simple approach, can be found in [374]. With the electrons IMFP in platinum taken from a publication of Cumpson, the method gives a platinum thickness of 0.38 nm [375]. It assumes a closed layer growth. Further the enclosed oxide layer is likely to affect the accuracy of the determined thickness.

Next, samples with different platinum coverages and evaporation temperatures were investigated. All these samples showed a clean LEED image with a $c(8 \times 2)$ or at least a (4×1) reconstruction as shown before. Never the less the corresponding XPS spectra at the lower evaporation temperatures reveal a clear amount of oxidized species. Figure 6.23 displays the 3d regions of arsenic and gallium for different samples (from top to bottom: A: GaAs:Te with 5 ÅPt at 300 K, B: GaAs:Si with 3 ÅPt at 300 K and C: GaAs:Te with 5 ÅPt at 570 K). Striking are the new features on the high binding energy side of the Ga 3d signals, which are most developed in the high temperature preparation (C). All these additional signals have FWHM of about 1.6 eV and are equally separated by about 2 eV. The parameters from this sample are used as starting point for the peak synthesis in the two other investigated preparations. The extra signals have the typical shape of plasmon loss peaks or shake up signals, especially at the 300 K preparation (B) with the decreasing peak intensity. The plasma energy for n-doped GaAs is in the range of tenth of meV (see figure 4.17 in section 4.1.5), granular nanoscopic Ga is found to have a plasma resonance at 0.69 eV. Metallic materials have higher plasma energies (Ga $\approx$ 15 eV, Pt = 5.1 eV) [376, 377]. For the $PtGa_2$ intermetallic compound transitions between $2 - 3$ eV were found (as reviewed in [378]). As these kind of signals are only found at the gallium signal and only for platinum preparation with a direct metal semiconductor contact they could be assigned to an alloy species between platinum and gallium. It is interesting that these signals form a plateau in the 570 K sample. Beside this both major 3d signals from Ga and As are best fitted by metallic peak shapes. In corresponding ARXPS measurements (discussed below) these features dominate the flat angle scans. In the course of the ARXPS measurement a single scan per incident resulted a Ga 3d signal without the high energy tail. This is shown in (C) as an overlay (black dots). Based on this scan the position of the Ga^{3+} oxide species and the asymmetric Ga line shape used in all shown measurements, was determined.

Table 6.3 contains also the calculated oxide and platinum layer parameters for the direct contact samples. Here the oxide layer thickness should be interpreted with care. The electron analyser covers a surface area of up to 10 mm diameter and thus samples both regions 3 and 4. The structural difference of both regions can be seen from the AFM measurements discussed before. The relative high oxygen content in the 300 K samples is most likely located in the outer sample region, the determined values should be interpreted as an equivalent thickness. The determined platinum thickness depicts the correct tendency but gives smaller amounts than expected.

Angular resolved XPS measurements recorded from the high temperature sample (C) are shown in figure 6.24. From this data the platinum thickness was determined in a full Lambert-Beer approach as described in section 5.1.2.3 by 0.49 nm, which is very close to the nominal value of 0.5 nm. Further from the logarithm of the ratio of intensities between grazing and normal take-off angle a relative depth plot can be created. While it does not give absolute information it reveals the stacking order of the constituents of a sample (figure 6.25). The loss of overall intensity upon rotation of the sample was compensated by normalization. A species with equal distribution over the complete accessible information depth would give a value of zero in the relative depth plot.

Three regions can be identified. Covalent or metallic gallium and arsenide together with the high binding energy signals from the unidentified Ga tail form the main group of bulk species. Stacked on top is platinum, arsenic in the 3+ oxidation state and oxygen itself. The third group deep below is comprised of the the two remaining Ga tail signals at 22 and 24 eV. This analysis reveals a direct platinum GaAs contact and in general a layered stacking. The Ga species is slightly elevated towards the arsenic component, this could either be an indication for the $PtGa_x$ species at the interface, or a signature

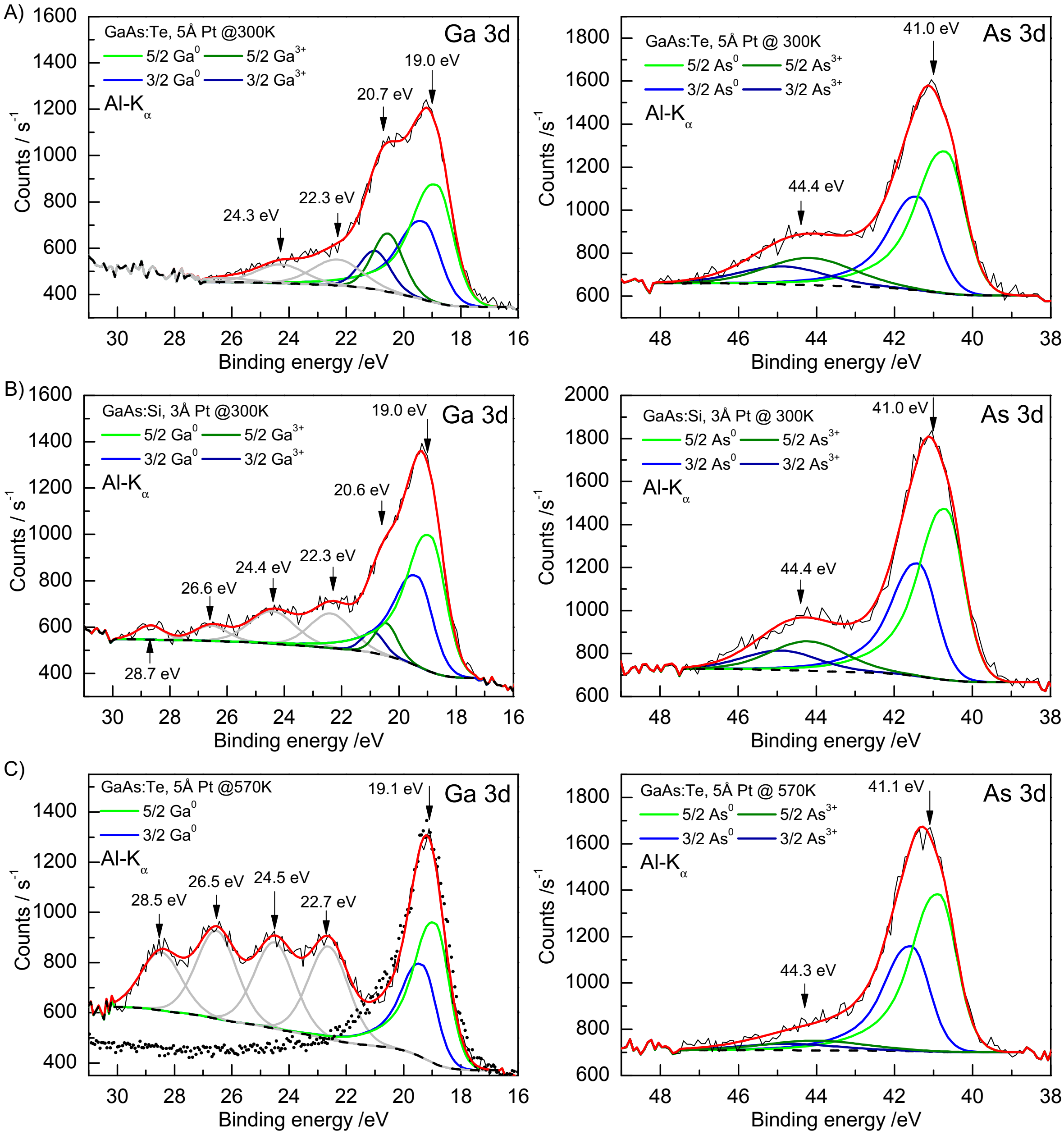

Figure 6.23.: XPS detail spectra of Ga 3d (left column) and As 3d (right column) in GaAs samples covered with different amounts of Pt and at varying evaporation temperatures. All spectra were recorded using the Al x-ray source. The arsenic 3d peaks of GaAs are fitted with an additional exponential blend with an amplitude of 1.2. The new features in the gallium region are discussed in the text.

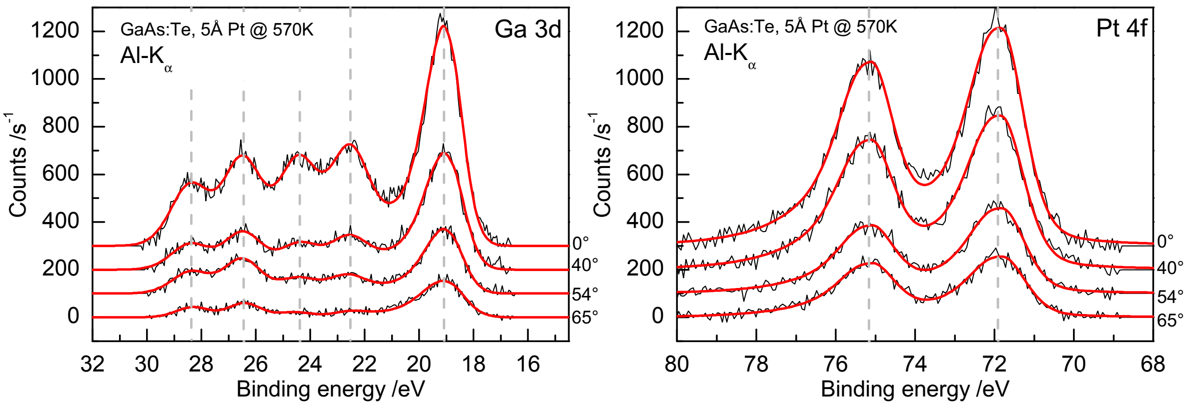

Figure 6.24.: Background subtracted XPS detail spectra of Ga 3d (left) and Pt 4f (right) in GaAs:Te samples covered with 5 Å Pt at 570 K at different analyser take-off angles and the corresponding envelope functions created by peak synthesis (red). All spectra were recorded using the Al x-ray source.

from the preferred arsenic removal and formation of the gallium rich reconstruction in the deoxdation process preceding the metallization (see figure 6.12 in this section). The Ga/As proportion is, as in the native oxide samples, shifted to gallium.

At first this seems to contrast the findings of Begley and Murarka discussed in section 4.2.1.1 where a $PtAs_2$ layer close to the interface, a $PtGa_x$ phase away from it and a resulting depletion of Ga in the semiconductor area below the interface was proposed. But in their studies 200 nm thick platinum layers were investigated [17, 242, 243], while the ultra thin 0.5 nm thick layers of the samples investigated here don't seem to be capable to allow such a defined and complex structure. Here the arsenic oxide layer (As^{3+} and O species) on top of the platinum would imply an out diffusion of As at this process temperatures. In general the quality of underlying data is high, with the exception of the As^{3+} species. The oxide intensity in the normal angle take-off configuration is already very low (right plot in 6.23C), at 65° in combination with the weak total signal strength, the accuracy of the resulting ratio has to be treated with caution.

While the 28 and 26 eV signal are at the same depth region as gallium, the 24 and 22 eV signals originate from suspiciously deep into the sample. This tendency is already evident from the raw Ga spectrum in figure 6.24. The strictly decreasing depth with increasing loss of kinetic energy fits into the picture of a plasmon loss feature, the final escape depth of a photoelectron after four plasmon interactions is consequently smaller than the average depth of an one time scattered photoelectron. But the large step between 26 and 24 eV neither fits into this scheme nor into a $PtGa_X$ intermetallic compound picture discussed initially.

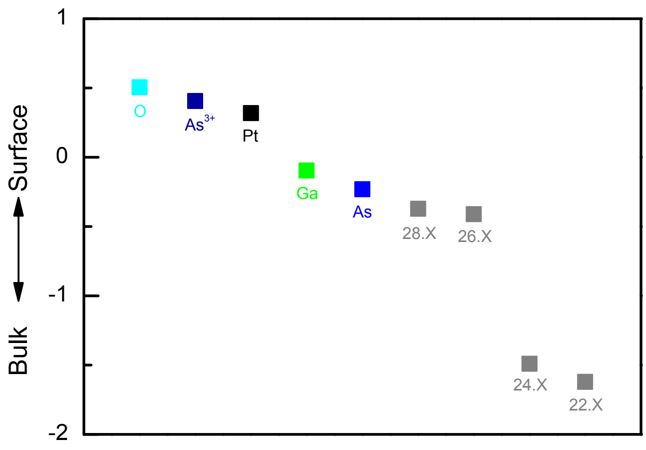

Figure 6.25.: Relative depth plot of the GaAs:Te, 5 Å @ 570 K sample. Analysed using the Al-source.

Further, carefully studies, best within a combined preparation and analysis environment to avoid the transport, are necessary to clarify the origin of these signals.

6.4. Superheated Substrates

By heating to temperatures larger than the 850 K required to prepare the $c(8 \times 2)$ reconstruction or by excessive sputter and anneal cycles the gallium arsenide substrate is subject to massive gallium diffusion. Macroscopically this is manifested as a dull, nebulous film, which reflects light diffusely and thus hampers optical investigations.

Microscopy

On a microscopic scale the surface outside the clamping regions is covered by coexisting smaller and lager droplets (figure 6.26). Inside the clamping region the surface is spotted by pits but is otherwise smooth in the same way as found by AFM measurements on the samples discussed before. Detailed SEM (S-3200N, *Hitachi*) scans show that the larger drops are surrounded by a depletion zone (figure 6.27 and figure C.7 in appendix C.3). Analysing this area by energy dispersive x-ray spectroscopy (EDX) reveals that the droplets consist of pure gallium while the remaining surface is composed of Ga and As in the same way as found on native oxide covered samples (table 6.4). The detected Cl signal is related to the microscopy and found on all samples. Oxygen was not found by the EDX which by its 20 keV electrons averages of a volume 15 nm deep into the

Element	**Atomic conc. /%**	
	Inside droplet	Outside droplet
Ga	62.5	35.7
As	0	29.2
C	38	34.7
Cl	0.5	0.4

Table 6.4.: Composition inside and outside the droplets of figure 6.27 determined by EDXs.

sample.

XPS

Subsidiary angle resolved XPS measurements give a differentiated picture of the surface near region. Both main As and Ga 3d peaks can be fitted by metallic asymmetric blend peak shapes (figure 6.28). A weak oxidized arsenic species can be assumed at 40° take-off angle only. Also the gallium 3d region does not show the typical signatures of oxidized species between $20 - 22$ eV (cf. appendix C.1.1) but a strong and broad signal at 23.3 eV instead. It dominates the gallium signal at 40° take-off angle. From its chemical shift, the similar oxygen concentration and its behaviour at different take-off angles it is assigned to a gallium in a high oxidation state related to the gallium diffusion reaction and the formation of droplets. The peak shape and energetic position also rule out a relation to the plasmon like signal tail on the platinum covered samples. In the literature (eg. [343]) and in the previous section on native oxide covered samples a signal in this region is discussed either as a hydroxide, a ternary oxide or as an interference with the O 2s peak. Based on this findings from superheated substrates it could also be a general sign of a surface diffused gallium species and the formation of droplets.

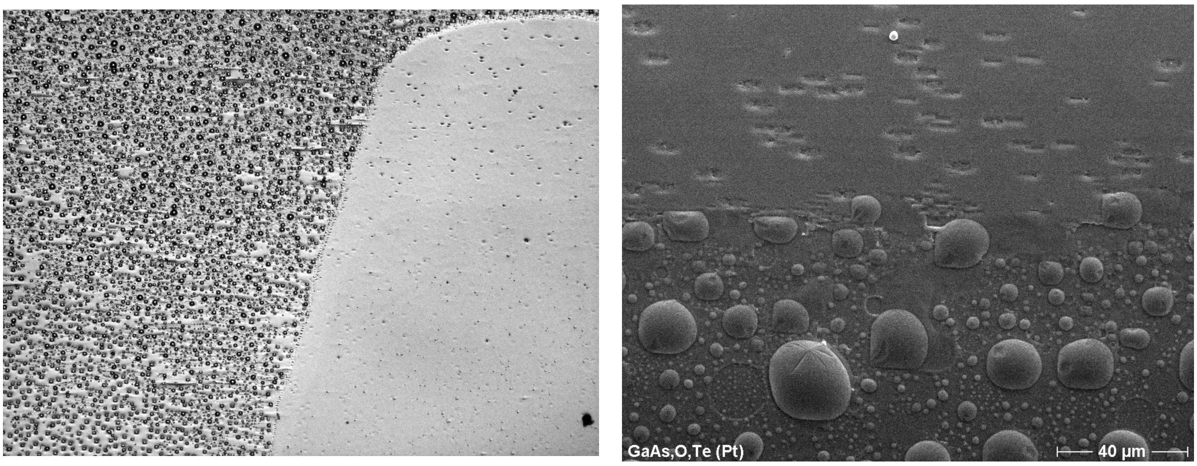

Figure 6.26.: Images of GaAs:Te heated to a temperature of 1070 K. Left: Light microscopy picture of the bracket imprint. Right frame: SEM picture of the same area with larger zoom. The features in the clamped area appear to be more like pits.

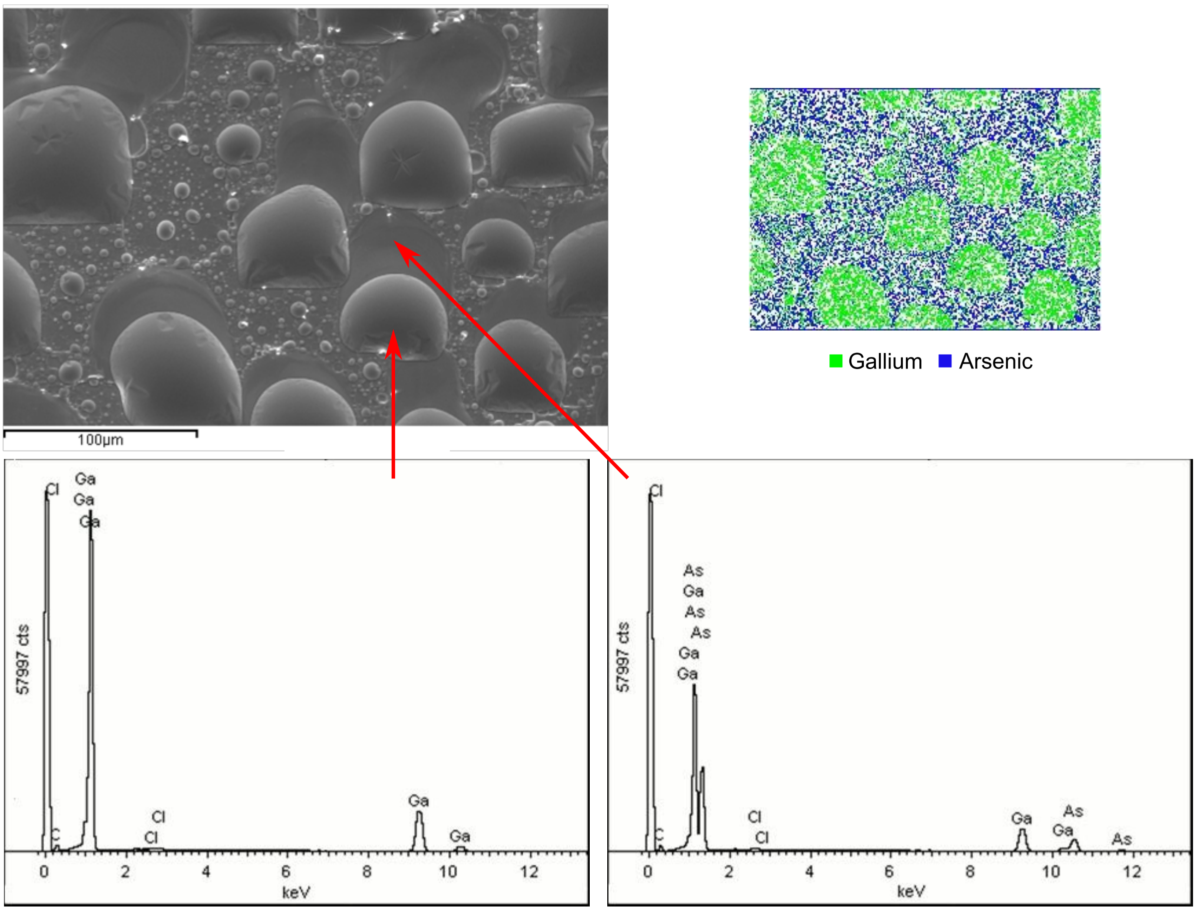

Figure 6.27.: SEM image of GaAs:Te heated to a temperature of 1070 K. Lower left and right: EDX spectra of blisters and craters at the indicated positions. In the upper right part the associated EDX map for Ga and As is shown.

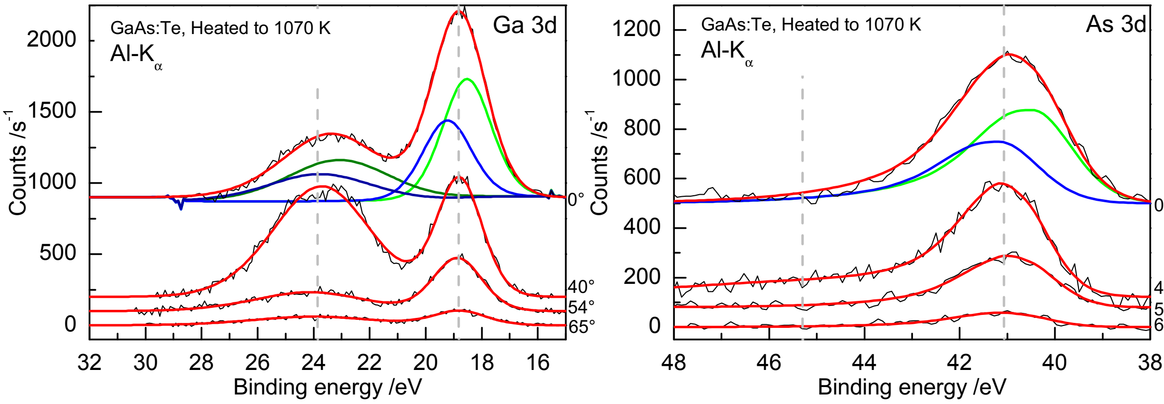

Signal	Species	BE (FWHM) /eV	Lit. BE /eV	Area /a.u.	Conc. /%
Ga $3d_{5/2}$	Ga-As	18.57 (2.05)	18.8 [348]	1416	32.69
Ga $3d_{3/2}$	Ga-As	19.27 (2.05)	19.3 [348]	935	
Ga^{3+} $3d_{5/2}$	Ga-O / Surface	23.15 (4.30)		1019	23.53
Ga^{3+} $3d_{3/2}$	Ga-O / Surface	23.85 (4.30)		673	
As $3d_{5/2}$	As-Ga	40.48 (1.99)	40.8 [341]	531	12.25
As $3d_{3/2}$	As-Ga	41.18 (1.99)	41.5 [341]	350	
O 1s		532.1	531.7 [345]	1391	19.34
C 1s		284.5	285.0 [345]	876	12.18

Figure 6.28.: Background subtracted XPS spectral details of Ga 3d (left frame) and As 3d (right frame) in GaAs:Te after heat treatment at 1070 K at different analyser take-off angles. All spectra were recorded using the Al x-ray source. Both main 3d peaks of GaAs are fitted with an additional exponential blend with an amplitude of 1.2.

6.5. Summary

The as-received gallium arsenide samples exhibit a grainy structure on a microscopic scale with a small surface roughness of $S_A = 0.214$ nm (Veeco measurements), which rises after removal of the protective coating to 0.758 nm. This native oxide structure largely consists of Ga_2O_3 and As_2O_3. On the outermost layer a sign of low oxidation state Ga_2O can be found. This species is commonly formed by heating of Ga_2O_3 under reductive conditions, but it could also be a x-ray induced effect [352, 353]. No further contamination beside oxygen and carbon could be found. The amount of carbon is typical for the residual of a protective coating [9]. Upon sample ageing the complexity of the oxide structure, as it appears in the 3d photoelectron spectra, increases. On the most aged sample an additional $Ga(OH)_3$ species was found. Beside the overall oxide thickness increase from 2.28(1.79) nm to 3.61(2.83) nm (using full TPP-2M), which fits to similar observations by Allwood [169]. In none of the investigated samples the presence of metallic arsenic at the interface, which is proposed to form a termination layer for the oxide growth, could be unambiguously verified. In general no principal difference between the tellurium and silicon doped samples could be found. The detailed composition varies with each sample and reflects the rather undefined process parameters of the wet chemical cleaning and the storage in ambient environment. The principal composition for of an aged sample is shown schematically in figure 6.29A.

Sputtering and annealing at elevated temperatures in principal removes the native oxide layer and produces a well defined surface reconstruction efficiently. Thermal desorption spectroscopy of the annealing step shows a two step desorption process starting at 620 K and 755 – 782 K respectively. A weak (1×1) bulk GaAs{100} lattice structure can be observed by LEED after cleaning cycles up to 620 K. From this the surface lattice constant can be determined with a deviation of only 0.5% from the published value of 3.99 Å [364]. By increasing the annealing temperature to 850 K LEED pictures reveal a partial (4×1) or full, gallium rich (relative surface concentration of 78%) $c(8 \times 2)$ reconstruction. According to Biegelsen the reconstruction consists of units of two gallium dimers in the top layer [160, 165].

On clean oxide-metal interface samples the chemical structure with respect to oxide and contamination composition matches that from unprocessed samples. But a metallic contribution to the As 3d signal and a shift of the Pt 4f signal indicate the formation of a $PtAs_2$ compound. This is initiated by the generation of metallic arsenic in a reduction step triggered by the annealing at high temperatures (see figure 6.29B).

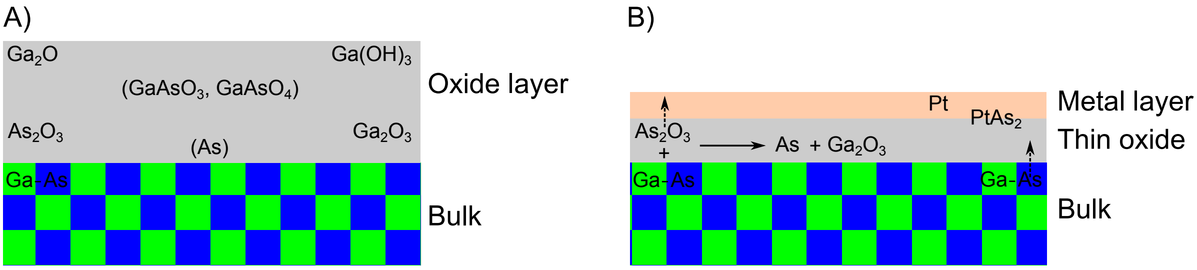

Figure 6.29.: Composition scheme of the samples investigated as found by analysis of different XPS signals and supporting scanning probe microscopy results. A) Native oxide in the aged state. The presence of mixed oxides and metallic As could not be unambiguously verified and are therefore given parentheses. B) Platinum on oxide. The topmost oxide and contamination layer was removed by a single cleaning step. The dashed lines indicate a diffusion process triggered by the elevated temperatures during annealing or a preferential removal. The solid line refers to a chemical reaction (non-stoichiometric formulation). The arsenic oxide on one hand reacts with GaAs giving gallium oxide and metallic arsenide but is also preferentially removed in the sputter and anneal step. The metallic As can react with platinum at the interface.

On the direct GaAs-Pt contact samples metallic gallium and arsenic are found. Furthermore the gallium region exhibits a distinct multi signal feature, which by shape and energetic spacing, resembles of a plasmon loss response. The energy difference fits to an interaction with a PtGa$_2$ species. On all samples oxidic species can be found. With increasing evaporation temperature its relative concentration diminishes while at the same time the loss feature in the Ga region becomes more dominant. The THICKOGRAM technique gives Pt coverages of only 50% of the target value, while a complete ARXPS analysis on the contrary returns layer thicknesses close to the desired value. Mainly responsible for the residual oxide and an inhomogeneous surface texture is a temperature gradient across the sample surface in the processing steps, caused by the sample holder design. The sample area below the brackets, protected from sputter ions and platinum coating, shows a flat surface with deep pits. These pits can be assigned to selective vaporization of volatile arsenic compounds as found by Allwood [169]. The outer sample region next to the brackets exhibits a grainy structure with larger, up to 30 nm wide, particles. Here the reduced temperature and sputter intensity causes either an incomplete oxide removal or a defect rich surface, prone to fast reoxidation. At low evaporation temperatures the central and hottest (with respect to the cleaning process) sample region shows a layered structure beneath a high dense coverage of individual particles. All regions feature a higher roughness compared to the native oxide samples, it peaks in the outer region with $S_A = 3.25$ nm for the sample evaporated at 100 K substrate temperature. Increasing the substrate temperature at evaporating from cryogenic temperatures up to 500 K results in an improvement of surface quality defined by roughness, especially in the central region important for the laser based experiments. The optimum is found a room temperature, where a well defined structure of terraces intermittent by monoatomic steps is found. At higher temperatures these layers start to decompose into individual drops, most likely a stress relief reaction or the sign of increased alloying and diffusion. The large sampling area of the electron analyser gives XPS results averaged over the clean central and outer region; the calculated oxide thickness is an equivalent thickness. Based on the SPM and XPS results and supported by STM, IRRAS and thermodynamic as well as lattice properties a thin, closed platinum layer is assumed, which reproduces the surface features of the underlying GaAs. A scheme model of the assumed composition is shown in figure 6.30 for a sample processed at elevated temperatures.

The central region on the 300 K and 500 K samples also exhibit impact crater like structures consisting of a protrusion and a high central nodule. Similar observations but on a larger scale were made by Begley [243]. There the central nodule was found to consist of a gallium rich compound diffused through the platinum layer on top.

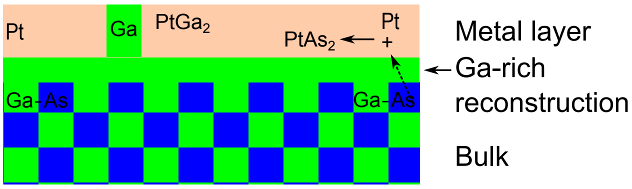

Figure 6.30.: Composition scheme of the direct contact metal interface samples investigated, as found by analysis of different XPS signals and supporting scanning probe microscopy results.The repeated sputtering and annealing cycles first create a Ga-rich surface. The subsequent metallization at elevated temperatures induces a Ga protrusion through the thin Pt layer. Both semiconductor constituents react with platinum, $PtAs_2$ preferentially at the interface, $PtGa_2$ on top.

There are two process in the preparation controlling the final composition. First the thermal treatment of the oxide layer will preferentially remove more volatile arsenic compounds and metallic As (pure arsenic sublimes at $\approx 890\,\mathrm{K}$), which in turn will be recovered by a redox reaction of As_2O_3 and GaAs yielding As and Ga_2O_3 [379]. Experiments on a GaAs substrate exposed to high temperatures, show large droplets of a gallium species and nearly no arsenic oxides (EDX). Corresponding XPS measurements boast a new Ga^{3+} oxide signal, which is assigned to the droplets. The second process is the diffusion into the platinum layer and consequent alloying. The impact crater features show that gallium diffuses through the layer. In combination with the shifted platinum signal, the metallic blend gallium 3d peak and the possible plasmon loss signals this gives a strong evidence for $PtGa_x$ formation. The evidence for a platin-arsenic species is weaker. Metallic arsenic peak shapes on the direct and oxide contact samples point to it. On thicker platinum layers $PtAs_2$ is located directly at the interface [230].

7. Results: Static Optical Characterization

The following section covers the static optical properties of the pure and metal coated samples obtained by rotational SHG and photo luminescence measurements. Theses experiments reveal information on the different contributions from the bulk, space-charge region and surface i.e. interface layer. Also the role of the individual susceptibility tensor elements is examined.

The discussion of this data is preceded by a brief outline of the properties of the static, unmodulated space-charge region in the analysed samples, which have a huge impact on the nonlinear response (cf. chapter 4.1.3). Further the density of free carriers generated by the probing pulse is calculated, as those modulate the optical properties by effects like depletion field screening or free carrier absorption.

Depletion zone properties

On n-doped {100} faced GaAs exposed to air the electronic bands are bended upwards raising a surface barrier $|eV_{surf}|$ of about 0.68 eV [1] (here e is the positive elementary charge and $V_{surf} = \Phi_{surf} - \Phi_{bulk}$ is the difference between surface and bulk potential). The amount of bending is mostly independent on the surface treatment [380]. At room temperature where $|eV_{surf}| \gg kT$ a simple depletion zone model can be used, where the acceptor surface states are occupied by dopant electrons, leaving behind fully ionized dopant donor states. Taking the z-axis perpendicular to the surface and pointing into the bulk, the space charge density ρ is approximately

$$\rho(z) = \begin{cases} eN_D^+ & 0 \leq z \leq L_D \\ 0 & z > L_D \end{cases}, \tag{7.1}$$

with $N_D^+ = N_D$ as the density of ionized dopant states (blue dashed line in the left graph of figure 7.1) and L_D as the space charge region thickness. This approach allows an approximate analytic solution of Poisson's equation [381]:

$$\frac{d^2\Phi}{dz^2} = \frac{dE_z}{dz} = -\frac{eN_D}{\epsilon_r\epsilon_0}. \tag{7.2}$$

Integrating twice and accounting for the boundary conditions $E_z(L_D) = 0$ and $\Phi(L_D) = \Phi_{bulk}$ gives the electric field in the depletion E_z zone and the potential Φ:

$$\begin{aligned} E_z(z) &= \frac{eN_D}{\epsilon_r\epsilon_0}(z - L_D),\ 0 \leq z \leq L_D \\ \Phi(z) &= \Phi_{bulk} - \frac{eN_D}{2\epsilon_r\epsilon_0}(z - L_D)^2. \end{aligned} \tag{7.3}$$

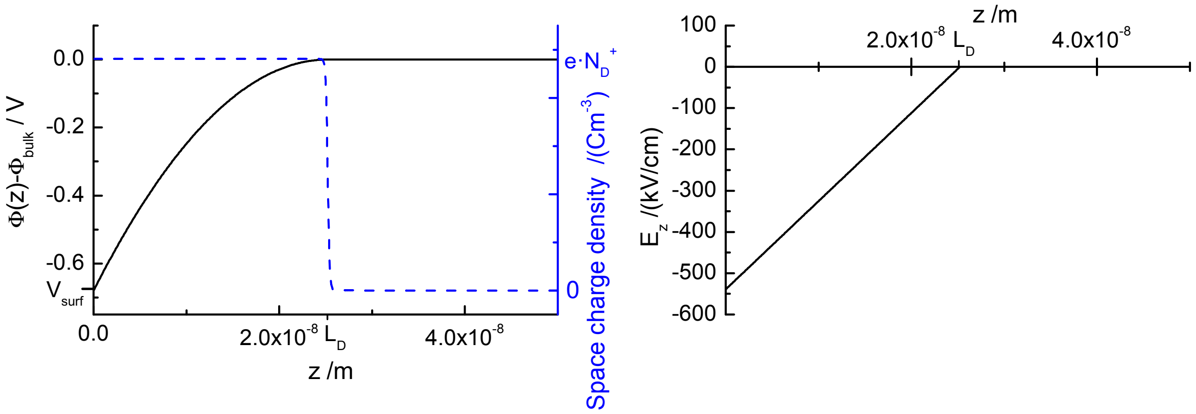

Figure 7.1.: Charge volume density, potential and depletion field according to Poisson's equation in the GaAs wafer, doped with 1.5×10^{18} /cm^3 Si.

Figure 7.1 shows the change of potential $\Phi(z) - \Phi_{bulk}$ (left) and electric field $E_z(z)$ (right) along the z-direction for the 1.5×10^{18} /cm^3 Si-doped sample. At the surface the potential is reduced by the amount of band bending V_{surf} compared to the bulk value. Using this experimentally established and basically invariant value, allows to obtain the depletion layer thickness L_D from equation 7.3:

$$L_D = \sqrt{\frac{-2\epsilon_r\epsilon_0 V_{surf}}{eN_D}} \tag{7.4}$$

For the GaAs:Si samples the electric field in the depletion zone is as large as −540 kV/cm and the depletion layer extends 25.2 nm deep into the crystal. Charge neutrality requires the surface charge to be equal to those in the depletion layer, but with opposite sign. So the concentration of ionized dopant states multiplied with the depletion width ($N_D^+L_D$) gives the number of surface state trapped electrons, i.e. the density of charged surface trap states, with 3.8×10^{12} /cm^2. At the second type of substrates investigated, the tellurium dopant concentration is specified with $1.1 - 2.2 \times 10^{18}$ /cm^3. The electric field is therefore in the range of -461 to -653 kV/cm. The space charge region is $20.8 - 29.5$ nm wide, the charged surface trap state density is in the range of $3.2 - 4.6 \times 10^{12}$ /cm^2.

Calculation of injected carrier densities

For the estimation of the laser pulse injected carrier density it is necessary to include the Gaussian spectral energy distribution, the adequate Fresnel equations for the laser polarization and the wavelength dependent absorption coefficient into the calculation. The peak irradiance as a function of laser power P and Gaussian waist of the focused beam ω_0, angle of incidence θ, as well as the repetition rate f of the laser, gives the total energy per pulse transferred to the sample surface within the elliptic spot area (parallel projection of beam with circular spot):

$$E_{tot} = \frac{2P\cos\theta}{\pi\omega_0^2 f}. \tag{7.5}$$

The amount of energy lost by reflection is determined by solving the Fresnel equation and accounted by the relative transmission factor T. The absorption length z_{ads} is defined as the distance at which the initial intensity has dropped to e^{-1}, so according to Beer's law (first line of equation 2.2) $z_{ads} = 1/\alpha(\lambda)$. Together with the spot diameter it defines the injection volume. Finally, after including the energy density distribution of the Gaussian pulse:

$$\epsilon(\lambda) = \sqrt{\frac{4 \cdot ln(2)}{\pi\Delta_\lambda^2}} \cdot exp\left(\frac{-4 \cdot ln(2)(\lambda - \lambda_0)^2}{\Delta_\lambda^2}\right), \tag{7.6}$$

with λ_0 as the central wavelength and Δ_λ the FWHM, and dividing by the photon energy hc/λ, the peak number of injected carriers per wavelength and volume is

$$\frac{dn}{d\lambda} = \frac{E_{tot} \cdot T \cdot \alpha(\lambda) \cdot \epsilon(\lambda) \cdot \lambda}{hc}, \tag{7.7}$$

from which by integration over the spectral region of interest the peak injected carrier density can be obtained:

$$n = \frac{E_{tot} \cdot T}{hc} \int \lambda\alpha(\lambda)\epsilon(\lambda)\, d\lambda. \tag{7.8}$$

In contrast to the calculations shown in figure 4.8, the transmission coefficient used here consists only of the first term of equation 2.3 as only the loss due to front side reflection has to be considered. A similar approach can be found in [150].

In the range between 775 – 950 nm the absorption coefficient for the corresponding dopant density was taken from [179]. For higher energies it was calculated from the extinction coefficient of intrinsic GaAs (cf. section 4.1.3). Figure 7.2 shows the strong doping influence on the band edge absorption. The system parameters used for the carrier density determination are summarized in table 7.1.

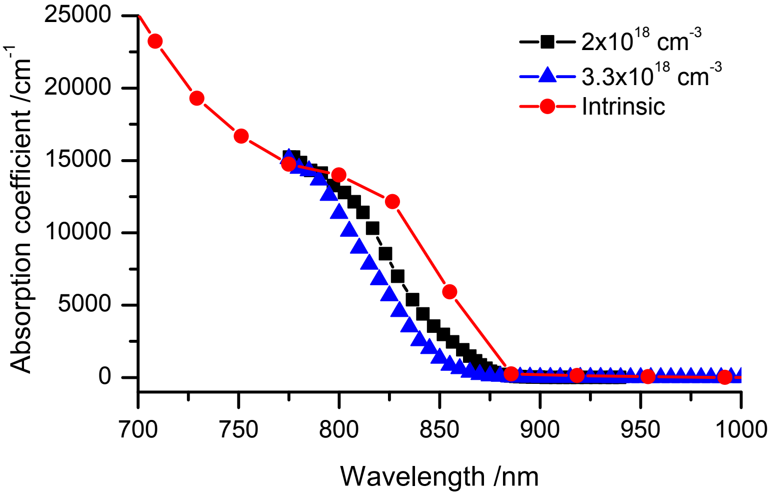

Figure 7.2.: Absorption coefficient of GaAs for different doping levels [178, 179].

Beam waist at focus spot	13 µm [a]
Angle of incidence	45°
Laser repetition rate	95 MHz

---

[a] Calculated from a beam with 6 mm diameter and a lens with $f = 15$ cm [153].

Table 7.1.: System parameters for injected carrier density calculations.

7.1. Rotational SHG Measurements

7.1.1. GaAs:Si

As mentioned in the chapter on sample preparation the silicon doped samples are of round shape and have no flat to denote the crystallographic orientation within the {100} plane (c.f. section 5.2). The assignment of azimuthal angle to a specific direction had to be made based on published data from other groups and on the measurements on GaAs-Te samples. Figure 7.3 shows typical rotational scans at 860 nm for two different polarization combinations, p-polarized input and output light (pp) on the left and s-polarized fundamental light and the SH light in p-polarization (sp) on the right side. In all measurements shown in this chapter laser pulses in the range of $35-40$ fs were used. The different excitation intensities in both experiments result from the polarization dependency of a beamsplitter (BS1 in figure 5.22) in the set-up. This is partly compensated by the difference in Fresnel factors for s- and p-polarization. Nevertheless both carrier densities are well below the doping density and are assumed to be uncritical regarding self photo modulation. The recorded SH signals (black dotted curves) have been normalized to the fundamental excitation beams in form of a nonlinear intensity reflection coefficient (equation 7.9). The red curves represent fits of the data to equation 4.5.

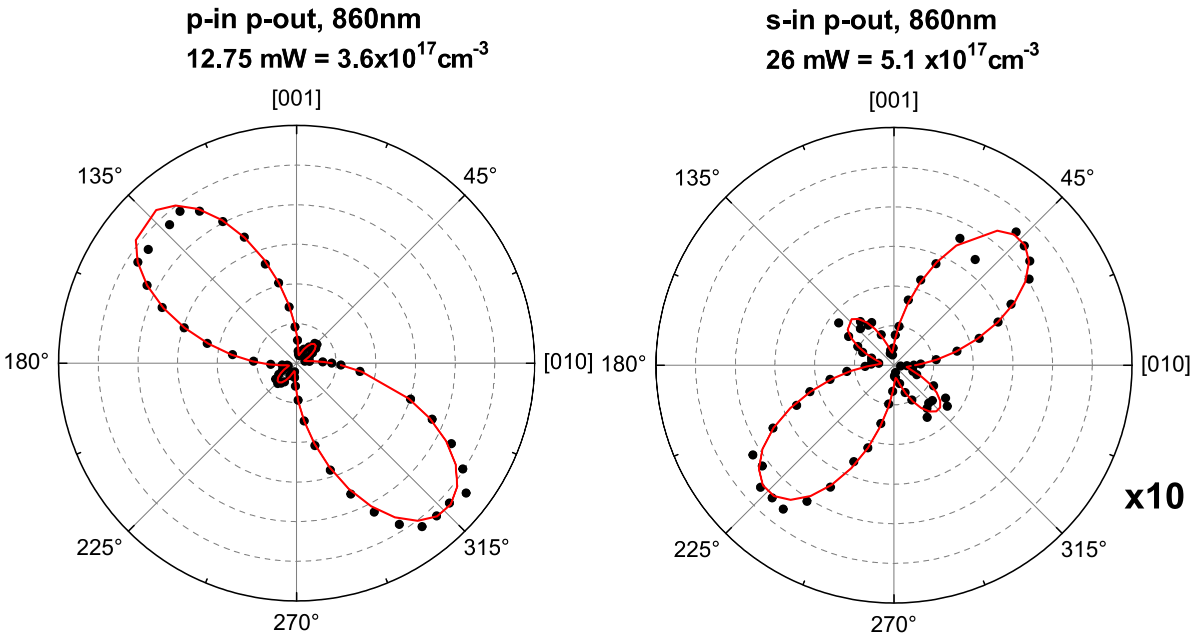

Figure 7.3.: SHG signal as a function of azimuthal angle from the GaAs:Si samples at 860 nm for pp and sp polarization configurations. Excitation pulse width $= 35-40$ fs.

For nearly all data shown satisfying fitting could be achieved with $m = 2$ and $B_1^{\alpha,\beta} = A_1^{\alpha,\beta} = 0$, reducing the model to:

$$R = \frac{I_{\alpha,\beta}(\Omega)}{I_\alpha^2(\omega)} = \left| A_0^{\alpha,\beta} + A_2^{\alpha,\beta}\cos(2\phi) + B_2^{\alpha,\beta}\sin(2\phi) \right|^2 . \tag{7.9}$$

The approximately ten times weaker SHG response in sp configuration results from different susceptibility tensor element contributions to the signal. Their assignment to the fitting coefficients is made in accordance to the work of Germer et al. [1]. Summarizing the susceptibility tensors of equations 2.46, 2.54 and 4.3 gives:

$$\chi_{ijk}^{eff} = \chi_{ijk}^{(2)} + 3\chi_{ijkz}^{(3)} E_z^{depl} + 6\chi_{ijkzz}^{(4)} E_z^{depl} E_z^{depl} + \chi_{ijk}^{(2),surf.}. \tag{7.10}$$

The factors before the depletion field terms originate from permutation of the zero frequency depletion field terms. All tensors are treated within the crystal using the default coordinates for $\bar{4}3m$ symmetry listed in table 4.3. The quadrupolar and magnetic contribution were found to be negligible [1]. The remaining unique, non-vanishing elements of $\chi_{ijkl}^{(3)}$ after elimination of those whose last index is not aligned to E_z^{depl} ($l \neq z$), form the sub set natural to $mm2$ symmetry. Similarly $\chi_{ijklm}^{(4)}$ reduces to three distinguishable elements. This finally yields for the case of SHG ($\omega_1 = \omega_2$) and for the cubic structure of GaAs were the y- and x-direction are physically indistinguishable ($x = y$) the following reduced forms for the depletion and bulk response: [1]

$$\begin{aligned}
3\chi_{xxzz}^{(3)} \cdot E_z^{depl} &= \chi_{xxz}^{eff} = \chi_{yyz}^{eff} = \chi_{xzx}^{eff} = \chi_{yzy}^{eff} \\
3\chi_{zxxz}^{(3)} \cdot E_z^{depl} &= \chi_{zyy}^{eff} \\
3\chi_{zzzz}^{(3)} \cdot E_z^{depl} &= \chi_{zzz}^{eff} \\
\chi_{xyz}^{(2)} + 6\chi_{xyzzz}^{(4)} \cdot E_z^{depl} \cdot E_z^{depl} &= \chi_{xzy}^{eff} = \chi_{yzx}^{eff} = \chi_{yxz}^{eff} = \chi_{xyz}^{eff} \\
\chi_{xyz}^{(2)} + 6\chi_{zxyzz}^{(4)} \cdot E_z^{depl} \cdot E_z^{depl} &= \chi_{zxy}^{eff} = \chi_{zyx}^{eff}.
\end{aligned} \tag{7.11}$$

Expressions for the second harmonic electric field at different input and output polarizations can be obtained by summing over all non-zero susceptibility elements and appropriate weighting factors which incorporate transmission factors, internal angles and terms holding information on the depletion field, as proposed by Sipe et al. [71, 99]. These elements are distributed to the fitting coefficients of equation 7.9 as shown in figure 7.4.

For example for the p-in / p-out (pp) the magnitude of the electric field is :

Configuration		Bulk + Depletion zone			Surface
		$\chi^{(2)}$	$\chi^{(3)}$	$\chi^{(4)}$	$\chi^{(2),surf}$
p-in / p-out	A_0		zzzz, zxxz, xxzz		zzz, zxx, xxz
	B_2	xyz		xyzzz, zxyzz	xyz, zxy
s-in / p-out	A_0		zxxz		zxx
	B_2	xyz		zxyzz	zxy
p-in / s-out	A_2	xyz		xyzzz	xyz
s-in + p-in / p-out	A_0		zzzz, zxxz, xxzz		zzz, zxx, xxz
	A_2	xyz		xyzzz, zxyzz	
	B_2	xyz		xyzzz, zxyzz	xyz, zxy

Figure 7.4.: Assignment of susceptibility tensor element to the fitting parameters for different polarization combinations [1, 71, 99].

$$\begin{aligned}E_{pp}(\Omega) = &\left(w^{pp}_{zzzz}\chi^{(3)}_{zzzz} + w^{pp}_{zxxz}\chi^{(3)}_{zxxz} + w^{pp}_{xxzz}\chi^{(3)}_{xxzz}\right) \cdot E^{depl}_{z} E^{2}_{0,p}(\omega) + \\ &\left(w^{pp}_{xyzzz}\chi^{(4)}_{xyzzz} + w^{pp}_{zxyzz}\chi^{(4)}_{zxyzz}\right) \cdot \sin(2\phi) \cdot E^{depl}_{z} E^{depl}_{z} E^{2}_{0,p}(\omega) + \\ &w^{pp}_{iso}\chi^{(2),surf}_{iso} \cdot E^{2}_{0,p}(\omega) + w^{pp}_{aniso}\chi^{(2),surf}_{aniso} \cdot \sin(2\phi) \cdot E^{2}_{0,p}(\omega) + \\ &w^{pp}_{xyz}\chi^{(2)}_{xyz} \cdot \sin(2\phi) \cdot E^{2}_{0,p}(\omega),\end{aligned} \tag{7.12}$$

where for simplicity the (an)isotropic surface elements were summarized to $\chi^{(2),surf}_{(an)iso}$. The rotational scan is aligned such that for p-polarized input light and 0° azimuthal angle the electric field is orientated along the crystallographic x-axis. In all measurements the angle of incidence was kept constant to 45° so that the total fundamental E-field is equally split in z-axis and xy-plane components. Accordingly for s-polarization the field is directed in the y-direction without any perpendicular component.

Both scans in figure 7.3 exhibit the expected $mm2$ symmetry with mirror axes along 45° and 135°. Responsible for the anisotropy is the isotropic parameter A_0 and thus the depletion zone $\chi^{(3)}$ and surface $\chi^{(2)}_{surf}$ elements, while the bulk $\chi^{(2)}_{xyz}$ dominates the sinusoidal part. In sp configuration the lobe in [011] direction has approximately the same strength as for the pp case (the right graph is zoomed by a factor of ten), while the other lobe is much weaker. This change manifests itself in a 90° phase shift between A_0

and B_2. The reduced intensity is caused by the absence of zzzz and xxzz tensor elements in A_0.

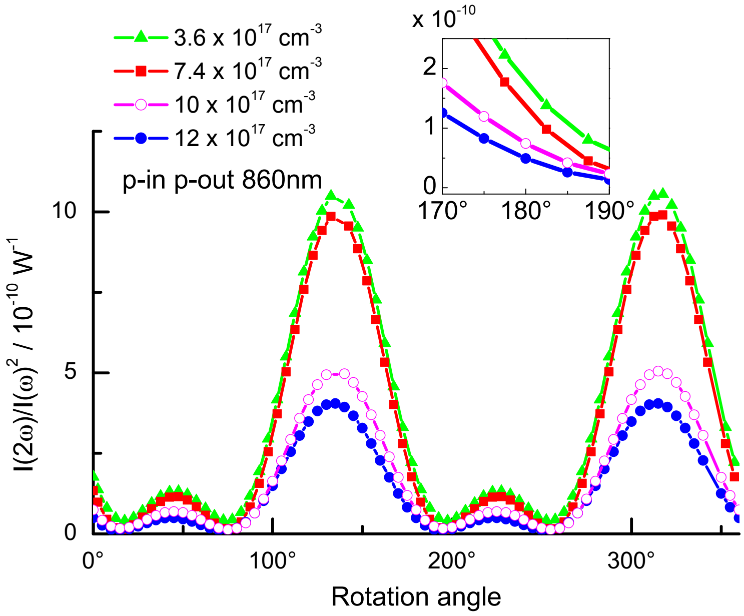

Figure 7.5.: Fitting curves of rotational scans on GaAs:Si at 860 nm at different excitation intensities. The inset shows a zoom into the region at 180° at which the anisotropic term is zero. The scale and units are the same as in the main graph. Excitation pulse width = 35 − 40 fs.

Figure 7.5 shows fits of 860 nm pp scans at different excitation intensities. At the lower blue dotted curve the injected carrier peak density is comparable to the doping concentration in this sample. It can be observed that the A_0 parameter decreases upon an increase in number of injected carriers (at $\phi = 0°, 180°$ the anisotropic term is zero) at the same time the total intensity decreases. This behaviour indicates the beginning of self photo modulation of the excitation beam in which the generated photo carriers screen the static space-charge field and thus reducing the $\chi^{(3)}$ and eventually also the $\chi^{(4)}$ tensors. The intensity ratio of the lobe at 135° to that at 45° as a measure of anisotropy remains constant, which implies that $A_0/B_2 \approx \mathit{const}$ in this carrier concentration regime and polarization configuration (cf. the highlighted fitting parameters in figure 7.9).

As it may be easily overlooked, it should be noted that the minima in the intensity signals differ from those expected for the square of a pure sine due to the shift by A_0. Further, most clearly seen at the green curve for 3.6×10^{17} /cm^3, the overall offset is caused by the phase difference between A_0 and B_2. This is illustrated in figure 7.6, were a phase shift of $\frac{\pi}{2}$ is added in the red curve.

At 800 nm both configurations exhibit a strong attenuation of anisotropy (figure 7.7)

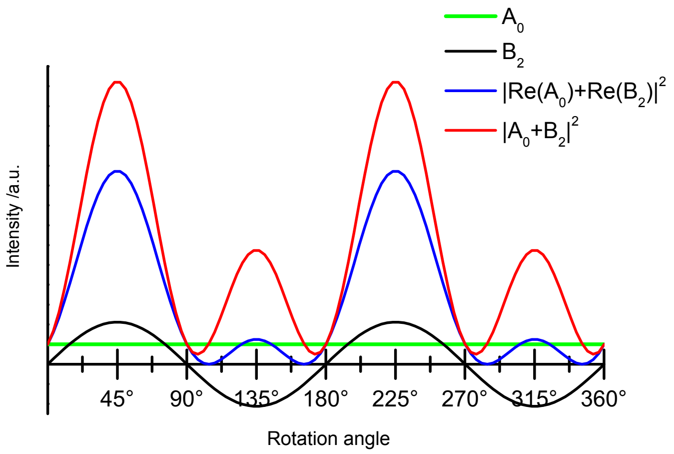

Figure 7.6.: Illustration of the shift in minima positions and change in anisotropy caused by the isotropic contribution and the phase shift between the complex quantities A_0 and B_2.

along with loss in total SHG reflectivity. In pp configuration R decreases about 67 %. while for the sp case the nonlinear reflection level is reduced by only 21 %. The different behaviour can be caused by the different susceptibility term contribution and their relation to the depletion field, or may be directly connected to wavelength dependence of the susceptibilities themselves. This will be discussed in the upcoming sections.

The strong change in absorption of GaAs within the wavelength range of the femtosecond laser source leads to a superposition of dispersive and depletion field screening effects upon measurement at different photon energies. Figure 7.8 shows that at nearly all probed wavelengths the number of photo carriers exceeds the doping density. When looking at the carrier density dependence of the fitting coefficients from various measurements in pp configuration over different photon energies (figure 7.9), a significant correlation of the isotropic fitting factor is found at 95 % significance level. The anisotropic part is independent from the carrier concentration. The cosine component A_2 which would indicate a mixed input polarization is ten times smaller than A_0 and below the noise level. The linear relation found between the A_0 and the carrier density suggests a dominating depletion field effect on the SHG signal from this GaAs surface. Similar findings are published by Germer et al. [1] where samples with different doping densities have been investigated and a direct relation to the depletion field could be established. They fitted the isotropic coefficient with a (nearly) zero intercept and thus postulated a negligible surface contribution. The effect of the photo carriers onto the space charge field and the depletion width has to be worked out to allow a classification of the results

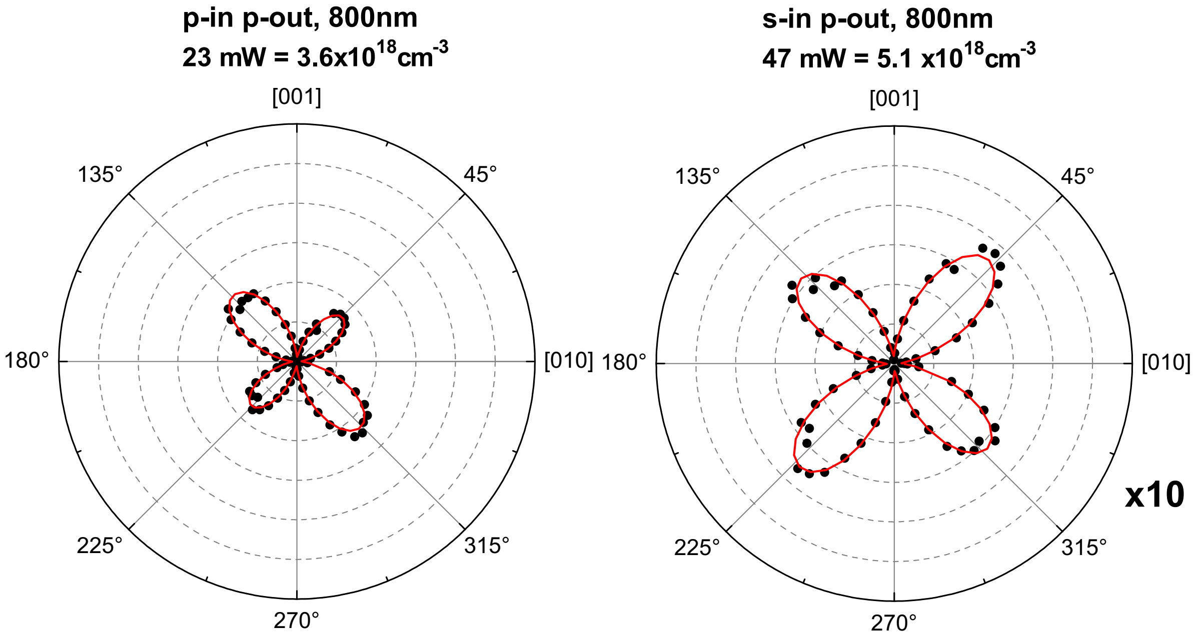

Figure 7.7.: SHG signal as a function of azimuthal angle from the GaAs:Si samples at 800 nm for pp and sp polarization configurations. Excitation pulse width = 35 − 40 fs.

presented in this thesis.

Depletion field screening

The electric field between the photon generated electron-hole pairs (Wannier-Mott type excitons) is in the order of:

$$|\vec{E}| \approx \frac{2R_x}{ea_x}, \tag{7.13}$$

where R_x is the exciton Rydberg constant and a_x is its Bohr radius. For GaAs this gives a field strength in the order of 6.5 kV/cm. The approximately 100 times stronger field in the depletion zone causes electron-hole separation and drift and as a consequence surface field screening.

To gain detailed understanding of the self-induced SHG modulation effects of the excitation laser pulse, the dynamics of the photo generated carriers within the time span of the pulse have to be included in the discussion. In a perturbation free system the carriers relax with their typical lifetimes to Fermi-Dirac distributions as described in section 4.1.4. Under the influence of heat or concentration gradients as they occur at excitation by strongly focused laser beams and under the influence of electric forces in the depletion zone, diffusion and the above mentioned drift of carriers play an import-

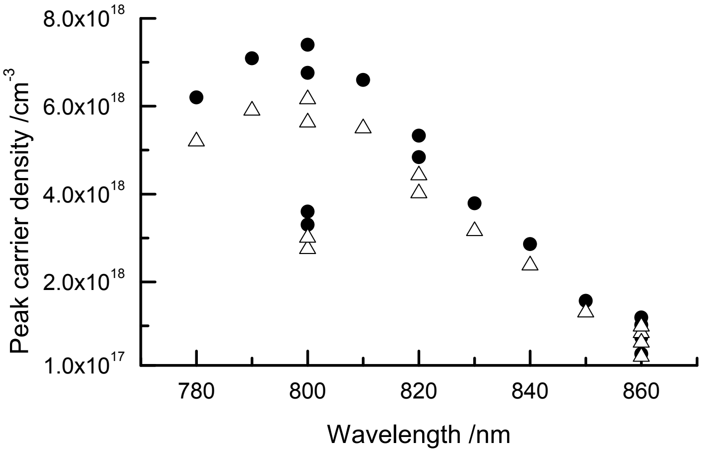

Figure 7.8.: Injected peak carrier density as a function of fundamental excitation wavelength for pp measurements (black dots). The dependence is based on the strong change of absorption properties in the band gap region and on the emission characteristics of the femtosecond laser. The open triangles include ambipolar diffusion and a surface recombination speed of 4×10^6 cm/s as described by equation 7.14 and show the carrier density state directly after arrival of the excitation pulse.

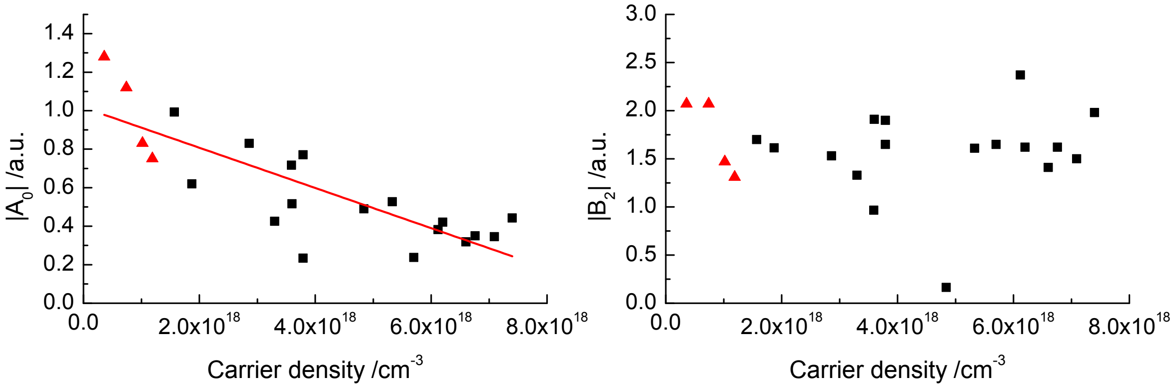

Figure 7.9.: Carrier density dependence of the isotropic and anisotropic fitting coefficients for pp polarization configuration. The data is superimposed by dispersive effects. The fitting parameters of the curves from figure 7.5 are highlighted by red triangles.

ant role. The resulting distribution functions are described by the Boltzmann transport equation (BTE) [108, 382]. The simplest solution which presumes carriers in thermal equilibrium with the (local) lattice is the drift-diffusion equation under the relaxation time approximation. Another common method is to simulate trajectories of individual particles in Monte Carlo simulations of carrier transport (e.g. in [207, 383]). To include all these processes and boundary conditions for high injection levels is a complicated task and the assumptions made in different publications often seem to be contradictory. A more detailed discussion on longer time scales will follow in the chapter on time-resolved measurements. Here only the self photo-modulation relevant results and approaches will be presented.

A simple approximation model considers only high photo carrier densities at which the original depletion field is completely screened [1]. For this case J. Long (as cited by Richter [384]) proposed an approximation for the photo generated carrier concentration to account for diffusion and surface recombination for a single wavelength, square laser pulse of duration t_{pulse} (see also [385]). Field drift is not included in this treatment and electrons and holes diffuse as bound excitons with an ambipolar diffusion coefficient $D =$ 20 cm^2/s [386]. Adapted to a spectrally broad Gaussian pulse this gives the expression for carrier injection introduced in the beginning of this chapter with additional terms for diffusion (D) and surface recombination (S):

$$n(z=0, t=t_{pulse}) = \frac{E_{tot}\cdot T}{hc(1+S\tau/\sqrt{D\tau})}\int \frac{\lambda\epsilon(\lambda)}{\alpha(\lambda)^{-1}+\sqrt{D\tau}}\, d\lambda. \tag{7.14}$$

The surface recombination lifetime lies typically in the range between $10^2 - 10^7$ cm/s [384]. It depends on the surface trap concentration and the energetic position of the trap states and the Fermi level. For GaAs the surface recombination speed scales with the doping density up to the point of degeneracy [387]. The reduced time is defined by $\tau^{-2} = t_{pulse}^{-2} + \tau_{recomb}^{-2}$. As the bulk recombination time is in the range of some nano seconds [388] and the femtosecond pulse emission interval of the laser is about 10 ns, τ is determined by the short pulse duration ($30 - 50$ fs). The diffusion length at the pulse duration is small and in the absence of surface recombination, the carrier densities equal those calculated by equation 7.8. At the maximum amount of surface recombination the carrier densities are approximately 17% lower than the initially determined values (see triangles in figure 7.8).

If at the same time the surface states are still charged (slow traps) and the bands directly at the surface are still bended, the screening of this remaining charge can be compared to the case in intrinsic semiconductors, where here the photo carriers are treated as intrinsic carriers [382]. The evolution of the electric field strength perpendicular to the surface can be expressed by:

$$E(z) = E(z=0) \cdot \exp\left(\frac{-z}{L_{inj}}\right), \tag{7.15}$$

where $L_{inj} = kT\epsilon_r\epsilon_0/2q^2n_{inj}$ is the Debye screening length in intrinsic material and n_{inj} the carrier concentration. The screening in this regime is much stronger. For the case shown in figure 7.7 at 800 nm and 3.6×10^{18} cm^{-3} (3.0×10^{18} cm^{-3} including diffusion and recombination) the screening length is only 1.7 nm. For weaker excitation at 860 nm (figure 7.3) the electric field extends 5.5 nm deep into the material. Figure 7.10 outlines the different lengths playing a role in the SHG signal. The absorption length of the reflected SHG signal defines the maximum information depth. With around 15 nm for 800nm photons it is smaller than the unperturbed depletion zone and much longer than the screening length in the modulated case. The second huge impact comes from the phase matching length $1/p$ (the signal strongly oscillates in z-direction with $\exp(-ipz)$), which further confines the signal response to the near surface region.

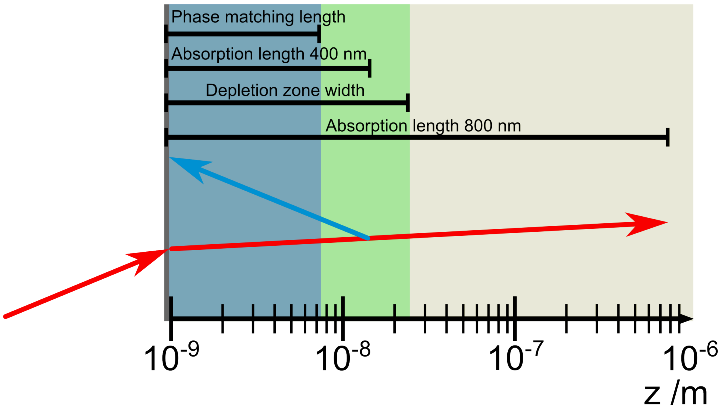

Figure 7.10.: Scheme of the relevant lengths for GaAs:Si at 800 nm fundamental wavelength in logarithmic representation.

In figure 7.11 the fitting coefficients for pp configuration averaged over different photon energies and their phase difference are shown as a function of the average electric field within the absorption length of the SHG response, including the phase matching length induced attenuation. For the fitting coefficients only data at carrier densities larger than the doping density are included such that the static depletion field can be treated as fully screened. Qualitatively the dependency of factors A_0 and B_2 is similar to that shown in figure 7.9. The magnitude of the isotropic part is linearly dependent on the electric field in the investigated range although the correlation is not very pronounced ($\overline{R}^2 = 0.43$) due to the interference with dispersive effects. The intercept at $E = 0$ is smaller than the large standard error of 0.27. The magnitude of the anisotropic part is still independent on the internal electric properties. The behaviour supports the suggestion of Germer that the influence of a directly surface related susceptibility tensor in the isotropic response is small and can be neglected. Nevertheless the Debye length becomes smaller with higher excitation levels; at the maximum level reached in pump-probe experiments, the model proposes L_{inj} to be in the range of only 0.3 nm. Any change at the surface that would affect the electric state within this layer would be reflected in a change of isotropic response. The phase matching length influence further amplifies the relative (near)surface contribution. In quasi pump-probe experiments where the depletion field was fully screened by strong 532 nm laser pulses at a fixed time delay prior to the wavelength variable probe pulse a decrease of only 50% was found over the complete photon energy range investigated [1]. This, compared to the reduction of the penetration depth of the electric field, small reduction of the SHG signal, is a further underlining of the importance of the near surface region and the surface trap charge on the reflected second harmonic signal.

The complex phase between A_0 and B_2 shows tendencies to shift by approximately 38° from higher (unmodulated depletion field) to lower electric field magnitude (lower curve in figure 7.11). This is reasonably well in sound with the model where the SHG signal is proportional to the integral of the electric field times the phase matching factor within the absorption depth of the SHG. In the unmodulated region the field is given by equation 7.3 while at the highest carrier concentration it is represented by equation 7.15. These relations predict a phase shift of $20 - 43°$ for the different photon energies and pulse intensities used to obtain the experimental data.

These results seem to contradict with those published by Qi et al. [170, 182]. They found, as mentioned already in section 4.1.3, a reduction in SHG intensity with an increase of the depletion field strength. Their described change is proportional to the square of the electric field and thus related to $\chi^{(4)}$ terms. They used s-out and p-in configuration which consists only of a A_2 factor with contributions from $\chi^{(2)}_{xyz}$, $\chi^{(4)}_{xyzzz}$ and $\chi^{(2)}_{surf.}$ terms [99]. For static depletion fields found at doping densities larger than 10^{16} cm^{-3} their observed behaviour saturates on a low level. Qi et al. could not find a similar change for pp configuration.

The doping of the samples investigated in this thesis falls into the saturation regime of the Qi results. Within this range the independence of B_2 upon the electric field is in

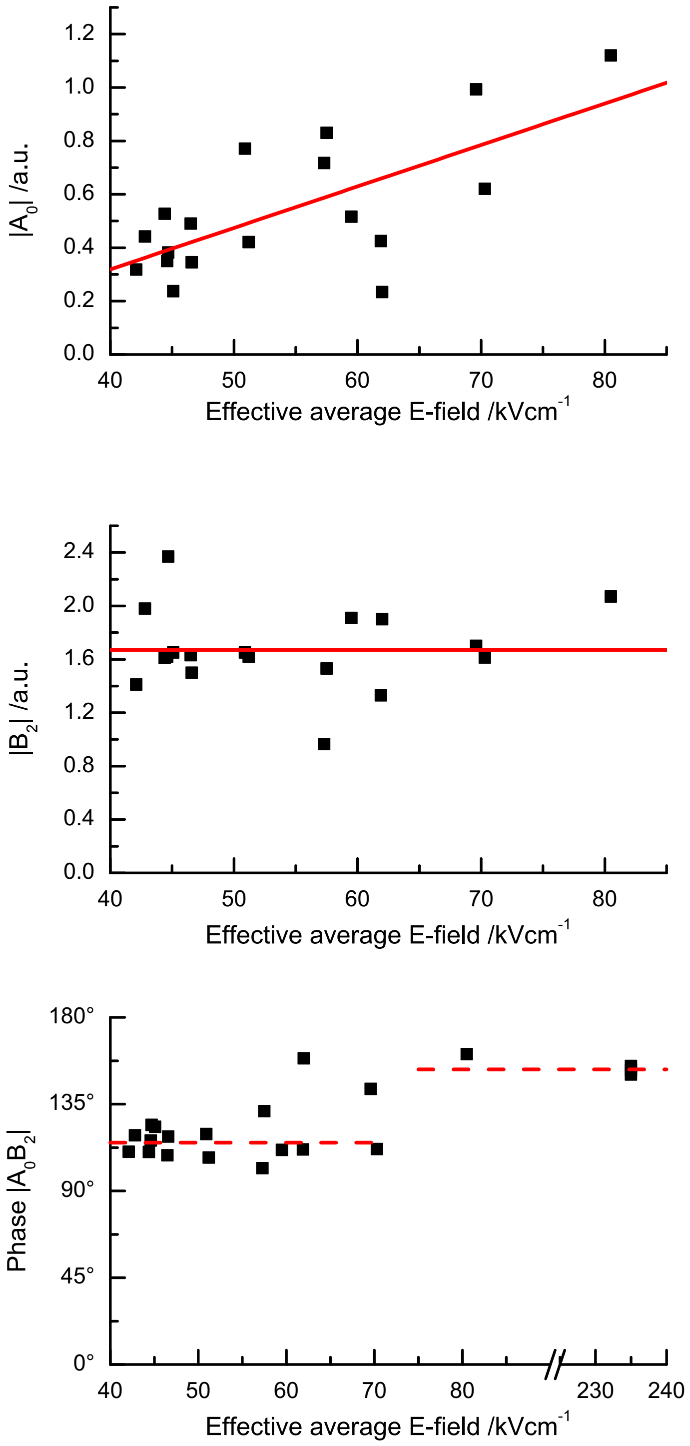

Figure 7.11.: Isotropic and anisotropic fitting coefficients for pp configuration on GaAs:Si as function of the effective average electric field within the absorption depth of the SHG signal. The experiments were done at various wavelengths. The upper two panels show the magnitude of the complex fitting parameters, while the lower panel shows their relative phase relation. Here the dotted lines indicate the mean phase angle for the two regimes, the flat band region at complete screening of the static depletion field and the high field region, at low injected carrier densities.

accordance with those findings. But neither an indication for an increase of B_2 at lower doping densities nor an explanation for the absence of $\chi^{(3)}$ contribution in the Qi work (the effective average electric field spans the range between $4 - 40\,\text{kVcm}^{-1}$) could be found. The experimental conditions at which Qi could observe the effects indicate that these results eventually could be related to the dynamics of the meta stable EL2* trap state [1].

Although the Germer model seems to work well, there are some flaws and uncertainties involved. First there is an abrupt change, respectively an undefined region between the unmodulated case with an average field of 270 kV/cm and a screening length of 25 nm on one side and the screened regime with average fields down to 40 kV/cm and corresponding Debye lengths of 1 nm. Partial depolarization of the space charge region is not explained. The experimental data for the fitting coefficients suggests a continuous linear relationship over the complete range of carrier densities, including the partial depolarized region shown as red triangles in figure 7.8.

Second in the model the defect states responsible for the Fermi pinning are allocated onto the oxide side of the interface to make them slow traps. A thin film of amorphous oxide has a band gap of 4.7 eV (Ga_2O_3) [389]. A direct absorption of fundamental or SH photons is impossible. Further the large band gap acts a quantum barrier and inhibits transport of electrons and holes from the GaAs side [170]. DFT calculations on models of amorphous gallium oxide yield a partially filled Ga interstitial acceptor state 2.5 eV over the valence band and an oxide vacancy donor state roughly 2 eV below the conduction band states. Both can not be charged by the photon source used [390]. With respect to the samples covered with platinum discussed later, it is worth noting that the authors found an insulator-metal transition at temperatures higher than 670 K triggered by the growth of local crystalline Ga_2O_3 domains. UHV based measurements on oxide free samples show a similar behaviour upon photo modulation [150]. It is more likely that the common candidate for Fermi pinning, the EL2 level (cf. figure 4.6 in section 4.1.2) is responsible for the space charge region.

Finally the application of the model to the regime of self modulation is problematic concerning drift and depolarization speed. Originally the lack of surface contributions was determined by investigating samples with different levels of doping at pulse intensities with negligible photo modulation. Completly screening the depletion field within the pulse duration of $30 - 50$ fs would require drift velocities of both carrier types of about 6.5×10^5 m/s, where a rough estimation of the high field electron drift velocity in GaAs gives values in the range of 8×10^4 m/s [12].

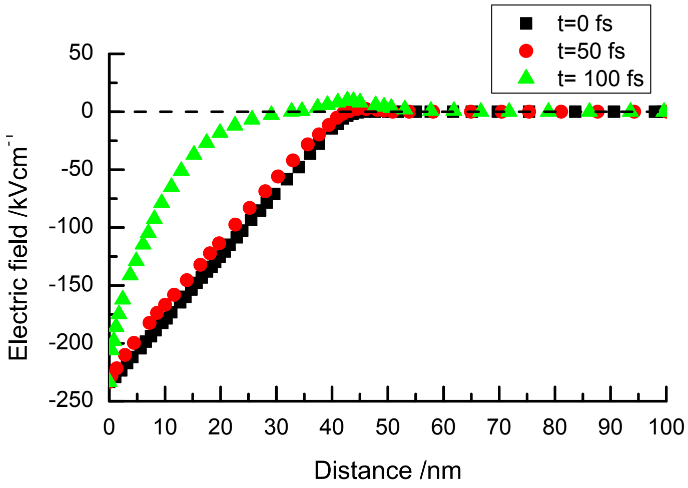

Figure 7.12.: Electric field in the depletion zone calculated by solving DDE. The sample is doped to a carrier level of 3×10^{17} cm^{-3}. The excitation is modelled with a 50 fs Gaussian intensity profile. The small positive electric field at the end of the depletion zone in the 100 fs curve is a result from the different electron and hole drift velocities (Dember effect) [391]. Data from [207].

BTE based approaches are needed to fully understand the dynamic charge and field distribution. Although not really appropriate for the length scales and high field range found in the depletion field some groups used drift and diffusion equation (DDE) to model the screening. For example Dekorsy et al. fitted electro optical sampling pump-probe measurements on n-doped GaAs with a dopant density of 3×10^{17} cm^{-3} and an excitation level of 5×10^{17} cm^{-3} and found that directly after the excitation pulse (50 fs) the average field strength in the depletion zone (43 nm) dropped by 12% [207]. After 100 fs the linear dependence on distance is lost and the average e-field is lowered to 60%. The calculated electric field profiles are shown in figure 7.12 for three different simulation times. These findings would indicate a much less pronounced self modulation than those calculated by the flat band model before. But for higher doped samples like those investigated in this thesis with their spatially stronger confined depletion zones, already smaller carrier injections and less electron-hole separation create strong counterfields to screen the space charge region. This will be discussed in more detail in chapter 8.2.1.

Determination of susceptibility values

With this plausible explanation of the influence of the internal electric fields on the nonlinear response, now the dispersive effects of susceptibility terms will be examined.

A direct measurement of absolute nonlinear susceptibility tensors requires a calibrated set-up. This can be achieved either by regular reference measurements of a standard, like well characterized α-quartz, or more advanced by a dual beam implementation, where the second excitation beam continuously measures the reference sample (e.g. in [392]). In this way also laser fluctuations can be suppressed. Due to technical limitations both schemes could not be implemented in the set-up used in this thesis.

Further the complex signal composition from various tensor elements hinders a simple direct measurement (cf. equation 7.12). More accessible are a number of susceptibility tensor element ratios. Based on the observations discussed in the previous sections the susceptibility expressions can be simplified by neglecting higher order, explicit surface as well as the $\chi^{(4)}$ terms, leaving behind the bulk contribution $\chi^{(2)}_{xyz}$ and the three depletion terms in first order to E_z. After examination of the field equations for different polarization configurations (cf. figure 7.4) with only these four contributions remaining, three complex ratios can be extracted. Each of them relates a third order depletion zone element to the bulk nonlinearity. The observed dispersion of the A_0/B_2 ratios are shown in figure 7.13 (black squares) as absolute values on the left and as relative change referenced to the value at 790 nm on the right axis. At each photon energy the ratio was averaged over different measurements at variable excitation levels. As the fundamental photon energies and the injected carrier density are not completely independent, the dispersive data at this stage is still afflicted by photo modulation effects.

For example for the pp configuration equations 7.9 and 7.12 define the ratios as:

$$\frac{A_0^{pp}}{B_2^{pp}} = \frac{w^{pp}_{zzzz}}{w^{pp}_{xyz}}\frac{\chi^{(3)}_{zzzz}}{\chi^{(2)}_{xyz}} + \frac{w^{pp}_{zxxz}}{w^{pp}_{xyz}}\frac{\chi^{(3)}_{zxxz}}{\chi^{(2)}_{xyz}} + \frac{w^{pp}_{xxzz}}{w^{pp}_{xyz}}\frac{\chi^{(3)}_{xxzz}}{\chi^{(2)}_{xyz}}. \tag{7.16}$$

In combination with appropriate expressions for ps and mixed input ($p + s = m$) ms configurations all three terms can be fully determined. As the s-output intensities were to small to be reliably detected, the relative tensor elements were obtained by fitting the relative susceptibilities to A_0 and B_2 values and their relative phases at different polarization combinations. For each excitation photon energy these fitting targets consisted at least of one pp, one ps and a mp dataset with variable relative p-polarization amount. Additional fits have been made under presumption of Kleinman symmetry ($\chi^{(3)}_{zxxz} = \chi^{(3)}_{xxzz}$) to reduce the models degree of freedom. Kleinman symmetry requires the absence of absorption which is a rough approximation, considering the large absorption length of about ≈ 800 nm and the small information depth of the SHG (≈ 7 nm). An example for a complex rotational scan in pm configuration can be found in the ap-

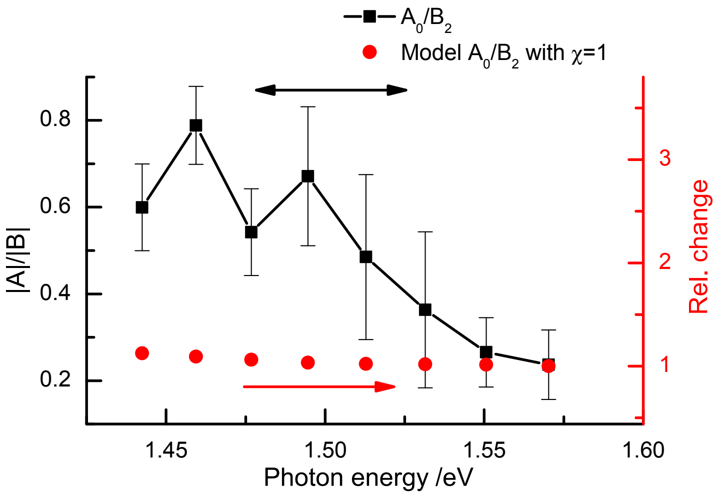

Figure 7.13.: A_0/B_2 ratio at different photon energies, averaged over variable excitation intensities (black squares). The standard deviation of each data point is given as error bar. The left axis represents the absolute value of the ratio, while the right, red axis shows the relative change referenced to the amount at 1.57 eV. The red circles display the change of the weighting factors of A_0 and B_2 under the assumption of constant susceptibility values.

pendix C.3.3. For each dataset the effective electric field was treated according to the respective regime by equation 7.3 or 7.15 and incorporated into the weighting factors. Figure 7.14 shows the relative magnitude and phase angles for the $\chi^{(3)}_{zzzz}$ element for the two different fits. Two critical point transitions are labelled in the dispersion curves. Those are the E_1 resonance along the Λ lines ($\langle 111 \rangle$ directions) at 2.92 eV and its spin-split separated transition $E_1 + \Delta_1$ at 3.13 eV [393]. The two-photon resonance point E_1 can be identified in both fits and also in the phase data of the non Kleinman fit. $E_1 + \Delta_1$ at 790 nm is at the lower end of the tunable wavelength range of the laser system and was therefore not measurable.

The absolute strength of the corresponding $\chi^{(3)}_{zxxz}$ and $\chi^{(3)}_{xxzz}$ elements is one magnitude smaller than that of the pure z orientated element. Further the resonance is shifted by ≈ 0.4 eV. It is accompanied by a pronounced phase shift of $45 - 55°$. Again the large $30 - 40$ nm FWHM Gaussian energy distribution in the excitation laser pulse has to be considered when interpreting this data. So within the experimental resolution (10 nm steps) this peak can be assigned to the E_1 point too.

To ensure that the measured signal dispersion is not related only to changes of the linear optical properties in the weighting factors, the relative change of calculated A_0/B_2 ratios for constant χ-values is plotted as red circles in figure 7.13. It becomes apparent that the small changes in the weighting coefficients of 12% can be neglected in light of the

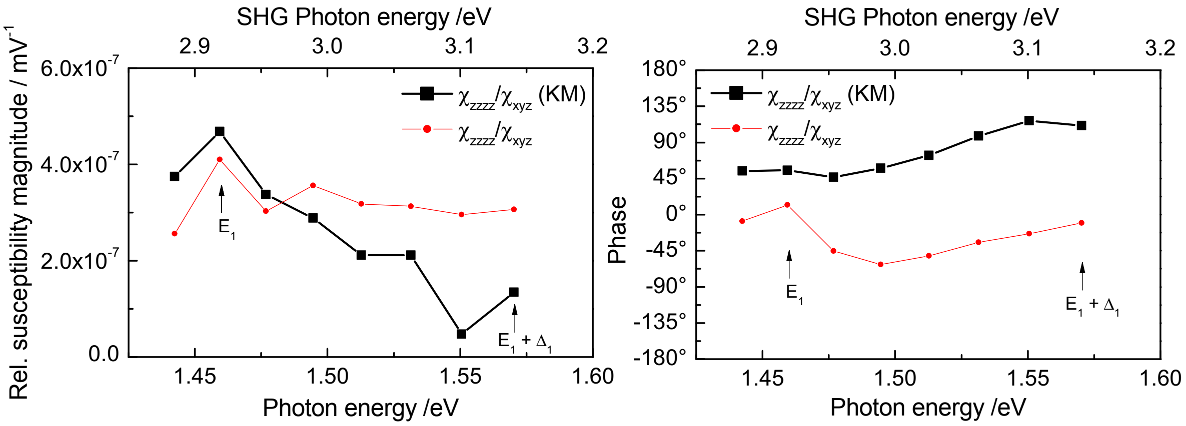

Figure 7.14.: Relative magnitude and phase of $\chi^{(3)}_{zzzz}/\chi^{(2)}_{xyz}$ terms, fitted with (black squares) and without (red circles) Kleinman symmetry. The solid lines are only a guide to the eye. The excitation pulse width is 35 – 40 fs. The combined average error of magnitudes and phase values is about 2%. The input data itself shows a standard deviation of around 12 % (mean value of error bars shown in figure 7.13).

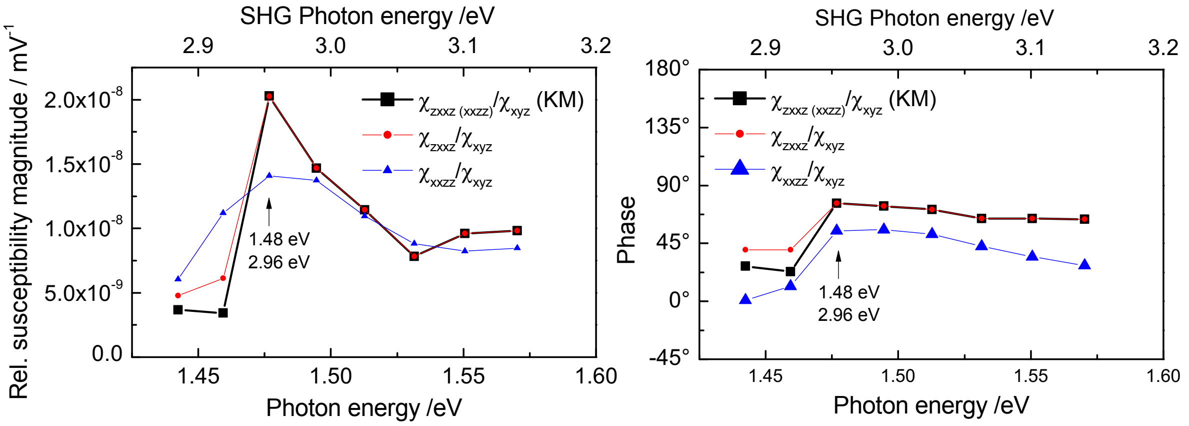

Figure 7.15.: Relative magnitude and phase of $\chi^{(3)}_{zxxz}/\chi^{(2)}_{xyz}$ and $\chi^{(3)}_{xxzz}/\chi^{(2)}_{xyz}$terms, fitted with (black squares) and without (red circles) Kleinman symmetry. The solid lines are only a guide to the eye. The excitation pulse width is 35 – 40 fs. The combined average error of magnitudes and phase values is about 2%. The input data itself shows a standard deviation of around 12 % (mean value of error bars shown in figure 7.13).

strong change of the experimental data.

Absolute values of $\chi^{(2)}_{xyz}$ were measured by different groups, whereas the depletion field was never included and magnitudes and dispersion properties differ significantly [392, 394]. The essence is that $\chi^{(2)}_{xyz}$ is in the order of 4×10^{-10} m/V and the third order elements have values of about 1×10^{-18} m^2/V^2. Calculation of optical properties in the large wavelength limit give the following ratios ([395] as summarized in [1]):

$$\begin{aligned} \chi^{(3)}_{zzzz}/\chi^{(2)}_{xyz} &= 4.0 \times 10^{-9}\ \mathrm{m/V} \\ \chi^{(3)}_{zxxz}/\chi^{(2)}_{xyz} &= 2.3 \times 10^{-9}\ \mathrm{m/V}. \end{aligned} \tag{7.17}$$

This fits quite well for the *zxxz* and *xxzz* elements at low photon energies, while in the resonance range their magnitude increases up to 2×10^{-8} m/V. The *zzzz* term is surprisingly large over the complete wavelength range, most likely caused by mutually reinforcing effects related to the depletion field aligned to the excitation pulse electric field.

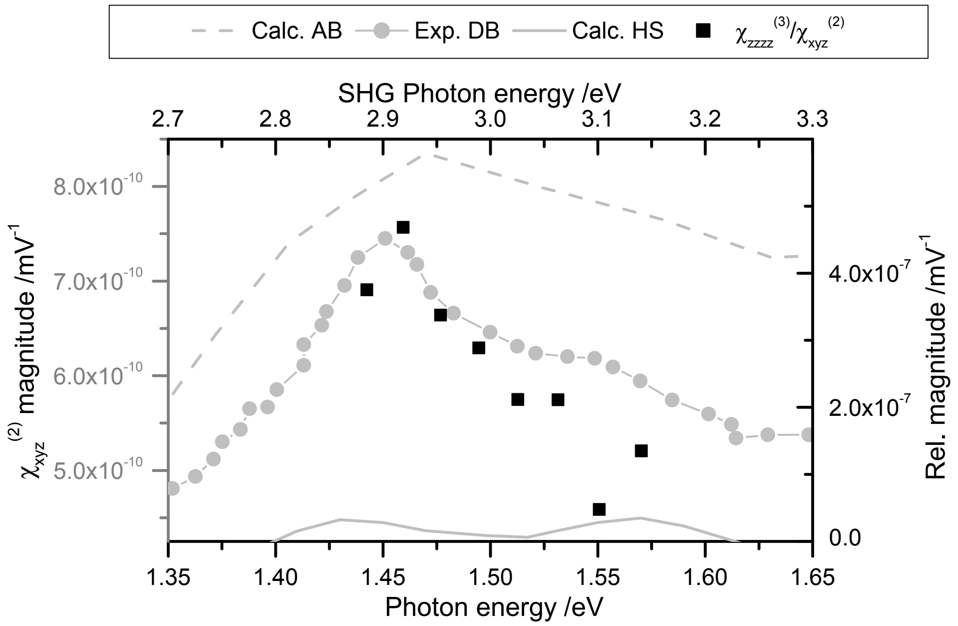

Figure 7.16.: Dispersion of $\chi^{(2)}_{xyz}$ (grey circles) as measured by Daum and Bergfeld [396] in comparison to the measured $\chi^{(3)}_{zzzz}/\chi^{(2)}_{xyz}$ ratios on GaAs:Si (black squares). Additionally theoretical $\chi^{(2)}_{xyz}$ dispersion calculations from Adolph and Bechstedt (dashed curve) [397] as well as Hughes and Sipe (solid curve) [398] are shown.

Especially interesting is the work of Daum and Bergfeld who measured $\chi^{(2)}_{xyz}$ values in a calibrated device of semi-insulating GaAs(001) samples in s-out, p-in configuration (ps) and the plane of incidence aligned to the [100] direction [396]. They followed the mathematical treatment of Sipe and Germer; fourth order terms were neglected, the surface and bulk term, as they are not separable, were combined to a single tensor element (cf.figure 7.4). In figure 7.16 an excerpt of their results (grey filled circles) together with the fitted $\chi^{(3)}_{zzzz}/\chi^{(2)}_{xyz}$ terms with Kleinman symmetry of figure 7.14 (black squares) are plotted. Additionally it displays two different theoretical calculations from Adolph/Bechstedt (AB) [397] and Hugh/Sipe (HS) [398] in the critical point energy corrected way of Daum et al.

The relative trend of the calculated $\chi^{(3)}_{zzzz}/\chi^{(2)}_{xyz}$ data with exception of the 1.55 eV point conforms with the bulk nonlinear susceptibility dispersion published by Daum and Bergfeld very well. This confirms the quality of the applied fitting procedure and the possibility to principally separate depletion field and dispersive effects, with the employed experimental set-up. In the final step absolute values for the third order susceptibility terms can be obtained from these measurements. They are given in table 7.2. The dispersion behaviour of these values qualitatively stays the same as that of the ratios.

Wavelength	Kleinman symmetry		Unrestricted fit		
	$\chi^{(3)}_{zzzz}$	$\chi^{(3)}_{zxxz}$, $\chi^{(3)}_{xzzz}$	$\chi^{(3)}_{zzzz}$	$\chi^{(3)}_{zxxz}$	$\chi^{(3)}_{xzzz}$
/nm		$\times 10^{-18}$	$/\mathrm{m}^2\mathrm{V}^{-2}$		
790	80	5.83	182	5.83	5.03
800	29.3	5.94	183	5.94	5.09
810	132	4.86	195	4.86	5.48
820	134	7.22	201	7.22	6.91
830	190	9.64	234	9.64	9.02
840	228	13.7	205	13.7	9.53
850	345	2.53	302	4.51	8.25
860	274	2.68	187	3.48	4.41

Table 7.2.: Absolute values of third order susceptibility elements for the GaAs:Si samples, calculated with the help of $\chi^{(2)}_{xyz}$ data from Daum et al. [396].

7.1.2. GaAs:Te

The rectangular GaAs:Te substrates are aligned with their long side parallel to the ⟨011⟩ axis, which allows a direct, self-contained alignment in the rotational scans. In contrast to Si Te has a lower diffusivity. The lower tendency to segregation makes it more suitable for higher doping levels [399]. The specifications of the tellurium and the silicon doped GaAs substrates concerning etch pit density, miss cut and dopant level are comparable, although the doping level of the GaAs:Te is less exactly specified. The ionization energies of both impurities differ only by 3×10^{-5} eV which is amply negligible at room temperature [382]. Nevertheless the rotational second harmonic reflection scans are considerably different. Figure 7.17 displays rotational scans in pp and ps configuration at 840 nm. In both configurations the signal intensities are about four times smaller than

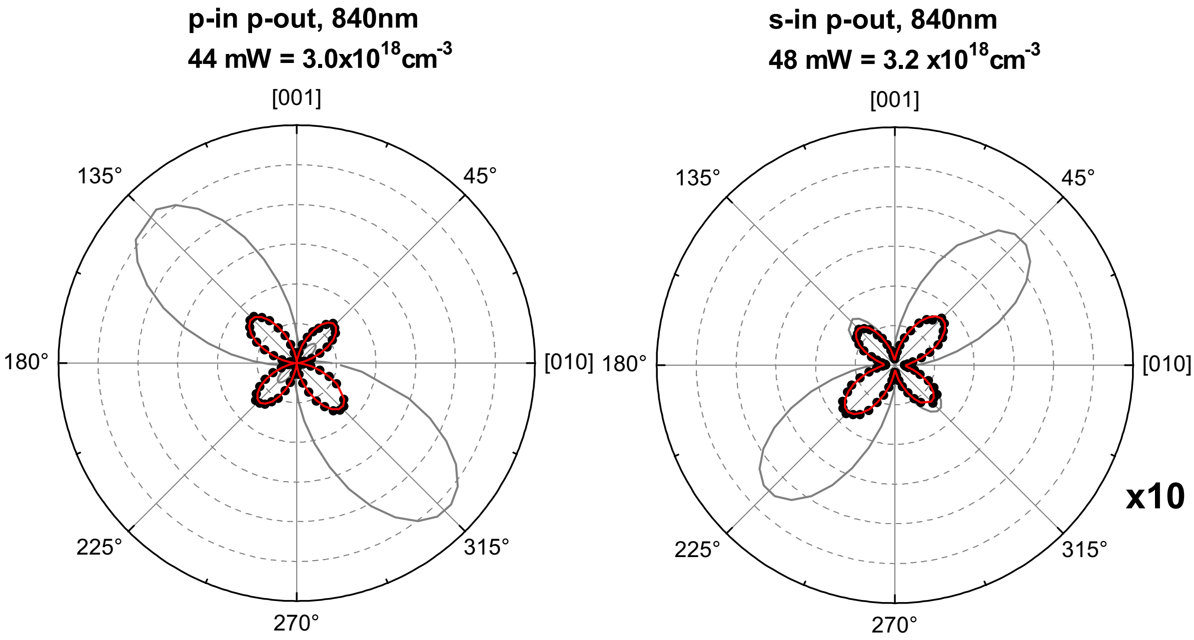

Figure 7.17.: SHG signal as a function of azimuthal angle from the GaAs:Te samples at 840 nm for pp and sp polarization configurations. The excitation pulse width is 35 – 40 fs.

those of the silicon doped substrates marked as reference as grey curves. It is even weaker than the 800 nm measurement on GaAs:Si. Further the anisotropy is much less pronounced and the symmetry is more bulk like, which, based on the discussion earlier, would indicate a smaller depletion zone effect. It should be noted that measurements at wavelengths larger than 840 nm were to weak for an reasonable analysis and that at this point, already photo modulation sets in. Again the ps signal is weaker as it lacks the contribution of the dominant $\chi^{(3)}_{zzzz}$ contribution. At 800 nm and higher excitation levels the rotational measurements result in curves like in figure 7.18. Similar to the previous results the ps signal changes only slightly, while the pp configuration, contrary to the expected trend at high carrier density and expected for the dispersion of the susceptibility term elements, increases by a factor of nearly two. Still with only weak $mm2$ symmetry.

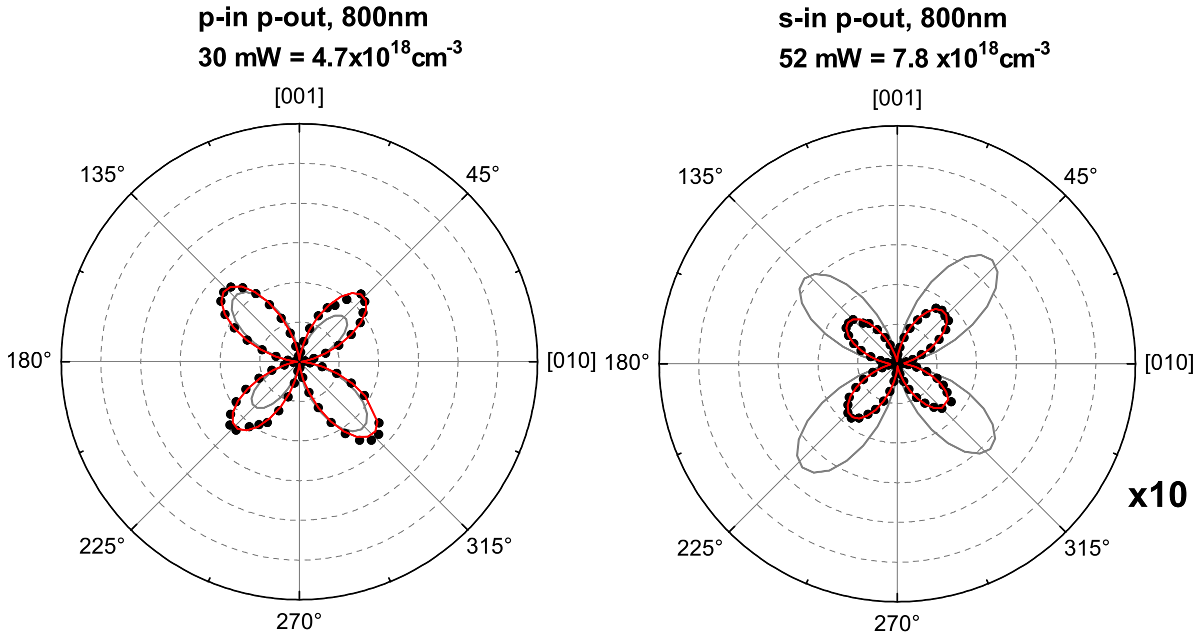

Figure 7.18.: SHG signal as a function of azimuthal angle from the GaAs:Te samples at 800 nm for pp and sp polarization configurations. The excitation pulse width is 35 – 40 fs.

In many measurements a low symmetry feature becomes apparent. While the lobes of low intensity in the [011] and $\left[0\overline{1}\overline{1}\right]$ directions are of similar strength and well fitted, the 90° shifted directions are non-uniform. This is demonstrated in figure 7.19, which depicts a scan in pp configuration at 840 nm. The possible relationship between the reduction of symmetry to m (C_1) and a miss cut of the {100} plane was presented in section 4.1.3. Takebayashi analysed and fitted rotational data in a similar way to the process shown here to extract tilt angles [192]. For a tilt of 2° already a large imbalance in the lobe intensities was found, much stronger than those seen in these measurements. A possible tilt would probably be smaller than 1° and be in accordance with the given specifications of the wafer.

Alternatively, as perfect alignment between the laser spot and the intercept between the surface and the axis of rotation is not always achieved, the excitation beam moves over the sample in a small circular motion; local microscopic or macroscopic surface variances could lead to a similar signal perturbation. Normally these effects show up as small dips in the signal as they are seen at around 135°. Regardless of the actual reason, this imbalance reduces the quality of the fit and of the obtained A_0 and B_2 coefficients.

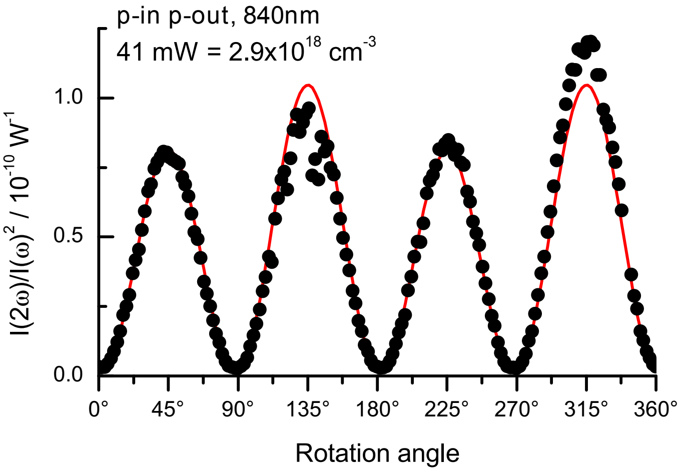

Figure 7.19.: SHG signal as a function of azimuthal angle from the GaAs:Te samples at 840 nm for pp configuration. The direction at 135° and 315° exhibit different intensities, which lower the overall symmetry of the SHG response to m.

The analysis of the experimental data follows the treatment of the GaAs:Si data. The most striking difference in the data is the much smaller dispersive effect of the isotropic response. While at the silicon doped sample the dispersive and field effects were strongly superimposed, here the influence of the space charge region is dominant. The effect is demonstrated in figure 7.20. It shows the data of four different sets of experimental data at different excitation levels (black to red curve). In the left graph the expected effect of higher carrier densities at lower wavelengths can be seen. The right graph depicts that within each data set the isotropic coefficient A_0 changes less compared to the change between different sets.

By averaging over all different sets, considering surface recombination and including the phase and absorption depth effects, the dependence of the different fitting coefficients on depletion zone properties can be determined, these results shows figure 7.21. In the upper panel, the effective electric field is calculated for the upper and lower limit (dashed red lines) and the average (bold red line) of the specified dopant density. The correlation with $\overline{R}^2 = 0.52$ is slightly higher than that of GaAs:Si. It intercepts at $E = 0$ with $A_0 = -0.25$ to -0.04 ($\sigma \approx 0.1$) depending on the assumed carrier concentration. A negative A_0 is physically meaningless, this hints that the exact doping density must be closer to 1.1×10^{18} cm^{-3} were the regression curve exhibits the smallest intercept. The effect of the static electric field in the material on the nonlinear response is smaller by nearly a half compared to GaAs:Si (grey curve). The bulk related value B_2 is still independent from the electric field, but deviates more strongly from its mean value.

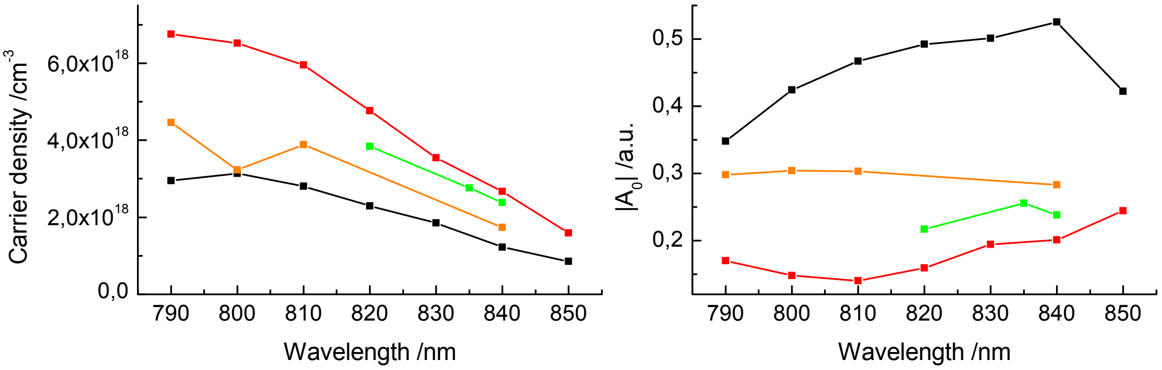

Figure 7.20.: Dependence of the injected peak carrier density and the isotropic fitting coefficient A_0 on the wavelength of the excitation beam for four different sets of experimental data with increasing intensity (black to red curve).

Finally also the relative phase between both factors in the flat band region is smoother and smaller.

The data set of averaged A_0/B_2 ratios of the tellurium doped samples used in the fitting process (black squares in figure 7.22) of susceptibility values is smaller than that of GaAs:Si (grey triangles). For photon energies smaller than 1.47 eV the rotational data was to weak for a reliable fit. The remaining data shows the same general trend but with a less steep progression towards smaller energies. The strongest feature is a step at 1.53 eV. Because of the less favourable signal intensity, the susceptibility fits were done under the assumption of Kleinman symmetry and repeated for the given minimum, maximum and average dopant densities mentioned before (black squares and dashed red lines in figures 7.23 and 7.24). The all perpendicular $\chi^{(3)}_{zzzz}/\chi^{(2)}_{xyz}$ term is once more dominant and one order of magnitude larger than the other two ratios. The intense E_1 transition region in the GaAs:Si data (grey triangles) is unfortunately not covered by this set of data, but for that the $E_1 + \Delta$ transition at the high energy limit of the dispersion data is pronounced.

This semi quantitatively reflects the observed behaviour of the raw rotational data shown before in graphs 7.17 and 7.18. Due to the lack of the zzzz contribution the sp polarized curve changes only little between 840 nm and 800 nm. But, also in contrast to the GaAs:Si data, the intensity at 800 nm is about two times stronger than at the long wavelength limit. As predicted, it is also stronger than the silicon data at this photon energy [1]. The fits for the lower and upper dopant density limit match the medium

---

[1] The susceptibility data would give reason to expect a stronger difference between GaAs:Si and GaAs:Te at 800 nm, but for comparing the raw rotational data from different sample types their

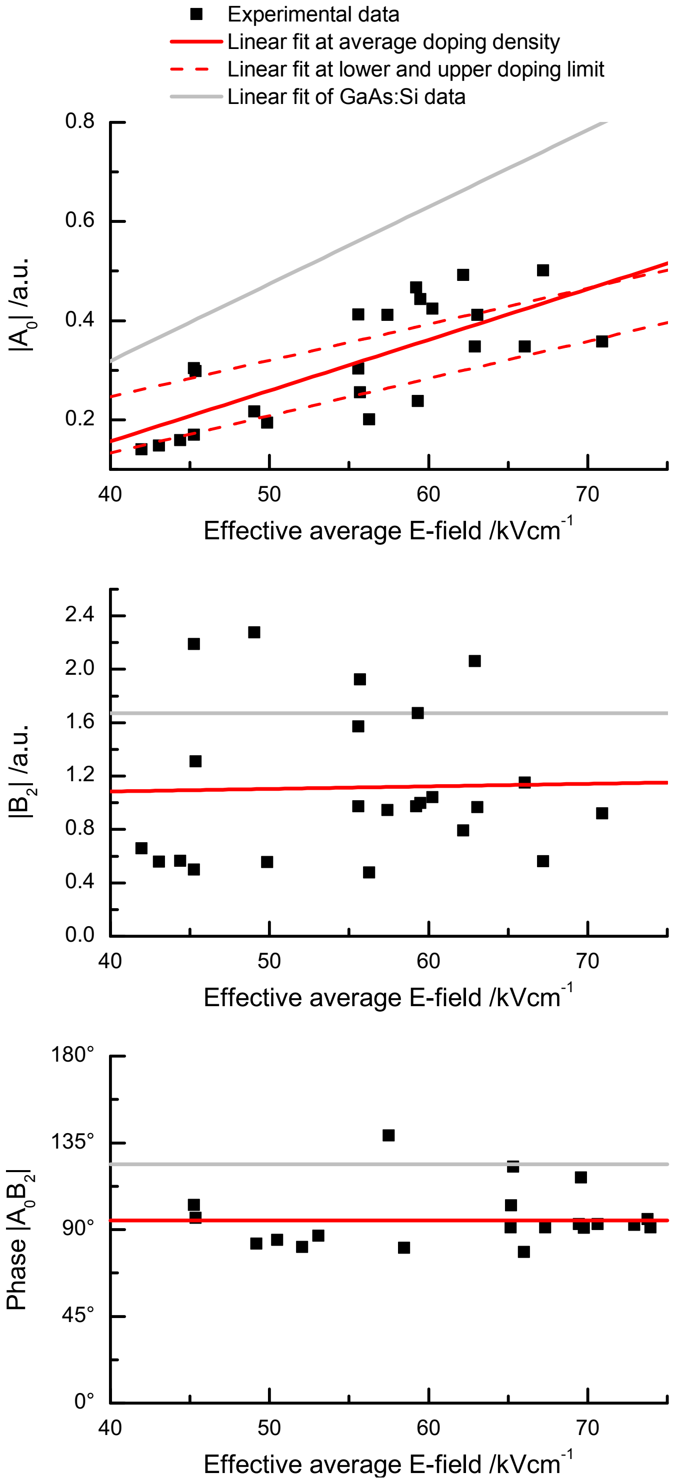

Figure 7.21.: Isotropic and anisotropic fitting coefficients for GaAs:Te as function of the effective average electric field within the absorption depth of the SHG signal. The upper two panels show the magnitude of the complex fitting parameters, while the lower panel shows their relative phase relation.

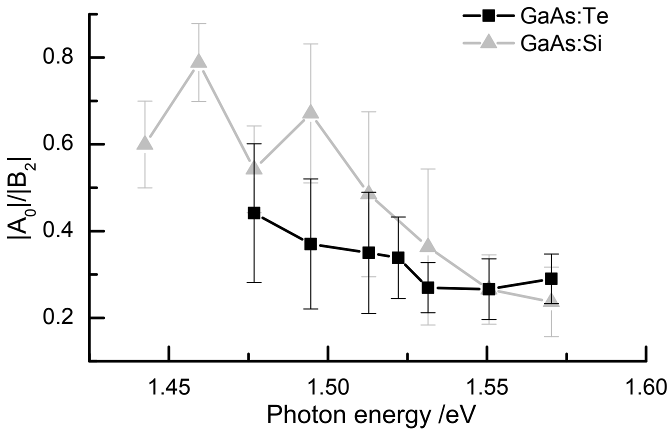

Figure 7.22.: A_0/B_2 ratio at different photon energies, averaged over variable excitation intensities (black squares). The standard deviation of each data point is given as error bar. The grey triangles show the corresponding data from GaAs:Si

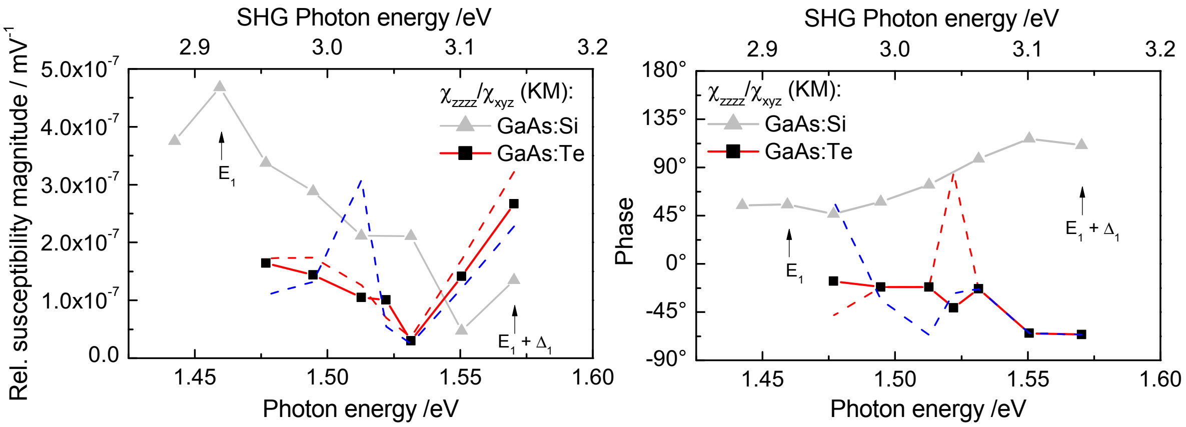

Figure 7.23.: Relative magnitude and phase of $\chi^{(3)}_{zzzz}/\chi^{(2)}_{xyz}$ terms, fitted with Kleinman symmetry (black squares) at a dopant density of 1.6×10^{18} cm^{-3}. The dashed lines show the corresponding fits for 1.1×10^{18} cm^{-3} (red) and 2.2×10^{18} cm^{-3} (blue). The calculated value for GaAs:Si are shown as grey triangles. The solid lines are only a guide to the eye. The excitation pulse width is 35 – 40 fs. The combined average error of magnitudes and phase values is about 2%. The input data itself shows a standard deviation of around 11 % (mean value of error bars shown in figure 7.22).

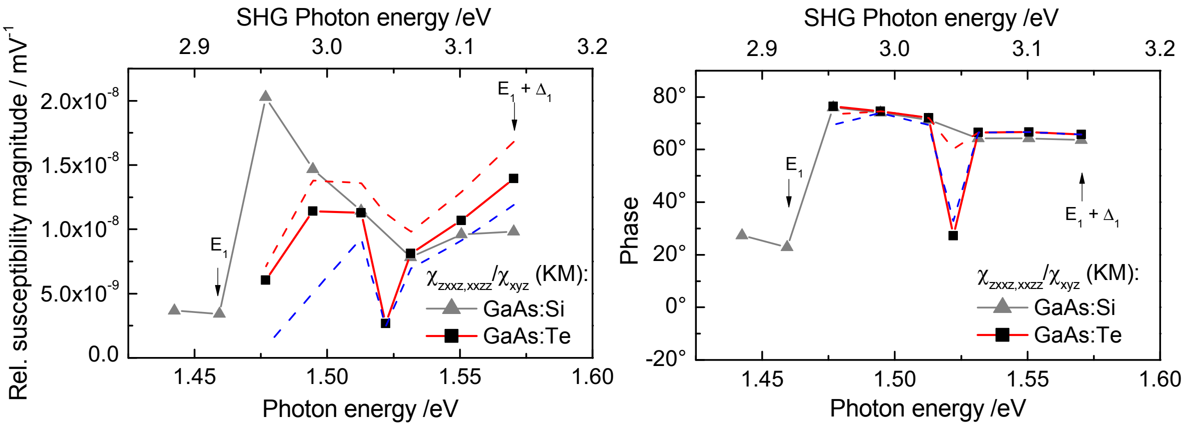

Figure 7.24.: Relative magnitude and phase of $\chi^{(3)}_{zxxz(xxzz)}/\chi^{(2)}_{xyz}$, fitted with Kleinman symmetry (black squares) at a dopant density of 1.6×10^{18} cm^{-3}. The dashed lines show the corresponding fits for 1.1×10^{18} cm^{-3} (red) and 2.2×10^{18} cm^{-3} (blue). The calculated value for GaAs:Si are shown as grey triangles. The solid lines are only a guide to the eye. The excitation pulse width is 35 – 40 fs. The combined average error of magnitudes and phase values is about 2%. The input data itself shows a standard deviation of around 11 % (mean value of error bars shown in figure 7.22).

density fit at 1.6×10^{18} cm^{-3}, only at 1.51 eV the high dopant density model jumps to a value found also in test runs without Kleinman symmetry limitation—which probably is a local minimum. The edge feature in the A_0/B_2 data appears also as (local) minima in the magnitude and phase value of $\chi^{(3)}_{zzzz}/\chi^{(2)}_{xyz}$. It does not correspond to any critical point transition. The phase values shift in the same way like GaAs:Si by approximately 40° at high energies but with opposite sign. The phase value is determined from the measured absolute value of the phase difference between A_0 and B_2, the fit can not distinguish between a positive or negative phase difference. This ambiguity leads also to the erratic behaviour of the phase in the fits for the other doping levels.

The fitting results for $\chi^{(3)}_{zxxz(xxzz)}/\chi^{(2)}_{xyz}$ especially the phase meet those from the silicon doped samples, beside the suspicious value at 1.53 eV. Again the $E_1 + \Delta$ critical point is more intense.

Also for this sample absolute susceptibility values were calculated from the ratios and the $\chi^{(2)}_{xyz}$ data from Daum [396] (table 7.3).

---

exact dopant density has to be considered.

Wavelength	Kleinman symmetry	
	$\chi^{(3)}_{zzzz}$	$\chi^{(3)}_{zxxz}$, $\chi^{(3)}_{xxzz}$
/nm	$\times 10^{-18}$ /m^{2}V^{-2}	
790	159	8.3
800	87	6.6
810	19	5.1
815	64	1.7
820	69	7.4
830	97	7.7
840	120	4.4

Table 7.3.: Absolute values of third order susceptibility elements, calculated with the help of $\chi^{(2)}_{xyz}$ data from Daum et al. [396].

7.1.3. GaAs-Pt

For the static and time-resolved optical measurements of the interface effects the deposited amount of platinum ($3 - 5$ Å) and the substrate temperature at the evaporation process ($100 - 570$ K) were systematically varied. Due to the limited supply of GaAs:Si substrates and their lack of recognizable angular orientation, the study focuses mostly on the tellurium doped samples.

Nevertheless first the results from the silicon doped samples are shown. The evaporation of platinum strongly changes the nonlinear signal of rotational scans. Figure 7.25 shows the result of a scan at 805 nm from GaAs:Si-Pt(3 Å@300 K) in comparison to a measurement at comparable injection levels and photo modulation strength from the oxide covered substrate at 800 nm (grey curve). The total signal is significantly weaker while the relative influence of the isotropic, depletion i.e. surface region contribution is larger. The latter effect is to strong that it may be explained by dispersive effects of the small photo energy difference between both scans. This effect shows up also at lower evaporation temperatures (red curve on left side of figure 7.26). While the absolute values of the fitting parameters $|A_0|$ and $|B_2|$ are still within the standard variance of the native oxide values (figure 7.11), their field dependent ratio illustrates the change upon Pt deposition (right side of figure 7.26). The proportion between the isotropic and anisotropic fitting parameter of the 300 K data equals that of GaAs:Si substrate values at much higher injection levels rather than those at a similar level. But these values, although on the upper end of the range, still could be explained as statistical variation of substrate data. So also the relative phase difference between both coefficients has

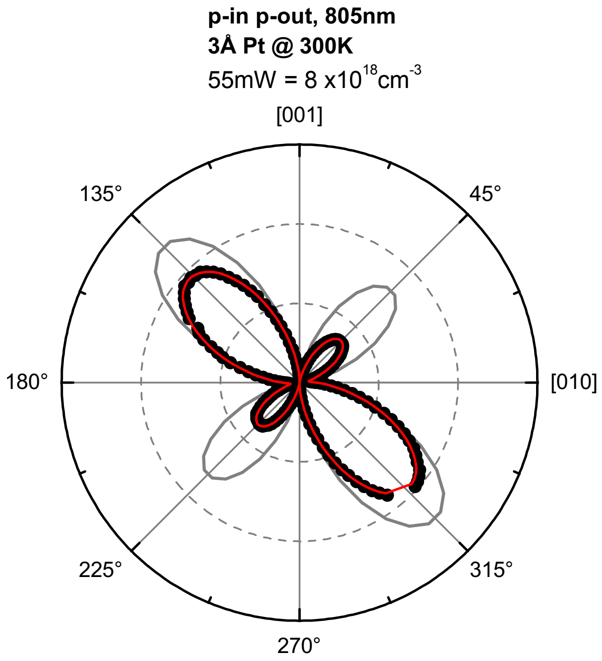

Figure 7.25.: Rotational SHG scan of GaAs(100):Si covered with 3 Å Pt evaporated at 300 K (black dots) and fit (red curve). The grey curve is a result on native oxide covered substrate at comparable wavelength and injection level.

to be considered. In the photo modulated flat band regime the phase difference on the native oxide samples is around 115°. For the platinum samples it is already at 147°. This directly reflects on the intensity ratio between the peaks at 135° and 45° which was already introduced as a simple measure of anisotropy in the beginning of this chapter. This parameter is on oxide covered samples for different wavelengths in the examined range between 1.34-1.47, while it is twice as large for the 300 K substrates(2.72 & 2.82) and even higher for the low temperature sample (3.77).

For a complete dispersion discussion, more experiments have to be done, but it seems that the effect saturates when looking at the ratio values for 805 nm and 815 nm. At least in its initial state directly after preparation in the UHV, the platinization of these samples comes with the removal of the oxide layer and the preparation of a defined and reconstructed GaAs surface. The origin of the observation made may be found in the changed GaAs surface itself, the lack of oxide layer or directly in the formation of the GaAs-Pt interface and its thickness and preparation temperature dependent nature. In the upcoming chapter on time-resolved experiments, more effects upon variation of theses properties become evident.

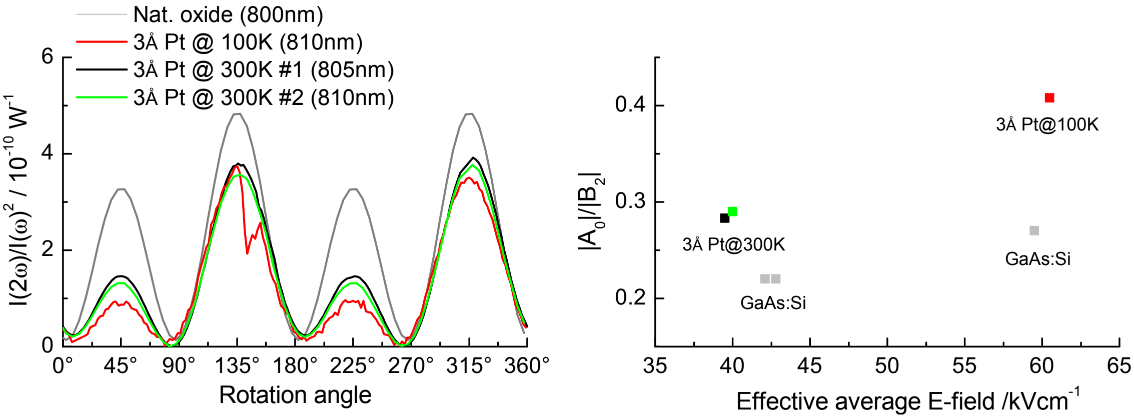

Figure 7.26.: Left: Rotational scans on native oxide GaAs:Si and Pt covered substrates. Right: Ratio between the magnitude of the isotropic parameter A_0 and that of B_2 at different effective average electric field strength and different samples.

GaAs:Te reference samples

A more solid and comparable investigation of interface effects can be done on the tellurium doped samples. To support the assignment of the measured effects to the properties at the metal-semiconductor interface, reference experiments were done. Figure 7.27 shows a rotational scan in pp configuration from a GaAs:Te sample on the left side which was sputtered and annealed in the UHV up to 850 K. As the optical experiments were done in air, the sample is expected to be reoxidized. The initial surface reconstruction is the same stable Ga-rich $c\,(8 \times 2)$ configuration prepared also for the platinum covered samples. Again in the background a scan at comparable configuration from a native oxide covered substrate is shown for comparison. Beside the weaker signal, the strong deformation of the opposite lobes at 135° and 315° is the most prominent feature. While the smaller deformation on some unprocessed tellurium samples is in the range of 10% and related to a surface tilt of 1° or less, here the imbalance reaches 40%. It has to be included in the fitting routine by an additional $B_1^{\alpha,\beta}\sin(\phi)$ term in equation 7.9. The fit is shown in the graph, too (red curve). The quality of this modelling is lower than that for the other samples, especially at the troughs and the skewed lobes, it is possible that more components, like a cosine A_1 term, contribute to the signal. The theory of SHG in GaAs(100) [1, 71, 99] contains no elements resulting in a low m symmetry, so the reason for the shape of the rotational SHG signal may either be found in a cleaning process caused surface tilt or by another hitherto unknown SHG active reduction of the surface symmetry. The sputter gun is aligned in a 45° angle to the target surface pointing in the [011] direction of the GaAs(100) sample. The work of Takebayashi [192] shows that for pp configuration those lobes with components in direction of the tilt get amplified while those in the opposite direction get attenuated. When the same principles apply to these samples, the tilt would be in along the $\left[01\bar{1}\right]$ and thus 90° shifted to a possible sputter effect. Also there is no evidence for a preferential sputtering. The $c\,(8\times 2)$ surface reconstruction changes the surface symmetry by relaxation and rearrangement of bonds. The [011] is characterized by stripes of Ga dimers, while the $\left[01\bar{1}\right]$ direction, perpendicular to the dimers, is periodically interrupted by missing Ga surface atoms and thus a reduced gallium density (cf. figure 4.2). The following reoxidation after removal of UHV conditions and the preferential Ga oxidation may lead to a different native oxide layer, which could induce the lowering of the symmetry in rotational scans. Finally, it could not be completely ruled out that residual oxidic species form partly ordered islands as discussed in section 4.1.1, although the LEED pictures do not indicate this behaviour. A further investigation of these effects, completely under UHV conditions is necessary.

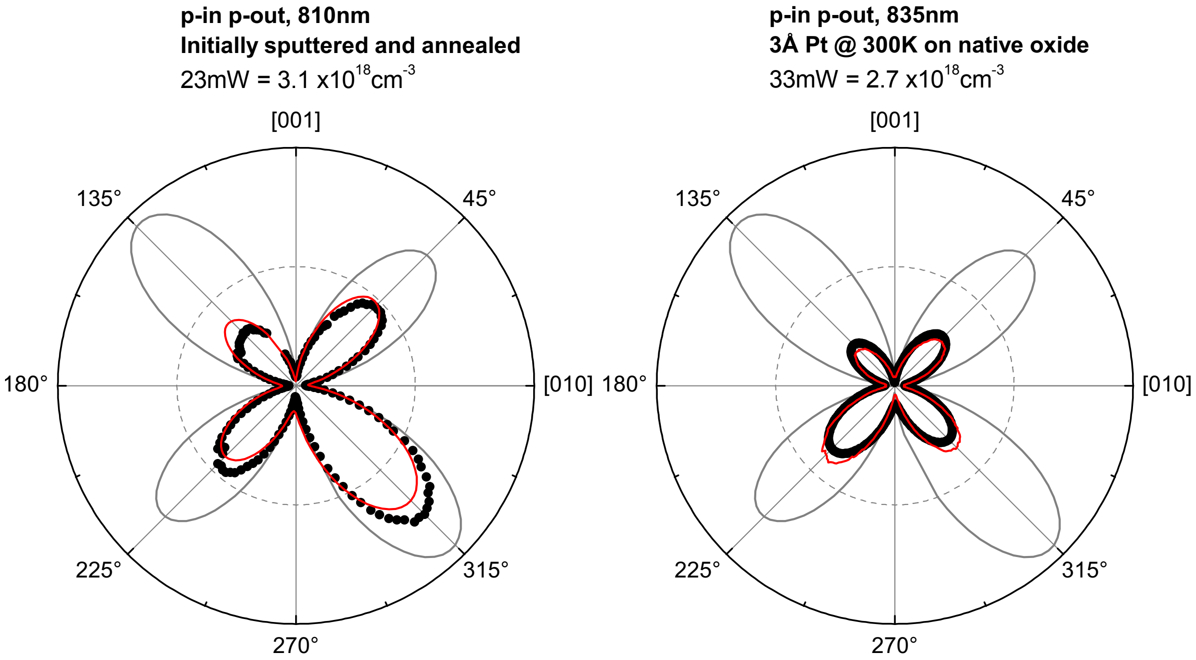

Figure 7.27.: SHG signal as a function of azimuthal angle from GaAs:Te samples at 810 nm for pp polarization configurations - on the left side after initial cleaning and preparation of a defined surface and on the right side after deposition of 3 Å Pt directly on a native oxide covered substrate. The excitation pulse width is 35 – 40 fs.

Standard fits and those including the low symmetry component give $|A_0|/|B_2|$ ratios of 0.26 at an effective field level of 61 kV/cm. They line up nicely with the values for silicon doped native oxide covered samples at the same depletion field strength (cf. right side of figure 7.26) and are only slightly larger than those of the oxidized GaAs:Te samples (0.12 to 0.21). The peak intensity ratios are obtained either by averaging over both deformed lobes or by subtracting out the B_1 component from the model. Both methods give similar values of 1.14 and 1.19 respectively, which are again lower than those values from native oxide samples. This permits a clear and significant distinction from the samples with a platinum interface.

The second reference samples consists of a 3 Å Pt deposition directly on an oxidic GaAs:Te sample. Measurements on a Pt(111) single crystal did not give any measurable SHG response. The face centred cubic crystal structure of platinum prohibits a bulk contribution to the nonlinear second order feedback and the surface terms of clean surfaces are apparently to small do be detected (see also [256] and section 4.2.3). So its surprising that rotational scans on this type of samples exhibit results which are different from the unprocessed native oxide samples (right side of figure 7.27). The measurement shown was recorded at 835 nm but at higher power, resulting in a similar photo modulation level as the sputtered only sample discussed before. The overall signal diminished even further and the intensities of all four lobes differ. A number of reasons can be thought of to explain the observed effect. The reduction of symmetry compared to the Pt-free samples could be caused by an SHG active metal-oxide interface, which due to a small alignment mismatch at the evaporation process exhibits a spatial inhomogeneous platinum thickness (The angle set at the cooling finger may have a small deviation from a perpendicular alignment of the substrate surface to the evaporator, see section 5.2.1). Alternatively as this type of sample corresponds to a MOS type capacitor, charges in the (spatial variant) metal layer upon ultrashort laser pulse excitation could transiently change the electronic system in the semiconductor. Also weak sputtering of the oxide layer by a small amount of heavy platinum ions escaping from the evaporator can not be ruled out.

Most likely is that the deposition of Pt onto the oxide layer evokes structural and chemical changes in the complex native oxide layer and at the interface between this and the bulk semiconductor. Kobayashi et al. discovered upon experiments on GaAs and Si that platinum, when applied on the semiconductors native oxide layer, acts as an oxidation catalyst [400, 401]. The catalytic behaviour already sets in directly after deposition, as shown in XPS spectra. In contrast to other metallic catalysts [402], the additionally formed oxide components do not accumulate on top of the metal layer but within the already present native oxide film, leading to a growth of the oxide thickness. Oxygen dissociatively adsorbs at Pt and moves in form of O^- or O^{2-} through the metal layer into the native oxide. From the semiconductor side gallium and arsenic diffuse into this region with different diffusion coefficients, leading to a layered system of binary and ternary oxides. Opposed to this, the XPS measurements of the MOS type sample shown in section 6.3 do not show an increased oxide growth.

The platinum film thickness is to small to absorb fundamental light to a significant amount, even though the absorption coefficient in this spectral region is high compared to the GaAs substrate [248]. The drop in SHG intensity compared to the Pt-free oxidic samples must be attributed either to an increased scattering of fundamental or SHG light at the oxide-semiconductor interface or to a reduced nonlinear susceptibility of the substrate induced by the interface modification.

In the scope of the characteristic properties $|A_0|/|B_2|$ (0.28) and the peak intensity ratio (1.17), this type of samples behave more like the sputtered samples and differ substantially from corresponding direct metal-GaAs interface samples. The intensity ratio matches that of the sputtered samples and is smaller than on the native oxides, while the $|A_0|/|B_2|$ is less unambiguous and higher.

GaAs:Te-Pt samples

With this background the metal-GaAs interface samples can be discussed. First the substrates with a 3 Å coverage are investigated. The sample preparation is equivalent to that of the silicon doped samples, with the same surface reconstruction. Due to the small cooling rate of the sample holder used for the rectangular GaAs:Te wafer pieces, 200 K was chosen for the low temperature deposition (red curve on left side of figure 7.28). The change in reflected SH intensity is different to that from GaAs:Si.

There, the SHG response on the oxidic samples was not only weaker than on the tellurium samples, but it reduced further upon platinum film preparation. Here the signal increases for the sample at 200 K process temperature. The effect is even stronger at the 300 K samples shown on the right side of figure 7.28 (red curve). This graph additionally includes the rotational scans from the previously discussed reference samples (green and blue) to demonstrate the strong sensitivity of this measurement method to the interface and surface constitution. At 500 K in turn the total SHG intensity drops below the native oxide level. On a number of samples, for example on the 200 K scan shown in figure 7.28, also a small to moderate A_1 term influence becomes apparent. The peak intensity ratio of all direct metal contact samples is strongly enhanced compared to the bare substrates and even more compared to the reference samples. Just as on the silicon doped wafer this is primarily caused by a shift of the relative phase between A_0 and B_2

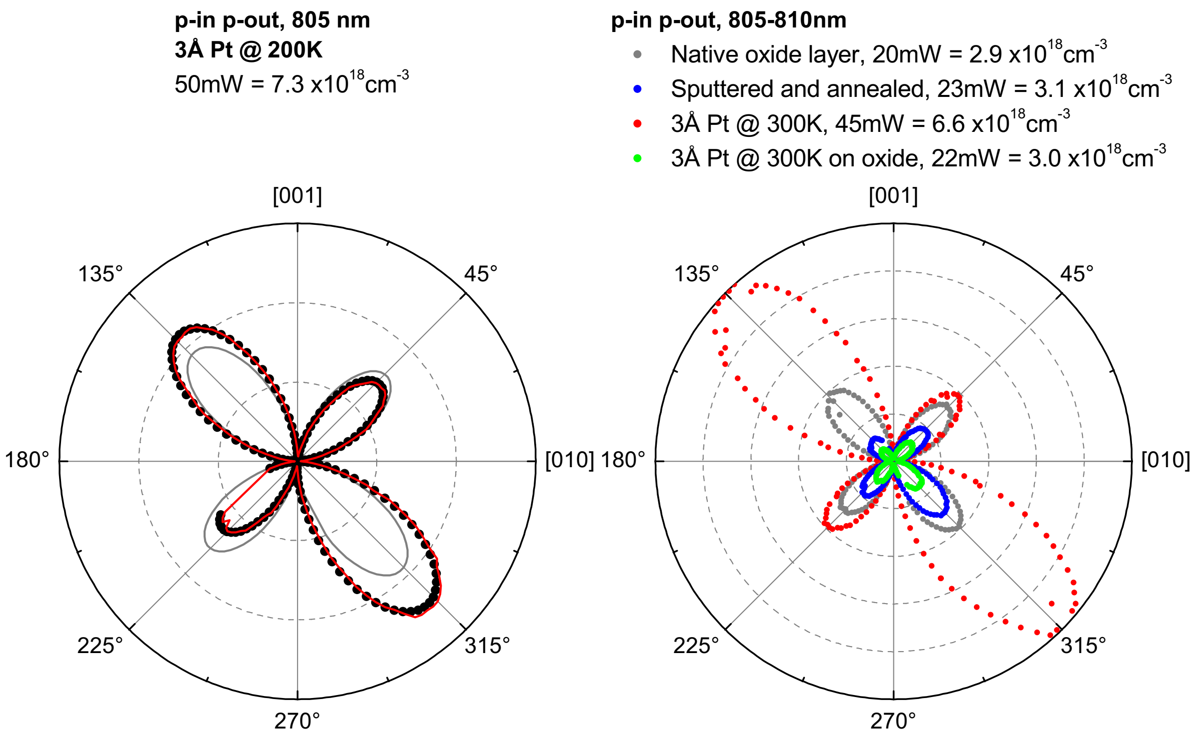

Figure 7.28.: Rotational SHG scans of GaAs:Te{100}, covered with 3 Å Pt. Left: 200 K substrate temperature (black dots), fit (red curve) and corresponding native oxide (grey curve). Right: 300 K substrate temperature and the previously presented references. The excitation pulse width is 35 – 40 fs.

from an average value of 95° to 147°, rather than from absolute changes in $|A_0|$ and $|B_2|$. Both characteristic anisotropy quantities follow the trend of the SHG intensity for the different substrate temperatures. This is summarized in the left side of figure 7.29 and table 7.4.

Similar results can be found when evaporating a nominal amount of 5 Å platinum (right side of figure 7.29.) In the 200 – 500 K temperature range the dynamics of the rotational signal is reduced compared to the substrates with lower metal coverage. Especially the sample at 300 K stands out less, while at the same time the average SHG level of the 200 K and 500 K scans is higher. The trend of decreasing anisotropy and SH intensity at high temperature preparations proceeds with increased rate.

The observed significant change of anisotropy and SHG intensity on the direct metal-semiconductor samples is caused and influenced by a system of different effects. The first and most obvious effect is the formation of a Schottky contact between the n-GaAs and platinum as described in section 4.2.2.1. The involved processes are complex and a simple barrier height prediction based on workfunction and electron affinity differences is in

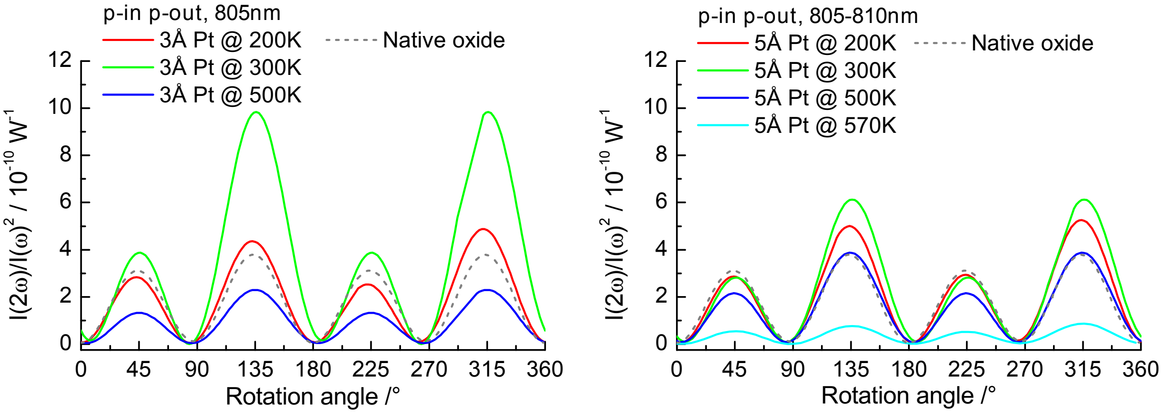

Figure 7.29.: Rotational scans of GaAs:Te covered with platinum at different substrate temperatures. Left: 3 Å Pt deposition. Right: 5 Å Pt deposition. The excitation pulse width is 35 – 40 fs.

Sample type	Peak ratio	$\|A_0\|/\|B_2\|$
Native oxide	1.28	0.16
Sputtered and annealed	1.19	0.26
3 Å Pt @ 300K on oxide	1.11	0.29
3 Å Pt @ 200K	2.14	0.24
3 Å Pt @ 300K	2.94	0.28
3 Å Pt @ 500K	1.75	0.20
5 Å Pt @ 200K	1.82	0.17
5 Å Pt @ 300K	2.16	0.21
5 Å Pt @ 500K	1.92	0.24
5 Å Pt @ 570K	1.56	0.17

Table 7.4.: Anisotropy parameters for Pt covered GaAs:Te samples in different configurations and reference values.

general not possible. The deposited amount of $3-5$ Å equivalent thickness corresponds to a coverage of 1.1-1.8 ML platinum, which is more than the approximately only 0.1 ML metal (Sn) coating necessary for saturation of Fermi level pinning (on a GaAs $\{110\}$ surface) [403]. The approximate threshold for Fermi pinning is at a surface state density of 10^{12} cm^{-2} and a monolayer on the $\{100\}$ face of gallium arsenide corresponds to an atomic density of 6.26×10^{14} cm^{-2} [404]. On the surface of a semiconductor the periodicity breaks and interface states with imaginary wave vectors are introduced in the band structure, filling the band gap (virtual induced gap states). The metal induced gap states (MIGS) at an ideal interface can be thought of as metal Bloch wave leaking into the band gap of GaAs where matching with the VIGS creates a continuum of allowed states, which due to the nature of the VIG states have partly valence and conduction band properties [381]. For sub monolayer metal amounts the metallic Bloch wave is replaced with electronic levels of the adsorbed atoms. For this regime another approach, the so called defect model, treats formation of an adsorbate layer as a source for surface defects in GaAs creating vacancies or antisites (cf. figure 4.6 in section 4.1.2). In both approaches the local properties at the interface including in-diffusion, reactivity and defect density determine the exact Schottky barrier.

The XPS and SPM experiments (section 6.3) discuss the diffusion and reaction principles on GaAs-Pt interfaces in connection with previous findings (section 4.2.1.1). In all direct contact samples metallic arsenic and gallium were found, indicating a possible alloying or the formation of intermetallic phases. At room and elevated process temperatures substantial chemical reactivity at the interface sets in [17, 242]. Here diffusion processes become dominant, with a fast transport of gallium atoms through the metal layer [244]. SPM shows craters of gallium on the platinum film and XPS data indicate a strong gallium platinum interaction, especially at the high temperature sample (570 K).

Beside the chemical composition the morphology, in particular the growth mode of platinum on the polar semiconductor surface, is probably the second major influence on the measured rotational SH scans. At both coverages the 300 K preparations show the strongest increase in anisotropy and the highest signal levels, indicating a high interface quality. At low temperatures the growth is more particle like, while at higher temperatures interface quality suffers from a droplet formation which may be a sign of a change to Stranski-Krastanov growth with island formation, connected to strain relief by misfit dislocation. The exact critical thickness of Pt on GaAs for this process is unknown, but it varies between $< 1-15$ nm for different substrates [405, 406].

The more pronounced SHG dynamics in the thinner 3 Å preparations may be related to

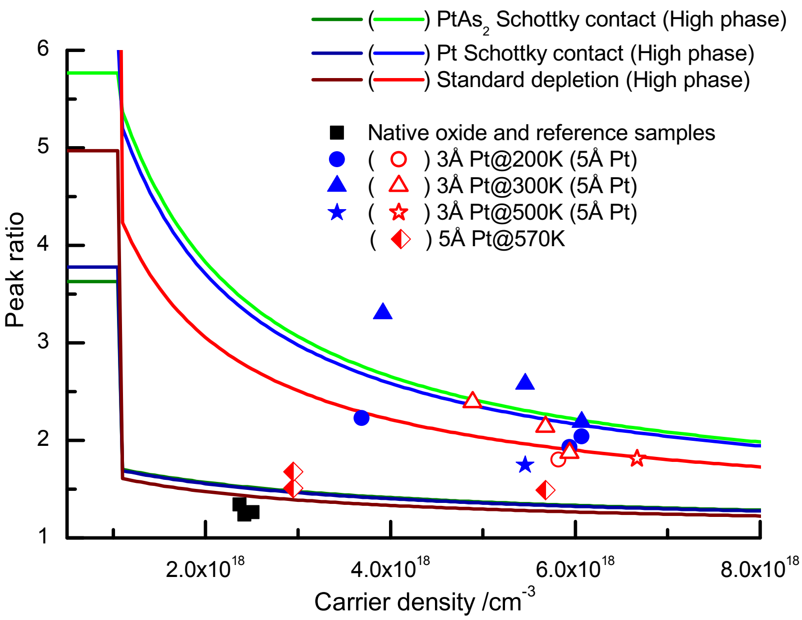

Figure 7.30.: Peak ratios from SHG rotational scans on samples with varying preparation parameters and calculated predictions based on different band bending parameters and A_0-B_2 phase relations.

a stronger intermixing or a more advanced consumption of the platinum layer. Also the Pt layer itself or the GaAs-Pt interface can affect the SHG signal by linear absorption or additional SHG activity.

To test the plausibility of the above discussion, injection density dependent peak ratio estimations for different contact types were performed for 805 – 810 nm scans (figure 7.30). Because the effective average field for a given injection density varies with different barrier heights, the carrier density is plotted on the abscissa. The lines represent the calculated peak ratio predictions for different states. They are based on the linear regression of 1.1×10^{18} cm^{-3} doping, $|A_0|/|B_2|$ values from the wavelength averaged data of figure 7.21 and the differential phase between both in the low wavelength region. The step at the doping level reflects the abrupt transition between the Germer model and the unmodulated regime which was already discussed in section 7.1.1. For the high phase labelled curves the additional average phase shift of 33° (805 – 810 nm measurements only) observed on platinum covered samples was included. From bottom to top they represent the low and high phase difference versions of a standard depletion zone with a barrier height of 0.68 V, a GaAs-Pt Schottky contact with $\phi_B = 0.94$ V and an interface with a PtAs$_2$ layer ($\phi_B = 0.99$ V). The low phase curves differ only slightly. The experimental values for the native oxide and reference samples (black squares) reside on the lower side of the expected standard depletion zone model. The dispersion relation of the different susceptibility tensor ratios in figures 7.23 and 7.24 exhibit a minimum in the $805 - 810$ nm range, which explains the negative deviation from the prediction curve based on wavelength averaged data. The low temperature data for 3 Å (blue circles) and 5 Å (red unfilled circles) lay in the range of the predicted phase shifted values for an uncovered GaAs:Te {100} surface with default band bending. The samples with the presumed highest interface quality at 300 K (blue triangles, ie. red unfilled triangles), are predominantly located in the range of the Pt and $PtAs_2$ high phase predictions and even above. With further increasing process temperatures the values first drop back down to pure GaAs:Te band bending regimes and for the 5 Å Pt@570 K samples even into the prediction band of the low phase region. In this picture two effects determine the peak ratio of a rotational SHG curve. On one hand the already familiar depletion zone properties and one the other hand the observed shift in the phase between A_0 and B_2. The (stepwise) loss of interface quality on the high temperature samples diminishes the peak ratio towards the low phase regime, so the phase shift can possibly be interpreted as a quality indicator of the interface, which can not be obtained from SPM and XPS measurements with this sensitivity. This graph allows also the discussion of two other possible explanations. First the metal layer could absorb substantial amounts of the pumping light, thus reducing the induced carrier density and shifting the system in the unmodulated region. Beside that this would be highly unlikely for such thin films, this would give peak ratios between 3.6 and 5.9 as given by plateaus on the low carrier density site of the prediction curves. Second platinum implanted into the semiconductor could act as second donor dopant. For a hypothetical resulting doping density of 6×10^{18} cm^{-3} the step in the peak ratio prediction shifts to this injection density value and the unmodulated region would give ratios in the range of the low temperature preparation (2-3). The usual temperatures for ion implementation are considerably higher than those investigated here [407], further defined doping is a difficult tasks which requires well defined processes. A further detailed investigation over a larger wavelength range, injection densities and polarization configurations as done on the native oxide samples could help to increase validity of the prediction based discussion. Also the implementation of UHV based rotational scans would be useful to rule out the unknown influence of a reoxidation.

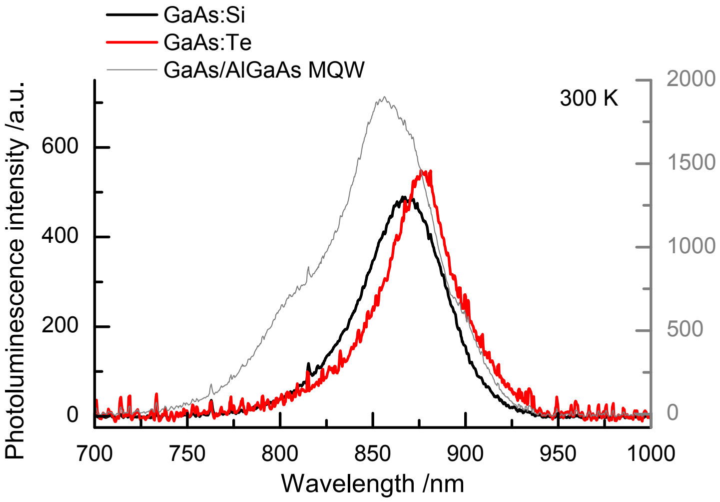

Figure 7.31.: Photoluminescence measurements at room temperature from GaAs:Si, GaAs:Te substrates with native oxide and from a GaAs/AlGaAs multi quantum well structure.

7.2. Photoluminescence

To support the discussion on the different behaviour found in rotational SHG scans on native oxide and metal coated samples, to a small extent photoluminescence measurements were performed. The measurements were recorded at room temperature (RT) with an excitation source at 527 nm (see section 5.3.5). This probes radiative transitions from the top ≈ 140 nm in the samples. Although measurements at room temperature suffer from the large $k_B T$ broadening and an insensitivity to exciton and donor transitions, they still can provide information on the band structure and alloying processes at the metal-semiconductor interface.

In figure 7.31 photoluminescence measurements from tellurium as well as silicon doped substrates are shown at comparable excitation intensities. Additionally the luminescence signal from a GaAs/AlGaAs multi quantum well (MQW) structure is displayed on the right axis of ordinates.

Both substrate signals peak at wavelengths, i.e. band gap energies, offset to the room temperature band gap of intrinsic material at 871 nm (1.424 eV). The amount of band gap narrowing for samples doped to a level of $1-2\times 10^{18}$ /cm^{-3} is expected to be -0.032 eV (891 nm) [408]. The GaAs:Te signal is shifted to 877 nm (1.414 eV). Compared to RT measurements from similar samples (e.g. [409]) the peak is more symmetric with an increased sub band gap emission up to 896 nm. On the silicon doped substrates, where the peak emission at 867 nm (1.431 eV) is shifted to the high energy side, the emission signal is even more symmetric. Broad photoluminescence peaks with sub band gap

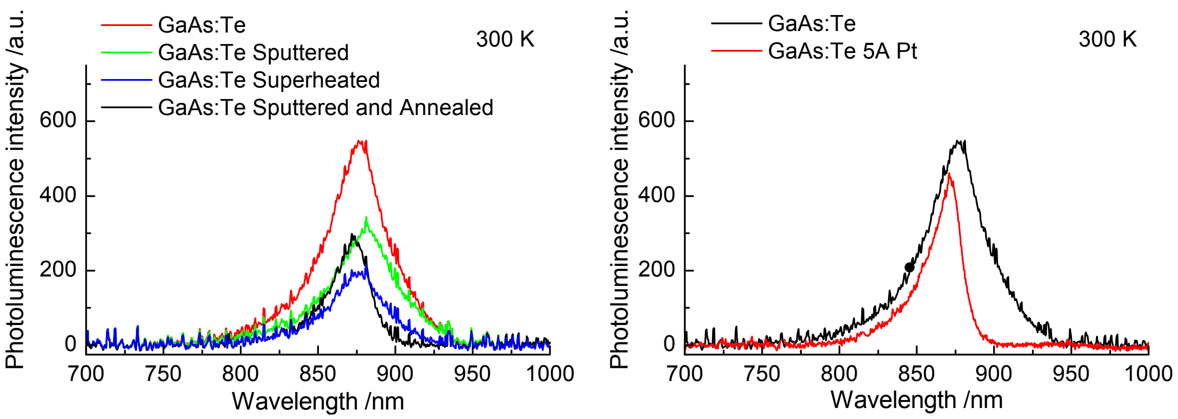

Figure 7.32.: Left: Photoluminescence spectra from GaAs:Te doped native oxide and after different cleaning and heating steps. Right: The luminescence signal of an unprocessed native oxide GaAs:Te substrate and after cleaning and deposition of 5 Å at 200 K.

emission are discussed in the scope of impurities and defect states at the surface by Gfroerer in [410]. Donor to band (DB) transitions from the silicon or tellurium gap states are shifted by 5.85 meV and 5.89 meV (874.7 nm) but also strain and dislocations at the interface to the native oxide layer can produce deep emission. The energetic position of the signal peaks can reveal information on interface indiffusion and alloying/reactivity. For example an arsenic rich interface layer in GaInP/GaAs hetero-structures is found to have a different band gap than the bulk phases of the materials [411]. In contrast to these graded interfaces, roughness or disordered alloys at the boundary between two materials again lead to a broadening of emission peaks [410].

The signal of the MQW structure is more complex. First it features a small shoulder at the expected band gap energy, but the peak intensity is shifted to higher energies too. The confinement of electrons in the multiple quantum layers evokes the broad signal at 800 nm. At same excitation energy the luminescence intensity from this sample is approximately three times stronger than that from the other two semiconductor samples. The relevant difference opposed to the other samples is, that the structure is grown on an undoped (100) substrate (see also the corresponding rotational scans in appendix C.3.5). The PL intensity is a measure of the efficiency and the density of radiative recombinations in the sample. A depletion layer, with its spatially separated holes and electrons is therefore known as a 'dead layer'. Its strength and depth significantly affects the measured intensity.

Surface treatment processes like ion bombardment and tempering consequently change the emission behaviour of the semiconductor samples (left side of figure 7.32). After sputtering at standard cleaning process parameters, the GaAs:Te emission red shifts at reduced intensity. This expresses the change and degradation of the interface quality which often goes along with an increase of (non-radiative) surface recombinations. A superheating of the GaAs surface at which gallium strongly accumulates at the surface, produces comparable PL signatures at even lower intensities. In contrast, a defined sputtering and annealing preparation with a LEED verified surface reconstruction emits light with a sharp spectral slope at the band edge and a peak position (873 nm) closer to the substrate band gap. But the intensity is still well below that from the native oxide covered samples. The later effect may arise from a reoxidation as the measurements were performed exposed to air.

After deposition of platinum also the intensity partially recovers (right side of figure 7.32). From the peak width and shape the Pt samples suggest an increase of interface quality compared to the native oxide samples. The expected reduced intensity upon an increased depletion layer at a GaAs-Pt Schottky barrier may be counteracted by a reduced number of defect states which determines the amount of surface recombination. Both effects couple in a complex way [410].

7.3. Summary

In this chapter the static second order nonlinear properties of differently doped GaAs(100) substrates and platinum covered samples were investigated. The contribution of different regions in the (hetero-)structures like bulk, depletion layer and surface and interface regions were examined and related to possible morphology effects like diffusion and contact roughness and chemical reaction like alloying. Complementary photoluminescence experiments at room temperature supported the findings.

Subject to the polarization configuration, the rotational SH scans could be reproduced by an isotropic complex component and one to three sinusoids. These themselves could be associated with different nonlinear tensor elements of the different sample regions. The isotropic part which formally is related to depletion and surface terms (dipole approximation) was found to be linearly dependent on the electric field in the depletion zone with a zero or at least negligible intercept. As suggested by Germer et al. [1] a specific surface term does not contribute significantly to the obtained SHG data. But even though the phase matching and the depletion field effects which strongly respond to changes in the surface states make SHG on these samples quite surface sensitive. By studying rotational scans at different wavelength and beam polarization configurations it was possible to calculate tensor element ratios and the dispersion behaviour in the accessible photon energy range of the femtosecond light source. The substrates doped with silicon and tellurium showed different properties concerning the dispersion relation and SHG efficiency but also in photoluminescence measurements.

The removal of the oxide layer, preparation of a well defined surface reconstruction and the deposition of platinum brought distinct changes to the SHG response. Next to variations in SHG intensity, an increase in anisotropy (peak ratio) could be observed. Comparative measurements on reconstructed samples without platinum and on samples with an oxide interlayer allowed an assignment of the observations to the formation of a direct platinum GaAs interface (Schottky barrier). The strength of these effects depend on the substrate temperature at the evaporation process and the deposited metal thickness. At cryogenic temperatures the insufficient surface mobility inhibits the formation of a high quality interface. At room temperatures the strongest changes in SHG scans were found. Elevated temperatures of 500 K and above enabled an increase of alloying and diffusion processes which again deteriorate the interface. Qualitatively these conclusions were supported by peak ratio predictions based on the depletion model and from photoluminescence measurements. Although the latter method was not much sensitive to changes in evaporation temperatures.

Also small tilts in the crystallographic plane can be measured by rotational SHG. They manifest in shape of a further reduction in symmetry which can be modelled by additional sine components.

For further validation and as reference also rotational measurement on (111) faces and undoped multi quantum well structures were performed (appendix C.3.4 and C.3.5).

8. Results: Time-Resolved Measurements

The static SHG experiments on native oxide covered and metal interfaced silicon and tellurium doped GaAs samples discussed in the previous chapter, show an interesting behaviour of the non-linear optical response upon changes in the depletion field and interface properties. One remaining open question is to what extend the claimed self modulation of the probing laser pulse can affect the SH response within the $30 - 50$ fs pulse duration with respect to carrier drift velocities.
To address the dynamics of the processes involved, pump and probe measurements as described in chapter 5.3.2, were performed to monitor the temporal evolution of the SH intensity. Following a discussion on signal processing, the first part of this chapter discusses these results under the topic of carrier dynamics, while the second part covers the weak oscillatory modulation of the time-resolved data related to coherent phonon excitation.

8.1. Signal Processing

In rotational SHG experiments the incoming fundamental beam is chopped, thus the lock-in amplifier directly monitors the photo current from the PMT, related to the intensity of the non-linear radiation. This signal normed to the square of the incoming fundamental beam intensity takes the form of a non-linear reflection coefficient $R = \frac{I(\Omega)}{I^2(\omega)}$. Time-resolved measurements monitor the change of this factor. For a better comparability the first step in data processing is thus the normalization in form of:

$$\Delta R_{rel.} = \frac{|\Delta R|}{R} = \frac{|R_p - R|}{R}, \tag{8.1}$$

where R_p refers to the pump modulated SH reflection of the probe beam. The pump chopped / lock-in amplifier set-up experiments yield $|R_p - R|$. Here the absolute SH

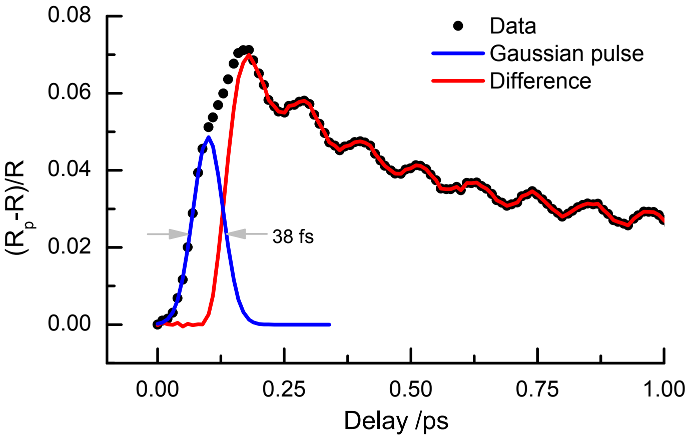

Figure 8.1.: Time-resolved SHG trace showing an autocorrelation feature on its rising edge (black dots), the corresponding Gaussian fit (blue curve) and the processed data after subtraction of the fit (red curve).

reflectivity R has either to be taken from accompanying rotational scans or by estimation using the findings of the previous chapter. Scans recorded with the shaker / storage oscilloscope based apparatus or with a probe chopped lock-in setup give R_p at positive and R at negative pump delays directly. From these parameters the normalized relative change signal $\Delta R_{rel.}$ can be constructed.

The next step is the potential removal of what hereafter is referred to as an autocorrelation feature. Figure 8.1 shows a time-resolved SHG scan (black dots) with such an autocorrelation feature, which can be fitted by a Gaussian (blue curve) with a fixed width corresponding to the laser pulse duration as determined by a FROG measurement. It is most likely related to energy transfer into the autocorrelation signal at pump delays in the range of the pulse width (cf. section 3.2.1 and see the inset of figure 5.17) or to a coherent coupling with the pump pulse. Its intensity varies with the choice of experimental parameters. Only at datasets with a distinct shoulder in the rising edge of the signal allowing an unambiguous localization of the pulse, the removal procedure is applied.

The remaining data is then fitted by a combination of a mono- or biexponential convergence function, one to two exponential decays and an optional constant offset:

$$fit(\tau) = \sum_{i=1}^{2} -A_i^{ex} \cdot exp\left(-\frac{\tau}{t_i^{ex}}\right) + \sum_{j=1}^{2} A_j^{dec} \cdot exp\left(-\frac{\tau}{t_j^{dec}}\right) + A_0 \qquad (8.2)$$

The number of exponentials in the fit is kept as low as possible without losing a significant

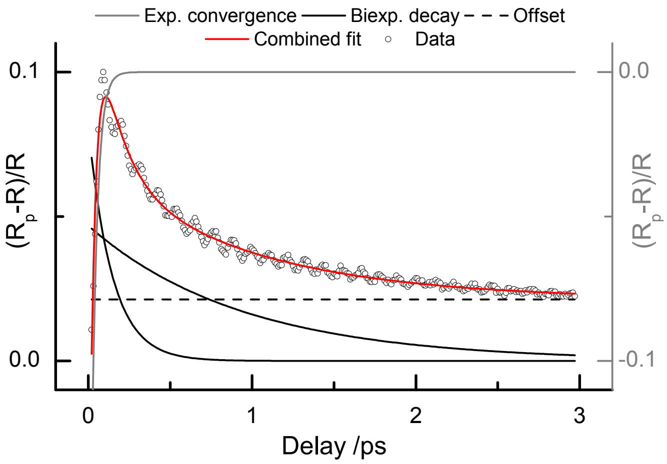

Figure 8.2.: Fit of the dataset shown in figure 8.1 after removal of the autocorrelation feature. The rising edge is fitted by a single exponential convergence function, while the relaxation is modelled by a biexponential decay and a constant offset. The outcome is a reconstruction of the signal at $R^2 = 0.9823$.

amount of determination. The initial guess of fit parameters is done by visual inspection of the curve. The offset represents another decay process with a very long lifetime compared to the temporal range covered by the dataset, which otherwise can only be poorly fitted. Figure 8.2 shows the combined fit (red curve) of the data set from figure 8.1 and the individual excitation (grey curve), decay (black curves) and offset components. The fit quality reaches a R^2 of 0.9823.

Processing of the phonon signal contribution

The minute oscillatory modulation of the transient SH signal is extracted from the data by subtracting the result of the fit according to equation 8.2. Residual low frequency components which mostly origin from an imperfect fitting at sharply peaked turning point after the initial excitation are then removed by applying a digital high pass filter. Also components beyond the Nyquist limit are removed by a corresponding low pass filter. Then linear prediction singular value decomposition (LPSVD) is applied to determine the initial guess for the subsequent fit. Originally the LPSVD technique was used in the field of nuclear magnetic resonance spectroscopy (NMR) to analyse the free induction decays, but as it allows the reconstruction of the initial amplitude and phase also from noise signals (in combination with Cadzow filtration) it seemed to be a good choice to fit the decay of coherent phonons too. Details on this method and their performance have been published [412] (see also references therein). In most cases the results of LPSVD are already of very good quality. In the next step the $4N$ parameters of the N guessed phonon modes (each characterized by its amplitude, phase, frequency and lifetime) are iteratively fitted in spectral and time domain. In an alternating fashion first the frequency and lifetimes of all modes are kept constant and the other parameters are fitted by a nonlinear least square method to the time signal. Afterwards the frequencies and lifetimes are fitted to the real and imaginary part of a FFT spectrum obtained from the time signal after apodization while the amplitude and phase are kept constant. Iterations of these procedure are performed until the targeted quality has been reached. The iterative fit method was previously also applied by Chang [150].

8.2. Carrier Dynamics

8.2.1. GaAs:Si

In time-resolved measurements the number of adjustable experimental parameters increases, as not only the wavelength, the polarization and power of the incoming probe beam and the polarization of the emitted SH signal can be varied, but also the power and polarization of the pumping beam and the azimuthal alignment of the sample. Based on the discussion so far, it would be optimal to probe the dynamics of the surface and interface SHG processes at azimuthal angles where the bulk contribution term B_2 is zero. For technical reasons, this is generally not possible. The absolute SH signal at the $\langle 001 \rangle$ and $\langle 010 \rangle$ directions is to small to uncover its temporal change with an acceptable SNR ratio, especially when also the phonon modulation should be revealed. Further an imperfect polarization purity of the probe has its biggest influence at these rotational orientations. Instead time-resolved scans are usually recorded at the lobes in $\langle 011 \rangle$ and $\langle 0\bar{1}1 \rangle$ directions. Figure 8.3A shows two scans at 860 nm in so called ppp and spp configuration, where the last letter indicates the polarization of the pump beam. Figure 8.3B denotes the samples azimuthal alignment, at which in both configurations the corresponding higher intensity peak is probed. These azimuthal positions are referred to as HP-1, as they denote the first higher intensity peak at each polarization configuration. Correspondingly the lower intensity peaks are labelled as LP-1.

Both measurements show a similar temporal curve shape with a biexponential excitation to an offset within the 6 ps scan range. The relative change of SHG reflectivity reaches in both configurations approximately 4.3 - 4.5 % of the unperturbed signal. The pump intensity in both scans is the same and the carriers induced by the probe pulse differ only

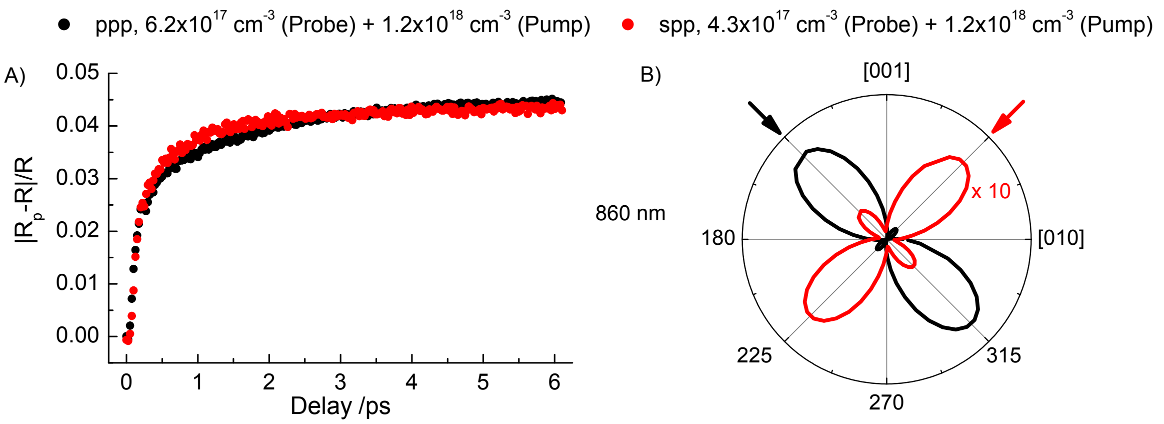

Figure 8.3.: A) Time-resolved relative SHG intensity measurements on native oxide covered GaAs:Si in p-in, p-out, p-pump (ppp) and s-in, p-out, p-pump (spp) configurations at 860 nm and identical beam power. B) Static rotational scan under the same probe beam conditions, indicating that in both time-resolved measurements the respective high peaks were investigated. The excitation pulse width is 35 – 40 fs.

slightly due to the different Fresnel coefficients for s- and p-polarization. The sharper rising edge of the spp signal suggests a faster underlying process, eventually due to the stronger relative change of injected carriers.

At 800 nm the anisotropy and the difference in R decreases (figure 8.4B), while the pump induced transient perturbation increases to 5.4 % for the ppp case and decreases down to 2.7 % for spp (figure 8.4A). Similar to the rotational experiments discussed before, the beam intensity at the smaller wavelength is much larger. Here the probe itself induces already enough carriers to completely screen the static depletion field, while at 860 nm the probe generated hot carrier density is in the 10^{17} cm^{-3} range which lays in the unperturbed range according to the Germer model. The 800 nm excitation transients exhibit different characteristics compared to those at longer wavelength. The two-stepped excitation process is faster, creating a peak in the waveform around 1 ps and a subsequent slower decay to an offset.

Looking at the pump and probe scans in the $\Delta R = |R_p - R|$ scale it can be seen that the absolute change of the non-linear reflection coefficient is stronger at 860 nm and that the ratio between ppp and spp configurations is considerably larger at 800 nm (≈ 10) than that at 860 nm (≈ 4) (figure 8.5).

To classify the relative signal peak intensities, their different waveforms and coupled to these, the lifetimes of excitation and decay processes, a series of measurements with varying pump power was recorded (figure 8.6). A central wavelength of 810 nm was chosen as it allows to access the higher range of injected carrier densities unavailable

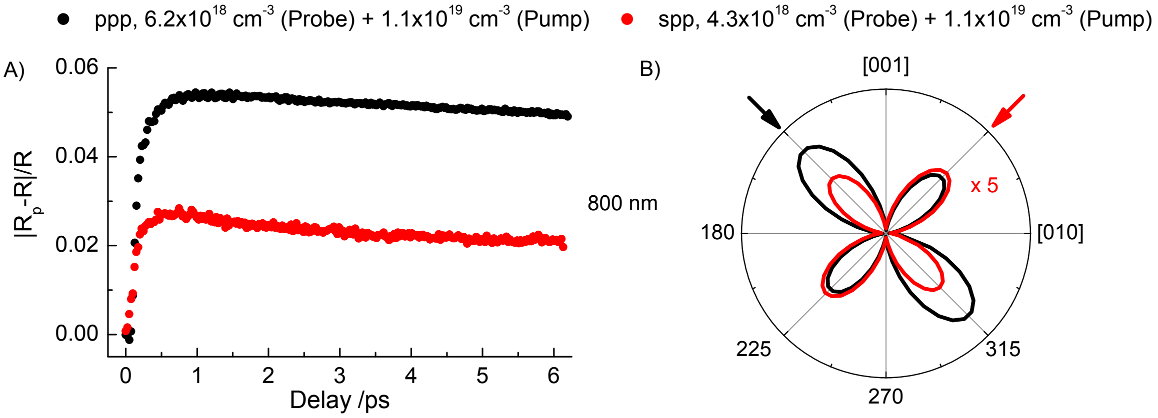

Figure 8.4.: A) Time-resolved relative SHG intensity measurements on native oxide covered GaAs:Si in p-in, p-out, p-pump (ppp) and s-in, p-out, p-pump (spp) configurations at 800 nm and comparable beam power. B) Static rotational scan under the same probe beam conditions, indicating that in both time-resolved measurements the respective high peaks were investigated. The excitation pulse width is 35 – 40 fs.

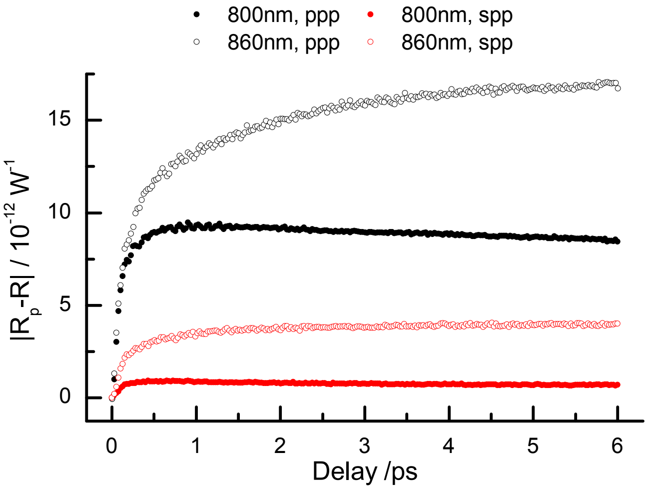

Figure 8.5.: Time-resolved SHG measurements on native oxide covered GaAs:Si at 800 nm and 860 nm for ppp and spp beam polarization configuration. The sample is aligned to the respective higher intensity peak of the corresponding rotational scans (HP-1). Displayed is the absolute magnitude of change in R. The excitation pulse width is 35 – 40 fs.

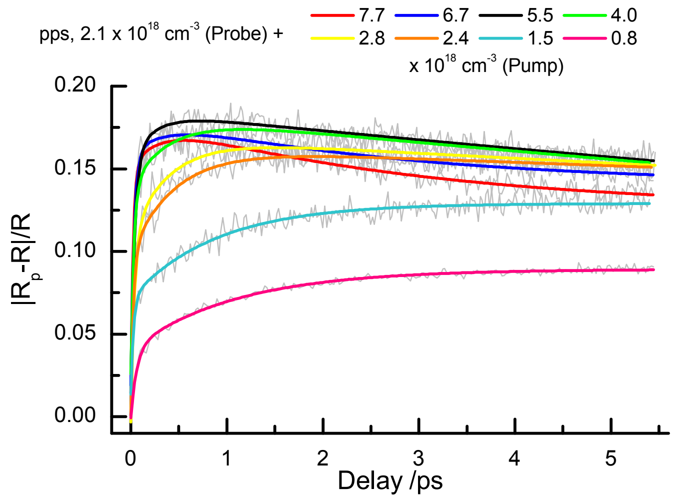

Figure 8.6.: Relative change of the non-linear reflection coefficient upon different levels of pump induced carrier injection. The measurements where performed at 810 nm and constant probe carrier injection level of 2.1×10^{18} cm^{-3} at HP-1. The excitation pulse width is $35 - 40$ fs.

at the large wavelength end of the tunable laser spectrum. The probe carrier density in these experiments was kept constant at 2.1×10^{18} cm^{-3}. The signal undergoes a strong change upon increase of pump power, from a biexponential convergence with large lifetime of the second process at low carrier densities to a peaked waveform with subsequent decaying. Also the maximum displacement of $\Delta R_{rel.}$ from its unperturbed value passes through a maximum. It is remarkable that while the waveforms of the previously discussed measurements (figures 8.3 and 8.4) fit well into this progression, the relative change of reflection in the high power 800 nm measurements is much smaller. This is shown in figure 8.7A. The black filled dots represent the data from 810 nm data set, showing the monotonic increase in peak $|R_p - R|/R$ up to a total carrier density of about 6×19^{18} cm^{-3} where a saturation sets in. The open circles show data from other experiments in the same wavelength range and different beam power configurations. The additional data suggests that for total carrier densities larger than 1×10^{19} cm^{-3} the relative peak intensity of pump and probe traces drops again. Also the 860 nm scan at the lower end peak carrier density range as well as the 800 nm signal (red filled dots) fit into this trend.

But already small deviations in the pump and probe beam focus and spot overlap on the sample surface affect the total carrier density strongly. A similar effect on the measured signals have different pump and probe ratios. The differential detection scheme of the chopper / lock-in amplifier set-up requires an external normalization, which makes the

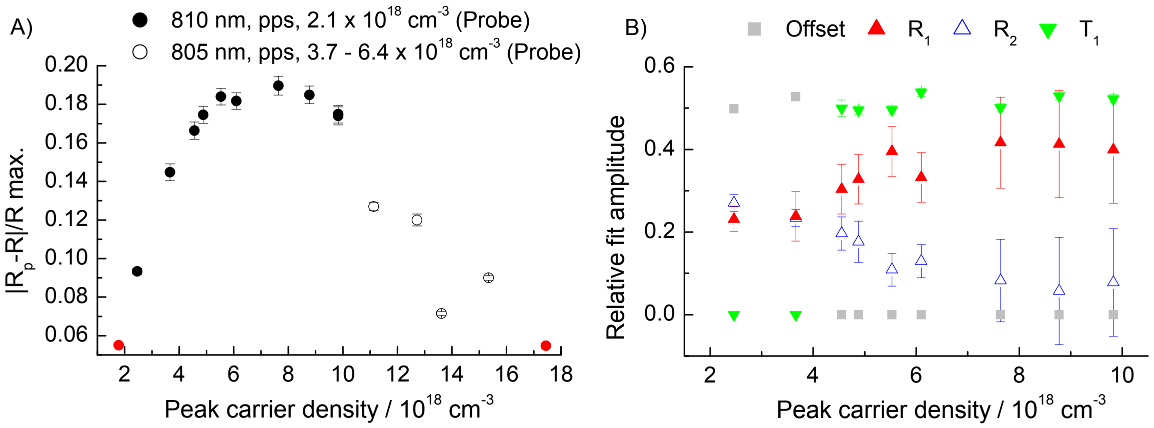

Figure 8.7.: A) Peak change of $|R_p - R|/R$ on native oxide covered GaAs:Si at HP-1 orientation for a measurement series at 810 nm (black filled circles) and further experiments at higher carrier densities (open black circles) as a function of maximum injected carrier density by pump and probe pulse at zero delay. Additionally the ppp scans at 800 nm and 860 nm are shown. The displayed error bars represent the error due to noise. B) Relative intensities of the excitation and decay mechanisms used to fit the waveforms of the 810 nm experiments. The error bars represent the uncertainty of the fit. The excitation pulse width is 35 – 40 fs.

data prone to long-term laser power and alignment stability errors. The first two effects change the waveform completely, while the latter affects its relative intensity only. Thus the comparison of results between different experiments can be a delicate task.

For this reasons figure 8.7B displays the contribution of the exponential excitation and relaxation processes used to fit the 810 nm data only. The graph shows the relative amplitudes of the exponentials normed to the complete fit (the sum of A_i^{ex}, A_j^{dec} and A_0 of equation 8.2 .

At low carrier densities the signals final values are fitted by a constant offset, the two excitation processes are of nearly same impact. With rising carrier density the slow second excitation process R_2 monotonically looses relevance down to 10 %, while the fast process R_1 increases and finally settles in the range of 40 %.

The lifetimes of the three processes R_1, R_2 and T_1 are displayed in figures 8.8A, B and 8.9. The values from the 810 nm scans are shown as filled triangles. To increase the statistical validity of the fits, also data from further experiments with appropriate pump and probe beam properties are included (open triangles). The lifetimes of these are not hampered by potential normalization errors. The first excitation process R_1 shows a weak carrier concentration dependency. While at densities larger than 4×10^{18} cm^{-3} it levels off at a value of 35 ± 2 fs, it increases to $60 - 70$ fs at low carrier densities. With respect to the other processes it may be fitted by an exponential decay function.

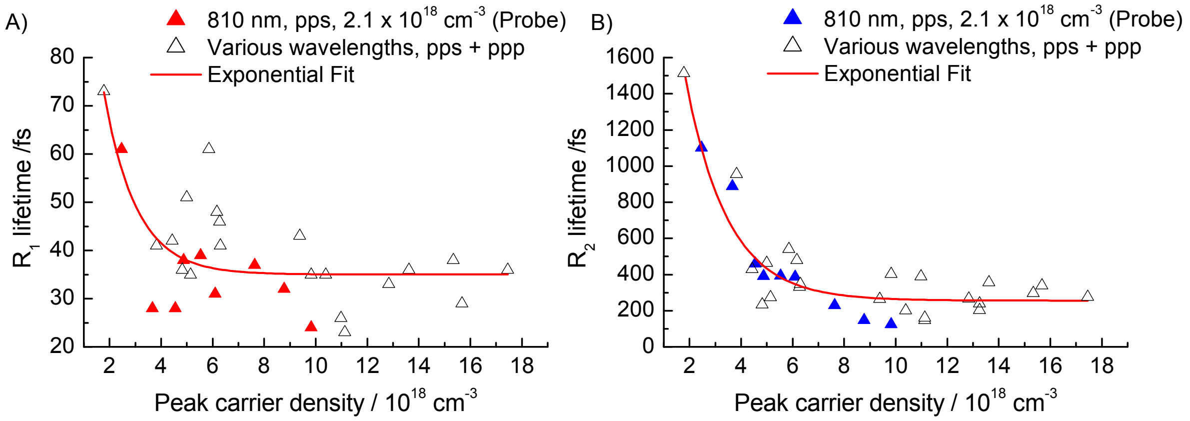

Figure 8.8.: Lifetimes of excitation processes R_1 and R_2 as a function of peak injected carrier density on native oxide covered GaAs:Si at HP-1 azimuthal orientation. The excitation pulse width is $35 - 40$ fs.

However the quality of this fit is low. The rather large scattering of R_1 values results from the short lifetime of this process and thus the small number of datapoint (The standard delay step is $20 - 25$ fs. It results a zero carrier injection limit of 154 ± 105 fs and a rate of $1.26 \pm 0.53 \times 10^{18}$ cm^{-3}. A similar but more unambiguous behaviour can be observed for R_2. The exponential fit is characterized by an amplitude of 3.8 ± 0.7 ps and an exponential constant of $1.63 \pm 0.2 \times 10^{18}$ cm^{-3}. The high carrier limit of this processes lifetime is 256 ± 27 fs.

Finally and with the highest fit quality also the carrier density dependency of the T_1 decay process can be modelled by an exponential decay. As a decay contribution to the transient SH signal within the 5.5 ps scan range can only be seen at carrier densities larger than 4×10^{18} cm^{-3}, the exponential function is offset to those of the excitation mechanisms. From this fit a zero carrier injection limit lifetime in the range of 9.6 ± 0.1 ns can be estimated. On the large carrier density side it reaches a level of 18 ± 3 ps. The decay rate of $9.1 \pm 2 \times 10^{17}$ cm^{-3} is stronger than those of R_1 and R_2.

No clear dispersive effect in the time-resolved SHG measurements at the HP-1 azimuthal positions could be observed (cf. Appendix C.4.1). Both the relative intensity as well as the waveform can be attributed to carrier injection properties.

Before the discussion and interpretation of the individual excitation and decay processes, the transient properties at the lower intensity peak (LP-1) are investigated. Analogous to the procedure at HP-1 figure 8.10A shows a set of measurements at LP-1 orientation with varying pump power. The change in SHG is with 2.5-7.5 % only half as intense as at HP-1, associated with this, also the noise in these scans is stronger. All transients can

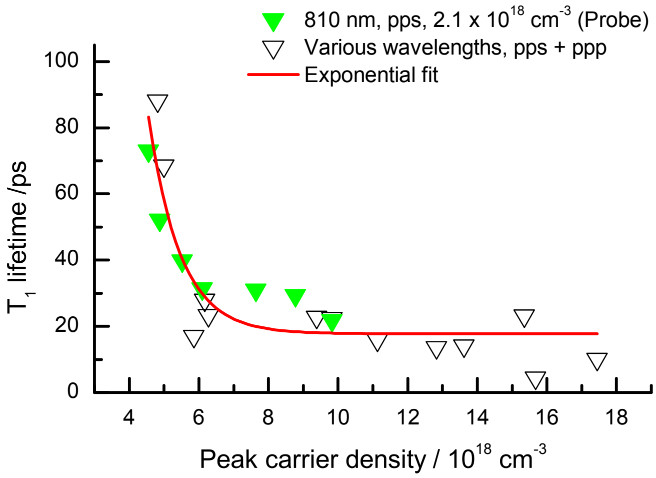

Figure 8.9.: Lifetime of the decay process T_1 as a function of peak injected carrier density on native oxide covered GaAs:Si at HP-1 azimuthal orientation. Notice the different scale compared to figure 8.8. The excitation pulse width is $35 - 40$ fs.

be modelled by a single excitation and decay exponential in combination with a constant offset. They too show the behaviour observed at HP-1 to run through a maximum in $\Delta R_{rel.}$ but at higher carrier densities in the range of 10^{19} cm^{-3}. In this carrier region the signal has a much more peaked shape than HP-1 measurements. The set of experiments shown here where done at 830 nm, which results from a possible dispersive effect found in the LP-1 signals as shown in figure 8.10B. It plots time-resolved SH curves at various central wavelengths between $800 - 830$ nm and medium to high intensity levels, recorded with the regular pump chopped lock-in amplifier set-up. At large wavelengths the signals show the single peak curve shape. With decreasing wavelength the T_1 decay process gains dominance accompanied with a decrease in lifetime. Between $807 - 810$ nm the SH transients change their shape creating an intermediate signal minimum and a consequent re-rise of intensity. To investigate this peculiar behaviour further measurements with a probe chopped lock-in setup were performed at both sides of peak shape change region. The absolute SHG intensity detection scheme is less sensitive but on the other hand allows the explicit determination of the sign of the transient SH change (figure 8.11A). It reveals that the initial excitation process actually decreases the SH intensity. The second process which before was taken as a decaying process to restore the SH radiation back to its unperturbed level, describes a different process here. While at 810 nm the process actually brings the signal back to the region of static SH intensity it overshoots this level at wavelengths smaller than that. This makes a third, real decaying process necessary which is modelled in the scans shown here by the offset. The figure shows also

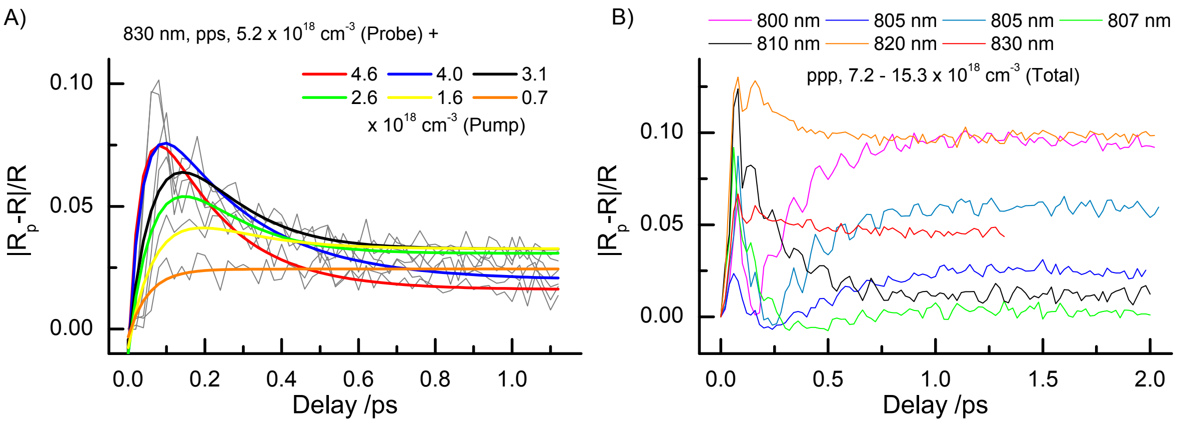

Figure 8.10.: A) Transient change of $\Delta R_{rel.}$ on native oxide covered GaAs:Si at LP-1 orientation for different pump beam intensities and the corresponding fits. B) Time-resolved SH signals at the same sample configuration for different wavelengths. It shows a monotonic change of signal from a single peaked shaped at high wavelengths to a more complex behaviour at low wavelength.

the signed change of $\Delta R_{rel.}$ for a HP-1 measurement, revealing a temporary decrease in SH intensity in this configuration, too. This will be discussed in detail further down in this chapter.

With this knowledge the scans from figure 8.10B can be unfolded to obtain their true peak shape shown in figure 8.11B. Based on this data and further measurements at different wavelengths, the peak $\Delta R_{rel.}$ as a function of carrier density is plotted in figure 8.12A. In the 830 nm data set the plateau formation at 10^{19} cm^{-3} can be seen, but the additional measurements at higher carrier densities give inconclusive responses not allowing a secured interpretation of the injected carrier density dependency. The relative fit amplitudes of the three processes used to model the transient LP-1 SH data are shown on the right side of figure 8.12. Most prominent are the large amplitudes and error bars of the R_1 process which are related to the fitting of the steep and short lived initial excitation in the signals. The second process, here still labelled as decay T_1 gains importance in the signal with increasing carrier density as much as the constant offset contribution diminishes.

The fitting amplitudes for excitation curves at different wavelengths (figure 8.11) are plotted in figure 8.13A. It shows the drop of the long-lifetime component and a dip of R_1 around the characteristic wavelength at 807 nm. The high carrier peak concentration in the region of 1.5×10^{19} cm^{-3} at which this effect is observed (figure 8.13B) could be an indication of a photo injected transient degeneracy type behaviour, where the Fermi level is shifted into the partially filled conduction band. Two counteracting processes

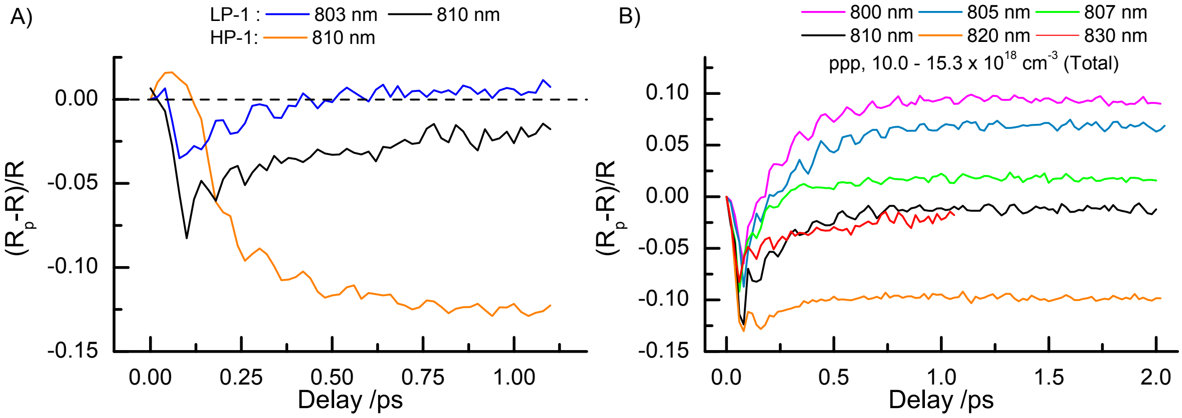

Figure 8.11.: A) Signed transient change of $\Delta R_{rel.}$ for different wavelength at HP-1 and LP-1 on native oxide covered GaAs:Si. The scans are obtained by probe chopped lock-in measurements. B) Unfolded transients from figure 8.10B.

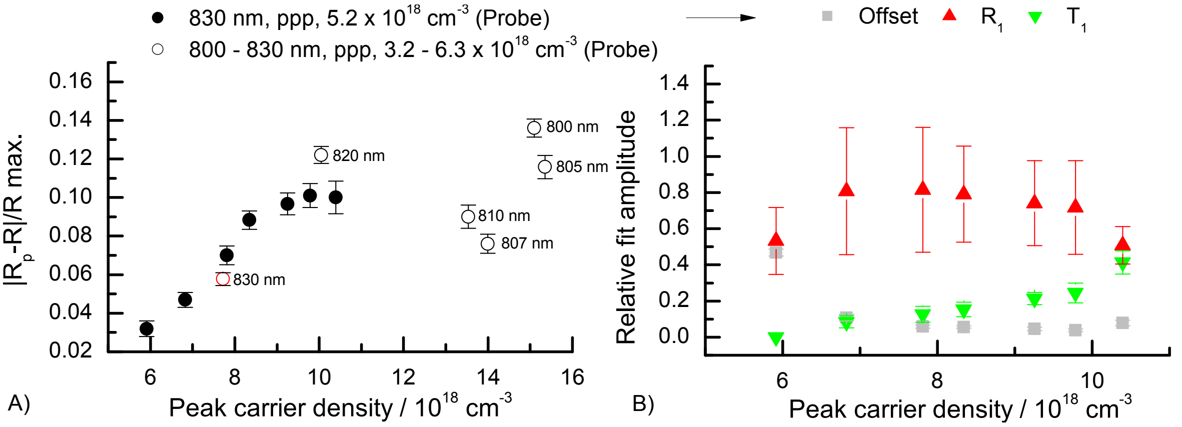

Figure 8.12.: A) Peak change of $\Delta R_{rel.}$ on native oxide covered GaAs:Si at LP-1 orientation for a measurement series at 830 nm (black filled circles) and further experiments, especially at higher carrier densities (open black circles) as a function of maximum injected carrier density by pump and probe pulse at zero delay. The displayed error bars represent the error due to noise. B) Relative intensities of the excitation and decay mechanisms used to fit the waveforms of the 830 nm experiments. The error bars represent the uncertainty of the fit. The excitation pulse width is 35 – 40 fs.

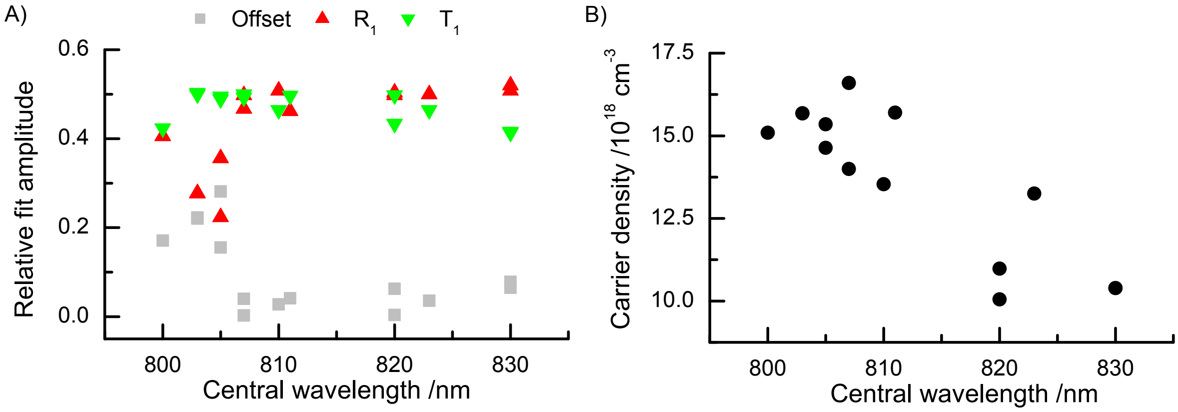

Figure 8.13.: A) Relative intensities of the R_1 andT_1 processes as well as the long delay offset from time-resolved scans at various wavelengths shown in figure 8.11B. The data shows a dip around 807 nm. B) Peak injected carrier density of the measurments of A). In the dip region the intensity is constant.

determine the behaviour of near band gap absorption: The band filling responsible for the Fermi shift (Burnstein-Moss effect) induces a blue shift of absorption while band gap renormalization moves the absorption edge to larger wavelengths [13, 408, 413]. Dominant for n-doped GaAs is the first process [414]. So a transient alteration of the band edge energy towards 807 nm could be responsible for the turn over of the SHG dynamics at wavelength smaller than this. A similar effect in the high carrier regime was found in transient absorption measurements by Shah (cf. chapter 4.13 (figure 4.13) [198]. The modification of the band edge with varying free carrier density is also shown in figure 7.2) which plots the absorption coefficient at different dopant levels.

Similar to the higher intensity peak data the lifetime of the rapid first excitation process does not exhibit a narrow distribution. It scatters roughly around the high carrier density limit of the corresponding HP-1 with a mean value of 27 ± 12 fs (cf. figure 8.14A). The lifetimes of the T_1 process fit nicely to those of R_2 at HP-1 (figure 8.14B), with a mean value of 233 ± 91 fs. This confirms the treatment of T_1 rather as a secondary excitation process equivalent to R_2. Due to the weak signal to noise ratio at weak beam power it was not possible to obtain useful information for low carrier densities.

In summary three processes were identified on native oxide covered GaAs:Si samples in HP-1 azimuthal orientation (cf. table 8.1). With the help of probe chopped lock-in measurements the sign of SHG change could be determined. The rapid initial excitation and the succeeding second process both diminish the SHG intensity which is brought back to its static level by a slow relaxation process. The secondary excitation looses relevance with increasing carrier density. At the low peak LP-1 a R_1 process equivalent

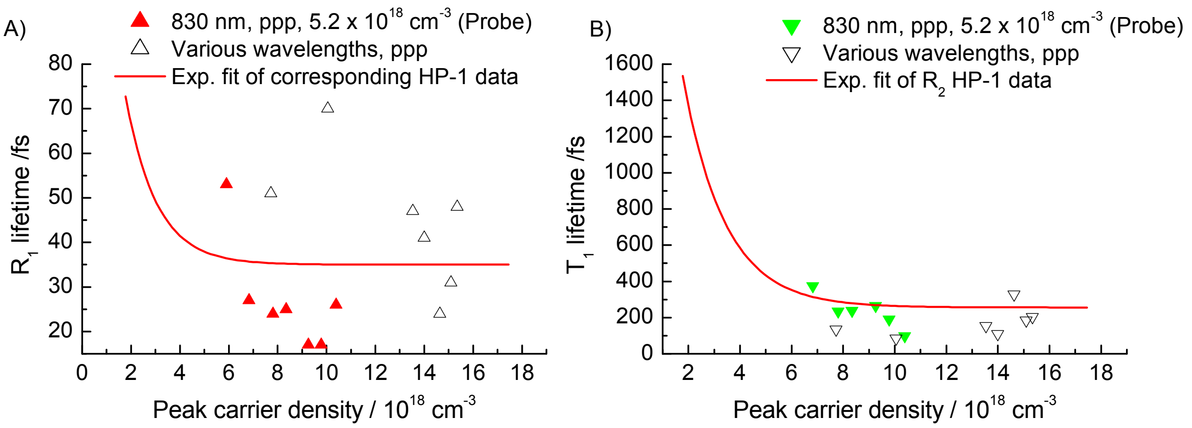

Figure 8.14.: Lifetimes of excitation process R_1 and 'decay' process T_1 as a function of peak injected carrier density on native oxide covered GaAs:Si at LP-1 azimuthal orientation.

to its HP-1 counterpart can be found with similar lifetimes and the same sign of SHG change. However the second process exhibits an opposite change of SHG. Here the combination of R_1 ,R_2 and the long lifetime component lead to a dispersive effect. The latter process could not be pinpointed and thus must be treated by an offset.

In many linear ultrafast transmission and reflection experiments on semiconductors and metals the obtained transient signals are related to carrier effects induced by the pump beam. The susceptibility terms are changed by additional free carrier absorption (eg. [11, 151]). Although their nonlinearities have been neglected in the discussion of the static rotational SHG measurements given the strong depletion field and bulk effects, these nonlinearities should be observable in time-resolved measurements monitoring the small change of SHG after carrier injection adding another term to the expression for the effective second order susceptibility (eq. 7.10). The concept of electron and hole dynamics in GaAs has been introduced in section 4.1.4. In the low to middle carrier regime ($< 10^{19}$ cm^{-3}) the initial excitation process R_1 increases with laser intensity. It's lifetime of $27 - 35$ fs is due to the convolution with the probe pulse at the lower limit of detectable time spans, so it is an upper limit. This allows the assignment to carrier injection and momentum randomization. The T_1 process at HP-1 and the long lifetime component at LP-1 respectively, with their decay behaviour may be attributed to thermalization of carriers and lattice by emission of optical phonons and finally radiative and non radiative recombination processes. The lifetime of the R_2 exponential would fit to carrier-carrier and carrier-phonon scattering events directly after the injection to establish a Fermi-Dirac distribution, but the observed different direction of SHG intensity modification make this questionable.

Alignment	Process	Low carrier density lifetime	High carrier density lifetime	Change of SHG
HP-1	R_1	154 ± 105 fs	35 ± 2 fs	Red.
	R_2	3.8 ± 0.7 ps	256 ± 27 fs	Red.
	T_1	9.6 ± 0.1 ns	18 ± 3 ps	Inc.
LP-1	R_1	-	27 ± 12 fs	Red.
	R_2 (T_1)	-	233 ± 91 fs	Inc.

Table 8.1.: Summary of process properties responsible for the transient change of SH intensity in pump-probe experiments on native oxide covered GaAs:Si. The low and high carrier injection level lifetimes are obtained by fitting the data of figures 8.8, 8.9 and 8.14. The last column indicates whether the process induced a transient increase or reduction in SHG intensity.

The second group of processes detectable in the time-resolved SHG measurements are related to the formation of free carriers indirectly. Considering again equation 7.10 theses are changes in the bulk susceptibility $\chi^{(2)}_{ijk}$, depletion field changes via $\chi^{(3)}_{ijkz}E^{depl}_z$ and directly surface symmetry break related effects $\left(\chi^{(2),surf}_{ijk}\right)$. The latter was already found to be negligible. The bulk value is affected especially at high carrier injection densities by the depopulation of electrons from the valence band. These valence electrons arise from the asymmetric bonds between adjacent gallium and arsenic so they are primarily responsible for the dipole allowed second harmonic generation in the bulk [63, 415]. Consequently a decrease of SHG intensity is expected in a time scale of the excitation pulse, both properties of the observed R_1 process. The most dominant effect is the transient screening of the surface depletion field by separation of electron-hole pairs subsequent to injection. The self photo modulation discussed in chapter 7.1 and the launching of coherent phonons by depletion field screening (TDFS, cf. section 2.4.1) require this process to be fast. The decrease in depletion field strength leads to a reduction of the isotropic parameter A_0 in the fitting of rotational SH scans (equation 7.9) and an increase of symmetry. For a higher intensity lobe this manifests in a transient relative decrease in SHG radiation, while the 90° shifted low peak gains SH intensity. This would explain the opposite signs of R_2 observed at HP-1 and LP-1. The $233 - 256$ fs lifetimes of these exponentials are in the expected range for a complete screening of the depletion field by electron and hole drift at the given dopant concentration. But for launching coherent phonons or self photomodulation the complete screening period is to long. The long-time relaxation processes can be related to diffusion and recombination ultimately restoring the static depletion field, band gap and bulk susceptibility.

Finally the inset of band filling and band gap renormalization discussed before affect the

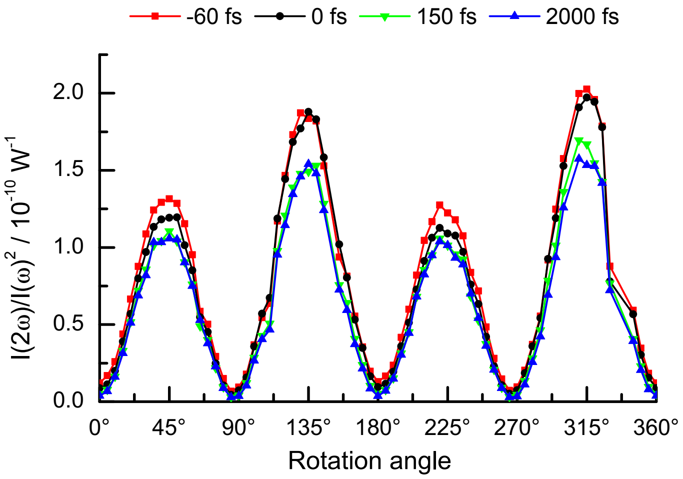

Figure 8.15.: Rotational SH scans at 810 nm on native oxide covered GaAs:Si in the presence of the pump beam at different delays. The induced peak carrier density is: 4.1×10^{18} cm^{-3} (Probe) + 4.8×10^{18} cm^{-3} (Pump). The excitation pulse width is 35 – 40 fs.

transient data in a nonlinear way by changes in absorption.

To gain more insight into the separation of transient bulk and depletion field effects a number of rotational SHG experiments in combination with the pump-probe technique have been performed. Due to the long time stability of the laser performance only selected time steps were investigated with this method. Although the SNR of this technique is lower than in pump chopped measurements, each single delay point is fitted by a complete rotational fit connecting the values at all high and low intensity peaks. Further this approach directly reveals the temporal evolution of the already familiar coefficients of section 7.1. Figure 8.15 shows rotational scans for some exemplary delay steps on GaAs:Si at 810 nm. Directly after the interaction with the rising edge of the pump pulse at zero delay the intensity at the lower lobes start to decrease. After 150 fs all peaks seem to have reached their final excited state. Fitting the rotational scans at all delay points gives the evolution of A_0 and B_2 and the phase difference between both, as shown in an absolute scale in figure 8.16. As before the anisotropic bulk dominated B_2 is initially about four times stronger than the isotropic depletion field term A_0. Both parameters decrease on a fast time scale comparable to the R_1 process, but while B_2 can be fitted by a single exponential, the decay of A_0 shows a biexponential behaviour with a larger second time constant. The isotropic component diminishes by circa 55 %, but the decrease of the stronger bulk contribution is superimposed on the otherwise expected simple intensity levelling between high and low peaks (transformation from $mm2$ symmetry to bulk $\bar{4}3m$).

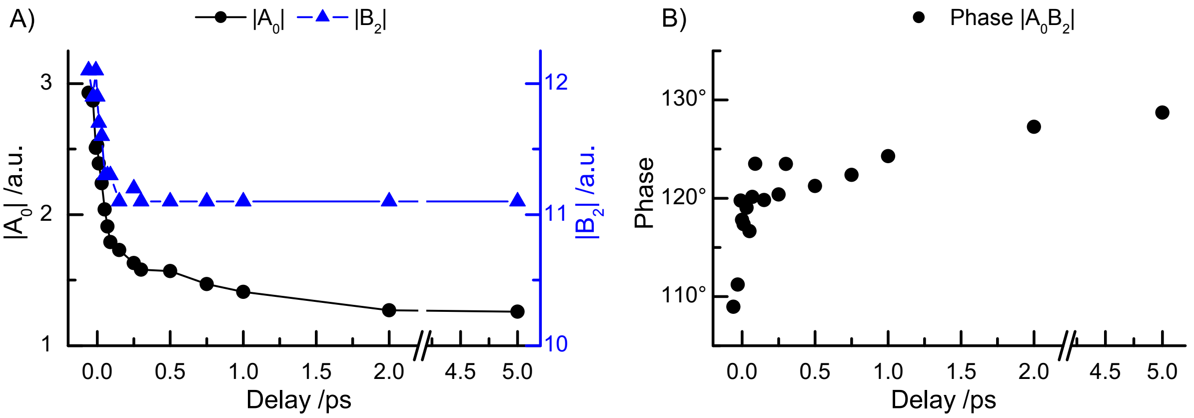

Figure 8.16.: Temporal evolution of fitting parameters and their phase difference of the rotation curves shown in figure 8.15 and at further delay points. The error of the fit is ca. 7 %.

The fitting of rotation scans confirms the assignment of bulk effects to R_1 only and the relation of depletion field screening with a combination of R_1 and R_2. This in turn implies that the measured R_1 is actual a convolution of a rapid bulk effect and an independent or related fast process changing the depletion field. So the depletion field screening can eventually be described by a quick component directly induced by the generation of a plasma in the depletion zone and a subsequent field drift of the separated electron hole pairs. This would not only explain the same lifetime of the quick bulk and depletion term but also the discrepancy discussed in the chapter on rotation scans between the fast photomodulation within the time span of the laser pulse and the much lower drift velocities (cf. section 7.1.1). The initial $|A_0B_2|$ phase at negative delays with a value of 109° fits to the expected phase angles for a self modulation at the given carrier injection density (cf figure 7.11), but the transient change up to 130° is unexpected in the context of the previously discussed static measurements. A second set of rotational scans at lower power and larger wavelength is shown in figure 8.17). Here, although the effect is small, the increase of LP-1 and LP-2 and the reduction of HP-1 and HP-2 can be observed directly. The injected carrier densities of 1.2×10^{18} cm^{-3} due to the probe and 1.8×10^{18} cm^{-3} added by the pump are far below the high carrier regime where the dispersive effect was found. The unperturbed A_0 term is larger than those at the previous experiment and decreases only by 25 %, the bulk term however changes even less. Both show the same exponential respectively biexponential delay time dependency as before. As the weak probe injects carriers below the doping level the starting phase of 150° fits nicely to those expected for the high depletion field regime (cf. figure 7.11). During the excitation it varies only slightly. Finally to draw a line

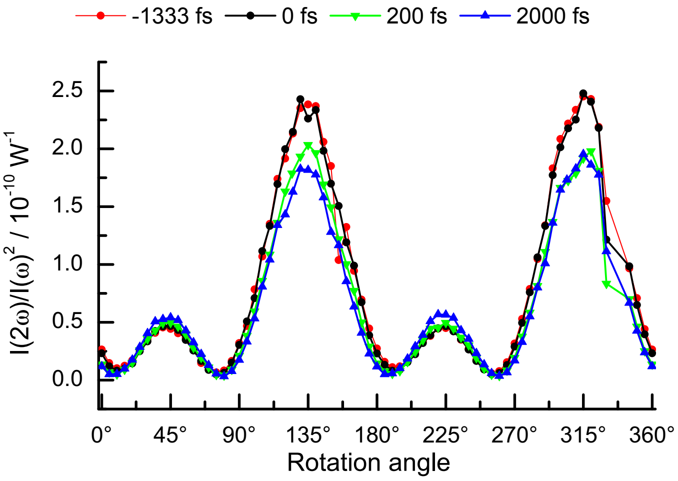

Figure 8.17.: Rotational SH scans at 850 nm on native oxide covered GaAs:Si in the presence of the pump beam at different delays. The excitation pulse width is 35 – 40 fs.

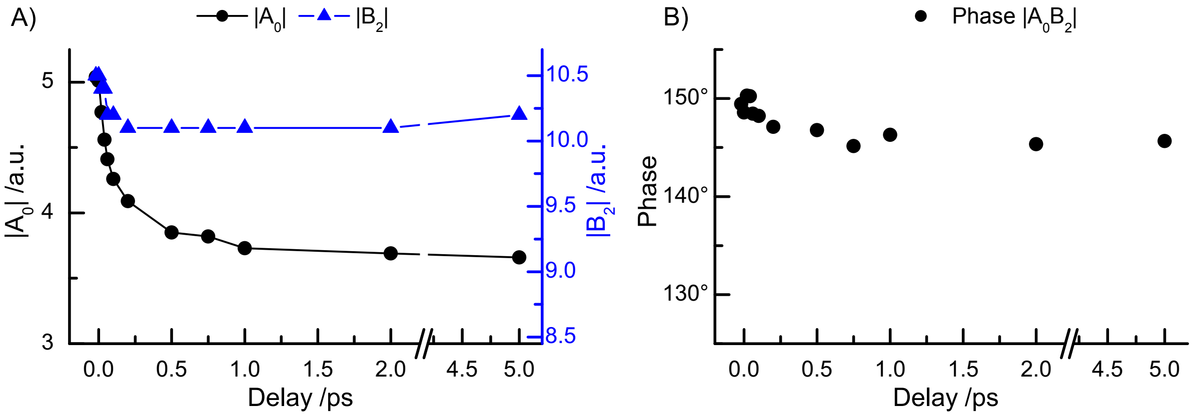

Figure 8.18.: Temporal evolution of fitting parameters and their phase difference of the rotation curves shown in figure 8.17 and at further delay points. The error of the fit is ca. 4 %

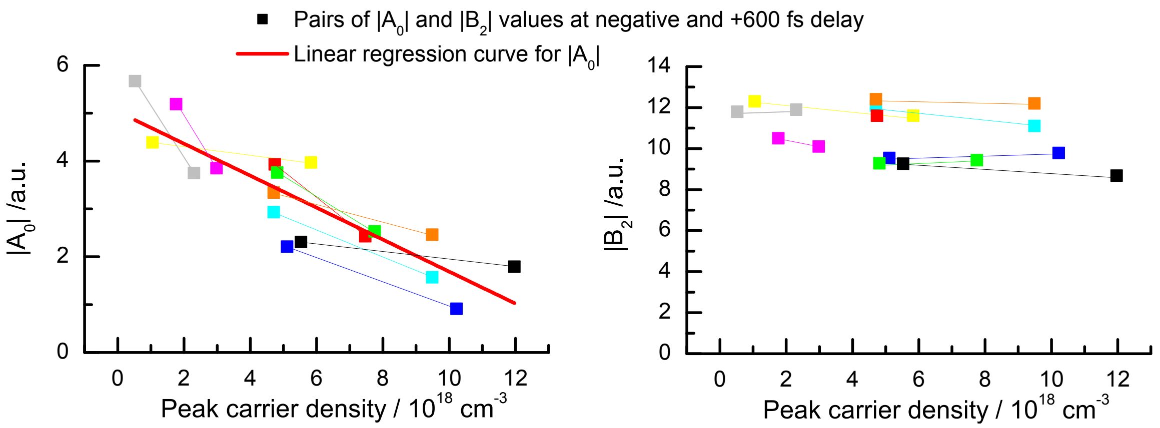

Figure 8.19.: Pairs of $|A_0|$ and $|B_2|$ fitting parameter values at negative and 600 fs delay from various measurements with different wavelength and peak carrier densities (. In average $|A_0|$ shows the same linear behaviour on total carrier densities as determined in the static optical measurements in chapter 7.1.1.

back to the static measurements plotting the fitting parameters at negative and 600 fs delays for many different experiments at varying excitation levels and wavelengths as a function of carrier density gives the established linear dependence upon carrier density and in first approximation injection independent B_2. To create this plot the negative delay value was taken as probe only injection and the value at 600 fs as combined pump and probe injection level.

8.2.2. GaAs:Te

The GaAs:Te samples already showed a distinct different SHG response compared to the silicon doped substrates in static rotational scans, although both are commercial wafers with comparable specifications. Their dynamic SHG properties are different too and will be briefly illustrated in the following section.

Figure 8.20 shows pump-probe experimental data at HP-1 and LP-1 azimuthal sample orientation for different wavelengths and excitation levels. The data is already plotted as signed change of $\Delta R_{rel.}$ to allow identification of transient increase or reduction of SH intensity compared to its unperturbed value. With the same procedure as on GaAs:Si the sign of SH scans was determined by additional probe chopped and shaker based measurements. Qualitatively the behaviour at LP-1 configuration is similar to that of the GaAs:Si with a fast initial decrease and a secondary slower process increasing the intensity of the generated second harmonic light (figure 8.20B). Also the higher power regime dispersive feature can be observed at similar spectral interval and carrier densities. The carrier density dependent peak signal amplitude (peak $\Delta R_{rel.}$) plotted as blue squares in figure 8.21A is in the expected range of 2-20 % and exhibits a weak maximum around 10^{19} cm^{-3}.

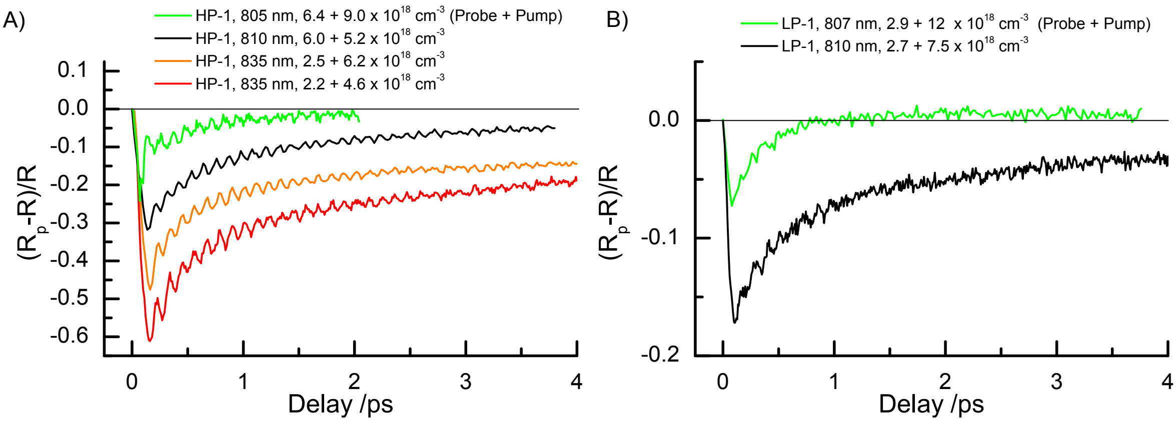

Figure 8.20.: Typical time-resolved SHG data from HP-1 and LP-1 peaks on native oxide covered GaAs:Te at different wavelength and peak carrier densities. The excitation pulse width is 35 – 40 fs.

At HP-1 however (figure 8.20A) the results strongly differ from those of the silicon doped samples (cf. figure 8.6). The signals exhibit the same strong peaked behaviour as those from LP-1. While the strongest transients (orange and red curve) may be fitted by single excitation and a biexponential decay but most scans can be described best by the LP-1 typical R_1, R_2 and an offset. At the 805 nm experiment the maximum change

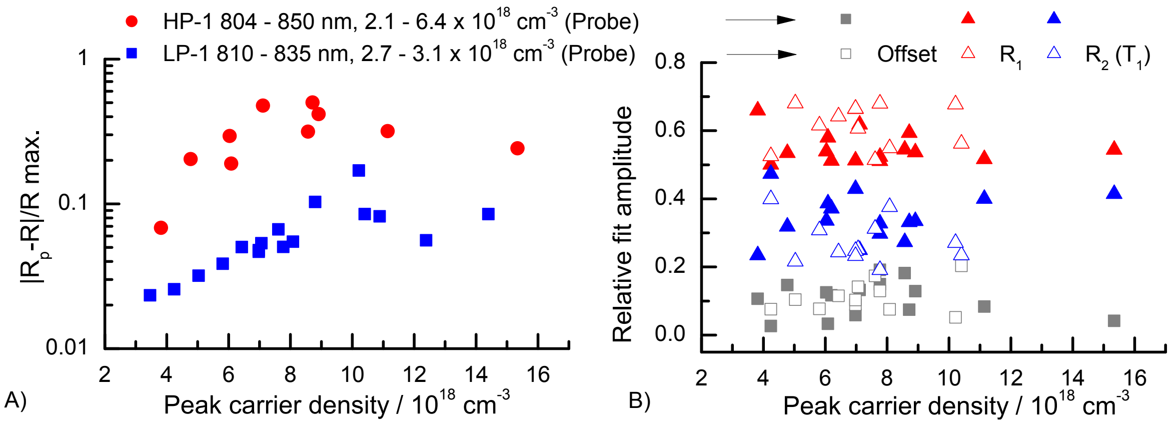

Figure 8.21.: A) Peak change of $\Delta R_{rel.}$ on native oxide covered GaAs:Te at HP-1 and LP-1 orientation as a function of maximum injected carrier density by pump and probe pulse at zero delay. The error bars are smaller than the dots. B) Relative intensities of the excitation and decay mechanisms used to fit the waveforms.

of SH reflectivity is in the common range up to 20 %, the much larger value of 45-60 % at large wavelengths is caused by the substantial weaker static SHG intensity at the high peak, which in turn was discussed before as a possibly less pronounced depletion field contribution to the SH signal (cf. chapter 7.1.2). This transient SHG behaviour is in disagreement with the discussion on GaAs:Si with respect to the depletion field screening effects. In contrast to the upward change of SHG after the initial excitation a R_2 with negative sign would be expected as a consequence of the reduction of isotropic depletion field driven SHG.

On the native oxide covered GaAs:Te samples neither in LP-1 nor in HP-1 alignment a clear carrier dependency of the relative fit function contributions could be found (8.21B). This applies also to their obtained lifetimes (figure 8.22). At both peaks R_1 is characterized by a 77 ± 30 fs rise and R_2 by a 811 ± 640 fs rise, both are not only quite imprecise but also considerably longer than the equivalent processes at GaAs:Si.

It seems that the dynamics in this sample are more complex and that the depletion field processes are convoluted with other not yet identified interface effects. Figure 8.23A compares the 835 nm TR-SHG trace in pps configuration obtained by a pump chopped experiment (red curve) with the results of a probe chopped experiment at similar wavelength and same polarization alignment (blue curve). In the latter a fast initial positive feature can be observed before the swing to a negative SH intensity change. This is not seen in the pure magnitude results obtained from standard pump chopped measurements. Mathematically the blue curve can be constructed from the magnitude results by folding the curve at 60 fs. Pump and probe beams are cross

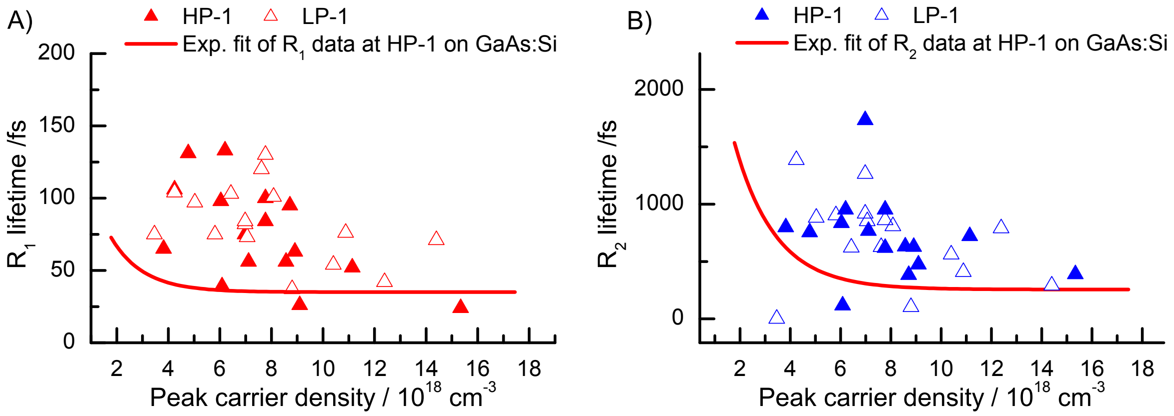

Figure 8.22.: R_1 and T_1 lifetimes of GaAs:Te oxide samples at HP-1 and LP-1 as a function of peak carrier concentration, averaged of different excitation wavelengths. The average lifetime of the first excitation process R_1 is 77 ± 30 fs, while the mean decay lifetime T_1 results in 811 ± 640 fs.

polarized to reduce the influence of an autocorrelation feature or coherent artefact as these initial features are commonly labelled (see [415] and references therein). In figure 8.23B shaker based measurements at 810 nm in pps (red curve) and ppp (black curve) are shown. The ppp data not only shows a strong AK feature but also the direction of the complete remaining signal is affected. Similar observations could not be made on GaAs:Si. Additionally time-resolved reflectivity measurements were performed on this substrate (cf. appendix C.4.2). More experiments on this issue especially by time-resolved rotational scans are currently carried out and will be published elsewhere.

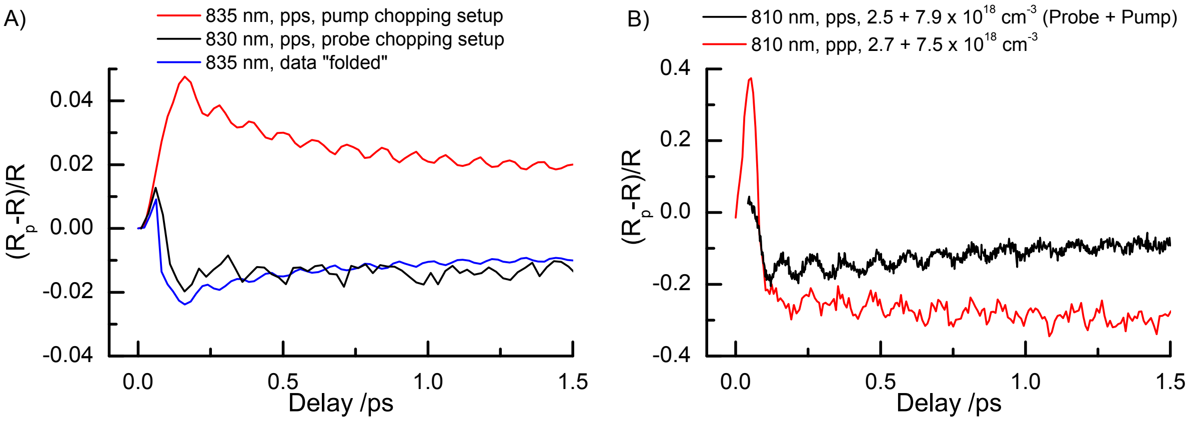

Figure 8.23.: A) Time-resolved SHG scans at 835 nm in pps configuration obtained by measurements with a pump chopped and a probe chopped setup. Both signal shapes can be transferred to each other by scaling and folding at 60 fs. B) Shaker based measurements at 810 nm with ppp and pps polarization alignment. The excitation pulse width is $35 - 40$ fs.

8.2.3. GaAs-Pt

The oxide layer removal, surface reconstruction and preparation of a metal adlayer already proved to have a strong effect on the static SHG response in rotational measurements. There the formation of direct metal-semiconductor interface with Schottky behaviour strongly increased the anisotropy between the higher and lower intensity lobes which was mainly related to a shift in the complex phase between A_0 and B_2 rotational scan fitting parameters. This section will compare the changes of TR-SHG data upon metallization at different evaporation temperatures and platinum coverages. The raw intensity of the temporal change in photo current detected by the photo multiplier is comparable at all samples investigated, but the strong increase in anisotropy would reflect as large changes in the relative scale of ΔR, which in turn would make a direct comparison of signal shapes difficult. For this reason in this section the transient data is plotted as unnormed, signed $\Delta R = (R_p - R)$.

First the GaAs:Si-Pt samples are discussed. Figure 8.24 shows transient SHG data at HP-1 (left side) and LP-1 (right side) for the 3 Å coverage at 100 K and 300 K compared to data from a native oxide covered sample at the same wavelength and comparable injection densities. At HP-1 the metal covered samples show a clear reduction of SHG change and a deceleration in all excitation and decay components. The change in anisotropy in static measurements between pure substrates and the platinum covered samples led to ca. 20 % decrease in SHG intensity at HP-1 but was constant between the low and room temperature preparation (cf. figure 7.26). In the time-resolved data however the change between those is even stronger than the difference to the native oxide sample.

Table 8.2 summarizes the properties of the parameters used to fit these specific data sets. The trend in relative amplitudes and lifetimes matches the carrier dependency of those on GaAs:Si at low carrier densities. The same behaviour was found for the anisotropy in the static rotation measurements. The noise in the transient data of the native oxide covered sample is actually a signature of the underlying coherent phonon oscillations discussed later which becomes visible after longer averaging. This signal is reduced on the metal samples and nearly not visible at the low temperature preparation. This can be related to decreased efficiency of coherent phonon launching due to the less instant depletion field change as the lifetime of R_1 is increased from 44 fs to 132 fs which is larger than the period of the dominant LO phonon mode (114 fs). Also a less pronounced coupling of phonon modes with the injected carrier plasma is expected.

At LP-1 (figure 8.24B) all signals exhibit the turnover behaviour discussed before for

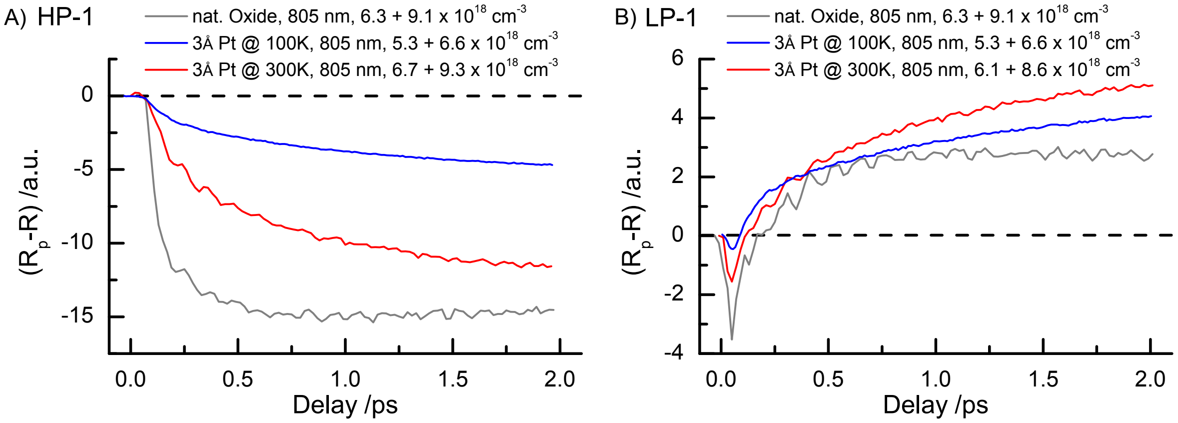

Figure 8.24.: Time-resolved SHG pump-probe data for GaAs:Si-Pt metal interface samples at different process parameters in HP-1 and LP-1 configuration along with reference data on native oxide covered samples. The excitation pulse width is 35 – 40 fs.

Sample	R_1	R_2	T_1
	Lifetime (rel. Amplitude)		
nat. Ox.	44 fs (0.71)	278 fs (0.09)	20.8 ps (0.20)
3 Å@300 K	100 fs (0.31)	766 fs (0.29)	Offset (0.40)
3 Å@100 K	132 fs (0.25)	1360 fs (0.31)	Offset (0.44)

Table 8.2.: Properties of the transient data fitting parameters (cf. equation 8.2) of the HP-1 GaAs:Si-Pt data shown in figure 8.24.

scans below 807 – 810 nm. In the same way as at HP-1 the phonon signature 'noise' decreases with metallization. The first rapid process in negative direction is affected most and could not be fitted satisfactory in the Pt covered samples. Further the subsequent rising edge shows a biexponential behaviour similar to those at HP-1 (cf table 8.3). This could eventually allow the separation of the previously proposed convolution of fast bulk and depletion field effect.

For the set of tellurium doped samples a number of reference samples were investigated to rule out nonlinear effects directly related to the sputtering and annealing as well transient nonlinear effects within the ultra thin metal layer itself. The static experiments revealed a decreased SHG efficiency with low anisotropy compared to the native oxide samples and for the sputtered sample a reduction of symmetry which was related to a different oxide growth mode on the reconstructed Ga-rich $c\,(8 \times 2)$ surface. Figure 8.25 summarizes the time-resolved results for these reference samples. All peaks exhibit qualitatively the expected properties of the pure GaAs:Te substrates. The deposition of the metal layer on the oxidic interface is not SHG active to an extend detectable

Sample	$R_1(neg.)$	$R_1(pos.)$	R_2	T_1
		Lifetime (rel.	Amplitude)	
nat. Ox.	20 fs (0.20)	256 fs (0.75)		Offset (0.05)
3 Å@300 K	no fit	112 fs (0.26)	886 fs (0.36)	Offset (0.38)
3 Å@100 K	no fit	132 fs (0.26)	1360 fs (0.31)	Offset (0.43)

Table 8.3.: Properties of the transient data fitting parameters (cf. equation 8.2) of the LP-1 GaAs:Si-Pt data shown in figure 8.24.

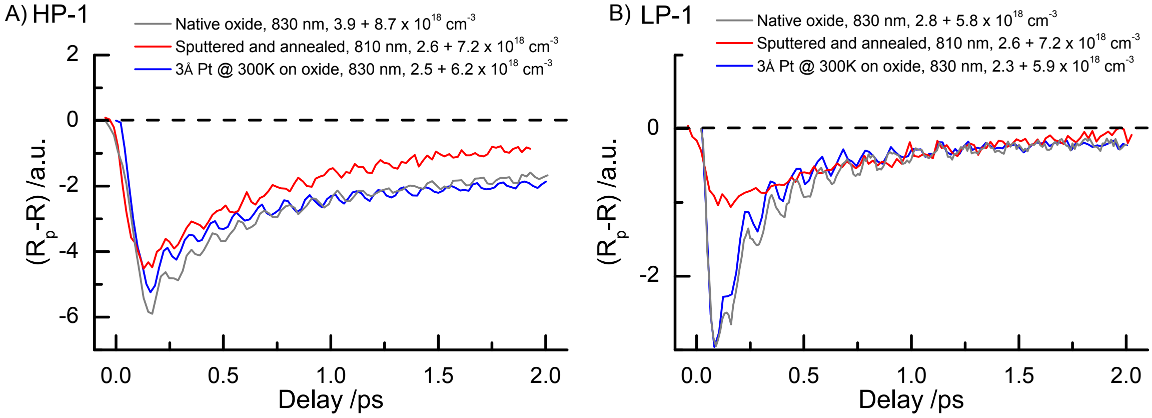

Figure 8.25.: Time-resolved SHG pump-probe data for GaAs:Te reference samples (see key in plot) at different process parameters in HP-1 and LP-1 configuration along compared to results obtained from pure native oxide covered substrate at similar experimental conditions. The excitation pulse width is 35 – 40 fs.

with this method. The sputtered sample shows particular at LP-1 much less transient nonlinear response to the initial carrier injection.

Based on the findings from metal coated silicon doped samples and the behaviour of the GaAs:Te reference samples the time-resolved data for the 3 Å platinum covered samples is surprising (figure 8.26). At HP-1 the signal shape has changed completely. The first initial excitation is now a process with positive sign and is followed by biexponential decrease. As on GaAs:Si-Pt the R_1 seems to be deconvoluted into two processes with opposite sign. The first process is strongest for the low temperature sample while the second is most pronounced for room temperature GaAs:Te-Pt. Further the weakest phonon signature is found on the high temperature preparation. The same picture is found at LP-1 with inverse sign. The 300 K preparation which is characterized by the highest anisotropy given by the HP-1/LP-1 peak ratio (table 7.4) and the best interface quality in the relevant central region of the sample as determined by AFM measurements (table 6.15) shows the strongest effect so far attributed to transient changes in the

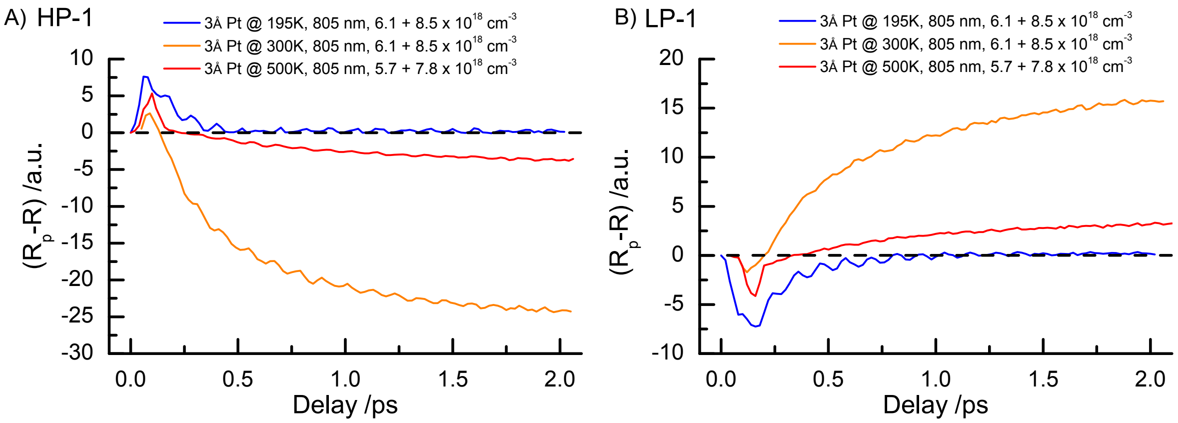

Figure 8.26.: Time-resolved SHG pump-probe data for 3 Å GaAs:Te-Pt metal interface samples at different process parameters in HP-1 and LP-1 configuration. The excitation pulse width is 35 – 40 fs.

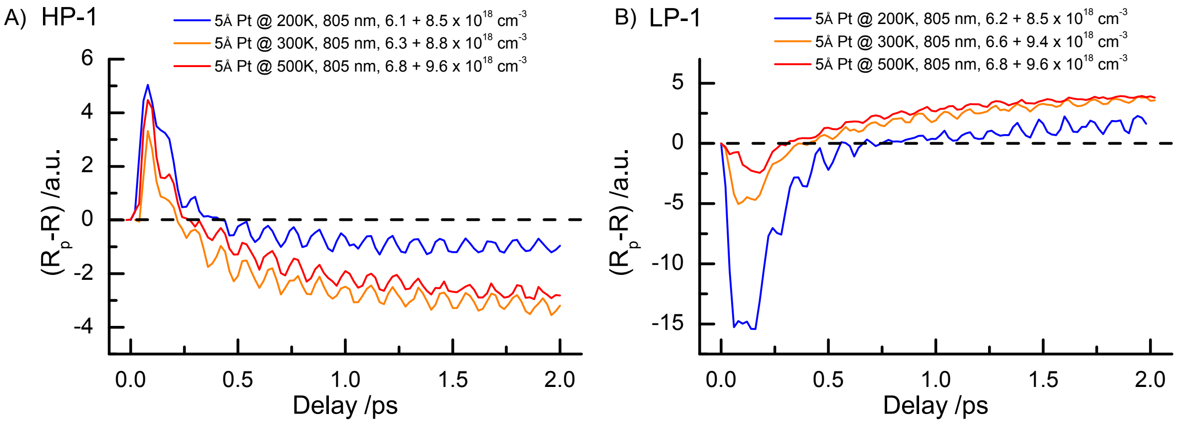

Figure 8.27.: Time-resolved SHG pump-probe data for 5 Å GaAs:Te-Pt metal interface samples at different process parameters in HP-1 and LP-1 configuration. The excitation pulse width is 35 – 40 fs.

depletion field. The morphological and static SHG results support this picture very well. The decrease of phonon amplitude with increased evaporation temperature is not yet fully understood. May be it is related to the inset of platinum diffusion and alloying at the interface.

The non oscillatory behaviour on the 5 Å samples is similar to those with less platinum coverage (please note the different scale in the graphs), where the difference between high and room temperature behaviour is less pronounced. Only at LP-1 the reduction of phonon oscillation at higher preparation temperatures can be observed. More experimental work at different wavelength and carrier densities is necessary to gain a more detailed understanding of these effects.

8.3. Phonon Dynamics

This final sections covers the analysis of the weak modulation in the results of time-resolved pump-probe SHG measurements attributed to coherent phonon oscillation. While the nonoscillatory part of the signal discussed before was mostly in the range of 10-20 % of the total SHG intensity, the phonon signal corresponds to merely 1% of it. This corresponds to the least SNR ratio of all shown laser based experiments. A long scan time is required, even when using the shaker baser set-up, in order to push it to a satisfactory level (see section 5.3.2). This makes the results prone to laser stability problems. Finally sufficiently long delay ranges have to be recorded to allow an identification of the often narrow spaced modes at GaAs. In the following only the principle results obtained from both types of substrates and different platinum coverages are shown. All data is normalized to the strongest peak, so amplitude of specific phonon modes are given in a relative scale.

8.3.1. Results for GaAs Surfaces

Figure 8.28A shows the relative Fourier power spectrum (black curve) of the oscillatory signal after removal of the background signal (inset). The red curve corresponds to the fit of time and spectral data as described in section 8.1, the individual modes found are colour coded to their spectral region. Their properties are summarized in the table below the figure. Finally the phase is plotted in the background as a dashed grey curve. The dominant mode is the longitudinal optical (LO) mode at 8.8 THz. Its initial phase of -2.6 rad corresponds to a cosine oscillation with negative amplitude, which supports the assignment of transient depletion field screening as the main excitation mode on GaAs (see section 2.4.1). Although LPSVD is used to estimate the initial amplitude and phase of each phonon mode as starting parameter for the iterative fit in time and spectral domain, it is not possible to obtain a pure cosine phase, particular for the weak modes. As the background is removed by subtracting the sum of exponentials describing the transient depletion field and bulk SHG effects the starting point of the phonon oscillation is not always easy to identify, especially at the peaked LP-1 data sets. Even though filtering frequencies below 3 THz and beyond the Nyquist limit is performed on the extracted data set. A FFT filtering of the complete signal including background is avoided, as it proved to create artificial signals in the region of interest. Beside the main component this spectrum shows signs of further modes discussed in literature (e.g. [150, 152, 207, 217, 218, 416, 417]). At 8.3 THz a mode can be identified

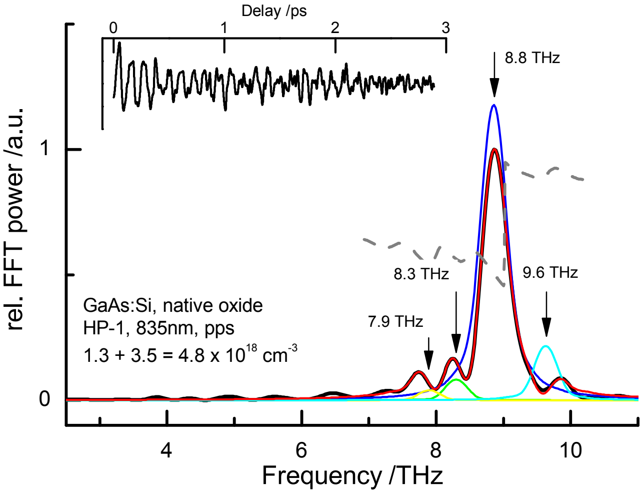

	Frequency /THz	Amplitude (rel.)	Lifetime /ps	Phase
▬	8.8	0.64	1.2	-2.5
▬	9.6	0.20	2.2	-0.9
▬	8.3	0.10	(5.1)	-2.6
▬	7.9	0.06	(21)	-2.9

Figure 8.28.: Phonons modes on native oxide covered GaAs:Si. Probed by 835 nm light in pps configuration and HP-1 azimuthal orientation. The excitation pulse width is 35 – 40 fs.

which at first was nonspecifically addressed as surface LO mode [202, 203] but could later be related to coupling between the LO mode and the hole plasma at the interface side of the depletion region [217]. Further the weak mode 7.9 THz is a first sign of a LOPC, the LO phonon-electron plasma coupled mode, which becomes more dominant at higher carrier densities ($> 5 \times 10^{18}$ cm^{-3}). Its carrier density dependence and the absence of a crystalline arsenic layer as determined in XPS measurements rule out a LO phonon mode of a pure As layer at the oxide-bulk interface. Finally the mode at 9.6 THz is of unknown origin, it shows a more sinusoidal phase which would make impulsive Raman scattering a possible excitation mechanism. It could be related to the high frequency branch of the LOPC mode at carrier densities below the anti-crossing point (see section 4.1.5).

As the launch of coherent phonons by TDFS depends only on the strength and speed of the field screening the results should be independent of wavelength and polarization apart from the different absorption coefficient. Figure 8.29A shows a phonon spectrum at a set of completely different parameters, given in the figure. Also here the response is dominated by the 8.7 THz LO phonon. Its lifetime is reduced to 700 fs which is in sound with findings of Min et al. for higher carrier densities [206]. The underlying time signal is quite short which reduces the spectral resolution. Nevertheless also shoulders

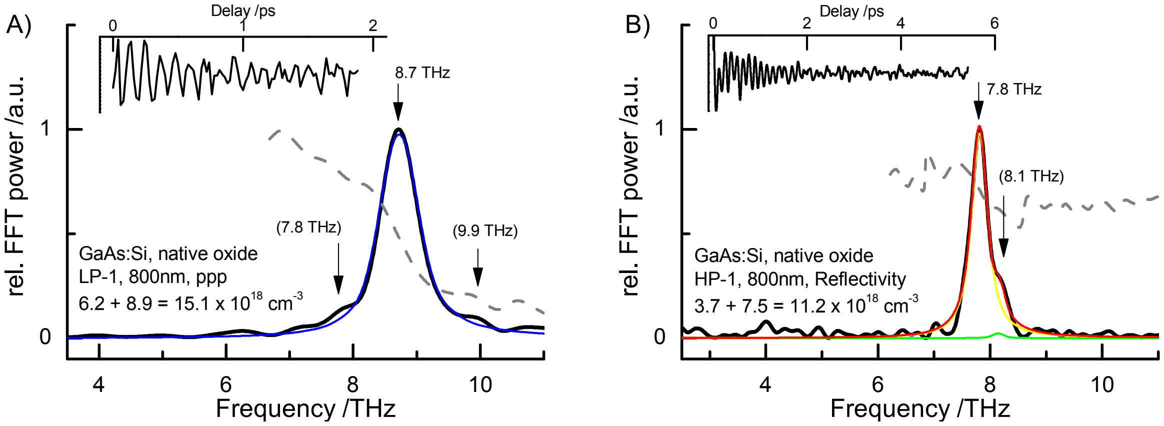

		Frequency /THz	Amplitude (rel.)	Lifetime /ps	Phase
A)	🟦	8.7	1	0.7	-2.4
B)	🟨	7.8	0.92	1.1	0.1
	🟩	8.1	0.08	2.4	-0.1

Figure 8.29.: Phonons on GaAs:Si at lower intensity peak azimuthal orientation (LP-1) and in reflectivity mode. The excitation pulse width is 35 – 40 fs.

at 7.8 THz and in the range of the new mode at 9.9 THz can still be seen. In strong contrast is the spectrum of a modulated signal extracted from a reflectivity measurement (figure 8.29B). The rotational alignment corresponds to a HP-1 angle in TR-SHG experiments. At 800 nm and a peak carrier density of 11.2×10^{18} cm^{-3} the spectrum shows a strong 7.8 THz oscillation and a small shoulder at 8.1 THz. While TR-SHG experiments monitor effects in the uppermost layers determined by the phase matching length, linear reflectivity studies at 800 nm sample a region of approximately 400 nm into the sample (cf. scheme 7.10). As the LO phonon couples with photo carriers as well as with free carriers caused by the high doping of 1.5×10^{18} cm^{-3}, the ω_- branch of the LOPC mode has transverse optical (TO) phonon properties (see figure 4.17A). The nonlinear probing method in contrast samples only LO phonons in the depth less than the depletion region which is free of carriers and therefore uncoupled. With respect to the high frequency component ($>$ 9.0 THz) both spectra in figure 8.29 contradict the assignment to the ω_+ LOPC branch. First at the injected carrier densities of the TR-SHG measurement at LP-1 the strong slope of the plasmon like branch would result in a higher frequency of this mode and second, this feature should be more dominant in the reflectivity scan due to the same reasons as there the ω_- signal is strong.

On the tellurium doped samples a stronger 8.5 THz mode was found next to the LO mode (figure 8.30A). Here the frequency of the LO mode is slightly shifted to higher energies (8.9 THz), while at the same time a dip at the hole plasma coupled mode

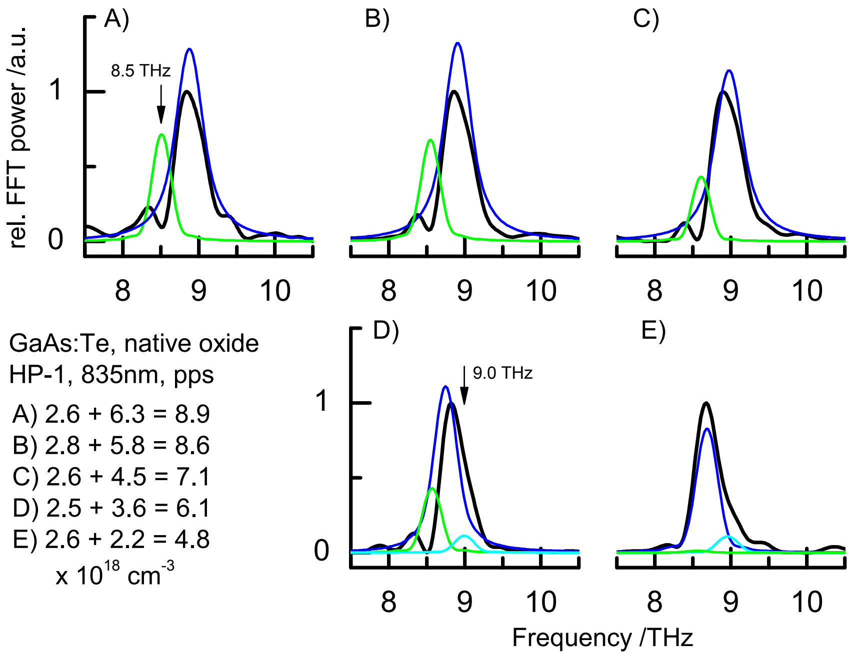

		Frequency /THz	Amplitude (rel.)	Lifetime /ps	Phase
A)	🟦	8.9	0.75	0.9	3.14
	🟩	8.5	0.25	4.5	0.9
B)	🟦	8.9	0.74	1	2.78
	🟩	8.5	0.26	3.7	0.44
C)	🟦	8.9	0.82	0.9	3.14
	🟩	8.6	0.18	(17)	0.68
D)	🟦	8.7	0.67	1.4	0.23
	🟩	8.5	0.21	(11)	-2.34
	▬	9.0	0.12	6	-0.39
E)	🟦	8.7	0.69	4.4	-1.52
	🟩	8.5	0.10	4	0.6
	▬	9.0	0.21	(14)	-1.9

Figure 8.30.: Phonon modes on native oxide covered GaAs:Te at HP-1. Probed by 835 nm light in pps configuration at varying injection levels. The excitation pulse width is 35 – 40 fs.

frequency appears. A similar situation was found by Matsumoto et al. [218]. The dip is a result of a strong frequency shift between both modes also found in the spectra shown here. With decreasing pump power this surface mode vanishes and the 9.0 THz oscillation sets in.

8.3.2. Results for GaAs-Pt Interfaces

The preparation of a clean GaAs surface and the subsequent metal coating has also a significant effect on the excitation of coherent phonon modes. The general trend is the formation of an intense set of peaks on the low frequency side of the bulk LO mode in the range $6-8.5$ THz. For example, at the 3 ÅPt@100 K sample the strongest feature is now the 8.3 THz oscillation. Also the LOPC mode in the range of 7.7 THz can be seen. Both show lifetimes around $500-600$ fs which for the hole plasma mode is longer than that detected on the native oxide covered GaAs:Te sample (on the silicon samples its amplitude is to small to extract a trustworthy lifetime) and for the LOPC mode shorter than that detected by reflectivity measurements. The accompanying LOPC frequency shift with respect to the reflectivity measurement is caused by the lower carrier density and the related shift of the ω_- branch towards the plasma frequency. The phase shift of both plasma modes to the LO bulk mode induces the large dip in the spectrum. In contrast to this, the spectrum of the room temperature 3 Å sample shows a broad peak, which can be fitted by two oscillations centred at 7.2 THz and 7.5 THz. Their lifetimes of 1.5 ps and 4.4 ps could by treated as signature of the good interface quality.

Spectra with the same tendency to form side peaks in the $6-8.5$ THz frequency range were also recorded by Chang in UHV based experiments on cleaned and reconstructed sufaces [150]. There these modes haven been labelled as surface phonon modes due to their frequencies which are forbidden in bulk GaAs (cf figure 4.16).

A clear assignment of the observed change in phonon response either to the reconstructed surface or the formation of a metallic contact could not be made so far. The phonon spectrum obtained by time-resolved SHG from the sputtered and annealed GaAs:Te reference sample gives more insight, as here nearly no pure bulk LO phonon mode is visible. The response is mainly caused by an oscillation at 7.5 THz with a sinusoidal phase and a lifetime of 2.4 ps and a smaller side peak at 7.0 THz. Whether this oscillation is a LOPC mode with a strong shift has still to be worked out, but it helps to identify the low peak shoulders at metal samples shown before as a feature related to the underlying surface reconstruction. As expected from the carrier dynamics discussion in the previous chapter the phonon response from the metal on oxide reference sample is in sound with those from the pure substrates.

The situation on the metal samples based on GaAs:Te substrates is shown in figure 8.33 for 3 Å preparations and in figure 8.34 for the 5 Å samples. For the smaller platinum coverages the low temperature sample shows two strong modes: one at 8.3 THz similar to the one found on the corresponding sample based on silicon doped substrates and one

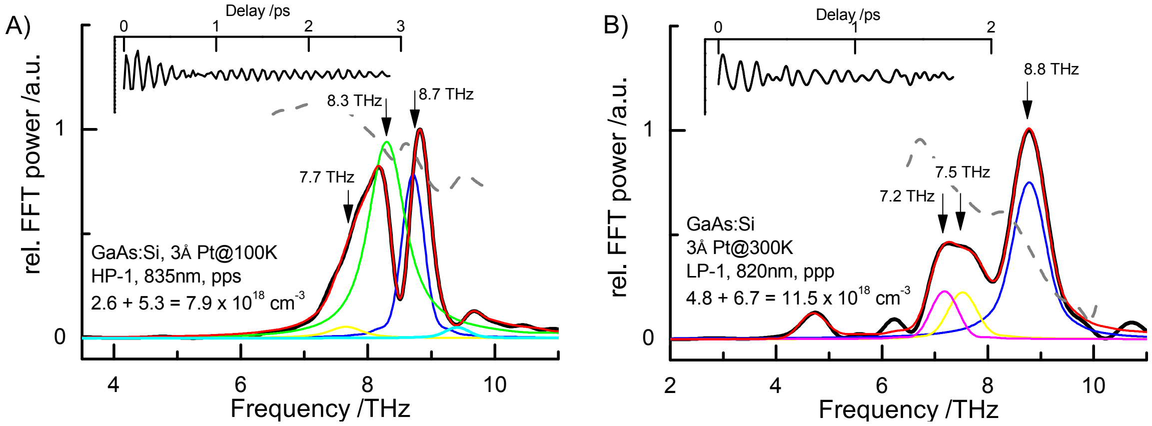

		Frequency /THz	Amplitude (rel.)	Lifetime /ps	Phase
A)	🟩	8.3	0.59	0.5	0.6
	🟦	8.7	0.21	2.6	-2.6
	🟨	7.7	0.13	0.6	1.6
	🟦	9.4	0.07	1.3	2.36
B)	🟦	8.8	0.36	0.7	-2.37
	🟨	7.5	0.14	1.5	0.39
	🟪	7.2	0.10	4.4	-0.34

Figure 8.31.: Phonons on GaAs:Si coated with 3 Å platinum at 100 K and 300 K. The excitation pulse width is 35 – 40 fs.

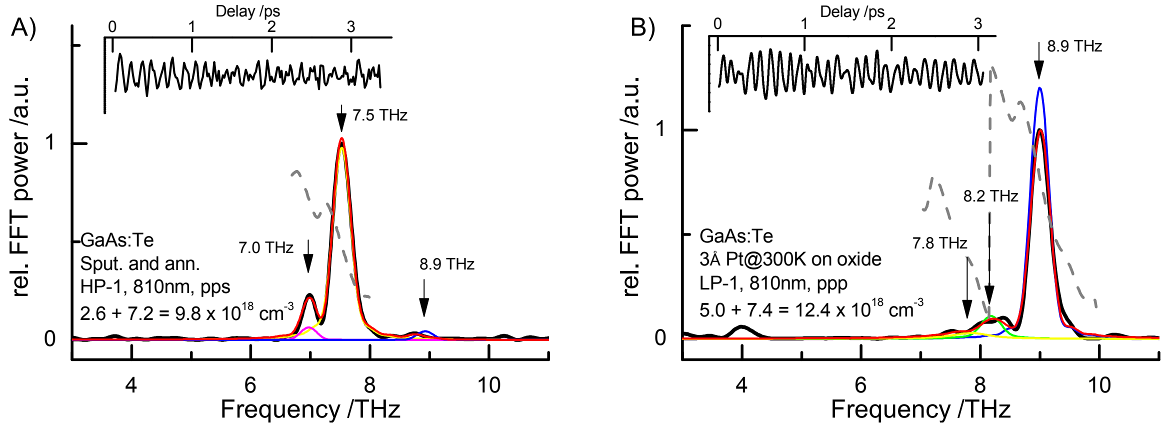

		Frequency /THz	Amplitude (rel.)	Lifetime /ps	Phase
A)	🟨	7.5	0.76	2.4	-1.58
	🟪	7.0	0.13	(25)	-0.49
	🟦	8.9	0.12	8.3	0.59
B)	🟦	8.9	0.51	5.0	-2.1
	🟨	7.8	0.27	0.5	-1.29
	🟩	8.2	0.22	1.7	-1.41

Figure 8.32.: Phonons on GaAs:Te reference samples. The left side shows the spectra from a sputtered and annealed sample with a Ga-rich $c(8 \times 2)$ reconstruction, while on the right side a spectrum from a 3 Å Pt on oxide sample is shown. The excitation pulse width is 35 – 40 fs.

at 9.1 THz. Both have a similar phase which rules out a phase shift induced interference which was responsible for the observed frequency shift on the bare tellurium doped GaAs samples (figure 8.30). This is so far the strongest manifestation of a peak beyond the LO phonon frequency. Furthermore an even higher frequency shoulder at 9.7 THz can be seen. The room temperature sample on which the strongest transient SHG change was found however gives only a simple LO phonon mode response with a weak 9.1 THz side peak. Increasing the preparation temperature gives again a broad spectrum containing the 7.7 THz mode, the bulk LO 8.7 THz oscillation and the new high frequency signal at 9.3 THz. Beside this latter oscillation component, the set of samples seem not to show a systematic behaviour upon variation of evaporation temperature. This can also be observed at the 5 Å samples where the room temperature sample boasts the strongest 9.2 THz mode and the high temperature sample gives a simple LO phonon oscillation only.

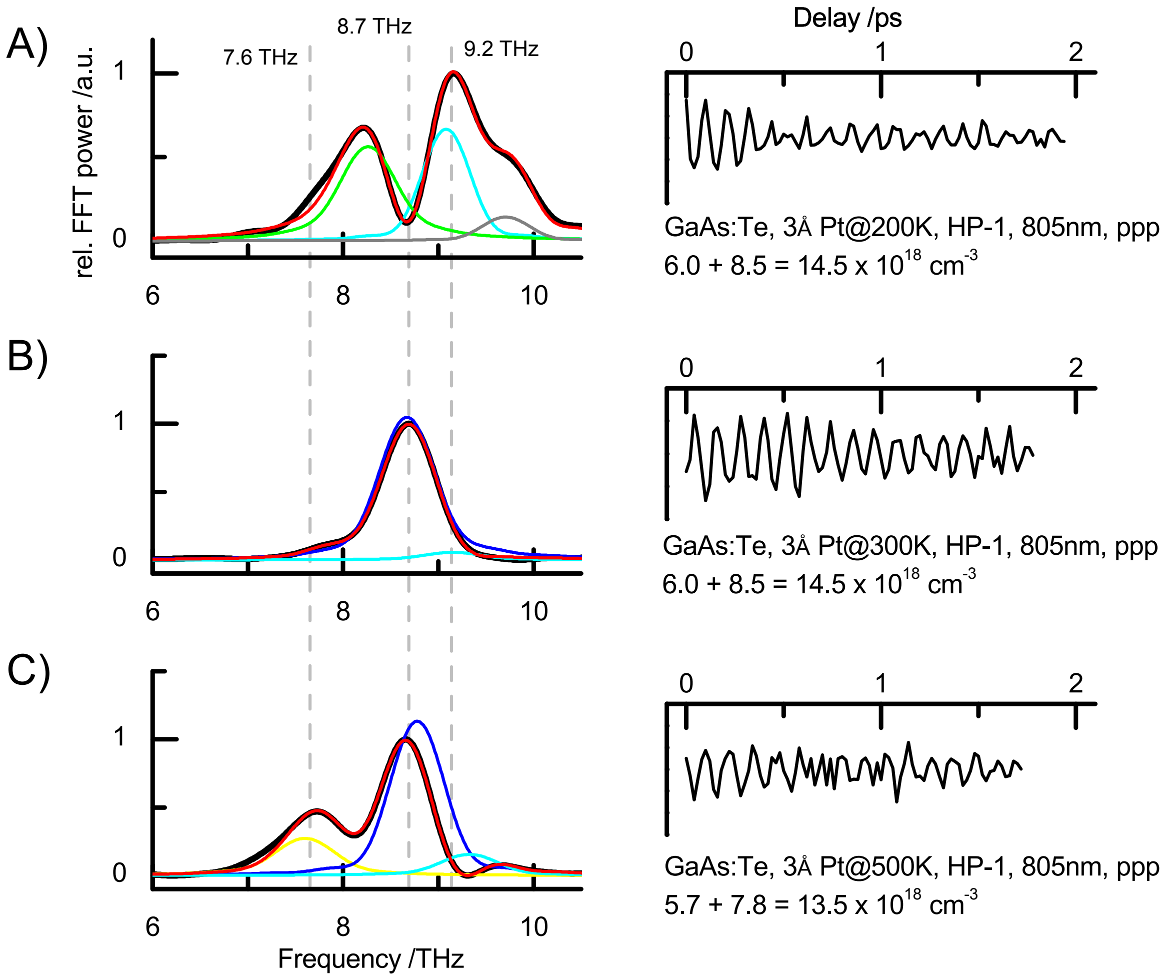

		Frequency /THz	**Amplitude (rel.)**	**Lifetime /ps**	**Phase**
A)	▬	8.3	0.51	0.7	0.97
	▬	9.1	0.33	2.4	1.09
	▬	9.7	0.15	2.2	0.01
B)	▬	8.7	0.75	1.1	-2.40
	▬	9.1	0.19	0.9	0.69
C)	▬	8.8	0.46	1.9	-0.10
	▬	7.6	0.32	0.8	2.21
	▬	9.3	0.22	1.1	1.69

Figure 8.33.: Phonons on GaAs:Te 3 Å platinum samples prepared at different evaporation temperatures.

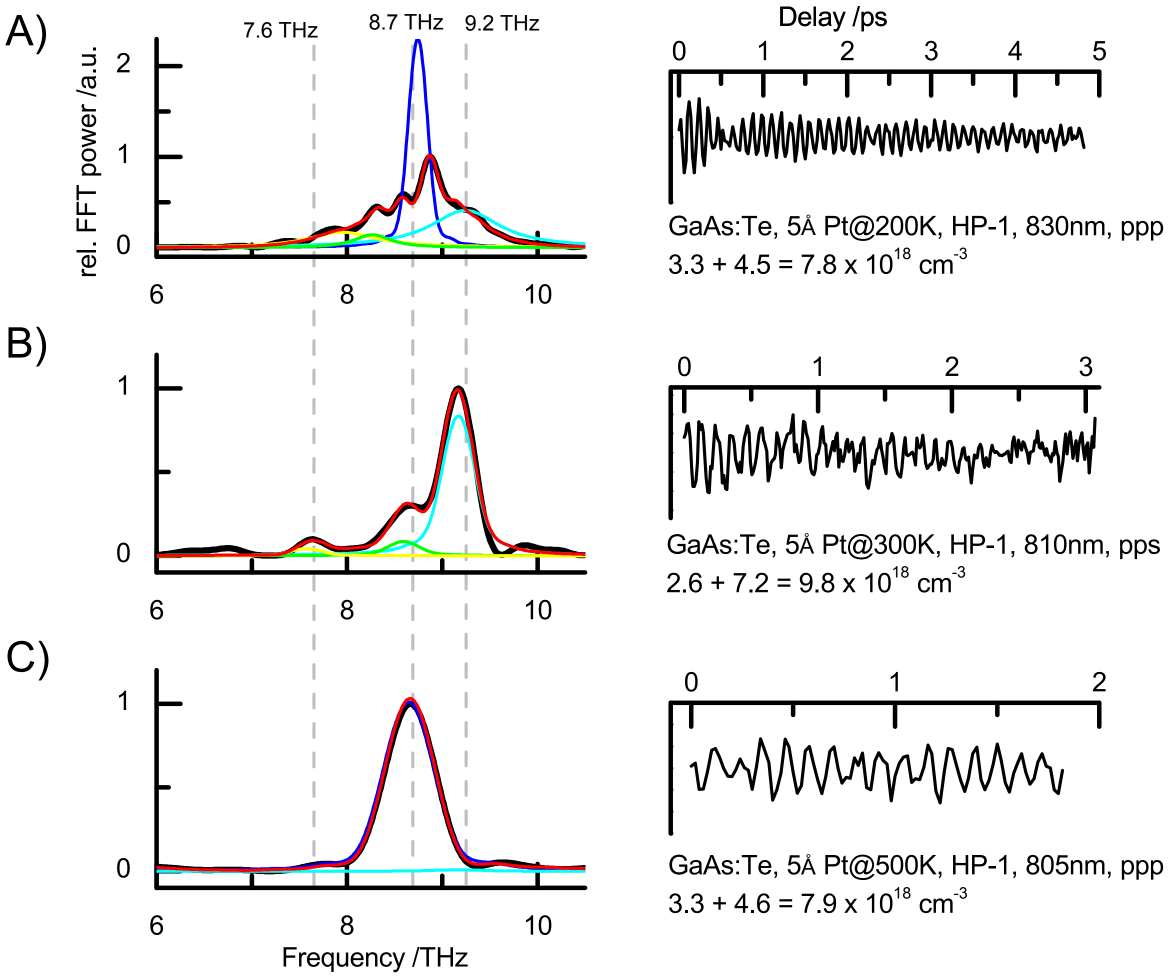

		Frequency /THz	Amplitude (rel.)	Lifetime /ps	Phase
A)	—	9.2	0.43	0.4	-1.58
	—	7.9	0.27	0.4	0.71
	—	8.7	0.17	5.3	2.43
	—	8.3	0.13	0.8	0.99
B)	—	9.2	0.66	1.8	-1.56
	—	8.5	0.20	1.8	-0.20
	—	7.6	0.14	2.1	1.13
C)	—	8.6	0.59	2.2	0.05
	—	9.2	0.05	2.6	2.58

Figure 8.34.: Phonons on GaAs:Te 5A platinum at different evaporation temperatures. The excitation pulse width is 35 – 40 fs.

8.4. Summary

In this chapter the transient change of second harmonic generation intensity from the pure and metal covered GaAs samples as a response to a variably delayed pump pulse was investigated. In the experiments presented in this chapter the pump pulse rapidly induced a non-thermal hot carrier distribution in the conduction band. Its influence on bulk optical properties and the depletion zone was studied at two different azimuthal orientations, namely in $\langle 011 \rangle$ and $\left\langle 0\bar{1}1 \right\rangle$ direction which correspond to the sum of the maxima of the bulk response and a 90° phase shifted isotropic contribution. Measurements on GaAs:Si at different wavelengths and carrier densities in combination with probe chopped experiments to identify the sign of the transient SHG response allowed the identification of different excitation and relaxation processes and their lifetimes. Rotation measurements in the presence of the delayed pump pulse allowed a correlation of the excitation and relaxation processes with the isotropic and anisotropic fitting components of rotational scans and thus with bulk and depletion zone effects. It was found that the bulk nonlinear susceptibility term responds on a time scale of the pump pulse with a decrease in SHG intensity most likely caused by depopulation of valence band electron states. The depletion field driven SHG term shows a biexponential behaviour: a quick process on the same time scale as the bulk response and a slower subsequent effect. Depending on the azimuthal orientation the two rapid processes add up or have opposite signs. The latter case occurs at the lower intensity lobes.

At the GaAs:Te substrates both lobes show the same behaviour with a quick sharply peaked decrease in SHG intensity. Here the lifetimes of all processes are larger than those on GaAs:Si. More work has to be done on this type of substrates to understand their behaviour with respect to the assumed depletion field screening. After surface cleaning and deposition of platinum the samples based on the the silicon doped substrates show a decelerated response with slightly smaller absolute SHG change, where the GaAs:Te-Pt samples changed their dynamic properties completely. They now feature a separated response too, with the difference that the single exponential process has an opposite sign to the biexponential process related to the depletion field dynamics at both azimuthal configurations. The samples which in rotational scans have been found to have the largest anisotropy and by chemical and morphological investigation are related to the highest interface quality with respect to surface roughness and composition, show the strongest transient SHG response upon pumping.

A further zoom into the SHG response revealed information about coherent lattice oscillation modes in the samples (coherent phonons). In SHG experiments with their immanent surface sensitivity due to symmetry conditions and the short phase matching length the oscillatory response of the native oxide covered samples is dominated by the longitudinal optical bulk phonon mode at 8.7 – 8.9 THz. Depending on the carrier density and signal quality of the investigated trace also features of a coupling between the LO bulk phonon and either electron and hole plasma can be found at 7.7 – 7.9 THz and 8.3 – 8.5 THz. While the signal from the uncoupled mode stems from the carrier free depletion zone, the hole plasma coupled mode is surface related as hot holes are pushed to the interface after excitation inside the space charge region. The electron plasma mode thus is located at the back of the depletion zone due to the opposite movement of hot electrons and inside the bulk itself where it couples with free carriers induced by the rather strong doping of $1.1 - 2.2 \times 10^{18}$ cm^{-3}. Reflectivity based phonon scans thus reveal only the LOPC mode at 7.5 THz due to their much less surface specific response. The scans often show a weak sign of a mode at frequencies larger than the LO phonon mostly in the range of 9.0 – 9.7 THz.

The platinum coated samples unfortunately do not show a clear interface quality or preparation temperature dependent behaviour. The strongest change on the GaAs:Si-Pt samples is a number of spectrally overlapped modes in the range of 6 – 8.5 THz. The sputtered and annealed reference sample already investigated in rotational and carrier dynamic measurements revealed a strong 7.5 THz mode and nearly no bulk LO signal. Thus this can be a feature of the surface reconstruction which can also be seen in the platinized samples. Finally the GaAs:Te-Pt samples exhibit no systematic response to a change of process parameters. Some samples give spectra with side peaks similar to those found on GaAs:Si-Pt while others simply oscillate at unperturbed LO phonon frequency. Only the high frequency component was found to be stronger in these samples. The origin of this oscillation mode is still unclear and needs more investigation. Its frequency is outside of the bulk allowed phonon band.

9. Discussion and Outlook

In this thesis the chemical and morphological properties of doped gallium arsenide semiconductor surfaces and metal-semiconductor hetero-interfaces were studied and related to their nonlinear optical response in static and time-resolved measurements. In the first step, x-ray photoelectron spectroscopy (XPS) and different scanning probe microscopy (SPM) methods were employed to analyse the chemical composition and its microscopic arrangement in the topmost layers of GaAs negatively doped either with silicon or tellurium. Stored in environmental atmosphere these materials form a so called native oxide layer with a complex oxidic structure. Defect states at the interface between oxide and bulk semiconductor are responsible for an upward band bending in the near interface layer of the material. This is a result of free electrons from the conduction band getting trapped in these surface states and thus create a negative surface charge repelling the remaining conduction band electrons away from the surface (depletion zone). In the next step these oxidic termination layers were effectively removed under ultra-high vacuum (UHV) conditions and replaced by a defined surface reconstruction layer. Finally hetero-interface structures were prepared by platinum evaporation onto these samples at different processing parameters. XPS and SPM experiments on these samples revealed information on the reactivity of platinum to gallium and arsenide at the interface, a possible reoxidation as well as diffusion and segregation processes.

Following this, the electronic and lattice vibration properties were investigated using optical nonlinear second order harmonic generation (SHG). In a simple picture the nonlinear response can be understood as a Lorentz oscillator representing any kind of vibration of free or bound electrons or the lattice itself, which at intense optical excitation becomes anharmonic. The polarization described by the Lorentz model now contains terms oscillating at harmonic frequency with respect to that of the incoming light. The material specific efficiency of these processes are expressed by the nonlinear susceptibility. The SHG process is allowed in non centrosymmetric systems only. This makes it very interface sensitive. Due to the zinkblende structure of GaAs, also the bulk regions of the investigated samples contribute to the nonlinear response. Each interface can be attributed a different susceptibility. As they are tensors, their non zero elements reveal the symmetry of the respective region. Also electric fields inside the sample (e.g. the space-charge region) contribute to the optical signal in form of third order terms (second order with respect to the optical excitation). By changing the input and output polarizations and the rotational alignment of the samples to the excitation light it is possible to select different groups of tensor elements to be probed. The information depth of the SHG signal is governed by the phase matching length between fundamental and harmonic light. In the GaAs based samples and the used wavelength range this is about 8 nm. Three levels of information were obtained analysing the SHG signal. First with the largest signal to noise ratio rotational scans were recorded. In this method the azimuthal orientation of the sample with respect to the lights plane of incidence is varied, yielding a sinusoidal intensity profile whose symmetry and strength is determined by the contribution of bulk, interface and depletion field terms. By probing at different polarization and wavelength combinations these influences could be separated and their dispersive behaviour established. The next weaker signal investigated, was the temporal change of SHG intensity upon impinging the sample with a strong pump laser pulse. Here the pump is treated as a source for a non thermal distribution of hot electrons and holes injected into the sample in a very short time span. The temporal evolution of the optical response revealed the dynamics of the hot carriers and their influence on the depletion field and the bulk optical parameters. The third signal detected with the smallest signal to noise ratio was an oscillatory modulation of the time-resolved data. It is caused by coherent phonons, the collective vibration of lattice constituents. Spectral analysis of these signals allowed the identification of different phonon modes and phonon carrier coupled modes.

Two types of (100) faced substrates were investigated: GaAs wafers doped with silicon at a concentration of 1.5×10^{18} /cm^{-3} and tellurium implanted samples with a concentration of $1.1 - 2.2 \times 10^{18}$ /cm^{-3}. Both types of samples have similar surface quality specifications, their impurity levels inside the band gap differ only slightly ($\Delta E = 3 \times 10^{-5}$ eV [382]). Using Poissons equation the depletion zone parameters were calculated. For the silicon doped sample it resulted in a 25.2 nm deep depletion zone, with an electric field at the interface of -540 kV/cm, while for GaAs:Te a depletion length range of $20.8 - 29.5$ nm with an electric field between $-461 - -653$ kV/cm was determined. After removal of the protective coating, atomic force microscopy measurements revealed a grainy structure with a surface roughness of about 0.76 nm. In XPS experiments the on top oxide layer showed to consist mostly of ${\mathrm{Ga}_3}^+$ and ${\mathrm{As}_3}^+$ in form of

Ga_2O_3 and As_2O_3. On the uppermost layer a weak indication of ${Ga_1}^+$ as Ga_2O was detected. Upon sample ageing the oxide layer thickness increases from initially 2.28 nm to 3.61 nm (or $1.79 - 2.83$ nm using a different model). On the most aged samples additionally $Ga(OH)_3$ was identified. The oxidation process is finally self limiting, which was attributed to the formation of a metallic arsenic layer at the interface [168], but the presence of such a species could not be unambiguously pinpointed here. Beside oxygen and spurious carbon no further contaminations have been found. Regarding the morphological and chemical aspects the two types of substrates did not show distinct differences.

In contrast to this are the results of the optical experiments, where the tellurium samples showed weaker dispersive effects in the depletion field related terms and in general a less pronounced asymmetry in rotational scans. For all types of samples the rotational SHG intensity distribution could be fitted by the square of the sum of an isotropic, constant term and an anisotropic sinusoidal contribution. The isotropic and anisotropic parts either add up or have opposite signs resulting in lobes in $\langle 011 \rangle$ and $\langle 0\bar{1}1 \rangle$ directions with different intensities. The amplitudes of both are complex. By changing the power of the probing laser pulse a linear dependency of the isotropic part upon injected carrier density, or related to this, the effective average electric field amplitude within the absorption depth of the SHG signal could be found, while at the same time the anisotropic part stays constant. This self photomodulation behaviour of the probe laser pulses confirmed the assignment of the isotropic fitting parameter to depletion zone nonlinearities depending on the electric field inside the material and the anisotropic term to the bulk contribution. A specific interface or surface related term is found to be to weak to play a role in the measured signals. The susceptibility terms contributing to the SHG signal depend on the polarizations of the excitation beam and the SH emission. From results at different polarization configurations susceptibility ratio terms relating depletion field elements to the bulk susceptibility could be fitted for different photon energies. Using the literature values for the bulk response, the dispersion behaviour of the electric field terms could be established for both substrate types. The results were discussed with respect to a model published by Germer et al. [1] which specifies two cases: For injected carrier densities below the doping level it treats the depletion field as unmodulated. For electron and hole densities above this threshold the model describes the original depletion field as completely screened. At the same time the surface trap states are still charged resulting in a remaining, very surface confined field of $0.5 - 3$ nm for the laser intensities employed. So for carrier densities up to the doping level threshold the effective average electric field is treated as being constant and only then it is related to the injected hot carrier concentration. A partial depolarization is not covered by the model. In contrast to this the experiments revealed a steady continuous linear relation between carrier injection and depletion zone term. Further at the transition between both cases the experimental results showed a shift of approximately 40° in the phase difference between the complex isotropic and anisotropic amplitudes. As the excitation pulse has a temporal width of ≈ 40 fs the observed photomodulation effect does not fit to drift and diffusion velocities of electrons and holes in GaAs material known from literature.

Time-resolved measurements at rotational alignments corresponding to the peaks in SHG intensity gave different results for the different alignments as well as for both substrate types.

On GaAs:Si at the high intensity lobes (HP) where depletion and bulk susceptibilities add up ($\langle 011 \rangle$ direction) a three step change in SH intensity upon pumping was found: A fast (R_1) and slow (R_2) excitation process transiently reducing SHG efficiency (negative change) followed by a slow decay (T_1) which restores the original SH intensity level (positive change). Both the lifetimes of the individual processes and their relative contribution to total SHG signal as well as the magnitude of the transient SHG intensity itself were found to depend on the carrier density injected by pump and probe pulses.

The first, fast excitation R_1 did not show a clear carrier relation. For high carrier densities it was found to be similar to the laser pulse width (35 fs), while for carrier densities below 3×10^{18} /cm^{-3} a weak tendency to increase to $60 - 70$ fs was obtained. The relative amplitude of R_1 increased between $2 - 10 \times 10^{18}$ /cm^{-3} in the same way the slower process R_2 lost its relevance. This affected also the total peak transient SHG change which was found to run through a maximum of approximately 18 % for carrier densities between $6 - 10 \times 10^{18}$ /cm^{-3}.

The slow excitation process R_2 showed a clear exponential dependency between lifetime and carrier density. By fitting, a high carrier density limit lifetime of 256 fs was found, while the fitting amplitude gave a lifetime of 3.8 ps at the low carrier density limit. The rate of this exponential was determined by $1.63 \pm 0.2 \times 10^{18}$ cm^{-3} which is remarkably close to the doping density in this sample.

The decay process T_1 exhibited a similar exponential relation with high carrier density lifetime of 18 ± 3 ps. For carrier injections smaller than 4×10^{18} /cm^{-3} the decay process was to weak to be fitted. An estimation close to the zero injected carrier limit resulted in a lifetime of about 10 ns which is similar to the reported carrier lifetimes in GaAs.

While at HP the negative change of SHG intensity at the R_1 and R_2 transients was in agreement with the expected screening of the depletion field, which results in a reduction of the isotropic fitting contribution and a subsequent levelling of the lobes in the different directions, measurements at the initially lower peaks (LP) were found to be different. Here it showed that R_1 and R_2 have opposite effects in the SHG efficiency. While R_2, in accordance to the peak levelling. leads to a transient positive change in SH intensity, the fast R_1 process strongly reduces it in a similar manner as at the high intensity lobe (HP). Further the interplay between both seems to be wavelength dependent. Only for wavelengths smaller than $807 - 810$ nm the R_2 process becomes stronger than R_1 leading to a transient increase of total LP SHG intensity, expected for the depletion dynamics (the positive signal R_2 is stronger than the negative contribution of R_1). The opposite signs of both processes results in a strongly peaked TR-SHG trace which was found to be more difficult to fit precisely.

The exponential carrier dependency of the excitations R_1 and R_2 could not be established but the high carrier limit values of 27 fs and 233 fs respectively fit well to those found at HP. The decaying part T_1 however could not be fitted at all.

Time-resolved rotational SHG scans were performed in order to unravel the previous findings. While standard pump-probe measurements yield information on the transient SHG intensity change at a given azimuthal orientation, rotational pump-probe scans give a complete rotational data set for each delay interval. Fitting these to bulk and depletion field terms, results in temporal change of the fitting coefficients for each contribution. It allows the interpretation from a different perspective. These measurements revealed two fast processes in the depletion and bulk parts, with lifetimes according to R_1 and third slower process in the depletion field term only. Its lifetime corresponds to R_2. The first, fast depletion field process was found to be responsible for the linear photomodulation effects observed in static rotational SHG scans. It must be directly related to the injection of electron-hole pairs in the depletion zone. The second, slower process shows the attributes expected for field induced opposite drift of holes and electrons, building up a counter field. The lifetime of this fits to drift velocities inside GaAs. The fast effect in the bulk additionally reduces the SHG efficiency, an effect superimposed on the depletion zone effect. Its wavelength dependency could be an indication for a transient band filling effect, where states close to the valley in the conduction band get completely filled. This increases the band gap and makes the SHG more non-resonant and thus lowers the SHG efficiency. Only for small wavelengths the photon energy is large enough to reach unsaturated parts of the conduction bands.

On the tellurium doped samples the electronic response differs considerably. At both lobes sharply peaked transient signals with an initial fast decreasing SHG intensity and subsequent slower process with opposite sign were found, an effect which is not yet understood and need more careful investigations.

The coherent phonon response in both sample types was found to be dominated by the longitudinal optical bulk phonon mode inside the carrier free depletion zone ($8.7 - 8.9$ THz). Further coupled modes with smaller amplitude could be found, either with the hole plasma direct at the surface oscillating at $8.3 - 8.5$ THz or with the free electrons at the back of the depletion zone ($7.7 - 7.9$ THz). In some measurements a weak and unidentified phonon signal in the range of $9.0 - 9.7$ THz became visible.

The metal interface samples were prepared in two steps. First the native oxide layer was removed by sputtering and annealing under UHV conditions. Subsequent tempering at specific temperatures created a Ga-rich $c\,(8 \times 2)$ surface reconstruction onto which the platinum was deposited. The metal evaporation process was varied by depositing 3 Å or 5 Å thick layers at different substrate temperatures in the range of $100 - 570$ K. The success of surface cleaning was verified by LEED measurements and by monitoring the desorption with the help of mass spectroscopy. Reference samples were prepared by sputtering and annealing a tellurium doped sample without final metallization and by creating a defined metal on oxide sample removing only the topmost oxide and contamination layer with short sputtering and annealing cycles. Caused by preferential removal and a reduction reaction at the elevated temperatures at the sputtering step arsenic oxide As_3O_3 was found to be depleted and the XPS spectra in the 3d region of As showed a metallic signature. Together with a shift of the platinum signals this indicated the formation of $PtAs_2$. On the direct metal contact samples scanning probe microscopy showed a varying surface structure which could be grouped into different regions. The design of the UHV sample holder was responsible for a temperature gradient across the sample resulting in colder outer regions. Further the sample was mounted by retaining brackets which shielded parts of the sample from cleaning and platinum deposition. As a consequence the outer regions exhibited a rough structure and poor LEED image quality. Further deep pits could be found, which were attributed to partial evaporation of unstable low oxide arsenic components. In the centre of the sample a layered structure became visible below a grainy coating. With increasing temperature the quality of the terraced structure increased and reached its maximum at room temperature preparations. At this preparation temperature mono atomic steps were found to separate individual flat terraces. At elevated temperatures a droplet formation set in, which could be a stress relief reaction or an increased alloying and diffusion. The roughness at low temperatures was in the range of 2.7 nm and thus larger than on the clean samples; it reached its minimum in the 300 K preparations with a value of only ≈ 0.5 nm. The Gibbs energy of the (100) surface of gallium arsenide allows the formation of a Pt wetting layer and the small lattice mismatch between both materials a layer by layer growth. Thus platinum deposition in the range of $3-5$ Å leads to the formation of an ultra thin platinum layer on top of the reconstructed GaAs surface. On all samples the terraces also featured crater like structures consisting of a protrusion and a central nodule, most likely a result of gallium diffusion through the platinum layer. In experiments where uncovered substrates were treated at temperatures larger than 850 K their surface became opaque. Optical and electron microscopy showed a strong blister and crater formation. The drops were found to consist of pure gallium. This gallium segregation to the surface supports the assignment of the protrusion features on the metal covered samples. The Pt deposition was calibrated using a quartz microbalance prior to evaporation and checked by different SPM and XPS methods. XPS based thickness approaches based on the THICKOGRAM technique resulted platinum thicknesses in the range of $0.15-0.38$ nm, a complete angle-resolved experiment on a high-temperature sample resulted in a thickness of the expected nominal value of 5 Å. The XPS measurements suffer from the large detection spot width of the analyser which is larger than the central region of the sample and thus include information from the outer regions. Detailed XPS measurements on the direct metal contact samples showed the same metallic arsenic signature as found on the Pt on oxide sample, further a strong multi signal feature in the Ga 3d energetic region was found, which resembles of a plasmon loss signal and was attributed to an interaction with a $PtGa_2$ species.

As discussed before, the depletion field terms manifest themselves in the SH intensity difference between the HP and LP lobes in rotational SHG measurements. On the sputtered and annealed reference sample measurements between $805-810$ nm with a carrier density in the range of 3×10^{28} /cm^{-3} resulted in a lobe intensity ratio of 1.19. This is smaller than that found on the untreated native oxide samples (1.28). The handling of this reference sample in ambient air, should have induced reoxidation of the initially clean surface, but the growth seems to be different from that on the native oxide samples. This showed also an additional low symmetry component in the rotational data. Together with the reduced overall SHG efficiency in this sample this indicates a less pronounced depletion zone effect, which in turn may be related to different defect states at the interface. A further investigation of this process may eventually help to determine the trap state responsible for the depletion field in n-doped native oxide samples. Also the metal on oxide sample yielded a low intense rotational SHG trace with an even less pronounced lobe ratio of only 1.11. This ruled out an optical effect from the platinum layer itself. The rotational scans from the direct contact, platinum covered GaAs:Te samples showed a similar trend as the structural and chemical characterization. The highest SHG efficiency was found at the room temperature samples, where it was stronger than that of the native oxide samples. In the low and high temperature preparations it dropped to a similar level or even below. The behaviour was found to be more distinct on samples with thin coverages of 3 Å. Beside the overall intensity change also the intensity ratio between the HP and LP lobes was strongly increased, reaching values of up to 2.94 for the 300 K, 3 Å samples at experimental parameters corresponding to those from the reference sample scans. Similar results were found on the GaAs:Si samples. Fitting the rotational data revealed that a phase shift of about 35° is responsible for the change in symmetry rather than the magnitude of the complex isotropic and anisotropic fitting parameters. The change in depletion field contribution can be discussed with the formation of a Schottky barrier interface and the quality of this contact. A simple modelling of carrier dependent peak ratios based on the previously determined depletion field susceptibility terms, the Poisson equation, ie. the Germer model, and published barrier heights from different interfaces was performed. It suggested a Pt or $PtAs_2$ Schottky contact for the room temperature preparations. The strong difference in the results from direct metal contact samples to those from the reference samples also ruled out a fast reoxidation of the reconstructed GaAs surface layer through the ultra thin platinum layer. Accompanying photoluminescence measurements at room temperature supported the increase of interface quality in the metallized samples compared to the native oxides.

Time-resolved experiments on GaAs:Si-Pt revealed a decelerated response upon pumping. The lifetimes of the fast processes at the investigated carrier densities rose to $100 - 132$ fs, those of the slow process to $766 - 1360$ fs. On the tellurium doped reference samples the temporal response was found to be similar to those on the native oxide covered samples. So the reoxdiation of an initially reconstructed GaAs surface and a platinum-oxide interface do not show a contribution to the temporal SHG change. On the tellurium implanted substrates however, the metallization gave rise to strong changes in the temporal response at the HP lobes. At both coverages and all preparation temperatures they now showed as similar biexponential transient reduction of SHG efficiency as found on GaAs:Si and GaAs:Si-Pt. The lifetimes of these two processes correspond to those found on the silicon doped, metal-interfaced samples. Additionally a fast process in the beginning of the signal in positive direction, increasing the SHG intensity, was found. It seemed to vary with the preparation temperature. The lower intensity peak signals changed less dramatic. They exhibited a stronger overshoot of the biexponential part than the corresponding native oxide samples. In general the traces from the samples prepared at room temperature once more were found to show the strongest response. The opposite signs of the fast processes in the HP traces may eventually be caused by differences in the fast bulk and depletion zone response investigated before on the GaAs:Si samples and thus may be related to changes in the electronic structure due to the Schottky barrier formation.

Also on the phonon spectrum the metallization had a strong effect, but a clear relation to the preparation parameters could not be found yet. In general the spectra showed an increased intensity of modes in a spectral region between $6.0 - 8.5$ THz, which still have to be investigated in more detail. Further a phonon mode at $9.2 - 9.7$ THz was found. As its frequency is larger than the LO bulk mode its origin could not be pointed out yet. Eventually it is a signature of the high frequency branch of the plasma coupled phonon mode. Oscillations at the Pt interface are expected at lower frequencies in the range of $2 - 5$ THz [115].

To summarize the results of the work presented in this thesis demonstrated the successful implementation of optical experiments which allow the detection of changes in reflectivity and in particular the detection of the nonlinear optical response of semiconductor based samples as a function of beam polarization, wavelength, power and crystallographic alignment. Two different variations of interferometric set ups have been build to perform the dynamic studies on hot carrier processes and coherent phonons and their influence on the optical response of the samples investigated. Beside the construction of the optical apparatus the work also included the set-up of the metrological equipment and the programming of the computerized measurements control and data acquisition as well as a complex database and analysis tool frame work.

The rotational SHG scans proved to be a quick and useful technique to investigate the near surface electronic properties of semiconductors. Compared to XPS and pure surface techniques like SPM, rotational measurements were found to be very sensitive to interface modifications. The implementation of a dual line experiment in which simultaneously a defined reference sample is measured would allow the determination of absolute susceptibility values. Also the time-resolved experiments especially in combination with pump-probe rotational scans showed to be a very useful tool helping to understand the dynamics of hot carriers and internal electric field changes in the investigated samples. To obtain reliable and reproducible results a meticulous alignment of beam focus and the pump and probe spots spatial and temporal overlap was necessary. The implementation of the shaker based set-up in principal should have allowed shorter scan times, but the lack of a differential detection scheme in which power fluctuations of the laser would have been compensated by simultaneously measuring the static response of a second sample, prevented this. Nevertheless, the absolute detection scheme and the higher sampling rate should have promoted the fitting and analysis of the data, but there were still a number of stability issues in this system. When time-resolved data with phonon sensitivity were required, a large number of individual scans had to be averaged resulting in long scan times of up to 8 hours. These experiments would benefit most from a further development of the shaker based set-up.

The time-resolved experiments revealed a different behaviour in the silicon and tellurium doped substrates which from their specifications were thought to be similar. On the first sample type rotational pump-probe scans allowed the distinction between depletion and bulk effects. Similar wavelength and polarization dependent experiments have to be done on the tellurium samples in order to learn more about the specific differences in its dynamic response. Also the dispersive properties of the metal covered samples are still an open question which need further investigations. In the scope of rotational scans the depletion field screening was discussed with a model which involves only two states: a completely screened field and an unmodulated field. The time-resolved scans however showed a dynamic behaviour which required a description including transient depolarization. Additional Monte Carlo simulations of carrier injection and transport within the time period of the initial fast processes in the complete native oxide and hetero-interface sample systems would be helpful to establish a dynamic depletion field screening description. For this purpose additional supporting experiments on samples with different doping densities and doping type (p-doping) should be done.

In this work some first experiments have shown that it is possible to investigate CO adsorption by infrared spectroscopy on the ultra thin platinum films deposited on the semiconductor substrates. Transient depletion field screening leads to a transient high density of hot holes confined to the interface (n-doped samples) and vice versa to a hot electron plasma at the interface for p-doped substrates. It would be interesting to investigate a possible interaction between these hot carriers and the photo desorption process of CO from the metallic adlayer. On thin alkali metal layers coherent phonon modes were found to oscillate in the range of 2.3 – 4.7 THz [115, 279]. These materials in combination with a different semiconductor substrate would eventually allow to study phonon coupling across an interface. An interesting material is InSb where a coherent phonon mode at 5.6 THz is expected [418, 419].

A. Mathematical Background

A.1. Maxwells Equations

Microscopic form

The Maxwell equations form the general basis for classical electrodynamics. Maxwell combined and extended the laws of Gauss and Ampere as well as Faraday's law of induction. In the vacuum they are:

$$\nabla \cdot \vec{E} = \frac{\rho}{\epsilon_0} \tag{A.1}$$

$$\nabla \cdot \vec{B} = 0 \tag{A.2}$$

$$\nabla \times \vec{E} = -\frac{\partial}{\partial t}\vec{B} \tag{A.3}$$

$$\nabla \times \vec{B} = \mu_0 j + \mu_0 \epsilon_0 \frac{\partial}{\partial t}\vec{E} \tag{A.4}$$

where ϵ_0 is the electric constant and μ_0 is the magnetic constant. Equation A.1 is the differential form of Gauss's law. It says that charges given by their density ρ are the origin of the electric field $\vec{E}$. Similar to this is eq. A.2 which expresses the non existence of magnetic monopoles. Faraday's law of induction relates the curl of $\vec{E}$ to the temporal change of the magnetic field $\vec{B}$. Ampere's law (eq. A.4) is extended by a displacement current term $\mu_0\epsilon_0\frac{\partial}{\partial t}\vec{E}$. Now it says that magnetic fields can be generated by current flow (given by the current density j) and by changing electrical fields.

From this framework wave equations for the magnetic and electric field can be derived. Considering a current and charge free environment ($\rho = j = 0$) equations A.1 and A.4 simplify to:

$$\nabla \cdot \vec{E} = 0 \tag{A.5}$$

$$\nabla \times \vec{B} = \mu_0 \epsilon_0 \frac{\partial}{\partial t} \vec{E} \tag{A.6}$$

Taking the curl of equations A.3 and A.6 and crosswise substituting the terms for $\nabla \times \vec{E}$ and $\nabla \times \vec{B}$ will result in:

$$\begin{aligned} \nabla \times (\nabla \times \vec{E}) &= -\mu_0 \epsilon_0 \frac{\partial^2}{\partial t} \vec{E} \\ \nabla \times (\nabla \times \vec{B}) &= \mu_0 \epsilon_0 \frac{\partial^2}{\partial t} \vec{B} \end{aligned} \tag{A.7}$$

Introducing $c = \frac{1}{\sqrt{\epsilon_0 \mu_0}}$ and using the identity: $\nabla \times (\nabla \times \vec{a}) = \nabla(\nabla \cdot \vec{a}) - \Delta \vec{a}$ gives for the one-dimensional case with $\Delta = \frac{\partial^2}{\partial x^2}$:

$$\begin{aligned} \frac{\partial^2}{\partial x^2} \vec{E} &= \frac{1}{c^2} \frac{\partial^2}{\partial t^2} \vec{E} \\ \frac{\partial^2}{\partial x^2} \vec{B} &= \frac{1}{c^2} \frac{\partial^2}{\partial t^2} \vec{B} \end{aligned} \tag{A.8}$$

These are standard wave equations also known from vibration of strings. A possible solution for $\vec{E}$, which is used also in different sections of this thesis, is:

$$E(x,t) = E_0 \cdot exp(i(kx - \omega t)) \tag{A.9}$$

where E_0 is the amplitude, k the wave vector and ω the angular frequency. More detailed versions of this derivation can be found for instance in [38, 41, 118].

Macroscopic form

The formulation of the Maxwell equations given above (eq. A.1 to A.4) are unhandy when dealing with macroscopic materials. For this case they can be related to material parameters whereby two new quantities, the electric displacement field $\vec{D}$ and the magnetic field strength $\vec{H}$ have to be included into the formalism:

$$\nabla \cdot \vec{D} = \rho_{free} \tag{A.10}$$

$$\nabla \cdot \vec{B} = 0 \tag{A.11}$$

$$\nabla \times \vec{E} = -\frac{\partial}{\partial t}\vec{B} \tag{A.12}$$

$$\nabla \times \vec{H} = j_{free} + \frac{\partial}{\partial t}\vec{D} \tag{A.13}$$

where ρ_{free} and j_{free} refer to the free charge density and the free current density respectively.

A.2. Fresnels Equations

Considering a situation as shown in figure A.1, where an incoming light wave with wave vector k_i hits the interface between two media with refractive indices n_1 and n_2, the amplitudes of the different electric and magnetic fields can be calculated using the equations developed by Fresnel. The idea is to to split the wave vectors into components parallel to the interface plane (x-axis) and perpendicular to it (z-axis). The boundary conditions at the interface require the $k_{||}$ components to be the same for all incorporated beams. From the definition of the wave vectors (eq. 2.6) and the trigonometric relations specified by the angles of incidence $\theta_{i,r,t}$ the laws of reflection and refraction can be obtained:

$$\begin{aligned} \theta_r &= \theta_i \\ \frac{sin\theta_t}{sin\theta_i} &= \sqrt{\frac{\epsilon_1}{\epsilon_2}} = \frac{n_1}{n_2} \end{aligned} \tag{A.14}$$

For the calculation of the amplitude s and p polarization have to be treated separately. For the case of the electric field perpendicular to the plane of incidence (s-polarization or transversal electric (TE)) the relation is:

$$E_{r0} = \frac{\sqrt{\epsilon_1}cos\theta_i - \sqrt{\epsilon_2 - \epsilon_1 sin^2\theta_i}}{\sqrt{\epsilon_1}cos\theta_i + \sqrt{\epsilon_2 - \epsilon_1 sin^2\theta_i}}E_{i0} \tag{A.15}$$

$$E_{t0} = \frac{2\sqrt{\epsilon_1}cos\theta_i}{\sqrt{\epsilon_1}cos\theta_i + \sqrt{\epsilon_2 - \epsilon_1 sin^2\theta_i}}E_{i0} \tag{A.16}$$

For the opposite case where the magnetic field is perpendicular to the plane of incidence (transversal magnetic (TM)- or p-polarization), the Fresnel equations are expressed by the magnetic field amplitude:

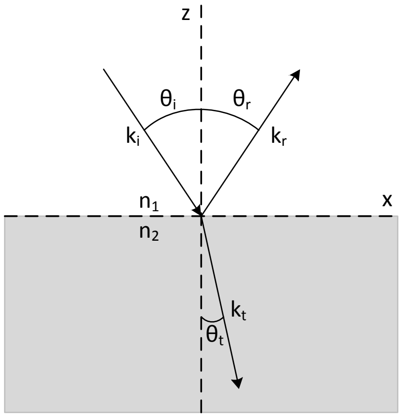

Figure A.1.: Reflection and refraction.

$$H_{r0} = \frac{\epsilon_2 cos\theta_i - \sqrt{\epsilon_1\epsilon_2 - \epsilon_1^2 sin^2\theta_i}}{\epsilon_2 cos\theta_i + \sqrt{\epsilon_1\epsilon_2 - \epsilon_1^2 sin^2\theta_i}} H_{i0} \tag{A.17}$$

$$H_{t0} = \frac{2\epsilon_2 cos\theta_i}{\epsilon_2 cos\theta_i + \sqrt{\epsilon_1\epsilon_2 - \epsilon_1^2 sin^2\theta_i}} H_{i0} \tag{A.18}$$

From these expression the reflection and transmission coefficients and, introducing the Poynting vector, the reflectivity and transmissivity can be calculated. More detailed derivations can be found i.a. in [38, 39].

A.3. Kinematic Theory of Single Scattering Events

The simplest theoretical description of low energy electron diffraction is the kinematic theory, considering a single elastic scattering at the sample surface.
According to de Broglie the wavelength of an electron with a given energy E_{kin} can be expressed by

$$\lambda = \frac{h}{p} = \frac{h}{\sqrt{2m_e E_{kin}}} \tag{A.19}$$

where h is the Planck constant, p the impulse of the electron and m_e its mass. For the typical energy range of 50 to 500 eV, the electrons have a wavelength comparable to the dimensions inside a crystal and thus are diffracted by the single lattice constituents. Another important point is that at these energies the scattering cross section in solids has a maximum, leading to a small mean free path λ inside the material (figure A.2).

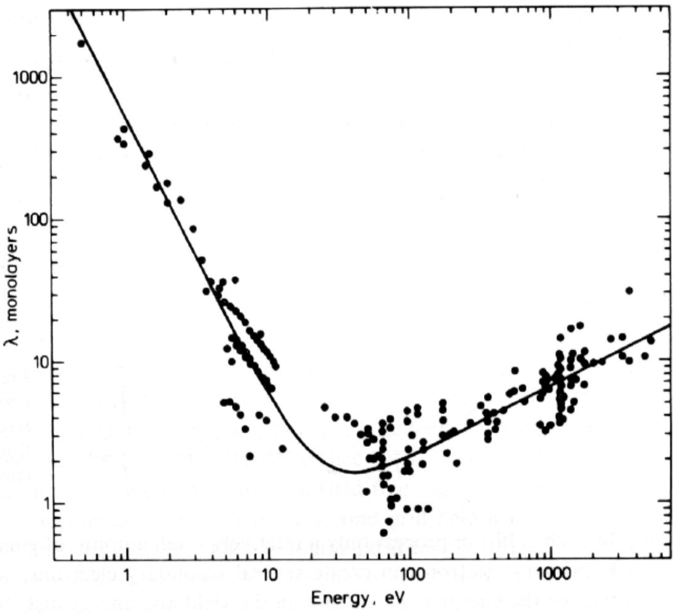

Figure A.2.: Inelastic mean free path (IMFP) for electrons in solids as function of kinetic energy. [290]

As usual, for constructive interference along a specific direction, the path difference of an incoming and outgoing electron wave has to be an integer multiple of its wavelength. Figure A.3 illustrates these constraints. The incoming and scattered electron waves are represented by their wave vectors $\vec{k}$ and $\vec{k}'$. The two scattering centers are related by a translation vector $\vec{R}$ of the Bravais lattice.

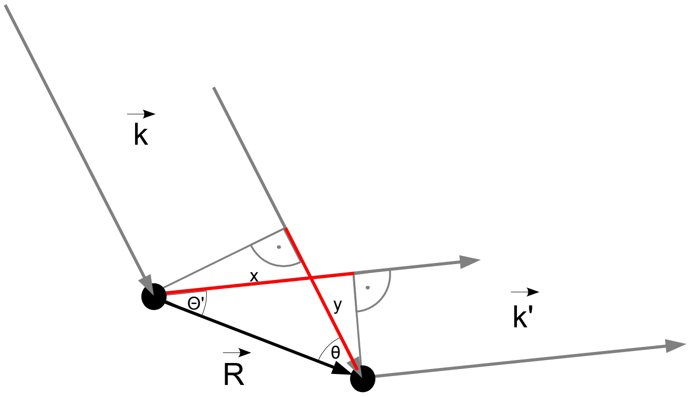

Figure A.3.: Scattering geometry according to Laue.

The overall path difference is the difference between the two red colored segments x and y, which in turn can be obtained by calculating the inner product between the translation vector and the unit vector $\vec{e}$ of the corresponding wave vector.

$$x - y = (\vec{R} \bullet \vec{e'}) - (\vec{R} \bullet \vec{e}) = n \cdot \lambda \qquad n \in \mathbb{Z} \tag{A.20}$$

$$x - y = \vec{R} \bullet (\vec{k'} - \vec{k}) = n \cdot 2\pi \tag{A.21}$$

Introducing the scattering vector $\Delta\vec{k} = \vec{k'} - \vec{k}$ and using the component representation results in the Laue equations:

$$\begin{aligned} \vec{a_1} \bullet \Delta\vec{k} &= m_1 \cdot 2\pi \\ \vec{a_2} \bullet \Delta\vec{k} &= m_2 \cdot 2\pi \\ \vec{a_3} \bullet \Delta\vec{k} &= m_3 \cdot 2\pi \end{aligned} \tag{A.22}$$

with $\vec{R} = \sum_{i=1}^{3} c_i \vec{a_i}$ and $m_i = n/c_i$.
To connect the Laue equations with the obtained diffraction pattern the reciprocal lattice and the Ewald sphere are introduced. In the reciprocal space the basis vector $\vec{b_1}$ of the lattice is perpendicular to the plane spanned by $\vec{a_2}$ and $\vec{a_3}$ in real space. It's length is the reciprocal height of the parallelepiped defined by the three basic vectors of the real lattice, which is the distance $\vec{d}$ of the lattice planes, multiplied by 2π (see figure A.4). $\vec{b_2}$ and $\vec{b_3}$ are defined accordingly.

$$\vec{b_1} = 2\pi \frac{\vec{a_2} \times \vec{a_3}}{\vec{a_1} \bullet \vec{a_2} \times \vec{a_3}} \tag{A.23}$$

$$|\vec{b_1}| = \frac{2\pi}{|\vec{a_1}| \cdot cos\angle(\vec{b_1}, \vec{a_1})} \Leftrightarrow \vec{b_1} \bullet \vec{a_1} = 2\pi \tag{A.24}$$

By using relation A.24 and creating a reciprocal translation vector $\vec{G} = \sum_{i=1}^{3} m_i \vec{b_i}$, the Laue equations A.22 can be simplified to

$$\Delta\vec{k} = \vec{G} \tag{A.25}$$

A constructive interference occurs whenever a scattering vector equals a reciprocal translation vector. In other words all visible diffraction spots are related by a $\vec{G}$. As LEED is surface sensitive the LAUE conditions simplify to a two dimensional problem with surface meshes instead of lattices. It is now possible by measuring the distances of reciprocal translation vectors and their included angles to construct the reciprocal surface

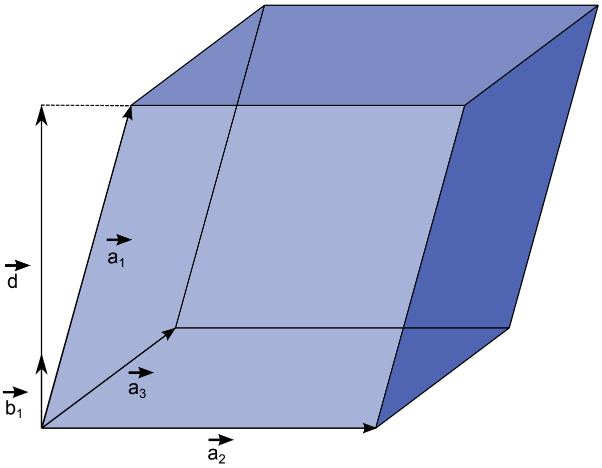

Figure A.4.: The volume created by the three basis vectors of the real space lattice. $\vec{d}$ is the distance vector between the lattice planes. The reciprocal basis vector $\vec{b_1}$ showing in the same direction as $\vec{d}$, it's length is the reciprocal height, multiplied with 2π.

mesh. To transfer the dimensions from the screen's coordinate system to that of the sample the distance between screen and sample r and the wave vector of the electron beam, defined by the set-up and it's kinetic energy have to be known. Equation A.26 describes this conversion:

$$|\vec{G}| = |\Delta\vec{k}| = |\vec{k}| \cdot sin(\theta) = |\vec{k}| \cdot \frac{x}{r} = \frac{\sqrt{2m_e E_{kin}}}{\hbar} \cdot \frac{x}{r} \tag{A.26}$$

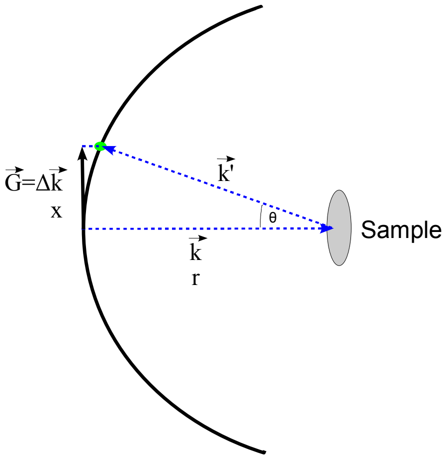

Figure A.5.: Relation between the geometry of a LEED experiment and the scattering vectors.

In the final step the received reciprocal surface mesh can be transformed back to real space to determine the lattice parameters of the surface region on the investigated sample.

A.4. Angle-Resolved XPS

The differential number of electrons emitted from an infinitesimal layer of material reaching the analyser as a function of rotation angle and depth z depends on a number of elements, as the x-ray flux at depth z, the number of atoms in the emission volume combined with an effective cross section for the emission, a term accounting the loss due to inelastic scattering and some analyser efficiency parameters [420]:

$$dN(\alpha) = \left[I_0(1-R)\frac{cos(\beta)}{cos(\beta')}exp\left(\frac{-z}{\lambda_x cos(\beta')}\right)\right] \cdot \left[\rho\sigma\frac{A_0}{cos(\alpha)}dz\right] \cdot \left[exp\left(\frac{-z}{\lambda_e cos(\alpha)}\right)\right] \cdot D_0 \tag{A.27}$$

Here I_0 is the initial x-ray intensity, R the reflection coefficient, β and β' the angles of the source beam outside and inside the material and λ_x the IMFP of the x-ray photons. The electron emission term is defined by the density ρ, the effective area of the sample seen by the analyser entrance $\frac{A_0}{cos(\alpha)}$ and a cross section σ. In the most important electron scattering term the argument of the exponential function is scaled in a way that after an electron path of $\frac{z}{cos(\alpha)} = \lambda_e$ the intensity is dropped to $\frac{1}{e}$ following the definition of the IMFP. Finally the analyser parameters are summarized in D_0.

After rearranging and summarizing: $C' = I_0 A_0 \sigma \rho D_0$ equation A.27 becomes:

$$dN(\alpha) = C'(1-R)\frac{cos(\beta)}{cos(\beta')cos(\alpha)}exp\left(\frac{-z}{\lambda_x cos(\beta')} - \frac{z}{\lambda_e cos(\alpha)}\right)dz \tag{A.28}$$

and after integration over a complete layer O with thickness t (see figure 5.6) the electron intensity is:

$$N_O(\alpha) = C'(1-R)\lambda_e\frac{cos(\beta)}{cos(\beta') + cos(\alpha)\cdot\lambda_e/\lambda_x}\left[1 - exp\left(\frac{-t}{\lambda_x cos(\beta')} - \frac{t}{\lambda_e cos(\alpha)}\right)\right] \tag{A.29}$$

This can be simplified by making two assumptions: For source beam angles smaller than the critical angle (ca. 88° for Au) absorption, reflection and refraction ($\beta = \beta'$) of the x-ray photons can be neglected. Further when considering that $\lambda_x >> \lambda_e$ and thus $cos(\beta') >> cos(\alpha)\cdot\lambda_e/\lambda_x$ the electron intensity can be described by:

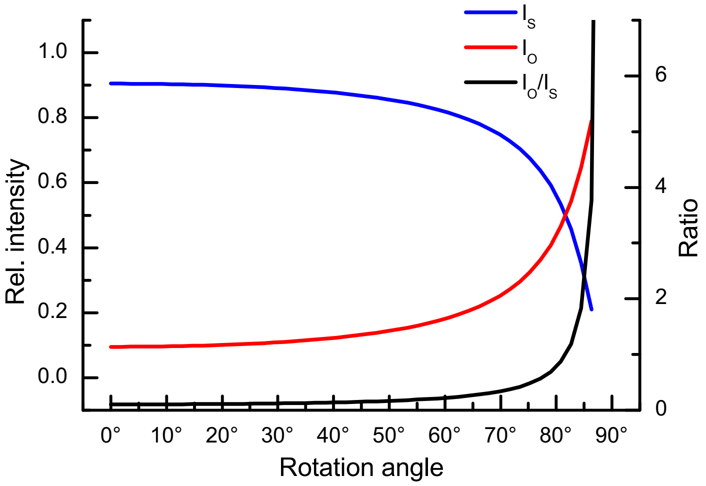

Figure A.6.: Relative intensities from substrate and overlayer photo electrons as a function of sample orientation. Also the ration between both signals is shown.

$$\begin{aligned} N_O(\alpha) &= N_\infty \left[1 - exp\left(\frac{-t}{\lambda_e cos(\alpha)}\right)\right] \\ N_\infty &= C'\lambda_e \end{aligned} \tag{A.30}$$

Here N_∞ shows that for an infinite thick sample, the intensity is not depending on the rotation angle. When taking the intensity ratios between different angles the N_∞ term can be eliminated and thus the layer width be calculated.

In an analogous approach the signal intensities N_O and N_S of a substrate S buried under an overlay O can be modelled. The expression for the overlayer is the same as in equation A.30 with $\lambda_e = \lambda_O(O)$ the mean free path of overlayer photo electrons inside the overlayer material. The substrate term is a combination of the infinite thick sample expression (A.30) with an additional damping of the electron intensity when travelling through the overlayer, defined by the IMFP of substrate electrons in overlayer material $\lambda_O(S)$:

$$\begin{aligned} N_S(\alpha) &= N_\infty \; exp\left(\frac{-t}{\lambda_O(S) cos(\alpha)}\right) \\ N_\infty &= C'\lambda_S(S) \end{aligned} \tag{A.31}$$

In figure A.6 the angular dependency of N_O, N_S as well as the ratio N_O/N_S is shown.

Also from the ratio of substrate signals at different angles the thickness can be calculated:

$$\begin{aligned} \frac{N_S(\alpha)}{N_S(0)} &= \frac{e^{\frac{-t}{\lambda_O(S) cos(\alpha)}}}{e^{\frac{-t}{\lambda_O(S)}}} \\ t &= -\ln(\frac{N_S(\alpha)}{N_S(0)}) \cdot cos(\alpha) \frac{\lambda_O(S)}{cos(\alpha) - 1} \end{aligned} \tag{A.32}$$

B. Technical Details

B.1. Calibration of the UHV Temperature Measurement

For the calibration process the sample temperature was simultaneously measured with the thermocouple mounted on the sample holder and a pyrometer. The pyrometer (Metis MS09, *SensorTherm*) is measuring the intensity of the black body radiation emitted from the sample at a wavelength of 900 nm with a silicon based detector. When the emissivity of the material is known, the temperature of the radiation source can be determined. A major problem in the application of this measurement method is the temperature dependent infrared transmissivity of many semiconducting materials, causing a superposition of the sample temperature signal and the dominating heat radiation from the subjacent filament. Figure 4.8 in section 4.1.3 shows the transmission and absorption properties of GaAs at room temperature. At the detector wavelength the transmissivity is about 20%. In figure B.1A the shift of the absorption coefficient for different temperatures is shown. This limits the operation to specific temperature regions. Another difficulty concerning a precise measurement is, that the emissivity ϵ, which is a correction factor of the actual heat radiation with respect to that of an ideal black body, is not only material specific but also depending on the surface properties and the temperature itself.

For all of the above stated reasons a silicon wafer with the same thickness of 500 µm was used for calibration. Featuring a lower band gap energy of 1.104 eV at room temperature, the transmissivity becomes important not before wavelengths larger than 1 µm. Also an emissivity factor of 68 % is known for red heat silicon (as specified by *SensorTherm*). The nearly three times higher thermal conductivity (Si: 145 W/m K, GaAs: 44 W/m K [327]) can be neglected for such thin samples.

The results of the calibration process are displayed in figure B.1B. The pyrometer is capable of measuring temperatures in a range between 820 K to 1670 K. Starting from 900 K the temperature difference is less than ± 2.5 K, but also at the lowest measurable

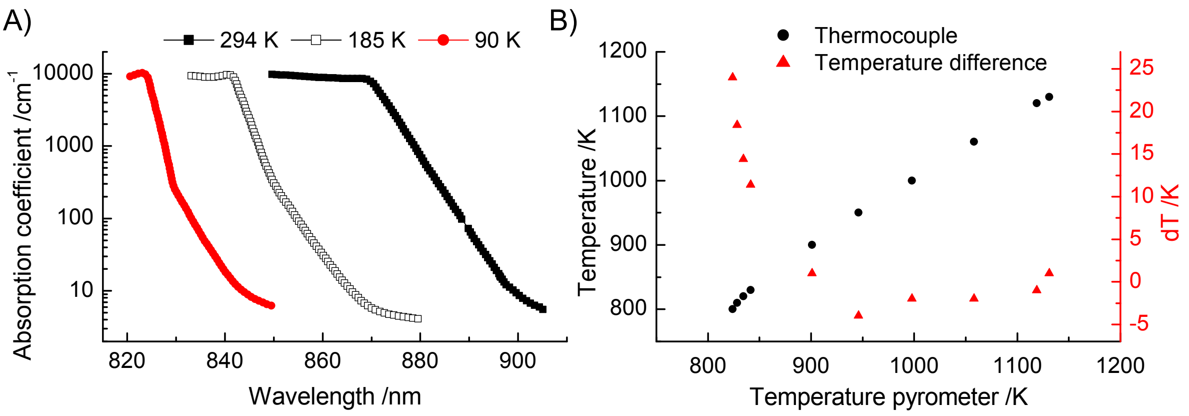

Figure B.1.: A) The absorption coefficient of GaAs at different temperatures as found by Sturge [421]. b) Comparison of temperatures measured by thermocouple and pyrometer.

temperature, the difference is only about 3 %.

B.2. SPM Calibration

STM

The quality of the self made tips and the calibration of the lateral displacement of the piezos was checked by measurements on freshly cleaved highly ordered pyrolytic graphite (HOPG) with its well established lattice parameters (figure B.2) [422].

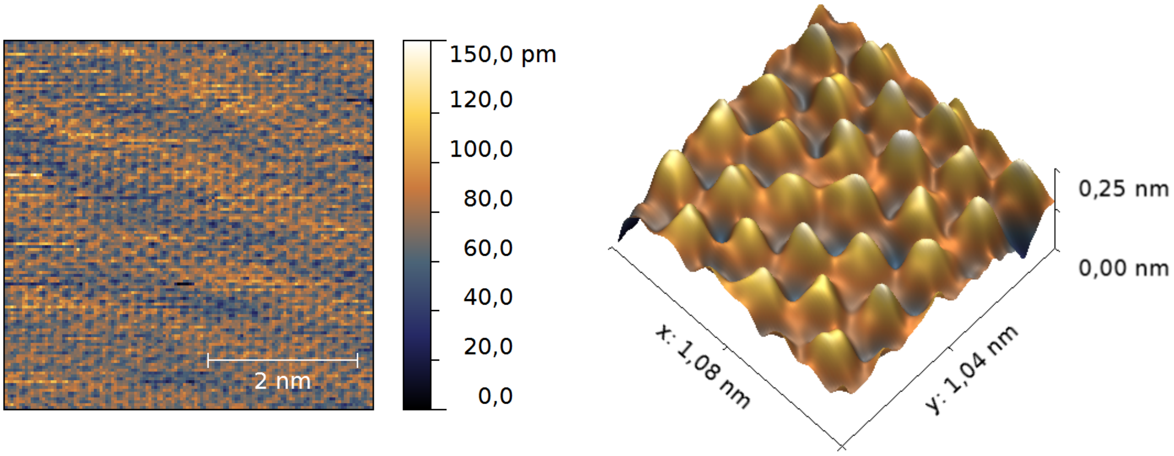

Figure B.2.: STM pictures of a freshly cleaved HOPG surface. Measurements like this were performed before each scan on GaAs samples to check the tip quality and calibrate the lateral scan axis.

AFM

The *Digital Instruments (Veeco)* atomic fore microscope and the condition of the cantilever-tip assemblies was verified by scanning self-assembled closed layers of polystyrene spheres, prepared by Peter Clawin [423]. The spheres itself are NIST certified size standards with 453 nm±4 nm diameter (3450A Nanosphere, *Duke Scientific*).

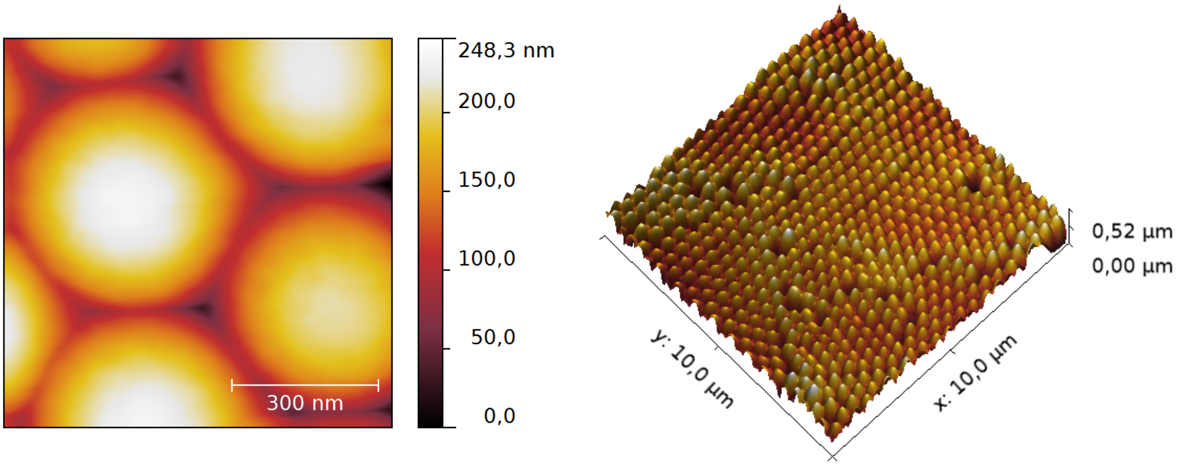

Figure B.3.: AFM pictures of a self-assembled layer of polystyrene spheres with 453 nm diameter used as calibration standard.

SNOM

The calibration of the SNOM is particularly important as the thermally pulled tips are under strong mechanical stress and tend to easily break. Figure B.4 shows the topographic information (left side) and the back reflection intensity from a 632 nm laser line (right side) of a pit grid with 10 µm interval (*Digital Instruments*).

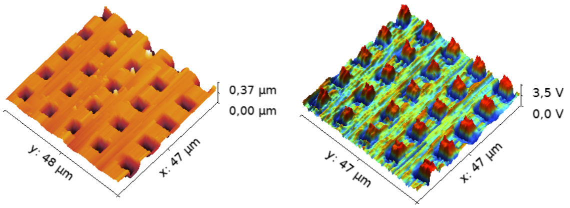

Figure B.4.: SNOM calibration with a 10 µm interval calibration lattice. Left: Topographic image. Right: Optical signal.

C. Further Data

C.1. XPS

C.1.1. References

References from the work of Sullivan et al. [343] unless otherwise noted:

B.E. /eV	Mod. A.P. /eV[1]	Signal	Species	Comment
425.8	1081.5	Ga LMM	Ga_2O_3	in Ga_2O_3 powder
424	1082.8	Ga LMM	Ga_2O	in Ga_2O_3 powder
424	1082.8	Ga LMM	Ga_2O_3	in Ga_2O_3 powder [349]
423.4	1083.1	Ga LMM	Ga_2O_3	in Ga_2O_3 powder [425]
420.3	1085.4	Ga LMM	Ga-As	(Doublet) cleaned wafer
418.7	1186.4	Ga LMM	Ga-As	metallic Ga
414.4	1091.3	Ga LMM	Ga-As	(Doublet) cleaned wafer
267.4	1263.2	As LMM	As_2O_3	in GaAs
267.4	1263.6	As LMM	As_2O_5	[425]
262	1266.6	As LMM	metallic As	based on data from [341]
261.6	1267	As LMM	metallic As	based on data from [425]
261.6	1266.1	As LMM	As−Ga	cleaned wafer

---

[1] Usually the modified Auger parameter is calculated as the sum of the dominant Auger lines kinetic energy and the binding energy of the strongest core level [424]. Instead Sullivan et al. used the binding energy difference of the Auger emission and the corresponding 3d line as Auger parameter [343], which is thus a function of excitation energy. As a compromise his values and those from other sources are transferred to the standard formalism but referenced to the 3d peak.

B.E. /eV	**Signal**	**Species**	**Comment**
46.3	As^{5+} 3d	As_2O_5	in As_2O_5 powder [349]
45.2-46	As^{5+} 3d	As_2O_5	NIST survey [426]
45.3	As^{3+} 3d	As_2O_3	in As_2O_3 powder [349]
45.2	As^{5+} 3d	As_2O_5	
45.2	As^{5+} 3d	$GaAsO_4$	NIST survey [426]
44.6	As^{3+} 3d	As_2O_3	in As_2O_3 powder [349]
44.3	As^{3+} 3d	As_2O_3	in GaAs
44-44.9	As^{3+} 3d	As_2O_3	NIST survey [426]
41.6-42	As 3d	elemental As	NIST survey [426]
41.1	As 3d	GaAs	in etched GaAs [349]
40.7-41.2	As 3d	GaAs	NIST survey [426]
23-24	O 2s	O-X	NIST survey
23.2	O 2s	O-X	For oxide conc. > 20%
21.6	Ga^{3+} 3d	$Ga(OH)_3$	By boiling GaAs inH_2O
20.7	Ga^{3+} 3d	Ga_2O_3	
20.6	Ga^{3+} 3d	Ga_2O_3	Ga_2O_3 powder [350]
20.4	Ga^{3+} 3d	Ga_2O_3	Ga_2O_3 powder and on Ga [349]
20.2-21.6	Ga^{3+} 3d	$Ga(OH)_3$	NIST survey [426]
20.2-21.6	Ga^{3+} 3d	$GaAsO_4$	NIST survey [426]
20.1	Ga^{1+} 3d	Ga_2O	
19.7-20.9	Ga^{3+} 3d	Ga_2O_3	NIST survey [426]
19.6-20.1	Ga^{1+} 3d	Ga_2O	NIST survey [426]
19.25	Ga $3d_{3/2}$	GaAs	HCl etched GaAs [348]
19.1	Ga 3d	GaAs	
19.0	Ga^{1+} 3d	Ga_2O	By reaction of Ga_2O_3 + Ga [350]
18.8	Ga $3d_{5/2}$	GaAs	HCl etched GaAs [348]
18.5-19.8	Ga 3d	GaAs	NIST survey [426]
18.5	Ga 3d	elemental Ga	[350]
18.2 -18.9	Ga 3d	elemental Ga	NIST survey [426]

C.1.2. Spectra from GaAs:Te

Figure C.1 shows the 2p core level signals of native oxide covered GaAs:Te samples, recorded using the Al K_α source. The intensity ratio between $2p_{1/2}$:$2p_{3/2}$ of 0.50 is in sound with the theoretical value. The split energy is 27.0 eV (26.84 eV [341]).

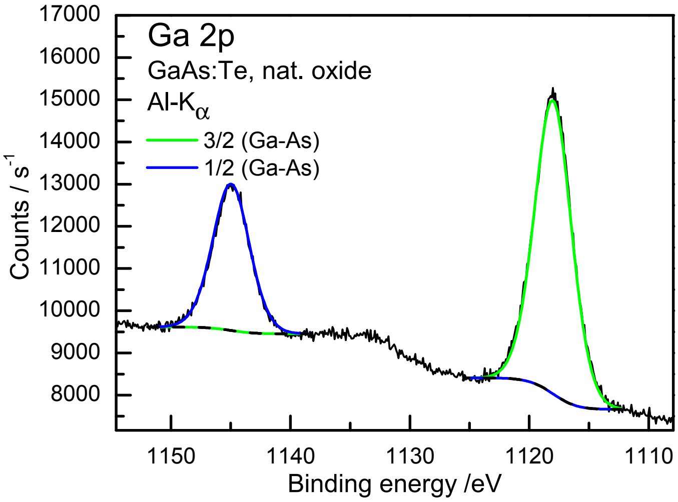

Signal	**Species**	**B.E. (FWHM) /eV**	**Lit. B.E. /eV**	**Area /a.u.**	**Conc. /%**
Ga $2p_{3/2}$	Ga_2O Ga_2O_3	1118.0 (3.68)	1118.0 [343] 1118.8 [343]	2655.3	66.5
Ga $2p_{1/2}$	Ga_2O Ga_2O_3	1145.0 (3.56)	1144.8 [341, 343] 1145.6 [341, 343]	1337.3	33.5

Figure C.1.: XPS Detail spectra of Ga 2p in GaAs:Te covered with native oxide layer using the Al x-ray source.

C.2. SPM

C.2.1. Platinum on Glass

In order to verify the amount of deposited platinum primarily determined by micro balance readings, 5 Å Pt were evaporated at room temperature on a high quality glass sample (D263T, *Schott AG*). Figure C.2 shows SEM images of the two bracket regions 1 and 2 (see section 6 for a definition). The clamping of the thermocouple in region 1, creates a gap between the retaining plate and the sample surface, which in turn causes the formation of the double edge in the left frame of figure C.2. The strong contrast in the SEM images is caused by the huge conductivity difference between the coated region and that below the brackets.

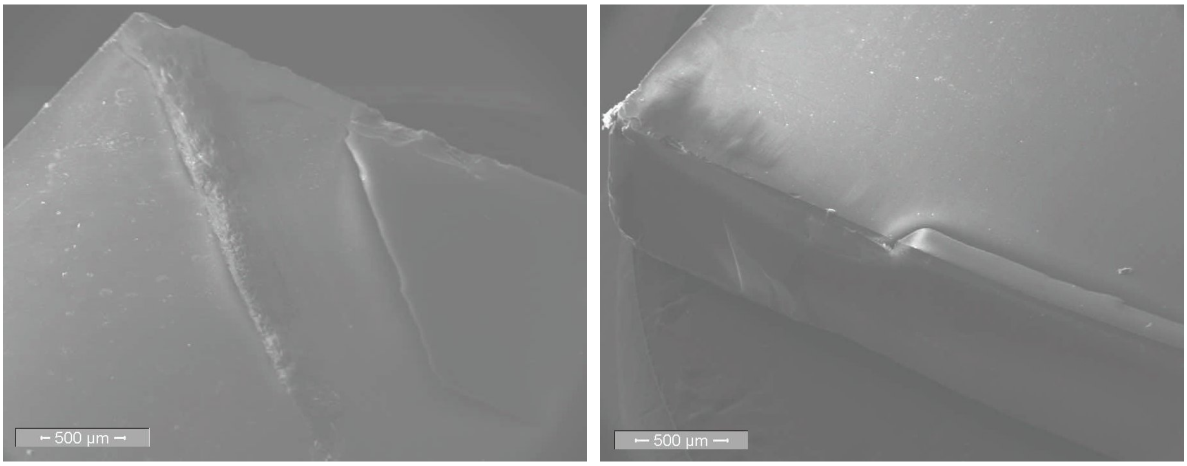

Figure C.2.: SEM images of a glass substrate (*Schott*) covered with 5 Å Pt deposited at room temperature. The left frame shows the bracket region 1, the right frame the opposite region 2.

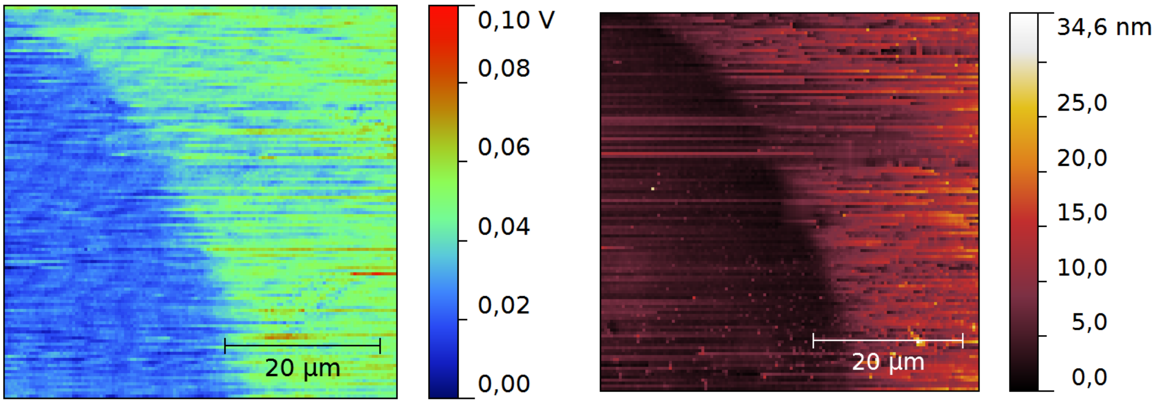

Figure C.3.: SPM images of a glass substrate (*Schott*) covered with 5 Å Pt deposited at room temperature. Left: SNOM image in reflection using a 632 nm HeNe laser. Right: Shear force image of the same area.

Also in SNOM measurements in reflection using a 632 nm HeNe laser source, a strong signal difference between the covered and uncovered regions can be found (left frames of figures C.3 and C.4). A height profile across the boundary, where the uncoated area is used as reference plane, gives a platinum layer thickness of 6 – 8 nm (figure C.5), which is more than ten times the nominal value. An inaccuracy of the micro balance in this dimension can be rejected based on the investigations on GaAs and earlier experiments by Al-Shemmary and Buchwald [29, 31]. This finding is also in contrast to the findings in XPS measurements on the metallized GaAs samples (cf. section 6.3). On a larger range into the metallized region the platinum layer thickness decreases again (right side of figure C.3 and figure C.5). In a simple picture it could be thought of a snow drift like behaviour. The growth mode and the mobility of platinum on top of the glass material must be responsible for this considerably different effect on the glass substrate compared to the gallium arsenide specimen.

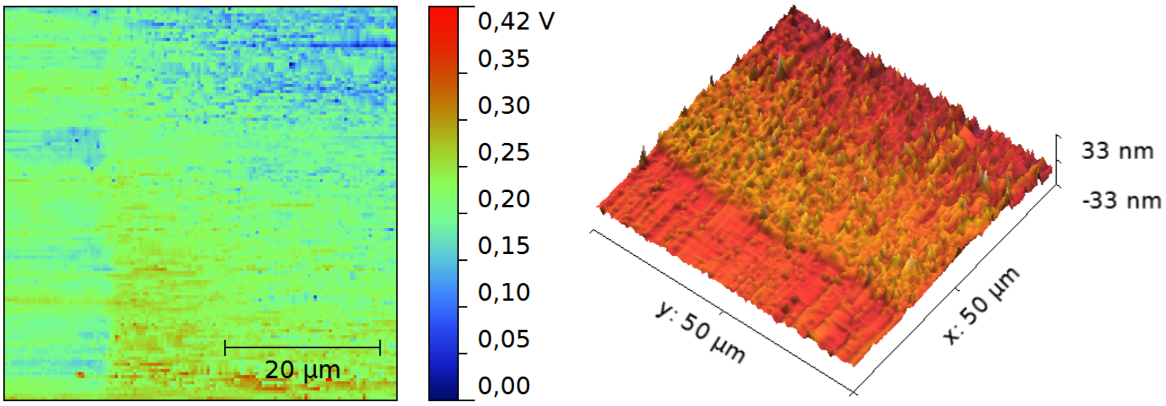

Figure C.4.: SPM images of a glass substrate (*Schott*) covered with 5 Å Pt deposited at room temperature. Left: SNOM image in reflection using a 632 nm HeNe laser. Right: Shear force image of the same area.

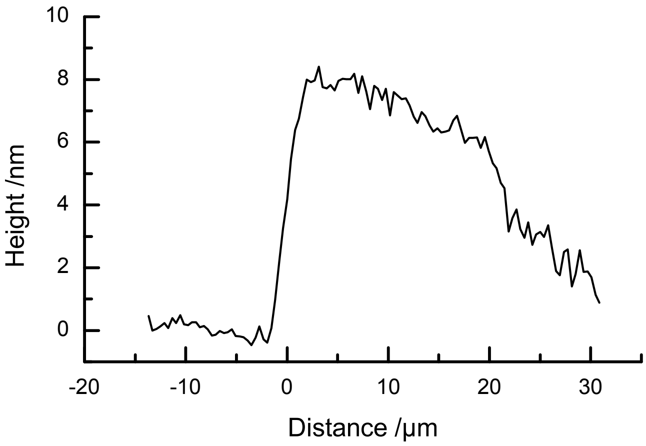

Figure C.5.: AFM height profile of a glass substrate (*Schott*) covered with 5 Å Pt deposited at room temperature.

C.3. Static Optical Measurements

C.3.1. Infrared Spectroscopy of CO on GaAs:Si-Pt

As shown in appendix B.1 and section 4.1.3, GaAs is transparent to infrared radiation. The stretching vibration mode of CO adsorbed at on-top sites measured by infrared reflection absorption spectroscopy (IRRAS) (figure C.6) is thus assigned to adsorption on platinum. CO is not known to adsorb on GaAs. To be able to detect this transmission signal, either a closed metal film or a high density of particles is necessary to reflect a sufficient amount of radiation. As references the corresponding CO signal from a flat Pt(111) single-crystal (2087 cm^{-1}) and from a PtCo_3 surface (2084 cm^{-1}) is shown as an example for a Pt-alloy. Compared to these the IR signal on GaAs:Si-Pt is weak and broad, which indicates a low order of adsorption sites. According to the Blyholder model the lower absorption energy (with respect to the transitions on the single crystals) is related to a stronger back bonding from the metal to carbon, which in turn depends on the metal and the adsorption site (coordination) [427]. Saturation coverages of CO on platinum particles evaporated at 300 K on alumina support show even stronger shifts to higher wave numbers (2090 – 2095 cm^{-1}) [29]. The observation of a CO adsorption on GaAs-Pt systems opens the door for further experiments on coupling between phonon modes at the semiconductor-metal interface and adsorbed molecules.

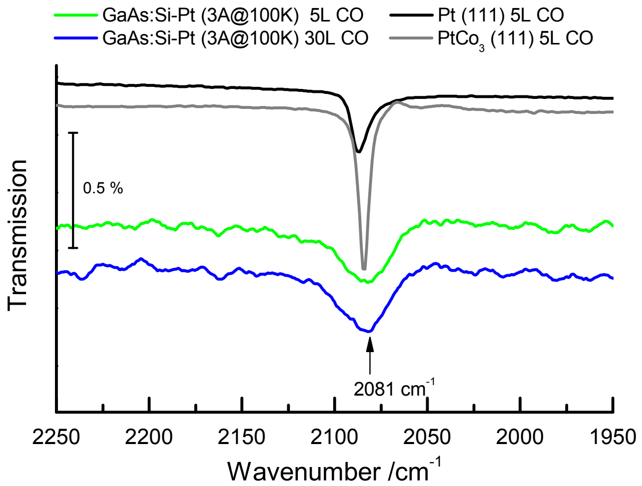

Figure C.6.: IRRAS spectrum of 5 and 30 L CO adsorbed to a 3 Å Pt coverage on GaAs:Si evaporated at 100 K. As reference corresponding saturation coverage data from a clean Pt(111) and a PtCo_3(111) single crystal alloy surface are shown.

C.3.2. Optical Microscopy of Superheated GaAs:Te Substrates

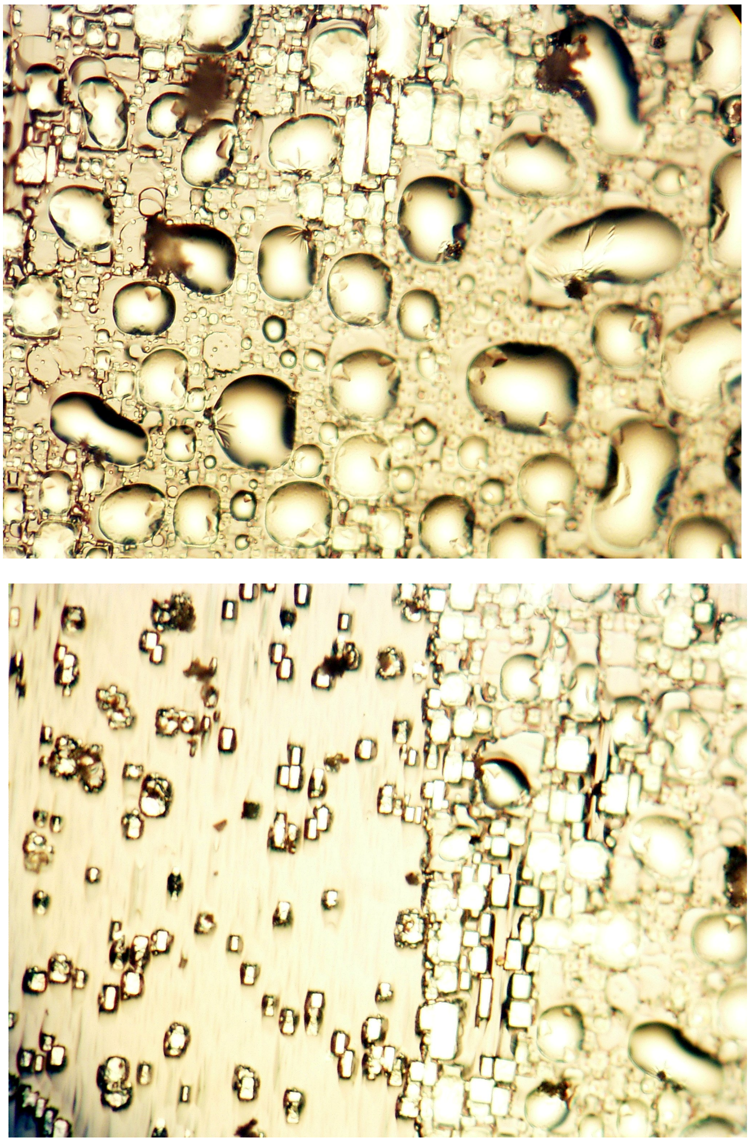

Figure C.7.: Light microscopy images of GaAs:Te heated to temperatures larger than 900 K. The initially polished substrates becomes opaque due to segregation of gallium and consequent blistering. The upper images shows the central region, while the lower one represents the transition between region 2 and 3 (for a description of the sample regions see section 6.1.1).

C.3.3. Rotational SHG Measurements on GaAs:Si

Figure C.8 shows a rotational scan on native oxide covered, Si-doped GaAs(100) surface with mixed input polarization and p-polarized output (mp). Due to the characteristic of a $\lambda/2$ plate the input polarization turned from nearly 100 % p to a mixed state and finally ends in a s-polarized input. At the intermediate states the cosine contribution of the mixed input causes the overall offset in the signal (phase contribution) and the unequal levels at the minima. These measurements proved to be very useful for the determination of susceptibility ratios as they provided information on different susceptibility components (cf. section 7.1.1) necessary for the fitting process.

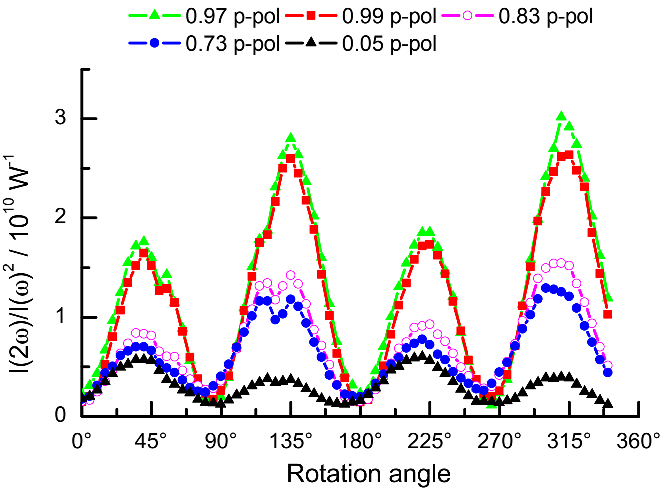

Figure C.8.: Rotational SHG scan of GaAs:Si (100), covered with oxide at different levels of p-polarized excitation beam and p-polarized output. The excitation pulse width is 35 – 40 fs.

C.3.4. Rotational SHG Measurements on GaAs(111)

The hexagonal GaAs(111) face can terminate with an arsenic or gallium layer, where the latter with only one dangling bond is energetically more stable than the As face with three dangling bonds. The (111) surface is only little studied by second-harmonic generation. Yamada et al. calculated the expected rotational behaviour for different polarization configuration without depletion zone treatment [193], while Scurtu et al. investigated GaAs(111) electrode interfaces in acid solutions by rotational SHG in combination with electrochemical methods [428]. Their predictions and findings correspond to the measurements in figure C.9. They exhibit the expected threefold symmetry for strongly doped samples. As on the GaAs:Te(100) substrates, this sample shows an increase in SHG intensity at lower wavelengths.

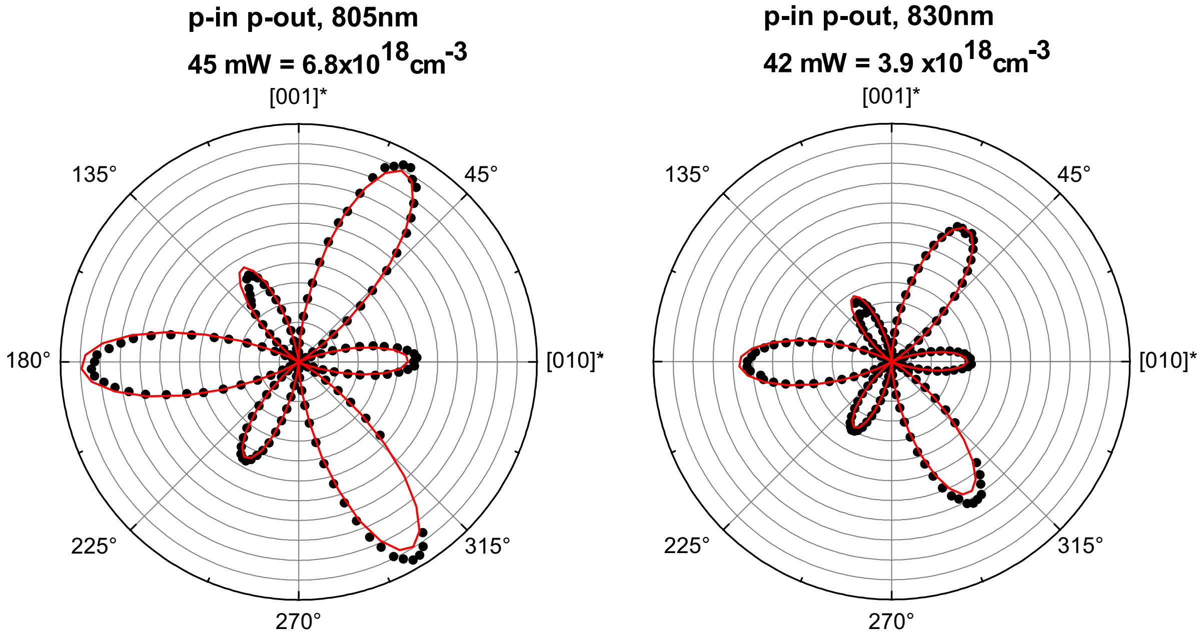

p-in p-out, 805nm
45 mW = 6.8x10^{18}cm^{-3}

p-in p-out, 830nm
42 mW = 3.9 x10^{18}cm^{-3}

Figure C.9.: SHG signal as a function of azimuthal angle from the GaAs (111) samples at 805 nm and 830 nm for pp polarization configuration. The [010]*, i.e. [001]* direction labels the projection of this vector to the (111) plane. The excitation pulse width is 35 – 40 fs.

C.3.5. Rotational SHG Measurements on GaAs(100)/AlGaAs Multi Quantum Well

Rotational SHG scans on multi quantum well structures made by repeated GaAs, $Al_{0.3}Ga_{0.7}As$ layers on an intrinsic GaAs(100) substrate are shown in figure C.10. The signal consists almost completely from bulk contribution, in a way typical for an undoped (100) substrate. Taking the optical information depth properties of standard GaAs as a basis, the SH signal should origin only from the topmost 20 to 30 nm, so only from the first quantum well layers (cf figure C.11).

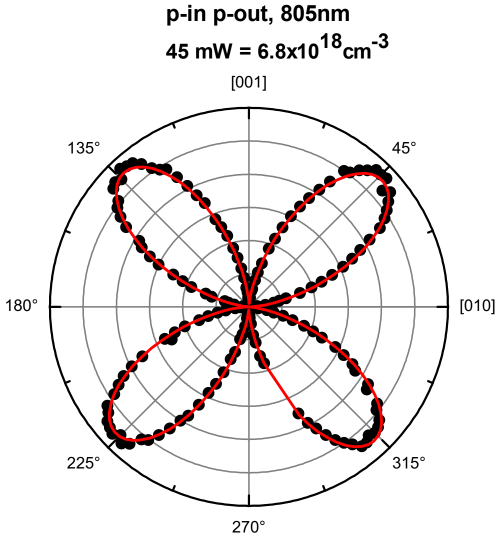

Figure C.10.: Rotational SHG scan of GaAs(100)/$Al_{0.3}Ga_{0.7}As$ multi quantum well structure in pp polarization configuration at 805 nm.

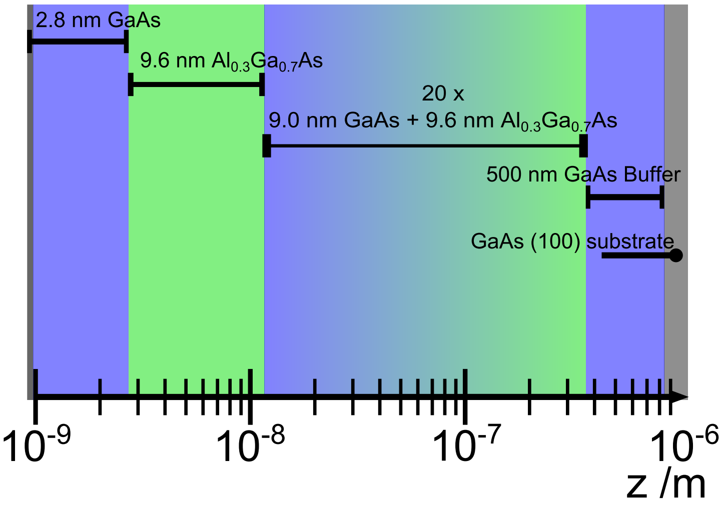

Figure C.11.: Composition of the $Al_{0.3}Ga_{0.7}As$ multi quantum well structure.

C.4. Time-Resolved Optical Measurements

C.4.1. Carrier Dynamics on GaAs:Si

Figure C.12 shows time-resolved SHG data on relative change in R scale at the higher intensity peak and different wavelengths. All measurements shown were recorded in pps or ppp configuration at intermediate carrier injection levels.

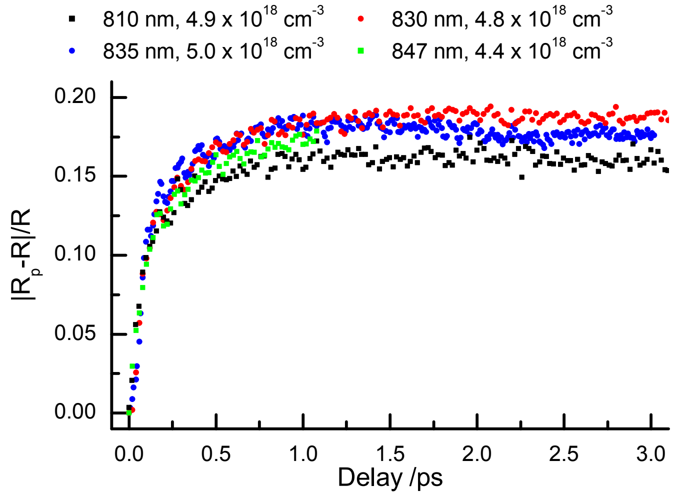

Figure C.12.: Relative temporal change of non-linear reflection coefficient R at different excitation wavelengths and similar peak carrier densities. All experiments were performed either in pps or ppp configuration at an azimuthal orientation associated to the higher intensity lobe at native oxide covered GaAs:Si. The excitation pulse width is 35 – 40 fs.

C.4.2. Carrier Dynamics on GaAs:Te

A small number of experiments were performed to investigate the temporal change of linear reflectivity on native oxide covered GaAs:Te upon pumping. Figure C.13 shows the response for different pump-injected carrier densities in pps configuration. The linear reflectivity response is isotropic, so no specific azimuthal orientation was chosen to record this data. In all scans a transient reduction of reflectivity can be observed, which qualitatively resembles the response of the non-linear SHG experiments, but with a much slower excitation of about 130 fs at the highest carrier density. The first relaxation process T_1 has a lifetime of 740 fs. With deceasing pump power not only the signals intensity decreases but also the shape of the response changes to an excitation and offset type.

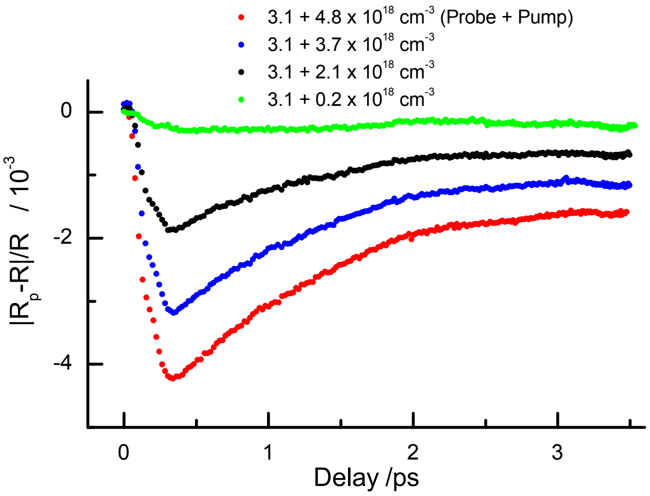

Figure C.13.: Relative temporal change of linear reflectivity R at different pump intensities on native oxide covered GaAs:Te. All experiments were performed in pps configuration. The initial rise at maximum injection density is about 130 fs long, while the following first relaxation process takes about 740 fs. The excitation pulse width is $35 - 40$ fs.

C.4.3. Carrier dynamics on GaAs(100)/AlGaAs Multi Quantum Wells

The multi quantum well structures on undoped GaAs (100) substrates exhibit a significantly different behaviour in their temporal SHG response than the pure doped oxide covered substrates and the metal interface samples. As shown in figure C.14A the signal at the given laser intensities consists of a sharp excitation R_1 and relaxation process T_1 with lifetimes in the range of $35 - 40$ fs each and a weak secondary relaxation process T_2 with an approximate lifetime of 230 fs quickly reaching a constant offset within the scan range. From scheme C.11 it can be seen that the information depth of the SHG signal confined by the phase matching length and the adsorption length of the frequency doubled SHG radiation is limited to the 2.8 nm thick GaAs capping layer and the first quantum well layer. The band gap in the wall material $Al_{0.3}Ga_{0.7}As$ is about 1.84 eV [429]. Absorption takes place in the thin top-layer which, based on the measurements on the substrates, is very likely heavily oxidized and inside the quantum well layer.

The quick establishment of a quasi-stationary equilibrium state may be attributed to the suppression of carrier diffusion into the bulk and the consequent high local carrier density. In contrast to the semiconductor and metal-interface samples, the signal gets weaker with increasing photon energy and laser intensity. Figure C.14B shows, unfortunately unnormalized, scans at different wavelength in pps configuration which support this trend.

As on the other samples the intensity of the fast excitation component is more pronounced when pump and probe pulse have the same polarization.

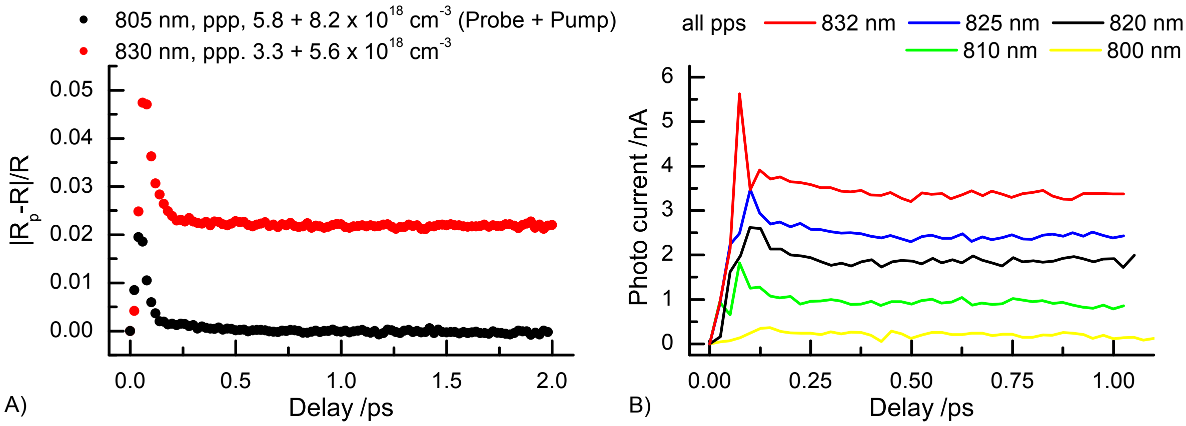

Figure C.14.: A) Relative temporal change of non-linear reflectivity at 805 nm and 830 nm on GaAs(100) multi quantum well structures. Measured at peak 1 (45°, compare figure C.10) in ppp configuration. B) Unnormalized change in SHG intensity for various wavelength in pps configuration, also measured at peak 1. The excitation pulse width is 35 – 40 fs.

List of Figures

List of Tables

Bibliography

[1] Germer, T. A. ; Kolasinski, K. W. ; Stephenson, J. C. ; Richter, L. J.: Depletion-electric-field-induced second-harmonic generation near oxidized GaAs(001) surfaces. In: *Physical Review B* 55 (1997), Nr. 16, 10694

[2] Hilbert, M. ; Lopez, P.: The World's Technological Capacity to Store, Communicate, and Compute Information. In: *Science* 332 (2011), Nr. 6025, 60-65. – 10.1126/science.1200970

[3] Thierse, Wolfgang: *Vortrag: Traditionswahrung und Modernisierung - Sozialdemokratie in der Entscheidung*. 2003

[4] *APS News - This month in Physics History, November 17-December 23 1947: Invention of the First Transistor*. `http://www.aps.org/publications/apsnews/200011/history.cfm`. (2000)

[5] *BBC News: How the CD was developed*. `http://news.bbc.co.uk/2/hi/6950933.stm`. (2007)

[6] Berners-Lee, Tim: *WorldWideWeb: Summary*. `https://groups.google.com/forum/#!msg/alt.hypertext/eCTkkOoWTAY/bJGhZyooXzkJ`. (1991)

[7] *Heise online: Rasanter Anstieg des mobilen Datenverkehrs durch iPhone & Co.* `http://heise.de/-1578508/`. (2012)

[8] Moore, G. E.: Cramming more components onto integrated circuits. In: *Electronics* 38 (1965), Nr. 8, S. 114–117

[9] Necke, M.: *Zersetzungsverhalten neuartiger, kohlenstofffreier Gold-Precursoren für den Einsatz in elektronenstrahlgestützten additiven Strukturierungsverfahren zur direkten Abscheidung von Metallen*, Carl von Ossietzky Universität Oldenburg, PhD thesis, (2010)

[10] Ahlf, Maraike: *Rare Earth Oxide Thin Films from Solution Based Inorganic Precursor Deposition as Potential Candidates for Insulators in Advanced Gate Stacks*, Carl von Ossietzky University of Oldenburg, PhD thesis, (2012)

[11] Othonos, A.: Probing ultrafast carrier and phonon dynamics in semiconductors. In: *Applied Physics Review* 83 (1996), Nr. 4, S. 1789

[12] Blakemore, J. S.: Semiconducting and other major properties of gallium arsenide. In: *Journal of Applied Physics* 53 (1982), Nr. 10, R123-R181

[13] Blakemore, J. S. ; Blakemore, J. S. (Hrsg.): *Gallium arsenide: Edited by John S Blakemore*. American Institute of Physics, 1987

[14] *Circuits Today: Ultra-fast Systems and GaAs VLSI Technology*. http://www.circuitstoday.com/ultra-fast-systems-and-gaas-vlsi-technology. (2011), Last checked: 1-3-2014

[15] Anwar, A.: Are silicon technologies poised to displace GaAs. In: *semiconductor-TODAY* 2 (2007), Nr. 10, 48-51

[16] Lechuga, L. M. ; Calle, A. ; Golmayo, D. ; Briones, F.: Hydrogen sensor based on a Pt/GaAs Schottky diode. In: *Sensors and Actuators B: Chemical* 4 (1991), Nr. 3-4, 515-518

[17] Murarka, S. P.: High-temperature stability of Au Pt/n-GaAs Schottky barrier diodes. In: *Solid-State Electronics* 17 (1974), Nr. 8, 869-876

[18] Masó, J. ; Barniol, N. ; Pérez-Murano, F. ; Aymerich, X.: Morphologic and spectroscopic characterization of porous Pt/GaAs Schottky diodes by scanning tunnelling microscopy. In: *Thin Solid Films* 261 (1995), Nr. 1-2, 299-306

[19] Voelcker, J.: The Gunn effect: puzzling over noise. In: *Spectrum IEEE* 26 (1989), Nr. 7

[20] Cengher, D. ; Hatzopoulos, Z. ; Gallis, S. ; Deligeorgis, G. ; Aperathitis, E. ; Androulidaki, M. ; Alexe, M. ; Dragoi, V. ; Kyriakis-Bitzaros, E. D. ; Halkias, G. ; Georgakilas, A.: Fabrication of GaAs laser diodes on Si using low-temperature bonding of MBE-grown GaAs wafers with Si wafers. In: *Journal of Crystal Growth* 251 (2003), Nr. 1-4, 754-759

[21] Ustinov, V. M. ; Zhukov, A. E.: GaAs-based long-wavelength lasers. In: *Semiconductor Science and Technology* 15 (2000), Nr. 8, R41

[22] *phys.org: World record solar cell with 44.7% efficiency.* http://phys.org/news/2013-09-world-solar-cell-efficiency.html. (2013), Last checked: 2-3-1014

[23] Wilson, Greg ; Mooney, Dave: *Research Cell Efficiency Records.* http://www.nrel.gov/ncpv/. (2014), Last checked: 2-3-2014

[24] Kost, C. ; Mayer, J. N. ; Thomsen, J. ; Hartmann, N. ; Senkpiel, C. ; Philipps, S. ; Nold, S. ; Lude, S. ; Schlegl, T.: *Studie: Stromgestehungskosten Erneuerbare Energien.* Fraunhofer-Institut für solare Energiesysteme ISE, 2013

[25] Rastedt, Maren: *Design und Optimierung organischer Nanoröhrchen (für die potentielle Anwendung in kostengünstigen organischen Photovoltaik-Bauteilen)*, Carl von Ossietzky Universität Oldenburg, PhD thesis, (2013)

[26] McFarland, E. W. ; Tang, J.: A photovoltaic device structure based on internal electron emission. In: *Nature* 421 (2003), Nr. 6923, 616-618. – 10.1038/nature01316

[27] Gratzel, M.: Applied physics: Solar cells to dye for. In: *Nature* 421 (2003), Nr. 6923, 586-587. – 10.1038/421586a

[28] Tisdale, W. A. ; Williams, K. J. ; Timp, B. A. ; Norris, D. J. ; Aydil, E. S. ; Zhu, X. Y.: Hot-Electron Transfer from Semiconductor Nanocrystals. In: *Science* 328 (2010), Nr. 5985, 1543-1547. – 10.1126/science.1185509

[29] Al-Shemmary, A.: *Model studies on photocatalysis: laser induced CO desorption from platinum nanoparticles at an alumina support*, Universität Oldenburg, PhD thesis, (2011)

[30] Al-Shemmary, A. ; Buchwald, R. ; Al-Shamery, K.: Surface photochemistry of CO adsorbed on alumina supported nanoparticulate platinum. In: *Journal of Physics: Condensed Matter* 22 (2011), Nr. 8, 084011

[31] Buchwald, Robert: *NO-Adsorption und laserinduzierte Adsorbatplatzänderungen an Platin-Nanopartikeln und Aufbau einer STM-UHV-Kammer*, Universität Oldenburg, PhD thesis, (2013)

[32] Funk, S. ; Bonn, M. ; Denzler, D. N. ; Hess, C. ; Wolf, M. ; Ertl, G.: Desorption of CO from Ru(001) induced by near-infrared femtosecond laser pulses. In: *The Journal of Chemical Physics* 112 (2000), Nr. 22, S. 9888–9897

[33] Wieckowski, A. (Hrsg.) ; Savinova, E. R. (Hrsg.) ; Vayenas, C. G. (Hrsg.): *Catalysis and Electrocatalysis at Nanoparticle Surface.* 1. Marcel Dekker, Inc., 2003

[34] Schwab, G. M.: Boundary-Layer Catalysis. In: *Angewandte Chemie International Edition in English* 6 (1967), Nr. 4, 375

[35] Park, J. Y. ; Lee, H. ; Renzas, J. R. ; Zhang, Y. ; Somorjai, G. A.: Probing Hot Electron Flow Generated on Pt Nanoparticles with Au/TiO_2 Schottky Diodes during Catalytic CO Oxidation. In: *Nano Letters* 8 (2008), Nr. 8, 2388-2392. – doi: 10.1021/nl8012456

[36] Ueba, H. ; Gumhalter, B.: Theory of two-photon photoemission spectroscopy of surfaces. In: *Progress in Surface Science* 82 (2007), Nr. 4-6, 193-223

[37] Mauerer, M. ; Shumay, I. L. ; Berthold, W. ; Höfer, U.: Ultrafast carrier dynamics in Si(111) 7x7 dangling bonds probed by time-resolved second-harmonic generation and two-photon photoemission. In: *Physical Review B* 73 (2006), Nr. 24, 245305

[38] Meschede, D.: *Optik, Licht und Laser.* 3. Vieweg+Teubner, 2008

[39] Bordo, V. G. ; Rubahn, H-G.: *Optics and Spectroscopy at Surfaces and Interfaces.* Wiley-VCH, 2005

[40] Kopitzki, K. ; Herzog, P. (Hrsg.): *Einführung in die Festkörperphysik.* 3. Teubner, 1993

[41] Fox, M.: *Optical Properties of Solids.* 1. Oxford University Press, 2007

[42] Franken, P. A. ; Hill, A. E. ; Peters, C. W. ; Weinreich, G.: Generation of Optical Harmonics. In: *Physical Review Letters* 7 (1961), Nr. 4, 118

[43] Maimann, T. H. M.: Stimulated optical radiation in ruby. In: *Nature* 187 (1960), 493

[44] Shen, Y. R.: *The Principles of Nonlinear Optics.* John Wiley & Sons, 1984

[45] Trebino, R.: *Frequency-Resolved Optical Gating.* Kluwer Academic Publishers, 2000. – ISBN 1–4020–7066–7

[46] Yariv, A.: *Quantum Electronics.* 3. John Wiley & Sons, 1989

[47] Mukamel, S.: *Principles of Nonlinear Optical Spectroscopy.* 1995

[48] Becker, P. C. ; Fork, R. L. ; Brito Cruz, C. H. ; Gordon, J. P. ; Shank, C. V.: Optical Stark Effect in Organic Dyes Probed with Optical Pulses of 6-fs Duration. In: *Physical Review Letters* 60 (1988), Nr. 24, 2462

[49] Mysyrowicz, A. ; Hulin, D. ; Antonetti, A. ; Migus, A. ; Masselink, W. T. ; Morko&ccedil ; , H. : "Dressed Excitons" in a Multiple-Quantum-Well Structure: Evidence for an Optical Stark Effect with Femtosecond Response Time. In: *Physical Review Letters* 56 (1986), Nr. 25, 2748

[50] Fröhlich, D. ; Nöthe, A. ; Reimann, K.: Observation of the Resonant Optical Stark Effect in a Semiconductor. In: *Physical Review Letters* 55 (1985), Nr. 12, 1335

[51] Miller, A. ; Miller, D. A. B. ; Smith, S. D.: Dynamic non-linear optical processes in semiconductors. In: *Advances in Physics* 30 (1981), Nr. 6, 697-800

[52] Schmitt-Rink, S. ; Chemla, D. S. ; Miller, D. A. B.: Theory of transient excitonic optical nonlinearities in semiconductor quantum-well structures. In: *Physical Review B* 32 (1985), Nr. 10, 6601

[53] Berman, P. R. ; Salomaa, R.: Comparison between dressed-atom and bare-atom pictures in laser spectroscopy. In: *Physical Review A* 25 (1982), Nr. 5, 2667

[54] Ruddock, I. S.: Nonlinear optical second harmonic generation. In: *European Journal of Physics* 15 (1994), Nr. 2, 53

[55] Kleinman, D. A.: Nonlinear Dielectric Polarization in Optical Media. In: *Physical Review* 126 (1962), Nr. 6, 1977

[56] Dailey, C. A. ; Burke, B. J. ; Simpson, G. J.: The general failure of Kleinman symmetry in practical nonlinear optical applications. In: *Chemical Physics Letters* 390 (2004), Nr. 1-3, 8-13

[57] Neumann, F. E.: *Vorlesungen über die Theorie der Elastizität der festen Körper und des Lichtäthers.* B. G. Teubner-Verlag, 1885

[58] Terhune, R. W. ; Maker, P. D. ; Savage, C. M.: Optical Harmonic Generation in Calcite. In: *Physical Review Letters* 8 (1962), Nr. 10, 404

[59] Pershan, P. S.: Nonlinear Optical Properties of Solids: Energy Considerations. In: *Physical Review* 130 (1963), Nr. 3, 919

[60] Adler, E.: Nonlinear Optical Frequency Polarization in a Dielectric. In: *Physical Review* 134 (1964), Nr. 3A, A728

[61] Bloembergen, N. ; Pershan, P. S.: Light Waves at the Boundary of Nonlinear Media. In: *Physical Review* 128 (1962), Nr. 2, 606

[62] Bloembergen, N.: Second Harmonic Reflected Light. In: *Optica Acta: International Journal of Optics* 13 (1966), Nr. 4, 311-322

[63] Bloembergen, N. ; Chang, R. K. ; Jha, S. S. ; Lee, C. H.: Optical Second-Harmonic Generation in Reflection from Media with Inversion Symmetry. In: *Physical Review* 174 (1968), Nr. 3, 813

[64] Shen, Y. R.: Optical Second Harmonic Generation at Interfaces. In: *Annual Review of Physical Chemistry* 40 (1989), Nr. 1, 327

[65] Heinz, T F.: Second-order Nonlinear Optical Effects at Surfaces and Interfaces. In: Ponath, H.-E. (Hrsg.) ; Stegeman, G. I. (Hrsg.): *Nonlinear Surface Electromagnetic Phenomena.* Elsevier Science Publishers, 1991

[66] Brown, F. ; Matsuoka, M.: Effect of Adsorbed Surface Layers on Second-Harmonic Light from Silver. In: *Physical Review* 185 (1969), Nr. 3, 985

[67] Heinz, T. F. ; Chen, C. K. ; Ricard, D. ; Shen, Y. R.: Spectroscopy of Molecular Monolayers by Resonant Second-Harmonic Generation. In: *Physical Review Letters* 48 (1982), Nr. 7, 478

[68] Chen, C. K. ; Castro, A. R. B. ; Shen, Y. R.: Surface-Enhanced Second-Harmonic Generation. In: *Physical Review Letters* 46 (1981), Nr. 2, 145

[69] Guyot-Sionnest, P. ; Chen, W. ; Shen, Y. R.: General considerations on optical second-harmonic generation from surfaces and interfaces. In: *Physical Review B* 33 (1986), Nr. 12, 8254

[70] Felderhof, B. U. ; Marowsky, G.: Linear optics of polarization sheets. In: *Applied Physics B: Lasers and Optics* 43 (1987), Nr. 3, 161-166

[71] Sipe, J. E.: New Green-function formalism for surface optics. In: *Journal of the Optical Society of America B* 4 (1987), Nr. 4, 481-489

[72] Shen, Y. R.: Nonlinear optical studies of surfaces. In: *Applied Physics A: Materials Science & Processing* 59 (1994), Nr. 5, 541-543

[73] Richmond, G. L. ; Robinson, J. M. ; Shannon, V. L.: Second harmonic generation studies of interfacial structure and dynamics. In: *Progress in Surface Science* 28 (1988), Nr. 1, 1-70

[74] Corn, R. M. ; Higgins, D. A.: Optical second harmonic generation as a probe of surface chemistry. In: *Chemical Reviews* 94 (1994), Nr. 1, 107-125. – doi: 10.1021/cr00025a004

[75] Heinz, T. F. ; Tom, H. W. K. ; Mate, C. M. ; Zhu, X. D. ; Crowell, J. E. ; Somorjai, G. A. ; Shen, Y. R.: Surface studies by optical second-harmonic generation: The adsorption of O2, CO, and sodium on the Rh(111) surface. In: *Physical Review Letters* 52 (1983), Nr. 5, S. 348

[76] Zhu, X. D. ; Shen, Y. R. ; Carr, R.: Correlation between thermal desorption spectroscopy and optical second harmonic generation for monitoring surface coverages. In: *Surface Science* 163 (1985), Nr. 1, 114-120

[77] Niemantsverdriet, J. W.: Thermal Desorption Spectroscopy. In: *Spectroscopy in Catalysis*. Weinheim, 1993

[78] Parker, D. H. ; Jones, M. E. ; Koel, B. E.: Determination of the reaction order and activation energy for desorption kinetics using tpd spectra: application to D_2 desorption from Ag(111). In: *Surface Science* 233 (1989), S. 65

[79] de Jong, A.M. ; J.W.Niemantsverdriet: Thermal desorption analysis: Comparative test of ten commonly applied procedures. In: *Surface Science* 233 (1990), S. 355

[80] King, D. A.: Thermal desorption from metal surfaces: A review. In: *Surface Science* 47 (1975), Nr. 1, 384-402

[81] Campbell, D. J. ; Lynch, M. L. ; Corn, R. M.: Second harmonic generation studies of anionic chemisorption at polycrystalline platinum electrodes. In: *Langmuir* 6 (1990), Nr. 11, 1656-1664. – doi: 10.1021/la00101a006

[82] Bourdon, A. ; Gomez, S. L. ; Lemal, M. ; Quelin, X.: Surface second-harmonic generation in Au:TiO2 cermet thin films. In: *The European Physical Journal D* 30 (2004), S. 217

[83] Efrima, S. ; Berkovic, G.: Second harmonic generation studies of silver metal liquidlike films. In: *Journal of Physical Chemistry* 95 (1991), S. 7422

[84] Anderson, S.: *Second-harmonic generation as a probe of chemically modified Si(111) surfaces and the initial oxidation of hydrogen terminated Si(111)*, Concordia University, PhD thesis, (2000)

[85] Baten, S. M. A. ; Taylor, A. G. ; Paul Wilde, C.: A second harmonic generation study of the oxidation of copper electrodes. In: *Electrochemistry Communications* 9 (2007), Nr. 9, 2393-2396

[86] Guo, C. ; Rodriguez, G. ; Taylor, A. J.: Ultrafast Dynamics of Electron Thermalization in Gold. In: *Physical Review Letters* 86 (2001), Nr. 8, 1638

[87] Guo, C. ; Rodriguez, G. ; Hoffbauer, M. ; Taylor, A. J.: Influence of electronic temperature and distribution on the second-order surface nonlinear susceptibility of metals. In: *Applied Physics Letters* 78 (2001), Nr. 21, 3211-3213

[88] Tom, H. W. K. ; Aumiller, G. D. ; Brito-Cruz, C. H.: Time-resolved study of laser-induced disorder of Si surfaces. In: *Physical Review Letters* 60 (1988), Nr. 14, 1438

[89] Lamprecht, B. ; Leitner, A. ; Aussenegg, F. R.: SHG studies of plasmon dephasing in nanoparticles. In: *Applied Physics B: Lasers and Optics* 68 (1999), Nr. 3, 419-423

[90] Klein-Wiele, J. H. ; Simon, P. ; Rubahn, H. G.: Size-Dependent Plasmon Lifetimes and Electron-Phonon Coupling Time Constants for Surface Bound Na Clusters. In: *Physical Review Letters* 80 (1998), Nr. 1, 45

[91] Glinka, Y. D.: Pump-probe second harmonic generation study of ultrafast spin dynamics in semiconductor multilayers. In: *Surface and Interface Analysis* 35 (2003), Nr. 2, S. 146–150

[92] Prybyla, J. A. ; Tom, H. W. K. ; Aumiller, G. D.: Femtosecond time-resolved surface reaction: Desorption of Co from Cu(111) in less than 325 fsec. In: *Physical Review Letters* 68 (1992), Nr. 4, 503

[93] McGilp, J. F.: Optical Second-Harmonic Generation as a Semiconductor Surface and Interface Probe. In: *physica status solidi (a)* 175 (1999), Nr. 1, 153-167

[94] McGilp, J. F.: A review of optical second-harmonic and sum-frequency generation at surfaces and interfaces. In: *Journal of Physics D: Applied Physics* 29 (1996), Nr. 7, 1812

[95] Driscoll, T. A. ; Guidotti, D.: Symmetry analysis of second-harmonic generation in silicon. In: *Physical Review B* 28 (1983), Nr. 2, 1171

[96] Guidotti, D. ; Driscoll, T. A. ; Gerritsen, H. J.: Second harmonic generation in centro-symmetric semiconductors. In: *Solid State Communications* 46 (1983), Nr. 4, 337-340

[97] Heinz, T. F. ; Loy, M. M. T. ; Thompson, W. A.: Study of Si(111) Surfaces by Optical Second-Harmonic Generation: Reconstruction and Surface Phase Transformation. In: *Physical Review Letters* 54 (1985), Nr. 1, 63

[98] Tom, H. W. K. ; Heinz, T. F. ; Shen, Y. R.: Second-Harmonic Reflection from Silicon Surfaces and Its Relation to Structural Symmetry. In: *Physical Review Letters* 51 (1983), Nr. 21, 1983

[99] Sipe, J. E. ; Moss, D. J. ; Driel, H. M.: Phenomenological theory of optical second- and third-harmonic generation from cubic centrosymmetric crystals. In: *Physical Review B* 35 (1987), Nr. 3, 1129

[100] Tom, H. W. K.: *Studies of Surfaces using Optical Second-Harmonic Generation*, University of California Berkley, PhD thesis, (1984)

[101] Kittel, Ch.: *Einführung in die Festkörperphysik*. 12. R. Oldenbourg Verlag, 1999

[102] Ashcroft, N. W. ; Mermin, N. D.: *Festkörperphysik*. Oldenbourg Verlag, 2001

[103] Wendler, L. ; Haupt, R. ; Bechstedt, F. ; Rücker, H. ; Enderlein, R.: Free carrier scattering from quasi-2D optical phonons in semiconductor quantum

wells and superlattices. In: *Superlattices and Microstructures* 4 (1988), Nr. 4/5, 577-580

[104] Leheny, R. F. ; Shah, J. ; Fork, R. L. ; Shank, C. V. ; Migus, A.: Dynamics of hot carrier cooling in photo-excited GaAs. In: *Solid State Communications* 31 (1979), Nr. 11, 809-813

[105] Byrnes, S. J. F.: *Basic theory and phenomenology of polarons.* http://sjbyrnes.com/. (2008), Last checked: 28-4-2012

[106] Vasileska, D.: *Polar optical phonon scattering.* http://nanohub.org/resources/11522. (2011), Last checked: 28-4-2012

[107] Lundstrom, M.: *ECE 656 Lecture 24: Phonon Scattering I.* http://nanohub.org/resources/12455. (2009), Last checked: 28-4-2012

[108] Lundstrom, M.: *Fundamentals of carrier transport.* 2nd edition. Cambridge University Press, 2000

[109] Balzer, F. ; Al Shamery, K. ; Neuendorf, R. ; Rubahn, H.-G.: Nonlinear optics of hexaphenyl nanofibers. In: *Chemical Physics Letters* 368 (2003), Nr. 3-4, 307-312

[110] Otto, A.: Excitation of nonradiative surface plama waves in silver by the method of frustrated total reflection. In: *Zeitschrift für Physik* 216 (1968), S. 398

[111] Kretschmann, E. ; Raether, H.: Radiative decay of nonradiative surface plasmons excited by light. In: *Z.Naturforsch A* 23 (1968), S. 2135

[112] Teng, Y. Y. ; Stern, E. A.: Plasma Radiation from Metal Grating Surfaces. In: *Physical Review Letters* 19 (1967), Nr. 9, 511

[113] Ropers, C. ; Park, D. J. ; Stibenz, G. ; Steinmeyer, G. ; Kim, J. ; Kim, D. S. ; Lienau, C.: Femtosecond Light Transmission and Subradiant Damping in Plasmonic Crystals. In: *Physical Review Letters* 94 (2005), Nr. 11, 113901

[114] Ropers, C. ; Stibenz, G. ; Steinmeyer, G. ; MÃ¼ller, R. ; Park, D. J. ; Lee, K. G. ; Kihm, J. E. ; Kim, J. ; Park, Q. H. ; Kim, D. S. ; Lienau, C.: Ultrafast dynamics of surface plasmon polaritons in plasmonic metamaterials. In: *Applied Physics B: Lasers and Optics* 84 (2006), Nr. 1, 183-189

[115] Matsumoto, Y. ; Watanabe, K.: Coherent Vibrations of Adsorbates Induced by Femtosecond Laser Excitation. In: *Chemical Reviews* 2006 (2006), Nr. 106, S. 4234

[116] Shah, J.: *Ultrafast Spectroscopy of Semiconductors and Semiconductor Nanostructures.* 2. Springer-Verlag, 1998 (Solid-State Sciences)

[117] Boyd, R. W.: *Nonlinear Optics.* 3. Academic Press, 2003

[118] Tipler, P. A.: *Physik.* 1. Spektrum Akademischer Verlag, 1998

[119] De Silvestri, S. ; Fujimoto, J. G. ; Ippen, E. P. ; Gamble, E. B. ; Williams, L. R. ; Nelson, K. A.: Femtosecond time-resolved measurements of optic phonon dephasing by impulsive stimulated raman scattering in [alpha]-perylene crystal from 20 to 300 K. In: *Chemical Physics Letters* 116 (1985), Nr. 2-3, 146-152

[120] Zeiger, H. J. ; Vidal, J. ; Cheng, T. K. ; Ippen, E. P. ; Dresselhaus, G. ; Dresselhaus, M. S.: Theory for displacive excitation of coherent phonons. In: *Physical Review B* 45 (1992), Nr. 2, S. 768

[121] Ippen, E. P. ; Dresselhaus, G. ; Dresselhaus, M. S. ; Moodera, J. S. ; Cheng, T. K. ; Brorson, S. D. ; Kazeroonian, A. S.: Impulsive excitation of coherent phonons observed in reflection in bismuth and antimony. In: *Applied Physics Letters* 57 (1990), Nr. 10, S. 1004

[122] Nakashima, S. ; Mizoguchi, K. ; Harima, H. ; Sakai, K.: Coherent phonon oscillations in photo-excited semiconductors and semimetals. In: *Journal of luminescence* 76 (1998), S. 6–14

[123] Kutt, W. A. ; Albrecht, W. ; Kurz, H.: Generation of coherent phonons in condensed media. In: *IEEE Journal of Quantum Electronics* 28 (1992), Nr. 10, S. 2434–2444

[124] Sun, C. K. ; Liang, J. C. ; Stanton, C. J. ; Abare, A. ; Coldren, L. ; DenBaars, S. P.: Large coherent acoustic-phonon oscillation observed in InGaN/GaN multiple-quantum wells. In: *Applied Physics Letters* 75 (1999), Nr. 9, 1249-1251

[125] Sun, C. K. ; Liang, J. C. ; Yu, X. Y.: Coherent Acoustic Phonon Oscillations in Semiconductor Multiple Quantum Wells with Piezoelectric Fields. In: *Physical Review Letters* 84 (2000), Nr. 1, 179

[126] Yee, K. J. ; Lim, Y. S. ; Dekorsy, T. ; Kim, D. S.: Mechanisms for the Generation of Coherent Longitudinal-Optical Phonons in GaAs /AlGaAs Multiple Quantum Wells. In: *Physical Review Letters* 86 (2001), Nr. 8, 1630

[127] Chern, G. W. ; Lin, K. H. ; Huang, Y. K. ; Sun, C. K.: Spectral analysis of high-harmonic coherent acoustic phonons in piezoelectric semiconductor multiple quantum wells. In: *Physical Review B* 67 (2003), Nr. 12, 121303

[128] Hodak, J. H. ; Martini, I. ; Hartland, G. V.: Observation of acoustic quantum beats in nanometer sized Au particles. In: *Journal of Chemical Physics* 108 (1998), S. 9210

[129] Hodak, J. H. ; Henglein, A. ; Hartland, G. V.: Size dependent properties of Au particles: Coherent excitation and dephasing of acoustic vibrational modes. In: *Journal of Chemical Physics* 111 (1999), Nr. 18, S. 8613

[130] Hartland, G. V.: Coherent vibrational motion in metal particles: Determination of the vibrational amplitude and excitation mechansim. In: *Journal of Chemical Physics* 116 (2002), Nr. 18, S. 8048

[131] Hartland, G. V. ; Hu, M. ; Wilson, O. ; Mulvaney, P. ; Sader, J. E.: Coherent Excitation of Vibrational Modes in Gold Nanorods. In: *Journal of Physical Chemistry B* 106 (2002), Nr. 4, S. 743

[132] Link, S. ; El-Sayed, M. A.: Optical Properties and Ultrafsat Dynamics of Metallic Nanocrystals. In: *Annual Review of Physical Chemistry* (2003), S. 331

[133] El-Sayed, M. A. ; Qian, W. ; Huang, W.: Coherent Vibrational Oscillation in gold Prismatic Monolayer Periodic Nanoparticle Arrays. In: *Nano Lett.* 4 (2004), Nr. 9, S. 1741

[134] Burgin, J. ; Langot, P. ; Del Fatti, N. ; Vallée, F. ; Huang, W. ; El-Sayed, M. A.: Time-resolved Investigation of the Acoustic Vibration of a Single Gold Nanoprism Pair. In: *Journal of Physical Chemistry* 112 (2008), S. 11231–11235

[135] Dekorsy, T. ; Leiderer, P. ; Habenicht, A. ; Merkt, F. ; Bartels, A. ; Hudert, F. ; Taubert, R.: Coherent acoustic oscillations of nanoscale Au traingles and pyramids: influcence of size and substrate. In: *New Journal of Physics* 9 (2007), S. 376

[136] Huang, W. ; Qian, W. ; El Sayed, M. A.: The Optically Detected Coherent Lattice Oscillations in Silver and Gold Monolayer Periodic Nanoprism Arrays: The Effect of Interparticle Coupling. In: *The Journal of Physical Chemistry B* 109 (2005), Nr. 40, 18881-18888. – doi: 10.1021/jp0526647

[137] Zijlstra, E. S. ; Tatarinova, L. L. ; Garcia, M. E.: Laser-induced phonon-phonon interactions in bismuth. In: *Physical Review B* 74 (2006), Nr. 22, 220301

[138] Dekorsy, T. ; Auer, H. ; Waschke, C. ; Bakker, H. J. ; Roskos, H. G. ; Kurz, H. ; Wagner, V. ; Grosse, P.: Emission of Submillimeter Electromagnetic Waves by Coherent Phonons. In: *Physical Review Letters* 74 (1995), Nr. 5, 738

[139] Shen, Y. C. ; Upadhya, P. C. ; Linfield, E. H. ; Beere, H. E. ; Davies, A. G.: Terahertz generation from coherent optical phonons in a biased GaAs photoconductive emitter. In: *Physical Review B* 69 (2004), Nr. 23, 235325

[140] Leitenstorfer, A. ; Hunsche, S. ; Shah, J. ; Nuss, M. C. ; Knox, W. H.: Femtosecond high-field transport in compound semiconductors. In: *Physical Review B* 61 (2000), Nr. 24, 16642

[141] Winnewisser, G.: Spectroscopy in the terahertz region. In: *Vibrational Spectroscopy* 8 (1995), Nr. 2, 241-253

[142] Beard, M. C. ; Turner, G. M. ; Schmuttenmaer, C. A.: Terahertz Spectroscopy. In: *The Journal of Physical Chemistry B* 106 (2002), Nr. 29, 7146-7159. – doi: 10.1021/jp020579i

[143] Roke, S.: *New ligth on hidden surfaces*, Universiteit Leiden, PhD thesis, (2004)

[144] Dhar, L. ; Rogers, J. A. ; Nelson, K. A.: Time-resolved vibrational spectroscopy in the impulsive limit. In: *Chemical Reviews* 94 (1994), Nr. 1, 157-193. – doi: 10.1021/cr00025a006

[145] Garrett, G. A. ; Albrecht, T. F. ; Whitaker, J. F. ; Merlin, R.: Coherent THz Phonons Driven by Light Pulses and the Sb Problem: What is the Mechanism? In: *Physical Review Letters* 77 (1996), Nr. 17, 3661

[146] Stevens, T. E. ; Kuhl, J. ; Merlin, R.: Coherent phonon generation and the two stimulated Raman tensors. In: *Physical Review B* 65 (2002), Nr. 14, 144304

[147] Menzel, D. ; Gomer, R.: Desorption from Metal Surfaces by Low Energy Electrons. In: *The Journal of Chemical Physics* 41 (1964), S. 3311

[148] Redhead, P. A.: Interaction of slow electrons with chemisorbed oxygen. In: *Canadian Journal of Physics* 42 (1964), Nr. 5, 886-905. – doi: 10.1139/p64-083

[149] Nisoli, M. ; De Silvestri, S. ; Cavalleri, A. ; Malvezzi, A. M. ; Stella, A. ; Lanzani, G. ; Cheyssac, P. ; Kofman, R.: Coherent acoustic oscillations in metallic nanoparticles generated with femtosecond optical pulses. In: *Physical Review B* 55 (1997), Nr. 20, S. 424

[150] Chang, Y. m.: *Study of Coherent Surface Phonons Using Time-Resolved Second-Harmonic Generation*, University of California, Riverside, PhD thesis, (1996)

[151] Cho, G. C. ; Kütt, W. ; Kurz, H.: Subpicosecond Time-Resolved Coherent-Phonon Oscillations in GaAs. In: *Physical Review Letters* 65 (1990), Nr. 6, S. 764

[152] Pfeifer, T. ; Dekorsy, T. ; Kütt, W. ; Kurz, H.: Generation Mechanism for Coherent LO Phonons in Surface-Space-Charge Fields of III-V-Compounds. In: *Apllied Physics A* 55 (1992), S. 482

[153] Eichler, J. ; Eichler, H. J.: *Laser*. 5. Springer-Verlag, 2003

[154] Diels, J. C. ; Fontaine, J. J. ; McMichael, I. C. ; Simoni, F.: Control and measurement of ultrashort pulse shapes (in amplitude and phase) with femtosecond accuracy. In: *Applied Optics* 24 (1985), Nr. 9, 1270-1282

[155] Naganuma, K. ; Mogi, K. ; Yamada, H.: Time direction determination of asymmetric ultrashort optical pulses from second-harmonic generation autocorrelation signals. In: *Applied Physics Letters* 54 (1989), Nr. 13, 1201-1202

[156] Naganuma, K. ; Mogi, K. ; Yamada, H.: General method for ultrashort light pulse chirp measurement. In: *Quantum Electronics, IEEE Journal of* 25 (1989), Nr. 6, S. 1225–1233

[157] Yang, W. ; Springer, M. ; Strohaber, J. ; Kolomenski, A. ; Schuessler, H. ; Kattawar, G. ; Sokolov, A.: Spectral phase retrieval from interferometric autocorrelation by a combination of graduated optimization and genetic algorithms. In: *Optics Express* 18 (2010), Nr. 14, 15028-15038

[158] Taft, G. ; Rundquist, A. ; Murnane, M. M. ; Christov, I. P. ; Kapteyn, H. C. ; DeLong, K. W. ; Fittinghoff, D. N. ; Krumbugel, M. A. ; Sweetser, J. N. ; Trebino, R.: Measurement of 10-fs laser pulses. In: *Selected Topics in Quantum Electronics, IEEE Journal of* 2 (1996), Nr. 3, S. 575–585

[159] Adachi, S.: GaAs, AlAs, and AlxGa1-xAs: Material parameters for use in research and device applications. In: *Journal of Applied Physics* 58 (1985), Nr. 3, R1-R29

[160] Biegelsen, D. K. ; Bringans, R. D. ; Northrup, J. E. ; Swartz, L. E.: Surface reconstructions of GaAs(100) observed by scanning tunneling microscopy. In: *Physical Review B* 41 (1990), Nr. 9, 5701

[161] Van Bommel, A. J. ; Crombeen, J. E. ; Van Oirschot, T. G. J.: Leed, aes and photoemission measurements of epitaxially grown GaAs(001), (111)A and (1[combining macron]1[combining macron]1[combining macron])B surfaces and their behaviour upon cs adsorption. In: *Surface Science* 72 (1978), Nr. 1, 95-108

[162] Drathen, P. ; Ranke, W. ; Jacobi, K.: Composition and structure of differently prepared GaAs(100) surfaces studied by LEED and AES. In: *Surface Science* 77 (1978), Nr. 1, L162-L166

[163] Mendez, M. A. ; Palomares, F. J. ; Cuberes, M. T. ; Gonzalez, M. L. ; Soria, F.: Characterization of GaAs(100) surfaces by AES and LEED. In: *Surface Science* 251-252 (1991), 145-149

[164] Armstrong, S. R. ; Hoare, R. D. ; Pemble, M. E. ; Povey, I. M. ; Stafford, A. ; Taylor, A. G. ; Joyce, B. A. ; Neave, J. H. ; Zhang, J.: Optical second harmonic generation studies of the nature of the oxide-covered and clean c(4x4) and (2x4) reconstructed GaAs(001) surfaces. In: *Surface Science Letters* 291 (1993), Nr. 3, L751-L755

[165] Biegelsen, D. K. ; Bringans, R. D. ; Northrup, J. E. ; Swartz, L.-E.: Erratum: Surface reconstructions of GaAs(100) observed by scanning tunneling microscopy. In: *Physical Review B* 42 (1990), Nr. 5, 3195

[166] Kumpf, C. ; Smilgies, D. ; Landemark, E. ; Nielsen, M. ; Feidenhansl, R. ; Bunk, O. ; Zeysing, J. H. ; Su, Y. ; Johnson, R. L. ; Cao, L. ; Zegenhagen, J. ; Fimland, B. O. ; Marks, L. D. ; Ellis, D.: Structure of metal-rich (001)

surfaces of III-V compound semiconductors. In: *Physical Review B* 64 (2001), Nr. 7, 075307

[167] Verheij, L. K. ; Freitag, M. K. ; Wiegershaus, F.: Oxygen adsorption on Ga-rich GaAs(100). In: *Surface Science* 342 (1995), Nr. 1-3, 55-62

[168] Rim, A. ; Beserman, R.: Oxidation processe in undoped GaAs and in Si-doped GaAs. In: *Journal of Applied Physics* 74 (1993), S. 897

[169] Allwood, D. A. ; Carline, R. T. ; Mason, N. J. ; Pickering, C. ; Tanner, B. K. ; Walker, P. J.: Characterization of oxide layers on GaAs substrates. In: *Thin Solid Films* 364 (2000), Nr. 1-2, 33-39

[170] Qi, J.: *Nonlinear optical spectroscopy of Gallium Arsenide interfaces*, University of Pennsylvania, PhD thesis, (1995)

[171] Demanet, C. M. ; Marais, M. A.: A multilayer model for GaAs oxides formed at room temperature in air as deduced from an XPS analysis. In: *Surface and Interface Analysis* 7 (1985), Nr. 1, 13-16

[172] Torkhov, N.: Formation of a native-oxide structure on the surface of n-GaAs under natural oxidation in air. In: *Semiconductors* 37 (2003), Nr. 10, 1177-1184

[173] Chelikowski, J. R. ; Cohen, M. L.: Gallium arsenide (GaAs), band structure. In: Madelung, O. (Hrsg.) ; Rössler, U. (Hrsg.) ; Schulz, M. (Hrsg.): *Landolt-Börnstein - Group III Condensed Matter.* 41A1b. 1976 (SpringerMaterials - The Landolt-Börnstein Database)

[174] Zumbühl, D.: *Introduction to Mesoscopic Physics and Quantum Dots.* Lecture, 2006

[175] Moench, W.: *Semiconductor surfaces and interfaces.* 3. Springer, 2001 (Springer series in surface sciences). – ISBN 9783540679028

[176] Allen, R. E. ; Dow, J. D.: Role of surface antisite defects in the formation of Schottky barriers. In: *Physical Review B* 25 (1982), Nr. 2, 1423-1426

[177] Allen, R. E. ; Sankey, O. F. ; Dow, J. D.: Theoretical interpretation of Schottky barriers and ohmic contacts. In: *Surface Science* 168 (1986), 376-385

[178] SOPRALAB: *SOPRA N&K Database*. http://www.sopra-sa.com/index2.php?goto=dl&rub=4/. (2011)

[179] Casey Jr, H. C. ; Sell, D. D. ; Wecht, K. W.: Concentration dependence of the absorption coefficient for n- and p- type GaAs between 1.3 and 1.6 eV. In: *Journal of Applied Physics* 46 (1975), S. 250

[180] Morrison, R. E.: Reflectivity and Optical Constants of Indium Arsenide, Indium Antimonide, and Gallium Arsenide. In: *Physical Review* 124 (1961), Nr. 5, 1314

[181] Haga, E. ; Kimura, H.: Free-Carrier Infrared Absorption in III-V Semiconductors IV. Inter-Conduction Band Transitions. In: *Journal of the Physical Society of Japan* 19 (1964), Nr. 9, S. 1596

[182] Qi, J. ; Yeganeh, M. S. ; Koltover, I. ; Yodh, A. G. ; Theis, W. M.: Depletion-electric-field-induced changes in second-harmonic generation from GaAs. In: *Physical Review Letters* 71 (1993), Nr. 4, 633

[183] Lee, C. H. ; Chang, R. K. ; Bloembergen, N.: Nonlinear Electroreflectance in Silicon and Silver. In: *Physical Review Letters* 18 (1967), Nr. 5, 167

[184] Bergfeld, S.: *Optische Dreiwellenspektroskopie an GaAs(001), Si(111) und Pt-Elektrolyt-Grenzflächen*, RWTH Aachen, PhD thesis, (2003)

[185] Stehlin, T. ; Feller, M. ; Guyot-Sionnest, P. ; Shen, Y. R.: Optical second-harmonic generation as a surface probe for noncentrosymmetric media. In: *Optical Letters* 13 (1988), S. 389–391

[186] Armstrong, S.: Optical second harmonic generation studies of the nature of the GaAs (100) surface in air. In: *Journal of Crystal Growth* 120 (1992), S. 94–97

[187] Krasnov, V. F. ; Prots', V. I. ; Rubenchik, A. M. ; Struts, S. G. ; Stupak, M. F.: Characteristics of second harmonic generation in GaAs plates. In: *Soviet Journal of Quantum Electronics* 20 (1990), Nr. 5, S. 532–536

[188] Yamada, C. ; Kimura, T.: Comments on "optical second harmonic generation studies of the nature of the GaAs(100) surface in air". In: *Journal of Crystal Growth* 130 (1993), Nr. 1-2, 321-322

[189] Armstrong, S. R. ; Hoare, R. D. ; Pemble, M. E. ; Povey, I. M. ; Stafford, A. ; Taylor, A. G.: Reply to comments on "optical second harmonic generation studies of the nature of the GaAs (100) surface in the air". In: *Journal of Crystal Growth* 130 (1993), Nr. 1-2, 323-324

[190] Kravetsky, I. V. ; Kulyuk, L. L.: Optical second harmonic generation as a crystalline surface symmetry probe for III-V semiconductors. In: *Surface and Interface Analysis* 22 (1994), Nr. 1-12, S. 605–608

[191] Yamada, C. ; Kimura, T.: Anisotropy in second-harmonic generation from reconstructed surfaces of GaAs. In: *Physical Review Letters* 70 (1993), Nr. 15, 2344

[192] Takebayashi, M. ; Mizutani, G. ; Ushioda, S.: Azimuthal angle dependence of optical second harmonic intensity from a vicinal GaAs(001) wafer. In: *Optics Communications* 133 (1997), Nr. 1-6, 116-122

[193] Yamada, C. ; Kimura, T.: Rotational symmetry of the surface second-harmonic generation of zinc-blende-type crystals. In: *Physical Review B* 49 (1994), Nr. 20, 14372

[194] Shah, J.: Hot electrons and phonons under high intensity photoexcitation of semiconductors. In: *Solid-State Electronics* 21 (1978), Nr. 1, 43-50

[195] Lin, W. Z. ; Fujimoto, L. G. ; Ippen, E. P. ; Logan, R. A.: Femtosecond carrier dynamics in GaAs. In: *Applied Physics Letters* 50 (1987), Nr. 3, 124-126

[196] Driel, H. M.: Influence of hot phonons on energy relaxation of high-density carriers in germanium. In: *Physical Review B* 19 (1979), Nr. 11, 5928

[197] Pötz, W. ; Kocevar, P.: Electronic power transfer in pulsed laser excitation of polar semiconductors. In: *Physical Review B* 28 (1983), Nr. 12, 7040

[198] Shank, C. V. ; Fork, R. L. ; Leheny, R. F. ; Shah, J.: Dynamics of Photoexcited GaAs Band-Edge Absorption with Subpicosecond Resolution. In: *Physical Review Letters* 42 (1979), Nr. 2, 112

[199] Dumitrica, T. ; Allen, R. E.: Femtosecond-scale response of GaAs to ultrafast laser pulses. In: *Physical Review B* 66 (2002), Nr. 8, 081202

[200] Huang, L. ; Callan, J. P. ; Glezer, E. N. ; Mazur, E.: GaAs under Intense Ultrafast Excitation: Response of the Dielectric Function. In: *Physical Review Letters* 80 (1998), Nr. 1, 185

[201] Tom, H. W. K. ; Xu, L. ; Chang, Y. m.: Observation of local-interfacial optical phonons at buried interfaces using time-resolved second-harmonic generation. In: *Physical Review B* 59 (1999), Nr. 19, S. 12220

[202] Chang, Y. m. ; Xu, L. ; Tom, H. W. K.: Coherent phonon spectroscopy of GaAs surfaces using time-resolved second-harmonic generation. In: *Chemical Physics* 251 (1999), S. 283

[203] Chang, Y. m. ; Xu, L. ; Tom, H. W. K.: Observation of Coherent Surface Optical Phonon Oscillations by Time-Resolved Surface Second-Harmonic Generation. In: *Physical Review Letters* 78 (1996), Nr. 24, S. 4649

[204] Patel, C. ; Parker, T. J. ; Jamshidi, H. ; Herman, W. F.: Gallium arsenide (GaAs), phonon dispersion, phonon frequencies and wavenumbers. In: Madelung, O. (Hrsg.) ; Rössler, U. (Hrsg.) ; Schulz, M. (Hrsg.): *Landolt-Börnstein - Group III Condensed Matter*. 41A1b. 1984 (SpringerMaterials - The Landolt-Börnstein Database)

[205] Kütt, W. ; Cho, G. C. ; Strahnen, M. ; Kurz, H.: Electro-optic sampling of surface space-charge fields on III-V compounds. In: *Applied Surface Science* 50 (1991), Nr. 1-4, 325-329

[206] Min, L. ; Miller, R. J. D.: Subpicosecond reflective electro-optic sampling of electron-hole vertical transport in surface-space-charge fields. In: *Applied Physics Letters* 56 (1990), Nr. 6, 524-526

[207] Dekorsy, T. ; Pfeifer, T. ; Kütt, W. ; Kurz, H.: Subpicosecond carrier transport in GaAs surface-space-charge fields. In: *Physical Review B* 47 (1992), Nr. 7, S. 3842

[208] Mooradian, A. ; Wright, G. B.: Observation of the interaction of plasmons with longitudinal optical phonons in GaAs. In: *Physical Review Letters* 16 (1966), Nr. 22, 999

[209] Kersting, R. ; Heyman, J. N. ; Strasser, G. ; Unterrainer, K.: Coherent plasmons in n-doped GaAs. In: *Physical Review B* 58 (1998), Nr. 8, 4553

[210] Kuznetsov, A. V. ; Stanton, C. J.: Coherent phonon oscillations in GaAs. In: *Physical Review B* 51 (1995), Nr. 12, 7555

[211] Cho, G. C. ; Bakker, H. J. ; Dekorsy, T. ; Kurz, H.: Time-resolved observation of coherent phonons by the Franz-Keldysh effect. In: *Physical Review B* 53 (1996), Nr. 11, 6904

[212] Cho, G. C. ; Dekorsy, T. ; Bakker, H. J. ; Hövel, R. ; Kurz, H.: Generation and Relaxation of Coherent Majority Plasmons. In: *Physical Review Letters* 77 (1996), Nr. 19, S. 4062

[213] Fuchs, R. ; Kliewer, K. L.: Optical Modes of Vibration in an Ionic Crystal Slab. In: *Physical Review* 140 (1965), Nr. 6A, S. 2076

[214] Tom, H. W. K. ; Chang, Y. m. ; Kwak, H.: Coherent phonon and electron spectroscopy on surfaces using time-resolved second-harmonic generation. In: *Applied Physics B* 68 (1999), S. 305

[215] Chang, Y. m. ; Chang, N. A.: Coherent longitudinal optical phonon and plasmon coupling in GaAs. In: *Applied Physics Letters* 81 (2002), Nr. 20, 3771-3773

[216] Hase, M. ; Hayashi, D. ; Lee, J. D.: Control of carrier transport in GaAs by longitudinal-optical phonon-carrier scattering using a pair of laser pump pulses. In: *Journal of Applied Physics* 109 (2011), S. 073715

[217] Chang, Y. m.: Interaction of electron and hole plasma with coherent longitudinal optical phonons in GaAs. In: *Applied Physics Letters* 80 (2002), Nr. 14, 2487-2489

[218] Watanabe, K. ; D.T., Dimitrov ; Takagi, N. ; Matsumoto, Y.: Coherent surface phonon at a GaAs(100)-c(8x2) surface. In: *Physical Review B* 65 (2002), S. 235328

[219] Boisvert, G. ; Lewis, L. J. ; Scheffler, M.: Island morphology and adatom self-diffusion on Pt(111). In: *Physical Review B* 57 (1998), Nr. 3, 1881

[220] Varga, P. ; Lundgren, E. ; Redinger, J. ; Schmid, M.: Ultrathin Films of Co on Pt(111): an STM View. In: *physica status solidi (a)* 187 (2001), Nr. 1, 97-112

[221] Sandy, A. R. ; Mochrie, S. G. J. ; Zehner, D. M. ; bel, G. ; Huang, K. G. ; Gibbs, D.: Reconstruction of the Pt(111) surface. In: *Physical Review Letters* 68 (1992), Nr. 14, 2192

[222] Ritz, G. ; Schmid, M. ; Varga, P. ; Borg, A. ; nning, M.: Pt(100) quasi-hexagonal reconstruction: A comparison between scanning tunneling microscopy data and effective medium theory simulation calculations. In: *Physical Review B* 56 (1997), Nr. 16, 10518

[223] Heinz, K. ; Barthel, A. ; Hammer, L. ; Müller, K.: Kinetics of the irreversible transition Pt(110) $1 \times 1 - - > 1 \times 2$ as observed by LEED. In: *Surface Science* 191 (1987), Nr. 1-2, 174-184

[224] Ferrer, S. ; Bonzel, H. P.: The preparation, thermal stability and adsorption characteristics of the non-reconstructed Pt(110)-1×1 surface. In: *Surface Science* 119 (1982), Nr. 2-3, 234-250

[225] Beurden, P. van: *On the surface Reconstruction of Pt-Group metals - A Theoretical Study of Adosrbate-Induced Dynamics*, Technische Universiteit Eindhoven, PhD thesis, (2003)

[226] Frank, F. C. ; Merwe, J. H. d.: One-Dimensional Dislocations. I. Static Theory. In: *Proceedings of the Royal Society of London.Series A, Mathematical and Physical Sciences* 198 (1949), Nr. 1053, 205-216

[227] Volmer, M. ; Weber, A.: Keimbildung in übersättigten Gebilden. In: *Zeitschrift für Physikalische Chemie* 119 (1926), S. 277

[228] Stranski, I. N. ; Krastanow, L.: Zur Theorie der orientierten Ausscheidung von Ionenkristallen aufeinander. In: *Monatshefte für Chemie / Chemical Monthly* 71 (1937), Nr. 1, 351-364

[229] McCaldin, J. O. ; McGill, T. C.: The semiconductor-conductor interface. In: Poate, J. M. (Hrsg.) ; Tu, K. N. (Hrsg.) ; Mayer, J. W. (Hrsg.): *Thin films - Interdiffusion and reactions.* John Wiley & Sons, 1978

[230] Sinha, A. K. ; Poate, J. M.: Metal-compund semiconductor reactions. In: Poate, J. M. (Hrsg.) ; Tu, K. N. (Hrsg.) ; Mayer, J. W. (Hrsg.): *Thin films - Interdiffusion and reactions.* John Wiley & Sons, 1978

[231] Yoder, M. N.: Ohmic contacts in GaAs. In: *Solid-State Electronics* 23 (1980), Nr. 2, 117-119

[232] Poate, J. M. (Hrsg.) ; Tu, K. N. (Hrsg.) ; Mayer, J. W. (Hrsg.): *Thin films - Interdiffusion and reactions.* John Wiley & Sons, 1978

[233] McGilp, J. F. ; McLean, A. B.: Schottky contacts to cleaved GaAs (110) surfaces. II. Thermodynamic aspects. In: *Journal of Physics C: Solid State Physics* 21 (1988), Nr. 4, 807

[234] Zhao, K. ; Wong, H. K.: Epitaxial growth of platinum thin films on various substrates by facing-target sputtering technique. In: *Journal of Crystal Growth* 256 (2003), Nr. 3-4, 283-287

[235] McIntyre, P. C. ; Maggiore, C. J. ; Nastasi, M.: Orientation selection in thin platinum films on (001) MgO. In: *Journal of Applied Physics* 77 (1995), Nr. 12, S. 6201–6204

[236] Al Shamery, K. ; Al Shemmary, A. ; Buchwald, R. ; Hoogestraat, D. ; Kampling, M. ; Nickut, P. ; Wille, A.: Elementary processes at nanoparticulate photocatalysts. In: *European Physical Journal B* 75 (2010), Nr. 1, 107-114

[237] Klimenkov, M. ; Kuhlenbeck, H. ; Nepijko, S. A.: Growth mode of Pt clusters deposited on g-Al2O3(111)/NiAl(110): a TEM study. In: *Surface Science* 539 (2003), Nr. 1-3, 31-36

[238] Bäumer, M. ; Libuda, J. ; Sandell, A. ; Freund, H. J. ; Graw, G. ; Bertrams, T. ; Neddermeyer, H.: The Growth and Properties of Pd and Pt on AI2O3/NiAI (110). In: *Berichte der Bunsengesellschaft für physikalische Chemie* 99 (1995), S. 1381–6

[239] Hsieh, L. Z. ; Yeh, D. H.: Comparative analysis of platinum diffusion parameters in GaAs and GaN semiconductors. In: *Journal of Applied Physics* 102 (2007), Nr. 2, 024507

[240] Vaisleib, A. V. ; Goldiner, M. G.: Effects of specimen size on the interstitial-substitution diffusion mechanisms in semiconductors. In: *Journal of Physics D: Applied Physics* 24 (1991), Nr. 10, 1832

[241] Chang, L. B. ; Yeh, D. H. ; Hsieh, L. Z. ; Zeng, S. H.: Enhanced modulation rate in platinum-diffused resonant-cavity light-emitting diodes. In: *Journal of Applied Physics* 98 (2005), S. 093504

[242] Yu, K. M. ; Walukiewicz, W. ; Jaklevic, J. M. ; Haller, E. E. ; Sands, T.: Effects of interface reactions on electrical characteristics of metal GaAs contacts. In: *Applied Physics Letters* 51 (1987), Nr. 3, S. 189–191

[243] Begley, D. L. ; Alexander, R. W. ; Bell, R. J. ; Goben, C. A.: Reaction at a platinum-gallium arsenide interface. In: *Surface Science* 104 (1981), Nr. 2-3, 341-353

[244] Schulz, K. ; Zheng, X. ; Lin, J. ; Chang, Y.: Morphological development during platinum/gallium arsenide interfacial reactions. In: *Journal of Electronic Materials* 19 (1990), Nr. 6, 581-589

[245] Rideout, V. L.: A review of the theory and technology for ohmic contacts to group III-V compound semiconductors. In: *Solid-State Electronics* 18 (1975), Nr. 6, 541-550

[246] Sinha, A. K. ; Smith, T. E. ; Levinstein, H. J.: Sintered ohmic contacts to n-and p-type GaAs. In: *Electron Devices, IEEE Transactions on* 22 (1975), Nr. 5, S. 218–224

[247] Palik, E. D. ; Ghosh, G.: *Handbook of Optical Constants of Solids*. Bd. Bd. 5: *Handbook of optical constants of solids*. Academic Press, 1998 `http://books.google.com/books?id=rxuG1kXvSqgC`. – ISBN 9780125444200

[248] Weaver, J. H.: Optical properties of Rh, Pd, Ir, and Pt. In: *Physical Review B* 11 (1975), Nr. 4, 1416

[249] Murata, K. ; Tanaka, H.: Surface-wetting effects on the liquid-liquid transition of a single-component molecular liquid. In: *Nature Communications* 1 (2010), 16. – 10.1038/ncomms1015

[250] Fenske, D.: *Synthese, Charakterisierung und Anwendung kolloidaler Nanopartikel in der heterogenen Katalyse - Struktur-Eigenschafts-Beziehungen*, Carl von Ossietzky Universität Oldenburg, PhD thesis, (2009)

[251] Van Hove, M. A. ; Koestner, R. J. ; Stair, P. C. ; Bibérian, J. P. ; Kesmodel, L. L. ; BartoS, I. ; Somorjai, G. A.: The surface reconstructions of the (100) crystal faces of iridium, platinum and gold: I. Experimental observations and possible structural models. In: *Surface Science* 103 (1981), Nr. 1, 189-217

[252] Brown, F. ; Parks, R. E. ; Sleeper, A. M.: Nonlinear optical reflection from a metallic boundary. In: *Physical Review Letters* 14 (1965), Nr. 25, S. 1029

[253] Grubb, S. G. ; DeSantolo, A. M. ; Hall, R. B.: Optical second-harmonic generation studies of molecular adsorption on platinum (111) and nickel (111). In: *The Journal of Physical Chemistry* 92 (1988), Nr. 6, 1419-1425. – doi: 10.1021/j100317a011

[254] Tom, H. W. K. ; Aumiller, G. D.: Observation of rotational anisotropy in the second-harmonic generation from a metal surface. In: *Physical Review B* 33 (1986), Nr. 12, 8818

[255] Lynch, M. L. ; Barner, B. J. ; Corn, R. M.: In situ second harmonic generation studies of chemisorption at well-ordered Pt(111) electrodes in perchloric acid solutions. In: *Journal of Electroanalytical Chemistry and Interfacial Electrochemistry* 300 (1991), Nr. 1-2, 447-465

[256] Lynch, M. L. ; Corn, R. M.: In situ second harmonic generation studies of the surface structure of a well-ordered platinum(111) electrode. In: *The Journal of Physical Chemistry* 94 (1990), Nr. 11, 4382-4385. – doi: 10.1021/j100374a002

[257] Lynch, M. L. ; Corn, R. M.: Surface phase transition of ordered iodine monolayers on a Pt(111) electrode as studied by normal incidence optical second harmonic generation. In: *Journal of Electroanalytical Chemistry and Interfacial Electrochemistry* 318 (1991), Nr. 1-2, 379-386

[258] McGlip, J. F. ; Yeh, Y.: Probing the buried metal-semiconductor interface by optical second harmonic generation: Au on Si(1 1 1) and Si(1 0 0). In: *Solid State Communications* 59 (1986), Nr. 2, 91-94

[259] O'Mahony, J. D. ; Kelly, P. V. ; McGilp, J. F.: Optical second harmonic generation from ordered Si(111)-Au interfaces. In: *Applied Surface Science* 56-58 (1992), Nr. Part 1, 449-452

[260] Song, K. J. ; Heskett, D. ; Dai, H. L. ; Liebsch, A. ; Plummer, E. W.: Dynamical Screening at a Metal Surface Probed by Second-Harmonic Generation. In: *Physical Review Letters* 61 (1988), Nr. 12, 1380

[261] Anisimov, S. I. ; Kapeliovich, B. L. ; Perelman, T. L.: Electron emission from metal surfaces exposed to ultrashort laser pulses. In: *Soviet Physics - JETP* 66 (1974), S. 776–781

[262] Sun, C. K. ; Vallée, F. ; Acioli, L. ; Ippen, E. P. ; Fujimoto, J. G.: Femtosecond investigation of electron thermalization in gold. In: *Physical Review B* 48 (1993), Nr. 16, 12365

[263] Groeneveld, R. H. M. ; Sprik, R. ; Lagendijk, A.: Femtosecond spectroscopy of electron-electron and electron-phonon energy relaxation in Ag and Au. In: *Physical Review B* 51 (1995), Nr. 17, 11433

[264] Lisowski, M. ; Loukakos, P. A. ; Bovensiepen, U. ; Stähler, J. ; Gahl, C. ; Wolf, M.: Ultra-fast dynamics of electron thermalization, cooling and transport effects in Ru(001). In: *Applied Physics A* 78 (2003), S. 165

[265] Garduño-Mejía, J. ; Higlett, M. P. ; Meech, S. R.: Morphology dependent ultrafast electron dynamics in ultrathin gold films. In: *Surface Science* 602 (2008), Nr. 20, 3125-3130

[266] Chang, Y. m.: Bias-dependent carrier and phonon dynamics in semiconductor–metal heterointerfaces. In: *Journal of Applied Physics* 96 (2004), Nr. 1, 928-930

[267] Hasselbrink, E. ; Wesenberg, C. ; Autzen, O.: Photochemistry on Thin Metal Films: Probe of Electron Dynamics in Metall-Semiconductor Heterosystems. In: *Physical Review Letters* 96 (2006), S. 196807

[268] Hasselbrink, E. ; Autzen, O. ; Wesenberg, C.: Photochemistry on ultrathin metal films: Strongly enhanced cross sections for NO2 on Ag/SI(100). In: *Journal of Chemical Physics* 125 (2006), S. 224707

[269] Zhdanov, V. P. ; Kasemo, B.: Substrate-mediated photoinduced chemical reactions on ultrathin metal films. In: *Surface Science* 432 (1999), Nr. 3, L599-L603

[270] Witt, G. L.: LTMBE GaAs: present status and perspectives. In: *Materials Science and Engineering: B* 22 (1993), Nr. 1, 9-15

[271] Lisiak, K. ; Milnes, A.: Platinum as a lifetime control deep impurity in silicon. In: *Journal of Applied Physics* 46 (1975), Nr. 12, 5229

[272] HÖFER, U.: Time-resolved coherent spectroscopy of surface states. In: *Applied Physics B: Lasers and Optics* 68 (1999), Nr. 3, 383-392

[273] CAO, J. ; GAO, Y. ; ELSAYED-ALI, H. E. ; MILLER, R. J. D. ; MANTELL, D. A.: Femtosecond photoemission study of ultrafast electron dynamics in single-crystal Au(111) films. In: *Physical Review B* 58 (1998), Nr. 16, 10948

[274] WATANABE, K. ; TAKAGI, N. ; MATSUMOTO, Y.: Impulsive excitation of a vibrational mode of Cs on Pt(111). In: *Chemical Physics Letters* 366 (2002), S. 606

[275] WATANABE, K. ; TAKAGI, N. ; MATSUMOTO, Y.: Femtosecond wavepacket dynamics of Cs adsorbates on Pt(111): Coverage and temperature dependences. In: *Physical Review B* 71 (2004), S. 085414

[276] HARTEN, U. ; TOENNIES, J. P. ; WÖLL, C. ; ZHANG, G.: Observation of a Kohn Anomaly in the Surface-Phonon Dispersion Curves of Pt(111). In: *Physical Review Letters* 55 (1985), Nr. 21, 2308

[277] KERN, K. ; DAVID, R. ; PALMER, R. L. ; COMSA, G. ; RAHMAN, T. S.: Surface phonon dispersion of platinum (111). In: *Physical Review B* 33 (1986), Nr. 6, 4334

[278] WATANABE, K. ; TAKAGI, N. ; MATSUMOTO, Y.: Direct Time-Domain Observation of Ultrafast Dephasing in Adsorbate-Substrate under the Influence of a Hot Electron Bath: Cs Adatoms on Pt(111). In: *Physical Review Letters* 92 (2003), Nr. 5, S. 057401

[279] MATSUMOTO, Y. ; WATANABE, K. ; TAKAGI, N.: Excitation mechanism and ultrafast vibrational wavepacket dynamics of alkali-metal atoms on Pt(1 1 1). In: *Surface Science* 593 (2005), Nr. 1-3, 110-115

[280] FUYUKI, M. ; WATANABE, K. ; MATSUMOTO, Y.: Coherent surface phonon dynamics at K-covered Pt(111) surfaces investigated by time-resolved second harmonic generation. In: *Physical Review B* 74 (2006), S. 195412

[281] WATANABE, K. ; TAKAGI, N. ; MATSUMOTO, Y.: Mode-selective excitation of coherent surface phonons on alkali-covered metal surfaces. In: *Physical Chemistry Chemical Physics* 2005 (2005), Nr. 7, S. 2697

[282] Davisson, C. ; Germer, L. H.: Diffraction of Electrons by a Crystal of Nickel. In: *Physical Review* 30 (1927), Nr. 6, 705

[283] Lagally, M. G. ; Martin, J. A.: Instrumentation for low-energy electron diffraction. In: *Review of Scientific Instruments* 54 (1983), Nr. 10, 1273-1288

[284] Hertz, H.: Ueber einen Einfluss des ultravioletten Lichtes auf die elektrische Entladung. In: *Wiedemanns Annalen der Physik und Chemie* 31 (1887), S. 983–1000

[285] Hallwachs, W.: Ueber den Einfluss des Lichtes auf electrostatisch geladene Körper. In: *Wiedemanns Annalen der Physik und Chemie* 33 (1888), S. 301–312

[286] Innes, P. D.: On the Velocity of the Cathode Particles Emitted by Various Metals under the Influence of Rontgen Rays, and Its Bearing on the Theory of Atomic Disintegration. In: *Proceedings of the Royal Society of London.Series A* 79 (1907), Nr. 532, 442-462. – 10.1098/rspa.1907.0056

[287] Rutherford, E.: The connexion between the b and g ray spectra. In: *Philosophical Magazine Series 6* 28 (1914), Nr. 165, 305-319

[288] Einstein, A.: Über einen die Erzeugung und Verwandlung des Lichtes betreffenden euristischen Gesichtspunkt. In: *Annalen der Physik und Chemie* 332 (1905), Nr. 6, S. 132–148

[289] Briggs, D. ; Seah, M. P.: *Practical Surface Analysis, Volume 1: Auger and X-Ray Photoelectron Spectroscopy*. Bd. 1. 2. Edition. John Wiley & Sons, 1990

[290] Seah, M. P. ; Dench, W. A.: Quantitative electron spectroscopy of surfaces: A standard data base for electron inelastic mean free paths in solids. In: *Surface and Interface Analysis* 1 (1979), Nr. 1, 2-11

[291] Seah, M. P. ; Gilmore, I. S.: Simplified equations for correction parameters for elastic scattering effects in AES and XPS for Q, β and attenuation lengths. In: *Surface and Interface Analysis* 31 (2001), Nr. 9, 835-846

[292] Tanuma, S. ; Powell, C. J. ; Penn, D. R.: Calculations of electorn inelastic mean free paths. II. Data for 27 elements over the 50 to 2000 eV range. In: *Surface and Interface Analysis* 17 (1991), Nr. 13, 911-926

[293] : Personal communication (2008)

[294] Fuess, H Goeppel W. ; Ziegler, C.: *Struktur der Materie: Grundlagen, Mikroskopie und Spektroskopie.* B. G. Teubner Verlagsgesellschaft, 1994

[295] Krieger, J.: *Photomultiplier Schema.* http://commons.wikimedia.org/wiki/File:Photomultiplier_schema_de.png/. (2007)

[296] Cumpson, P. J.: Angle-resolved XPS depth-profiling strategies. In: *Applied Surface Science* 144-145 (1999), 16-20

[297] Schmid, M.: *STM Schematic.* http://commons.wikimedia.org/wiki/File:ScanningTunnelingMicroscope_schematic.png. (2005)

[298] *Creative commons Lizenz: Weitergabe unter gleichen Bedingungen. (CC BY-SA 2.0 AT).* http://creativecommons.org/licenses/by-sa/2.0/at/. (2014)

[299] Binnig, G. ; Rohrer, H. ; Gerber, C. ; Weibel, E.: Surface studies by scanning tunneling microscopy. In: *Physical Review Letters* 49 (1982), Nr. 1, S. 57–61

[300] Tersoff, J. ; Hamann, D. R.: Theory of the scanning tunneling microscope. In: *Physical Review B* 31 (1985), Nr. 2, 805

[301] Wiesendanger, R.: *Scanning Probe Microscopy and Spectroscopy.* Cambridge University Press, 1994

[302] Vickerman, J. C. ; Gilmore, I. S.: *Surface Analysis - The Principal Techniques.* 2. Johny Wiley and Sons, 2009

[303] Synge, E. H.: A suggested method for extending microscopic resolution into the ultra-microscopic region. In: *Philosophical Magazine Series 7* 6 (1928), Nr. 35, 356-362

[304] Pohl, D. W. ; Denk, W. ; Lanz, M.: Optical stethoscopy: Image recording with resolution lambda/20. In: *Applied Physics Letters* 44 (1984), Nr. 7, 651-653

[305] Betzig, E. ; Trautman, J. K. ; HARRIS, T. D. ; Weiner, J. S. ; KOSTELAK, R. L.: Breaking the Diffraction Barrier: Optical Microscopy on a Nanometric Scale. In: *Science* 251 (1991), Nr. 5000, 1468-1470. – 10.1126/science.251.5000.1468

[306] Betzig, E. ; Finn, P. L. ; Weiner, J. S.: Combined shear force and near-field scanning optical microscopy. In: *Applied Physics Letters* 60 (1992), Nr. 20, 2484-2486

[307] Dunn, R. C.: Near-Field Scanning Optical Microscopy. In: *Chemical Reviews* 99 (1999), Nr. 10, 2891-2928. – doi: 10.1021/cr980130e

[308] Hitzel, F.: *Usage of reusable fiber holders for the DS45/DS95 SNOM scanners.* Danish Micro Engineering, 2005 (Application Note)

[309] De Serio, M. ; Zenobi, R. ; Deckert, V.: Looking at the nanoscale: scanning near-field optical microscopy. In: *TrAC Trends in Analytical Chemistry* 22 (2003), Nr. 2, 70-77

[310] Betzig, E. ; Trautman, J. K.: Near-Field Optics: Microscopy, Spectroscopy, and Surface Modification Beyond the Diffraction Limit. In: *Science* 257 (1992), Nr. 5067, 189-195. – 10.1126/science.257.5067.189

[311] Kaupp, G.: *Atomic Force Microscopy, Scanning Nearfield Optical Microscopy and Nanoscratching: Application to Rough and Natural Surfaces.* 1. Springer, 2006

[312] Kaupp, G. ; Herrmann, A.: Chemical contrast in scanning near-field optical microscopy. In: *Journal of Physical Organic Chemistry* 10 (1997), Nr. 9, 675-679

[313] Leist, U.: *Spektroskopische Untersuchung zur Adsorption und Photochemie von Wasser an geordneten Eisenoxid-Filmen*, Carl von Ossietzky Universität Oldenburg, Diplomarbeit, (1999)

[314] Leist, U.: *Untersuchung zur Adsorption und Photochemie von Wasser an geordneten Eisenoxid-Filmen als Modellsystem von Elementarprozessen der Atmosphärenchemie an Staubpartikeln*, Universität Oldenburg, PhD thesis, (2002)

[315] Hoogestraat, D.: *Ultrakurzpulsdynamik laserinduzierter Prozesse an Einkristalloberfläche*, Carl von Ossietzky Universität Oldenburg, Diplomarbeit, (2005)

[316] Schutzrecht (28 2008). Leist, U. ; Winkler, A. ; Carl von Ossietzky Universität Oldenburg (Erfinder). EP1411527

[317] Wille, A.: *Untersuchungen zu laserinduzieren Adsorptionsplatzänderungen im Modellkatalysatorsystem CO/Pd/Al2O3*, Carl von Ossietzky Universität Oldenburg, PhD thesis, (2003)

[318] Leist, U. ; Winkler, A. ; Büssow, J. ; Al-Shamery, K.: Mobile sample holder applying multiple heating systems with a variable heating and cooling rate. In: *Review of Scientific Instruments* 74 (2003), Nr. 11, S. 4772–4778

[319] Winkler, A.: *Untersuchung der Deposit-Substrat Wechselwirkungen und des Oxidationsverhaltens von Nanopartikeln auf einem oxidischen Träger am Beispiel der Systeme Ni/Al10O13/NiAl(110) und Ge/Al10O13/NiAl(110)*, Carl von Ossietzky Universität Oldenburg, PhD thesis, (2005)

[320] Neuendorf, S.: *Röntgenphotoelektronenspektroskopische und infrarotspektroskopische Untersuchungen an Platin-Cobalt-Oberflächenlegierungen*, Carl von Ossietzky Universität Oldenburg, PhD thesis, (2007)

[321] Greshnykh, D.: *Oberflächenspektroskopische Untersuchungen an Platin-Cobalt-Oberflächenlegierungen*, Carl von Ossietzky Universität Oldenburg, Diplomarbeit, (2005)

[322] Schnars, H.: *Abscheidung und Zersetzung von Selten-Erd-Oxid-Precursorn auf der H-terminierten Si(111)- und der SiO2-Oberfläche*, Carl von Ossietzky Universität Oldenburg, PhD thesis, (2009)

[323] Ridgway, J.W.T. ; Haneman, D.: The Diffusion of Iron and Nickel to Silicon Surfaces. In: *physica status solidi (b)* 38 (1970), Nr. 1, S. K31–K33

[324] Anderson, W. T. ; Christou, A. ; Davey, J. E.: Development ot ohmic contacts for GaAs devices using epitaxial Ge films. In: *IEEE Journal of Solid-State Circuits* 13 (1978), Nr. 4, S. 430

[325] Robinson, G. Y.: Metallurgical and electrical properties of alloyed Ni/Au—Ge films on n-type GaAs. In: *Solid-State Electronics* 18 (1975), Nr. 4, 331-338

[326] Ogawa, M.: Alloying reaction in thin nickel films deposited on GaAs. In: *Thin Solid Films* 70 (1980), Nr. 1, 181-189

[327] Maycock, P. D.: Thermal conductivity of silicon, germanium, III-V compounds and III-V alloys. In: *Solid-State Electronics* 10 (1967), Nr. 3, 161-168

[328] IRENE, E. A.: *Surfaces, Interfaces, and thin films for microelectronics.* John Wiley & Sons, 2008

[329] NÖLLER, H. G. ; POLASCHEGG, H. D. ; SCHILLALIES, H.: A step towards quantitative electron spectroscopy measurements by improved electron optics. In: *Journal of Electron Spectroscopy and Related Phenomena* 5 (1974), Nr. 1, 705-723

[330] CRIST, V.: *Handbook of Monochromatic XPS-Spectra - Semiconductors.* Bd. 3. John Wiley & Sons, 2000

[331] CRIST, V.: *Handbook of Monochromatic XPS-Spectra -The elements and native oxides.* Bd. 1. John Wiley & Sons, 2000

[332] SHIRLEY, D. A.: High-Resolution X-Ray Photoemission Spectrum of the Valence Bands of Gold. In: *Physical Review B* 5 (1972), Nr. 12, 4709

[333] WENDEROTH, M. ; GREGOR, M. J. ; ULBRICH, R. G.: Luminescence from gold-passivated gallium arsenide surfaces excited with a scanning tunneling microscope. In: *Solid State Communications* 83 (1992), Nr. 8, 535-537

[334] FEENSTRA, R. M. ; FEIN, A. P.: Surface morphology of GaAs(110) by scanning tunneling microscopy. In: *Physical Review B* 32 (1985), Nr. 2, 1394

[335] FEENSTRA, R. M.: Electronic states of metal atoms on the GaAs(110) surface studied by scanning tunneling microscopy. In: *Physical Review Letters* 63 (1989), Nr. 13, 1412

[336] ASAKI, M. T. ; HUANG, C. P. ; GARVEY, D. ; ZHOU, J. ; KAPTEYN, H. C. ; MURNANE, M. M.: Generation of 11-fs pulses from a self-mode-locked Ti: sapphire laser. In: *Optics letters* 18 (1993), Nr. 12, S. 977–979

[337] HAMAMATSU: *Photomultiplier Tubes - Basics and Application.* 1999

[338] SYSTEMS, Stanford R.: *Signal Recovery with PMTs.* 2006

[339] OAK, S. M. ; CHARI, R. ; VIJAYARAGAVAN, A. R.: Achieving high signal-to-noise ration in transient reflectivity measurements. In: *Indian Journal of Pure & Applied Physics* 44 (2005), S. 330

[340] ROSKER, M. J. ; WISE, F. W. ; TANG, C. L.: Femtosecond Relaxation Dynamics of Large Molecules. In: *Physical Review Letters* 57 (1986), Nr. 3, 321

[341] Moulder, J. F. ; Stickle, W. F. ; Sobol, P. E. ; Bomben, K. D.: *Handbook of X-ray photoelectron spectroscopy.* 2. Physical Electronics Inc., 1995

[342] Crist, V.: A Review of XPS Data-Banks. In: *XPS Reports* 1 (2007), S. 1

[343] Surdu-Bob, C. C. ; Saied, S. O. ; Sullivan, J. L.: An X-ray photoelectron spectroscopy study of the oxides of GaAs. In: *Applied Surface Science* 183 (2001), Nr. 1-2, 126-136

[344] Stoever, J.: Personal communication (2011)

[345] Crist, V.: *Binding energies and sensitivity factors data set (Mg Scofield) of Spectral Data Processor (SDP) software.* 2006

[346] Krawczyk, M. ; Jablonski, A. ; Tougaard, S. ; Toth, J. ; Varga, D. ; Gergely, G.: The inelastic mean free path and the inelastic scattering cross-section of electrons in GaAs determined from highly resolved electron energy spectra. In: *Surface Science* 402-404 (1998), Nr. 0, 491-495

[347] Tanuma, S. ; Powell, C. J. ; Penn, D. R.: Calculations of electron inelastic mean free paths (IMFPS). IV. Evaluation of calculated IMFPs and of the predictive IMFP formula TPP-2 for electron energies between 50 and 2000 eV. In: *Surface and Interface Analysis* 20 (1993), Nr. 1, 77-89

[348] Kang, M. G. ; Park, H. H.: Effect of GaAs surface treatments using HCl or $(NH_4)_2Sx$ solutions on the interfacial bonding states induced by deposition of Au. In: *Thin Solid Films* 332 (1998), Nr. 1-2, 437-443

[349] Mizokawa, Y. ; Iwasaki, H. ; Nishitani, R. ; Nakamura, S.: Esca studies of Ga, As, GaAs, Ga2O3, As2O3 and As2O5. In: *Journal of Electron Spectroscopy and Related Phenomena* 14 (1978), Nr. 2, 129-141

[350] Carli, R. ; Bianchi, C. L.: XPS analysis of gallium oxides. In: *Applied Surface Science* 74 (1994), Nr. 1, 99-102

[351] Iwakuro, H. ; Tasuyama, C. ; Ichimura, S.: XPS and AES Studies on the Oxidation of Layered Semiconductor GaSe. In: *Japanese Journal of Applied Physics* 21 (1981), 94

[352] Butt, D. P. ; Park, Y. ; Taylor, T. N.: Thermal vaporization and deposition of gallium oxide in hydrogen. In: *Journal of Nuclear Materials* 264 (1999), 71-77

[353] Rama Rao, M. V. ; Shripathi, T.: Photoelectron spectroscopic study of X-ray induced reduction of CeO2. In: *Journal of Electron Spectroscopy and Related Phenomena* 87 (1997), Nr. 2, 121-126

[354] Bekezina, T. P. ; Mokrousov, G. M.: Preparation of GaAs surfaces of desired composition. In: *Inorganic materials* 36 (2000), Nr. 9, S. 857–863

[355] Lu, Z. H. ; Bryskiewicz, B. ; McCaffrey, J. ; Wasilewski, Z. ; Graham, M. J.: Ultraviolet-ozone oxidation of GaAs(100) and InP(100). In: *Journal of Vacuum Science & Technology B: Microelectronics and Nanometer Structures* 11 (1993), Nr. 6, 2033-2037

[356] Negrila, C. C. ; Logofatu, C. ; Ghita, R. V. ; Cotirlan, C. ; Ungureanu, F. ; Manea, A. S. ; Lazarescu, M. F.: Angle-resolved XPS structural investigation of GaAs surfaces. In: *Journal of Crystal Growth* 310 (2008), 1576-1582

[357] Hinkle, C. L. ; Milojevic, M. ; Brennan, B. ; Sonnet, A. M. ; Aguirre-Tostado, F. S. ; Hughes, G. J. ; Vogel, E. M. ; Wallace, R. M.: Detection of Ga suboxides and their impact on III-V passivation and Fermi-level pinning. In: *Applied Physics Letters* 94 (2009), Nr. 16

[358] Cossu, G. ; Ingo, G. M. ; Mattogno, G. ; Padeletti, G. ; Proietti, G. M.: XPS investigation on vacuum thermal desorption of UV/ozone treated GaAs(100) surfaces. In: *Applied Surface Science* 56-58 (1992), Nr. 0, 81-88

[359] Thermo-Scientific: *Applicaton Notes*. Bd. 31014: *Angle Resolved XPS*. 2012 https://static.thermoscientific.com/images/D16069~.pdf

[360] Hill, J. M. ; Royce, D. G. ; Fadley, C. S. ; Wagner, L. F. ; Grunthaner, F. J.: Properties of oxidized silicon as determined by angular-dependent X-ray photoelectron spectroscopy. In: *Chemical Physics Letters* 44 (1976), Nr. 2, 225-231

[361] Powell, C. J. ; Jablonski, A.: *NIST Electron Inelastic-Mean-Free-Path Database, SRD 71*. Version 1.2. National Institute of Standards and Technology, 2010

[362] Guillen-Cervantes, A. ; Rivera-Alvarez, Z. ; Lopez-Lopez, M. ; Lopez-Luna, E. ; Hernandez-Calderon, I.: GaAs surface oxide desorption by annealing in ultra high vacuum. In: *Thin Solid Films* 373 (2000), Nr. 1-2, 159-163

[363] SpringThorpe, A. ; Ingrey, S. J. ; Emmerstorfer, B. ; Mandeville, P. ; Moore, W. T.: Measurement of GaAs surface oxide desorption temperatures. In: *Applied Physics Letters* 50 (1987), Nr. 2, 77

[364] Adachi, S.: *GaAs and related materials: bulk semiconducting and superlattice propteries*. 1. World Scientific Publications, 1994

[365] Zdyb, A. ; Olchowik, J. M. ; Mucha, M.: Dependence of GaAs and Si surface energy on the misorientation angle of crystal planes. In: *Materials Science - Poland* 24 (2006), S. 1109–1114

[366] Dablemont, C. A. ; Lang, P. ; Mangeney, C. ; Piquemal, J. Y. ; Petkov, V. ; Herbst, F. ; Viau, G.: FTIR and XPS Study of Pt Nanoparticle Functionalization and Interaction with Alumina. In: *Langmuir* 24 (2008), Nr. 11, 5832-5841. – doi: 10.1021/la7028643

[367] Wagner, C. D. ; Naumkin, A. V. ; Kraut-Vass, A. ; Allison, J. W. ; Powell, C. J. ; Rumble, J. R.: *NIST X-ray Photolectron Spectroscopy Database*. `http://srdata.nist.gov/xps/`. (2013), Last checked: 2013

[368] Lide, D. R.: *CRC Handbook of Chemistry and Physics: A ready-reference book of chemical and physical data*. 90. edition. CRC Taylor & Francis, 2009

[369] Allred, A. L. ; Rochow, E. G.: A scale of electronegativity based on electrostatic force. In: *Journal of Inorganic and Nuclear Chemistry* 5 (1958), Nr. 4, 264-268

[370] Godbey, D. J. ; Somorjai, G. A.: The preparation and characterization of rhenium modified Pt(111) and Pt(100), and platinum modified Re(0001) single crystal surfaces. In: *Surface Science* 202 (1988), 204-226

[371] Kim, Y. K. ; Baugh, D. A. ; Shuh, D. K. ; Stanley Williams, R. ; Sadwick, L. P. ; Wang, K. L.: Structural and chemical stability of thin films of Pt-Ga intermetallic compounds of GaAs(001). In: *Journal of Materials Research* 5 (1990), Nr. 10, S. 2139–2151

[372] Kuroda, T. ; Iwakuro, H.: X-ray photoelectron spectroscopy of Si/Pt and Pt/Si layers on GaAs. In: *Journal of Applied Physics* 66 (1989), Nr. 3, 1486-1488

[373] Iwakuro, H. ; Kuroda, T.: X-Ray Photoelectron Spectroscopy of Pt/GaAs Interfacial Reactions. In: *Japanese Journal of Applied Physics* 28 (1988), Nr. Part 1, No. 2, S. 223

[374] Cumpson, P. J.: The Thickogram: a method for easy film thickness measurement in XPS. In: *Surface and Interface Analysis* 29 (2000), Nr. 6, 403-406

[375] Cumpson, P. J. ; Seah, M. P.: Elastic Scattering Corrections in AES and XPS. II. Estimating Attenuation Lengths and Conditions Required for their Valid Use in Overlayer/Substrate Experiments. In: *Surface and Interface Analysis* 25 (1997), Nr. 6, 430-446

[376] Kozhevnikov, V. F. ; Diwekar, M. ; Kamaev, V. P. ; Shi, J. ; Vardeny, Z. V.: Fabrication and properties of gallium metallic photonic crystals. In: *Physica B: Condensed Matter* 338 (2003), 159-164

[377] Ordal, M. A. ; Bell, R. J. ; Alexander, J. ; Long, L. L. ; Querry, M. R.: Optical properties of fourteen metals in the infrared and far infrared: Al, Co, Cu, Au, Fe, Pb, Mo, Ni, Pd, Pt, Ag, Ti, V, and W. In: *Applied Optics* 24 (1985), Nr. 24, 4493-4499

[378] Blaber, M. G. ; Arnold, M. D. ; Ford, M. J.: A review of the optical properties of alloys and intermetallics for plasmonics. In: *Journal of Physics: Condensed Matter* 22 (2010), Nr. 14, 143201

[379] Riedel, A.: *Anorganische Chemie.* 4. edition. de Gruyter, 1999

[380] Glembocki, O. J. ; Tuchman, J. A. ; Ko, K. K. ; Pang, S. W. ; Giordana, A. ; Kaplan, R. ; Stutz, C. E.: Effects of electron cyclotron resonance etching on the ambient (100) GaAs surface. In: *Applied Physics Letters* 66 (1995), Nr. 22, 3054-3055

[381] Lueth, Hans: *Solid Surfaces, Interfaces and Thin Films.* 5th edition. Springer, 2010 (Graduate Texts in Physics)

[382] Wolfe, C. M. ; Holonyak, N. ; Stillmann, G. E.: *Physical properties of semiconductors.* 1. edition. Prentice-Hall International, 1989 (Prentice Hall Series in Solid State Physical Electronics)

[383] Zhou, X. ; Hsiang, T. Y. ; Miller, R. J. D.: Monte Carlo study of photogenerated carrier transport in GaAs surface space-charge fields. In: *Journal of Applied Physics* 66 (1989), Nr. 7, 3066-3073

[384] Richter, L. J. ; Cavanagh, R. R.: Mechanistic studies of photoinduced reactions at semiconductor surfaces. In: *Progress in Surface Science* 39 (1992), Nr. 2, 155-226

[385] Tyagi, M. S. ; Nijs, J. F. ; Van Overstraeten, R. J.: Effect of surface recombination on the transient decay of excess carriers produced by short wavelength laser pulses. In: *Solid-State Electronics* 25 (1982), Nr. 5, 411-415

[386] Ruzicka, B. A. ; Werake, L. K. ; Samassekou, H. ; Zhao, H.: Ambipolar diffusion of photoexcited carriers in bulk GaAs. In: *Applied Physics Letters* 97 (2010), Nr. 26, 262119-3

[387] Aspnes, D. E.: Recombination at semiconductor surfaces and interfaces. In: *Surface Science* 132 (1983), Nr. 1â??3, 406-421

[388] Rastegar, B. ; Wager, J. F.: Surface recombination velocity and bulk lifetime in GaAs and InP. In: *Semiconductor Science and Technology* 1 (1986), Nr. 3, 207

[389] Harrop, P. J. ; Campbell, D. S.: Selection of thin film capacitor dielectrics. In: *Thin Solid Films* 2 (1968), Nr. 4, 273-292

[390] Nagarajan, L. ; De Souza, R. A. ; Samuelis, D. ; Valov, I. ; Borger, A. ; Janek, J. ; Becker, K. D. ; Schmidt, P. C. ; Martin, M.: A chemically driven insulator-metal transition in non-stoichiometric and amorphous gallium oxide. In: *Nature Materials* 7 (2008), Nr. 5, 391-398. – 10.1038/nmat2164

[391] Dember, H.: Über eine photoelektronische Kraft in Kupferoxydul-Kristallen. In: *Physikalische Zeitschrift* 32 (1931), S. 554

[392] Yeganeh, M. S. ; Qi, J. ; Culver, J. P. ; Yodh, A. G. ; Tamargo, M. C.: Interference in reflected second-harmonic generation from thin nonlinear films. In: *Physical Review B* 46 (1992), Nr. 3, 1603-1610

[393] Lautenschlager, P. ; Garriga, M. ; Logothetidis, S. ; Cardona, M.: Interband critical points of GaAs and their temperature dependence. In: *Physical Review B* 35 (1987), Nr. 17, 9174-9189

[394] Burns, W. K. ; Bloembergen, N.: Third-Harmonic Generation in Absorbing Media of Cubic or Isotropic Symmetry. In: *Physical Review B* 4 (1971), Nr. 10, 3437-3450

[395] Ching, W. Y. ; Huang, M. Z.: Calculation of optical excitations in cubic semiconductors. III. Third-harmonic generation. In: *Physical Review B* 47 (1993), Nr. 15, 9479-9491

[396] Bergfeld, S. ; Daum, W.: Second-Harmonic Generation in GaAs: Experiment versus Theoretical Predictions of χ_{xyz}. In: *Physical Review Letters* 90 (2003), Nr. 3, 036801

[397] Adolph, B. ; Bechstedt, F.: Ab initio second-harmonic susceptibilities of semiconductors: Generalized tetrahedron method and quasiparticle effects. In: *Physical Review B* 57 (1998), Nr. 11, 6519-6526

[398] Hughes, J. L. P. ; Sipe, J. E.: Calculation of second-order optical response in semiconductors. In: *Physical Review B* 53 (1996), Nr. 16, 10751-10763

[399] Kamp, M. ; Morsch, G. ; Graber, J. ; Lueth, H.: Te doping of GaAs using diethyl-tellurium. In: *Journal of Applied Physics* 76 (1994), Nr. 3, 1974-1976

[400] Kubota, T. ; Nakato, Y. ; Yoneda, K. ; Kobayashi, H.: Platinum-enhanced oxidation of GaAs. In: *Physical Review B* 56 (1997), Nr. 12, 7428-7434

[401] Kobayashi, H. ; Yuasa, T. ; Nakato, Y. ; Yoneda, K. ; Todokoro, Y.: Low temperature catalytic formation of Si-based metal–oxide–semiconductor structure. In: *Journal of Applied Physics* 80 (1996), Nr. 7, 4124-4128

[402] Oshima, M. ; Kawamura, T. ; Maeyama, S. ; Miyahara, T.: Combined surface analysis by synchrotron radiation photoemission spectroscopy and surface extended x-ray absorption fine structure of oxidation features of metal-deposited GaAs. In: *Journal of Vacuum Science & Technology A: Vacuum, Surfaces, and Films* 6 (1988), Nr. 3, 1451-1455

[403] Mattern-Klosson, M. ; Lueth, H.: The Schottky barrier of Sn on GaAs(110). In: *Surface Science* 162 (1985), 610-616

[404] Kolasinski, Kurt W.: Surface and Adsorbate Structure. In: *Surface Science*. John Wiley & Sons, Ltd, 2012. – ISBN 9781119941798

[405] Evans, B. L. ; Maaroof, A. I. ; Xu, S.: Nucleation and growth of platinum and nickel films on amorphous carbon substrates. In: *Journal of Applied Physics* 77 (1994), Nr. 2, 900-907

[406] Shrestha, P. ; Gu, D. ; Tran, N. ; Tapily, K. ; Baumgart, H. ; Namkoong, G.: Investigation of Volmer-Weber Growth during the Nucleation Phase of ALD Platinum Thin Films and Template Based Platinum Nanotubes. In: *ECS Transactions* 33 (2010), Nr. 2, S. 127–134

[407] Grimaldi, M. G. ; Paine, B. M. ; Nicolet, M. A. ; Sadana, D. K.: Ion implantation and low-temperature epitaxial regrowth of GaAs. In: *Journal of Applied Physics* 52 (1981), Nr. 6, 4038-4046

[408] Hudait, M. K. ; Modak, P. ; Krupanidhi, S. B.: Si incorporation and Burstein-Moss shift in n-type GaAs. In: *Materials Science and Engineering: B* 60 (1999), Nr. 1, 1-11

[409] Zhou, X. ; Wei, Q. ; Wang, L. ; Joshi, B. ; Wei, Q. ; Sun, K.: Enhanced photoluminescence from gallium arsenide semiconductor coated with Au nanoparticles. In: *Applied Physics A* 96 (2009), Nr. 3, 637-641

[410] Gfroerer, Timothy H.: Photoluminescence in Analysis of Surfaces and Interfaces. In: *Encyclopedia of Analytical Chemistry.* John Wiley & Sons, Ltd, 2006. – ISBN 9780470027318

[411] Guimaraes, F. E. G. ; Elsner, B. ; Westphalen, R. ; Spangenberg, B. ; Geelen, H. J. ; Balk, P. ; Heime, K.: LP-MOVPE growth and optical characterization of GaInP/GaAs heterostructures: interfaces, quantum wells and quantum wires. In: *Journal of Crystal Growth* 124 (1992), Nr. 1â??4, 199-206

[412] Hoogestraat, D. ; Al Shamery, K.: Application of linear prediction and singular value decomposition for the analysis of periodic oscillations in coherent excitation spectra of condensed media and solid interfaces. In: *Journal of Physics: Condensed Matter* 22 (2010), Nr. 8, S. 084015

[413] Shah, J. ; Leheny, R. F. ; Lin, C.: Dynamic Burstein shift in GaAs. In: *Solid State Communications* 18 (1976), Nr. 8, 1035-1037

[414] Holtz, P. O. ; Zhao, Q. X.: *Impurities Condined in Quantum Structures.* Springer-Verlag, 2004

[415] Saeta, P. ; Wang, J. K. ; Siegal, Y. ; Bloembergen, N. ; Mazur, E.: Ultrafast electronic disordering during femtosecond laser melting of GaAs. In: *Physical Review Letters* 67 (1991), Nr. 8, 1023-1026

[416] Ishioka, K. ; Basak, A. K. ; Petek, H.: Allowed and forbidden Raman scattering mechanisms for detection of coherent LO phonon and plasmon-coupled modes in GaAs. In: *Physical Review B* 84 (2011), Nr. 23, 235202

[417] Zhao, H. B. ; Fan, Y. ; LÃ¼pke, G. ; Hanbicki, A. T. ; Li, C. H. ; Jonker, B. T.: Detection of coherent acoustic phonons by time-resolved second-harmonic generation. In: *Physical Review B* 83 (2011), Nr. 21, 212302

[418] Misochko, O. V. ; Gu, P. ; Sakai, K.: Coherent phonons in InSb and their properties from femtosecond pump-probe experiments. In: *Physica B: Condensed Matter* 293 (2000), Nr. 1-2, 33-37

[419] Schütte, Lars: Personal communication (2014)

[420] Fadley, C. S. ; Baird, R. J. ; Siekhaus, W. ; Novakov, T. ; Bergström, S. Å. L.: Surface analysis and angular distributions in x-ray photoelectron spectroscopy. In: *Journal of Electron Spectroscopy and Related Phenomena* 4 (1974), Nr. 2, 93-137

[421] Sturge, M. D.: Optical Absorption of Gallium Arsenide between 0.6 and 2.75 eV. In: *Physical Review* 127 (1962), Nr. 3, 768

[422] Delhaès, P.: *Graphite and precursors*. Gordon & Breach, 2001 (World of carbon). `http://books.google.com/books?id=7p2pgNOWPbEC`. – ISBN 9789056992286

[423] Clawin, P.: *Ultrakurspuls-Laser unterstützte Untersuchungen an Goldnanopartikeln und deren Präparation*, Carl von Ossietzky Universität Oldenburg, Diplomarbeit, (2008)

[424] Gaarenstroom, S. W. ; Winograd, N.: Initial and final state effects in the ESCA spectra of cadmium and silver oxides. In: *The Journal of Chemical Physics* 67 (1977), Nr. 8, 3500-3506

[425] Bahl, M. K. ; Woodall, R. O. ; Watson, R. L. ; Irgolic, K. J.: Relaxation during photoemission and LMM Auger decay in arsenic and some of its compounds. In: *The Journal of Chemical Physics* 64 (1976), Nr. 3, 1210-1218

[426] *NIST X-ray Photoelectron Spectroscopy Database, Version 4.1 (National Institute of Standards and Technology, Gaithersburg).* http://srdata.nist.gov/xps/. (2012)

[427] BLYHOLDER, G.: Molecular Orbital View of Chemisorbed Carbon Monoxide. In: *The Journal of Physical Chemistry* 68 (1964), Nr. 10, 2772-2777. – doi: 10.1021/j100792a006

[428] SCURTU, R. ; IONESCU, N. I. ; LAZARESCU, M. ; LAZARESCU, V.: Surface states- and field-effects at p- and n-doped GaAs(111)A/solution interface. In: *Physical Chemistry Chemical Physics* 11 (2009), Nr. 11, 1765-1770

[429] EL ALLALI, M. ; SOERENSEN, C. B. ; VEJE, E. ; TIDEMAND-PETERSSON, P.: Experimental determination of the GaAs and $Ga_{1-x}Al_xAs$ band-gap energy dependence on temperature and aluminum mole fraction in the direct band-gap region. In: *Physical Review B* 48 (1993), Nr. 7, 4398-4404

Curriculum Vitae

Personal details

Name	Dirk Hoogestraat
Birthday, -place	29th April 1979, Emden
Nationality	German

Education

1985 - 1989	Primary school: Grundschule Bad Lauterberg
1989 - 1991	Orientierungsstufe der KGS Bad Lauterberg
1991 - 1995	Grammar school: Gymnasialzweig der KGS Bad Lauterberg
1995 - 1998	Grammar school: Oberstufe des Ernst-Moritz-Arndt Gymnasiums Herzberg

Scientific education / Professional career

09/1998 - 10/1999	Non-military service (Zivildienst) at the AOK Klinik Pfaffenberg, Bad Sachsa
10/1999 - 07/2005	Diploma study of chemistry at the Carl von Ossietzky University of Oldenburg
2000 - 2005	Member of student's representatives council (Fachschaftsrat)
05/2002	Preliminary exams (Vordiplom): • Organic Chemistry, Inorganic Chemistry, Physical Chemistry, Physics
12/2002 - 04/2004	Student assistant in the Industrial Chemistry group of Prof. Dr. Rößner

	• Development of a multimedia learning units for the learning managment system “Vernetztes Studium Chemie” (now: “Chemgapedia”)
2004	Member of the curricula panel of the Fakultät 5 (Studienkommission)
11/2004	Exams (Diplom): • Inorganic Chemistry, Physical Chemistry, Industrial Chemistry, Computer Engineering
01/2005 - 07/2005	Diploma thesis on ultrashort laser pulse induced processes on single crystal surfaces
09/2005 - 08/2011	Research assistant in the “Nanophotonik and Grenzflächenchemie” group of Prof. Dr. Al-Shamery
since 03/2009	Doctoral studies in the group of Prof. Dr. Al-Shamery

Scientific Work

Publications / Scientific work

D. Hoogestraat, K. Al-Shamery

Application of linear prediction and singular value decomposition for the analysis of periodic oscillations in coherent excitation spectra of condensed media and solid interfaces

Journal of Physics: Condensed Matter, 22, 084015 (2010)

K. Al-Shamery, A. Al-Shemmary, R. Buchwald, D. Hoogestraat, M. Kampling, P. Nickut, A. Wille

Elementary processes at nanoparticulate photocatalysts

European Physical Journal B, 75, 107 (2010)

D. Fenske, D. Greshnykh, S. Neuendorf, D. Hoogestraat, H. Borchert, K. Al-Shamery

Ligand effects observed for the adsorption of CO on Co-Pt alloys

Surface Science, 602, 2101 (2008)

D. Fenske, W.-L. Yim, S. Neuendorf, D. Hoogestraat, D. Greshnykh, H. Borchert, T. Klüner, K. Al-Shamery

Pitfalls in interpreting temperature programmed desorption spectra of alloys: The CO/CoPt puzzle

ChemPhysChem, 8, 654 (2007)

D. Hoogestraat

Ultrakurzpulsdynamik laserinduzierter Prozesse an Einkristalloberflächen

Diplomarbeit, Universität Oldenburg (2005)

Talks / Poster presentations

D. Hoogestraat, K. Al-Shamery

Real-time investigations of energy dissipation processes at interfaces between semiconductors and thin metallic films

From the witches cauldrons in materials science, Goslar, Germany (2014)

D. Hoogestraat, K. Al-Shamery

Time-resolved phonon spectroscopy at metal-semiconductor junctions

Gordon Research Conference on Surface Dynamics, Andover, New Hampshire, USA (2009)

D. Hoogestraat, K. Al-Shamery

Time-resolved phonon spectroscopy at metal-semiconductor junctions

Femto-Plasmon Day, Sønderborg, Denmark (2009)

D. Hoogestraat, K. Al-Shamery

Femtosecond spectroscopy on semiconductors and nanoparticles

International Meeting on New Materials in Interface Schience, NanoSYS/MCI Sønderborg, Denmark (2007)

W.-L. Yim, T. Klüner, D. Fenske, D. Hoogestraat, D. Greshnyk, S. Neuendorf, H Borchert, K. Al-Shamery

Effects of Composition and Atomic Arrangement in Pt-Co on the Strength of CO Chemisorption: First-Principles and Infrared Absorption Studies

Winterschool 2006: Challenges in Theoretical Materials Schience: From Structure to Dynamcis, HWK, Delmenhorst (2006)

D. Hoogestraat, E. Suslov, D. Fenske, K. Topp, J. Kehres, K. Al-Shamery

Ultrafast phonon spectroscopy at coinage metal nanoparticles

Center of Interface Science (2006)

Statement of Authorship - Selbstständigkeitserklärung

I hereby testify that the present thesis is composed by myself and is based on my own original research. No further resources beside those specified have been used to write this thesis. No part of the dissertation has been previously published. Neither the complete thesis nor parts of it have been presented to any other university in order to obtain a doctorate.

Hiermit bestätige ich, dass die vorliegende Arbeit von mir selbständig angefertigt wurde. Es wurden keine weiteren Hilfsmittel als die angegebenen verwendet. Die Dissertation wurde zu keinem Teil im Vorfeld bereits veröffentlicht. Die vorliegende schriftliche Arbeit hat weder in Teilen noch in Gänze einer anderen wissenschaftlichen Hochschule zur Begutachtung in einem anderen Promotionsverfahren vorgelegen.

Dirk Hoogestraat, Oldenburg, 12th May 2014